JP0050851

JAERI-Review
2000-024

TIARA Annual Report 1999

October 2000

Advanced Radiation Technology Center

日本原子力研究所
Japan Atomic Energy Research Institute

本レポートは，日本原子力研究所が不定期に公刊している研究報告書です。
入手の問合わせは，日本原子力研究所研究情報部研究情報課（〒319-1195　茨城県那珂郡東海村）あて，お申し越しください。なお，このほかに財団法人原子力弘済会資料センター（〒319-1195　茨城県那珂郡東海村日本原子力研究所内）で複写による実費頒布をおこなっております。

This report is issued irregularly.
Inquiries about availability of the reports should be addressed to Research Information Division, Department of Intellectual Resources, Japan Atomic Energy Research Institute, Tokai-mura, Naka-gun, Ibaraki-ken, 319-1195, Japan.

© Japan Atomic Energy Research Institute, 2000

編集兼発行　　日本原子力研究所

JAERI-Review 2000-024

TIARA Annual Report 1999

Advanced Radiation Technology Center

Takasaki Radiation Chemistry Research Establishment
Japan Atomic Energy Research Institute
Watanuki-cho, Takasaki-shi, Gunma-ken

(Received September 25, 2000)

This annual report describes research and development activities which have been performed with the JAERI TIARA (Takasaki Ion Accelerators for Advanced Radiation Application) facilities from April 1, 1999 to March 31, 2000. Summary reports of 106 papers and brief descriptions on the status of TIARA in the period are contained. A list of publications, the type of research collaborations and organization of TIARA are also given as appendices.

Keywords: JAERI TIARA, Ion Accelerators, Solid State Physics, Radiation Effects in Materials, Materials for Space, Semiconductors, Organic Materials, Inorganic Materials, Nuclear Fusion Reactor, Functional Materials, Radiation Chemistry, Radiation Biology, Nuclear Medicine, Biotechnology, Radioisotope Production, Nuclear Chemistry, Radiation Shielding, Materials Analysis, Microbeam Technology, Accelerator Technology, Safety Control

(Eds.) Masahiro SAIDOH, Akio TORAISHI, Hisayoshi ITOH, Tamikazu KUME, Shigeru TANAKA, Shoji HASHIMOTO, Atsushi TANAKA, Hiroshi NARAMOTO, Toshiaki SEKINE, Kazuo ARAKAWA, Hisashi SEKINO, Satoshi TAJIMA and Susumu TANAKA

原研イオン照射研究施設（ＴＩＡＲＡ）平成１１年度年次報告

日本原子力研究所高崎研究所
放射線高度利用センター

(2000年9月25日受理)

本年次報告は、原研イオン照射研究施設で、1999年4月1日から2000年3月31日までの間に行われた研究活動の概要をまとめたものである。１）宇宙用半導体、２）バイオテクノロジー、３）放射線化学及び有機材料、４）無機材料、５）材料解析、６）核科学およびラジオアイソトープ製造、７）マイクロビーム応用、８）加速器施設の放射線遮蔽、９）加速器技術の９部門にわたる１０６編の研究報告に加えて、施設の運転保守・利用状況、公表された文献、企業・大学等との研究協力関係、研究開発・施設運営組織を収録する。

高崎研究所：〒370-1292 群馬県高崎市綿貫町 1233
編集委員：西堂雅博、虎石昭雄、伊藤久義、久米民和、田中　茂、橋本昭司、楢本　洋、
田中　淳、関根俊明、荒川和夫、関野　寿、田島　訓、田中　進

PREFACE

This report covers research and development activities which have been conducted with TIARA (Takasaki Ion Accelerators for Advanced Radiation Application) during the period from April 1999 to March 2000, and also gives an outline of the operation of TIARA in the same period.

All accelerators in TIARA, the AVF cyclotron, the 3MV tandem accelerator, the 3MV single-ended accelerator and the 400kV ion implanter, have been operated steadily since the construction were completed in 1993, and have supplied the beam-time to the research programs as had been recognized in advance by the Program Advisory Committee. In the same time, available species and energy ranges of ions have been widened to meet requirements from users, and the quality of ion beams have been improved gradually.

In the R & D of semiconductor and electronic devices for space application, multiple bit upsets (MBUs) have been observed in highly integrated memory devices like 16 Mbit dynamic random access memories (DRAMs). The radiation resistance of newly developed solar cells, i.e., backside-junction (BJ) cells has been examined. To investigate mechanisms behind single event phenomena, a new experimental system using lasers and ion micro-beams has been designed and installed. In the development of radiation resistant silicon carbide (SiC) devices, post-oxidation annealing has been found to improve the channel mobility of SiC field effect transistors (MOSFETs) fabricated with P or N ion implantation. It has been also found that n-type electrical conduction of $CuInSe_2$ is controlled by Cl ion implantation. In the fabrication of n-type diamond, hot-and C co-implantations have been demonstrated to be quite an effective means for reducing defects introduced during implantation.

In the field of biotechnology, broad researches have been performed using the following techniques in TIARA; (1) ion-beam irradiation for mutation induction, (2) microbeam technology for resolving problems in biology, (3) positron emitting tracer imaging system (PETIS) for plant physiology, and (4) ion-beam irradiation chemistry and plant biology. Several new mutants have been produced in plants and microorganisms by taking advantage of effective DNA damage caused by ion beams. Microbeam technology has also greatly progressed. Especially, the fate mapping of silkworm by microbeams has been established to offer an essential basis for the study on embryogenesis. Whereas, nitrogen and water uptake or transportation have been intensely studied using PETIS in many plant such as pea family, rice and tomato. Also, fundamental biological knowledge about post embryonic leaf development in *Brassica napus* and apoptosis-like cell death in maize have been elucidated using ion beams.

In the field of radiation chemistry and organic materials, ion track structures in polymers have been studied by irradiation of heavy ions. Space environment durability of newly developed polymeric materials was estimated for spacecraft. The thermo-responsive ion track filters were developed to regulate the permeability of solutes. The study on crosslinking of polydimethyl-siloxane and polysilane in ion track show that the ion beam irradiation is unique and powerful technique to produce nanowires. The effect of LET on primary process was studied by ion pulse radiolysis and the effective photon counting system was constructed for the analysis in irradiated gaseous nitrogen.

In the field of nuclear fusion materials and inorganic materials, various kinds of experimental studies were carried out. Especially, in order to simulate the effects of He and H produced by 14 MeV neutron-induced transmutation reactions, dual or triple ion-beams including He^+ ions and/or H^+ ions were widely used to irradiate the candidate fusion materials (ferritic/martensitic steels, vanadium alloys, SiC/SiC composites, Al_2O_3, and copper, etc.). Effects of implanted helium and/or hydrogen atoms on physical property (thermal diffusivity) and thermo-chemical properties (He embrittlememt, hardness, high temperature strength) as well as microstructure evolution by irradiation damage were intensively investigated with the support of calculation codes, TRIM/SRIM. In the area of basic studies of radiation effects, the simple defects were introduced by electron irradiation at low temperatures or low energy light ions in order to study the nature of simple defects. The dense electronic excitation was also employed to know the track structure which is common in many cases of radiation effects in non-metals.

In the field of material analysis, the research activities can be typically classified into two areas: (1) analysis by ion or particle beams and (2) analysis by electron or positron beams. In the area (1), the spectroscopy of secondary electrons generated under ion shadowing illustrated the effectiveness on the crystallographic analysis of low Z elements at the surface. This technique is unique, and complements the standard chemical analysis such as Auger spectroscopy. The use of ion-induced neutrons is also unique to analyze the hydrogen distribution, and further efforts are expected to accumulate the basic data for materials analysis applications. In the area (2), the analysis during materials processing gives us new ideas for materials design, and the use of positron beams is getting important for vacancy-related structure which can not be performed by other technique.

In radioisotope production and nuclear chemistry, development of positron emitters has been continued for study of plant physiology. The metallic-element positron emitter Fe-52 was newly available. Using an isotope separator on-line, short-lived isotopes of light elements such as Li-8 with a half-life of 0.838 sec have been produced in the $^{12}C + {}^{12}C$ reaction, and mass-separated for experiments on materials science with a nuclear probe. The isotope separator was also used in off-line mode for a medical purpose: by implantation of Xe-133 radioactive atoms into "stents", radioactive stents to prevent restenosis after coronary angioplasty were produced.

In the in-air micro-PIXE analysis system, success of elemental distribution mapping in a single bovine aortic endothelial cell and single aerosol particle with spatial resolution of 1 μm are worthy of note. The scanning transmission ion microscopy (STIM) technique was successfully applied to make direct beam positioning to sample for in-air micro-PIXE analyses.

In the field of radiation shielding for accelerator facilities, measurements were performed to obtain the nuclear data such as the double-differential charged particle emission (n, xz) or (p, xz) cross sections for neutron or proton with medium energies, the elastic-scattering cross sections for neutron and radioactivities of residual radionuclides generated by heavy ion reaction. Measurement of absorbed dose distributions in a plastic phantom under neutron irradiation with medium energies have also been made and the results were compared with calculated ones.

In the field of ion beam engineering, the absolute beam energy and the energy width of the cyclotron were measured within 0.1% accuracy by using a movable TOF counter system. The sources of instability of cyclotron beam intensities were analyzed as the function of elapse time after switching-on the AVF cyclotron. From experimental monitoring and simulation calculation, it is clear that the cause of beam instability is correlated closely with the change of magnetic field through the temperature change of the magnet yokes and pole tips.

The reception of users, general management of the facilities, safety management of the radiation controlled areas, support on utilization of facilities, and other duties have also been practiced smoothly; a computer code system to calculate induced activity, IRAC, have been developed and practically used for the evaluation of radiation safety in irradiation experiments.

The ninth TIARA Research Review Meeting was held on June 22 and 23 2000 in Takasaki, of which subjects were reported in this issue. 14 oral and 77 poster papers, and one invited lecture were presented. 303 persons participated the meeting. In contrast with the earlier meetings, numerous results of TIARA utilization were presented, suggesting the TIARA is now becoming a fruitful facility.

We owe the progress mentioned above to advices of the Consultative Committee for the JAERI-Universities Joint Research Project, Advisory Council JAERI's Research Facilities and their subcommittees.



Masahiro Saidoh, Director
Advanced Radiation Technology Center
Takasaki Radiation Chemistry Research Establishment

Contents

1. Semiconductors for Space ····· 1
1.1 Development of Collimated Swift Heavy-ion Micro-beams for Investigation of Single Event Phenomena ····· 3
1.2 Evaluation of Single-ion Multiple-bit Upsets on Recent Commercial DRAMs ····· 5
1.3 Radiation Tolerance of the Both-side Junction Space Solar Cell ····· 8
1.4 The Development of a New Data Collection System and Chamber for Microbeam and Laser Investigations of SEU Phenomena ····· 11
1.5 Improvement of Electrical Characteristics of SiC MOSFETs by Post-oxidation Annealing of Gate Oxide ····· 14
1.6 Effect of Cl Implantation on Electrical Properties of Chalcopyrite $CuInSe_2$ Thin Films ····· 17
1.7 ESR Characterization of Diamond Implanted with High Energy Phosphorus Ions at High Temperature ····· 20

2. Biotechnology ····· 23
2.1 Differential G-value of Tyrosine Isomers in the Radiolysis of Aqueous Phenylalanine Solution by Energetic Heavy Ions ····· 25
2.2 Development of Cell Surgery Technique by Ion Beam Exposure ····· 28
2.3 Effects of $^{4}He^{2+}$ and $^{12}C^{5+}$ Ion Beams on Plant Regeneration from Protoplasts of Chrysanthemum (*Dendranthema grandiflora* Tzvelev.) ····· 31
2.4 The Examination of the Fungal Pathogen (Glomerella cingulata) Resistance of the Ion Beam Irradiated Individuals in Strawberry ····· 33
2.5 Effects of Helium Ions and Gamma Rays Irradiation of Early Globular and Torpedo Embryos on Postembryonic Leaf Development in *Brassica napus* L. ····· 35
2.6 Mutation Rate and Molecular Nature of Mutations Induced by Carbon Ions in *Arabidopsis Thaliana* ····· 38
2.7 Mutation Induction with Ion Beam Irradiation in Rose ····· 41
2.8 Mutation Breeding using Ion-beam Irradiation in Aster ····· 43
2.9 Removal of Pollutants by Mutant Strains of Microorganisms Induced by Ion-beam Irradiation — Fixation of CO_2 by Microalgae — ····· 45
2.10 Use of a Collimated Heavy Ion Microbeam for Irradiating Mammalian Cells Individually to Study the Effect of High-LET Single Ion Irradiation ····· 48
2.11 Fate Mapping of the Cellular Blastoderm Stage Egg of the Silkworm, *Bombyx mori*, by Localized Irradiation of Heavy Ion Microbeams ····· 51
2.12 Morphological Analysis of Apoptosis-like Cell Death Induced by Ion Beam Irradiation in Plant Cells ····· 54
2.13 Breeding New Shiitake (*Lentinula edodes*) Variety at High Temperature using Ion Beam Irradiation ····· 56
2.14 Analysis of a Brassinolide-insensitive Mutant from *Arabidopsis Thaliana* Irradiated with Ion Beam ····· 58
2.15 Study on Plant Responses to Environmental Pollutants ····· 61

2.16 $^{13}NO_3^-$ and $^{13}NH_4^+$ Uptake and Assimilation-sites on a Single Root of Leguminous Crops Visualized by a Positron Emitting Tracer Imaging System: A Study Relating to the Locality of *Rhizobium* Infection Site ····· 64
2.17 Effect of NH_4^+ on $^{13}NO_3^-$ Absorption and Transport in Soybean Plant ····· 67
2.18 Ammonium ($^{13}NH_4^+$) Absorption and Translocation under Various Environmental Conditions in Rice Visualized by PETIS ····· 70
2.19 Effect of Phytohormones on ^{13}N Distribution in Rice Plants Detected by PETIS Detector ····· 73
2.20 Water and Trace Element Behavior in Plant ····· 76
2.21 Uptake of ^{18}F-Water and ^{15}O-H_2O in Tomato Plants ····· 78
2.22 Fundamental Study on Radiotherapy of Tumors to Beneficial Companion Animals using Heavy Ion Beam ····· 80
2.23 Development of Pollen-mediated Gene Transfer Technique using Penetration Controlled Irradiation with Ion Beams ····· 83

3. Radiation Chemistry/Organic Materials ····· 85
3.1 Study on Space Environment Durability of Newly Developed Polymeric Materials for Spacecraft ····· 87
3.2 Permeation Control of PEG Molecules by a Thermo-responsive Ion-track Filters ····· 89
3.3 Cross-linking of Polymers in Heavy Ion Tracks ····· 91
3.4 Ion Track Structure in Polysilane Thin Films ····· 94
3.5 Primary Process of Radiation Chemistry Studied by Ion Pulse Radiolysis ····· 97
3.6 Photon Counting System for Gaseous Nitrogen Irradiated with 175-MeV Ar Ion ····· 99
3.7 Application of Thin Film Dosimeters to Measurement of Ion Beam Dose Distribution ····· 101

4. Inorganic Materials ····· 105
4.1 He Ions Implantation Effect on the Thermal Diffusivity of CVD-SiC and CVI-SiC/SiC Composite ····· 107
4.2 Effect of Transmutant Gas Atoms on Microstructure Evolution by Displacement Damage of SiC/SiC Composites for Fusion Systems ····· 110
4.3 Implantation Mode Dependence of Damage Structure Depth Profiles in Al_2O_3 Irradiated with Triple Beam of H, He and Heavy Ions ····· 113
4.4 Damage Evolution in High Energy Ion-irradiated Metals and the Interaction between Gas Atoms (H and He) and Damage Defects ····· 116
4.5 Synergistic Effects of Hydrogen and Helium on Microstructural Evolution in Vanadium Alloys by Triple Ion Beam Irradiation ····· 119
4.6 Effects of Heat Treatment and Gas Atom Production on Hardness and Microstructure of F82H Steel Irradiated by Dual/Triple Ion Beams ····· 122
4.7 Evaluation of He Embrittlement in Reduced Activation Ferritic/Martensitic Steels ····· 125
4.8 Cavity Formation in Reduced Activation Ferritic/Martensitic Steels Irradiated with Dual Ions ····· 128
4.9 Basic Study on the Mechanisms of Helium Embrittlement and Reduction of High Temperature Strength on Reduced Activation Ferritic Steel ····· 130

4.10 Research on Formation Process of Irradiation Defects for Light Water Reactor Pressure Vessel Steel ····· 133
4.11 Mechanical Characterization of Ion Implanted Layer by Microindentation Test using Different Apex Angle Indenters ····· 136
4.12 Effect of Oxygen on Characteristics of Austenitic Stainless Steels as Cladding Tube in Light Water Reactor ····· 139
4.13 Investigation of the Resonant Vibration Modes of Self Interstitial Atoms in Metals by Low Temperature Specific Heat Measurement ····· 141
4.14 Effects of Electron Irradiation on Pd-H System ····· 143
4.15 Negative Magnetoresistance of Pyrolytic Carbon and Effects of Low-Temperature Electron Irradiation ····· 144
4.16 Measurement of Defect Recovery Spectrum in Al by means of Constant Heating Method ····· 146
4.17 Stability of Dislocation Loops in α-Al_2O_3 and $MgO \cdot nAl_2O_3$ Crystals under Displacive and Ionizing Radiation ····· 148
4.18 Carrier Control of β-$FeSi_2$ by 1.2 MeV-Au^{++} Ion Implantation ····· 151
4.19 Formation Process and Stability of Radiation-induced Non-equilibrium Phase in Silicon ····· 154
4.20 Ion Irradiation Effect on Carbon-related Thin Films ····· 157
4.21 Non-equilibrium Growth of Ni+C_{60} on MgO(100) ····· 160
4.22 Epitaxial Re-Crystallization of the Ni/MgO(100) Interface ····· 162
4.23 Characterization of Steps on Annealed Sapphire Surfaces ····· 164
4.24 Development of Micro-processing Technique of Ceramics using Rare-gas Ion Beam Irradiation ····· 167
4.25 Electrical and Optical Properties of Cr Ion Implanted TiO_2 ····· 170
4.26 Lattice Defects Created in Quartz of Uranium Ores ····· 172

5. Material Analysis ····· 175
5.1 Hydrogen Distribution Features in Epitaxial Cu(111)/Nb(110) Multilayer Characterized with Ion Beam Analysis ····· 177
5.2 Structure-sensitive Electron Spectroscopy: Continuum and Auger Electron Yields Induced by Fast Ions ····· 179
5.3 Chemical Effect on X-Ray Spectra Induced by Multiple Inner-shell Ionization (III) ····· 181
5.4 Quantitative Analysis of Hydrogen in Solid Surface using Fast Neutrons Produced by Nuclear Reaction ····· 184
5.5 In-situ Observation of Formation of Graphitic Onions under Ion Implantation ····· 187
5.6 In-situ Observation of Growth Processes of Transition Metal Compound Thin Films by Ion-Implantaion ····· 190
5.7 Depth-selective Damage Analysis of C_n^+ (n=1-4) Cluster Irradiated Polycarbonate by a Variable-energy Positron Beam ····· 193
5.8 Positron Annihilation Study of Defects Produced in Pd by Ion Implantation and their Effects on Hydrogen Storage ····· 196
5.9 Magic Number Vacancy Clusters in Si by High Precision Positron Lifetime Measurements with Internal Positron Source of ^{22}Na ····· 199

6. Nuclear Science and Radioisotope Production ····· 203
6.1 Production of the Positron Emitters of Metallic Elements for Plant Physiology: ^{52}Fe ····· 205
6.2 Development of a Radioactive Endovascular Stent by Implantation of ^{133}Xe Ions (2) ····· 207
6.3 Effectiveness of ^{133}Xenon Implanted Radioactive Stent to Prevent Restenosis after Balloon Injury ····· 208
6.4 Production of Polarized Beam of Unstable Nuclei via Ion Surface Interaction at Grazing Incidence and Tilted Foils ····· 209
6.5 Internal Conversion Electron Measurements of Neutron-deficient Isotopes in Rare-earth Region with a Si (Li) Detector ····· 211
6.6 Ion-source Development for the TIARA On-line Isotope Separator ····· 213
6.7 Systematic Behavior on Mössbauer Isomer Shifts of ^{133}Cs Implanted into Transition Metals ····· 216

7. Microbeam Application ····· 219
7.1 Study on Uptake of Europium by the Mixture of Apatite and Smectite using RBS and Micro-PIXE ····· 221
7.2 Application of In-air Micro-PIXE Camera to the Metabolic Study of Cultured Single Cells ····· 224
7.3 Application of Micro-PIXE to the Analysis of Single Raindrop and Single Aerosol Particle ····· 227
7.4 Target Preparation of Tissue Slices for In-air Micro-PIXE ····· 230
7.5 Development of Atmospheric Micro-PIXE System for High-efficiency Elemental Analyses ····· 233
7.6 Analysis of Uranium in Minerals by SEM, TEM, Micro-PIXE, XPS and XAFS ····· 236
7.7 Energy Stabilization Test for TIARA 3MV Single-ended Accelerator ····· 239
7.8 Development of the Measurement Method of Fluoride Distribution in Teeth ····· 242
7.9 Development of a High-energy Microbeam Single-ion-hit Technique for Bio-medical Applications ····· 245
7.10 Radiation Damage in Si PIN Diodes Induced by Heavy Ion Microbeam Single Hits ····· 248

8. Radiation Shielding for Accelerator Facility ····· 251
8.1 Measurements of Radioactivities of Residual Radionuclides Generated by Heavy Ion Reactions below the Coulomb Barrier (II) ····· 253
8.2 Light Charged-particle Production in Proton-induced Reactions on ^{58}Ni, ^{90}Zr, ^{197}Au, and ^{209}Bi at 42 and 68 MeV ····· 256
8.3 Study of Cross Section Measurement Methods using the Self-TOF High Energy Neutron Detector ····· 259
8.4 Measurement of Absorbed Dose Distributions in a Plastic Phantom Irradiated by 40- and 65- MeV Quasi-monoenergetic Neutrons ····· 262
8.5 Charged-particle Production and Neutron Scattering Cross Sections for 55-75 MeV Neutrons ····· 265

9. Accelerator Technology ····· 269
9.1 Beam Energy Measurement by the Time-of-flight Technique ····· 271
9.2 Acceleration Test of M/Q=2 and 4 Cocktail Beams and Study of Multiturn Extraction ····· 273

9.3 Measurement of Beam Energy and Its Spread using Nuclear Reaction Resonances at the Single-ended Accelerator ····· 276
9.4 Prolongation of a Filament Lifetime using SF_6 Plasma Method ····· 279
9.5 Development of Transparent-type Beam Current Monitor ····· 280
9.6 Cooling System for Beam Stabilization of JAERI AVF Cyclotron ····· 282
9.7 Model Test of the Flat Top Cavity for the JAERI AVF Cyclotron ····· 285
9.8 Present Status of JAERI AVF Cyclotron System ····· 288
9.9 Modification of the HY Beam Scanner for JAERI AVF Cyclotron ····· 291
9.10 Improvement of the Switching Magnet Current Controller of Tandem Accelerator ····· 292
9.11 Renewal of the Computer Control System for JAERI AVF Cyclotron (II) ····· 294
9.12 Renewal of Rotary Shutter for JAERI Cyclotron System ····· 296

10. Status of TIARA 1999 ····· 299
10.1 Utilization of TIARA Facilities ····· 301
10.2 Operation of JAERI AVF Cyclotron System ····· 303
10.3 Operation of the Electrostatic Accelerators ····· 304
10.4 Radiation Control & Radioactive Waste Management in TIARA ····· 305

Appendix ····· 309
Appendix 1. List of Publication ····· 311
Appendix 2. Type of Research Collaboration ····· 323
Appendix 3. Organization and Personnel of TIARA ····· 325

This is a blank page.

1. Semiconductors for Space

1.1 Development of Collimated Swift Heavy-ion Micro-beams for Investigation of Single Event Phenomena ····· 3
H. Mori, T. Hirao, T. Ohshima, S. Onoda and H. Itoh

1.2 Evaluation of Single-ion Multiple-bit Upsets on Recent Commercial DRAMs ····· 5
N. Nemoto, H. Shindou, A. Makihara, S. Kuboyama, S. Matsuda, T. Ohshima, T. Hirao and H. Itoh

1.3 Radiation Tolerance of the Both-side Junction Space Solar Cell ····· 8
O. Anzawa, K. Aoyama, M. Imaizumi, S. Matsuda, T. Ohshima, T. Hirao, H. Itoh, M. Saito and Y. Matsumoto

1.4 The Development of a New Data Collection System and Chamber for Microbeam and Laser Investigations of SEU Phenomena ····· 11
J.S. Laird, T. Hirao, H. Mori, S. Onoda and H. Itoh

1.5 Improvement of Electrical Characteristics of SiC MOSFETs by Post-oxidation Annealing of Gate Oxide ····· 14
T. Ohshima, M. Yoshikawa and H. Itoh

1.6 Effect of Cl Implantation on Electrical Properties of Chalcopyrite $CuInSe_2$ Thin Films ····· 17
T. Tanaka, T. Ohshima, H. Itoh, A. Wakahara and A. Yoshida

1.7 ESR Characterization of Diamond Implanted with High Energy Phosphorus Ions at High Temperature ····· 20
J. Isoya, T. Ohshima and Y. Morita

This is a blank page.

1.1 Development of Collimated Swift Heavy-ion Micro-beams for Investigation of Single Event Phenomena

H. Mori*, T. Hirao, T. Ohshima, S. Onoda* and H. Itoh
*Graduate School of Engineering, Tokai University
Department of Materials Development, JAERI

1.Introduction

It is well known that single-event phenomena (SEP) occur in large-scale integrated circuits (LSIs) installed in artificial satellites. The SEP have three different modes, single-event upset (SEU), single-event latch up (SEL) and single-event burn out (SEB). They are all induced by an energetic particle passing through the sensitive area in the devices and are one of the most serious problems for operating LSIs in space. In recent LSIs such as dynamic random access memory (DRAM) and static random access memory (SRAM), the advance of process enables more integration. In order to investigate the mechanisms of the SEP in LSIs, heavy ion micro-beams are regarded as a useful tool[1-2]. To evaluate SEP for LSIs used in space environments, heavy ions with LETs greater than 20 MeV/mg/cm^2 and projected ranges longer than 40 μm in Si are required. At present, it is difficult to focus the high energy ion beams produced by cyclotron to a beam size of several micro-meters. We have been developing the technique of micro-beam formation using micro-collimators to study the mechanisms of the SEP.

2.Experimental

The heavy ion beams used in this study are 150 MeV $^{40}Ar^{8+}$ and 400 MeV $^{56}Fe^{15+}$ accelerated with an AVF cyclotron at JAERI Takasaki TIARA facilities. The beams are collimated by two sets of double slits (1 mm square) with a distance of 11.2 m between the slits. For the final collimation of the beams, a micro-collimator is used. It is made of Mo and has selectable diameter of either 100 μm or 20 μm. The angle of the micro-collimator to the incident beam direction can be adjusted to an accuracy of 0.1° so as to minimize the energy difference between the collimated and direct beams.

The collimated beams are evaluated from the energy spectra and beam profiles. The former are measured with a silicon surface barrier detector (SSD) and multi channel analyzer (MCA). The latter are measured by the SEU mapping technique using a 16Mbit DRAM[3]. This technique has a spatial resolution of 2 μm x 2μm.

3. Results and Discussion

Figure 1 shows energy spectra of a 150 MeV Ar-ion beam (a direct beam) and collimated beams formed after the micro-collimators with diameters of 100 μm and 20 μm. The energy spectrum and FWHM obtained with the 100 μm or 20 μm collimator were almost the same as those of the direct Ar-ion beam, indicating the scattered fraction was negligibly small. From the comparison of the energy spectra, the collimated 100 μm or 20 μm beams have been achieved. Figure 2 shows beam profiles of Ar-ion beams passing through the micro-collimators with diameters of 100 μm and 20 μm. As shown in Fig.2, SEU occurs within an area of 100 μmϕ or 20 μmϕ. It is also found from the beam profiles that the collimated 100 μm or 20 μm beams are achieved.

Figure 3 shows energy spectra of a 400 MeV Fe-ion beam (a direct beam) and the collimated beams after the micro-collimator with a diameter of 20 μm. As compared with the direct beam, the position of the energy spectral peak after the 20 μm collimator shifted to the low energy side by about 14 MeV, and the FWHM increased from 7.1 to 25 MeV. These results are attributable to ion scattering at the edge of the micro-collimator, which is due to insufficient adjustment of the collimator to the incident beam direction. Similar to the result obtained for 150 MeV Ar, the formation of a Fe-ion beam with 20 μm diameter is expected by careful adjustment of the collimator.

4. Summary

The energy spectra and the beam profiles obtained in our experiments demonstrate that the formation of high energy (100 MeV over) ion beams in diameter of 20μm can be achieved using the micro-collimator method. By using such high energy heavy ion micro-beams, we will investigate the mechanisms of the SEP.

References

1) T. Hirao, et al. "Effect of micro-beam induced damage on single-event current measurements", Nucl. Instrum. Methods in Phys. Res. B104, 508 (1995).

2) T. Hirao, et al. "Effect of ion position on single-event transient current", Nucl. Instrum. Methods in Phys. Res. B130, 486(1997).

3) H. Mori, et al. "Development of a Collimated Swift Heavy-ion Microbeam (III)", JAERI-Review 99-025, 3 (1999).

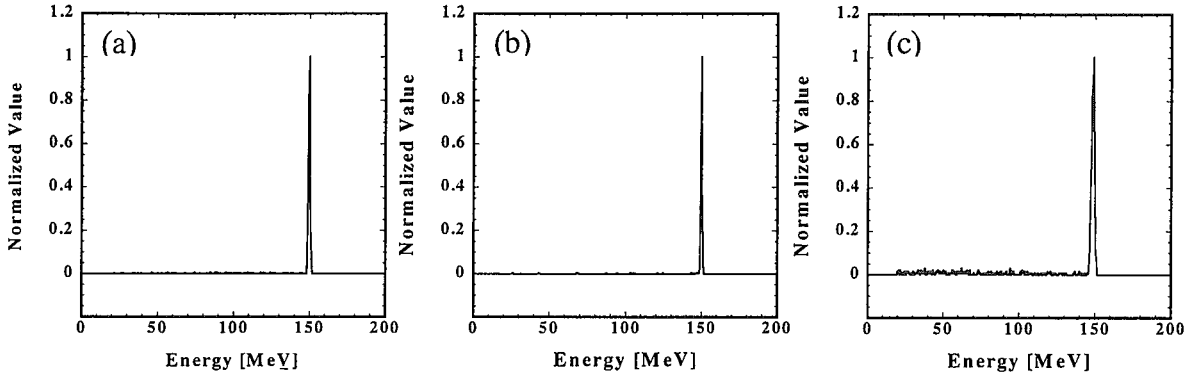


Figure 1. Energy spectra of a direct Ar-ion beam (a) and collimated Ar-ion beams after the micro-collimators with diameters of 100 μm (b) and 20 μm (c). The ordinate P/Pmax indicates the ion count normalized by the peak count.

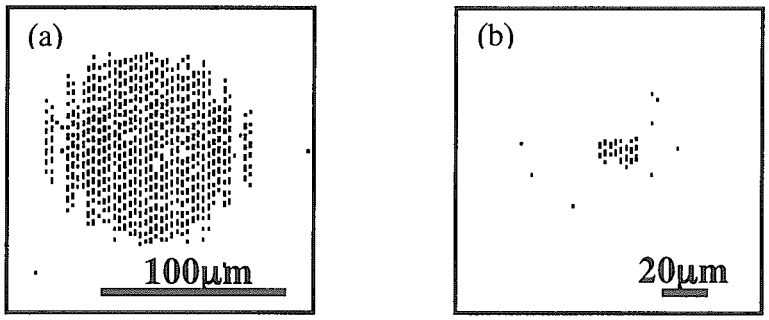


Figure 2. Beam profile of the collimated Ar-ion beams after the micro-collimators with diameters of 100 μm (a) and 20 μm (b).

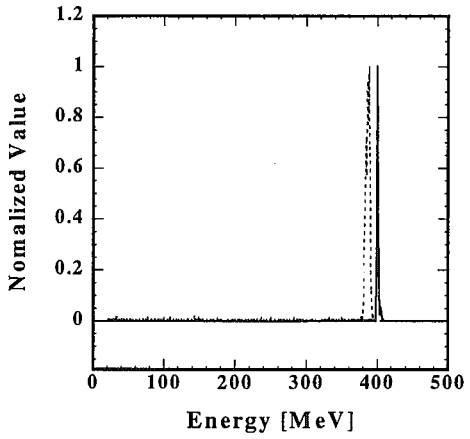


Figure 3. Energy spectra of a direct Fe-ion beam (solid line) and a collimated Fe-ion beam after the micro-collimators with a diameter of 20 μm (broken line).

1.2 Evaluation of Single-Ion Multiple-bit Upsets on Recent Commercial DRAMs

N. Nemoto, H. Shindou, A. Makihara, S. Kuboyama, S. Matsuda,
T. Ohshima*, T. Hirao*, H. Itoh*

National Space Development Agency of Japan (NASDA)
* Department of Materials Development, JAERI

1.Introduction

Semiconductor devices used in space are exposed to high energy particles such as solar protons and galactic cosmic rays. For this reason, semiconductor devices installed in spacecrafts have been designed and fabricated according to severe specifications. This fact increases the device cost and prolongs the development time of qualified devices. In recent years, reduction in the mission cost is regarded as a critical factor, and much effort has gone into reducing the cost of electronic components used in spacecrafts without diminishing their performance. On this policy, there has been a growing interest in space application of commercial devices such as highly integrated memory ICs because of their low prices and high performance.

High density DRAMs are very attractive for mass memory system such as Solid State Data Recorder (SSDR) intended for space applications. However the DRAMs are very sensitive to Single Event Upset (SEU) phenomenon caused by heavy ions and high energy protons. To prevent data errors caused by SEU, error correction circuitry is an essential element for these systems. It is well known and understood that DRAMs have several types of MBU modes other than normal single-bit upset. For effective error correction circuitry, one should know the characteristics of those MBU modes. As density of DRAMs increase, it is expected that some new types of MBU modes will be introduced. In previous work[1], SEU characteristics of 16Mbit DRAMs were evaluated in the radiation environment of space and compared with ground test data. For better interpretation of those data, additional ground testing with heavy ions was conducted on 16Mbit and 64Mbit DRAMs. Based on the results, some of the uncertainty on the previous data was clarified and several new MBU modes were identified. The mechanisms for the new upset modes were proposed based on detailed physical bit map analysis.

2.Experiment

Sample devices used for the experiments were 16Mbit and 64Mbit DRAMs manufactured by NEC. For these devices, design information summaries were published in their technical journals[2,3].

The devices were controlled by small MPU card. Specific data was written prior to irradiation and refreshed with RAS only refresh mode during irradiation. After the irradiation, stored data was readout. The refresh cycle time was programmable. Supply voltage was fixed to their minimum recommended value, because built-in internal voltage sources supply constant voltage not depending on the external voltage. The upset of memory cells are usually caused by discharging of charge stored in a cell[4]. Therefore most of the upsets are observed on cells in charged state (As described later, the upsets are also observed even if in the discharged state). To clarify the extent of disturbance caused by an incident ion, most of the experiments were conducted on the devices in which all cells were in charged or discharged state instead of all "0", all "1" or checkerboard pattern. For example the cells in the 16Mbit DRAMs that have even row addresses are charged in "1" data and discharged in "0" data, and the cells that have odd row addresses are in opposite state.

The experiments were performed with mono-energetic ions obtained from the heavy ion accelerator at Japan Atomic Energy Research Institute (JAERI) and Brookhaven National Laboratory (BNL). Ions were irradiated normal and 60° to the chip surface. The devices were rotated so that ions were incident along the word or bit lines in the case of angled irradiation.

3.Results and discussion

Figure 1 shows typical bit maps of the cells in MBU clusters caused by I, Br and Ni ions with incident angles of 0° and 60°. Apparently the patterns of the clusters correspond to the extent of charge diffusion around the ion track. The appearances are different from previous work[1] that indicates logical cell layout, because the maps are converted to the physical cell layout as shown figure 2. It should be noted that the conversion changes the appearance of the clusters to half the width and double the height. The conversion showed that most of the patterns of the clusters could be considered as a result of charge diffusion around the ion track.

Upsets of cells in discharged state were not observed in the experiments mentioned above, because of the lower fluence required to separate each MBU clusters. However the upsets were observed in the experiment in which all cells were set in discharged state. Most of the upsets were single bit. Observed MBU clusters, which is shown in figure 3, were quite different from those observed in charged state. The MBU clusters were always on a word line and ranging from 2 to 5 bits. Cells in each second column were upset, since cells in the adjacent column are connected to the adjacent word line as shown in figure 2. To confirm the hitting position of ion, the same experiments were repeated with all "0" written condition. In this case, each column is charged and discharged alternatively. Observed clusters were ranging from 6 to 10 bits for charged state and only single bit upsets were observed for discharged state, because fluence was limited to separate each clusters. Those clusters for charged state and single bit upsets for discharged states were clearly separated and never overlapped. This is evidence that the upsets of discharged state are caused by ion hitting to a part other than the cell array area. Because the access transistors are located in cell array area, the access transistor hit mechanism[4] is not the case. The unique pattern of the MBU clusters can be created only when the pre-charge or sense amplifier circuits were disturbed during refresh operation. In this experiment, observed rate of the MBU was relatively low, because of the slower refresh rate (5.2us). This MBU mode will be become more important for faster cycle times used in actual applications. The MBU mechanism may be reported for the first time.

Entire word line upsets were observed several times. Upsets were observed randomly in words that have a specific row address. The fact means that eight physical word lines were disturbed simultaneously in the DRAMs. To cause this mode of upsets, deselected word line drivers in x address decoder circuitry should be erroneously selected by an ion hit. The MBU mode will be a serious problem, because it destroys multiple bits in a word.

64Mbit DRAMs were also evaluated with the same manner mentioned above. Figure 4 shows typical MBU clusters created by several ion species with normal incidence. The observed cluster sizes were smaller than 16Mbit DRAMs. It may be caused by higher doping density of active transistors. Results were qualitatively the same as 16Mbit DRAMs with some exception. The first difference was that no entire word line upsets were observed. The second difference was found in the experiment in which all cells were set in the discharged state. The observed clusters were extended to several word lines as the clusters observed in charged cell arrays (See figure 5). However the clusters for charged and discharged cells never overlapped as in 16Mbit DRAMs. To create these types of clusters without hitting the cell array area, sticking of the sense amplifiers or another control circuit will be required. This MBU mode may also have not been reported.

4. Conclusions

As a result of this study, several MBU modes were observed and the responsible circuitry was identified. Also possible mechanisms were proposed as follows:

(1) MBUs in charged cell arrays : Caused by the diffusion of the generated charges around an incident ion track.

(2) MBUs in discharged cell arrays : Caused by an ion hit to the precharge or sense amplifier circuitry. This mode may also cause MBUs in charged cell arrays, although the rate is very low.

(3) Entire word line MBUs : Caused by an ion hit to the x decoder circuitry.

(4) Large MBUs in discharged cell arrays : Caused by an ion hit to the sense amplifier. Sticking of the sense amplifier is required for the MBU mode. Additional characterization is needed.

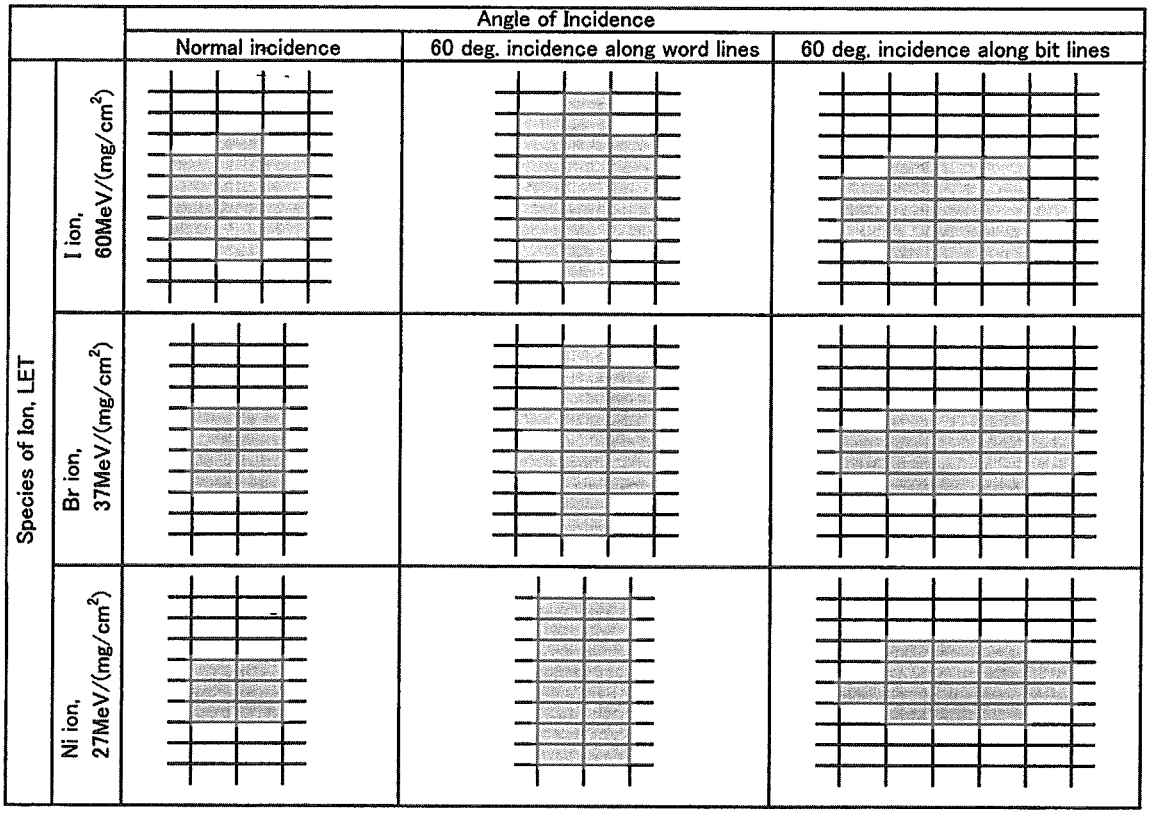


Figure 1. Typical patterns of MBU clusters in 16Mbit DRAMs created by various ions
(Each rectangular represents a cell area that has a size of 2.48x1.24μm)

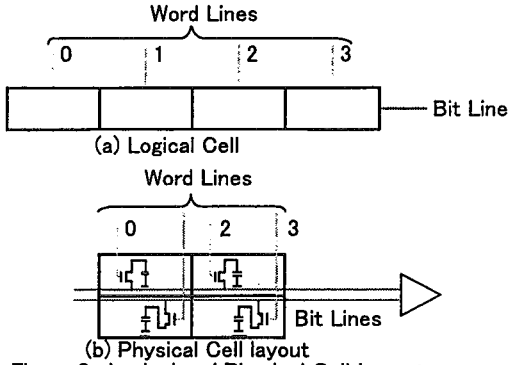
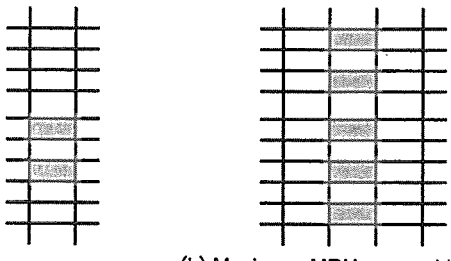
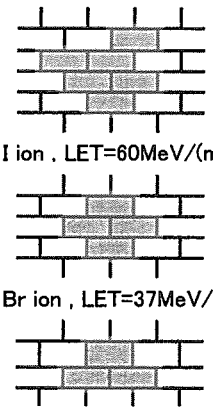


Figure 2. Logical and Physical Cell Layout



(a) Typical MBU (b) Maximum MBU created by I ion with 60 deg. incidence along word lines

Figure 3. Patterns of MBU clusters observed with a condition that all cells were set in discharged state.



(a) I ion , LET=60MeV/(mg/cm²)
(b) Br ion , LET=37MeV/(mg/cm²)
(c) Ni ion , LET=27MeV/(mg/cm²)

Figure 4. Typical patterns of MBU clusters created by several ions with normal incidence on 64Mbit
(Each rectangular represents a cell area that has a size of 1.30x0.65μm)

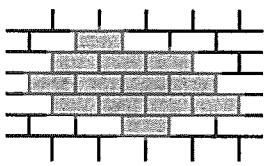


Figure 5. Pattern of a MBU cluster observed with the experiment in which all cells were set in discharged state

REFERENCES

[1] S. Buchner et al., "Investigation of Single-Ion Multiple-Bit Upsets in Memories on Board a Space Experiment," to be published in RADECS '99, (1999)
[2] S. Koshimaru et al., "2nd Generation 16Mbit DRAM," NEC Technical Journal, Vol. 46, No. 2, pp. 90-93, (1993)
[3] S. Tsukada et al., "Development of 64Mbit DRAM (3rd Generation)," NEC Technical Journal, Vol. 50, No. 3, pp. 23-27, (1997)
[4] L. W. Massengill et al., "Cosmic and Terrestrial Single-Event Radiation Effects in Dynamic Random Access Memories," IEEE Trans. Nucl. Sci., Vol. NS-43, No. 2, pp. 576-593, (1996)

1.3 Radiation Tolerance of The Both-side Junction Space Solar Cell

Osamu Anzawa, Kazuhiro Aoyama, Mitsuru Imaizumi, Sumio Matsuda, Takeshi Ohshima*, Toshio Hirao*, Hisayoshi Itoh*, Masashi Saito, Yusuke Matsumoto**
National Space Development Agency of Japan (NASDA), Department of Material Development, JAERI*, Advanced Engineering Service(AES) corporation**

1. Introduction

Degradation of silicon space solar cells by radiation occurs mainly due to the degradation of minority-carrier diffusion length. The irradiation of high energy electrons/protons causes the generation of defects in Si crystal[1]. These defects act as carrier recombination centers, resulting in a decrease of the minority-carrier diffusion length.

The structure of current Si space solar cells is shown in Fig. 1. The thickness of the silicon substrate is about 100 μ m, and a p/n junction is formed in a very shallow region of the cell. On the other hand, longer-wavelength lights generate minority-carriers in deeper region of the cell. Therefore, degrading the minority-carrier diffusion length reduces the output of a solar cell since the number of minority-carriers reaching the depletion region has been reduced.

The both-side junction (BJ) space solar cell, of which structure is shown in Fig. 2, has been developed to suppress the radiation effect[2),3)]. The backside junction improves the minority-carrier collection efficiency after the degradation.

In this study, radiation hardness of the BJ cell was examined after the irradiation of protons with a variety of energies.

2. Experiments

A number of 2×2 cm^2 BJ cells were used as samples for irradiation. The thickness of the cells was ~70 μ m. The substrate of the cells was boron-doped p-type CZ Si. A n-type layer was formed in the surface region by thermal diffusion of phosphorous. The surface was textured and covered with a SiO_2 passivation layer, and an anti-reflection (AR) coating was formed over the SiO_2 layer. In the backside region, p+-type regions for back-surface-field (BSF) and n-type regions for backside junction are alternatively formed. A SiO_2 passivation layer is formed on this side as well.

Proton irradiation with a energy of 10 MeV, 3 MeV, and 100 keV to the cells were carried out by the AVF cyclotron accelerator, the tandem accelerator, and the ion implanter, respectively, at JAERI Takasaki. After the irradiations, the cells were thermally treated at 60 °C for 24 hours.

The current-voltage (I-V) characteristics of the cells were measured under light from the AM0 solar simulator at NASDA. The temperature of the cells was kept at 28 °C during the measurement. The spectral response (SR) for the cells was measured under AM0 bias light without bias voltage. In the SR measurement, output currents under three kinds of condition were measured; I) total: current between the p-electrode and the both n-electrodes (front and back n-electrodes were connected), II) front: current between the front n-electrode and the back p-electrode, and III) back: current between the back n-electrode and the back p-electrode.

3. Results and Discussion

Figure 3 indicates the SR for the BJ cell before and after the irradiation of 100 keV protons with the fluence of 2×10^{14} cm^{-2}. Before the irradiation, the surface SR shows wide wavelength range response between 300 and

1200 nm, while the back SR shows only in the long-wavelength range (700-1200 nm). The summation of the front and the back SRs exactly corresponds to the total. After irradiation, the surface SR decreases especially in the short-wavelength range, and it is reflected on the total SR. The projection range of 100 keV proton in Si is about 1 μm so that the defects should be generated only in the surface region of the cell where short-wavelength photons are mainly absorbed. This causes severe degradation of SR in the short-wavelength range whereas it has almost no effect on SR in the long-wavelength range.

The SRs for the current cell and the BJ cell before and after the irradiation of 10 MeV protons with the fluence of 3×10^{12} cm^{-2} are exhibited in Fig. 4 and Fig. 5, respectively. The long-wavelength range SR decreases drastically for the current cell. However, it does not decrease so much for the BJ cell. This is due to the effect of the backside p/n junction which enhances collection of carriers generated in the backside region of the cell.

Comparing irradiation effect on the front and the back SRs, the response in the long-wavelength region decreases for the front SR, while the response over whole region decreases for the back one. The projection range of 10 MeV proton in Si is about 700 μm, thus defects caused by irradiation should be distributed uniformly throughout the cell. The defects degrade the minority-carrier diffusion length and cause the decrease in long-wavelength response of both of the front and the back outputs.

Figure 6 shows the remaining factor of the short circuit current (I_{SC}) for the BJ cell as a function of proton fluence with energies of 100 keV, 3 MeV, and 10 MeV. The data of the current cell with 10 MeV proton fluence is also shown in the figure. The degradation of I_{SC} by 100 keV proton is relatively small because only the SR in the short-wavelength region is decreased by the irradiation. Contrary, the degradation of I_{SC} by 3 MeV and 10 MeV protons is large, and the output of the cell becomes zero at fluences of 3×10^{13} cm^{-2} and 2×10^{14} cm^{-2}, respectively. This is caused by generation of the uniform defects in the cell. Also, 3 MeV protons generate larger number of defects than 10 MeV protons, and a larger degradation is therefore observed for the 3 MeV proton irradiation.

Note that the remaining factor of I_{SC} in the fluence region of less than 3×10^{13} cm^{-2} was effectively improved by the insertion of the backside p/n junction. The fluence of 10 MeV proton which gives 75% of the initial I_{SC} for the current and BJ cells was estimated to be 1.6×10^{12} cm^{-2} and 1.1×10^{13} cm^{-2}, respectively. This corresponds to a relative damage coefficient for the current and BJ cell of about 6.9. Thus, it is recognized that the radiation hardness was greatly improved by the BJ structure.

4. Conclusions

This study clarified that the insertion of the backside p/n junction greatly improved the radiation hardness of the Si space solar cell. Also, roles of front and back junctions were confirmed. Furthermore, dependence of energy of proton on the degradation of Si space cells were realized. These results of irradiation would be significant to estimate the power level generated from the solar cell paddle of the BJ cell.

References

1)M.Yamaguchi et al.:J.Appl.Phys.Vol86(1999), p.217-223.

2)Y.Tonomura et al.:2nd WCPEC(1998), p.3511-3514.

3)Y.Tonomura et al.:Tech.Dig.of Int.PVSE-11 (1999),p179-180.

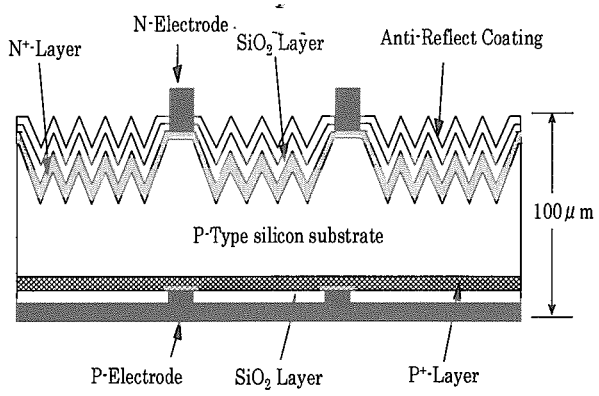


Fig.1 Schematic cross-section of conventional cell

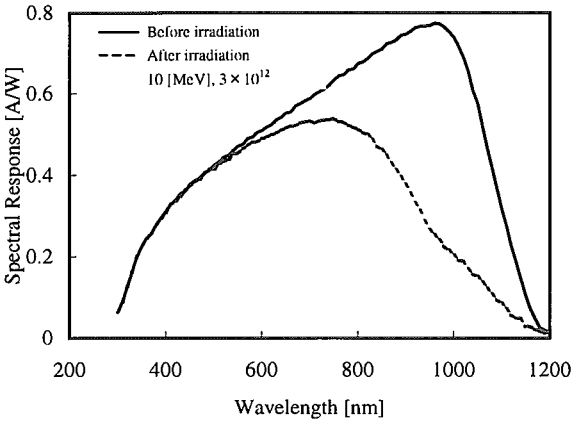


Fig.4 Spectral response of current cell before and after irradiation

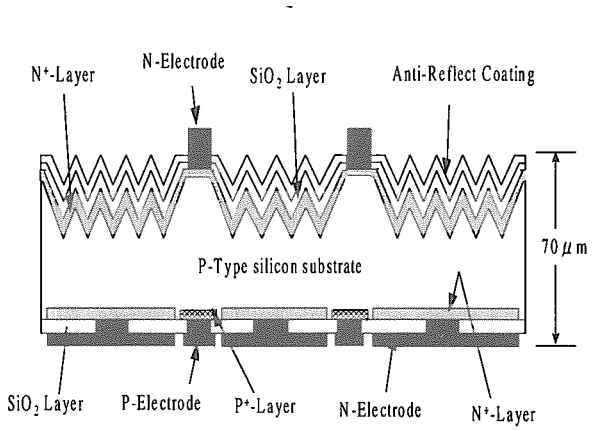


Fig.2 Schematic cross-section of BJ cell

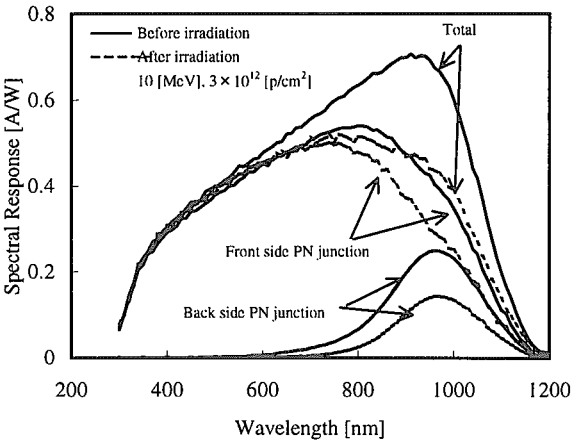


Fig.5 Spectral response of BJ cell before and after irradiation

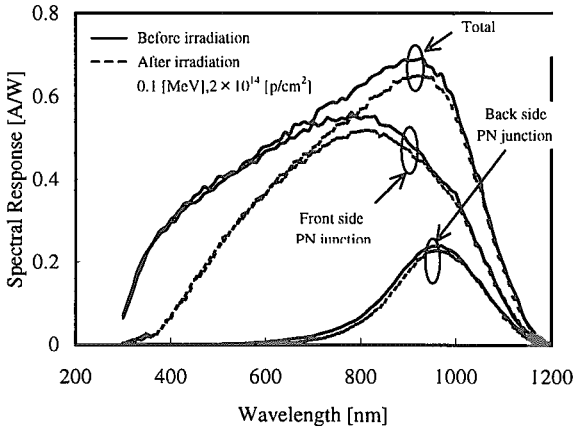


Fig.3 Spectral response of BJ cell before and after irradiation

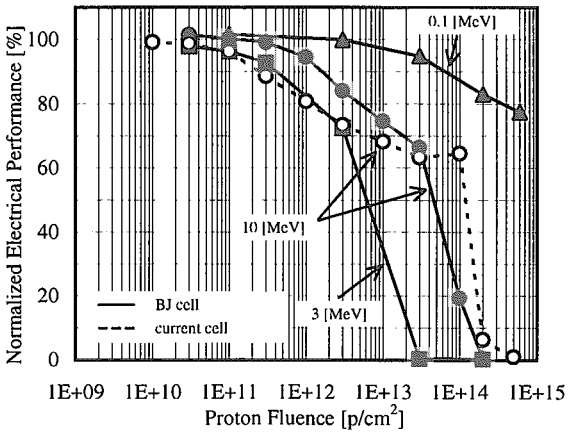


Fig.6 Degradation characteristics of Isc

1.4 The Development of a New Data Collection System and Chamber for Microbeam and Laser Investigations of SEU Phenomena

J.S.Laird, T.Hirao, H.Mori, S.Onoda and H.Itoh
Department of Materials Development, JAERI.

Introduction

In this paper we detail specifications of the new target chamber and data collection system for Laser and Ion microbeam Transient Ion (or Laser) Beam Induced Current measurements as a function of position and temperature. Transient I(L)BIC measurements are the basis of numerous techniques for quantitative analysis of semiconductor devices, a notable one being the analysis of the SEU susceptibility of a device.

A Single Event Upset (SEU) occurs when the amount of charge generated by ionizing radiation which is subsequently collected at a relevant electrode, is in excess of the critical value required to maintain the state of the cell [1]. Measuring the transient current waveform induced by heavy ions has been a useful method for investigating charge collection processes which lead to an SEU [2]. Focused lasers have also been widely applied for research into SEU phenomenon due to their ease of use and the additional timing control available to pulsed laser [3].

To date though there has been little work investigating the current transient dependence with temperature. Since charge collection is a strong function of device temperature a cryogenic target chamber, where the device temperature can be controlled between 77K and 450K, is extremely useful. The chamber will also be used for further development of the Scanning Ion Deep Level Transient Spectroscopy (SIDLTS) technqique which allows the quantitative imaging of defects within a semiconductor [4].

Design of the Target Chamber

The main function of the chamber is for ion and laser measurements as a function of several variables, the most notable being temperature. For microbeam experiments it will be attached to the end of the JAERI heavy ion microbeam. For laser analysis the chamber is a stand alone system as shown in Figure 1. In this configuration the chamber and vacuum system are mounted onto a custom deisgned optical bench. The overall design of the chamber and measurement system is given in Figure 2.

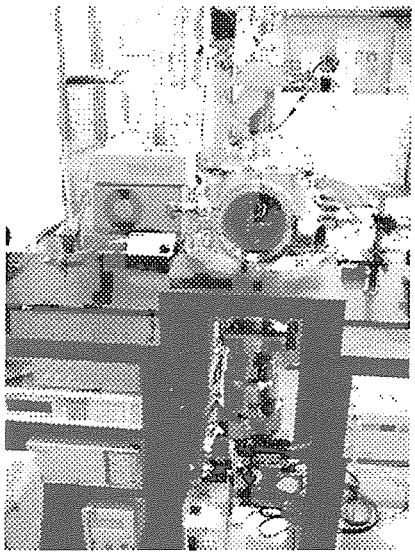


Figure 1: The new target chamber mounted on the custom designed optical bench.

The optical bench contains an assortment of components for the collimation, circularisation and detection of ultra-fast laser pulses (~50ps FWHM) from several Hamamatsu Picosecond Lasers (either 405nm or 780nm). An aspheric lens mounted in the chamber is used for final focusing. Focusing uses stage motion in the beam direction. Device cooling is provided by a constant flow liquid nitrogen (LN2) feedthrough system. A Lakeshore 340 Temperature Controller with a 50W heater and temperature sensor is used for feedback control (PID). The cryohead contains numerous connections including 2 50Ω RF feedthroughs, internal A250 amplifier supply lines, a temperature sensor and 2 LN2 lines. Since they must all move together, all connections are made through the top port of the XYZ stage. An assortment of wide bandwidth oscilloscopes allows the measurement of ultra-fast to

relatively slow charge collection processes. For example, the transient current resulting from drift within the depletion region is typically hundreds of *ps's* long, whereas the charge transient resulting from carriers detrapping from a defect can be seconds long depending on the defect. The XYZ stage and controller are fully automated for quick sample location, laser focusing and imaging (step size is 1μm).

Data Collection System

The data collection system uses the Labview software environment for easy integration of all system components. A GPIB and DAQ card are used to control all of the relevant equipment. The scanning system can perform either electrostatic scanning of the ion beam or stage scanning of the laser beam. The complete system as configured on the ion microbeam is shown in figure 3 (top). The focused ion or laser beam enters from the far right. For the ion case, beam scanning is controlled by the DAQ card in conjunction with 4 Kepco power supplies. Single event triggering (to minimize beam damage) is triggered by the GATE output of the collecting oscillospcope and a CLOCK signal from the DAQ card.

The collected transient current (or charge) can be correlated with scan position and images readily formed. Transient-IBIC data collected using the new system is presented for the case of a 50μm diameter p-n junction. Shown in figure 3 (bottom) is an image of the charge collection efficiency (CCE) of the device calculated by integrating the current transient at each position. Also shown are transients extracted from the centre and edge of the device. The current transient as a function of bias is also shown. Such data can be used for both testing theroretical models of charge collection and quantitative analysis of semiconductors.

References

[1] A.Holmes-Siedel, Handbook of Radiation Effects 1993.
[2] T.Hirao, Nucl. Inst. Meth B130 1997.
[3] A.H.Johnston, IEEE Trans. Nuc. Sci. Vol 40, 6, Dec 1993.
[4] J.S.Laird, Nucl. Ins. Meth. B158, 1999.

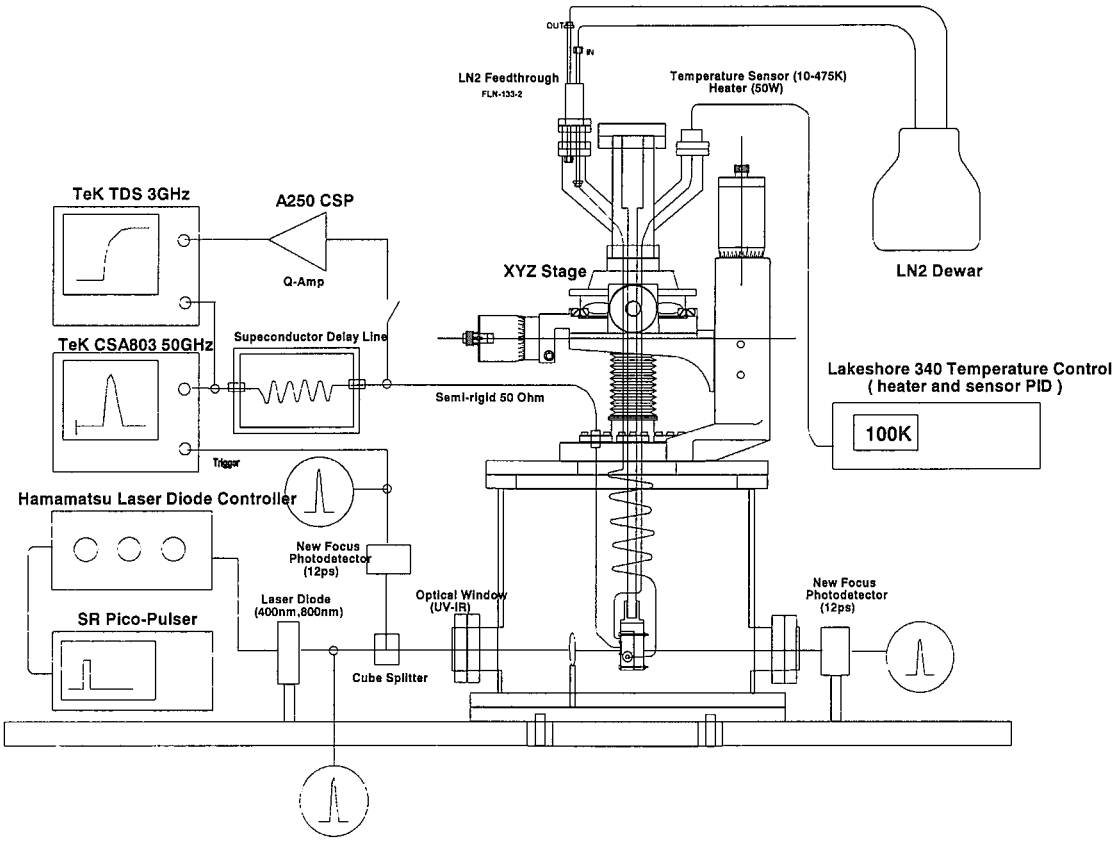


Figure 2: The complete chamber system for laser and ion microbeam experiments as a function of temperature. The temperature controller can accurately set the device to any temperature between 77K and 450K.

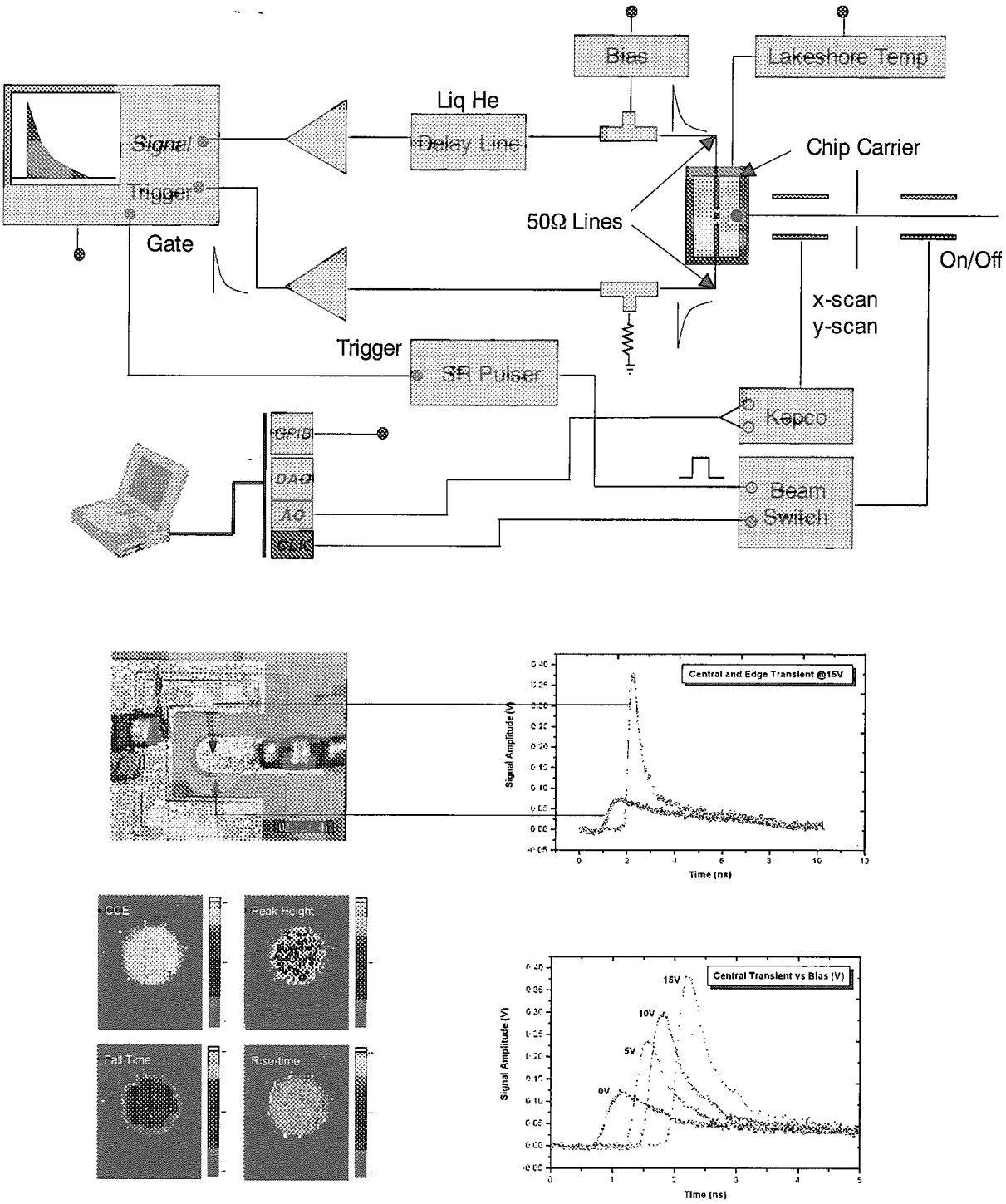


Figure 3: Top: The Transient-IBIC data collection system diagram. Bottom:Transient-IBIC results collected on a pn junction. Top left shows a photograph of the device. Images produced from the transient current data are shown in the lower left. The top right plot shows typical transients extracted from the centre and edge region of the diode. The bottom plot shows the centre transient behaviour with bias.

1.5 Improvement of Electrical Characteristics of SiC MOSFETs by Post-Oxidation Annealing of Gate Oxide

T. Ohshima, M. Yoshikawa, and H. Itoh
Department of Material Development, JAERI

1. Introduction

Silicon Carbide (SiC) is regarded as a promising candidate for high-power and high-frequency devices. SiC is also expected to be applied to electronic devices used in radiation environments such as space and nuclear reactors because of its strong radiation resistance[1]. For device production, it is important to optimize each fabrication process. Especially, oxidation technique necessary for the fabrication of metal-oxide-semiconductor (MOS) devices is one of the key techniques because interface states between gate oxide and SiC affect strongly performance of SiC MOS field effect transistors (FETs). Interface traps in SiC MOS structures have been studied using capacitance-voltage (*C-V*) measurements mainly[2-4]. Lipkin *et al.*[3] reported that *C-V* characteristics of 6H-SiC MOS structures are improved by post-oxidation annealing at 950°C in a wet oxidizing ambient. Fukuda *et al.*[4] reported that defects in the interface between SiO_2 and n-type 4H-SiC are reduced by annealing in hydrogen (H_2) at 1000 °C. However, the influence of post-oxidation annealing on channel mobility and threshold voltage in SiC MOS FETs has not yet been clarified.

In this study, we have demonstrated that the channel mobility in 6H-SiC MOSFETs is improved by post-oxidation annealing of gate oxide in steam and in H_2.

2. Experiments

The enhancement-type n-channel MOSFETs used in this study were fabricated on p-type 6H-SiC epitaxial films with a thickness of 4 μm grown on 6H-SiC substrates (3.5° off, Si-face). The source and drain were formed by phosphorus (P) or nitrogen (N) ion implantation at 800 °C and subsequent annealing at 1500 °C for 20 min in Ar atmosphere. The gate oxide was fabricated at 1100 °C for 1 hour in pyrogenic condition; H_2:O_2 =1:1. The gate length x width of the MOSFETs was 10 x 200 μm^2. Steam-annealing for the gate oxide was performed at 700 °C to 1000 °C for 30 min in the same atmosphere as the oxidation process. As for H_2 annealing, the samples were annealed at 400 °C to 900 °C for 30min in dry H_2 at a pressure of 20 Torr. The thickness of the gate oxide after annealing was determined by *C-V* measurements. The electrical characteristics of the MOSFETs were measured under the dark condition at room temperature (RT). The channel mobility was derived from drain current (I_D) -drain voltage (V_D) curves in the linear region. The threshold voltage (V_T) was determined as the value at the intersection between the gate voltage (V_G) axis and the line extrapolated from the curve of the square root of I_D versus V_G in the saturation region.

3. Results and Discussion

Figure 1 shows the steam-annealing temperature dependence of channel mobility (closed symbols) and threshold voltage (open symbols) for 6H-SiC MOSFETs. The channel mobility after annealing normalized by that before annealing (μ_{ann}/μ_0) is shown in the figure. The shift of V_T due to steam annealing (ΔV_T) is also plotted. The highest mobility of 52.2 cm^2/Vs, which is about 1.2 times as high as that before

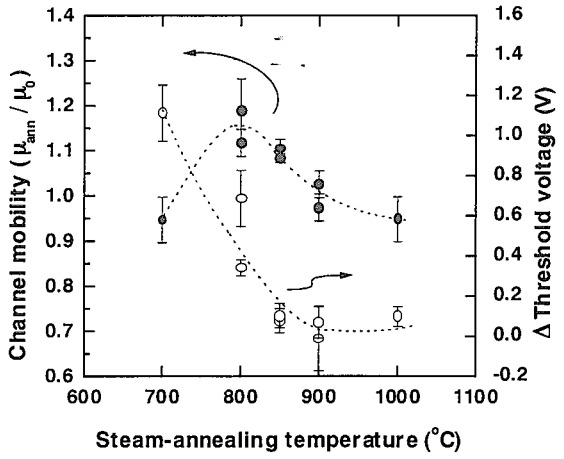


Fig. 1 Dependence of channel mobility (closed symbols) and threshold voltage (open symbols) on temperature of steam-annealing for 6H-SiC MOSFETs. The channel mobility in the MOSFET after steam annealing (μ_{ann}) normalized by that in the unannealing sample μ_{ann}/μ_0 is plotted in the figure. The shift of V_T upon the steam annealing (ΔV_T) is also plotted.

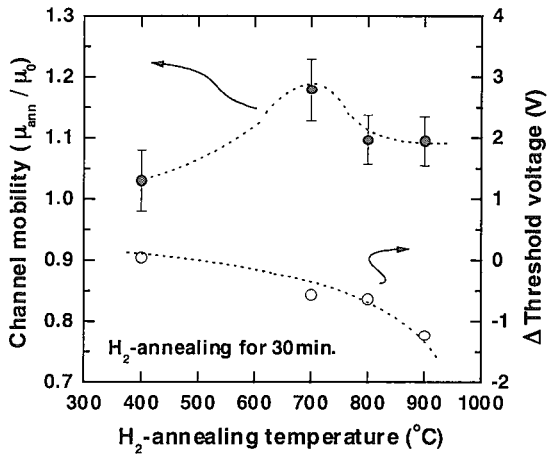


Fig. 2 Dependence of μ_{ann}/μ_0 (closed symbols) and ΔV_T (open symbols) on temperature of H_2-annealing for 6H-SiC MOSFETs.

annealing, is obtained for the samples annealed at 800 °C. No significant change in V_T is observed in an annealing temperature range between 900 and 1000 °C, and V_T increases with decreasing annealing temperature below 900 °C.

It was reported that carbon compounds, which probably degrade channel mobility, reside in oxide near the SiO_2/SiC interface after oxidation[5]. The increase of channel mobility due to the steam-annealing can be interpreted by the speculation that the number of residual carbon compounds decreases by the reactions among carbon and oxygen-related species during the annealing. The reaction rate probably increases with increasing annealing temperature. The steam annealing above 800 °C could give rise to further oxidation of SiC, which leads to the reproduction of carbon compounds. The formation of carbon compounds is enhanced when steam annealing temperature is raised. It is most likely that competition between the reduction and production of carbon compounds during steam annealing causes the annealing temperature dependence of channel mobility shown in Fig. 1.

Figure 2 shows the dependence of μ_{ann}/μ_0 (closed) and ΔV_T (open) on temperature of H_2-annealing for 6H-SiC MOSFETs. After H_2-annealing above 700 °C, the channel mobility is high compared with that in the sample fabricated without annealing. The highest mobility is obtained for the sample annealed at 700 °C. The channel mobility in this MOSFET is 51.8 cm^2/Vs, which is about 1.2 times as high as that in the one before annealing. After annealing at 400 °C, no significant change in mobility and V_T is observed. V_T shifts toward the negative voltage side with increasing annealing temperature. This shift indicates an increase of oxide-trapped positive charges and/or interface traps located near the middle region of the band gap. It is unlikely that such oxide-trapped charges and/or interface traps generated by H_2-annealing reduce channel mobility. Taking account of the fact that the shift of V_T by H_2-annealing differs from that by steam-annealing, it is most probable that mechanisms of the post-oxidation annealing

effects on the electrical characteristics of MOSFETs are different between H_2- and steam-annealings. To clarify this point, further investigations are necessary.

4. Conclusions

Enhancement-type n-channel MOSFETs with gate oxide annealed in steam or dry H_2 up to 1000 °C were fabricated on 6H-SiC. The influence of the post-oxidation annealing on channel mobility and threshold voltage was examied. The channel mobility is improved by steam-annealing as well as H_2-annealing of gate oxide. As for steam-annealing, the MOSFET whose gate oxide was annealed at 800 °C shows the highest channel mobility 52.2 cm^2/Vs, which is approximately 1.2 times as high as that in unannealed MOSFET. H_2-annealing of gate oxide above 700 °C also increases the channel mobility in MOSFETs, and the highest mobility of 51.8 cm^2/Vs is obtained in the MOSFET annealed at 700 °C. The threshold voltage is found to be affected by both post-oxidation annealings.

References

(1) H. Itoh, M. Yoshikawa, I. Nashiyama, S. Misawa, H. Okumura, S. Yoshida, In: G. L. Harris, M. G. Spencer, C. Y. Yang (Eds.), Amorphous and Crystalline Silicon Carbide III, Springer-Verlag, Berlin, (1992) 143.

(2) J. A. Cooper, Jr.: Phys. Stat. Sol. (a) **162** (1997) 305.

(3) L. A. Lipkin, D. B. Slater, Jr., J. W. Palmour: Mat. Sci. Forum **264-268** (1998) 853.

(4) K. Fukuda, K. Nagai, T. Sekigawa, S. Yoshida, K. Arai, M. Yoshikawa: Jpn. J. Appl. Phys. **38** (1999) 2306.

(5) B. Hornetz, H-J. Michel, J. Halbritter: J. Mater. Res. **9** (1994) 3008.

1.6 Effect of Cl implantation on electrical properties of chalcopyrite $CuInSe_2$ thin films

T.Tanaka[a)], T.Ohshima*, H.Itoh*, A.Wakahara, and A.Yoshida
Department of Electrical and Electronic Engineering, Toyohashi University of Technology,
*Department of Material Development, JAERI, Takasaki.

1.Introduction

I - III - VI_2 chalcopyrite semiconductors, such as $CuInSe_2$ and $Cu(In,Ga)Se_2$, have been one of the leading candidates for absorbers in heterojunction photovoltaic devices. These devices have demonstrated high conversion efficiency close to 19%[1)], which is comparable to that for polycrystalline Si solar cells.

The electrical properties, both the conductivity type and the carrier concentration, of $CuInSe_2$ strongly depend on the Cu/In and Se/(Cu+In) compositional ratio. For fabricating high efficiency solar cells, one must control the Cu/In ratio to slightly In-rich range, since Cu-rich $CuInSe_2$ contains a semi-metallic $CuSe_x$ phase. The crystallinity also depends on the Cu/In ratio. At present, $CuInSe_2$ thin films for high efficiency solar cells are fabricated by co-evaporation technique with precise control of the Cu/In ratio. In order to achieve a solar cell with higher efficiency and larger area, it is important to establish the doping technique using extrinsic dopants.

Several groups have investigated the doping effect of impurities like Cd, Zn, Br, Cl, Xe, Ne, O, N, P, Sb, and Bi in $CuInSe_2$.[2-7)] Yu et al. reported the ion implantation of Cd, Br. Cl, and Zn into p-$CuInSe_2$, and fabricated the pn junction diode.[3)] In spite of these investigations, the detailed roles of doped impurity have not yet been clarified.

Recently, we have reported that the Mg atoms implanted into $CuInSe_2$ films act as donors, and that the carrier concentration can be controlled by Mg implantation.[8)] Group VII atoms are also promising elements as donor in $CuInSe_2$. In this study, we have implanted Cl ions into the $CuInSe_2$ films epitaxially grown on GaAs (001) substrates by RF sputtering, and investigated the effects of Cl implantation on the electrical properties of $CuInSe_2$.

2.Experiments

$CuInSe_2$ thin films were grown on GaAs(001) substrate by RF diode sputtering at the substrate temperature of 450℃. The film thickness of the films was about 600nm.

Cl ions were implanted into the thin films using five kinds of accelerating energies, in order to achieve a constant concentration of Cl within a depth of 300nm from the surface. Figure 1 shows the distribution of Cl ions implanted at each energy and the total distribution, simulated by TRIM95 program.[9)] The mean concentration of Cl in the implanted layer was changed in the range of $5\times10^{17}\sim5\times10^{19}cm^{-3}$. After implantation, the layer was annealed at 400℃ for 10min in N_2 atmosphere, to eliminate the damages, and to activate Cl ions implanted.

The composition of the films were evaluated by electron prove microanalysis (EPMA). Reflection high-energy electron diffraction (RHEED) was used to determine the crystallographic structure and orientation. The

[a)]Present address: Department of Electrical and Electronic Engineering, Faculty of Science and Engineering, Saga University, 1 Honjyo, Saga 840-8502, Japan.

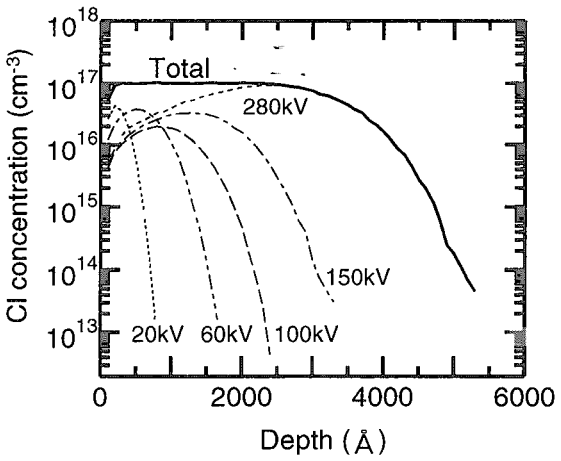


Fig.1. Simulation results for distribution of Cl atoms implanted at 20, 60, 100, 150, and 280keV, and total distribution.

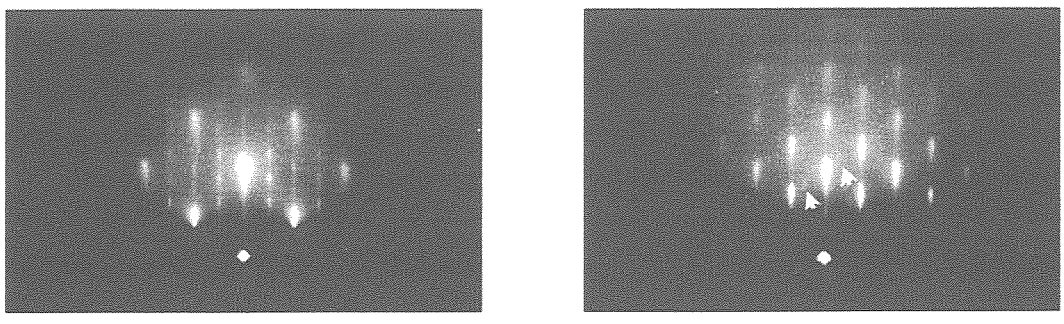
conductivity type, the resistivity, and the carrier concentration of the films were determined by hot-probe method and Hall measurements using van der Pauw technique, respectively. The electrical properties of all implanted films were characterized after the annealing.

3.Results and discussion

The compositional ratios of [Cu]/[In] and [Se]/([Cu]+[In]) of as-grown films were 0.90 and 1.01, respectively. Figures 2 (a) and 2(b) show the RHEED patterns of as-grown films, in which the electron beam was incident in the [-100] and [-110] direction of (001) GaAs, respectively. It was confirmed that $CuInSe_2$ layer with chalcopyrite structure, where the c-axis of $CuInSe_2$ was perpendicular to the surface of (001) GaAs substrate, was epitaxially grown on GaAs. The additional but very weak spots indicated by arrows in the figure show the existence of twin type defects. However, the amount of the twinned-region estimated from the diffraction intensity does not seem so large.

A halo-like pattern with weak spots was observed after the implantation, indicating that the lattice defects were produced by ion implantation. After annealing, the diffraction spots appeared clearly, similar to that in the as-grown film. The damages in film due to ion implantation are removed by this annealing procedure. This tendency is similar to the result of Mg implantation.[8)]

The electrical properties were characterized by hot probe method and Hall measurements using van der Pauw method. The conduction type and the carrier concentration in as-grown films were n-type and around $3\times 10^{16}cm^{-3}$, respectively. By the annealing of as-grown films, the carrier concentration was decreased to the order of $10^{14}cm^{-3}$. Figure 3 shows the dependence of the resistivity on the Cl concentration in the thin films. All films implanted showed n-type conduction. The resistivity is decreased linearly from the order of $10^{3}\,\Omega$ cm to $10^{0}\,\Omega$ cm with increasing Cl concentration. The dependence of carrier concentration on Cl concentration in the thin films is shown in figure 4. The carrier



(a) (b)

Fig.2. Reflection high-energy electron diffraction patterns of $CuInSe_2$ film grown on GaAs(001) substrate: (a) [-100] azimuth of (001) GaAs. (b) [-110] azimuth of (001) GaAs.

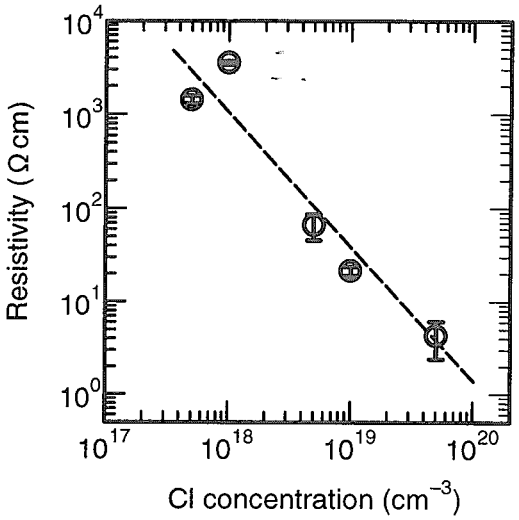


Fig.3. Dependence of resistivity of films on Cl concentration

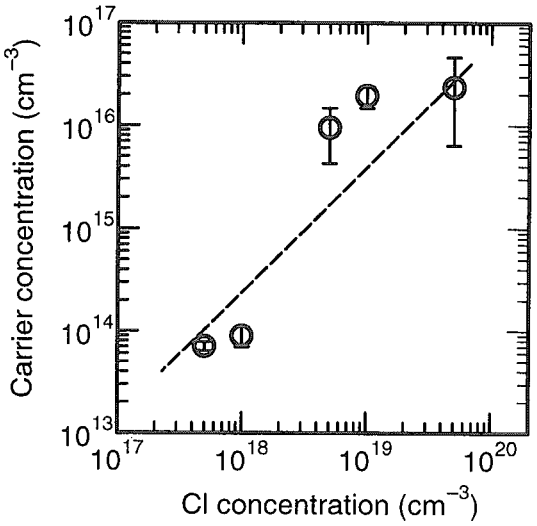


Fig.4. Dependence of carrier concentration of films on Cl concentration

concentration was changed almost linearly in the range of Cl concentration between 5×10^{17} and 5×10^{19}cm^{-3}. Consequently, the Cl atoms were found to act as donor in $CuInSe_2$. This result is consistent with the previous report.[3] As can be seen from figure 4, the ratio of carrier concentration to implanted Cl concentration is very small. Although the reason of this behavior is not clear at present, the electrical properties of $CuInSe_2$ films can be controlled by Cl ion implantation.

4.Conclusions

We have implanted Cl ions into $CuInSe_2$ epitaxial thin films using multi-energy implantation technique. All thin films implanted showed n-type conduction. The resistivity and the carrier concentration changed linearly with increasing the Cl concentration. As a consequence, Cl is found to act as donor in $CuInSe_2$. The control of carrier concentration of $CuInSe_2$ is possible by Cl ion implantation.

References

[1]D.Haneman, Crit. Rev. Solid State Mater. Sci. **14** (1988) 377.

[2]P.W.Yu, Y.S.Park, S.P.Faile, and J.E.Ehret, Appl.Phys.Lett. **26**, 717 (1975).

[3]P.W.Yu, Y.S.Park, and J.T.Grant, Appl. Phys. Lett. **28**, 214 (1976).

[4]R.D.Tomlinson, A.E.Hill, M.Imanieh, R.D. Pilkington, A.Roodbarmohammadi, M.A.Slifkin, and M.V.Yakushev, J.Electron.Matter. **20**, 659 (1991).

[5]S.Kohiki, M.Nishitani, T.Negami, and T.Wada, Appl.Phys.Lett. **62**, 1656 (1993).

[6]M.Nishitani, T.Negami, S.Kohiki, M.Terauchi, T.Wada, and T.Hirao, Appl. Phys. Lett. **62**, 1656 (1993).

[7]S.Kohiki, M.Nishitani, T.Negami, and T.Wada, Thin Solid Films, **226**, 149 (1993).

[8]T.Tanaka, T.Ohshima, H.Itoh, S.Okada, A. Wakahara, and A.Yoshida, J.Appl.Phys. **87**, 3283 (2000).

[9]J.P.Biersack, and L.J.Haggmark, Nucl. Instrum. Methods, **174**, 257 (1980).

1.7 ESR Characterization of Diamond Implanted with High Energy Phosphorus Ions at High Temperature

J. Isoya, T. Ohshima* and Y. Morita*
University of Library and Information Science, Department of Material Development, JAERI*

1. Introduction

In both high-pressure synthetic crystals and CVD films, p-type semiconducting diamond is easily obtainable by incorporating boron at the growth stage. Recently, n-type conductivity has been achieved in phosphorus doped homoepitaxial diamond thin film grown by CVD method.[1] We have been searching a condition for n-type doping by using high-energy (9-21 MeV) phosphorus ion implantation. In diamond, not only electric conductivity might be caused by damage-induced graphitization but also clusters of vacancies formed by post-implantation annealing act sometimes as donors[2]. Thus, electric measurements alone are not sufficient to characterize ion-implanted diamond. We use electron spin resonance (ESR) technique to identify both the radiation-induced defects and the defects remaining after annealing. Information obtained by ESR measurements is utilized to search both implantation and annealing conditions that should increase the concentration of phosphorus without increasing the concentration of defects.

The formation of amorphous phase as lattice-damages is monitored by the isotropic ESR signals of carbon dangling bonds. In an implantation at room temperature, even at a low fluence, microscopic amorphous particles are produced with a rate of 2.5×10^2 particles/ion[3]. Although the amorphous phase disappeared after the annealing at 1800°C under high pressure of 6 GPa, the electric activation of implants by the annealing seems to be difficult. The formation of amorphous phase, which was also observed after implantation at 400°C, is suppressed by using the high target temperatures of 700°C, 1000°C and 1500°C, in the case of a low fluence. The ESR-active defects remaining after high-temperature implantation are mainly vacancy-clusters. The lack of ESR signals of isolated substitutional phosphorus suggests that phosphorus ions are likely to be captured by vacancy-clusters. In phosphorus doping by ion implantation, optimizing both implantation and annealing conditions from a point of view of defect-control is crucially important.

In the course of searching condition for n-type doping, we have investigated the following implantation conditions in our present work: (1) high fluence phosphorus ion implantation at 1000°C, (2) carbon ion implantation at 1500°C after phosphorus ion implantation at 1500°C, (3) phosphorus ion implantation at 1800°C.

2. Experimental

Synthetic diamond crystals of type IIa were irradiated using a 3 MV tandem accelerator with either phosphorus of nine different energies between 9 MeV and 21 MeV or with carbon ions of nine different energies between 5 MeV and 9 MeV. By employing these acceleration energies, both phosphorus and carbon ions are implanted into a wide depth range from 2 μm to 4 μm. The samples had a shape of regular plate with a size, typically, of $3\times3\times1$ mm^3. The implantation was carried out along the [100] axis. For the high temperature implantation experiments, diamond crystals were heated through direct contact with a graphite heater of an electric furnace.

The ESR spectra were recorded on a Bruker ESP300 X-band spectrometer by using an Oxford Instrument ESR-900 to control the sample temperature.

3. Results and Discussion

(1) High fluence phosphorus ion implantation at 1000°C

In the target temperature range between 700°C and 1000°C, two dominant defects produced after phosphorus ion implantation

of a low fluence (2×10^{12} ions/cm^2 × 9 energy steps) are vacancy-chains along [110] having an effective spin of S=1 and an orthorhombic-I symmetry. The values of D_z (the principal value of the zero-field splitting along [110]) at 120 K are 14.34 mT and 7.33 mT, respectively. Vacancy-chain of a smaller zero-field splitting has a longer chain-length. With the increase of the target temperature, the concentration of defects decreases and the fraction of vacancy-chain of longer length increases.

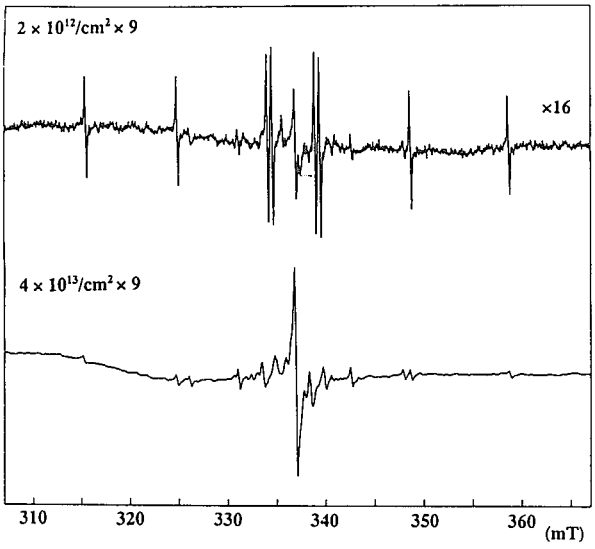


Fig.1. ESR spectra (120K) of type-IIa diamond crystals implanted with phosphorus ions at 1000°C.

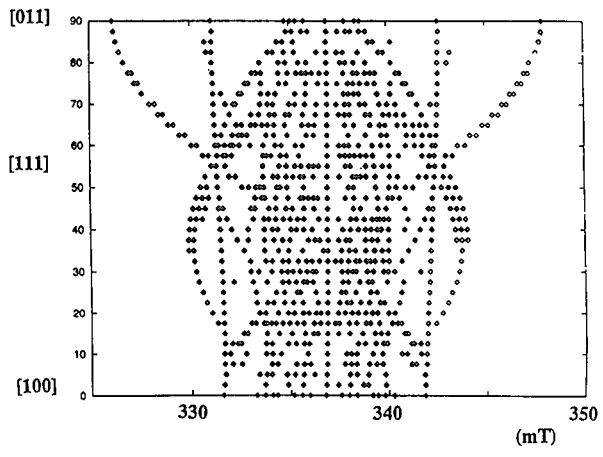


Fig.2. Angular dependence of the ESR line positions (10 K) of type-IIa diamond crystal which was implanted with phosphorus ions at 1000°C with fluence of 4×10^{13} ions/cm^2 for each of 9 steps of the energy.

We have investigated how the size of the vacancy-clusters depends on the fluence. We compare the defects formed after phosphorus ion implantation at 1000°C between two fluence conditions, one with fluence of 2×10^{12} ions/cm^2 for each of 9 steps of the energy between 9 MeV and 21 MeV and the other with fluence of 4×10^{13} ions/cm^2 for each of 9 steps of the energy (Figs.1,2). After the high fluence implantation, the concentration of defects increased and the vacancy-chain of longer length with a smaller zero-field splitting (D_z=7.33 mT) became predominant. Thus, in the case of implantation at 1000°C, a higher fluence seems to be not favorable for electric activation of phosphorus ions implanted, since phosphorus ions are likely to be captured by vacancy-clusters.

We note that the signal of S=1/2 with the g-value close to that of free electron is strongly observed in the case of the high fluence. The microscopic structure of the defect, which gives rise the strong signal, has not been identified.

(2) Carbon implantation after phosphorus implantation

Defects formed by high temperature implantation are mostly vacancy-clusters. Although the concentration of vacancy-clusters decreases by using annealing at elevated temperatures, vacancy-clusters of longer chain lengths, which are presumably formed by combining smaller clusters, remain after the annealing. Carbon ion implantation might be helpful in decreasing the vacancy-clusters.

Carbon ions with fluence of 1×10^{14} ions/cm^2 for each of 9 steps of the energy between 5 MeV and 9 MeV were implanted at 1500°C to a crystal which had been implanted with phosphorus ions with fluence of 1×10^{13} ions/cm^2 for each of 9 steps of the energy between 9 MeV and 21 MeV.

The concentration of the defects, which were observed after the carbon implantation, was similar to that after the phosphorus implantation (Fig.3). Thus, subsequent carbon ion implantation did not increase the concentration of the defects. The size of vacancy-clusters which remains after

phosphorus ion implantation at 1500°C might be too large to be filled with carbon ions implanted. It is likely that choosing a suitable target temperature should optimize the effect of implantation of carbon ions upon removing the defects formed by phosphorus ion implantation.

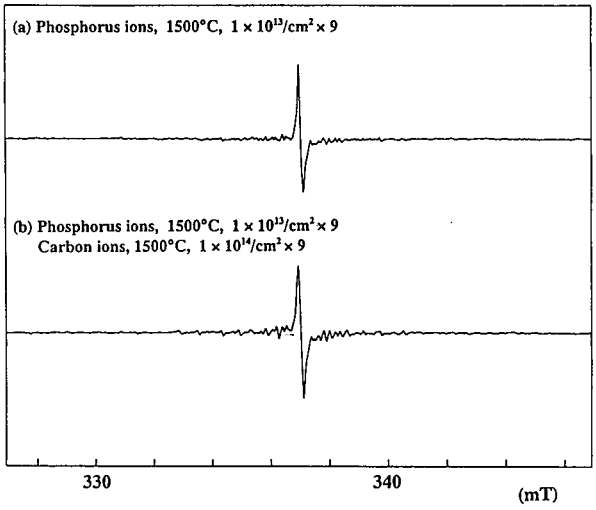


Fig.3. ESR spectra of type-IIa diamond crystals (a) After implantation of phosphorus ions (b) After implanted with carbon ions subsequent to phosphorus implantation.

(3) Implantation at 1800°C

It has been found that the concentration of the ESR-active defects after the implantation at 1500°C is remarkably lower than that after the implantation at 1000°C followed by the annealing at 1700°C (14 hrs under high pressure of 6 Gpa). In decreasing the defects, it is much more efficient to try to restore the crystallinity during implantation by using high target temperature than to try to decrease the defects by post-implantation annealing.

To investigate a higher target temperature, a type-IIa synthetic diamond crystal was implanted at 1800°C with phosphorus ions with fluence of 5×10^{13} ions/cm^2 for each of 9 steps of the energy between 9 MeV and 21 MeV. After the implantation, the color of the implanted layer turned to black. In the ESR measurements, the dielectric loss of the microwave cavity indicated that the crystal was conductive in the temperature range between 4 K and 300 K. In the ESR spectra obtained, the signal of dangling bonds in the amorphous phase was not observed (Fig.4). However, Raman spectra indicated that the implanted layer was converted to a carbon phase other than diamond. Since diamond is a metastable state of carbon at an ambient pressure, the target temperature for phosphorus doping by ion implantation should not increase to such a high temperature as 1800°C.

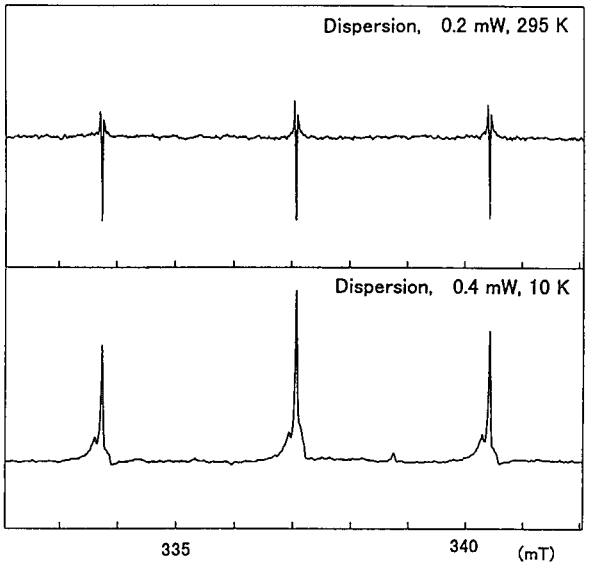


Fig.4. ESR spectra of type-IIa diamond crystal implanted with phosphorus ions at 1800°C. The three-line spectra are arising from nitrogen impurity.

Acknowledgments

The type-IIa synthetic diamond crystals used in the present work were supplied from Sumitomo Electric Industries. The Raman measurements were carried out by Dr. Hisao Kanda (NIRIM).

Reference

1) S. Koizumi, M. Kamo, Y. Sato, H. Ozaki and T. Inuzuka, Appl. Phys. Lett. 71, 1065 (1997)
2) J. F. Prins, Phys. Rev. B. 39, 3764 (1989)
3) J. Isoya, H. Kanda, I. Sakaguchi, Y. Morita and T. Ohshima, Radiat. Phys. Chem. 50, 321 (1997)

2. Biotechnology

2.1 Differential G-value of Tyrosine Isomers in the Radiolysis of Aqueous Phenylalanine Solution by Energetic Heavy Ions ····· 25
M. Taguchi, Y. Kobayashi, K. Hayano, H. Hiratsuka and S. Ohno

2.2 Development of Cell Surgery Technique by Ion Beam Exposure ····· 28
K. Shimono, M. Yamaguchi, M. Inoue, N. Shikazono, A. Tanaka, Y. Hase and H. Watanabe

2.3 Effects of $^{4}He^{2+}$ and $^{12}C^{5+}$ Ion Beams on Plant Regeneration from Protoplasts of Chrysanthemum (*Dendranthema grandiflora* Tzvelev.) ····· 31
T. Nakahara, K. Hirashima, H. Murakami, A. Tanaka, N. Shikazono, S. Hase and H. Watanabe

2.4 The Examination of the Fungal Pathogen (Glomerella cingulata) Resistance of the Ion Beam Irradiated Individuals in Strawberry ····· 33
M. Iizuka, N. Kudo, Y. Kimura, A. Tanaka, N. Shikazono and H. Watanabe

2.5 Effects of Helium Ions and Gamma Rays Irradiation of Early Globular and Torpedo Embryos on Postembryonic Leaf Development in *Brassica napus* L. ····· 35
H. Minami, N. Sakurai, N. Shikazono, A. Tanaka and H. Watanabe

2.6 Mutation Rate and Molecular Nature of Mutations Induced by Carbon Ions in *Arabidopsis Thaliana* ····· 38
N. Shikazono, A. Tanaka, H. Watanabe and S. Tano

2.7 Mutation Induction with Ion Beam Irradiation in Rose ····· 41
H. Yamaguchi, S. Nagatomi, A. Tanaka, N. Shikazono, T. Morishita and K. Degi

2.8 Mutation Breeding using Ion-beam Irradiation in Aster ····· 43
T. Baba, F. Nakamura, H. Nishi, S. Haraguchi, A. Tanaka, N. Shikazono and H. Watanabe

2.9 Removal of Pollutants by Mutant Strains of Microorganisms Induced by Ion-beam Irradiation — Fixation of CO_2 by Microalgae — ····· 45
M. Takigami, Nguyen, T.B., T. Ito, H. Ito and S. Hashimoto

2.10 Use of a Collimated Heavy Ion Microbeam for Irradiating Mammalian Cells Individually to Study the Effect of High-LET Single Ion Irradiation ····· 48
Y. Kobayashi, M. Taguchi, S. Wada, T. Funayama, T.V. Khoa, T. Kamiya, H. Watanabe and K. Yamamoto

2.11 Fate Mapping of the Cellular Blastoderm Stage Egg of the Silkworm, *Bombyx mori*, by Localized Irradiation of Heavy Ion Microbeams ····· 51
K. Kiguchi, Y. Kinjoh, K. Masahashi, Z.T. Tu, H. Tamura, K. Shirai, K. Kanetatsu, Y. Kobayashi, M. Taguchi and H. Watanabe

2.12 Morphological Analysis of Apoptosis-like Cell Death Induced by Ion Beam Irradiation in Plant Cells ····· 54
M. Kawai, Y. Kobayashi, Y. Oono and H. Uchimiya

2.13 Breeding New Shiitake (*Lentinula edodes*) Variety at High Temperature using Ion Beam Irradiation ····· 56
H. Akaishi, I. Narumi, M. Kikuchi and H. Watanabe
2.14 Analysis of a Brassinolide-insensitive Mutant from *Arabidopsis Thaliana* Irradiated with Ion Beam ····· 58
Y. Sasuga, K. Ichikawa, R. Kuwano, Y. Kobayashi, Y. Oono, Y. Kobayashi, S. Tanaka and H. Takenaga
2.15 Study on Plant Responses to Environmental Pollutants ····· 61
S. Matsuhashi, C. Mizuniwa, T. Ito, S. Hashimoto, N.S. Ishioka, S. Watanabe, A. Osa and T. Sekine
2.16 $^{13}NO_3^-$ and $^{13}NH_4^+$ Uptake and Assimilation-sites on a Single Root of Leguminous Crops Visualized by a Positron Emitting Tracer Imaging System: A Study Relating to the Locality of *Rhizobium* Infection Site ····· 64
H. Matsunami, Y. Arima, K. Watanabe, S. Matsuhashi, N.S. Ishioka, S. Watanabe, T. Itoh, C. Mizuniwa, T. Sekine, S. Hashimoto, A. Osa, H. Uchida and A. Tsuji
2.17 Effect of NH_4^+ on $^{13}NO_3^-$ Absorption and Transport in Soybean Plant ····· 67
N. Ohtake, T. Ohyama, K. Sueyoshi, T. Kawachi, H. Fujikake, A. Osa, M. Koizumi, S. Hashimoto, N. Ishioka, S. Watanabe, T. Sekine, S. Matsuhashi, T. Ito, C. Mizuniwa, H. Uchida and A. Tsuji
2.18 Ammonium ($^{13}NH_4^+$) Absorption and Translocation under Various Environmental Conditions in Rice Visualized by PETIS ····· 70
S. Kiyomiya, H. Nakanishi, H. Uchida, A. Tsuji, N. Harada, H. Tsukada, S. Matsuhashi, S. Hashimoto, T. Sekine and S. Mori
2.19 Effect of Phytohormones on ^{13}N Distribution in Rice Plants Detected by PETIS Detector ····· 73
H. Hayashi, H. Mano, N. Suzui, S. Matsuhashi, C. Mizuniwa, T. Ito, S. Hashimoto, N.S. Ishioka, T. Watanabe, T. Sekine, A. Osa, H. Uchida and A. Tsuji
2.20 Water and Trace Element Behavior in Plant ····· 76
T.M. Nakanishi, J. Furukawa, K. Tanoi, M. Yokota, S. Ueoka, N.S. Ishioka, S. Watanabe, T. Sekine, T. Ito, C. Mizuniwa, S. Matsuhashi, S. Hashimoto, A. Osa, H. Uchida and A. Tsuji
2.21 Uptake of ^{18}F-Water and ^{15}O-H_2O in Tomato Plants ····· 78
A. Tsuji, H. Uchida, T. Yamashita, S. Matsuhashi, T. Ito, C. Mizuniwa, N.S. Ishioka, S. Watanabe, A. Osa, S. Hashimoto and T. Sekine
2.22 Fundamental Study on Radiotherapy of Tumors to Beneficial Companion Animals using Heavy Ion Beam ····· 80
S. Wada, M. Natsuhori, Y. Kobayashi, K. Yamamoto and N. Ito
2.23 Development of Pollen-mediated Gene Transfer Technique using Penetration Controlled Irradiation with Ion Beams ····· 83
Y. Hase, A. Tanaka and H. Watanabe

2.1 Differential G-value of tyrosine isomers in the radiolysis of aqueous phenylalanine solution by energetic heavy ions

Mitsumasa Taguchi[1)*], Yasuhiko Kobayashi[1)], Kazuki Hayano[2)], Hiroshi Hiratsuka[2)], and Shin-Ichi Ohno[3)]
[1]Department of Radiation Research for Environment and Resources, JAERI,
[2]Department of Chemistry, Gunma University, and
[3]Theoretical Radiation Laboratory.

1.Introduction

Investigation of the decomposition reaction of biological substances in water irradiated with high Liner Energy Transfer (LET) particle is necessary for understanding irradiation effects on living organisms. However, LET effects on radiation damage of biological substances have not been observed clearly. The purpose of this study is to understand LET effects on living organisms from the viewpoint of the chemical field by analyzing LET dependence of decomposition reactions of DNA, proteins and amino acids in water.

In the present report, we investigated the LET dependence of production yields of tyrosine isomers by the irradiations of He-saturated phenylalanine aqueous solution with several hundreds MeV Ne ions. The yields decrease with an increase of LET of the ion.

2.Experimental

He-saturated aqueous phenylalanine solution (13 mM) was put into an aluminum cell, which has an aluminum window of 15-μm thickness for the irradiation. The volume of the sample solution was 4.7 mL and its depth was about 4 mm.

Irradiations were performed with 220-MeV C^{5+}, 350-MeV Ne^{8+} and 460-MeV Ar^{13+} ions by using Irradiation Apparatus for Seed[1)] in TIARA facility. Energy of the ion was attenuated by a set of aluminum foils (10- to 500-μm thickness) installed on the cell. The incident energies (E_0), the energies of the ion at the surface of the sample solution after penetrating the aluminum foils and the windows, were calculated by the TRM code[2)]. Penetration depth of the ion was less than 1.1 mm in water. Therefore, the sample solution was stirred during the irradiation by a magnetically coupled stirrer chip to keep the homogeneity. The sample solution was also irradiated with γ-ray as a low LET radiation.

Absorption spectra were recorded on the spectrophotometer before and after irradiation. The irradiated solutions were analyzed by High Performance Liquid Chromatography (HPLC) with a reversed phase column at 40 °C. Water with 3 % of acetonitrile was used as an eluent and its flow rate was 0.8 mL/minute.

3.Results and discussion

Aqueous phenylalanine solution has strong absorption bands in the ultraviolet region. After the irradiation with the ions, the absorption due to products was observed in the longer wavelength region, 260-450 nm, than the original absorption bands, and increased with an increase of dose.

We selected 275 nm as a monitor wavelength for analyzing the products by HPLC. The productions of *p*-, *m*-, and *o*-tyrosine, which are the adducts of one hydroxyl group on phenyl ring of phenylalanine, were reported after γ-ray irradiation of aqueous phenylalanine solution[3)]. The peaks of these tyrosine isomers (Tyrs) on the chromatogram were also observed after the ion irradiations.

Yields of the productions of Tyrs were estimated from the area of the peaks. The yields of Tyrs increased linearly with an increase of dose. *G*-value (molecules per 100 eV absorbed energy) of the production of total tyrosine isomers by γ-ray irradiation was estimated to be 0.30±0.03. In the

case of the ion irradiation, average G-value (G) is estimated by a following equation:

$$G = C \times 0.0047 / E_0 / F \times N_a \times 100 \quad (1)$$

where C is the concentration of tyrosine isomers estimated, and F and N_a are the fluence of the ion and the Avogadro number, respectively. Average G-value varies from 0.32 at 207 MeV to 0.19 at 67.6 MeV of the incident energy of the C ion. This means that the yield of total Tyrs along the trajectory decreases with decreasing energy of the ions.

We estimated the number of total molecules of Tyrs (N_t) produced by the single ion irradiation from the fluence dependence of the concentration of Tyrs:

$$N_T = C \times 0.0047 / F \times N_A . \quad (2)$$

All the ions used stop completely in the sample solution so that N_T is the number of molecules of Tyrs integrated over the trajectory. As can be seen from Figure 1, N_T increased steeply with increasing E_0. The increments were different among the ions used. The number of the radicals, which escape from the recombination process and react with the solute, is considered to increase with increasing energy because the ion having a higher energy has a lower LET value.

The yield of Tyrs will be determined by the concentration and distribution of transient species, *e.g.*, OH radical, produced in the track. The distribution of transient species at a very fast time is determined by the distribution of dose in the track. However, the reactions in the track is not clearly understood despite the fact that the dose distribution was investigated theoretically and experimentally. The differential G-value(G'), the G-value at a particular energy of the ion in the sample solution, of OH radical increases with the energy of C ion having 419- to 1022-eV/nm LET[4]. Therefore, as the first approximation, the production yield of Tyrs along the trajectory was assumed to be linearly proportional to the energy of the ion in the region up to 300 MeV:

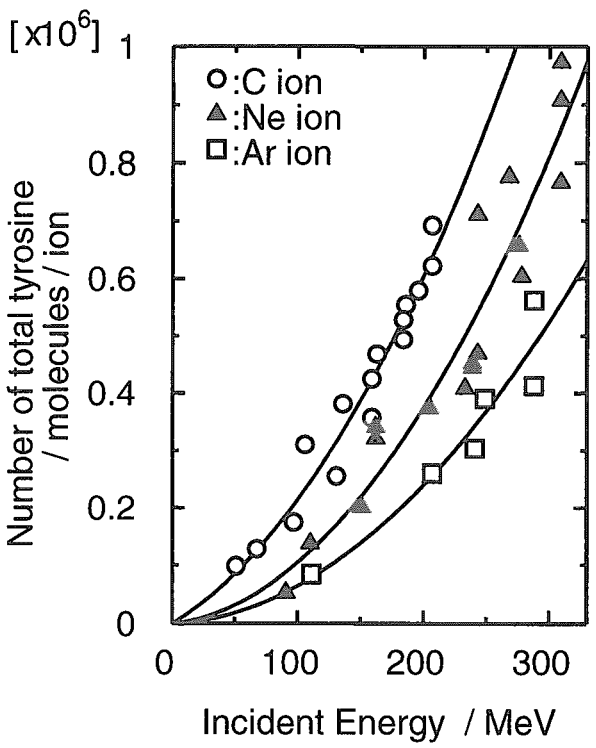


Figure 1.
Number of molecules of tyrosine isomers integrated over the one ion trajectory as a function of incident ion energy. The solid line was obtained by a least squares fitting method.

$$G' = a + bE \quad (3)$$

where E is the energy of the ion in the sample solution, and a and b are parameters for fitting the experimental results.

N_T corresponds to the value of the G'-value integrated over the trajectory:

$$N_T = \int_0^{E0} G' \, dE \times 100 . \quad (4)$$

Satisfactorily fitted curves were obtained by the least squares fitting method as shown in Figure 1. The G'-values were estimated by differentiating the fitted curve and plotted as shown in Figure 2. The G'-value increases with decreasing LET value of the same ion. Furthermore, the G'-value appears to increase with increasing atomic number of the ion at the same LET value.

The G'-values of OH and HO_2 radicals, and H_2O_2 molecules were estimated in aqueous formic acid solution irradiated with C ions in the 419- to 1022-eV/nm LET region[4]. The G'-value of OH radical decreased monotonously with the LET value as the same as the G'-value of Tyrs. However, G'-values of HO_2 radical and H_2O_2 increased monotonously with the LET value in water. Therefore, the production of Tyrs will be principally induced by OH radical(reaction(a)). Assuming that the G'-value of OH radical for all the ions used here decreases similarly to the G'-value of OH radical, the G'-values of Tyrs will decrease with the LET value from 0.3 obtained by the γ–ray irradiation. However, G'-values estimated here are partly greater than that expected.

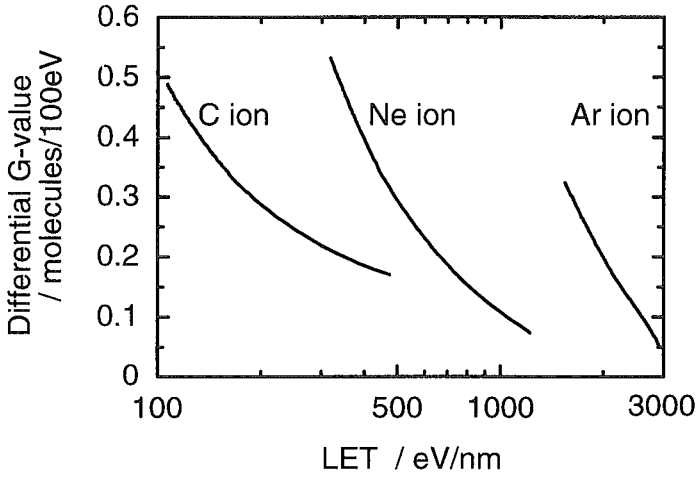
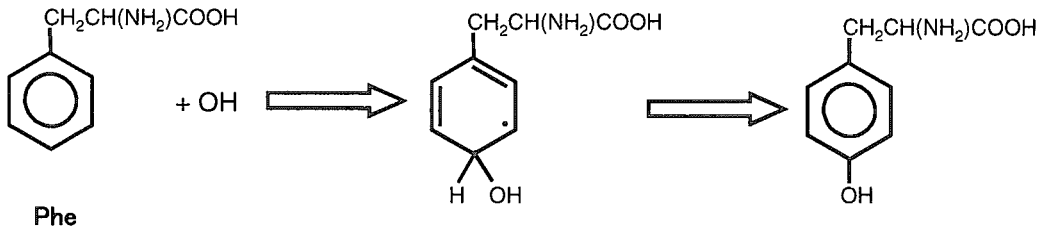


Figure 2
Differential G-value of total tyrosine isomers as a function of LET was obtained the slope of plots of number of total tyrosine in figure 1.



(5)

The G-value of total Tyrs in the oxygen-saturated aqueous Phe solution was estimated to be about three times that in the absence of oxygen after the irradiation with γ–ray. The oxidizing agents such as O_2 and $Fe(CN)_6^{3-}$ increase the efficiency of the reaction (b)[5-7]. The ions produce the oxidizing species, *e.g.*, O_2 molecule and HO_2 radical, which are rarely produced by the γ–ray irradiation and increase with the LET value, because these species would be produced by the recombination of transient species in the track . The increment of the G'-value would be caused by the oxidizing species produced in the track.

References

1. M. Kikuchi et al., *TIARA Annual Report* 1,159(1992).
2. J.F. Ziegler, et al., The Stopping Power and Range of Ions In Solid, vol. 1, Pergamon Press, New York, 1985.
3. O.H. Weeler and R. Montalvo, *Radiat. Res.*, **40**, 1(1989).
4. J.A., LaVerne, *Radiat. Phys. Chem.*, **34**, 135(1989).
5. P.Kranjnic, et al, *Z. Naturforsch.*, **50a**, 864,(1995).
6. Wang *et al.*, *Z.Naturforsch.* **48b**, 761(1993).
7. Volkert and Schulte-Fronhlinde, *Tetrahedron Lett.*, **18**, 2151(1968).

2.2 Development of Cell Surgery Technique by Ion Beam Exposure

K. Shimono, M. Yamaguchi, M. Inoue, N. Shikazono*,
A. Tanaka*, Y. Hase*, H. Watanabe*
Faculty of Agriculture, Kyoto Prefectural University,
*Department of Radiation Research for Environment and Resources, JAERI

1. Introduction

Ion beams have higher LET (Linear Energy Transfer), in comparison with that of X-rays or Gamma-rays, and the penetration range of ion beams in the target material can be controlled. Taking advantages of these characteristics of ion beams, a lot of energy can be deposited on the focused point of material exposed. Previously, we reported the phenomenon specific for ion beam exposure, " leaky pollen ", in which internal substance leaked through an opening in the outer wall of pollen grain[1,2]. The frequency of the leaky pollen increased with the increase of dose. The leaky pollen is thought to result from a physical lesion(s) induced by the combined action of electron stopping and nuclear stopping, suggesting that ion beam can be available for surgical treatment in plant cells.

This study aims to analyze biological effects following the ion beam irradiation to different parts of the cell, and to develop the procedure of cell surgery.

In the present paper, we describe primary data on the chromosome aberration induction and the repair of lesions in root tip cells exposed to C ions and electrons.

2. Experimental

The seeds of *Nicotiana tabacum* L. cv Tsukuba 1, were monolayered and exposed to scanning beam of 220 MeV C ions with different LET ranging from 93 to 242 keV/μm, from AVF Cyclotron. They were allowed to germinate and to grow at 25℃ under light condition. Immediately after germination, root tips with length of 0.2~0.3mm were fixed in a solution of ethanol : acetic acid (3:1, v/v) and used for determining the frequency of cells with chromosome aberration. Survival rate of the seeds exposed was also determined 7 weeks after imbibition.

Furthermore, the roots (length, 1~5mm) of the seeds imbibed for 96hr, were continuously exposed to 220 MeV C ions (LET, 111keV/μm ; penetration depth, 1mm) of 1Gy. Simultaneously, fractional exposure of 1Gy, i.e. 0.5 plus 0.5Gy with the interval time of 1 and 2hr, was performed. To make a comparison between radiation with different LETs, continuous (10Gy) and fractional (5 plus 5Gy) exposure of electrons (0.2keV/μm, 9mm) were also

performed under same exposure conditions as those in the ion exposure. The chromosome aberration frequency was determined in root tip cells fixed after 24hr of the exposure performance.

3. Results and Discussion

The dose-response curve for survival rate in the seeds exposed to C ions with different LETs was shown in Fig.1. The degree of survival reduction increased with the increase of LET up to 226 keV/μm, and decreased at 242 keV/μm. This feature was same on the chromosome aberration induction (Fig. 2). These results support the reports of other studies, i.e. the peak RBE at 252 keV/μm for the survival reduction in *Arabidopsis thaliana* exposed to different ions[3] and the increasing RBE over 111 keV/μm for the chromosome aberration induction in *N. tabacum* exposed to C ions[4]. As shown in Table 1, frequencies of the chromosome aberrations following continuous exposure with C ions of 1Gy and electrons of 10Gy were 50.2 and 53.0%, respectively. This implies that each of exposures has almost same effect on the induction of chromosome aberration in the present exposure system. When the dose was fractionized, the chromosome aberration frequencies in the electron exposure with the interval time of 1 and 2hr significantly decreased (46.5 and 45.0%, resp.), compared to that in continuous exposure. However, in case of the C ion exposure, the frequencies were same in both continuous and fractional exposure. These results mean that the repair of lesions induced by C ions is different from that by electrons.

References

1) M. Inoue et al., TIARA Annual Report. 3, 44, 1993
2) A. Tanaka et al., Nucl. Instr. and Meth. in Phys. Res. B129, 42, 1997
3) A. Tanaka et al., Int. J. Radiat. Biol. 72,121, 1997
4) Y. Hase et al., Radiat. Environ. Biophys. 38, 111, 1999

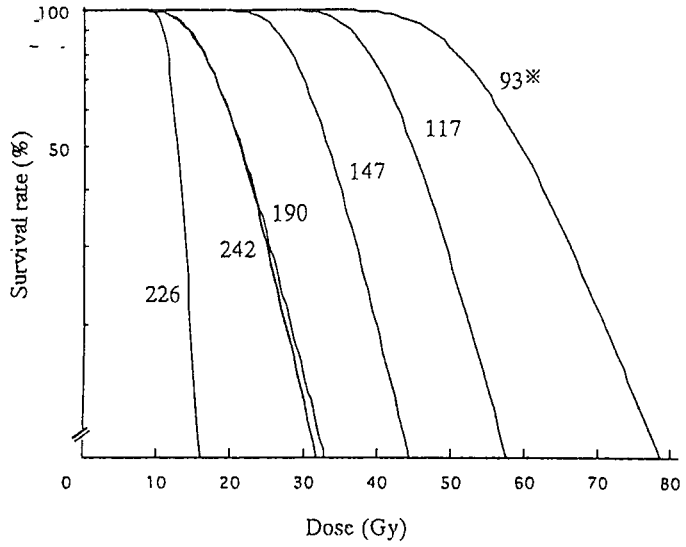


Fig. 1 Dose-response curve for survival rate of tobacco seeds exposed to 220 MeV $^{12}C^{5+}$ with different LETs.
※ LET, keV / μm.

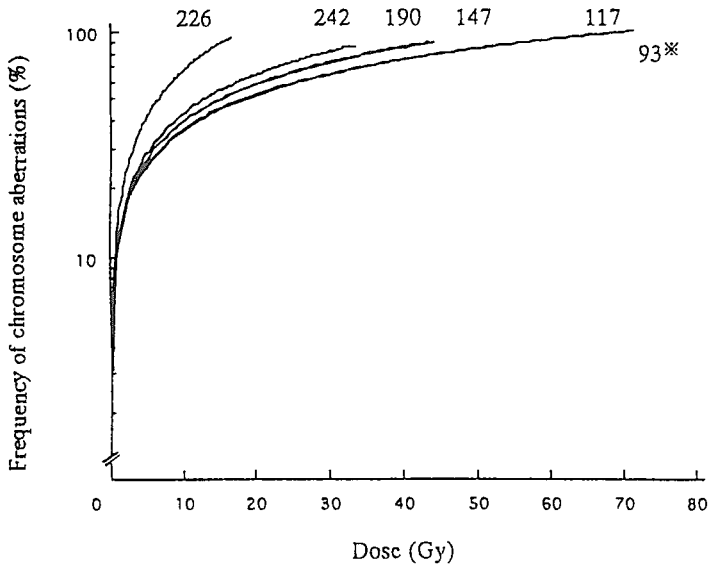


Fig. 2 Dose-response curve for the chromosome aberration induction in root tip cells exposed to 220 MeV $^{12}C^{5+}$.
※ LET, keV / μm.

Table 1 Frequency of chromosome aberrations observed in root tip cells following fractional exposure to carbon ions and electrons

Exposure						
Radiation	Total dose (Gy)	Interval time (hr.)	No. of roots observed	No. of mitotic cells observed	No. of mitotic cells with chromosome aberrations	Frequency of mitotic cells with chromosome aberrations (%)
$^{12}C^{5+}$	1	0	15	234	118	50.2±1.9
		1	15	227	113	50.1±2.7
		2	15	231	118	50.8±1.9
e^-	10	0	15	259	139	53.0±2.8
		1	15	229	106	46.5±2.4
		2	15	402	181	45.0±1.3

2.3 Effects of $^{4}He^{2+}$ and $^{12}C^{5+}$ Ion Beams on Plant Regeneration from Protoplasts of Chrysanthemum (*Dendranthema grandiflora* Tzvelev.)

T. Nakahara[1], K. Hirashima[1], H. Murakami[1], A. Tanaka[2], N. Shikazono[2], S.Hase[2] and H. Watanabe[2]

Fukuoka Agricultural Research Center[1]

Department of Radiation Research for Environment and Resources, JAERI[2]

1. Introduction

Ion beams have high LET (linear energy transfer) and are applied to induce various mutants of plant. Recently it have been irradiated many species of plant and acquired many mutants[1]. In many case, ion beams were irradiated to seed, meristem tip and callus, but there happened to raise chimera and were limited regenerated plant. So we tried to irradiate mesophyll protoplast of chrysanthemum with ion beams to prevent chimera and to acquire many regenerated plant.

2. Experimental methods

Chrysanthemum cultivar, 'Shuho-no-chikara' (White flower) was used for the experiments. Mesophyll protoplasts of chrysanthemum were isolated by the modified method of Nakahara et al[2]. Isolation and embedding of mesophyll protoplast were conducted according to previous report[2]. The protoplasts were irradiated with 50MeV $^{4}He^{2+}$ and 220 MeV $^{12}C^{5+}$ ion beams from the AVF cyclotron in JAERI. The protoplasts were cultured by the method of Nakahara et al[2].

3. Results and Discussion

In $^{4}He^{2+}$ ion beams, according to the increase of dose from 1 Gy to 10 Gy , the callus induction decreased gradually. At higher than 15 Gy, only few callus were induced. No callus was induced at higher than 20 Gy.

The LD_{50} was estimated to be existed around 4.9 Gy. In $^{12}C^{5+}$ ion beams,the relationship of the dose and the callus induction was similar to the case of $^{4}He^{2+}$. The LD_{50} was estimated to be existed around 3.3 Gy. The success of regeneration from protoplasts irradiated with ion beams has been achieved for the first time in the world. In this study, 658 regenerants were acquired and the regeneration of plant are in progress furthermore. Now the traits of the regenerants are being examined outdoors.

References

1) S.Nagatomi, A.Tanaka, A.Kato, H.Yamaguchi, H.Watanabe and S.Tano, TIARA Annual Report 6:41-43 (1998)

2) T.Nakahara, K.Hirashima, M.Koga, A.Tanaka, N.Shikazono and H.Watanabe, TIARA Annual Report 7:28-29 (1999)

Table 1. Plant regeneration from chrysanthemum mesophyll protoplast irradiated with ion beams.

Ion	Energy (MeV)	Dose (Gy)	No. of callus cultured	No. of callus regenerated	Rate of callus regenerated (%)
$^{4}He^{2+}$	50	2	1061	84	7.9
		5	3578	329	9.2
		10	1160	108	9.3
$^{12}C^{5+}$	220	2	97	6	6.2
		5	2015	131	6.5
Total			7911	658	8.3
Control			1000	67	6.7

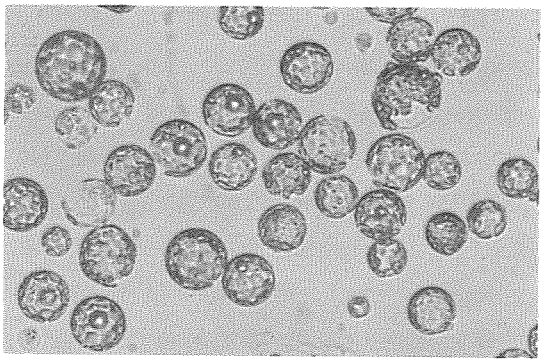


Fig.1 Mesophyll protoplast of chrysanthemum

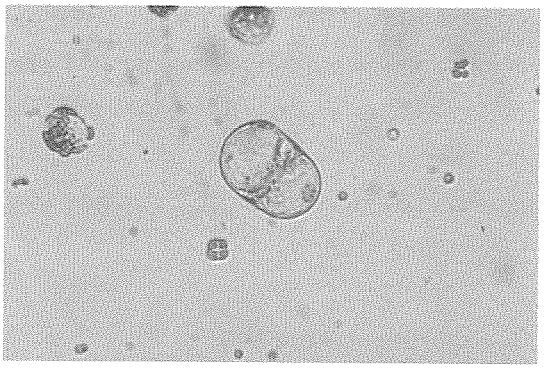


Fig.2 First division of mesophyll protoplast irradiated with ion beams

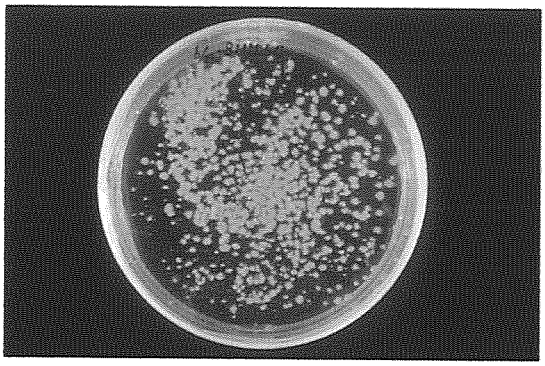


Fig.3 Callus induction from mesophyll prptoplast irradiated with ion beams

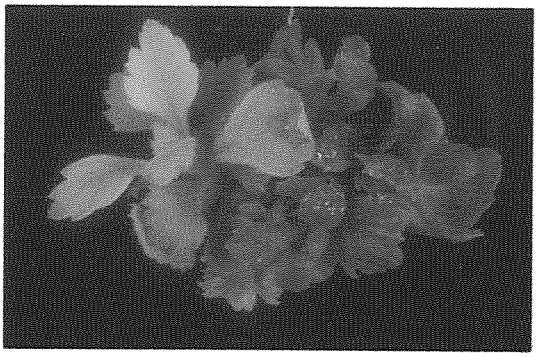


Fig.4 Plant regeneration from mesophyll protoplast irradiated with ion beams

2.4 The examination of the fungal pathogen (Glomerella cingulata) resistance of the ion-beam irradiated individuals in strawberry

Masahide IIZUKA[1],Nobuhiro KUDO[1], Yasuo KIMURA[1], Atushi TANAKA[2], Naoya SHIKAZONO[2] and Hiroshi WATANABE[2]
[1]Gumma Horticultural Experiment Station,
[2] Department of Radiation Research for Environment and Resources, JAERI.

1.Introduction

Ion beams, which have a higher linear energy transfer (LET) than X and gamma rays do, is one of efficient mutagenic agents, which is applicable to mutation breeding of many horticultural crops. However, there have been few studies on the effects of ion beam irradiation on induction of mutation in vegetables and ornamental crops. And, the acquisition of some disease resistance is reported, too. The lethal dose of the $^{4}He^{2+}$ and $^{12}C^{5+}$ ion beam irradiation to strawberry and hydrangea seed became clear [1),2)].

At present paper, ion beams are irradiated in the strawberry, and a fungal pathogen (Glomerella cingulata) resistance is individualy selected.

2.Materials and Methods

The strawberry GSC-1 seed after irradiation of the 220MeV $^{12}C^{5+}$ beam of 30 - 70Gy, were germinated and the seedlings were used follow the examination. Glomerella cingulata were isolated from strawberry leaf. It was maintained and cultured on 20 ml PDA (Bact- Potato Dextrose Agar, 39gfl, Difco Laboratories) medium in 9 cm-diameter petri dishes. After incubation under fluorescent light (16h/day photoperiod) at 25 ℃ for 4 weeks, PDA plate was covered with spore. Glomerella cingulata spore concentration is adjusted to 10^{4} /ml, and spray has a spore suspension in the whole of the stock. Seedlings of strawberry which had spreid by its spore suspension was managed in the greenhouse of 80% of the humidity at 28℃ after the inoculation, and getting sick was investigated after 1 week, 1month, and 2 months.

3.Results and Discussion

There were many seedlings in which sickness spots appeared by the investigation after the inoculation 1 week, and getting sick was recognized in 98% after 1 month. It could get two plants with no symptom and five plants with little symptom by the investigation after two months in 220plants.

References

1)N. Kudo et al. TIARA Ann. Rep., 16:62-64. (1998)

2)M. Iizuka et al. TIARA Ann. Rep., 2.3:30-31. (1999)

Table1. Glomerella cingulata getting sick of the ion beam irradiated strawberry plants

	After 1week	After 1month	After 2month
No symptom	22	4	2
Little symptom	132	68	5
Large symptom	66	104	18
Wilt	0	34	74
Dead	0	10	121

inoculated 13/9/1999
A number is the number of plants

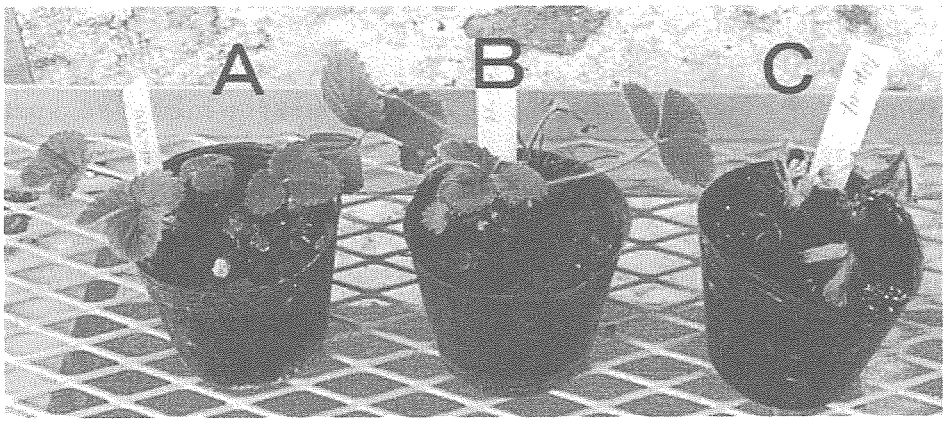


Fig 1 .Strawberry plantlets after two months, inoculated by the Glomerella cingulata
A : No symptom B : Little symptom C : Wilt

2.5 Effects of Helium Ions and Gamma Rays Irradiation of Early Globular and Torpedo Embryos on Postembryonic Leaf Development in *Brassica napus* L.

H.Minami,N.Sakurai*,N.Shikazono**,A.Tanaka**and H.Watanabe**

Oshima Horticultural Research Center, Tokyo Metropolitan Agricultural Station; *Radiation Laboratory, Tokyo Metropolitan Industrial Technology Institute; **Department of Radiation Research for Environment and Resources, JAERI

1.Introduction

The effects of gamma rays on whole plants in sexual reproductive stages have been intensively examined in plant mutation breeding. It is especially important in mutation breeding to increase mutation ratio. The ratio varies in life stages in which plant was irradiated. It is well known that reproductive organs ranging from differentiation to development and immature embryo during embryogenesis are more radiosensitive than the other organs[1].

Lardon *et al*[2]. made the flower culture method for developing an isolated whole flower (a flower with a pedicel) of *Brassica napus* into a mature pod within 50 days after pollination. The embryogenesis in sexual reproductive stages proceeds synchronously.

The purpose of this study is to investigate the effects of ion beams in sexual reproductive stages on embryogenesis and mutation of *B. napus* through flower culture method. In this paper, we report the effects of helium ions and gamma rays of the early globular and torpedo embryos on postembryonic leaf development of *B. napus*.

2.Materials and Method

2.1 Plant

B. napus cv. Lisandra were grown at 15/10℃ under natural daylight. Flowers of the terminal racemes were used and cultured through flower culture method. Whole flowers, which were unpollinated on the morning of anthesis during middle flowering period, were collected to be transferred on 1.5 ml tube (eppendorf) in Murashige and Skoog's macro and micro elements medium[3] supplemented with 3 % sucrose pH 5.8 using a procedure modified from that of Lardon *et al*..

2.2 Determination of early globular and torpedo stages after pollination under microscopy

Figure 1 shows the embryo stages after pollination. The early globular and globular embryos were observed five days and six days, respectively, after pollination. The torpedo embryo was observed 10 days after pollination.

2.2 Irradiation

Early Globular Stage

Whole flowers were irradiated five days after pollination at 30 Gy dose using helium ions (AVF cyclotron) and gamma rays (^{60}Co).

Torpedo Stage

Whole flowers were irradiated 10 days after pollination at 30 Gy dose using gamma rays.

3.Results and Discussion

The helium ions and gamma rays irradiation of early globular embryos showed some drastic effects on first true leaf development. Those effects were classified into four types: cup-shaped, funnel-shaped, shrunk and the other varied leaves (Figure 2). Those types were observed in 40 % of plants developed first true leaf (Table 1 and 2). The types of cup-shaped, funnel-shaped leaves were observed over 15%. It is reported that the upper tier of the regions is destined to develop into the apical part of the seedling with cotyledons and apex in *Arabidopsis thaliana*, while the lower tier gives rise to the hypocotyl and root[4]. These findings suggest that the malformed development of first true leaves caused the damage of the upper tier of globular embryo by helium ions and gamma rays irradiation to inhibit and/or to stop their cell division. On the other hand, the irradiation of gamma rays of torpedo embryo had not stronger effects than that of globular embryo, while caused sectors lacking chlorophyll in some first true leaves.

We investigate the effects of ion beams and gamma rays irradiation of developmental embryo on postembryonic development through flower culture of *Brassica napus* in progress.

4. References

1) H. Gaul: Radiation Bot. 4(1964)155-232

2) A. Lardon, A.M. Triboi-Blondel and C. Dumas:Sexual Plant Reproduction6(1993)52-56

3) T. Murashige and F. Skoog: Physiologia Plantarum 15(1962)473-497

4) G. Jürgens:"Arabidopsis",(E.M. Meyerowitz and C.R. Somerville eds.), pp.297-312, CSHL PRESS, New York(1994)

Table 1 Effects of helium ion irradiation of early globular embryo on first true leaf development

Number of plants developed first true leaf	Number of plants undeveloped first true leaf	Number of plants developed varied first true leaf			
		Types			
		Cup	Funnel	Shrunk	Others
55	2	3	3	7	6

Table 2 Effects of gamma rays irradiation of early globular embryo on first true leaf development

Number of plants developed first true leaf	Number of plants undeveloped first true leaf	Number of plants developed varied first true leaf			
		Types			
		Cup	Funnel	Shrunk	Others
54	4	5	3	7	5

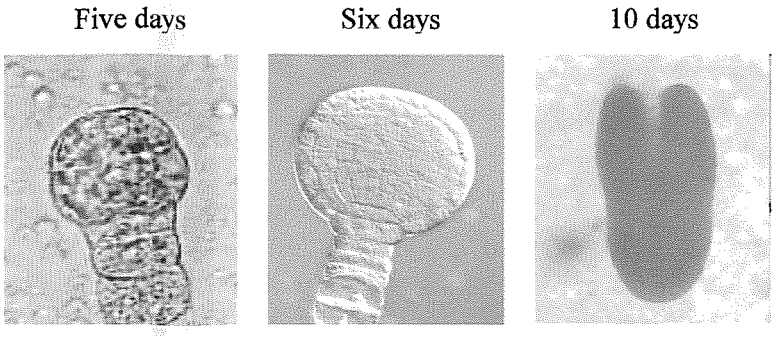


Fig. 1 Embryo stages after pollination

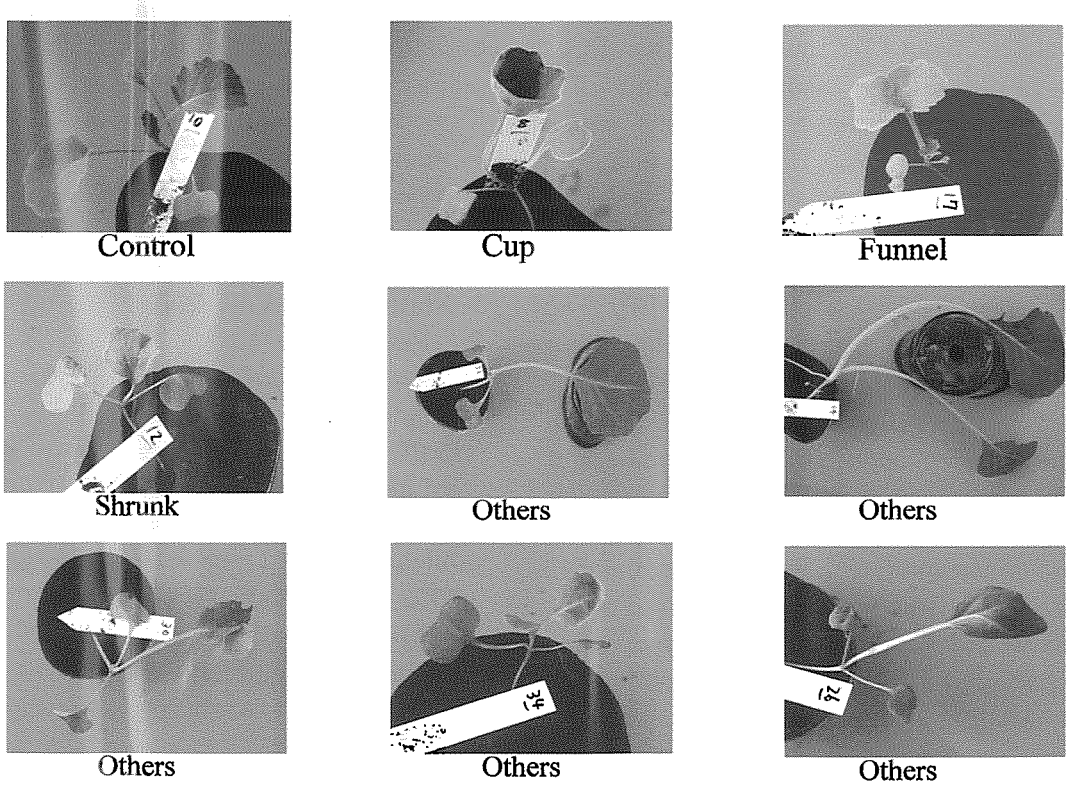


Fig.2 Postembryonic first true leaf development after irradiation on early globular and torpedo embryos

2.6 Mutation rate and molecular nature of mutations induced by carbon ions in *Arabidopsis thaliana*

Naoya Shikazono, Atsushi Tanaka, Hiroshi Watanabe and Shigemitsu Tano

Department of Radiation Research for Environment and Resources, JAERI

1. Introduction

High linear energy transfer (LET) radiation such as ion particles causes more localized, dense ionizations within cells compared with low LET radiation such as X-rays or γ-rays [1]. Based on microdosimetric and radiobiological considerations, it is assumed that high LET radiation could produce double strand breaks with damaged end groups whose reparability would be low [2,3]. Therefore, it seems plausible to assume that high LET radiation could generate mutations more frequently than low LET radiation. In addition, high LET radiation may induce a specific type of mutation.

Ion particle-induced mutations have been investigated using various plants [4]. The highest RBE was found around the linear energy transfer (LET) of 100～200keV/μm.

However, these studies were focused on mutant phenotypes where the numbers of the corresponding genes were unknown, or on somatic mutations. There are few reports on the mutation rate of a locus at the M2 generation after ion particle irradiation, which would be of great importance when ion particle-mutagenesis was applied to plant mutational breeding.

Some investigations on the molecular nature of mutations induced by X-rays, γ-rays and fast neutrons have been carried out in plants. It was shown that these radiations frequently induced deletions whose lengths were larger than several thousand base pairs. Bruggemann et al. [5] reported that 13 out of 18 *long hypocotyl 4* (*hy4*) mutants of *Arabidopsis* induced by fast neutrons carried deletions larger than 5 kb. However, there are few investigations in plants on the type of mutation induced by high LET ion particles. Mei et al. [6] reported that a rearrangement was induced in the semi-dwarf mutant of rice by argon ions, using a random genomic clone as a probe. Recently, we analyzed the characteristics of the carbon ion-induced mutations by PCR and Southern blot analyses and found that, out of four mutants, one had a total gene deletion, two contained inversions and/or translocations, and one had a point-like mutation [7].

In order to investigate the nature of mutations induced by high LET radiation in plants, mutation rates at the M2 generation for carbon ions and electrons were estimated. Further, a PCR analysis and a sequence analysis using carbon ion-induced *Arabidopsis* mutants were carried out.

2. Materials and methods

2.1. Plant material

Plants of *Arabidopsis thaliana* ecotype Columbia were grown on metro-mix (HYPONEX Co. Ltd., Japan) or on rock wool at temperatures around 25 °C in an air-conditioned greenhouse, and were subirrigated at 3- or 4-day intervals with 0.03% HYPONeX (HYPONEX Co. Ltd., Japan). Seeds of the mutants used for the complementation test were provided from the Nottingham Arabidopsis Stock Center (NASC).

2.2. Irradiation and mutant isolation

Irradiation of dry seeds was carried out as previously described [8]. The energy of carbon ions and of electrons was 220 MeV and 2 MeV, respectively. The dry seeds were irradiated with a dose of 150 Gy for carbon ions and with a dose of 750 Gy for electrons. Irradiated M1 seeds (26,200 seeds for carbon ions and 9,600 seeds for electrons) were sown and selfed to obtain M2 seeds. *gl*, *tt*, and *hy* mutants were selected from M2 plants. For the

complementation test, *gl* mutant lines were crossed with *gl1-1*, *gl2-1* and *gl3-1* mutants, and *tt* mutant lines were crossed with *tt3-1*, *tt4-1*, *tt5-1*, *tt6-1* and *tt7-1* mutants.

2.3. DNA extraction and molecular analysis

Genomic DNA was extracted from the M3 mutants following the procedure described by Konieczny and Ausubel [9]. The amplified DNA fragments were analyzed by agarose gel electrophoresis in TAE buffer, followed by visualization by ethidium bromide staining. For sequence analysis, rearranged fragments were cloned by colony hybridization or by TAIL PCR. The cloned fragments were subsequently sequenced by dideoxy termination method. Point mutations were analyzed by direct sequencing.

3. Results and Discussion

The doses for mutagenesis (150 Gy for carbon ions and 750 Gy for electrons) were determined from the relative biological effectiveness of carbon ions compared with that of electrons on the survival of the plants, which was approximately 5, and further from the fact that both doses are at the shoulder of each survival curve [8]. Mutation rates per locus per diploid cell per dose for carbon-induced *tt*, *gl*, and *hy* were 2.6×10^{-6}, 1.9×10^{-6}, 2.3×10^{-6}, respectively and for electron-induced *tt*, *gl*, and *hy*, mutation rates were 0.08×10^{-6}, 0.25×10^{-6}, and 0.14×10^{-6}, respectively (Table 1). It was demonstrated from the present result that mutation rates of carbon ions were 7.6 fold to 33 fold higher than those of electrons.

The results of the PCR analysis of the 26 mutants, which were induced in the present study, are schematically shown in Table 2. The PCR analysis indicates that a characteristic of the carbon ion-induced mutations was that large structural alterations were induced at similar frequency with point mutations.

The sequence analysis of carbon-ion-induced *gl1-3*, *tt4*(C4), and *ttg1-21* mutants revealed that inversions or translocations were accompanied with short deletions at the breakpoints. Furthermore, the inversion or translocation was found to be originated from recombinations between short homologous ends, indicating an involvement of non-homologous end joining (NHEJ) pathway for rejoining double strand breaks. It was found that all of the carbon ion-induced point mutations contained a short deletion.

From the present study, it was hypothesized that the characteristics of the mutation induced by carbon ions were the high mutation rate and the high frequency of inducing null mutations at a single gene. To verify this hypothesis, an analysis of the carbon ion-induced deletions, a comparison of the frequencies of the type of mutations induced by carbon ions with that of electrons, and analyses of deletions and point mutations induced by electrons will be needed.

References

[1] G. Kraft et al., Radiat. Environ. Biophys., 31, 161, 1992.

[2] U. Hagen, Radiat. Environ. Biophys., 33, 45, 1994.

[3] D. T. Goodhead, (1995), Radiat. Environ. Biophys., 34, 67, 1995.

[4] H. H. Smith, pp75-93 in *Induced Mutations and Plant Improvement*, 1972.

[5] E. Bruggemann et al., Plant J., 10, 755, 1996.

[6] M. Mei et al., Adv. Space Res., 10, 363, 1994.

[7] N. Shikazono et al., Genes Genet. Syst., 73, 173, 1998.

[8] A. Tanaka et al., Int. J. Radiat. Biol., 72, 121, 1997.

[9] A. Konieczny, A. and F. M. Ausubel, Plant J., 4, 403, 1993.

Table 1. Mutation rates of carbon ions and of electrons

Mutagen	Mutant group (loci)	Number of M1 seeds sown	Total number of M2 plants	Number of mutants in M2	Average mutant frequency/ locus ($X10^{-3}$)	Mutation frequency/ locus/ diploid cell/ dose (Gy) ($X10^{-6}$)
Carbon ions (150 Gy)	*tt3, tt4, tt5, tt6, tt7, ldox, (ttB)*	26200	104088	62	0.09	2.6
	gl1, gl2, gl3, ttg1	26200	104088	26	0.06	1.9
	hy1, hy2, hy3, hy4, hy5, hy6	14400	52407	23	0.07	2.3
Electrons (750 Gy)	*tt3, tt4, tt5, tt6, tt7, ldox, (ttB)*	9600	44026	4	0.01	0.08
	gl1, gl2, gl3, ttg1	9600	44026	7	0.04	0.25
	hy1, hy2, hy3, hy4, hy5, hy6	9600	44026	6	0.02	0.14

Table 2. PCR analysis of carbon ion-induced mutations

locus	point-like mutations	large structural alterations	
		rearrangements	total deletions
tt3	1	0	0
tt4	4	1	1
tt5	2	1	0
tt6	1	1	1
ldox	2	0	1
ttg1	2	2	0
gl1	1	1	4
total	13	6	7

2.7 Mutation Induction with Ion Beam Irradiation in Rose

H. Yamaguchi , S. Nagatomi , A. Tanaka*, N. Shikazono* ,
T. Morishita and K. Degi
Institute of Radiation Breeding, NIAR, Department of Radiation Research for Environment and Resources, JAERI *

1. Introduction

A combined method of gamma ray irradiation with in vitro culture is valid to enhance mutation frequency. In ion beams, its application is also effective. Nagatomi et al. reported that the specific flower color mutants in chrysanthemum, which were not obtained by gamma rays, were induced with this method[1-2].

In vitro culture enabled to originate a plant from single cell. Consequently, in using this technique, chimera-formation is avoided and solid mutants can be obtained. However, it is difficult to apply this technique to some species and some varieties.

The cutting-back has also been used for the production of solid mutant and some mutants are obtained with this method in some crops. This method is available for various vegetatively propagated crops.

In this study, we investigate the efficiency of mutation induction by means of a combined method of ion beam irradiation with the cutting-back in using rose.

2. Materials and Methods

Rose cultivar 'Orange rosamini' treated sterilely was used for this study. Stems were cut in one node with one bud and plated on MS media supplemented with 2mg/l BA, 0.01mg/l NAA, 2% sucrose and 0.9% agar. They were irradiated with various doses of accelerated ion particles, $^{4}He^{2+}$(100 MeV, 20 nA), $^{12}C^{5+}$(220 MeV, 0.02 nA), and $^{20}Ne^{8+}$(350 MeV, 0.02 nA) using an AVF Cycrotron in JAERI and with various doses of gamma rays. After irradiation, buds were plated on new media. The number of survival buds was investigated 2 month after irradiation.

Elongated shoots from C ion irradiated buds were cut in a short stem with a few buds and then plated on new media. Afterwards, newly elongated shoots from those buds were treated likewise. After plants raised were rooted and acclimated, the mutants were investigated for visible trait in applying the cutting-back.

3. Results and Discussion

The influence of ion beam irradiation and gamma rays on rose buds was showed on Fig 1. In He ion beams, the survival ratio decreased with increasing dose and the median lethal dose (LD50) was estimated 50-75Gy. The survival ratio also decreased with C ion beam irradiation. However, the relation between irradiation dose and survival ratio was not apparent. Ne ion beams irradiation did not affect on survival. These results were probably due to the penetration of beams.

In plants derived from eighty-eight buds irradiated C ion beams, the effects of mutation induction were investigated. Mutations were observed in plants derived from twelve irradiated buds (Table 1). Mutations were observed not only in higher doses but also in lower doses, 5 Gy, with which the influence of irradiation was hardly observed. Mutants in flower color, in the number of petals and in flower shape were selected. Drastic mutation

which observed in flower color in chrysanthemum could not be observed.

We investigate further the efficient irradiation dose for the obtainment of mutants and the effect of He ion beams on mutation induction.

References

1) S. Nagatomi et al., Breed. Sci.,46(Suppl.1),62,1996

2) S. Nagatomi et al., Breed. Sci.,48(Suppl.1),200,1998

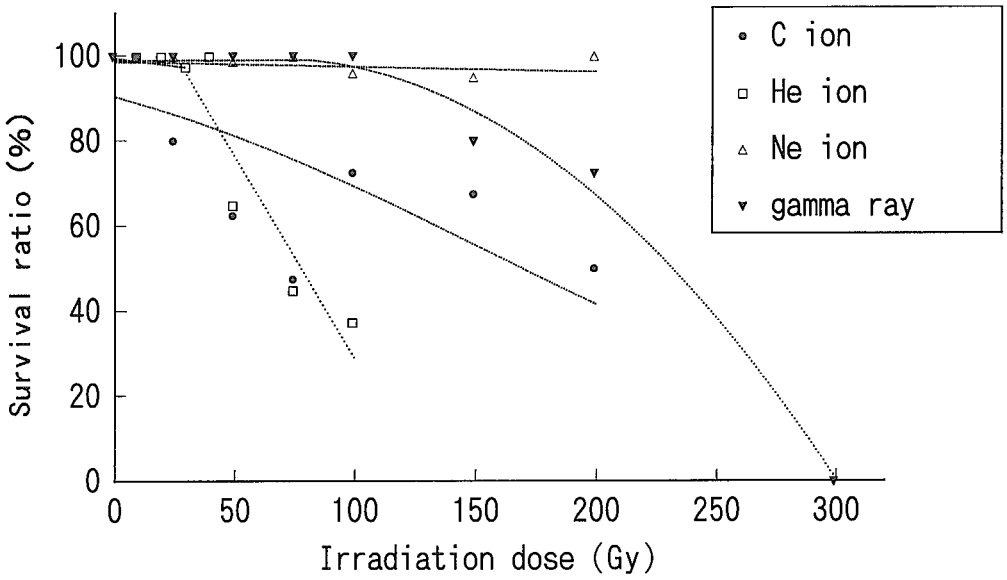


Fig.1 The influence of ion beams and gamma rays on rose buds.

Table 1 The number of buds obtained mutants with C ion beam irradiation.

Dose (Gy)	No. of irradiated buds	No. of buds obtained mutants
100	7	2
70	10	1
50	12	0
40	11	1
30	11	0
20	10	0
10	10	1
5	17	7

2.8 Mutation breeding using ion-beam irradiation in Aster

T.Baba[1], F. Nakamura[1], H. Nishi[1], S.Haraguchi[1], A.Tanaka[2], N.Shikazono[2] and H.Watanabe[2]
Fukuoka Pref. Federation of Agricultural Co-operative Association.[1]
Department of Radiation Research for Environment and Resources, JAERI[2].

1. Introduction

Aster belongs to a group of the chrysanthemum family and is cultivated for important cut flower in Fukuoka. Ion beams have higher LET (linear energy transfer) than gamma rays and X rays. Nagatomi et al[1) 2)], have reported that specific chrysanthemum mutants such as complex and stripe flower color mutants were induced by a combined method of ion-beam irradiation with *in vitro* culture, which were not induced by gamma rays. We expect that ion beam irradiation will be a new mutation- breeding method for many horticultural plants.

We supposed that ion beam induced specific mutation not only flowers color but also flower shape. The purpose of this study is to investigate the effects of ion beam on the mutant of flower shape.

We obtained results from our previous experiments[3)] showed threshold of injury of explants was at 10Gy with carbon ion and at 5-15Gy with helium ions.

In this paper, we report the effects of ion beam on shoot regeneration from the irradiated explants of leaf of aster.

2 . Materials and Methods

Aster cultivar, 'Yae - purple' of A. *hybrida Hort* (purple color and double flower) was used in this study. The explants of leaf was placed in petri dish containing M S media (Murashige and Skoog) supplemented with 2mg/l benzylaminopurine (BA), 1mg/l naphtalene acetic acid (NAA), 30g/l sucrose and 2g/l gellan gum for callus induction. The samples covered with Kapton film were irradiated with 220MeV carbon and 50MeV helium ion beams from the TIARA AVF cyclotron. After irradiation, the sample was transferred to the same fresh callus induction medium and was incubated under dark place at 25 ℃ for 7 days,and then incubated under 2500~3000 lux at 25℃. The cultured callus was transferred onto MS medium supplemented with 0.3mg/l BA, 15g/l sucrose, and 2g/l gellan gum in order to induce shoot regeneration. We investigated number of shoot regenerated from the irradiated explants of leaf.

3. Result and Discussion

Fig.1 shows rate of shoot regeneration induced from callus. In the case of carbon, shoot regeneration was rapidly decreased at higher than 5Gy, and was almost suppressed at higher than 10Gy. In the helium, they were decreased as dose increased and was suppressed at 20Gy. Effect of ion-beam on the number of shoot induced from an explant was shown in fig.2. At 5Gy, the shoot number of both carbon and helium ion was not different from control (0Gy). But at higher 10Gy, they were rapidly decreased and were almost suppressed at 20Gy.

Previous reports showed that callus well induced from the irradiated explains at 10Gy with carbon and helium ion, respectively, however, this data (fig.1,2) showed shoot was not well regenerate from callus at higher 10Gy.

These results suggest that dose to obtain mutants efficiently is 5-10Gy with carbon and helium ion .

References

1) S.Nagatomi, A.Tanaka, A.Kato , H.Watanabe and S.Tano, TIARA Annual Report 5:50-52(1996)
2) S.Nagatomi, A.Tanaka, H.Watanabe and S.Tano, TIARA Annual Report 6:48-50(1997)
3) T.Baba, S.Tanaka, S.Haraguchi, A.Tanaka, N.Shikazono and H.Watanabe TIARA Annual Report 2:48-49(1999)

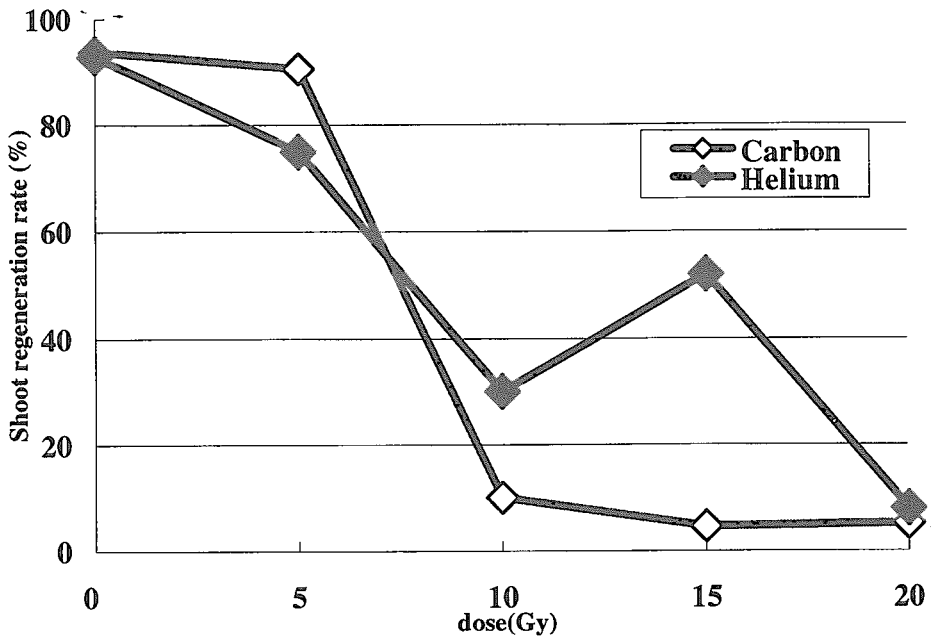


Fig.1 Effect of carbon and helium ion beam on shoot regeneration rate of sion callus

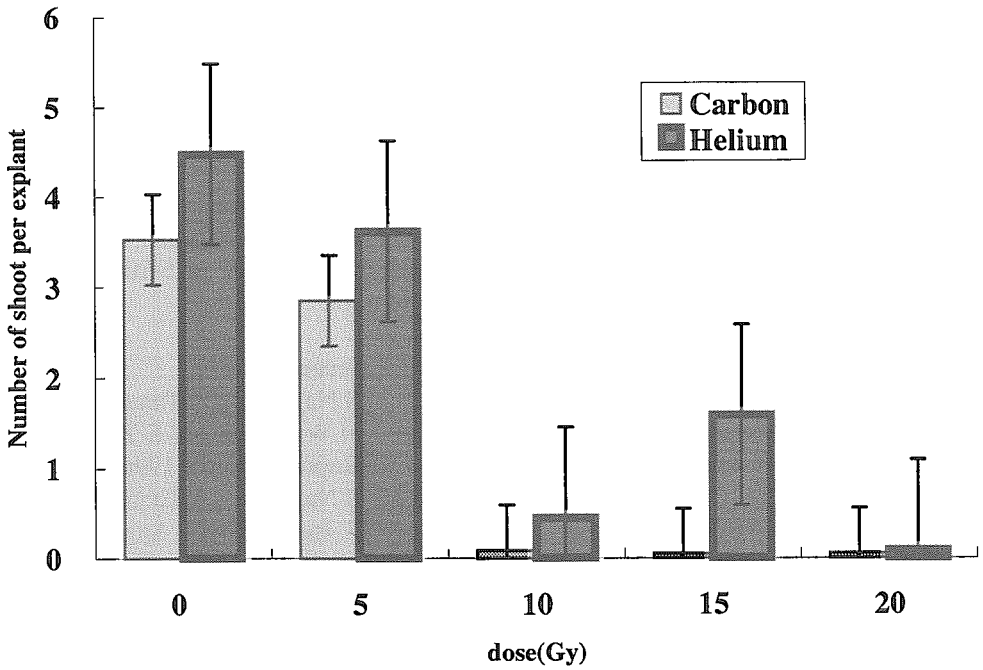


Fig.2 Effect of carbon and helium ion beam on shoot number per an explant

2.9 Removal of Pollutants by Mutant Strains of Microorganisms Induced by Ion-Beam Irradiation —— Fixation of CO_2 by Microalgae ——

M. Takigami, Nguyen T. B., T. Ito, H. Ito, S. Hashimoto
Department of Radiation Research for Environment and Resources, JAERI

1. Introduction

Pollutants accumulated in the circumstances are matters of utmost concern by the public. Generally speaking, pollutants in restricted area are treated by chemical and physical methods; on the other hand, pollutants spread in the circumstances are treated by biological methods, bioremediation. Pollutants that are accumulated in the circumstances mean that they are compounds difficult to be decomposed by common microorganisms. Therefore, efforts were made to find out effective microorganisms to decompose or fix them and trials were carried out to induce mutant strains of microorganisms. As we had found that the ion-beam irradiation to microorganisms was an effective method to induce mutation to microorganisms[1,2], some kinds of microalgae were irradiated with ion-beams. Using the mutant strains, fixation of CO_2 was examined.

2. Experimental

Microalgae

Microalgae subjected to the experiments were *Chlamydomonas reinhardtii* C-9 and *Chlorella vulgaris* C-135.

Preparation of Samples for Irradiation

C. reinhardtii C-9 and *C. vulgaris* C-135 were incubated in C medium (pH 7.5) and 1/2 MC medium (pH 6.0), respectively, at 20℃ for 6 days under illumination of 4500 lux.

Microalgae were filtered with membrane filters with a pore size of 0.45 μm, the membrane filters were put on small piece of agar gel, and wrapped with polyvinylidene chloride film.

C^{5+}-Irradiation

Samples were irradiated with C^{5+} beams (220 MeV) at room temperature changing dose from 100 Gy to 1000 Gy. After irradiation, the samples were kept at 4 ℃ for 2 days until the radioactivity of the samples decreased to a background level.

Inoculation and Incubation of Samples

The irradiated samples were suspended into medium and inoculated onto agar plates. The plates were incubated at 20 ℃ under illumination in sample bags which contain air, 10 % or 50 % carbon dioxide. After one week, the number of colonies was counted and survival fraction, N_i/N_0, was calculated, where N_i and N_o were number of colonies in irradiated and unirradiated samples, respectively.

Screening of Mutant Strains

The screening of mutant strains was carried out as follows. The survived colonies of microalgae were inoculated on the agar plates and incubated under illumination at 20℃ in a sample bag containing 100% carbon dioxide. The survived colonies were incubated in the medium broth after adjusting the pH value of the broth to 3.7 at 20℃ under illumination. The strains which grew well in the medium with low pH value were subjected to the following experiments.

Incubation of Mutant Strains

The screened mutants were inoculated into a fresh medium. The initial OD values of the medium were the same for all the strains. Then they were incubated at 20 and 30℃ under illumination of 4500 lux with a flow rate of 25 ml gas/min/100 ml medium broth. The

gas was composed of CO_2 and air. The rates of CO_2 in the gas were 0, 30 and 50 %.

3. Results and Discussion

Survival fraction decreased with increase of dose in the same manner regardless of the species of microalgae and concentration of carbon dioxide as shown in Fig. 1.

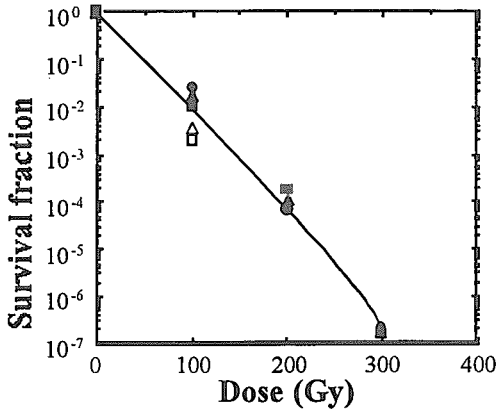


Fig. 1 Survival curves for microalgae irradiated with C^{5+} ion-beams. Open and closed symbols are for *C. reinhardtii* C-9 and *C. vulgaris* C-135, respectively. Microalgae were incubated in : ○,●: air; △,▲: 30% CO_2; ■□: 50% CO_2

While colonies from parent strains did not survive in carbon dioxide atmosphere, colonies from irradiated samples survived in high ratio as shown in Fig. 2. Therefore, it can be said that C^{5+}-irradiation to microalgae induces mutation. Although the relation between dose and mutation is not definite because of the lack of the number of colonies examined, there was a tendency that the higher the dose, the higher the mutation ratio.

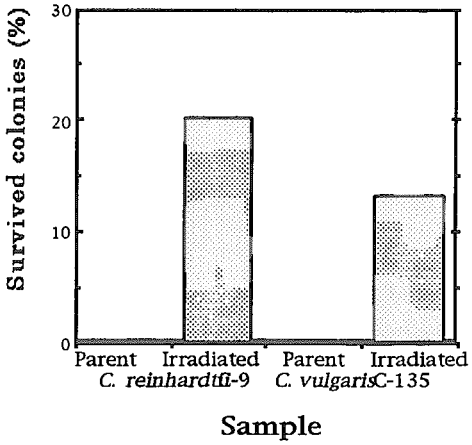


Fig. 2 Survived colonies of microalgae incubated in CO_2 atmosphere (≒100%)

The parent and mutant strains were incubated at 30℃ in various atmosphere with different concentration of CO_2 and the results are shown in Fig. 3 and 4. The rate of growth at 20℃ was much less than that at 30℃. All the strains grew better when incubated in 30% CO_2 than in air. OD_{750} of mutant strain of *C. reinhardtii* C-9 was higher than that of parent strain by 40-50% when incubated in 30% CO_2 at 30℃.

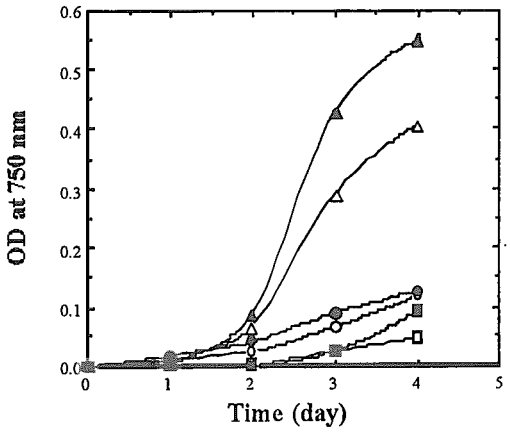


Fig. 3 Growth curves for *C. reinhardtii* C-9 incubated at 30℃. Open and closed symbols are for parent and mutant strains, respectively. Captions for the symbols are the same with those shown in Fig. 1.

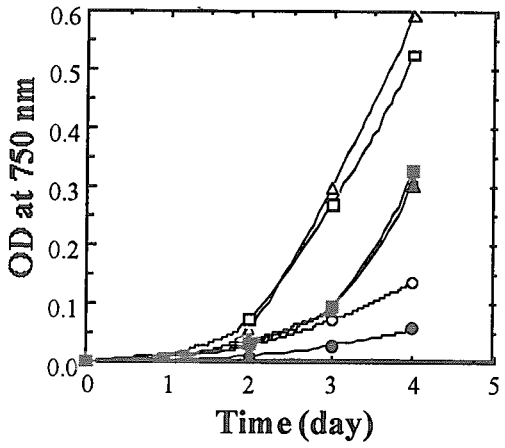


Fig. 4 Growth curves for *C.vulgaris* C-135 incubated at 30℃. Captions for symbols are the same with those shown in Fig. 3.

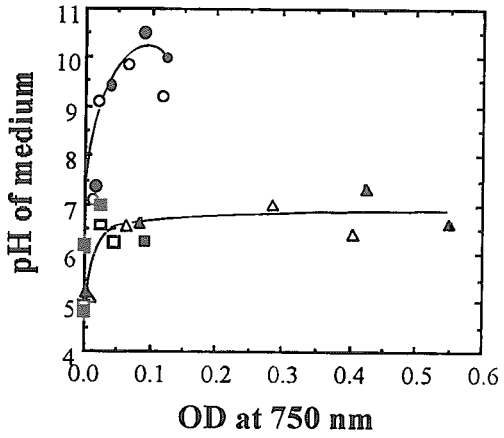


Fig. 5 Relation between OD at 750 nm and pH value of medium when *C. reinhardtii* was incubated at 30℃. Captions are the same for those shown in Fig. 3.

The relation between OD at 750 nm and pH value of medium for *C. reinhardtii* C-9 incubated at 30℃ is shown in Fig. 5. pH value increased with the increase of OD regardless of the strains. The result at 20℃ was almost the same with that at 30℃. Only the concentration of CO_2 affected pH of medium.

Although the details are not clear yet, some mutant strains show interesting characteristics. For example, one strain can survive in the atmosphere with high concentration of carbon dioxide, another strain can grow very fast in the air compared to the parent strains. Therefore, it is possible to say that ion beam irradiation is an effective method to induce mutation to microalgae.

References

1) N. Sermkiattipong, M. Takigami, S. Pongpat, O. Sukusudej, S. Charoen and H. Ito, Biocontrol Sci., 4(2), 109(1999)

2) A. Amsal, M. Takigami and H. Ito, Food Sci. Technol. Res., 5(2), 153(1999)

2.10 Use of a collimated heavy ion microbeam for irradiating mammalian cells individually to study the effect of high-LET single ion irradiation

Y. Kobayashi, M. Taguchi, S. Wada*, T. Funayama, T. V. Khoa, T. Kamiya, H. Watanabe and K. Yamamoto
Department of Radiation Research for Environment and Resources, JAERI
*Department of Veterinary Medicine, Kitasato University

1. Introduction

In recent years there has been an increasing interest in the use of microbeams in radiobiological research. The use of a heavy ion microbeam provides a unique way to control the number of ions traversing individual cells and localization of dose within the cell. High-LET heavy ions transfer their energy to biological organisms through high-density ionization and excitation along the ion track even by uniform irradiation.

At the very low fluences of occupational and environmental radiation exposure, individual cells only rarely experience traversals by a densely ionizing particles. The time intervals between the tracks on the individual cells may be much longer than the cell cycle or even longer than the turnover time. However, the biological radiation effects of exactly one particle are unknown because of the *Poisson* random distribution of tracks. One approach is to select cells with the desired exposures from a randomly irradiated population.

Using conventional track segment broad-field irradiation methods and sophisticated ion track recording techniques, the position of the target cells and the ion tracks can be measured together. However, this conventional approach is not practical, because it is required to measure all response of many cells that do not contribute to the aim of the irradiation experiment.

Microbeam will be able to overcome this limitation by delivering exactly counted number of ions per cell nucleus[1-3]. Furthermore, the microbeam allows highly localized irradiation of each cell. By local irradiation of a part of the nucleus or the cytoplasm using microbeam techniques, the dynamics of cellar repair and the intra-cellular process of functions such as *apoptosis* will be analyzed[4,5]. And through the irradiation of the immediate neighbor cells of a given cell, the cell to cell communication such as " bystander" effects, radiation effects of heavy ions transmitted from irradiated cells to neighboring un-irradiated cells, will be investigated directly[6,7].

Therefore, to study the distinct radiobiological effects of heavy ions, we are making an attempt to deliver a single or precise numbers of heavy ions with a spatial resolution of a few microns using our heavy ion microbeam apparatus at JAERI-Takasaki.

2. Delivery of counted heavy ions

The heavy ion microbeam apparatus has been installed under a vertical beam line of AVF-cyclotron, which provides 12.5 MeV/u $^{4}He^{2+}$, 18.3 MeV/u $^{12}C^{5+}$, 13.0 MeV/u $^{20}Ne^{7+}$ and 11.0 MeV/u $^{40}Ar^{13+}$ ions. These relatively high-energy heavy ions can be detected with a plastic scintillator and a photomultiplier tube (PMT) after they have passed through the biological samples to be irradiated.

Figure 1. shows a schematic diagram of the principle connections between the inverted microscope control system for sample targeting and beam shutter control system for

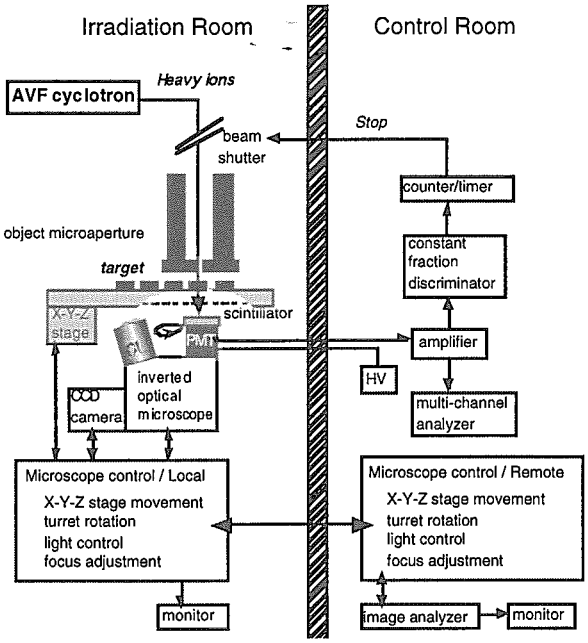


Figure 1. Schematic diagram of the connections between inverted microscope at the end of vertical beam line for sample observation and targeting, and the beam control system for delivery of counted heavy ions.

delivery of counted heavy ions. The desired irradiation point on biological sample was aimed to the beam position (end of the microaperture) viewed through object lens by remote controlling the X-Y-Z stage of the inverted microscope.

Then the object lens was replaced with a plastic scintillator and a photomultiplier tube (PMT) assembly mounted on the microscope turret. The collimated ions were detected with the PMT assembly after passing through a target cell and a 100 μm thick nuclear track detector CR-39 that is used for the evaluation of the targeting accuracy. The energy spectrums of collimated ions were measured with a multi-channel analyzer by detecting of scintillator light pulses. The number of ions traversed the sample were counted with a constant fraction discriminator and a preset counter/timer. Every irradiation was terminated by the action of beam shutter, which was controlled by the preset counter/timer module or by manual. The number of ions can be determined also by microscopic counting of etched CR-39 film exposed to the ion beams at the sample position. The exposed CR-39 film was developed by etching in 6 M NaOH at 60°C for about 0.5 to 1 hr, depending on the LET value of the penetrated ions.

To investigate the transformational and mutational events caused by a single ion irradiation, at least 10^3–10^4 mammalian cells need to be irradiated at one experiment, and those cells can not survive the exposure to the atmosphere more than 15 minutes. Therefore, we have introduced an automated target recognition system and a single ion hit system that controls beam choppers as a fast beam switch to achieve rapid targeting of mammalian cells and rapid delivery of precise numbers of heavy ions.

The target recognition system is installed to the off-line microscope in the Control Room (sample preparation room) to obtain positional data of individual cells in a short period before irradiation. Subsequently these cells are to be automatically targeted next to next on the X-Y-Z stage of the microbeam apparatus in the Irradiation Room according to the previously obtained positional data. This work is currently in progress to upgrade the cell recognition algorithm.

3. Dose response curves of mammalian cells

As a preliminary experiment, Chinese hamster ovary (CHO) cells were exposed to the broad-field heavy ions provided from the AVF cyclotron with a dose rate of about 0.1 Gy/sec using the vertical beam line at the HY1 port. Scanned beams of 50 MeV $^4He^{2+}$ (LET = 14 keV/μm), 220 MeV $^{12}C^{5+}$ (116 keV/μm), 260 MeV $^{20}Ne^{7+}$ (420 keV/μm), and 460 MeV $^{40}Ar^{13+}$ (1800 keV/μm) ions were used, Cells were maintained in F-12 medium supplemented with 10% fetal bovine serum (FBS) at 37°C in a humidified 5% CO_2 incubator. About 5-7 days after the irradiation, colonies of the cells were stained and counted to calculate surviving fractions.

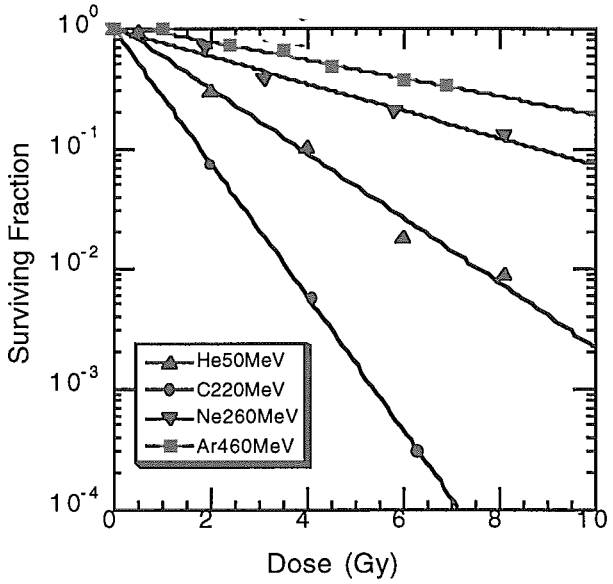


Figure 2. Survival curves of CHO cells exposed to "broad-field" $^{4}He^{2+}$, $^{12}C^{5+}$, $^{20}Ne^{7+}$ and $^{40}Ar^{13+}$ ions.

Figure 2 shows the dose response curves of CHO cells irradiated randomly with heavy ions in a "broad-field" way. Particle fluences were determined using a track detector CR-39 by counting the number of ion tracks after chemical etching. LET values were calculated with ELOSS code developed in JAERI. To convert particle fluences to doses in Gy, the following relationship was used: Dose [Gy] = 1.6 x 10^{-9} x LET [keV/μm] x Fluence [p/cm^2]. The survival fractions plotted against the given doses were almost linear in logarithmic scale and showed no shoulder.

The dose response curve for C ions irradiation (LET=116 keV/μm) was steeper than that for He ions (14 keV/μm), however other two curve for Ne and Ar ions with higher LET values (420 and 1800 keV/μm each) showed less lethal effect than He ions. This LET dependence of the cell lethality (RBE peak) has been ascribed to the "clustered damage" or specific irreparable DNA damage which can be introduced most effectively at the LET value around 100-200 keV/μm.

The decrease in RBE for Ne and Ar ion irradiation may be the result of "overkill" effect with higher LET values. However, the *Poisson* random distribution of ion hit on the target may cause the decrease of lethality. From the track structure model, the penumbra size of these ion tracks was estimated at about 10-20 μm in diameter, which is similar to the size of cellular nucleus. The survival fractions of CHO cells which was irradiated with particle fluences that gives "probability" of being penetrated by only one ion in their nucleus were estimated from Figure 2. at about 87% for Ne ions and 69% for Ar ions; those are close to that for C ions, 92%.

Does single hit of high-LET heavy ions in nucleus really kill the cell? This question will soon be answered.

References

1) C. R. Geard, D. J. Brenner, G. Randers-Pehrson, and S. A. Marino, *Nucl. Instr. and Meth.* **B54**, 411-416 (1991)
2) L. A. Braby, *Scanning Microscopy*, **6**, 167-175 (1992)
3) M. Folkard, B. Vonjnovic, K. M. Prise, A. G. Bowey, R. J. Locke, G. Schettino, and B. D. Michael, *Int. J. Radiat. Biol.* **72**, 375-385 (1997)
4) R. C. Miller, G. Randers-Pehrson, C. R. Geard, E. J. Hall, and D. J. Brenner, *Proc. Natl. Acad. Sci. USA*, **96**, 19-22 (1999)
5) L.-J. Wu, G. Randers-Pehrson, A. Xu, C. A. Waldren, C. R. Geard, Z. L. Yu, and T. K. Hei, *Proc. Natl. Acad. Sci. USA*, **96**, 4959-4964 (1999)
6) K. M. Prise, O. V. Belyakov, M. Folkard and B. D. Michael, *Int. J. Radiat. Biol.* **74**, 793-798 (1998)
7) H. Zhou, G. Randers-Pehrson, C. A. Waldren, D. Vannais, E. J. Hall, and T. K. Hei, *Proc. Natl. Acad. Sci. USA*, **97**, 2099-2104 (2000)

2.11 Fate mapping of the cellular blastoderm stage egg of the silkworm, *Bombyx mori*, by localized irradiation of heavy ion microbeams

K. Kiguchi*, Y. Kinjoh*, K. Masahashi*, Z. T. Tu*, H. Tamura*, K. Shirai*, K. Kanetatsu*, Y. Kobayashi**, M. Taguchi**, and H. Watanabe**

*Faculty of Textile Science and Technology, Shinshu University,

** Department of Radiation Research for Environment and Resources, JAERI.

1. Introduction

A collimated heavy ion microbeam apparatus has been installed under the vertical beam line of an AVF-cyclotron at JAERI-Takasaki as part of an experimental system designed to develop a novel cell surgery technique by local irradiation of living organisms with targeted heavy ion beams [1-2]. The use of heavy ion microbeams is expected to be extremely helpful to inactivate nuclei or cells in the irradiated region.

Prior to and in conjunction with use of this system, accurate fate maps will be necessary for analysis and correct interpretation of the results obtained from various types of developmental experiments using the silkworm, *Bombyx mori*. Although several fate maps of *Bombyx mori* have already been established [3-5], none of them are adequate for the cellular blastoderm stage eggs. In previous reports[6], we showed that spot irradiation of heavy ions aimed at the cellular blastoderm stage eggs caused abnormal embryos, which showed localized defects such as deletion, duplication, and fusion, depending on the dose and site of the irradiation. We also showed that the location and frequency of the defects correlated closely to the site of irradiation. In this experiment, we tried to establish a detailed fate map, based on the correlation between the site of irradiation and the site of defects in the resultant larval cuticle, of the *Bombyx* eggs at the cellular blastoderm stage.

2. Materials and Methods

Larvae of the *pnd* (pigmented non-diapausing) mutant were routinely reared on a commercial artificial diet (Yakult Inc.). Egg collection was performed on a polyester film every 20 minutes. The eggs were kept at 25℃ and subjected to ion beams at the cellular blastoderm stage (11–12 hrs after oviposition). A total of 111 points of the eggs (Fig.1) were locally irradiated with 500

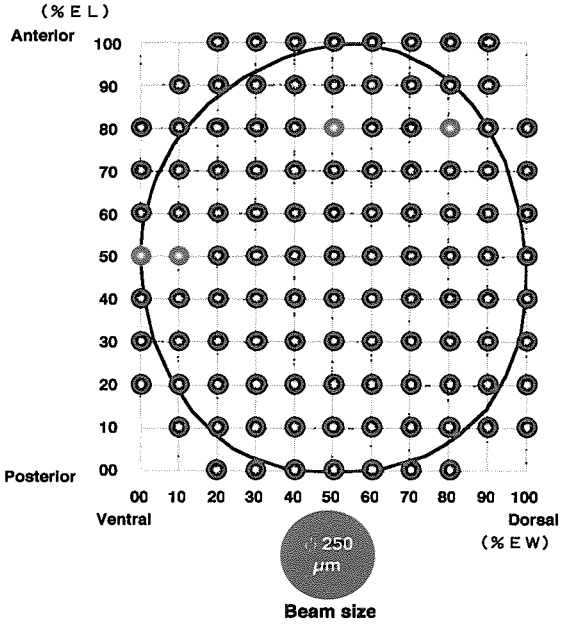


Fig. 1 An illustration showing the sites of spot irradiation by heavy ion microbeams.

Gy of carbon ion microbeams ($^{12}C^{5+}$; 18.3 MeV/u; range in water = 1.2mm) using a 250 μmϕ aperture. After irradiation, the treated eggs were kept in a moist chamber at 25℃ to allow embryonic development for 10-12 days. Hatched larvae were fixed in glycerol-acetic acid (1:4) for a few hrs at 60℃. The chorion of unhatched larvae was removed with a surgical knife, then fixed in the same manner as that used for the hatched larvae. Then the morphology of the resultant larvae was carefully examined under a dissecting microscope. Based on the pooled data of the sites of irradiation and sites of induced defect, presumptive regions were located and a fate map was prepared according to the method previously described [5].

3. Results and Discussion

(1) Relationship between beam size and area of defect induced

To determine an appropriate beam size of irradiation for fate mapping, heavy ions were irradiated to the center (50% of the total egg width / 50% of total egg length: 50/50) of the cellular blastoderm stage eggs using apertures of various sizes. None of larvae that developed from the eggs irradiated with small beams of 60 and 90 μmϕ showed cuticle defects. The defect frequency was less than 50 % when the beam size was smaller than 180 μmϕ, while it was higher than 90% when the beam size was larger than 200 μmϕ. In addition, the center of the defective regions was always the posterior part of the 3rd larval segment, irrespective of beam size (Fig. 2). Therefore, we adopted the beam size of 250 μmϕ for fate mapping.

(2) Preparation of a fate map

Among a total of 111 center points irradiated

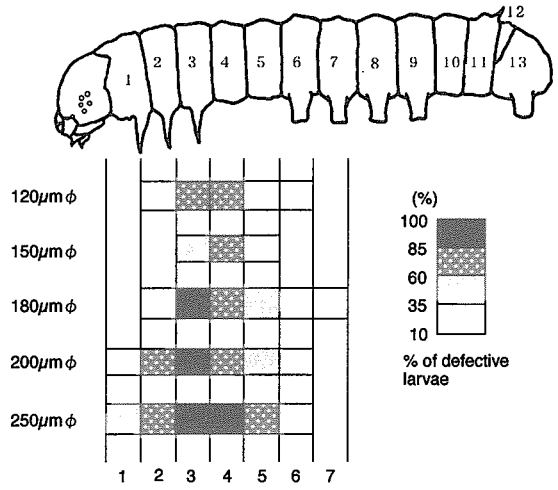


Fig. 2 Relationship between beam size and the defective region.

with 250 μmϕ (Fig.1), only the positions inducing defective cuticles are shown in Fig. 3. When eggs were irradiated near the anterior(85-100%EL), posterior (0-15%EL), or dorsal periphery (83-100EW), no defective larvae were observed. These areas are considered to be the presumptive extra-embryonic region, while the rest of the egg surface can be considered as the presumptive embryonic region, for the larval cuticle. A close correlation was observed between the site of irradiation and the site of the defect induced. Head defects were induced only by irradiation at the anterior half of the egg, whereas defects in thoracic and abdominal segments were induced by irradiation at the middle and the posterior part of the egg, respectively.

Based on these correlations, a fate map of the *Bombyx mori* egg at the cellular blastoderm stage was established (Fig. 4). The fate map at the cellular blastoderm stage, established here by heavy ion microbeams, is almost identical to the previous map of the fertilization stage made by

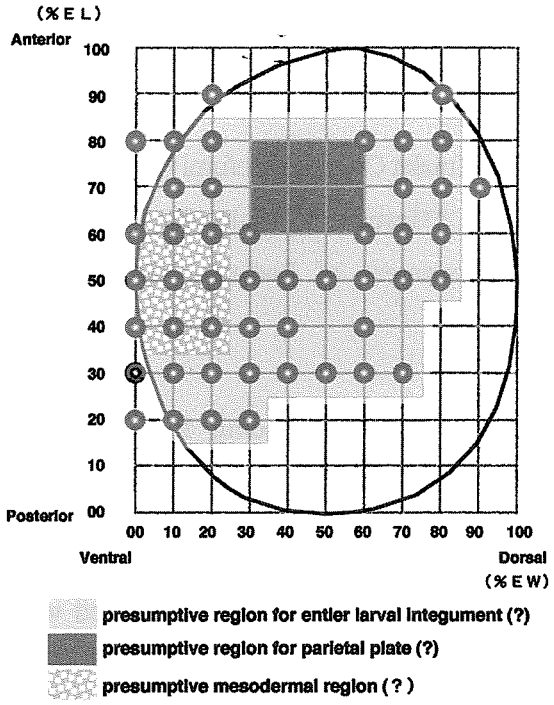


Fig. 3 An illustration showing the site where irradiation resulted in defective cuticles.

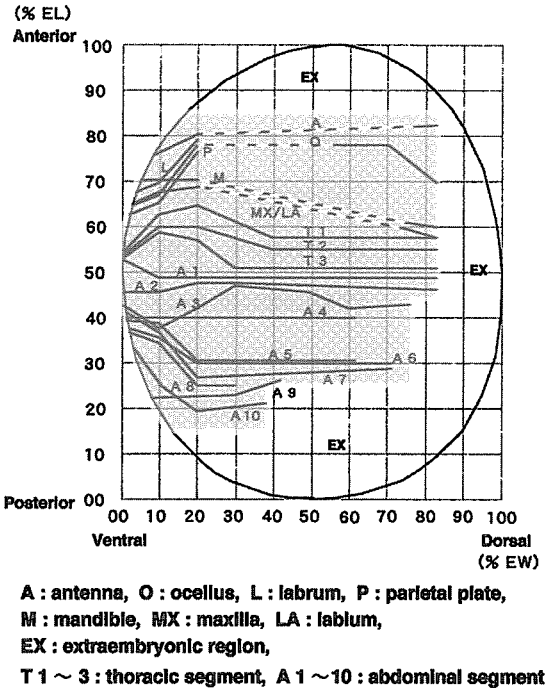


Fig. 4 A fate map of the *Bombyx* egg at the cellular blastderm stage.

UV-laser[5]. However, a few differences were observed between them; (1) the ventral region is regarded as the extraepidermal area in the laser map, while in the new map it is considered that the region contains the presumptive epidermal area, because irradiations on the ventral egg surface caused cuticular defects with high frequency, (2) the new fate map is considerably distorted compared with the laser map, probably due to the active cell division and movement at the stage of irradiation.

The fate map established here offers an essential basis necessary not only for understanding of the study on embryogenesis, but also for analyses of biological effects of heavy ions to eggs of the silkworm, *Bombyx mori*.

References

1) Y. Kobayashi, M. Taguchi and H. Watanabe , JAERI-Review, 97-015, 30-32 (1997).

2) Y. Kobayashi, M. Taguchi and H. Watanabe , JAERI-Review, 98-016, 27-29 (1998).

3) J. Kuwana and T. Takami, In Embryology of Invertebrates (eds. M.Kume and K.Dan), pp.287-343, Tokyo:Baifykan (1957).

4) M. Katsuki, A. Murakami and I. Watanabe, Zool. Mag., 89, 269-276 (1980).

5) M. Myohara, Development, 120,2869-2877 (1994).

6) K. Kiguchi, S. Yamasaki, Y. Kobayashi and H. Watanabe, JAERI-Review, 97-015, 45-47 (1997)

2.12 Morphological analysis of apoptosis-like cell death induced by ion beam irradiation in plant cells

Maki Kawai*,** Yasuhiko Kobayashi*,***, Yutaka Oono*, Hirofumi Uchimiya*,**
*Advanced Science Research Center, JAERI, **Institute of Molecular and Cellular Biosciences, University of Tokyo, ***Department of Radiation Research for Environment and Resources, JAERI

1. Introduction

Programmed cell death (PCD) is a process of self-directed death of specific cells and represents an important physiological process during growth and development of multicellular organisms. In plants, such events are characteristic of aerenchyma formation[1,2], developing tracheary cells, root cap cells, tapetum cell degradation, leaf senescence and other processes[3]. Several investigation have suggested parallels between PCD in plants and apoptosis[4], which is a specific type of PCD, in animal cells characterized by several morphological features. Although its importance is well known, very little is understood about the underlying cellular mechanisms of cell death in plants. In this regard, it is difficult to study developmentally regulated PCD because death is not synchronous and only occurs in a small number of cells.

In mammalian cells, apoptosis can be induced by radioactive rays such as X- or γ-rays. Such experimental models have contributed to our understanding of the molecular and cellular processes of programmed cell death. Here we report that a treatment of maize seedlings with ion beam ($^{20}Ne^{8+}$) causes apoptosis-like cell death, suggesting that this tool can serve as a effective mean of inducing PCD in plant cells.

2. Experiments

Maize (*Zea mays* L.) kernels treated with 10% sodium hypochlorite for 5 min were placed on 1% agar, followed by incubation at 23 ℃ under continuous illumination. Two-day-old seedlings on agar plates were irradiated with $^{20}Ne^{8+}$ (350 MeV) generated by the AVF cyclotron (JAERI) in the atmosphere. LET values and projectile ranges were calculated with ELOSS code developed by Japan Atomic Energy Research Institute (JAERI). All irradiations were carried out within 2 min at room temperature (25 ℃). After irradiation, seedlings were maintained at 25℃ under continuous light conditions and seminal roots were used for further analysis.

3. Results and discussion

To determine the biological effects of ion beam irradiation on two-day-old maize plants, we analyzed the root growth at 48 h after treatment. Irradiation resulted in a marked shortening of the relative root length as well as coleoptile, and such shortening was $^{20}Ne^{8+}$-dose dependent. Plant species are well known to be highly resistant to ionized

radiation compared to animal cells. Our results are consistent with these early findings, i.e., root elongation was not completely inhibited at 10 kGy.

During the early stages of apoptosis in animals, specific endonucleases attack nuclear DNA at the internucleosomal linker regions between nucleosomal cores, resulting in the production of low molecular weight oligonucleosomal DNA fragments, about 180 bp in size. To confirm whether or not radiation induced-growth defect of maize seedlings is associated with similar nuclear changes, we analyzed the irradiated plants for the appearance of DNA laddering. Roots of maize seedlings treated with different doses of Ne ions were used for DNA analysis. DNA fragmentation was observed at a relatively high dosage. Low molecular weight DNA fragments were noted at 100 Gy, and DNA laddering increased significantly with higher dosages.

To analyze the cytological changes induced by the irradiation, the seminal roots (5-mm long from the tip) of the seedlings (48 h after irradiation) were fixed and examined by DAPI staining. Chromatin condensation and fragmentation were identified in cells irradiated with 10 kGy. Further analysis showed that these morphological changes in nuclei appeared at 24 h after irradiation (data not shown).

The cellular structural changes observed in this study mimicked those of apoptosis in animal cells. Since necrosis is characterized by cell swelling and lysis associated with leakage of cellular contents, the observed ion beam-induced changes noted in our study does not represent necrosis but rather a cell death process that resembles apoptosis of animal cells.

In general, the irradiation dosage required to induce apoptosis of animal cells is < 10 Gy. Significantly, about 10-100 times higher dose was required for the induction of apoptotic changes in plant cells.

Since ion beam constitutes one form of higher LET ionizing radiation; it can deposit high energy on the target as opposed to low LET radiations such as electron beam, X- and γ-rays. Furthermore, it has been suggested that the ion beams cause clustered damage of DNA which is difficult to repair rapidly. Thus, the ion beam may be a useful alternative to low LET radiation such as X- and γ-rays as a powerful inducer of apoptosis-like cell death in plants.

References

1) M. Kawai et al. Planta 204, 277 1998
2) P. Samarajeewa et al. Planta 207, 354 1999
3) M. Kawai et al. Ann. Bot. in press 2000
4) M. Kawai et al. FEBS Lett. 464, 143, 1999

2.13 Breeding new shiitake(*Lentinula edodes*) variety at high temperature using ion beam irradiation

H. Akaishi, I. Narumi*, M. Kikuchi* and H. Watanabe*
Research and Development Division, Mori and Company, LTD,
*Department of Radiation Research for Environment and Resources, JAERI

1. Introduction

Shiitake(*Lentinula edodes* (Berkeley) Pegler) is the sort of edible mushroom widely cultivated in Japan, and it is possible to cultivate all the year round. However, it is difficult to produce the high quality mushroom in summer. Ion beams, which belong to high LET radiation, are considered to be an efficient mutagenic agents applicable to mutation breeding of shiitake. The present study were initiated aiming to obtain high quality mutant mushroom at high temperature by ion beam irradiation. In this paper, we report the ratio of monokaryon to dikaryon after helium ion beam irradiation to shiitake protoplasts .

2. Material and Method

(1) Protoplast isolation

Two cultivars, MIL1052 and MIL2212 of Shiitake(*Lentinula edodes* (Berkeley) Pegler) , were used in this study. To prepare protoplast from mycelium, the dikaryon was grown in GMY liquid medium(1% glucose, 0.4% yeast extract and 1% malt extract) at 25℃ for 7 days. After the incubation , the mycelium was harvested, washed 3 times with 0.6M mannitol solution by centrifugation at 5,000 rpm for 10 min, and then was incubated in an enzyme solution at 30℃ for 4 hr shaking at 200 rpm. The enzyme solution at pH 5.5 consisted of Cellulase(1.0%) and 0.6 M mannitol. The protoplasts were washed 3 times with 0.6 M mannitol solution by centrifugation at 2,000 rpm for 10 min.

The density of the protoplast suspension was adjusted to about 1 x 10^5 per ml for the following experiment.

(2)Irradiation

The protoplasts suspension was spread on SMY medium(0.6 M sucrose, 1% malt extract, 0.4% yeast extract and 1.5% agar) in a 3.5 cm petri dish. After being covered with Kapton film, the protoplasts were irradiated by ion beams from the AVF cyclotron in JAERI. The ion beam used was 50 MeV $^4He^{2+}$ with the dose of 25 Gy, 50 Gy and 125 Gy.

(3)Protoplast Culture

After irradiation, the protoplasts were incubated at 25℃ for 6 days. Colonies regenerated from protoplasts were transferred on GMY medium containig 1.5 % agar.

3. Results

Table 1 shows the isolation number of colonies regenerated from the protoplasts irradiated with helium ions. Isolation number of regenerated colonies in MIL2212 was 273 with the dose of 25 Gy, 327 with the dose of

50Gy and 113 with the dose of 125 Gy. The ratio of monokaryon to the isolation number was 7.7%, 11.3% and 19.5% with the dose of 25 Gy, 50 Gy and 125 Gy, respectively. Isolation numbers of regenerated colonies in MIL1052 was 276 with the dose of 25Gy and 9.4% of them were monokaryon. The ratio of monokaryon with the dose of 25 Gy in MIL2212 was almost the same as that in MIL1052. An increase in the ratio of monokaryon was dose-dependently observed. The cultivation experiment of strains selected is in progress.

References

1) H. Akaishi et al., TIARA Annual Report 98-016:58-59(1998)
2) H. Akaishi et al., TIARA Annual Report 99-025:57-58(1999)

Table 1 Isolation number of protoplast-derived colonies by helium ion beam irradiation.

Strain	Radiation	No. of colonies isolated		B/(A+B) (%)
		Dikaryon A	Monokaryon B	
MIL2212	He^{2+} - 25Gy	252	21	7.7
	He^{2+} - 50Gy	290	37	11.3
	He^{2+} - 125Gy	91	22	19.5
MIL1052	He^{2+} - 25Gy	250	26	9.4

2.14 Analysis of a brassinolide-insensitive mutant from *Arabidopsis thaliana* irradiated with ion beam

Y. Sasuga, K. Ichikawa*, R. Kuwano*, Y. Kobayashi*, Y. Oono**, Y. Kobayashi***, S. Tanaka and H. Takenaga*

Department of Bioscience, Tokyo University of Agriculture, *Department of Applied Biology and Chemistry, Tokyo University of Agriculture, **Advanced Science Research Center, JAERI, ***Department of Radiation Research for Environment and Resources, JAERI

1. Introduction

Brassinolide (BR), first isolated from pollen of rape (*Brassica napus L.*), bears a similarity in structure to animal steroid hormones. BR-like active substances, called brassinosteroids (BRs) collectively, are also found in a wide variety of plants. BRs show not only growth-modulating activity but also other various physiological effects on the growth and development of plants[1]. The mechanism of BRs actions, however, remains unclear. BR-deficient or insensitive mutants have provided valuable tools for research in the molecular mechanisms of BR.

Ion beam irradiation characterized by high linear energy transfer (LET) and relative biological effectiveness (RBE) is expected to be a new mutagen. Studies on the structural alteration of the DNA in ion-induced mutants demonstrated that ion beam irradiation causes large genetic changes, such as deletions, inversions, or translocations. Detection of polymorphism of genome DNA and genome subtraction have been used as efficient approach to identification of variant genome structure and as first step for positional cloning of genes of interest [2, 3]. Amplified fragment length polymorphism (AFLP) is a detection technique of polymorphism of DNA, which detect amplified fragments with high reproducibility[4]. Representational difference analysis (RDA) is an evolutional method of genome subtraction, which compare representation of the whole genome produced by whole genomic PCR[3].

A mutant brr1 (brassinolide resistant 1) was isolated from *Arabidopsis thaliana* after exposure of their dry seeds to 220 MeV carbon ions[5]. This mutant was capable of elongating the root in the presence of BR, whereas BR inhibited the root growth in wild type. The main objective of the present investigation was to evaluate AFLP and RDA for detection of the genomic structural alterations induced by ion beam irradiation.

2. Materials and Methods

1) Plant materials

A brr1 mutant was induced from wild type ecotype Columbia irradiated with carbon ions (220 MeV) to their dry seeds at TIARA. The mutant has been self-pollinated through 4 generations.

2) Genomic DNA extraction, AFLP analysis and RDA

Genomic DNA was extracted from 14-day-old plants using the method of cetyltrimethylammonium bromide (CTAB). AFLP was carried out following the protocol (Protocol for AFLP Mapping using Li-Cor Automated Sequencer). In brief, the genomic DNA was digested with *Eco*RI and *Mse* I. The digested DNA fragments were ligated with *Eco*RI and *Mse* I adaptors, and then amplified with pre-selective

primer and IRD-41 labeled selective primer. The selective PCR product was analyzed with Li-Cor autosequencer.

RDA was accomplished according to the manufacture's protocol (GeneFisher PCR Subtraction System, TaKaRa). The genomic DNA was digested with *Hind* III, and then ligated with R24/12 adaptor. The ligated DNA was amplified with R24 primer (whole genomic PCR). The PCR products were used for hybridization and amplify (kinetic enrichment). The enrichment products were subjected to 1.4% agarose gel electrophoresis for the further analysis.

3. Results and Discussion

1) Phenotype of brr1 mutant

M_4 seedlings of brr1 showed new dwarf phenotype (Figure 1 A and B). Namely, M_3 generation of brr1 only antagonized BR-induced retardation in root elongation, but dwarf mutants of the M_4 generation unexpectedly exhibited significant levels of resistance to BR in the aerial part as well as root. Thirty-day-old brr1 M_4 plants grew to the height of 2 cm or less, whereas wild type plants of the same age were greater than 20 cm in height (Figure 1 B). However, not all M_4 generation was the dwarf phenotype, almost showed non-dwarf phenotype. Dwarf and non-dwarf mutants of M_4 generation were observed to occur in a segregation ratio of 5 to 1. These results suggest the phenotypic changes in brr1 through 4 generations may be caused by multiple genes involved in the resistance to BR.

2) AFLP analysis and RDA

AFLP was used for positional cloning of genes responsible for the resistance to BR. The DNA fragments prepared from either brr1 or the wild type plants were amplified using 128 primer sets (Table 1). To detect fragments specific to brr1 mutant the fragments amplified were screened by comparison with the fragments from the wild type. Of 44 fragments identified, 40 fragments seemed to be derived exclusively from brr1 whereas the rest of them were from the wild type.

In an attempt to confirm that RDA is efficient in detecting structural alterations of DNA in ion-induced mutants, genomic DNA prepared from wild type were digested with *Hind* III and subtracted from those obtained from brr1 mutant. The whole genomic PCR products were composed largely of DNA fragments of 0.1 to 1.5 Kbp (Figure 2 A). The 5^{th} RDA products were electrophoresed on agarose gel to detect several major bands and no difference between 6^{th} and 7^{th} RDA products were detected, indicating that a series of 7 RDA was enough for subcloning (Figure 2 B). These results suggest that a combination of AFLP and RDA may be a useful technique of ion beam-induced mutant analysis, particularly of making of specific markers of chromosome. Further studies are now in progress to analyze F_2 population derived from a cross between brassinolide-resistant mutant brr1 and the wild type Columbia by means of AFLP as well as the absence of 7^{th} RDA fragments in genomic DNA of brr1 mutant by Southern blotting.

4. References

1) N. B. Mandava, Annu. Rev. Plant Physiol. Plant Mol. Biol., 39, 23-52 (1988)

2) A. Konieczny and F. M. Ausubel, Plant J. 4, 403-410 (1993)

3) N. Lisitsyn et al., Science 259, 946-951 (1993)

4) V. Pieter et al., Nucleic Acids Res., 23, 4407-4414 (1995)

5) Y. Sasuga et al., JAERI-Review 99-025, 59-61 (1999)

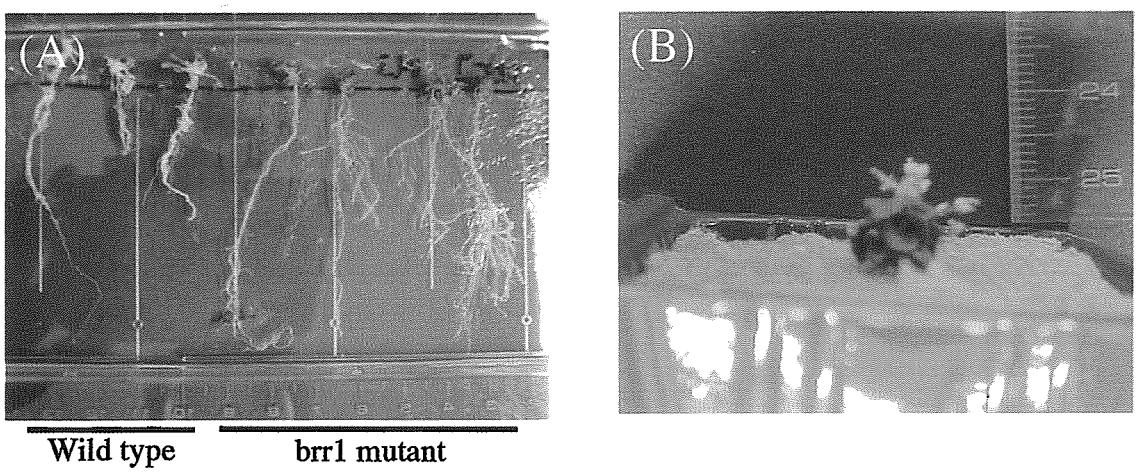


Figure 1. A dwarf phenotype of brr1 mutant of M4 generation. (A) Plants were grown on 1/2 MS medium containing 10^{-6} M brassinolide for14 days after germination. (B) A 30-day-old dwarf brr1 mutant.

Table 1. Genetic analysis of a brr1 mutant by AFLP.

IRD-41 labeled *Eco*RI primer

	M-CAA	M-CAC	M-CAG	M-CAT
E-ACA	1	2	3	4
E-ACC	5	6	7	8
E-ACG	9	10	11	12
E-ACT	13	14	15	16
E-AGA	17	18	19	20
E-AGC	21	22	23	24
E-AGG	25	26	27	28
E-AGT	29	30	31	32

IRD-41 labeled *Eco*RI primer

	M-CCA	M-CCC	M-CCG	M-CCT
E-ACA	33	34	35	36
E-ACC	37	38	39	40
E-ACG	41	42	43	44
E-ACT	45	46	47	48
E-AGA	49	50	51	52
E-AGC	53	54	55	56
E-AGG	57	58	59	60
E-AGT	61	62	63	64

IRD-41 labeled *Eco*RI primer

	M-CGA	M-CGC	M-CGG	M-CGT
E-ACA	65	66	67	68
E-ACC	69	70	71	72
E-ACG	73	74	75	76
E-ACT	77	78	79	80
E-AGA	81	82	83	84
E-AGC	85	86	87	88
E-AGG	89	90	91	92
E-AGT	93	94	95	96

IRD-41 labeled *Eco*RI primer

	M-CTA	M-CTC	M-CTG	M-CTT
E-ACA	97	98	99	100
E-ACC	101	102	103	104
E-ACG	105	106	107	108
E-ACT	109	110	111	112
E-AGA	113	114	115	116
E-AGC	117	118	119	120
E-AGG	121	122	123	124
E-AGT	125	126	127	128

Figures printed in red and blue letters indicate the primers of detectable DNA fragments characteristic of brr1 and wild type, respectively.

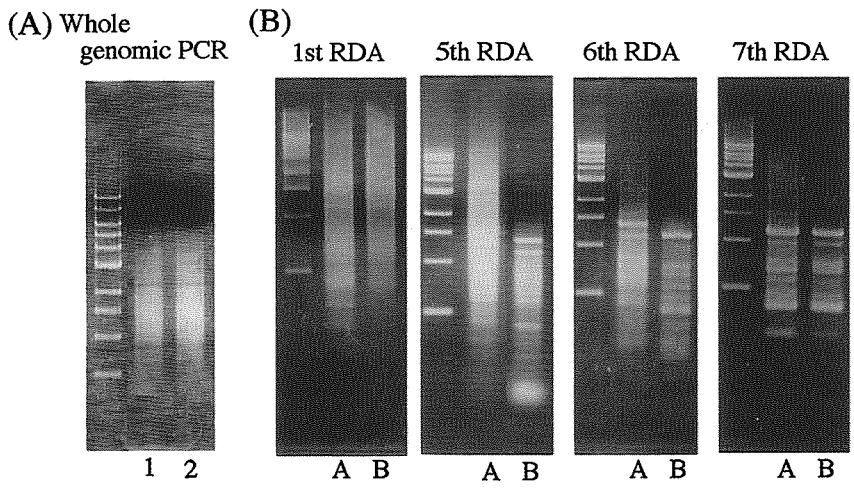


Figure 2. Agarose gel electrophoresis of amplicon DNA and RDA products.
Lane 1: wild type.
Lane 2: brr1.
Lane A: control.
Lane B: RDA product.
1Kbp DNA ladder was used as a size maker.

2.15 Study on Plant Responses to Environmental Pollutants

S. Matsuhashi, C. Mizuniwa, T. Ito, S. Hashimoto, N. S. Ishioka, S. Watanabe, A. Osa*, T. Sekine
Department of Radiation Research for Environment and Resources, JAERI, Takasaki
Department of Material Science, JAERI, Tokai*

1. Introduction

Responses of plants to environmental pollutants were studied with the positron emitting tracer imaging system (PETIS)[1] which is able to measure the translocation of a positron emitting tracer labeled compound in a plant continuously. In this study, a soybean was chosen as a sample plant, and a herbicide as an environmental pollutant. The translocation of $[^{13}N]$-NO_3^- ion as a nutrient tracer and that of $[^{18}F]$-F^- ion as a water tracer was measured with PETIS. Although there is some concern on the movement of $[^{18}F]$-F^- ion, it is considered to be a good tracer of water movement in the apoplast, because F^- ions are not easily taken up by plant cells[2]. Effects of a herbicide to nutrient uptake and water transportation in soybean plant were discussed.

2. Experiments

Three weeks old soybeans (*Glycine max* L. cv. Yahagi) and metsulfuronmethyl (MSM), as a herbicide, were used for the present experiment. A 3 cm x 4 cm piece of tissue paper soaking up 400 μl of 100 ppm MSM solution was put on the face of a leaflet of a young trifoliate for 12 hours (MSM treatment); as shown in fig. 1, the left leaflet of the trifoliate was chosen for this treatment. For comparison, distilled water treatment was done simultaneously in the same manner as MSM treatment to the right leaflet. Aqueous solutions of $[^{13}N]$-NO_3^- ion and $[^{18}F]$-F^- ion were produced by bombarding a water target with a proton or a helium ion beam, respectively, generated by the TIARA AVF cyclotron. One or three days after MSM treatment, positron imaging analysis was performed. A $[^{13}N]$-NO_3^- ion or $[^{18}F]$-F^- ion aqueous solution was fed from a cut stem, and the two-dimensional distribution of ^{13}N or ^{18}F in the

MSM-treated trifoliate was measred as a function of time with PETIS for 60 minutes. The PETIS used in the present experiment had a field of view of 5 cm x 5 cm.

3. Results and Discussion

Figure 1 shows the distribution of counts from ^{13}N or ^{18}F, accumulated for 60 minutes, taken 1 day after MSM treatment. One can notice an effect of MSM treatment on the transportation and accumulation of the ^{13}N tracer. The radioactivity in the MSM-treated leaflet was lower than those in the other leaflets. On the other hand, the ^{18}F tracer was distributed to all of the leaflets with its high accumulation at the petiole and the main vein. The experimental data suggest that the herbicide did not effect strongly the translocation and accumulation of the ^{18}F tracer.

Figure 2 shows a distribution of counts from ^{13}N and ^{18}F in a trifoliate, taken 3 days after MSM treatment. These data indicate that effect of MSM spread to the other leaflets from the MSM-treated one: the translocation and accumulation of the ^{13}N tracer was strongly suppressed by MSM treatment; small counts of ^{13}N were observed even at the petiole, the main vein, and the joint of the leaflets. The distribution of the ^{18}F tracer indicated a similar trend to that of the ^{13}N tracer, although the counts of ^{18}F at the petiole and the joint of the leaflets were almost the same as those of the trifoliate 1 day after MSM treatment.

These results show that the MSM treatment on a part of a leaflet of soybean trifoliate affected the entire leaflet in 1 day and the other leaflets of the same trifoliate in 3 days or less. The herbicide did not seem to suppress water transportation to the MSM-treated trifoliate even 3 days after the treatment at least to the petiole, but the transportation of the $[^{13}N]$-NO_3^- ion was strongly suppressed even in a day. These observations suggest that MSM treatment inhibited the transportation of $[^{13}N]$-NO_3^- ion from water to the MSM-treated trifoliate selectively. Possibly, the $[^{13}N]$-NO_3^- ion transport was controlled at the joint of leaflets.

References

1) T. Kume *et al.*, *Appl. Radiat. Isot.*, 48, 1035-1043, 1997

2) R. M. Macay *et al.*, *Plant Cell Environ.*, 11, 851-861, 1988

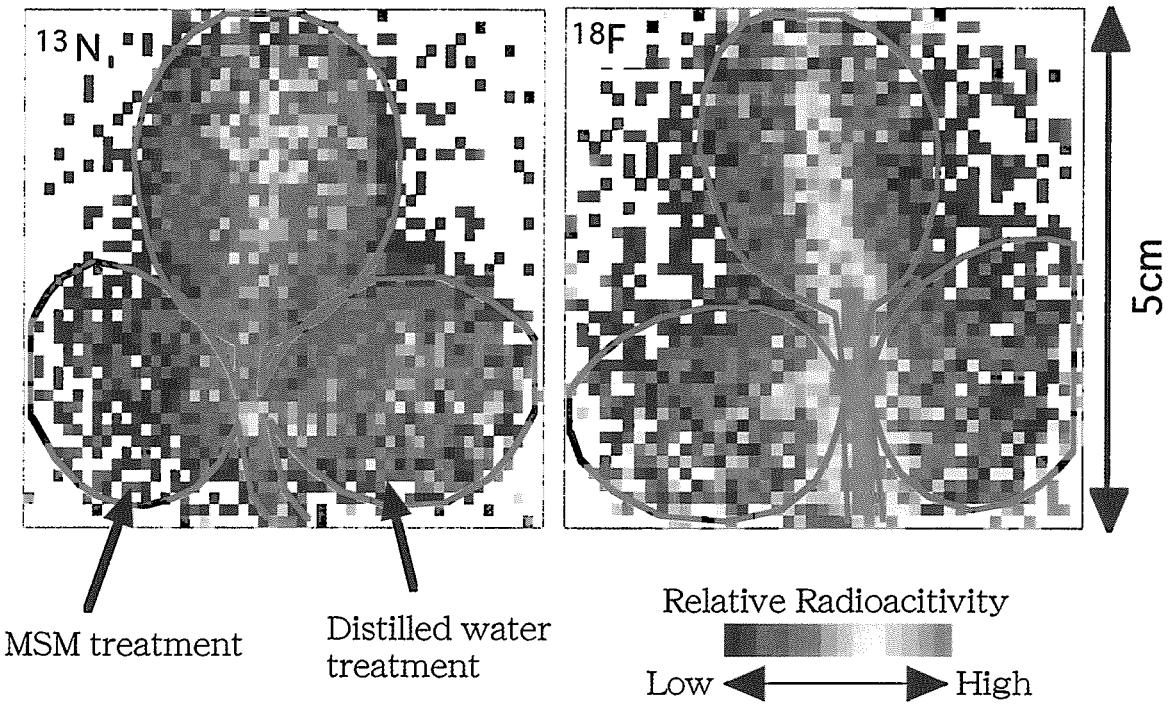


Fig. 1 Distributions of counts from ^{13}N (left) and ^{18}F (right) in the trifoliates of soybean 1 day after MSM treatment (see text). The outlines of trifoliates were shown with red lines in the figures.

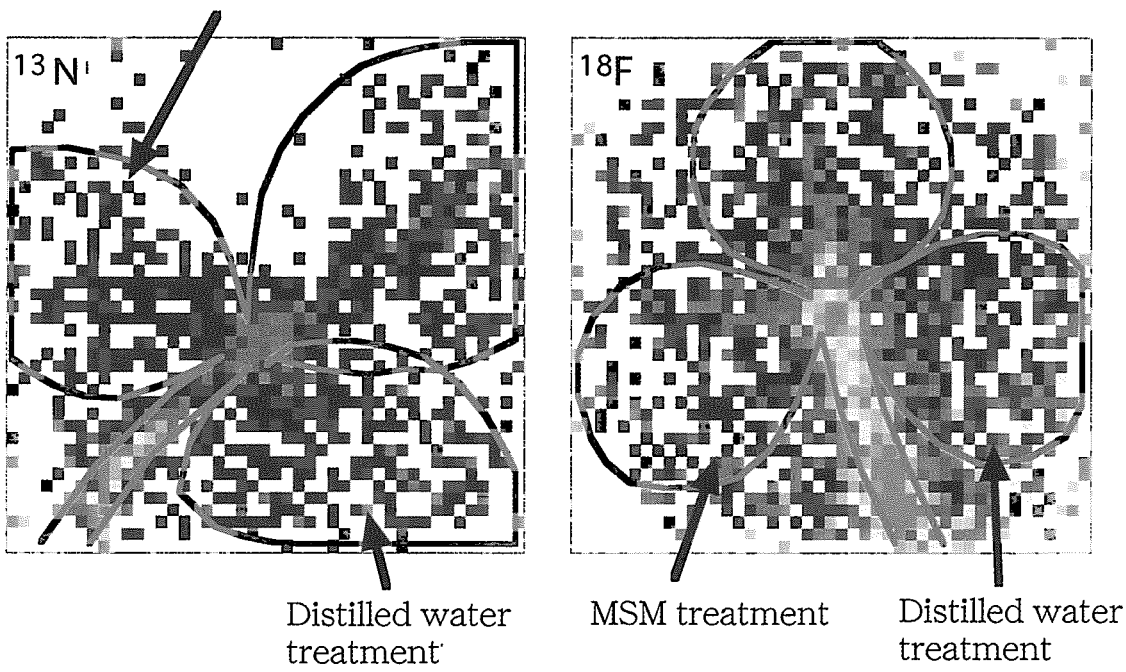


Fig. 2 Same as Fig. 1, except for the fact that the trifoliates of soybean were MSM-treated 3 days before.

2.16 $^{13}NO_3^-$ and $^{13}NH_4^+$ uptake and assimilation-sites on a single root of leguminous crops visualized by a positron emitting tracer imaging system : A study relating to the locality of *Rhizobium* infection site

H. Matsunami*[1], Y. Arima*[1], K. Watanabe*[1], S. Matsuhashi*[2], N. S. Ishioka*[2], S. Watanabe*[2], T. Itoh*[2], C. Mizuniwa*[2], T. Sekine*[2], S. Hashimoto*[2], A. Osa*[3], H. Uchida*[4], A.Tsuji*[4]
*1:Fac. of Agric., Tokyo Univ. Agric. and Tech., *2:Dept. Radiat. Res. Environ. Resources, JAERI, *3: Dept. Material Science, JAERI,
*4:Hamamatsu Photonics, Co.,

1.Introduction

Common bean is one of the most important leguminous crop as well as soybean in the world. Efficient utilization of root-nodule functions is much meaningful for establishing sustainable agricultural system. However, it is generally difficult to get high level yield of common bean depending on nodule nitrogen fixation, because nodule activity is insufficient and/or unreliable in the plants grown in fields [1,2].

With the artificial medium containing little amount of combined nitrogen, common bean plants revealed considerable capacity in nodulation and nitrogen fixation, while growth of the plant was inferior[3,4]. When application level of fertilizer nitrogen was increased, nodulation and nodule activity was more sensitively repressed in common bean than in soybean[5]. Results of a experiment, in which plant roots were fed with ^{15}N-nitrate, suggested that such a higher sensitivity of common bean to combined-nitrogen corresponded to higher activity in uptake, reduction and assimilation of ^{15}N-nitrate comparing to that of soybean.

In our previous report[6,7], it was clarified that a positron emitting tracer imaging system(PETIS) with ^{13}N was a powerful tool to obtain direct evidence for the location of the site where ^{13}N-nitrate was actively uptaken on a single root of common bean and soybean.

In this study, nitrate and ammonium uptake-sites was specified on a single root of common bean and soybean using ^{13}N and PETIS, and then the positional relationship was discussed between the nitrate uptake-site and the root hair elongating region, where *rhizobium* infection capably initiates.

2.Materials and Methods

For PETIS analysis of nitrate uptake-sites on a single root, common bean (*Phaseolus vulgaris* L.cv.Himetebou) and soybean (*Glycine max* (L.)Merr. cv. Enrei) were grown for ca. 10days after sowing in 300 mL pots filled with vermiculite. The pots were supplied with a nutrient solution containing 0.36 or 4.3 mmol L^{-1} NO_3^--N. The plants were transplanted to the 200 mL plastic bottle prior to PETIS experiment. One of the lateral roots generating on upper part of the tap root was taken out from the bottle and introduced into a polypropylene tube filled with ca.7mL of a nutrient solution containing 1.4 μ mol, 0.36 mmol or 4.3 mmol L^{-1} of NO_3^-(^{14}N-medium).

^{14}N-medium in the tube was replaced by a corresponding radioactive (ca.11-16MBq/ tube) nutrient solution containing $^{13}NO_3^-$. After feeding the radioactive medium for 2 min, ^{13}N-medium was discarded, and then the

root and tube were washed several times with corresponding ^{14}N-medium for 2 min. After filling the tube with new ^{14}N-medium, imaging process by PETIS was started by 1min time-frame and continued for 30min.

In case of analysis of ammonium uptake-sites, on a single root of common bean (*Phaseolus vulgaris* L. cv. Himetebou) was used. The plants were grown for ca.10 days after sowing by hydroponics with a nutrient solutioncontaining 0.36 mmolL^{-1} NH_4^+-N.

3.Results and Discussion

(1) $^{13}NO_3^-$-N- uptake sites and Rhizobium-infectible region on a single root of common bean and Soybean[7,8)]

1) The distribution images in a single root of common bean or soybean acquired by PETIS successfully gave under different applied concentration of nitrate in the medium .

2) On a single root of common bean and soybean, dense distribution site of ^{13}N was one or two, regardless of nitrate concentration in the ^{13}N medium. The first dense site extended within ca. 10 mm above root apex, and the second one extend over region of ca.10 to 23 mm from root apex. The former was detected in all roots examined, while the latter was not always distinct in examined roots. This distribution pattern did not change through detection period, and common in the all plants grown with different concentration of the medium nitrate. These facts suggested that a single root of common bean or soybean had two sites of active nitrate uptake and assimilation.

3) Microscopic observation revealed that root hair generation started at the point of 2.5-2.7 mm from root apex on the root of common bean, and root hair elongation zone shifted to root hair maturing zone at the point of 5.6-5.8 mm. In soybean, root hair elongation zone was slightly shorter and nearly to root apex than in common bean.

It was clarified that the ^{13}N dense region within about 1cm from root apex, which was interpreted to be the site of nitrate uptake and assimilation, wrapped over entirely root hair elongation zone, and partially root hair maturing zone on the single root of common bean and soybean.

(2) $^{13}NH_4^+$-N-uptake sites on a single root of common bean

Using $^{13}NH_4^+$-N, as well as $^{13}NO_3^-$-N, the distribution image of ^{13}N in a single root of common bean was successfully analyzed by PETIS (Fig.1). Dense distribution of ^{13}N was located at two positions of 10-25 and 30-45 mm from the root apex. This distribution pattern did not change through detection period (Fig.2). These facts suggested that a single root of common bean had two sites of active ammonium uptake and assimilation.

4.Conclusion

PETIS is a powerful tool to obtain direct evidences for location of the site where 13N-nitrate or ammonium are actively uptaken and assimilated. It was clarified that the ^{13}N dense region within about 1cm from root apex, which was interpreted to be the site of nitrate uptake and assimilation by PETIS analysis, wrapped over entirely root hair elongation zone, and partially root hair maturing zone on the single root of common bean and soybean.

5.Reference

1) LaRue, T. A. and Patterson,T.G.,1981, *Adv. Agron.*, 34, 15-38.

2) Nishimune, A., Konno, T., Saito, G. and Fujita, I., 1983, *Res.Bull Hokkaido Natl. Agric. Exp. Stn.*, 137, 81-106.
3) Arima, Y., 1993, Jpn. J. Soil Sci. Plant Nutr., 64, 118-125.
4) Piha, M. I. and Munns, D. N., 1987, Plant Soil., 98, 169-182.
5) Arima, Y. and Shirai, M., 1996, Jpn. J. Soil Sci. Plant Nutr., 67, 605-612.
6) Matsunami, H. et al, 1998, TIARA Annual Report 1997 (JAERI-Review 98-016), 47-49.
7) Matsunami, H. et al, 1999, TIARA Annual Report 1998 (JAERI-Review 99-025), 65-66.
8) Matsunami, H. et al, 1999, Soil Sci. Plant Nutr., 45, 955-962.

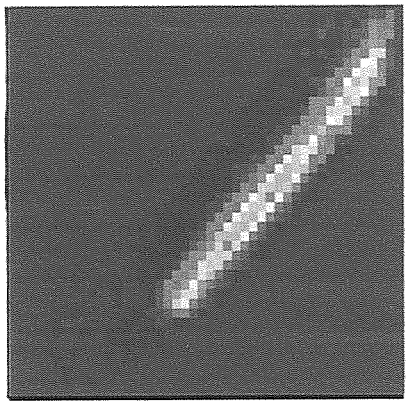
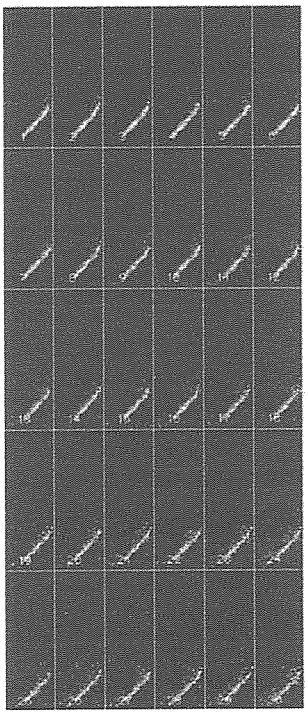


Fig. 1 ^{13}N distribution image in a single root of common bean. γ -ray emission was integrated for 30min After ^{13}N H_4-N pulse-feeding for 2 min.

10mm



10mm

Fig.2 Changes in the distribution after medium pulse-feeding of $^{13}NH_4$-N in common bean single root

2.17 Effect of NH_4^+ on $^{13}NO_3^-$ Absorption and Transport in Soybean Plant

N. Ohtake, T.Ohyama, K. Sueyoshi. T. Kawachi, H. Fujikake, A. Osa*, M. Koizumi *, S. Hashimoto**, N.Ishioka*, S. Watanabe*,T Sekine S. Matsuhashi**, T. Ito**, C. Mizuniwa**, H.Uchida*** and A. Tsuji***

Faculty of Agriculture, Niigata University, * Department of Material Science, JAERI, ** Department of Radiation Research for Enviroment and Resources, JAERI ,*** Hamamatsu Photonics Co.

1. Abstract

NO_3^- and NH_4^+ are the most important N forms for plant nutrition under agricultural as well as natural conditions. Many studies have shown that the presence of NH_4^+ in nutrient solution inhibits NO_3^- uptake in the plant roots. Conversely, a stimulation of NO_3^- uptake by low concentrations of NH_4^+ has also been reported. This was attributed to the acidification of the medium associated with NH_4^+ utilization, and consequently it increases H^+ gradient across the plasmamembrane which drives NO_3^- influx into cells. However, at a high concentration of NH_4^+ (5mM) this beneficial effect was no longer observed and the inhibitory effect is overwhelmed (Forde and Clarkson 1999). One possibility of the inhibition of NO_3^- absorption was due to depolarization of membrane potential in the plasma membrane.

In hydroponically grown soybean plants, when NH_4^+ was added into the culture medium, the NO_3^- absorption rate decreased after 60 minutes of time-lag. This result may suggest that the period of accumulation of the assimilatory products from NH_4^+ reaching the critical level may be required for the inhibiting of NO_3^- uptake (Ohyama et al. 1989).

In this report, we investigated that the effect of application of NH_4^+ on nitrate absorption and transport to the shoot in short time, especially leaf petiole, using ^{13}N-labeled nitrate and detected with PETIS(Positron Emitting Tracer Imaging System) .

2. Materials and methods

Soybean plants (cv. Williams) were inoculated with *Bradyrizobium japonicum* strain USDA 110 and were hydroponically cultivated with N free medium. After 32 days of planting, 1m*M* KNO_3 was added to the medium. The first experiment was conducted

at 35 days after planting. Imediately before $^{13}NO_3^-$ feeding, the medium was changed to the solution containing 1m*M* of KNO_3 (control) or the solution with 1 m*M* KNO_3 plus 10 m*M* NH_4Cl (NH_4^+ treatment). Then $^{13}NO_3^-$solution (control: 26.0 Mbq mL^{-1}, NH4 treatment: 26.0 Mbq mL^{-1}) was supplied to them.

In the second experiment, a plant was initially supplied with the medium containing 1m*M* KNO_3 labeled with ^{13}N (control: 15.6 Mbq, NH_4 treatment: 12.9 MBq). At 10 minutes after the commencement of $^{13}NO_3^-$ feeding, NH_4Cl were added to the medium for the final concentration as 10m*M* in NH_4 treatment. In both experiments, the radioactivities in the petiole at the position of second trifoliate leaves was observed by PETIS.

3. Results and discussion

In the first experiment, the radioactivity at the petiole increased about 10 minutes after the addition of ^{13}N-nitrate feeding (Figure 1). On the other hand, when the plant was previously supplied with 10m*M* NH_4^+ before nitrate feeding, the radioactivity at the point of petiole was significantly lower than that of control plants (Figure 1).

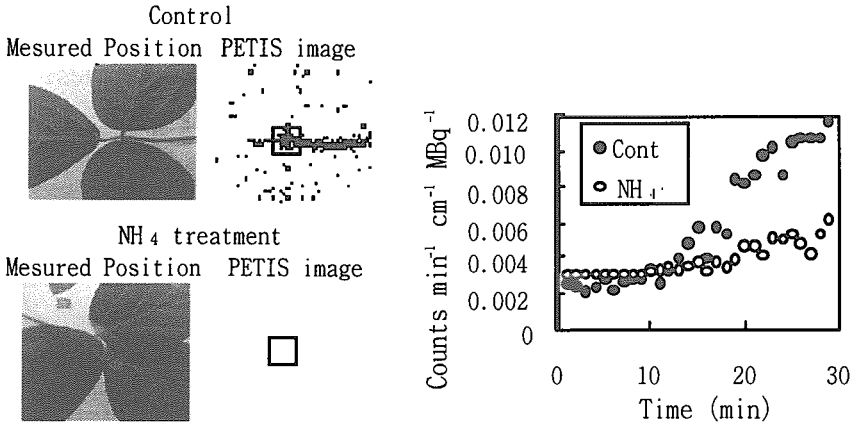


Figure 1 ^{13}N accumulation at leaf petiole co-exist with NH_4^+ (at final concentration as 10 m*M*) or without NH_4^+ (control) in culture medium。 ^{13}N labeled nitrate was fed to the root with 1 m *M* KNO_3 as a nitrate carrier. Radioactivity was mesured at the position of petiole node (open squer in PETIS image) every one minuit. The PETIS image shows average radioactivity of 30 minuits.

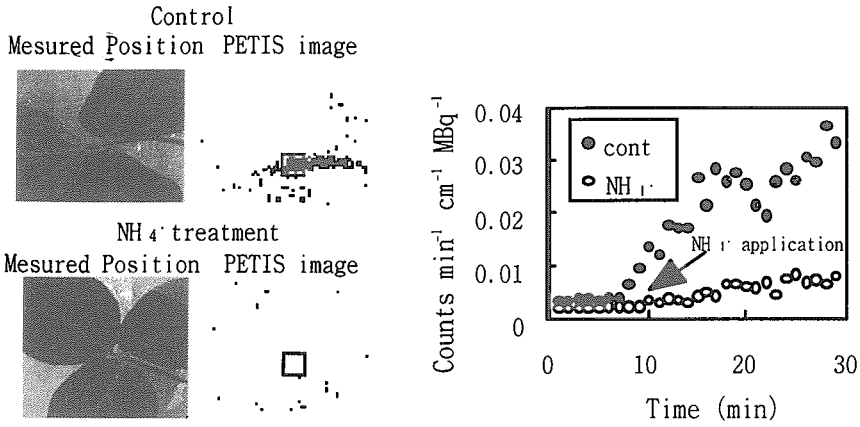


Figure 2 ^{13}N accumulation at the point of leaf petiole. The control plants fed $^{13}NO_3^-$ with 1m*M* KNO_3 as a nitrate carryier (basal medium) and NH_4^+ treated plants was fed basal medium with 10m *M* NH_4Cl as a final concentration 10 minuits after the commencement of $^{13}NO_3$ feeding. Radioactivity was mesured at the position of petiole node (open squer in PETIS image) every one minuit. The PETIS image shows average radioactivity of 30 minuits。

In the second experiment, the application of NH_4^+ at 10 minutes after addition of $^{13}NO_3^-$ also depressed the increase in the radioactivity at the point of petiole compared with control plant (Figure 2). These results indicated that the application of NH_4^+ depressed immediately the transport of N drived from NO_3^- to the petiole. The depressive effect of NH_4^+ application on NO_3^- transport to the petiole was assumed that NO_3^- influx into the roots was decreased or that the efflux from roots was enhanced by the exogenous NH_4^+. Alternatively it may be due to the decrease in transpiration. It is reported that nitrate transferred to the leaves in short time was related with transpiration (Sato et al. 1998). NH_4^+ application may repressed plant transpiration and transport of absorbed N originating from NO_3^-.

References

B.G. Forde and B.G. Clarkson BG. Advances in Botanical Reserch; J.A. Callow Ed.; 1 (1999) 2

T. Ohyama et al., Soil Sci. Plant Nutr., 35 (1989) 33

T. Sato et al., TIARA Ann. Rep. (1997) 53

2.18 Ammonium ($^{13}NH_4^+$) Absorption and Translocation Under Various Environmental Conditions in Rice Visualized by PETIS

S. Kiyomiya, H. Nakanishi, H. Uchida*, A. Tsuji*, N. Harada*, H. Tsukada*, S. Matsuhashi†, S. Hashimoto†, T. Sekine†, S. Mori
Graduate School of Agricultural and Life Sciences, The University of Tokyo, *Hamamatsu Photonics K. K., †Department of Radiation Research for Environment and Resources, JAERI

1. Introduction

Nitrogen is one of the major elemental plant nutrients, and ammonia is an essential nitrogen source for paddy rice. Though radioisotopes are often used for the studies of uptake and translocation of various nutrients in plants, stable isotope ^{15}N was only available for plant's nitrogen research. Therefore, it was impossible to measure the translocation rate of nitrogen in plants. Recently, ^{13}N-labelled compounds, $^{13}NH_4^+$ and $^{13}NO_3^-$, are coming to use. They have been adopted in the plant nutrition research, and allow researchers to visualize nitrogen by autoradiography and to detect nitrogen flow with ease. Here, we used $^{13}NH_4^+$ and a new method, a positron-emitting tracer imaging system (PETIS), to visualize real time ^{13}N translocation in rice. Some environmental conditions that might affect ^{13}N translocation were tested.

2. Experimental conditions

The radiotracer ^{13}N (half-life = 9.96 min) was produced by proton irradiation of water. The produced $^{13}NO_3^-$ with high radiochemical purity was converted to $^{13}NH_4^+$ using Devard's alloy.

Rice (*Oryza sativa* L. cv. Nipponbare) were hydroponically cultured. The $^{13}NH_4^+$ absorption experiments were performed when the plants had 1-3 tillers and there were 4-6 leaves on the main shoot. Roots of single plant were placed in a polyethylene bag that contained 15 ml of an aerated culture solution without NH_4^+. The plant and bag were placed between acrylic boards centered between PETIS detectors. $^{13}NH_4^+$ (100 to 500 MBq, carrier free in 1 ml) was added to culture solution immediately after synthesis. The γ-rays emitted from decaying positrons ^{13}N were counted over time using the coincident method by the paired detectors. The data were automatically crrected using 9.96 min as the half-life of ^{13}N. After 60-min trace analysis, the plants were removed and placed under a Bio-imaging plate (BAS-1500, Fuji Film) inside a cassette.

Dark, 1 mM methionine sulfoximine (MSO), 10 μM abcscisic acid (ABA), nitrogen deficiency (-N) for 3 days, and NO_3^- treatments were employed to evaluate their influence on the $^{13}NH_4^+$ translocation.

3. Results and Discussion

$^{13}NH_4^+$ was absorbed by the roots of control rice and ^{13}N translocation was monitored by PETIS. Within 60 min, $^{13}NH_4^+$ was absorbed from roots and ^{13}N was translocated to all the tissues of the plant (Fig. 1). Discrimination center, the basal part of the shoots, was especially strongly labelled. Recently, the importance of the discrimination center in Fe and methionine transport in barley was shown by using ^{59}Fe-mugineic acid and ^{11}C-methionine[1), 2)]. The discrimination center plays an important role

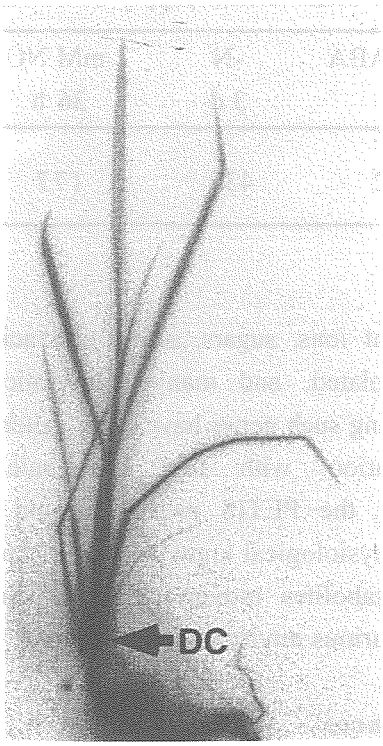


Figure 1 Image of the distribution of ^{13}N using BAS-1500 (Fuji Film, Japan) after a 60 min PETIS analysis.

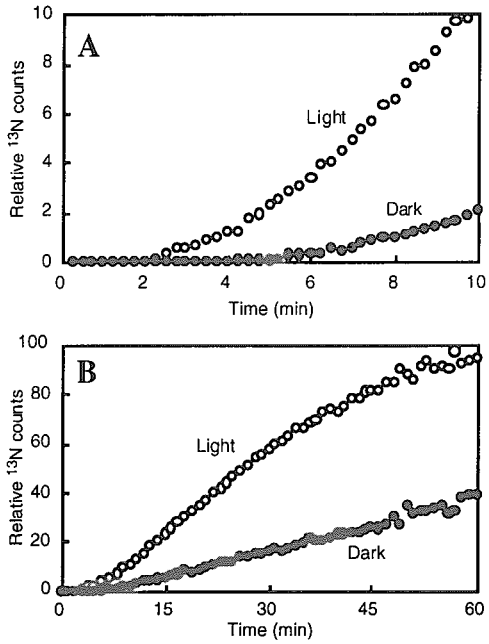


Figure 2 Time-course study of the ^{13}N translocation into the discrimination center under control (light) and dark conditions. **A.** Accumulation of radioactivity within 10 min. **B.** Accumulation of radioactivity for 60 min.

in the translocation of minerals and metabolites in graminaceous monocot plants. The younger leaves were also strongly labelled, while the oldest leaf was not. Absorbed ^{13}N would be predominantly translocated to the sink parts of the plant. The PETIS detectors were focused on the discrimination center, and real time ^{13}N translocation was monitored (Fig. 2). The accumulation curve determined from the PETIS data showed that ^{13}N accumulation in the discrimination center began at 2 min and then increased (Fig. 2A). The ^{13}N counts of the discrimination center increased with time through the experiment (Fig. 2B). Ammonium assimilation was blocked by 1 mM MSO, which decreased ^{13}N translocation to the discrimination center to 13% after 10 min (Table 1). ^{13}N distribution in control plant tissues must reflect metabolic activity of glutamine synthetase. In xylem loading step, it is considered that the main nitrogen solutes were ammonium assimilated products, but not NH_4^+ itself. Since root-absorbed ammonium is first converted to glutamine before translocation, our results show that this process proceeds remarkably quickly.

Some environmental conditions that might affect ^{13}N translocation were tested. In the dark, plants close stomata and suppress transpiration. When a plant was kept in the dark for 2 h, the initial detection time of ^{13}N was delayed and the amount of accumulated ^{13}N was decreased to 20% of the control level (Fig. 2, Table 1). The plant hormone abscisic acid (ABA) acts on stoma closing and completely suppresses the transpiration system in the xylem of rice. Contrary to our

Table 1 ^{13}N accumulation at the discrimination center after 10-min supply of $^{13}NH_4^+$

pre-treatment	1 mM MSO 0.5 h	dark 2h	10 μM ABA 1 h	-N 3 d	2 mM NO_3^- 36 h
^{13}N accumulation % of control	13	20	222	433	177

expectations, pre-treatment with 10 μM ABA for 1 h increased the ^{13}N accumulation by 222% (Table 1).

Nitrogen deficiency treatment for 3 days remarkably enhanced the ^{13}N accumulation in the discrimination centre by 433% (Table 1). This corresponds with the induction of an ammonium transporter gene (*AtAMT1*) and the increased NH_4^+ influx observed with nitrogen deficiency[3]. Pre-treatment with 2 mM NO_3^- for 36 h as the only nitrogen source also enhanced the ^{13}N accumulation by 177% (Table 1). These three phenomena have never been reported.

In studies using a gamma counter to monitor ^{13}N, many plants have to be prepared for a time course study. PETIS enables us to visualise the movement of labelled substances in one intact plant in real time reproducibly[4), 5), 6)]. We have already demonstrated real time amino acid movement in Fe-deficient barley using ^{11}C labelled methionine for the first time[1)]. Now, nine positron-emitting nuclides are available: ^{11}C, ^{13}N, ^{15}O, ^{18}F, ^{22}Na, ^{48}V, ^{52}Mn, ^{52}Fe, and ^{62}Zn. Many transporter genes for metal ions, sugars, and amino acids have been isolated, and many transgenic plants harbouring such genes have been generated. In combination with this transgenic plant research, the PETIS method should provide novel physiological knowledge about nutrients and metabolites movement in a plant body under various environmental stresses.

References

1) H. Nakanishi *et al.*, *J. Exp. Bot.* **50**, 637-643, 1999.
2) S. Mori, *in* Iron transport and storage in microorganisms, plants and animals, Vol. 35. Metal ions in biological systems (eds. A. Sigel & H. Sigel) 215-237 (Marcel Decker Inc., New York), 1998.
3) S. Rawat *et al.*, *Plant J.* **19**, 143-152, 1999.
4) T. Kume *et al.*, *Appl. Radiat. Isot.* **48**, 1035-1043, 1997.
5) H. Hayashi *et al.*, *Plant and Soil* **196**, 233-237, 1997.
6) T. Sato *et al.*, *Radioisotopes* **48**, 450-458, 1999.

2.19 Effects of phytohormones on ^{13}N distribution in rice plants detected by PETIS detector

H. Hayashi[1], H. Mano[1], N. Suzui[1], S. Matsuhashi[2], C. Mizuniwa[2], T. Ito[2], S. Hashimoto[2], N.S. Ishioka[2], T. Watanabe[2], T. Sekine[2], A. Osa[3], H. Uchida[4], A. Tsuji[4]

[1]Department of Applied Biological Chemistry, Univ. Tokyo, [2]Department of Radiation Research for Environment and Resources, JAERI, [3]Department of Material Science, JAERI, Central Research Laboratory, Hamamatsu Photonics Co.

1. Introduction

Nitrogen (nitrate in this experiment) absorbed by roots is transported to the leaves through xylem vessels and then retranslocated to the new leaves, root and storage organs through sieve tubes. These processes are highly regulated by surrounding conditions and plants by themselves by the action of phytohormones. It is very important to know how this nitrogen movement is regulated by phytohormones and what mechanisms are involved in controlling these movements in order to increase the efficiency of nitrogen fertilizer.

In this paper, we detected the nitrate movement absorbed in roots is affected by the treatment of phytohormones, such as Zeatin and ABA

2. Experiments

Rice plants (Oryza sativa L. var. Kantou) were grown in a complete nutrient solution. The plants of the 7th- or 8th- leaf stage were used for the experiments.

An aqueous solution containing $^{13}NO_3^-$ (a positron emitter with a half life of 9.9 minutes) was produced from the reaction of $^{16}O(P, \alpha)^{13}N$ by bombarding water with $1\,\mu A$ of 20 MeV H^+ particles from the TIARA AVF cyclotron. The water containing $^{13}NO_3^-$ was purified through a cation exchange column to separate from $^{13}NH_4^+$.

Around 50~100 MBq solution of $^{13}NO_3^-$ was added to the 5 mL of the nutrient solution which contain nitrate (0.71 mM) as an only nitrogen already in a small box (5cm x 0.5cm x 10cm) from which the rice plant was absorbing the nutrients. The rice plants were pretreated by adding biological level of Zeatin and ABA ($1x10^{-6}$ M) to the absorption solution for 1 hr. After washing the phytohormones by normal absorption solution, plants starts to absorb radioactive nitrogen. Absorption solution was replaced by the same solution without tracer at

10 minute after tracer was added.

For the detection of nitrogen transport, the plant was placed at the midposition between two separate two-dimensional block detectors (5 x 6-cm square x3) which were composed of a $Bi_4Ge_3O_{12}$ scintillator array coupled to a position sensitive photomultiplier tube (Hamamatsu Photonics Co., Japan). Two annihilation γ-rays from samples are detected in coincidence. The original position of the annihilation is localized at the intersection of the object plane, where the plant is set, in a line connecting the two detection points on the detectors. .

3. Results and discussion

The results show that this system provides a convenient system for displaying nitrogen movements in plants even though the spatial detection limit is only 2 mm and measurement lasting more than 30 minutes may be difficult because of decay of ^{13}N.

Our results (Figure1) show that in rice plants supplied with nitrate as the nitrogen source, the absorbed nitrogen was translocated through xylem vessels to the leaf top within 1 minute in control plant. The rice plants treated with phytohormones showed slow rate of nitrogen distribution compared with that of control plants. In case of Zeatin treatment, almost half amount of ^{13}N was distributed to the leaves compared with that of control plant. Rice plant treated with ABA also reduced amount of nitrogen distribution to the shoot. In this case, lag time of nitrogen distribution to the shoot was longer than that of control plant and the plant treated with Zeatin.

These results suggest the difference effect of Zeatin and ABA on the distribution processes through xylem vessels. Nitrate is first absorbed through plasma membrane by the action of nitrate transporters and then move to the pericycle cells through plasmodesmata. Finally, nitrate is released form pericycle cells to the apoplast and loaded into xylem vessels. Moreover, nitrate absorbed in root cells is stored in vacuoles temporally. Zeatin and/or ABA may affect of these nitrate movement processes differentially.

It is very important to know on which process these phytohormones effect by more detail observation using this PETIS system.

References

H. Hayashi, Y. Okada, H. Mano, T. Kume, S. Matsuhashi, N. S-Ishioka, H. Uchida and M. Chino, Plant and Soil, 196(1997)233.

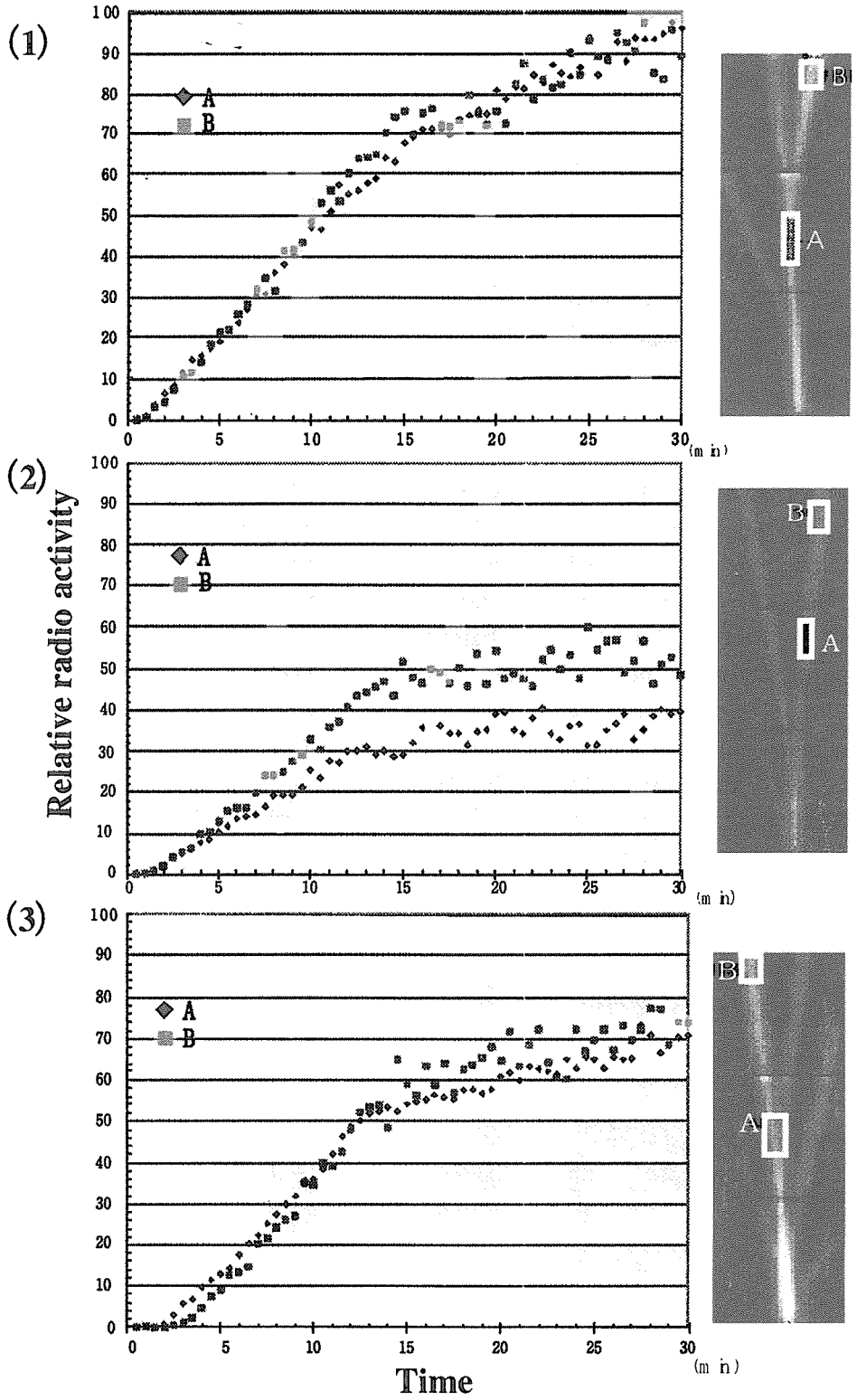


Figure 1 Effects of phytohormones on ^{13}N distribution detected by PETIS detector

(1); Control;$^{13}NO_3^-$ was applied with 0.71 mM nitrate for 10 min. (2); Roots were treated with 1μ M Zeatin for 1 hr before experiment start. (3); Roots were treated with 1μ M ABA for 1 hr before experiment start. A(◆) and B (■) showed the positions of counting. Photos in each figure show the accumulation pattern of ^{13}N for 30 min.

2.20 Water and Trace Element Behavior in Plant

T.M.Nakanishi[1], J.Furukawa[1], K.Tanoi[1], M.Yokota[1],S.Ueoka[1]
N.S.Ishioka[2], S.Watanabe[2], T.Sekine[2], T.Ito[2], C.Mizuniwa[2], S.Matsuhashi[2],
S.Hashimoto[2], A.Osa[3], H.Uchida[4] and A.Tsuji[4]

[1]Graduate School of Agricultural and Life Sciences, The University of Tokyo,

[2] Department of Radiation Research for Environment and Resources, JAERI

[3] Department of Material Science, JAERI

[4]Hamamatsu Photonics Co.

1. Introduction

Since real-time movement of chemicals in living plant is expected to provide new information in plant physiology, the authors measured the absorption and transfer of water (^{18}F-H_2O) and vanadate (^{48}V) in a plant by PETIS (Positron Emission Tracer Imaging System) method. This research has been performed for these three years and water movement was mainly performed last year as was reported[1]. Therefore, this year we mainly present a trial to measure vanadate uptake manner in soybean plant. Vanadium is produced by exhaustion gas from cars, fly ash or other industrial waste materials and has been one of the serious pollutant to the environment. Vanadium tends to be accumulated in root and causes serious problem for plant growth. Therefore, the initial effect of V appears in the root. However, the mechanism of V toxicity to a plant has not been extensively studied. What has been known is that vanadate (5^+) is a powerful inhibitor of ATPase activity in plant cells. In order to know V behavior directly in living plant, we performed PETIS.

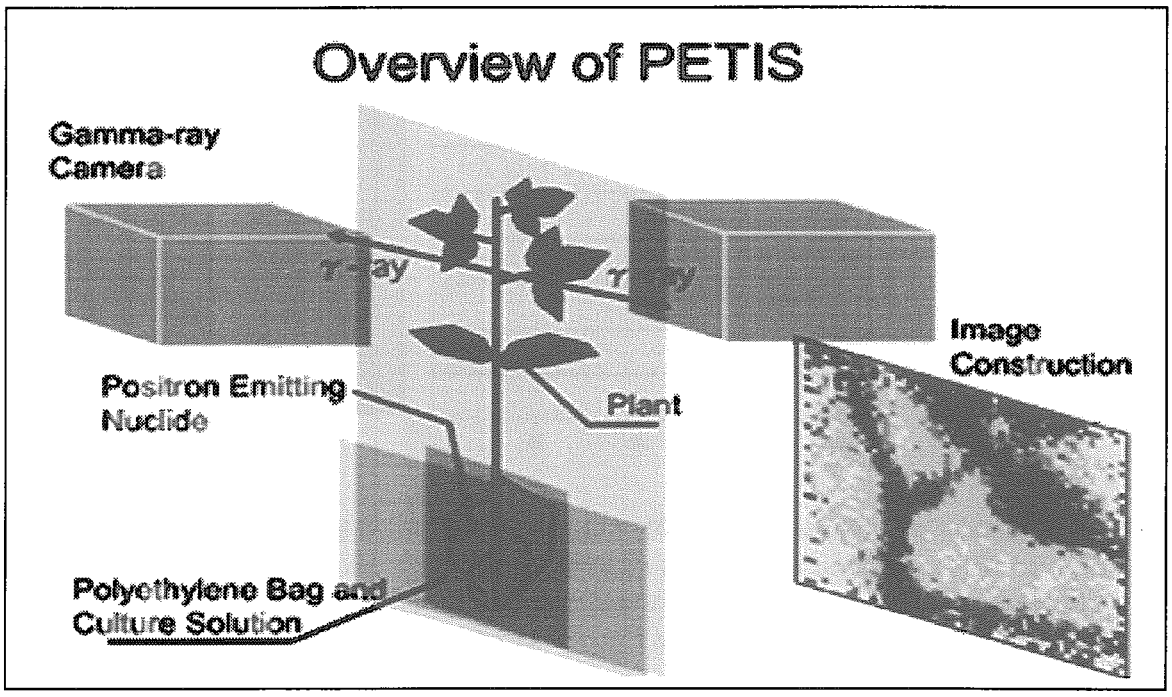


Fig. 1 Overview of PETIS (Positron Emission Tracer Imaging System)

2. Experimental

During the first two years, as was reported, the roots were cut off from plants and the chemicals were absorbed from the lower part the stem because of the difficulty in designing the plant target. This year a new target system was tried to measure V uptake manner from a root (Fig. 1). A cowpea plant, grown in a phytotron was transferred to a small plastic bag where 10ml of culture solution was added just before the experiment. An air from a small pump was conducted to the bag to mix the culture solution gently throughout the experiment. The upper part of the plant was fixed on an acrylic board with a tape and covered with a nylon mesh. Vanadium (^{48}V) solution was added to the culture solution and radioactivity from the target area (5cm x 6cm) as well as the lower part of the stem was collected every 15 seconds.

3. Results and discussion

In the series of $^{18}F\text{-}H_2O$ absorption, we used soybean from last year. Though we added heavy elements, such as Cr, Hg or Cd, we could not find out any difference in $^{18}F\text{-}H_2O$ absorption and transfer manner in a plant. Water absorption manner was not changed even spraying an abcdic acid to the plant to shut the guard cells of stomata. These result suggested that $^{18}F\text{-}H_2O$ movement was not the same as that of water itself. It seems that $^{18}F\text{-}H_2O$ is acting as a fluorine tracer. To know water moving manner in detail, it is preferable if the same experiment could be performed using $^{15}O\text{-}H_2O$ as a water tracer.

In the case of V absorption, when a cowpea plant was cultured without phosphate for 4 days, high absorption of V was observed (fig. 2). Since there is a similarity of vanadate and phosphate in chemical form, V might be absorbed to compensate the phosphate deficiency. Figure 3 shows BAS image of V.

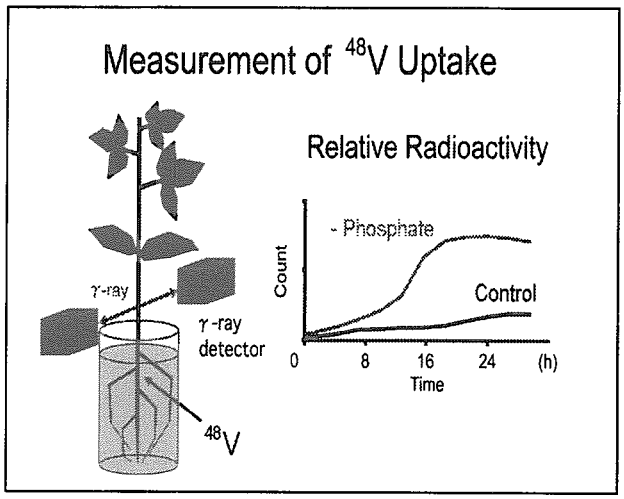


Fig.2 48V uptake in a cowpea plant.

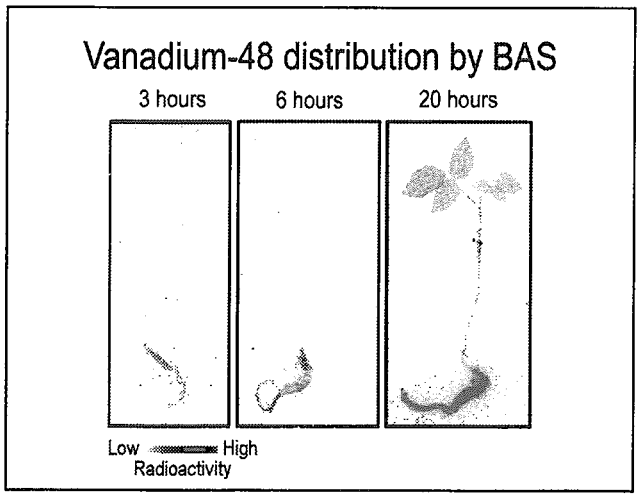


Fig. 3 BAS image of V in a cowpea plant.

References

1) T.M.Nakanishi et al.,
J.Radioanal.Nucl.Chem.,(in press)

2.21 Uptake of ^{18}F-Water and ^{15}O-H_2O in Tomato Plants

A.Tsuji, H.Uchida, T.Yamashita, S.Matsuhashi*, T.Ito*, C.Mizuniwa*, N.S.Ishioka*, S.Watanabe*, A.Osa**, S.Hashimoto*, T.Sekine*
Central Research Lab., Hamamatsu Photonics K.K.,
*Department of Radiation Research for Environment and Resources, JAERI,
**Department of Material Science, JAERI

1.Introduction

Conventionally, behavioral observation of water in plants and vegetation, optical compounds, and other elements has mainly been carried out by static methods such as autoradiography and other methods of image measurement using RI. We have developed a dynamic image measurement method using positron emitting nuclides, allowing us to investigate the biological functions of plants and vegetation from a new angle.

The Positron Emitting Tracer Imaging System (PETIS) which we have developed is comprised of two planar detectors, which detect radioactive rays. This measurement method enables dynamic movements of substances within the plant to be obtained as a two-dimensional image without contact.

Currently, this method is being used to carry out fundamental research such as the observation of the uptake and transport of water, minerals and nutrients. In addition, we are now finding ourselves able to compile measurement data that supports the behavior of matter inside plants.

2.Experiments

PETIS was used this experiment. The system consists of two-dimensional block detectors which are composed of a $Bi_4Ge_3O_{12}$ scintillator array coupled to a position sensitive photomultiplier tube (PS PMT; Hamamatsu R3941-2). The mosaic BGO array is formed with 27(X) x 23(Y) array of 2 mm square cross section x 20 mm deep BGO pillars, where each segment is placed with 2.2 mm pitch.

$^{18}F^-$ was produced by TIARA AVF cyclotron. And ^{15}O was produced by the $^{14}N(d,n)^{15}O$ reaction in a nitrogen gas target. The target gas contains 0.5% oxygen as carrier and was kept a continuous flow with flow rates of 500ml/min at a pressure of 3kg/cm^2. The gas in the target chamber was irradiated with a 10 MeV deuteron beams at a current of 15 μA using the cyclotron (SUMITOMO CYPRIS-HM) at Hamamatsu Photonics PET Center.

Tomato plants were grown in barmuculite from seed at 25°C and maintained in controlled environmental chamber. The plants cultivated for 6 weeks (about 40 cm height) were used for the experiment.

The water containing ca. 10 MBq/ml of ^{18}F-water or ca. 200Mbq/ml of ^{15}O-H_2O was fed to the root of the plants.

3. Results and discussion

Figure 1 shows the time activity curves of ^{18}F-water. Under dark and bright condition, ^{18}F-water uptake was observed and was similarly increased. Figure 2 and figure 3 show the time course curves and images of ^{15}O-H_2O tracer activity in a tomato stem. Images were shown every minute.

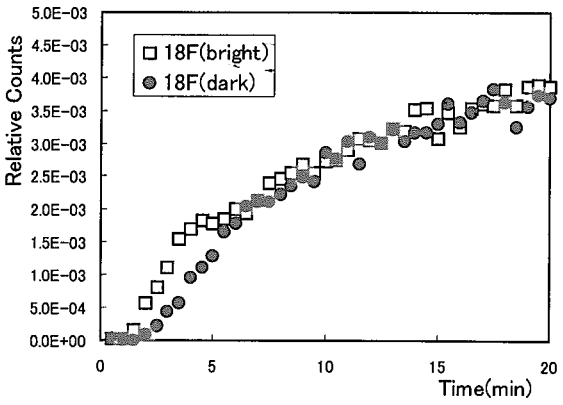


Figure 1 Time course study of ^{18}F-water uptake at the tomato stem.

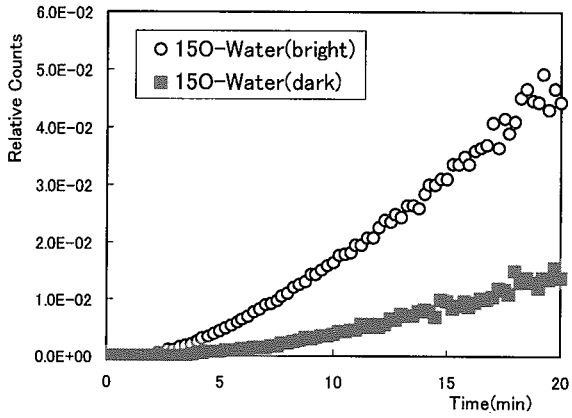


Figure 2 Time course study of ^{15}O-H_2O uptake at the tomato stem.

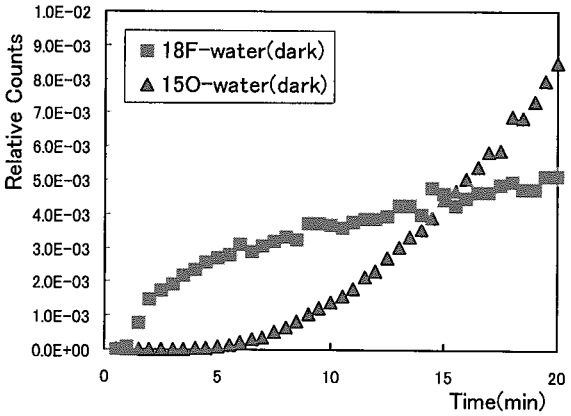


Figure 4 Time course study of ^{15}O-H_2O and ^{18}F-water uptake under dark condition.

The uptake velocity of ^{15}O-H_2O was 2.0~2.5 cm min^{-1} at bright condition. There was slightly uptake under dark condition as expected. Figure 4 shows the relation between ^{18}F-water and ^{15}O-H_2O at dark condition. ^{18}F-water uptake was rapid compared to ^{15}O-H_2O, and the shape of graph was different from. The first ^{18}F-water signal was noticed 2 minute after beginning the experiment. But, ^{15}O-H_2O signal was noticed 5 minute after beginning.

These results suggest that ^{18}F-water uptake only shows "^{18}F uptake" but not "water uptake".

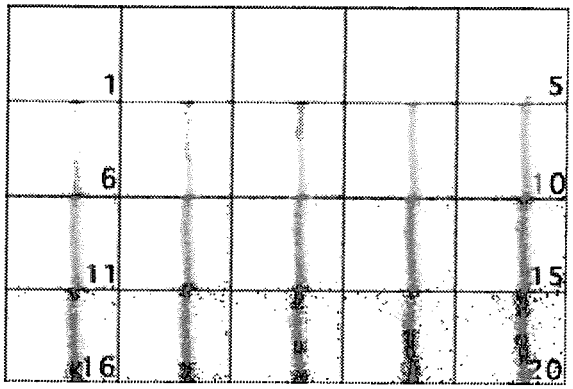


Figure 3 Image of ^{15}O-H_2O uptake in a tomato stem. (Images were shown every minute)

2.22 Fundamental Study on Radiotherapy of Tumors to Beneficial Companion Animals using Heavy Ion Beam

S.Wada[a], M.Natsuhori[a], Y.Kobayasi[b], K.Yamamoto[b], N.Ito[a]
[a]Department of Veterinary Medicine, Kitasato University
[b]Department of Radiation Research for Environment and Resources, JAERI

1.Introduction

Recently, due to improvements of environmental condition including the spread of social understanding of animal diseases and preventive medication including vaccination and premedication, companion animals can live much longer than before. These improvements made it possible to reduce severe infectious diseases. Instead, diseases of companion animals are shifting from the infectious diseases to the aging-related metabolic disorders and neoplasm (cancer) formation. Among the companion animals, beneficial animals that assist the people both mentally and physically, and that highly contribute to the people in many occasions. For example, they work for the handicapped people who are physically disordered, blind, deaf or mentally disordered, or they work together with quarantine (inspection), police, fire service, or a rescue team in case of big trouble such as earthquake and so forth. Production of these beneficial animals is costly and therefore limited in number, but gradually increasing as its need increase. Since such animals are socially essential to human life and its bond between the particular people and the animal is so close, disease controls including cancer therapy are often required to such animals. Radiotherapy is one of the choices for the medical treatment against cancer. However, there is limited number of data on X ray and γ ray radiotherapy to dogs and cats. Moreover, there is no study on ion beam radiotherapy to these animals. Therefore our purpose is to investigate the fundamental aspects of the effects of radiation on cancer cells to forecast the proper protocol for radiotherapy on such animals and if possible, feed the data back to human being.

2.Materials and methods

Cell lines used for this experiment were squamous cell carcinomas, fibrosarcoma and hemangiopericytoma that originated from spontaneously generated canine tumor. Cell lines were kept and grown in MEM medium with 10% serum supplemented. These were incubated at 37℃ in humidified atmosphere of 95% air and 5% carbon dioxide mixture. These cells were irradiated ^{12}C ion beam at 220 MeV (116keV/μm) or γ ray radiation (60Co-γ source) at a dose rate of 2.0 Gy/min.

After irradiation, the survival rates of the cells were examined. To examine the rates of cell survival, exponential growing cells were removed from dishes by adding 0.05% tripsin. The cells were washed and resuspended to a density of 1×10^5 cell/ml. Then the cells were irradiated at a given dosage at a room temperature and plated on 6-cm tissue culture dishes at a given density to calculate the rate of surviving cells. About 10 days after the irradiation, colonies of the cells were stained and counted. The survival rates against the given doses were plotted and fitted to the following linear-quadratic model,

$$\ln S = -\alpha D - \beta D2$$

where S is the survival fraction and D is the radiation dose.

3.Result and Discussion

Figure.1 shows the effect of radiation on the survival rates of the three cell lines after carbon ion beam or γ ray irradiation. The survival curves of ion beam irradiation showed almost linear in logarithmic scale and had no shoulder. But the survival curves of γ ray irradiation showed to have shoulders. As shown in figure 1, the lethal effect was much higher by ion beam than γ ray irradiation. The cells appeared to have the different radiosensitivity by the γ ray irradiation, depend on the type of tumor. Squamous cell carcinoma was the most radioresistant and hemangiopericytoma was the most sensitive to the γ ray irradiation. On the contrary, the ion beam irradiation showed almost no difference on the rate of survival, which appeared to be independent from the type of tumor.

The relative biological effectiveness (RBE) of the dose required to give 10% of survival by ion beam to γ ray on squamous cell carcinoma, fibrosarcoma and hemangiopericytoma, was 2.6, 2.2 and 1.9, respectively (table1). There was a tendency that the more the tumor is radioresistant on γ ray, the higher the RBE becomes. Therefore it is indicated that the therapeutic effect of the low LET (γ ray) irradiation on the radioresistant tumor becomes much higher by the use of ion beam.When in use of the fractionated irradiation, the survival curves have repeating shoulders. Based on the shoulder, the total dose is calculated from the intercept of the line. Predictive survival fraction is calculated from survival curve fitted to the linear-quadratic model, since this method is regarded as one of methods for making protocols of radiotherapy. Fortunately, this in vitro experimental model is worth for screening the sensitivity of the tumor in the target species. This means that this experimental model can be expanded to apply for the target individuals.

Consequently, these data will be significantly useful for making good protocols of radiotherapy by the use of low LET and ion beam radiation. Together with this in vitro experiment, in vivo experimental radiotherapy for the target animal will give good indication for making the better protocols of the radiotherapy.

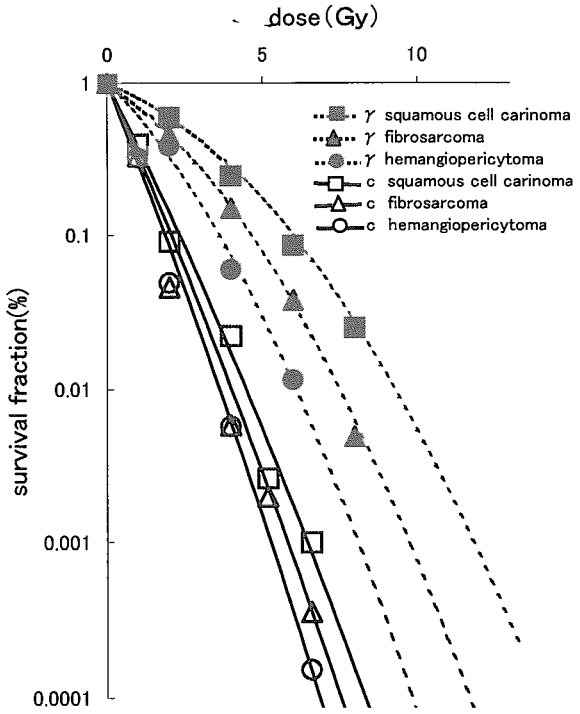


Fig.1.survival curve of three canine tumor cell lines following exposure to ^{12}C ion beam and γ ray.

Table.1.RBE of three canine tumor cell lines following exposure to ^{12}C ion beam.

	D_{10} (Gy)		RBE
	γ ray	220MeV ^{12}C ion	
Squamous cell carcinoma	5.97	2.34	2.56
fibrosarcoma	4.62	2.07	2.23
Hemangioperi-cytoma	3.59	1.87	1.92

2.23 Development of pollen-mediated gene transfer technique using penetration controlled irradiation with ion beams

Y. Hase, A. Tanaka and H. Watanabe
Department of Radiation Research for Environment and Resources, JAERI

There are several gene transfer techniques in plants such as *Agrobacterium*-mediated transformation and direct gene introduction by electroporation. However, the range of applicable plant species is restricted by the host range in the *Agrobacterium*-transfection method, and also plant species that are capable of protoplast regeneration are limited in the electroporation method. If pollen can be used as a carrier of DNA vector, it could make up a large part of these disadvantage. However, no stable method in pollen transformation have been established yet.

We have reported that the transient β -glucuronidase (GUS) expression was observed at a high frequency (55.1%) when tobacco pollen was incubated in a DNA (pBI221) solution following ion-beam irradiation with the penetration depth of 4 μm[1,2]. Although tobacco pollen has a endogenous GUS-like activity, GUS expression frequency was increased as the concentration of DNA solution was increased[1]. Those results suggest that the foreign DNA can be efficiently introduced into the pollen using penetration-controlled irradiation with ion beams. The amount of seeds obtained by pollination of those DNA-introduced pollen was not decreased significantly[2]. However, apparent transformants were not obtained in the screening of more than 10,000 seeds. Accordingly, the pollen transformation may not be achieved only by raising the transient GUS expression frequency which indicates the incorporation efficiency of the foreign DNA into the cell.

There are several possible reasons why transformants could not be obtained. One of them is the nucleases that were released from pollen. In our current method, those nucleases completely digested the plasmid DNA less than 2 hour after suspension of the irradiated pollen[3]. Since Matousek and Tupy reported no further release of nucleases was observed after 2 min of incubation of tobacco pollen[4], we have tried to remove nucleases by washing. Although degradation of DNA was reduced by washing, it could not be removed completely[3]. The plasmid DNA was cut within 4 hour after washing. Although the addition of EDTA suppress the nuclease activities, EDTA can not be used in our system because the addition of EDTA, even in 0.3mM, greatly reduce the pollen germination activity[3]. Pollen germination was also suppressed as incubation time increased. It was thought that incubation time in the DNA solution should be less than 1 hour[3].

Another possible hindrance in pollen transformation is the characteristics of the pollen itself. Following meiosis, microspore nucleus divides in an unusual manner to form two daughter cells, the vegetative and generative cell. Consequently the generative cell lies free in the cytoplasm of the vegetative cell. In order to obtain transformants in the next generation, the foreign DNA has to be transferred into the genome of the generative nucleus. In our studies, the foreign DNA was

successfully introduced into the vegetative cells through the outer wall and membrane of the vegetative cells. However, it is still unclear whether the foreign DNA could be introduced into the generative nucleus that is covered by cell membrane and nuclear membrane. On the other hand, the generative nuclei of mature tobacco pollen are in just before M-phase. Therefore, the introduction frequency of foreign DNA into the genome might be in a low level. Thus, nucleases, cell membranes and DNA introduction frequency have been unsolved problems in our pollen transformation system. We will attempt the other vector system or method such as *Agrobacterium* transfection and electroporation to reveal the reason why transformants has not been obtained.

References

1) A.Tanaka et al., *JAERI Rev.* 97-015:21-23(1997).
2) Y.Hase et al., *JAERI Rev.* 98-016:81-83(1998).
3) Y.Hase et al., *JAERI Rev.* 99-025:82-83(1999)
4) J.Matousek and J.Tupy, *Plant Sci.Lett.* 30:83-89(1983).
5) Guan-Ning Ye et al., *Plant Journal* 19: 249-257 (1999).

3. Radiation Chemistry/Organic Materials

3.1 Study on Space Environment Durability of Newly Developed Polymeric Materials for Spacecraft ····· 87
Y. Nakayama, H. Seino, K. Imagawa, M. Sugimoto, H. Kudoh, N. Morishita and Y. Morita

3.2 Permeation Control of PEG Molecules by a Thermo-responsive Ion-track Filters ····· 89
M. Asano, H. Koshikawa, Y. Maekawa, M. Yoshida and T. Kume

3.3 Cross-linking of Polymers in Heavy Ion Tracks ····· 91
H. Koizumi, M. Taguchi, Y. Kobayashi and T. Ichikawa

3.4 Ion Track Structure in Polysilane Thin Films ····· 94
S. Seki, K. Maeda, Y. Kunimi, S. Tagawa, Y. Yoshida, H. Kudoh, M. Sugimoto, Y. Morita, T. Seguchi and H. Shibata

3.5 Primary Process of Radiation Chemistry Studied by Ion Pulse Radiolysis ····· 97
Y. Yoshida, S. Seki, A. Saeki, K. Okamoto and S. Tagawa

3.6 Photon Counting System for Gaseous Nitrogen Irradiated with 175-MeV Ar Ion ····· 99
M. Taguchi, K. Furukawa, H. Namba and S. Ohno

3.7 Application of Thin Film Dosimeters to Measurement of Ion Beam Dose Distribution ····· 101
T. Kojima, H. Sunaga, H. Takizawa and H. Tachibana

This is a blank page.

3.1 Study on Space Environment Durability of Newly Developed Polymeric Materials for Spacecraft

Y.Nakayama, H.Seino, K.Imagawa,
M.Sugimoto*, H.Kudoh*, N.Morishita*, Y.Morita*
Office of Research and Development, NASDA,
*Department of Material Development, JAERI

1.Introduction

Polymeric materials such as polymer films for thermal control play important roles for use in spacecraft. Among the properties required for a spacecraft material are the durability against space environment effects.

Ground simulation tests that utilize single or combined irradiation of ions (proton, iron ion, carbon ion, etc.), electron beam (EB), ultraviolet rays (UV), and atomic oxygen (AO), as well as flight experiments, are very useful to examine the space-environment durability of spacecraft materials[1].

Polyimides and fluoropolymers are typical polymeric materials used for spacecraft. Polyimides are stable against EB and UV irradiations. Durability of polyimides against AO, however, is as low as other polymeric materials. Challenges to improve the AO durability of polyimide is being done[2]. We have developed several polyimide films as candidates of thermal control materials with improved AO durability.

Although fluoropolymers have higher durability against AO compared to other polymeric materials, they are not strong against EB, UV and ions. Recently, it has been found that EB irradiation to poly(tetrafluoro ethylene) (PTFE) at a narrow temperature range around the melting point of PTFE caused cross-linking[3]. The cross-linked PTFE (X-PTFE) can have improved durability against space environments.

Polyimide films are also applied as a base film for flexible solar array panels, where tensile force is loaded to the film. Such a tensile force can affect the durability against space environments of polymeric materials. Thus irradiation tests of polymer films under tensile forces are necessary.

In the present work, we report the results of evaluation of thermal control materials under ground simulation tests.

2.Experimental

Samples studied in the present work are shown in Table 1. The thickness of the polyimide films was about 0.05mm and that of the PTFE and X-PTFE was about 0.5mm.

Table 1 Samples

Name	Composition
PI1	Metal oxide[10nm]/UPILEX-S
PI2	Siloxane layer [2-3 μ m]/UPILEX-R
PI3	Siloxane-containing[0.9wt%]UPILEX-R
PI4	Siloxane-containing[2.7wt%]UPILEX-R
PI5	Fluorine-containing[16.7wt%]polyimide
PI6	BPDA-ODA(UPILEX-R)
PI7	BPDA-PDA(UPILEX-S)
X-PTFE	cross-linked PTFE
PTFE	poly(tetrafluoro ethylene)

BPDA-ODA: [biphenyl tetracarboxylic dianhydride] -[4,4' oxydianiline]
BPDA-PDA: [biphenyl tetracarboxylic dianhydride]-[paraphenylene diamine]

Proton(H^+: 1, 3 MeV), iron ions(Fe^+: 1MeV, Fe^{5+}: 15MeV) and carbon ion (C^+: 1MeV) irradiations were carried out with Tandem accelerator of TIARA, JAERI. Proton(H^+: 10 MeV) irradiation was carried out with AVF

cyclotron of TIARA. Fluences of ions were equal to 10-year irradiation on geostationary orbit (GEO) (proton: $2x10^{11}$[cm^{-2}], iron ion: $5x10^{7}$[cm^{-2}], carbon ion: $5x10^{8}$[cm^{-2}]) or more.

EB irradiation was applied to UPILEX-R film cut in the size of dumbbell shape type 4 of JIS K-7127 under tensile forces, 0, 7.5, 15.0, 26.0 MPa. Fluence of electron was equal to 10-year irradiation on geostationary orbit (GEO) ($2x10^{16}$[cm^{-2}]) or more.

Thermo-optical properties (solar absorptance: α_S and normal infrared emittance: ε_N) were evaluated with instruments in NASDA.

3.Results and Discussion

PI1 with ultra-thin metal oxide on UPILEX-S showed a little smaller α_S and larger ε_N compared to PI7(UPILEX-S). The α_S and ε_N values for PI2 with siloxane layer on UPILEX-R were a little larger than those for PI6(UPILEX-R). Siloxane-containing materials, PI3 and PI4, also showed a little larger α_S and ε_N compared to PI6. Fluorine-containing polyimide PI5 gave a little smaller α_S and ε_N compared to PI6 and PI7. X-PTFE showed a almost same α_S as PTFE and smaller ε_N than PTFE. Solar absorptance values of proton-irradiated samples are shown in Fig.1. All the samples showed a little change in α_S.

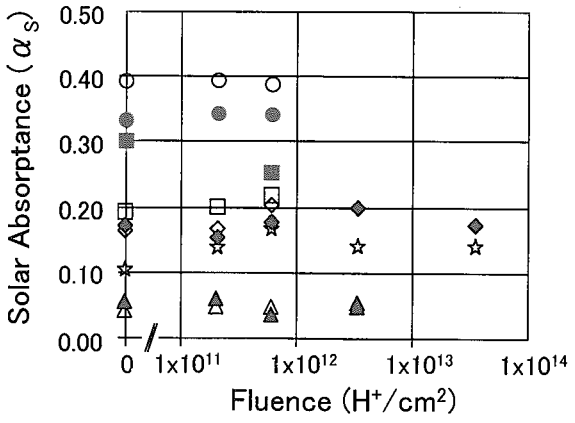


Fig.1 Solar absorptance (α_S) values with increase of proton fluence.
●:PI1, ■:PI2, ◇:PI3, ◆:PI4, ☆:PI5, □:PI6, ○:PI7. ▲:X-PTFE, △:PTFE.

Values of ε_N were almost constant under proton irradiation. Irradiations with iron ions and carbon ion did not cause large changes in α_S and ε_N values.

The values of tensile strength and elongation at break for the dumbbell sample (UPILEX-R) after EB-irradiation under tensile force are shown in Fig.2. EB-irradiated samples became a little larger in tensile strength and smaller in elongation at break compared to the control sample. The difference of tensile force during the EB irradiation and of EB fluence did not affect the tensile strength and elongation at break. These results seem to suggest that EB irradiation increased the brittleness of the polyimide by causing cross-linking under the present conditions.

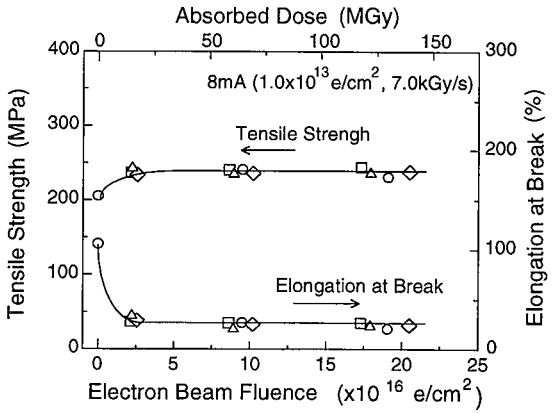


Fig.2 Mechanical properties of UPILEX-R after EB irradiation under tensile force.
○:0MPa, □:7.5MPa, ◇:15MPa, △:26MPa.

References

1) Y.Nakayama, K.Imagawa, M.Tagashira, M.Nakai, H.Kudoh, M.Sugimoto, N.Kasai, T.Seguchi, Proceedings of 8th ISMSE-5th ICPMSE, Arcachon, France, June(2000).
2) M.R.Reddy, J.Mater.Sci., 30, 281(1995).
3) E.Katoh, H.Sugisawa, A.Oshima, Y.Tabata, T.Seguchi, T.Yamazaki, Radiat.Phys.Chem., 54, 165(1999).

3.2 Permeation control of PEG molecules by a thermo-responsive ion-track filters

M. Asano, H. Koshikawa, Y. Maekawa, M. Yoshida and T. Kume

Department of Material Development, Takasaki Radiation Chemistry Research Establishment, Japan Atomic Energy Research Institute,
Watanuki-machi 1233, Takasaki, Gunma 370-1292, Japan

Introduction

Heavy ions are ionizing particles that create zones of high density excitations and ionizations as they pass through materials. These damage zones are called latent tracks and they can be converted into useful ion-track pores by chemical etching[1]. Among these materials, a poly(ethylene terephthalate) (PET) is a very favorable film for the preparation of fine cylindrical ion-track pores with an uniform size[1].

We are interested in developing a thermo-responsive filter to regulate the size of pore in nano-order scale; this regulation would behave similarly to biological membrane. In order to achieve this goal, we utilized a chemical linkage (like grafting) method as a filter modification. Poly(N-isopropylacrylamide) (PNIPAAm), which has a lower critical solution temperature (LCST) around 32°C in water, can be linked chemically onto the wall of pores in the filter by γ-ray radiation. Therefore, PNIPAAm was incorporated as a chemical valve onto the PET ion track to prepare the thermo-sensitive filter[2]. The corresponding gel layer palys an important role in appearance of open-close function for the pore according to changes in a slight amount of temperature. The thermo-sensitivity of the PNIPAAm-linked PET filter was confirmed by the permeability of poly(ethylene glycol)s (PEGs) through the filter.

Experimental

Ion track PET filters with a cylindrical pore were prepared by irradiation of ^{129}Xe ions with an energy of 450 MeV at a fluence of 6 x 10^6 ions/cm^2, followed by etching in 6 M aqueous solution of NaOH (1.0 μm in diameter and 38 μm thickness). The uncrosslinked PNIPAAm (like linear polymer) was obtained by irradiating a mixture of 9 g of its monomer in 30 ml of acetone for 1 hour at 25°C using a ^{60}Co γ source (dose rate : 10 kGy/h). A thermo-responsive layer based on the uncrosslinked PNIPAAm was chemically linked onto the wall of cylindrical pores in the filter as follows. Ion-track PET filters and a 10% water-acetone (60 /40) solution of uncrosslinked PNIPAAm was placed into a glass ampoule; then the ampoule was sealed after several times of degassing at -78°C (dry ice-ethanol system). γ-Ray radiation of this ampoule was carried out at 0°C (ice-water system) for 3 hours at a dose rate of 10 kGy/h. The irradiated sample was immediately immersed in a thermostated water bath at 60°C. After chemical linkage (grafting), the unreacted PNIPAAm was removed in a Soxhlet-type extractor in methanol for 24 hours. The capability of such a thermo-responsive PNIPAAm-linked ion-track PET filter was evaluated from the permeability of PEGs with Mw of 106 - 70,000 as a function of temperature.

Results and Discussion

Figure 1 shows the chemically grafting yield of PNIPAAm at 60°C based on the weight of ion-track PET filters as a function of grafting time. The grafting yield reached to 9% yield for 180 minutes of the reaction.

Figure 2 shows permeability of PEG with a Mw of 106 through ion track PET filters with the different grafting yields of PNIPAAm at 31°C as a swollen state and 33°C as a shrunken state of PNIPAAm. The permeability was evaluated using permeation ratios between permeating amounts of PEG with and without grafted PNIPAAm gel layer at each temperature. In a swollen state of PNIPAAm

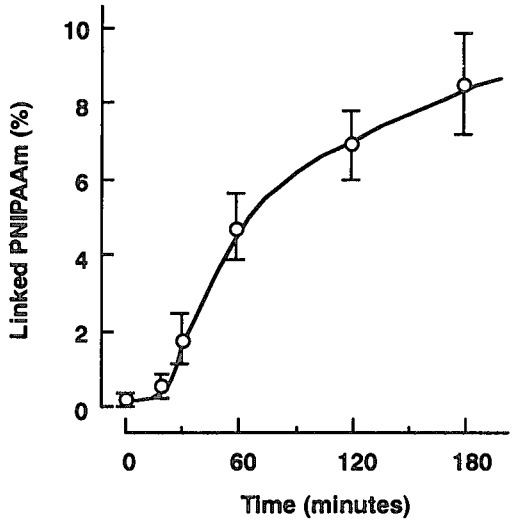


Figure 1 Chemical grafting yield of PNIPAAm onto ion-track PET filters as a function of grafting time.

at 31°C the permeability (M_t / M_∞) decreased with increase of the grafting yield and in an approximately 7% yield the permeation of PEG was completely blocked. The pores of ion track PET filters were completely covered by the highly swollen gel layer, which was observed by an optical microscope. In contrast, in a shrunken state at 33°C, the permeability was constant up to 5% of grafting yield and decreased to 30% in 7% grafting yield. The pores of ion track PET filters were partially covered by the gel layers in shrunken state, which looked like a mosaic structure by a microscopic observation. Therefore, PEG molecules with a Mw of 106 should permeate

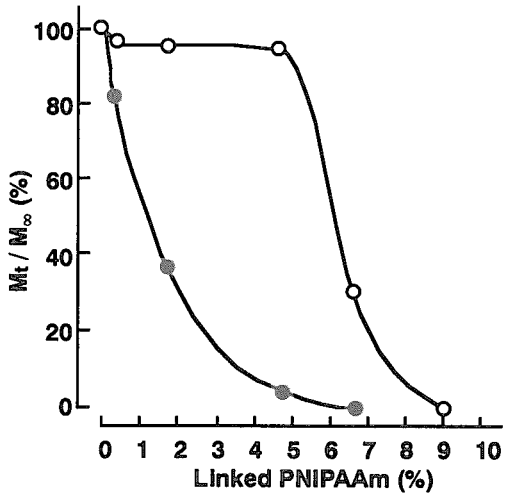


Figure 2 Permeability control of PEG with a Mw of 106 through PNIPAAm-linked ion-track PET filters at temperatures of (●) 31°C and (○) 33°C.

through the labyrinth-like porous gel layer in PET filters. In the case of ion track filters with 7% grafting yield, no PEG was permeated through those filters even in a shrunken state at 33°C.

In conclusion, we described an interesting result of solute permeation behavior on the PNIPAAm-linked ion-track PET filter. This functional filter is characterized by a unique "open-close" permeation profile, that is the PNIPAAm-linked porous filter regulates the permeability of solutes at a certain temperature due to a thermo-sensitivity of linked PNIPAAm layers.

References

1)R. Spohr : Ion tracks and microtechnology (Ed. by K. Bethge), Vieweg Verlag, Germany, 1990.

2) A. Hiroki, M. Yoshida et al., *Radiat. Effects & Defects in Solids,* 147,165-175 (1998).

3.3 Cross-linking of Polymers in Heavy Ion Tracks

H. Koizumi, M. Taguchi*, Y. Kobayashi* and T. Ichikawa
Division of Molecular Chemistry, Graduate School of Engineering, Hokkaido University; *Department of Radiation Research for Environment and Resources, JAERI

1. Introduction

Heavy ions deposit energy along the ion tracks with high density. The high local dose may cause chemical effects different from those by γ-rays and fast electrons. Relationship between the dose distribution in the ion tracks and the chemical effects of ion beam irradiation will be important to develop new applications of ion beams for material modification and fabrication of micro-structure[1-4].

In the present study, we have examined formation of "gel strings" of poly-dimethylsiloxanes by ion irradiation. Gelation dose of polydimethylsiloxane is 10^4-10^6 Gy[5] (table 1). Dose near the center of heavy ion tracks exceeds the gelation dose[1-3]. Single gel string will be generated in any single ion track[4]. Measurements of the size and the yield of the strings will give information on the chemical reactions in heavy ion tracks.

2. Experimental

Polydimethylsiloxanes supplied by Shin-Etsu Chemical Co., Ltd. were degassed under vacuum. They were put in metal cells with a window of Aluminum foil of 25 μm thickness for ion-beam irradiation. Ion beams from the AVF cyclotron were irradiated at the HY1 port. The irradiated samples were dissolved in hexane. The insoluble residue was separated by filtration with membrane filters (Millipore LSWP04700, pore size 10.0μm). Weight of insoluble residue was measured.

3. Results and Discussion

The weight of the insoluble residue of polydimethylsiloxane irradiated with 256 MeV Ar ion is plotted in figure 1 as a function of the ion fluence. The weight increases proportional to the ion fluence. The yield increases as increasing the initial molecular weight of polydimethyl-siloxanes.

The gel fraction for the ion-irradiated polydimethyl-siloxane of the initial weight of 60,000 is plotted in figure 2 as a function of average dose within the ion range. The gel fraction is proportional to the average dose. This dependence on the dose is different from that for γ-irradiation in figure 3. It is zero at doses lower than a gelation dose. It abruptly increases at higher doses than the gelation dose, and approaches to unity. The difference arises from that in local dose distributions for ion- and γ-irradiations. Local dose within the radius of several nm in the heavy ion tracks exceeds the gelation dose; the gelation occurs in any single track. The amount of the gel hence proportionally increases with increasing number of the irradiated ions. Crosslinking by

γ-irradiation occurs homogeneously over the sample. The gelation occurs only when the macro dose exceeds the gelation dose.

The yield of the insoluble residue per ion is shown in table 2. Single gel string with the length of the ion range will be generated in any single ion track. The average radius of the string is then calculated from the yield and with the density of the sample. It is also shown in table 2. It increases with increasing the initial molecular weight of the polymers. The radial dose distribution decreases with increasing the distance(r) from the center in proportion to $1/r^2$. The gelation dose decreases with increasing the initial molecular weight (M) in proportional to 1/M. The radius of the area with higher dose than the gelation dose hence increases in proportion to $\sqrt{M}$: the weight of the gel strings increase in proportion to M. It agrees with the experimental results.

The radius of the gel string is estimated from radial dose distribution in ion tracks: the radius at which the dose is the gelation dose is calculated by using the dose distribution proposed by Chatterjee and Schaefer[6]. The estimated values are comparable with the experimental values. The chemical effects in polydimethylsiloxane by the ion-irradiation can be estimated with the dose-yield relationship for γ-irradiation and the local dose distribution in the ion tracks. The single gel string is generated in single ion track due to high local dose in the heavy ion tracks.

References

1) H. Koizumi, M. Taguchi, H. Namba, T. Ichikawa, H. Yoshida, Nucl. Instr. and Meth. B, **132** (1997) 633.
2) H. Koizumi, T. Ichikawa, H. Yoshida, H. Namba, M. Taguchi, and T. Kojima, Nucl. Instr. and Meth. B, **117** (1996) 431.
3) H. Koizumi, T. Ichikawa, H. Yoshida, H. Shibata, S. Tagawa, and Y. Yoshida, Nucl. Instr. and Meth. B, **117** (1996) 269.
4) H. Koizumi, M. Taguchi, and T. Ichikawa, TIARA Annual Report 1998, JAERI-Review 99-025 (1999) 93.
5) C. G. Delides, Radiat. Phys. Chem. **16** (1980) 345.
6) A. Chatterjee and H. J. Schaefer, Radiat. Environ. Biophys. **13** (1976) 215.

Table 1. Gelation dose of polydimethyl-siloxane. The value of 2.7 (ref. 5) is used for the G-value of the crosslinkng to estimate the dose.

Molecular Weight	Gelation Dose / kGy
30,000	60
60,000	30
103,000	18
165,000	10

Table 2. Dependence on the initial molecular weight (mw) of the yield of gel (Y) and the radius(r) of "gel string" generated in polydimethylsiloxane irradiated with 256 MeV Ar ions.

mw.	Y / 10^{-14}g ion^{-1}	r / nm	
30,000	1.2	5.4[a]	6-11[b]
60,000	2.0	7.0[a]	9-16[b]
165,000	6.0	12[a]	14-25[b]

[a] calculated from Y, the range of the ion (133μm), and the density of the sample.
[b] estimated from the radial dose distribution in the ion tracks (see text).

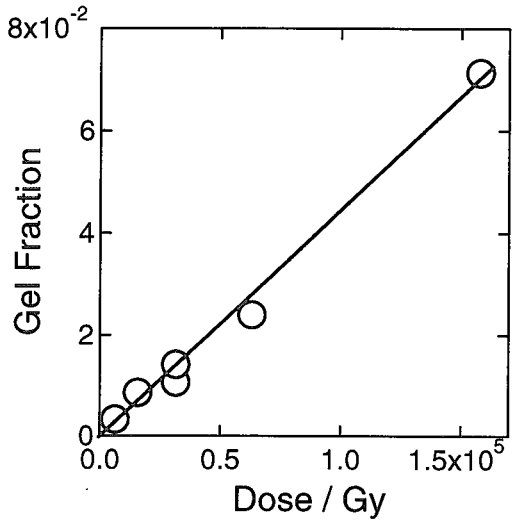


Figure 2. Gel fraction of polydimethyl-siloxane irradiated with 256 MeV Ar ions as a function of dose. The molecular weight of polydimethylsiloxane is 60,000. The dose is average dose within the range of the ion.

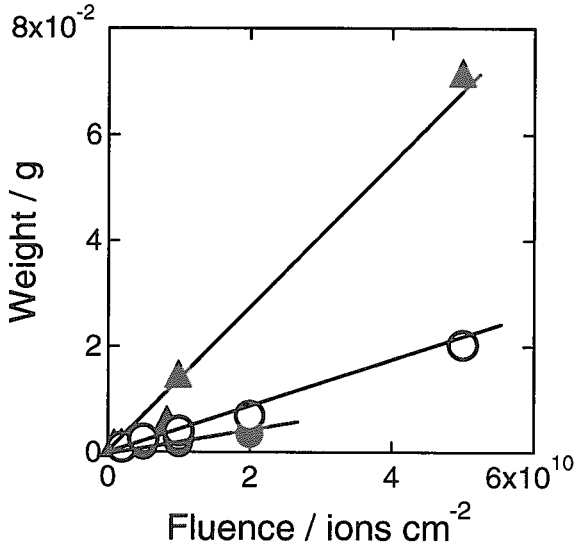


Figure 1. Weight of the insoluble residue (gel) of polydimethylsiloxane irradiated with 256 MeV Ar ion as a function of the ion fluence; the initial molecular weights of polydimethylsiloxane are 30,000 (●), 60,000(○), and 165,000(▲). The irradia-tion area is 19.6 cm^2.

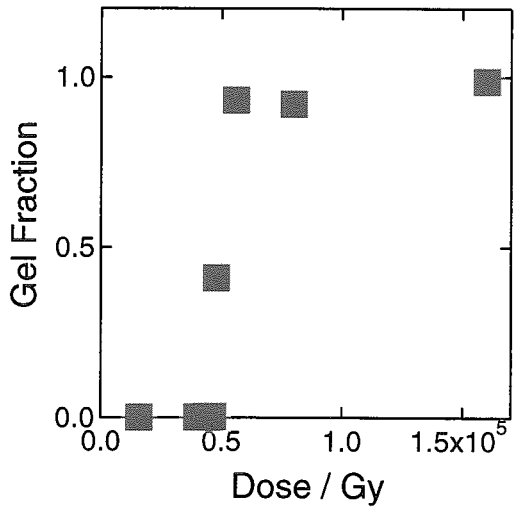


Figure 3. Gel fraction of polydimethyl-siloxane irradiated with γ–ray as a function of dose. The molecular weight of polydimethylsiloxane is 60,000.

3.4 Ion Track Structure in Polysilane Thin Films

S. Seki [a], K. Maeda[a], Y. Kunimi[a], S. Tagawa[a], Y. Yoshida[a], H. Kudoh[b], M. Sugimoto[b], Y. Morita[b], T. Seguchi[b], H. Shibata[c]

[a]The Institute of Scientific and Industrial Research, Osaka University.

[b]Department of Material Development, JAERI, Takasaki

[c]RCNST, The University of Tokyo.

Introduction

Polysilane derivatives are themselves one dimensional semiconducting wires that exhibit interesting features such as thermo- and solvato-chromism [1,2], nonlinear optical property [3], and photoconductivity [4]. These features of polysilanes have been ascribed to the σ electrons delocalized along the skeleton. The UV-light induced reactions in polysilanes have been widely studied because of their high efficiency of main chain scission [5]. We reported the radiation effects of ion beams on polysilanes and the dependence of reaction processes on LET (linear energy transfer: energy deposition rate of incident particles per unit length) of the characteristic radiation [6]. Polymers seem to be cross-linked by high LET ion beam irradiation. On the other hand a main chain scission reaction was predominantly seen for low LET radiation. The difference in radiation induced reactions was ascribed to a variation of density of reactive intermediates. The spatial distribution of deposited energy by charged ions played a significant role in promoting chemical reactions in the target materials [7-11], and we suggested that the ion beam produced a non-homogeneous field of chemical reactions, where the reactive intermediates produced by an incident ion are radially distributed from the projectile. The size of the field depended not only on LET but also on the kind of reactive intermediate species. It is called as "chemical track radii" which should be defined for each target materials.

Experimental

PMPS was synthesized by the reaction of methylphenyldichlorosilane with sodium in refluxing toluene or *n*-undecane (Kipping method). The reaction was carried out under an atmosphere of predried argon with or without 12-crown-4 ether. The PMPS was fractionated by separatory precipitation leading to **PS1** (Mn = 4.6 ~ 2.2 x 10^5), **PS2** (Mn = 1.5 ~ 1.1 x 10^5), **PS3** (Mn = 2.6 ~ 2.1 x 10^4), **PS4** (Mn = 1.0 x 10^4 ~ 9.0 x 10^3), and **PS5** (Mn = 5.0 ~ 4.0 x 10^3) with small dispersion less than 1.5. PMPS was spin-coated on Si substrate which had been treated by NaOH solution in ethanol/water = 1/1 during 5 min. These films were irradiated in a vacuum chamber (< 1 x 10^{-6} hPa) with ion beams listed in the table from a cyclotron accelerator at Japan Atomic Energy Research Institute, Takasaki Radiation Chemistry Resarch Establishment. The ion beams from a Van de Graaff accelerator was also of use at the Research Center for Nuclear Science and Technology, University of Tokyo. The irradiated films were developed by acetone, diethylether, dibutylether, and benzene in this order, respectively for 2 min. AFM measurements were performed at RT and in air using Seiko Instruments

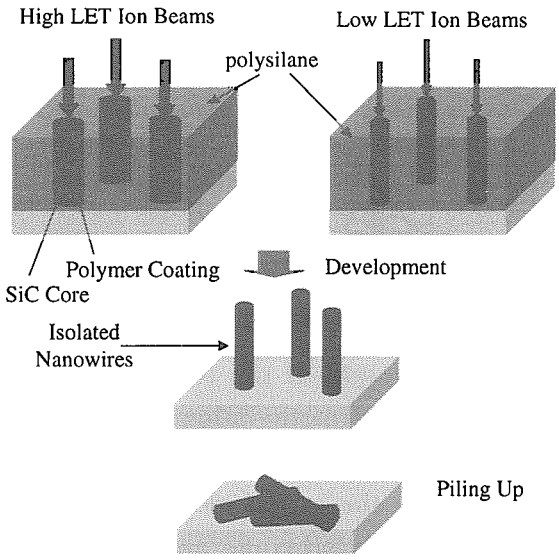


FIG 1. Schematic view showing the formation of nanowires in a polysilane thin film. Development gives individual nanowires and the number density of wires.

SPI-3800.

Results and discussion

Cross-linking reactions in a polysilane thin film is revealed to occur within chemical track, which renders the film insoluble against any kinds of solvents. The following equations give good interpretation to the gelation in polysilane films [6],

$$s = \{1-(r+\delta r)\}^f$$

$$g = 1-\{1-(r+\delta r)\}^f$$

where s and g denote the fraction of sol and gel, respectively, r is the radius of a chemical track determined by the energy deposition rate of an incident ion, δr is the differential radius of the track which depends on the shape and size of a individual polymer molecule, and f is the fluence of the incident ion beams. The schematic of the gelation in the polymer system is presented in figure 1. An incident ion densely deposits its energy within a limited area, and a cross-linked, cylinder-like polymer gel is formed along the projectile. The uncross-linked part of a film is washed by solvent, leading to the isolated nanowires of cross-linked polysilanes. The wires are piled up by the procedures when the film is irradiated at high fluence of ion beams, thus we can determine the size of a nanowire by trace of the gel fraction. The estimated values of the nanowire radii are summarized in the table for poly(methylphenylsilane): PMPS.

Table Chemical core sizes in PMPS with different molecular weights for a variety of ion beams.

Ion Beams	LET (eV/nm)	$r+dr$ [a] (nm) PS1	PS2	PS3	PS4	PS5
450 MeV Xe	8500	13.4	-	9.3	-	7.4
520 MeV Kr	4100	10.2	-	8.9	-	6.7
175 MeV Ar	2200	6.3	5.9	-	5.1	4.3
2 MeV N	960	5.1	4.8	-	3.8	3.0
2 MeV C	810	5.0	4.3	4.0	3.4	2.7
0.5 MeV C	420	4.1	-	2.9	-	2.2

a $r+dr$ denotes the radius of a chemical track, i.e., the radius of a nanowire formed by each ion beam.

The radii apparently increase with an increase in the LET of ion beams and the molecular weight of a target polymer: PMPS, representing that the diameter of a nanowire is perfectly under control. The IR spectra of the irradiated products showed the typical features of β-SiC ceramics [12], however the ratio of β-SiC conversion did not reach to 100 % for all the specimens (~25 % for **PS1** and ~65 % for **PS5** upon irradiation to 450 MeV $^{129}Xe^{23+}$). Thus the β-SiC ceramic structure is formed only at the center part of each nanowire because of the extremely high energy density. The conversion ratio also estimates the corresponding size of SiC core for PS1 (11.8 nmϕ) and PS5 (12.4 nmϕ). This suggests that the β-SiC core size: r depends only on LET, and the thickness of the cross-linked polymer coating: δr can be individually controlled by the molecular weight of the polymer.

The variation of δr in **PS1-PS5** is discussed based on the theoretical aspects on the physical interaction of ion beams to a matter. The following formulas were already given on the values of the coaxial energy in an ion track [12],

$$\rho_c(r) = \frac{LET}{2}\left[\pi r_c^2\right]^{-1} + \frac{LET}{2}\left[2\pi r_c^2 \ln\left(\frac{e^{1/2} r_p}{r_c}\right)\right]^{-1} \qquad r \le r_c$$

$$\rho_p(r) = \frac{LET}{2}\left[2\pi r^2 \ln\left(\frac{e^{1/2} r_p}{r_c}\right)\right]^{-1} \qquad r_c < r \le r_p$$

where ρ_c and ρ_p are the deposited energy density at core and penumbra area, respectively, r_c and r_p are the radii of core and penumbra area, e is an exponential factor. The equations give a value of deposited energy density at a boundary of a nanowire by using its radii. The density is estimated as 1.2 ~ 1.6 eV/nm^3 for all the ion beams in **PS5**. The small discrepancy in the density indicates that the radial distribution of deposited energy influences the size of a nanowire and its surface structure. The density (~1 g/cm^3) and molecular weight of **PS5** give the volume of a molecule roughly as 10^2 nm^3. The deposited energy per molecule is ~150 eV indicating that the ion beams form only a few cross-linking points at the boundary because the G-value of cross-linking (number of reactions per absorbed 100 eV) has been already reported as 0.5~1. Thus simple cross-linking of polymer molecules occurs at the nanowire surface. It suggests the structure of a nanowire having a β-SiC core lapped by the cross-linked polysilanes.

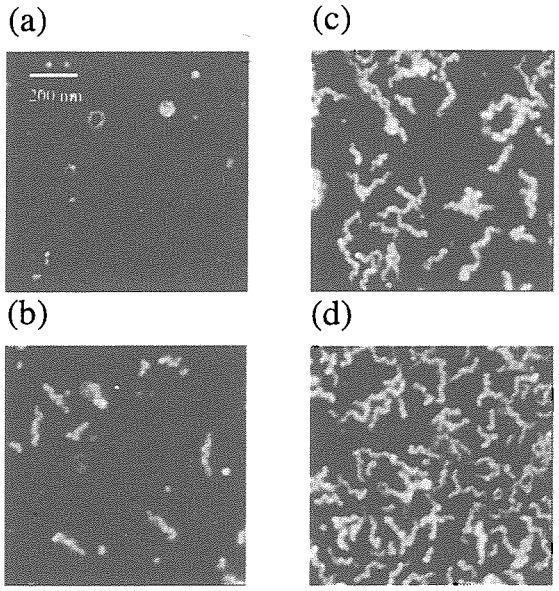


FIG 2. AFM images of the nanowires. a) Top view observed after development of non-irradiated films. Images b), c), and d) indicate the surface morphology of the developed films after ion irradiation by $^{129}Xe^{23+}$ at 2.2 x 10^9, 7.1 x 10^9, and 1.1 x 10^{10} ions/cm^2, respectively. The tone changing from dark to bright in this figure implies the height as much as 24 nm.

Figure 2 shows a series of atomic force microscope (AFM) images for the nanowires formed on a Si substrate, together with the enlarged view of a wire and the schematic of a cross section. The cross section is obtained by the deconvolution that takes the shape of the AFM tip into accounts. The section of a wire indicates a complete cylindrical shape. It shows a corresponding value of radius to that estimated by the piling up of the wires as listed in the table. The number of observed nanowires in a unit area shows good agreement with that of incident particles. In spite of a development procedure by solvents, the wires remain adhered to the Si substrate and the nanowires remain isolated from each other. This indicates that one end of the wire is tightly connected to the substrate by chemical bonds. Another attractive feature of the wires is their length. The film with 170 nm initial thickness is used to obtain the images in figure 2. The mean length of the nanowires in figure 2 is 180 ± 9 nm estimated for 80 % middle of total distribution of the wire length. We conclude that the length of a wire is also controlled by simply changing the thickness of a target film.

Conclusion

The ion beam irradiation is very unique and powerful technique to produce nano-sized cylindrical structures as displayed in the present study. It not only produces isolated nanowires on Si surface but also controls their size and length of wires. The size-controllability is also supported by the theoretical models of an energy distribution in a single ion track. We believe that the present technique has the potential to be developed for producing nano-structure materials other than SiC nanowires in the future.

References

1) Trefonas III, P., Damewood, J. R., & West, R. *Organometallics* **4**, 1318-1319 (1985).
2) Harrah, L. A. & Zeigler, J. M. *J. Polym. Sci., Polym. Lett. Ed.* **23,** 209-211 (1985).
3) Kazjar, F., Messir, J., & Rosillio, C. *J. Appl. Phys.* **60,** 3040-3044 (1986).
4) Kepler, R. G., Zeigler, J. M., Harrah, L. A., & Kurtz, S. R. *Phys. Rev.* **B35,** 2818-2822 (1987).
5) Trefonas III, P., West, R., & Miller, R. D. *J. Am. Chem. Soc.* **107,** 2737-2742 (1985).
6) Seki, S., et al. *J. Phys. Chem.* **B103**, 3043-3048 (1999).
7) Magee, J. L. & Chattarjee, A. Kinetics of Nonhomogenious Processes, G. R. Freeman Ed., Chapter 4, p.171-214 (1987).
8) LaVerne, J. A. & Schuler, R. H. *J. Phys. Chem.* **98**, 4043-4049 (1994).
9) Kobetich E. & Katz, R Phys. Rev. **170**, 391-396 (1968).
10) Wilson, W. E. *Radiat. Res.* **140**, 375-381 (1994).
11) Varma, M. N., Baum, J. W., & Kuehner, A. J. *Radiat. Res.* **62**, 1-11 (1975).
12) Seki, S., et al. *Radiat. Phys. Chem.* **48**, 539-544 (1996).

3.5 Primary Process of Radiation Chemistry Studied by Ion Pulse Radiolysis

Y.Yoshida, S. Seki, A. Saeki, K. Okamoto, S Tagawa,
M. Taguchi*, H. Nanba**
ISIR, Osaka University, *Department of Radiation Research for Environment and Resources, JAERI, **Department of Material Development, JAERI

1. Introduction

It is important to realize the mechanism of the irradiation effect of high energy ion beams, which shows the different effects from the low LET radiation such as γ rays and electron beams. To investigate the irradiation effects, the behavior of the excited state of polymer was studied by using the ion beam pulse radiolysis [1-3]. Figure 1 shows the time-dependent behavior of the emission from polystyrene excimer obtained in 520 MeV Kr^{+20} ion pulse radiolysis of 3, 10, and 100 mM polystyrene solutions in cyclohexane monitored at 330 nm. The emission intensities at various concentrations were normalized at the ion pulse end. In 100 mM solution, the lifetime of polystyrene excimer was 20 ns, which was agreement with the lifetime of solid polystyrene excimer. In 10 and 3 mM, the fast and the slow decay components were observed. The lifetime of the slow components corresponded to 20 ns. The ratio of emission intensity of the fast component to that of the slow component increased in decreasing of the concentration of polystyrene.

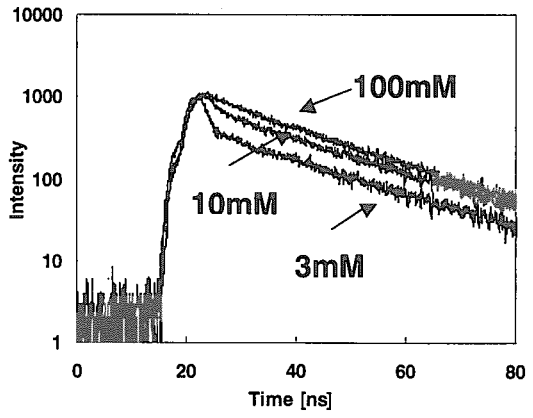


Fig. 1 Time-dependent behavior of polystyrene excimer obtained in 520 MeV Kr+20 pulse radiolysis of polystyrene solution in cyclohexane monitored at 330 nm

If the fast and slow components are given by the polystyrene excimer, the difference can be explained by a reaction of polystyrene excimer with other short-lived intermediates. To confirm the mechanism on the LET effect, the emission spectrum should be measured. The emission spectroscopy by using a streak camera with a monochorometor has been done instead for the photon counting technique.

2. Experimental

The time-resolved emission spectroscopy was done at HX1 irradiation port by using 460MeV Ar^{+13} or 520 MeV Kr^{+20} ion pulse beams from the AVF cyclotron. The repetition of the continuous pulse train was reduced to be 1/6 by using the s-chopper. The time-dependent emission was measured by a streak camera with a monochromator or a photon counting system. A trigger for the streak camera and a start signal were provided from a signal from the s-chopper.

A specially designed cell (made of stainless steel) for liquid sample was used. The sapphire window for UV-emission was used.

The molecular weight of polystyrene was 10000. All samples were degassed and irradiated at room temperature.

3. Results and Discussion

Figure 2 shows an emission spectrum obtained in the 460MeV Ar^{+13} ion beam pulse

radiolysis of 3 mM polystyrene solution in cyclohexane observed the streak camera. The emissive intermediate is only polystyrene excimer, because the spectrum shows a typical gaussian shape with the central wavelength of 330 nm. Although the experiment on 520 MeV Kr^{+20} has not been done, the emissive intermediate as shown in fig. 1 should be polystyrene excimer, because the LET effect could be observed in the case of the 460MeV Ar^{+13}.

In solid polystyrene, polystyrene excimer is produced in the following reaction scheme.

$$PS \rightarrow PS^{\cdot+} + e^- \quad (1)$$
$$PS^{\cdot+} + e^- \rightarrow PS^* \quad (2)$$
$$PS^* + PS \rightarrow PS_2^* \quad (3)$$
$$PS^{\cdot+} + PS \rightarrow PS_2^{\cdot+} \quad (4)$$
$$PS_2^{\cdot+} + e^- \rightarrow PS_2^* \quad (5)$$

Where PS, $PS^{\cdot+}$, $PS_2^{\cdot+}$, PS^*, and PS_2^* represent polystyrene, and its monomer cation radical, dimmer cation radical, monomer excited state, and excimer, respectively.

The polystyrene excimer is formed through monomer excited state (reactions 2 and 3) or through the geminate ion recombination of daimer cation radical of polystyrene (reactions 4 and 5). Although yields of polystyrene excimer should be changed by the LET effect, the decays of polystyrene excimer are constant in solid polystyrene. It means that polystyrene excimer does not react with other polystyrene excimer.

On the hand, the reaction mechanism of polystyrene is very complicated in alkane liquid, as follows.

$$RH \rightarrow RH^{\cdot+} + e^- \quad (6)$$
$$RH^{\cdot+} + e^- \rightarrow RH^* \quad (7)$$
$$RH^* + PS \rightarrow RH + PS^* \quad (8)$$
$$PS^* + PS \rightarrow PS_2^* \quad (9)$$
$$RH^{\cdot+} + PS \rightarrow RH + PS^{\cdot+} \quad (10)$$
$$PS^{\cdot+} + e^- \rightarrow PS^* \quad (11)$$
$$PS^* + PS \rightarrow PS_2^* \quad (12)$$
$$PS^{\cdot+} + PS \rightarrow PS_2^{\cdot+} \quad (13)$$
$$PS_2^{\cdot+} + e^- \rightarrow PS_2^* \quad (14)$$
$$X + PS_2^* \rightarrow ? \quad (15)$$

Where RH, $RH^{\cdot+}$, and RH^*were alkane, cation radical of alkane, excited state of the alkane, respectively. There are three formation processes of polystyrene excimer through the excited states (reactions 7, 8, and 10), through the cation radicals (reactions 10, 11, and 12), and through dimmer cation radicals (reactions 10, 13, and 14).

The LET effect as shown fig.1 is caused by the decay of the polystyrene excimer (reaction 15). X means an unknown short-lived intermediate. One of the unknown intermediates is though to be alkane excited state, because the rapid decay of polystyrene excimer is good agreement to the lifetime of alkane excited state.

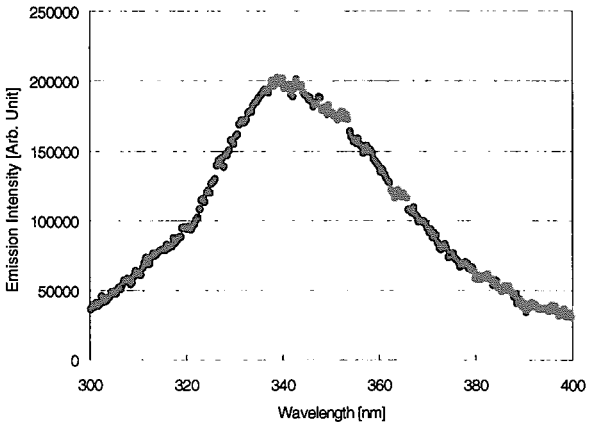


Fig. 2 Emission spectra obtained in ion beam pulse radiolysis of 3mM polystyrene solution in cyclohexane.

References

1) H. Shibata et al. Nuclear. Instrum. Meth.,A327, 53, 1993
2) Y. Yoshida et al., Nuclear. Instrum. Meth, A327, 41, 1993
3) H. Shibata et al., Nucl. Instrum. Meth., B105, 42, 1995

3.6 Photon counting system for gaseous nitrogen irradiated with 175-MeV Ar ion

M.Taguchi[a], K.Furukawa[b], H.Namba[c], and S.Ohno[d]
[a]Department of Radiation Research for Environment and Resources, JAERI,
[b]Department of Material Science, JAERI,
[c]Department of Material Development, JAERI,
[d]Theoretical Radiation Research Laboratory.

1.Introduction

We have been studying on spatial distribution of energy deposited by high energy heavy ions traveling through matters, which gives the nature of ion irradiation effects[1,2]. The distribution of deposit-energy for various ions can be estimated by the theoretical equations in water, which is the most important substances from the microdosimetrical point of view relating to health physics because of the main component of living bodies. The deposit-energy decreases steeply with an increment of a radial distance from the incident ion beam.

Two types of emission were observed in nitrogen irradiated with 330 MeV Ar^{11+} ion[3]; the (0,0) transition of the first negative system of nitrogen molecular ion at the wavelength of 391.4 nm, and the (0,0) transition of the second positive system of nitrogen molecules observed at 337.1 nm ($C^3\Pi_u$-$B^3\Pi_g$). The former has an excitation cross section proportional to the total ionization cross section[4]. While the latter is known to be induced exclusively by low energy electrons, about 20 eV[5]. Thus the analysis of the distribution of these transitions will be important to understand the energy distribution in the track in detail.

In the present report, we constructed the photon counting system, which coincides with the acceleration frequency of the AVF cyclotron, for the measurement of the low yield of photons from the gaseous nitrogen irradiated with 175 MeV Ar^{8+} ions.

2.Experimental

Ion irradiation and fluorescence measurement were performed at the beam port of HX-1 of the AVF cyclotron in TIARA facility, which is called the Experimental Apparatus for Basic study of Radiation Chemistry with Heavy Ions (EA-BRACHI)[1,3,6]. The ion used in this study was 175 MeV Ar^{8+}. The pressure of nitrogen gas in the target chamber was controlled to 18 Torr at ambient temperature, using pressure sensors, a throttling valve, pressure controller and mass flow controller that previously described[6]. Ar ions were induced through a tantalum collimators with 2 mm hole, which was sealed Kapton film (7.5μm thick) to keep the gas pressure in the

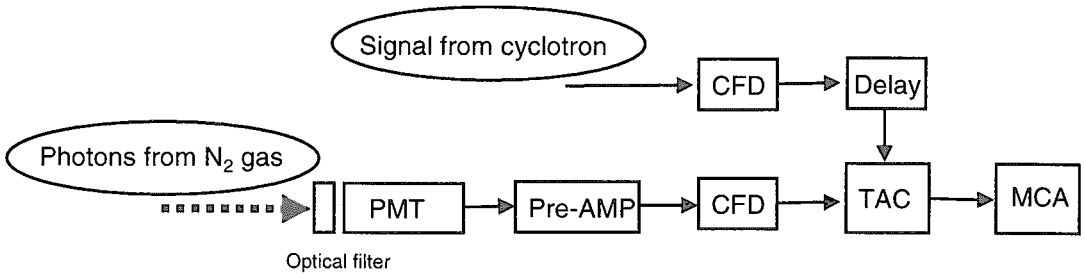


Fig. 1
Block diagram of coincidence system between photons from nitrogen gas irrdiated and timing signal from AVF-cyclotron. CFD: constant fraction discriminator, TAC: time-to-amplitude converter, MCA: multichannel analyzer.

target chamber, set on the upper streams of the ion beam to a target chamber. The fluence of the Ar ion has been measured by counting photons from plastic scintillators induced by one Ar ion irradiation before and after measurements, and was $6x10^7$ ions/sec.

Optical system was constructed with three slits to collect photons of the excited nitrogen molecules from the restricted two-dimensional area. The space resolution of the area was 2 mm. The distance of the restricted area from the center of the ion beam was changed with moving target chamber itself. In this study the optical system was placed at the radial distance of from –2 mm to 50 mm. The photons were measured by a single photon counting system with a photomultiplier tube (PMT). The block diagram of this system is shown in Figure 1.

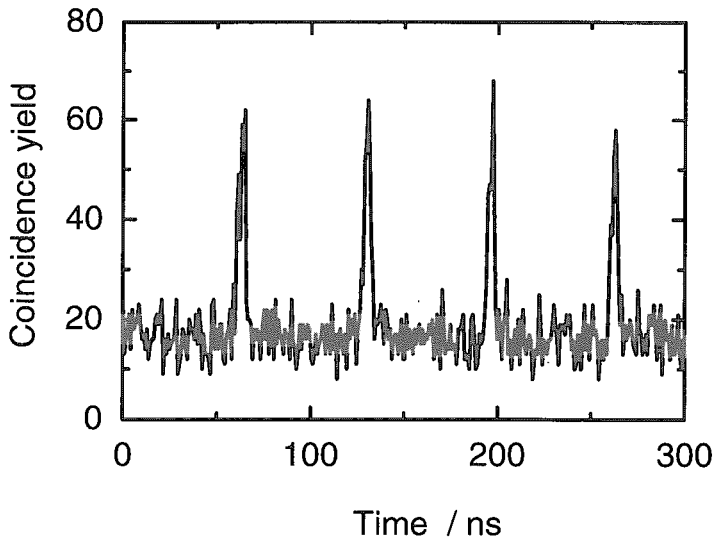


Fig. 2
Yield of photons from gaseous nitrogen irradiated with 175-MeV Ar ion coincided with the acceleration frequency of the AVF-cyclotron.

3.Results and Discussion

The (0,0) transition of the second positive system of nitrogen molecules is induced by low energy electrons[5]. Thus it is suitable for estimation of the contribution to the energy deposition from the low energy electrons. The photons from other emissive transitions were eliminated using the interference filter of 338 nm.

Being the week emission from the transition of the gaseous nitrogen at low pressure, the thermal noise of PMT prevents the accurate measurement of the photons. Therefore, we constructed the photon counting system, which coincides with the acceleration frequency of the AVF cyclotron.

Figure 2 shows the time profile of photons measured by PMT. The coincident yield had sharp peaks with peak width of about 5 ns FWHM, and time intervals between the peaks of about 67 ns. The 175-MeV Ar ion from the AVF cyclotron consists of fine structure pulses with a high frequency at 15.067 MHz, which is in good agreement with measured time intervals (66.7 ns = 1 / 15.067 MHz). Small peaks observed between the big peaks is the thermal noise from PMT.

Further experiments on energy distribution around heavy ion trajectory are in progress.

References

1. M.Taguchi, H.Namba, K.Furukawa, and S.Ohno, Radiat. Phys. Chem., **55**,511(1999).
2. S.Ohno, K.Furukawa, M.Taguchi, H.Namba and H.Watanabe, Radiat. Phys. Chem., **55**,503(1999).
3. M.Taguchi, H.Namba, Y.Aoki, K.Furukawa and S.Ohno, JAERI-Review, **97-015**, 72(1996).
4. W.L.Borst and E.C.Zipf, Phys. Rev., **A1**,834(1970)
5. M.Imai and W.L.Borst, J. Chem. Phys., **61**,1115(1974).
6. M.Taguchi, K.Furukawa, M.Moriyama, and S.Ohno, JAERI-Review, **99-025**, 91(1999).

3.7 Application of Thin Film Dosimeters to Measurement of Ion beam Dose Distribution

T. KOJIMA, H.SUNAGA, H.TAKIZAWA and H.TACHIBANA
Advanced Radiation Technology Center, JAERI

1. Introduction

Ion beams provided by the TIARA AVF cyclotron (e.g. $^{1}H^{+}$: max. 90 MeV) have been widely applied to various material science and biological studies. Practical evaluation of absorbed dose is essential for interpretation of radiation effects of ion beams on materials or biological substances under consideration of different radiation qualities and inhomogeneity of energy deposition in interested volume. Dosimetry required in these research works should cover the doses of 0.005–200 kGy with high precision within ±5% and the spatial resolution of about 10 μm. Thin film dosimeters of about 10-200 μm in effective thickness, e.g. alanine-PE, cellulose triacetate (CTA), Gafchromic film and RCD (radiachromic dye film, FWT-60), have been well-characterized for ^{60}Co γ-rays and MeV electrons in the above dose range so far. These dosimeters have a potential to be applied also to ion beams. The linear energy transfer (LET) characteristics of their dose responses have been studied for their application to ion beams[1, 2]. Reliability of the real-time fluence monitoring employing a Faraday cup was also confirmed in advance to this study, by simultaneous use with a total-absorption calorimeter in the uniform-fluence radiation field under scanning beams.Such a preliminarily characterized Gafchromic dosimeters was tested for

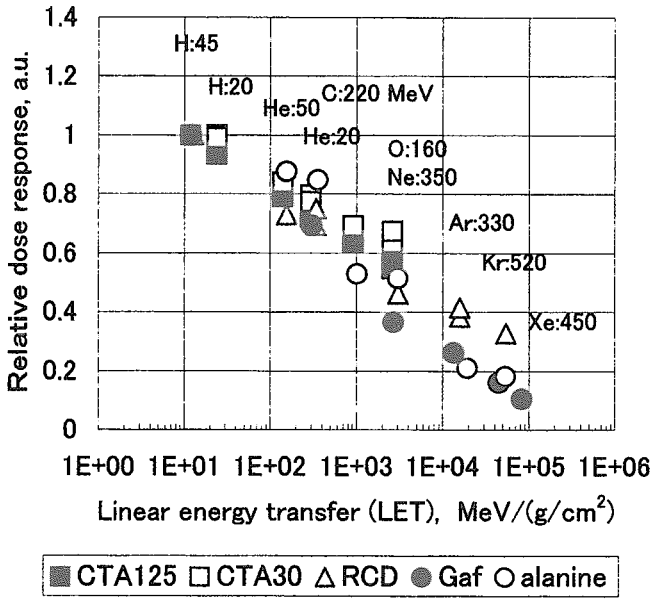


Fig.1 LET characteristics of dose responses of thin film dosimeters: CTA dosimeters(125 and 30 μm in thickness), RCD (50 μm), Gafchromic (8 μm) and alanine films (223 μm)

measurement of the lateral and depth dose distributions in the plastic phantom.

2.Experimental

The detailed experimental procedure to study dose response characteristics of film dosimeters is found in elsewhere[1, 2]. Dosimeters were irradiated in the 100x100mm^2 scanning ion beams under vacuum about 2x10^{-4} Pa. Doses give to dosimeters were controlled using a Faraday cup (suppression: -100V) so as to be doses in their linear dose response range when irradiated by low LET radiation, e.g. 10-160 kGy for CTA, 1-10 kGy for alanine, 2-8 kGy for RCD and 0.5-5 kGy for Gafchromic dosimeters. The uncertainties in fluence measurement in terms of coefficients of variation was ±2% at a 68 % confidence level (1σ) for studied ion beams[1].

The Gafchromic dosimeter having 8-μm thick sensitive layer on the surface was also tested for dose distribution measurement. For the study on depth dose distribution measurement, the dosimeters were irradiated through a stack of 7.5-μm thick polyimide films having many steps of different thickness[6]. Color changes of Gafchromic films were measured in terms of optical density at the wavelength of 580 nm using a spectrophotometer. For the study on the lateral dose distribution measurement, the dosimeters were irradiated with 450-MeV Xe ions through a 10-μm thick metal mask having 10-μm dia. holes at 60-μm center-to-center distance. Color change of irradiated area relevant to the hole pattern on the mask was analyzed using a laser microscope.

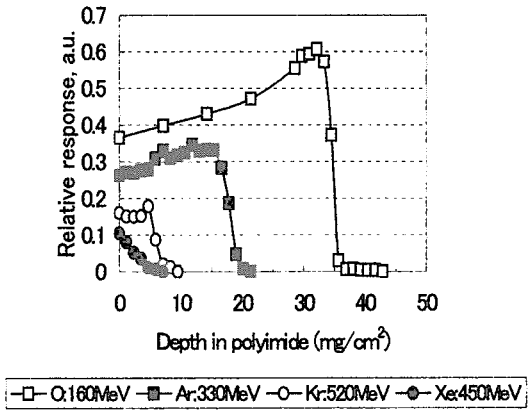


Fig.2. Depth dose distribution in the polyimide phantom measured using Gafchromic dosimeters.

3.Results and discussion

Dose response characteristics of four film dosimeters were studies for ion beams. These beams have enough energies to pass through films completely except for 520 MeV Kr and 450 MeV Xe ions. Average values of the mass electronic collision stopping power, represented as 'LET values' in this study, were calculated using ELOSS code[3] on the basis of the data table of Ziegler et al.[4], taking into account of change of LET values in the entire dosimeter. Dose responses which were calculated in terms of relative ESR signal amplitude per unit mass and dose for alanine, or net optical absorbance per unit thickness and dose for other films, were normalized to those for the low LET radiations. Dose responses, electron spin resonance signal amplitude per unit dose for alanine and optical density change per unit dose for others estimated from linear fitting of four dose points were normalized to those for ^{60}Co γ-rays or 2-MeV electrons. Such relative effectiveness values are plotted as the

function of LET, as shown in Fig.1. All the film dosimeters have a similar tendency showing decrease of relative dose response with increase of LET higher than about 100 MeV/(g/cm^2). The scattering limit of one plot is about ±4% at 1σ. It suggests applicability of these dosimeters to ion beams when calibrated by low LET radiations with appropriate correction on dose responses using the relations in Fig.1

Depth dose distributions in polyimide phantom for relatively heavier ion beams measured by the stacks of Gafchromic dosimeters are shown in Fig.2 as the preliminary result. It shows a potential to measure depth dose distributions showing Bragg-peaks with spatial resolution of 1.2 mg/cm^2 (7.5 μm). The relative dose values at the surface are mostly agreed with those in Fig.1.

Color change on the Gafchromic dosimeter irradiated by 450 MeV Xe through as shown in Fig.3. Color change patterns relevant to irradiated areas were clearly observed with sufficient sharpness of the spot edge. It suggests that the film dosimeters have a potential to know exact position of irradiated area with the spatial resolution of 10μm

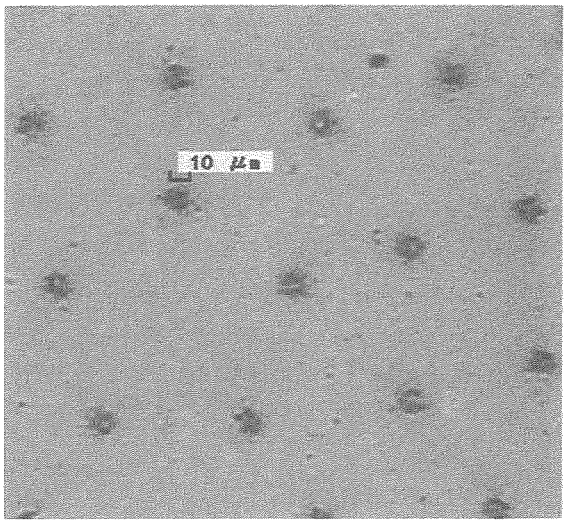


Fig.3 Color change pattern on the Gafchromic film irradiated by 450-MeV Xe ions through metal foil having 10-μm dia. holes with 60-μm center distance.

3.Conclusion

Overall uncertainty in ion beam dosimetry using film dosimeters is ultimately estimated better than ±5% at 1σ, as the sum in quadrature of uncertainty components in fluence measurement ±2% and film dosimetry ±4% at 1σ.

Gafchromic dosimeters have a potential to measure depth dose distribution with the spatial resolution of 1.2 mg/cm^2(7.5 μm) for lateral, and to know exact position of irradiated area with the spatial resolution of 10μm in lateral.

These results meet mostly the requirement to ion beam dosimetry in material science and biological research using a TIARA cyclotron, although higher spatial resolution and quantitative measurement should be achieved for lateral dose distribution

References

1)T.Kojima et al.: *Radiat.Phys.Chem.*, **53**, (1998) 115

2)T.Kojima et al.:IAEA-TECDOC-1070 (1999) 197.

3)K.Hata and H.Baba: JAERI-M 88-184 (1988)

4)J.F.Ziegler, J.P.Biersack and U. Littmark : "The stopping power and range of ions in solids", Vol.1(1985) (Permagon Press, Oxford).

5)T.Kojima et al.:JAERI-Conf 2000-1 (2000), 31

This is a blank page.

4. Inorganic Materials

4.1 He Ions Implantation Effect on the Thermal Diffusivity of CVD-SiC and CVI-SiC/SiC Composite ····· 107
T. Taguchi, N. Igawa and S. Jitsukawa

4.2 Effect of Transmutant Gas Atoms on Microstructure Evolution by Displacement Damage of SiC/SiC Composites for Fusion Systems ····· 110
S. Nogami, A. Hasegawa, T. Taguchi, K. Abe and R. Yamada

4.3 Implantation Mode Dependence of Damage Structure Depth Profiles in Al_2O_3 Irradiated with Triple Beam of H, He and Heavy Ions ····· 113
T. Aruga, Y. Katano, S. Yamamoto, T. Nakazawa and D. Yamaki

4.4 Damage Evolution in High Energy Ion-irradiated Metals and the Interaction between Gas Atoms (H and He) and Damage Defects ····· 116
Y. Shimomura, I. Mukouda, D. Yamaki, T. Nakazawa, T. Aruga and S. Jitsukawa

4.5 Synergistic Effects of Hydrogen and Helium on Microstructural Evolution in Vanadium Alloys by Triple Ion Beam Irradiation ····· 119
N. Sekimura, S. Yonamine, T. Okita, A. Kurui, Y. Arai, T. Iwai, S. Ohnuki, A. Naito, S. Hamada and Y. Miwa

4.6 Effects of Heat Treatment and Gas Atom Production on Hardness and Microstructure of F82H Steel Irradiated by Dual/Triple Ion Beams ····· 122
E. Wakai, T. Sawai, H. Tanigawa, A. Naito, T. Taguchi and S. Jitsukawa

4.7 Evaluation of He Embrittlement in Reduced Activation Ferritic/Martensitic Steels ····· 125
T. Hirose, H. Tanigawa, E. Wakai, Y. Miwa, S. Jitsukawa, H. Sakasegawa, Y. Katoh, A. Kohyama and M. Narui

4.8 Cavity Formation in Reduced Activation Ferritic/Martensitic Steels Irradiated with Dual Ions ····· 128
A. Naito, S. Jitsukawa, E. Wakai, H. Tanigawa, I. Ioka, A. Hishinuma and A. Kohyama

4.9 Basic Study on the Mechanisms of Helium Embrittlement and Reduction of High Temperature Strength on Reduced Activation Ferritic Steel ····· 130
H. Tanigawa, H. Abe, S. Jitsukawa, T. Iwai, H. Serizawa and Y. Katoh

4.10 Research on Formation Process of Irradiation Defects for Light Water Reactor Pressure Vessel Steel ····· 133
T. Tobita, M. Suzuki, Y. Idei, A. Iwase, K. Aizawa, H. Amezawa and N. Sekimura

4.11 Mechanical Characterization of Ion Implanted Layer by Microindentation Test using Different Apex Angle Indenters ····· 136
I. Ioka, M. Futakawa, T. Wakui and A. Naito

4.12 Effect of Oxygen on Characteristics of Austenitic Stainless Steels as Cladding Tube in Light Water Reactor ····· 139
S. Hamada, I. Ioka, C. Kato and K. Kiuchi
4.13 Investigation of the Resonant Vibration Modes of Self Interstitial Atoms in Metals by Low Temperature Specific Heat Measurement ····· 141
M. Watanabe
4.14 Effects of Electron Irradiation on Pd-H System ····· 143
K. Yamakawa, Y. Chimi, K. Adachi and A. Iwase
4.15 Negative Magnetoresistance of Pyrolytic Carbon and Effects of Low-Temperature Electron Irradiation ····· 144
N. Ishikawa, A. Iwase, T. Iwata, Y. Chimi and T. Nihira
4.16 Measurement of Defect Recovery Spectrum in Al by means of Constant Heating Method ···· 146
Y. Chimi, A. Iwase and N. Ishikawa
4.17 Stability of Dislocation Loops in α-Al_2O_3 and $MgO \cdot nAl_2O_3$ Crystals under Displacive and Ionizing Radiation ····· 148
K. Yasuda, C. Kinoshita and H. Abe
4.18 Carrier Control of β-$FeSi_2$ by 1.2 MeV-Au^{++} Ion Implantation ····· 151
Y. Maeda, K. Umezawa, T. Ito, S. Yamamoto and I. Nashiyama
4.19 Formation Process and Stability of Radiation-induced Non-equilibrium Phase in Silicon ····· 154
S. Ohnuki, S. Watanabe, T. Suda, M. Takeda, F. Arimoto, S. Suzuki and H. Abe
4.20 Ion Irradiation Effect on Carbon-related Thin Films ····· 157
H. Naramoto, J. Vacik, S. Yamamoto, K. Narumi and Y. Xu
4.21 Non-equilibrium Growth of Ni+C_{60} on MgO(100) ····· 160
J. Vacik, H. Naramoto, S. Yamamoto and K. Narumi
4.22 Epitaxial Re-Crystallization of the Ni/MgO(100) Interface ····· 162
J. Vacik, S. Yamamoto, H. Naramoto and K. Narumi
4.23 Characterization of Steps on Annealed Sapphire Surfaces ····· 164
K. Narumi and H. Naramoto
4.24 Development of Micro-processing Technique of Ceramics using Rare-gas Ion Beam Irradiation ····· 167
S. Ohtsuka, A. Hasegawa, M. Satou, K. Abe and T. Taguchi
4.25 Electrical and Optical Properties of Cr Ion Implanted TiO_2 ····· 170
T. Sumita, T. Yamaki, S. Yamamoto, H. Abe, A. Miyashita and I. Nashiyama
4.26 Lattice Defects Created in Quartz of Uranium Ores ····· 172
S. Toyoda, K. Komuro and H. Isobe

4.1 He ions implantation effect on the thermal diffusivity of CVD-SiC and CVI-SiC/SiC composite

T.Taguchi, N.Igawa, and S.Jitsukawa
Department of Material Science, JAERI

1. Introduction

Ceramic matrix composites show excellent mechanical properties at high temperature. These composites, therefore, are expected to be used for structural applications at high temperatures. In particular, SiC/SiC composite is expected to be used for first wall and blanket components in a fusion reactor because of low activation. In the fusion reactor, the material has to have high thermal diffusivity for heat exchange and thermal shock.

Under fusion conditions, He and H are produced by 14MeV neutron-induced transmutation reactions which are (n, α) and (n,p) respectively. These transmutation rates in SiC are larger than those in the other candidate materials such as ferritic steels and vanadium alloys.[1),2)] It is important to investigate He and/or H effects on the thermal and mechanical properties. In this study, we investigated He ions implantation effect on the thermal diffusivities of β-SiC and SiC/SiC composite.

2.Experimental procedure

2.1 materials

The β-SiC was fabricated by Chemical Vapor Deposition method and obtained from Toshiba Denko Co.Ltd., Japan. This density was 3.21g/cm^3. The SiC/SiC composite was fabricated by Chemical Vapor Infiltration method and obtained from Nippon Carbon Co. Ltd., Japan. This density was 2.25g/cm^3. The specimen size was 10mm in diameter and 0.7mm in thickness

2.2 Measurement of thermal diffusivity and thermal conductivity

The thermal diffusivity of the specimens were measured in the temperature range from 15 to 1100℃ using a laser flash thermal diffusivity analyzer (PS-2000, Rigaku Co. Ltd., Japan) with a ruby laser of 20J in the maximum power. The transient temperature response at the rear surface of the specimen was monitored with an IR detector. The thermal diffusivity, α, was obtained by $t_{1/2}$ method using the following equation:

$$\alpha = 1.388L^2/\pi^2 t_{1/2} \qquad (1)$$

where $t_{1/2}$ is the time required to reach half of the total temperature rise on the rear surface of the specimen, and L is the specimen thickness.

2.3 Implantation

An irradiation apparatus was installed in Light Ion Room No.2 of cyclotron facility at TIARA. β-SiC and SiC/SiC were implanted 50MeV He ions for 19 hours with this apparatus using an Al-foil energy degrader in order to obtain the uniform He distribution in the specimens.

3. Results

Figure 1 shows the distribution of He concentration calculated by TRIM code.[3)] It was found that He ions could be implanted uniformly in the specimen toward the depth of about 760μm. The β-SiC and SiC/SiC were implanted approximately 25.5appm.

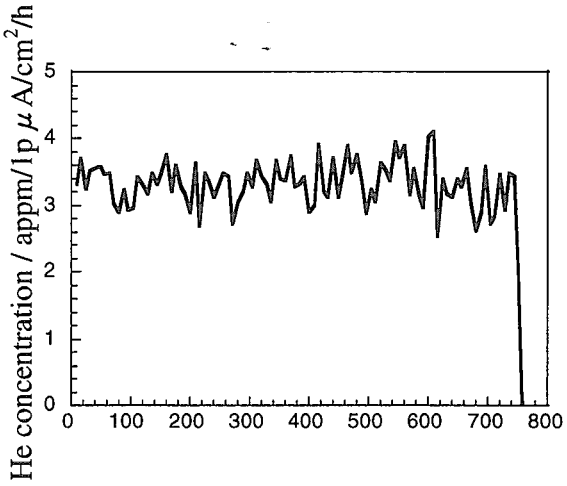


Fig.1 Depth distribution of He in β -SiC calculated by TRIM code.

Figures 2 and 3 show the results of thermal diffusivities of the β -SiC and SiC/SiC composite, respectively. The thermal diffusivities of β -SiC and SiC/SiC decreased after implantation of He^+ ions. He atoms combine with lattice defects easily and become stable because they are not soluble in SiC. Consequently the thermal diffusivities of He implanted specimens decreased. The thermal diffusivity of β -SiC measured in the 2nd run was higher than that measured the 1st run. It is reported that He release from SiC starts at 500 ℃ and tended to increase with increasing

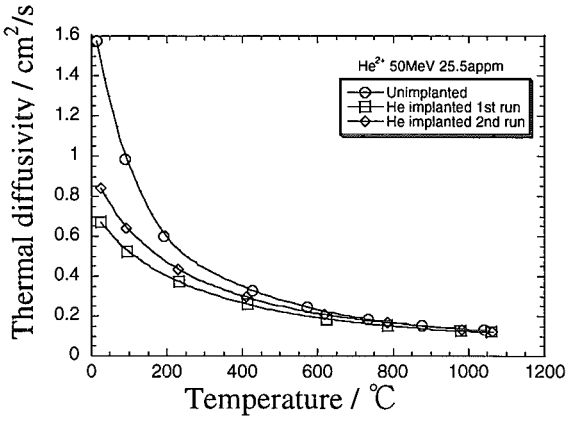


Fig.2 The thermal diffusivities of as-received β -SiC and He implanted β -SiC as functions of temperature.

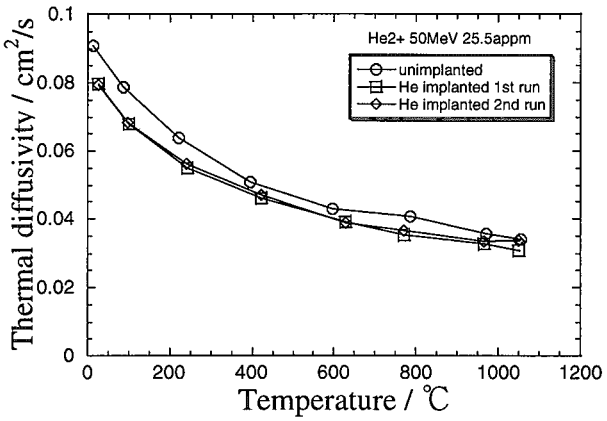


Fig.3 The thermal diffusivities of as-received SiC/SiC and He implanted SiC/SiC as functions of temperature.

temperature[4]. The specimen was heated up to 1100 ℃ during the 1st measurement. Therefore, the thermal diffusivity of the 2nd measurement was higher than that of 1st measurement. However, the thermal diffusivity of 2nd measurement was lower than those of as-received β -SiC and SiC/SiC. By annealing at higher temperature than 1100℃, it is expected that the thermal diffusivity of specimen recover higher.

4. Discussion

The thermal conductivity K is calculated from the thermal diffusivity α by the following equation:

$$K = \alpha \rho C_P \quad (2)$$

where ρ is the density and C_P is the specific heat capacity at constant pressure. Because heat conduction in SiC takes place by phonon-phonon scattering, K is also given as Debye equation:

$$K = 1/3 \rho C_P V l_{thermal} \quad (3)$$

where $l_{thermal}$ is the mean free path of phonons and V is the mean phonon velocity which we

Table 1. $l_{irradiaition}$ and $X_{irradiation}$ of β-SiC and SiC/SiC calculated from eqn(6) and eqn(7)

	First run		Second run	
Specimen	$l_{irradiation}$ / 10^{-9}m	$X_{irradiation}$ / appm	$l_{irradiation}$ / 10^{-9}m	$X_{irradiation}$ / appm
β-SiC	9.1	14.5	18.1	2.2
SiC/SiC	3.5	310.8	3.9	244.7

assume to be equal to the velocity of sound in SiC. In this study V is given by the following equation:

$$V=\sqrt{E/\rho} \quad (4)$$

where E is the elastic modulus of the SiC. By setting eqn(2)=eqn(3), we obtain

$$l_{thermal}=3\alpha/V \quad (5)$$

When additional phonon scattering by defects are introduced into a solid after irradiation, the mean free path is reduced from $l_{thermal}$ to l_I. The mean free path attributable to irradiation induced defects, $l_{irradiation}$, is approximated by:

$$1/l_I=1/l_{thermal}+1/l_{irradiation} \quad (6)$$

Finally, the defect concentration induced by irradiation, $X_{irradiaiton}$, is calculated from $l_{irradiaiton}$ by the following equation,

$$X_{irradiation}=M/(2\rho\, l_{irradiaiton}{}^3 N_A) \quad (7)$$

where M is the molecular weight of SiC and N_A is Avogadro's constant.

Table 1 shows the $l_{irradiaiition}$ and $X_{irradiation}$ of β-SiC and SiC/SiC calculated from eqn(6) and eqn(7). In the result, the $l_{irradiaiition}$ and $X_{irradiation}$ of β-SiC was much lower than those of SiC/SiC. The $X_{irradiation}$ of β-SiC was lower than He concentration implanted, while that of SiC/SiC was higher than He concentration implanted. The $X_{irradiation}$ calculated from 2nd measurement data in both materials was lower than that from 1st measurement. The reason for this is that the induced defects were recovered when the specimens were heated up to 1100℃ during the 1st measurement.

5. Conclusion

He ion implantation effect on the thermal diffusivities of β-SiC and SiC/SiC was investigated. The results obtained in this study are summarized as follows:

(1) The thermal diffusivities of β-SiC and SiC/SiC decreased after implantation of He ions.

(2) The thermal diffusivity measured in the 2nd run was higher than that measured in the 1st run because He was released from β-SiC and SiC/SiC during the 1st run.

(3) The defect concentration induced by irradiation, $X_{irradiation}$, was estimated. In the result, The $X_{irradiation}$ of β-SiC was lower than He concentration implanted, while that of SiC/SiC was higher than He concentration implanted.

References

1) L.L.Snead et al., Journal of Nuclear Materials **233-237** (1996) 26-36

2) T.Noda et al., Journal of Nuclear Materials **233-237** (1996) 1491-1495

3) J.F.Ziegler et al., The Stopping and Ranges of Ions in Matter, vol.1, Pergamon Press, New York, 1985

4) K.Sasaki, T.Yano, T.Maruyama and T.Iseki, Journal of Nuclear Materials **179-181** (1991) 407-410

4.2 Effect of Transmutant Gas Atoms on Microstructure Evolution by Displacement Damage of SiC/SiC Composites for Fusion Systems

S. Nogami [1], A. Hasegawa [2], T. Taguchi [3], K. Abe [2], R. Yamada [3]

[1] Graduate School of Engineering, Tohoku University, [2] Department of Quantum Science and Energy Engineering, Tohoku University, [3] Department of Material Science, JAERI

1. Introduction

Fusion reactor materials are required to have the radiation resistance and the low induced-radioactivity by high energy neutron irradiation. Silicon carbide (SiC) has been considered as the blanket-shield and the first-wall material because of its inherently lower induced-radioactivity by 14 MeV neutron irradiation, high temperature strength and dimensional stability after irradiation. SiC-fiber reinforced SiC-matrix (SiC/SiC) composites have been developed because monolithic SiC is so brittle for structural materials. Displacement damages and transmutant gas atoms such as helium and hydrogen will be formed in materials after neutron irradiation. Additionally, the number of helium formed in SiC after 14 MeV neutron irradiation is considered to be larger than those in ferritic steels and vanadium alloys. Effects of helium and hydrogen on microstructural evolution due to displacement damage at high temperature of SiC/SiC composites have not been studied yet.

The purpose of this study is to investigate effects of displacement damage with helium and hydrogen on microstructural evolution of SiC/SiC composites using simultaneous triple-ion-beam (self-ion, He-ion and H-ion) irradiation.

2. Experimental

Specimen preparation

SiC/SiC composites used in this study were fabricated with 0/90 SiC fiber weaves infiltrated with β-SiC using chemical vapor infiltration (CVI) process. SiC fiber in this composite was Hi-Nicalon[1] which is composed of small β-SiC grain (about 5 nm), 0.5 wt. % oxygen and free carbon. The pyrolitic carbon was deposited by CVD (Chemical Vapor Deposition) process as a fiber / matrix interface material and the thickness of C-layer was 1.2 or 0.15 μm. These composites were fabricated by DuPont Lanxide in USA. These samples were cut perpendicularly to the layers of textile and mechanically polished into mirror-like surface with 300 μm in thickness and then cut into the form of disk 3 mm in diameter.

Irradiation

Simultaneous triple ion beam irradiations were carried out using 4.30 MeV C^{2+} ions or 7.84 MeV Si^{2+} ions from a tandem accelerator, 1.20 MeV He^{+} ions from a single-ended accelerator and 380 keV H^{+} ions from an ion-implanter. Irradiation temperatures were 600, 800 and 950℃, and measured with an infrared pyrometer during irradiation. The irradiation at 950℃ was carried out only for dual-beam condition. The projected range of three ion beams in Hi-Nicalon was about 3 μm, which was calculated with TRIM code[2] using 45 eV as the displacement threshold energy[3] and 2.74 g/cm^3 as the density. Figure 1 shows the calculated depth distribution of displacement damage, helium and hydrogen concentration. The peak displacement damage by

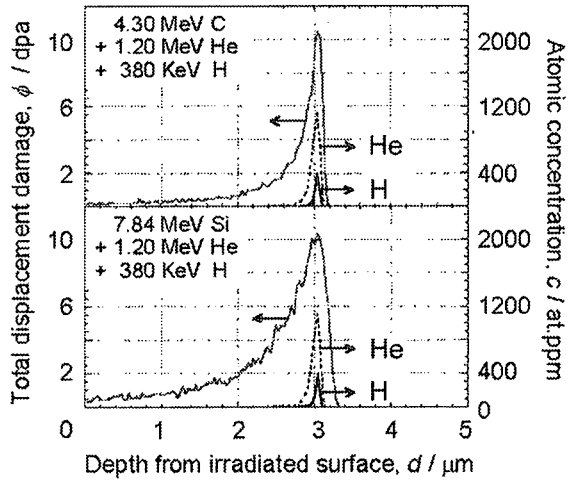


Figure 1. Depth distribution of displacement damage, helium concentration and hydrogen concentration calculated by TRIM code.

self ions was about 10 dpa and the displacement damage rate was about 1.1 x 10^{-3} dpa/sec. The concentrations of helium and hydrogen were 1000 at.ppm and 385 at.ppm at the damage peak of self ions, respectively.

Post irradiation experiment

After irradiation, morphological observations and step-height measurements of irradiated surface were made by a scanning electron microscope (SEM) at 10 kV and a scanning probe microscope (SPM), respectively. To prepare TEM samples, irradiated samples were thinned into about 50 nm by a focused ion beam (FIB) device using 30 kV Ga ion beam at Tohoku University. The cross-sectional microstructural observations from irradiated surface to region behind the projected range were performed by a TEM at 200 kV.

3. Results and Discussion

Figure 2 shows a typical microstructure of SiC/SiC composites after triple-beam irradiation. This specimen was irradiated at 600 ℃. The shrinkage in SiC-fiber at irradiated region, the high dense black-dot at damage peak region of C-layer and debondings or micro cracks in C-layer were observed for all the irradiation conditions. These microstructural changes were also observed after dual-beam irradiation[4,5].

Figure 3 shows the SEM observation of the specimens surface after irradiation. Results of SEM observations and step-height measurements showed shrinkages of SiC-fiber and C-layer. These

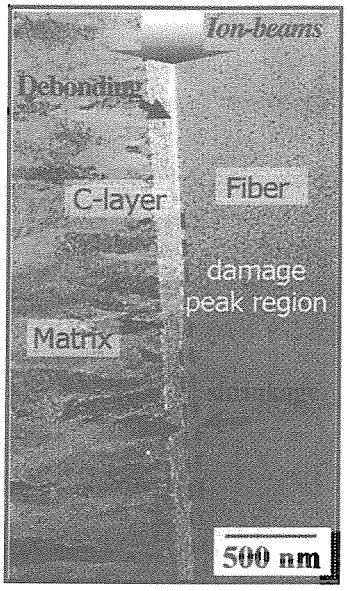


Figure 2. A typical microstructure of SiC/SiC composite after triple beam irradiation. Irradiation conditions; Displacement damage: 10 dpa (by Si-ion), He concentration: 1000 at.ppm, H concentration: 385 at.ppm

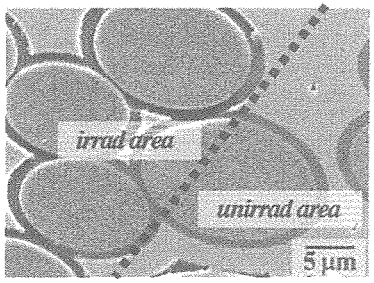


Figure 3. A SEM observation of irradiated surface of SiC/SiC composite.

dimensional changes were considered to be attributable to the shrinkage of irradiated parts of SiC-fiber and C-layer[6]. These morphological changes were also observed for all the irradiation conditions.

Microstructural development of SiC-fiber

Figure 4 shows the results of the shrinkage rate of SiC-fibers calculated with the following equations.

$$\Delta V / V_{TEM} \sim \{\pi r^2 - \pi(r-\Delta r)^2\} / \pi r^2 \times 100\,(\%) \quad (1)$$

$$\Delta V / V_{SPM} \sim (L_{fm} - L_m) / R_p \times 100\,(\%) \quad (2)$$

where R_p is the projected range of ion beams calculated by TRIM code, r is the radius of SiC-fiber before irradiation, Δr is the change of the radius of SiC-fiber by irradiation and L_{fm} is the step-height between the surface of SiC matrix and that of SiC fiber after irradiation, respectively. L_m is the assumed bump-height of SiC matrix caused by only displacement damage, which was calculated with the results of the volumetric swelling of CVD processed β-SiC after neutron irradiation (a few dpa) reported by Snead et al.[7]. The volumetric swelling (ΔV_m) of $\beta\text{-SiC}_{CVD}$ caused by displacement damage was about +0.7 % at 600℃, +0.4 % at 800℃ and +0.3 % at 950 ℃ [7]. The volumetric swelling is generally expressed by the following equation in terms of the linear swelling.

$$\Delta V_m \sim L_m / R_p \times 100\,(\%) \quad (3)$$

Using these results and this equation, bump-height (L_m) caused by only displacement damage may be about 21 nm at 600℃ and about 12 nm at 800℃, respectively.

From this figure, the shrinkage of SiC-fiber was mainly attributable to the displacement damage. Shrinkage of SiC-based-fibers after neutron irradiation was also reported[1] and the grain growth of β-SiC in SiC-based-fibers from amorphous SiC phase was considered to be the major cause of this shrinkage. The shrinkage in this study was con-

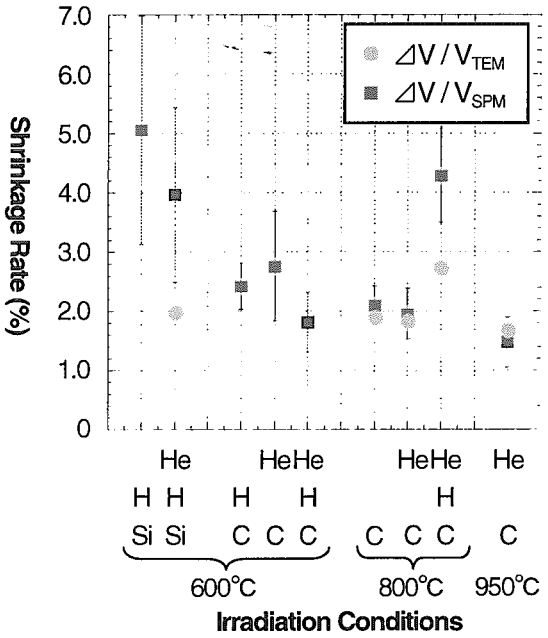


Figure 4. Dependence of the shrinkage rate of SiC-fiber on irradiation conditions

sidered to occur through the same mechanism as this.

On the other hand, almost no effect of helium on the shrinkage was observed. Hasegawa et al. [8] reported helium in β-SiC_{CVD} and Hi-Nicalon was immobile below 900 to 1000℃. Effect of helium on microstructure evolution may be small in this irradiation conditions. This result also shows hydrogen might affect the shrinkage of SiC-fibers. The temperature dependence looks complicated. Hi-Nicalon contains 17 atomic % excess carbon, therefore, the release as forms of CH_n at 800℃ might also enhance the shrinkage of SiC fibers.

The shrinkage of SiC-fiber after irradiation by Si-ion as the self-ion was larger than that by C-ion. This is considered to be attributable to the difference of the total displacement damage from irradiated surface to damage peak region as is shown in figure 1.

Microstructural change of SiC-matrix

No microstructural change in SiC-matrix was observed for specimens irradiated at 600 and 800℃. On the other hand, helium-bubbles were only observed in SiC-matrix of the specimen irradiated at 950℃ by C and He-ion. Figure 5 shows the damage peak region of SiC-matrix irradiated at 950℃.

No helium-bubbles were observed in the monolithic β-SiC_{CVD} specimen, which was irradiated by only 3 MeV He-ions up to 1000 at.ppm and annealed at 950℃ for 2.5 hours after irradiation.

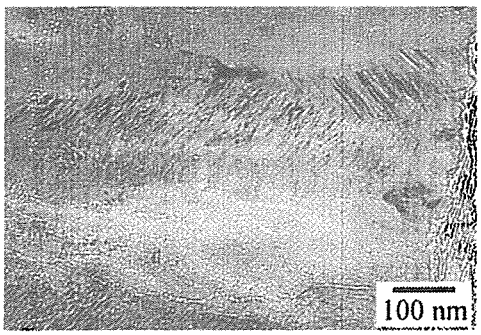


Figure 5. Helium-bubbles in the damage peak region of SiC-matrix.

Price [9] reported the void-formation in β-SiC after neutron irradiation (< 1.2 dpa, E > 0.18 MeV) above 1250℃. Hasegawa et al. [8] reported helium in β-SiC_{CVD} was immobile below 900 to 1000℃. Helium-bubbles observed at 950℃ irradiation were formed at temperatures lower than in the previous work. Simultaneously irradiated helium might enhance void formation above 950℃. More systematic irradiation is required to clarify the irradiation response above 950℃.

4. Summary

Simultaneous triple-ion-beam irradiations of SiC/SiC composites were carried out. Shrinkage of SiC-fiber and C-layer was observed in the temperature range of 600 to 950 ℃, but microstructural development which was enhanced by simultaneous helium and hydrogen irradiation was not observed at 800℃.

References

1) G. E. Youngblood et al., J. Nucl. Mater., 258-263 (1998) 1551-1556.
2) J. F. Ziegler et al., The Stopping and Ranges of Ions in Matter, vol. 1, Pergamon Press, New York, 1985.
3) I. A. Honstvet et al., Philos. Mag. A41 (1980) 201.
4) S. Nogami et al., JAERI-Review 99-025 TIARA Annual Report 1998 pp 135-137.
5) S. Nogami et al., J. Nucl. Mater. in press
6) G. B. Engle and B. T. Kelly, J. Nucl. Mater. 122 & 123 (1984) 122-129.
7) L. L. Snead et al., J. Nucl. Mater., 253 (1998) 20-30.
8) A. Hasegawa et al., J. Nucl. Mater. in press
9) R. J. Price, J. Nucl. Mater. 48 (1973) 47-57.

4.3 Implantation Mode Dependence of Damage Structure Depth Profiles in Al_2O_3 irradiated with Triple Beam of H, He and Heavy Ions

T. Aruga[a], Y. Katano[a], S. Yamamoto[b], T. Nakazawa[a], D. Yamaki[a]
[a]Department of Material Science, JAERI
[b]Department of Materials Development, JAERI

1. Introduction

The synergetic effects of displacement of atoms from lattice sites and implanted H, He atoms on damage structure developments in α-Al_2O_3, which is proposed for electrical insulators and diagnostic materials in the fusion reactor environment, have been studied using samples irradiated with multiple beams of hydrogen (H), helium (He) and self ions of oxygen (O) or alminum (Al) from TIARA [1,2]. In the present study, the damage structures in Al_2O_3 after triple ion beam (H^+, He^+ and N^{2+} or O^{2+}) irradiation were examined with a cross-sectional transmis-sion electron microscopy (XTEM). Major interests are placed on microstructural differences brought about by atomic displacements due to N- or O-ions penetrating He- and H-ion damaged region of depths.

2. Experimental procedure

The materials used in this study were single crystal alumina (α-Al_2O_3). The procedures of sample preparation and irradiations have been described elsewhere [3]. The samples were irradiated mainly with triple ion beams (0.25MeV H^+, 0.6MeV He^+, 4.7MeV $O^{2+}$and /or 4.7MeV N^+) at 923 K (0.4Tm). The ion energies are so chosen that the depths for projected ranges of the He- and H ions in Al_2O_3 coincide around 1.45 μm and O or N ions are predicted to penetrate the He- and H-ion damaged region and to stop around 2.3~2.4 μm. Table 1 summarizes the irradiation conditions examined and respective damage parameters obtained with TRIM89 code [4], using a common displacement energy of 40 eV. After irradiations, XTEM observations were performed using a JEM-2000FX electron microscope operating at 200kV. Depth profiles of implanted H atoms in the as-irradiated samples were measured utilizing a resonant nuclear reaction analysis (NRA) of ^{15}N, $^{15}N(H, \alpha\gamma)^{12}C$, details of which have been already described in ref. [5].

3. Results and discussion

Depth profiles of damage structures in the sample irradiated with triple beam of (0.25MeV H^+, 0.6MeV He^+, 4.7MeV N^{2+}) are given in fig. 1 for (a)dislocation component in dark field and (b) cavity component . The number density of loops increases from a depth very close to the surface to a depth of 2.4 μm, and peaks around 1.4 μm of He- and H-ion ranges and around 2.3 μm of N-ion ranges(fig. 1(a)). Cavities are formed around 1.4 and 1.55 μm in depth, and apparently the former are observed to be aligned to c-axis and the latter associated with grown dislocation lines and distributed inhomogeneously. Furthermore, the former and the latter are identified to be associated with implanted He- and H-atoms,

Table 1. Beam conditions used and corresponding damage parameters obtained by TRIM

Energy/Ion (MeV)	Flux (10^{16}/m^{2}s)	Fluence (10^{20}/m^2)	Calculated values (TRIM)			
			damage peak		implanted atom peak	
			depth(μm)	(dpa)	depth(μm)	concentration(at%)
Sample ID [#97-08], triple beam						
0.25H$^+$	3.7	4.0	1.40	0.066	1.44	2.2
0.6 He$^+$	4.1	4.5	1.44	0.78	1.46	1.9
4.7 N^{2+}	0.41	0.45	2.40(1.40)	0.47(0.44)	2.44	0.21
Sample ID [#98-04], triple beam						
0.25H$^+$	2.2	5.1	1.40	0.084	1.44	3.1
0.6 He$^+$	1.7	4.0	1.44	0.7	1.46	2.3
4.7 O^{2+}	0.43	1.0	2.2(1.44)	1.0 (0.17)	2.28	0.4
Sample ID [#97-09], sequentially						
0.25H$^+$ (1-st)	5.0	5.4	1.40	0.09	1.44	3.3
0.6 He$^+$(2-nd)	5.6	6.0	1.44	1.05	1.46	2.6

respectively, judging from the similarity observed previously in the samples irradiated with practically single beam of He- and H-ions [1,2]. Two peaks are observed in the depth profile of the number densities of cavity measured within 0.05 μm width around the He- and H-ions' ranges, as shown in fig. 2. Cavity formation behaviors around the He- and H-ion implanted region differ from the depth profiles of He- and H-ion ranges prediction by TRIM, which is given in fig. 3: the separation of ~ 0.15μm between the two peaks observed in fig. 2 far exceeds the predicted distance of 0.04 μm between the two. The observed discrepance between two peaks suggests stopping powers used in TRIM may be problematic.

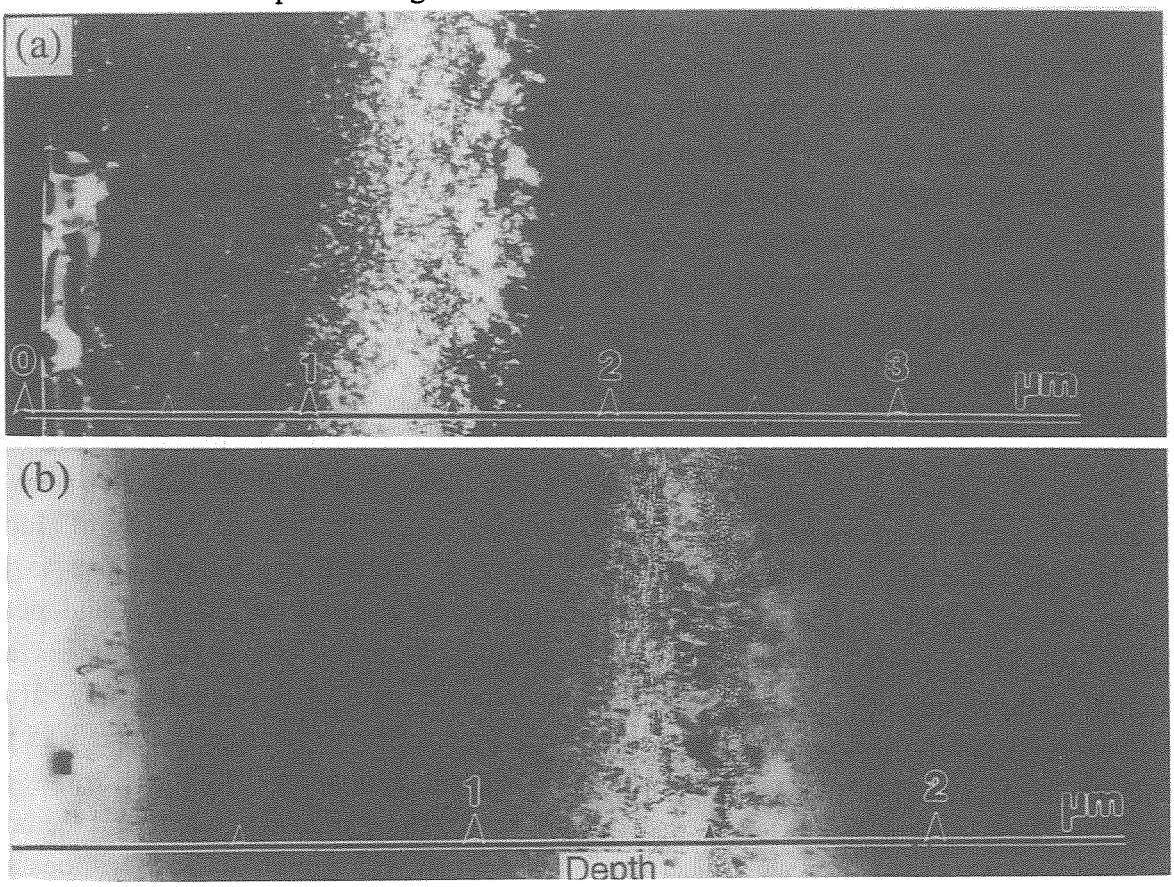


Fig.1. Cross sectional damage strauctures of α-Al_2O_3 irradiated with triple beam of H^+-, He^+- and N^{2+} ions at 923 K ; (a) dislocation component in dark field and (b) cavity component around ion ranges.

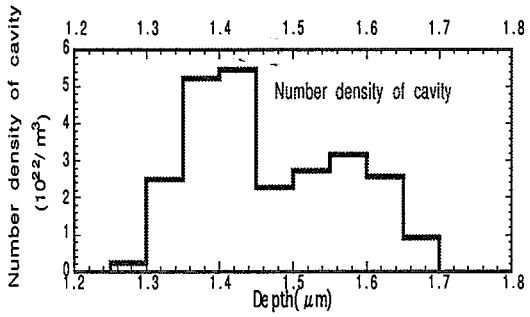


Fig.2. Depth profiles of the number densities of cavities.

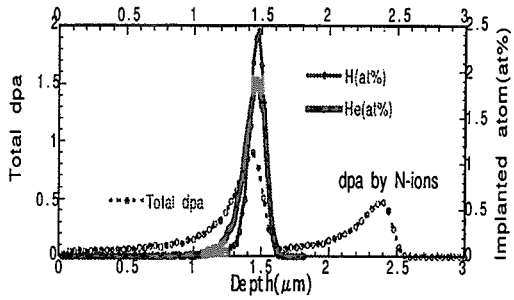


Fig.3. Depth profiles of damage parameters by TRIM89.

On the other hand, in the cross-sectional damage structures in Al_2O_3 irradiated with triple beams (0.25MeV H^+, 0.6MeV He^+, 4.7MeV O^{2+}) at 923K to almost the same doses both in dpa and at% of He and H, as those in the case of triple beam involving N-ion's, however, with a damage rate about one half of N-ion's case, growth of cavities is considerably retarded. The retardation of cavity growth is remarkable in the sample irradiated in sequence with firstly 0.25MeV H-ions and then 0.65 MeV He-ions to comparable doses; of course, each dose rate is lower than that of the case of triple beam irradiation. These facts above demonstrate that growth of cavity is strongly influenced by the rate of point defects, presumably vacancies, supplied under the irradiation, since the rates of gas atom implantation in above three cases are almost comparable. Detailed analysis on cavity growth as a function of dpa/s, at%/s is under way.

In relation to the peak separation in the depth profile of cavity number density, depth profiles of H atoms in the samples reveals that the profile for the irradiation with single beam of 0.25MeV H-ions is peaked at 1.51μm, whereas the profile for triple beam irradiation with 4.7MeV N-ions penetrating He and H damaged region has two peaks; larger one at 1.52 μm and the other smaller peak at 1.40 μm. The fact seems to be well corresponding to the cavity density profile having the peak at depth around the He-ion's average projected range. However, in the case of dual beam irradiation with He- and H-ions without heavy ions penetrating He and H damaged region, H atoms are distributed in the more similar form of Gaussian than that in the single H-ion beam irradiated sample. Therefore it seems that He atom traps point defects (vacancies) along with H atoms, under the condition that enough flow of point defects is provided at the irradiation temperature at 923 K.

Reference

[1] Y. Katano, T. Nakazawa, D. Yamaki, T. Aruga, K. Hojou, K. Noda, J. Nucl. Mater.233-237 (1996)1325.

[2] Y. Katano, T. Nakazawa, D. Yamaki, T. Aruga, and K. Noda, Nucl. Instr. and Meth. B. 141 (1998) 411.

[3] Y, Katano, H. Ohno and H. Katsuta, J. Nucl. Mater. 155-157(1988)366.

[4] J.F. Ziegler, J.P. Biersak and U.L. Littmark, The stopping and Range of Ions in Solids (Pergamon, New York, 1985).

[5] Y.Katano, T. Aruga, S. Yamamoto, T. Nakazawa, D. Yamaki, and K. Noda, Nucl. Instr. and Meth. B 140 (1998) 152.

4.4 Damage evolution in high energy ion-irradiated metals and the interaction between gas atoms (H and He) and damage defects

Y. Shimomura, I. Mukouda, D. Yamaki*, T. Nakazawa*, T. Aruga*
and S. Jitsukawa*
Faculty of Eng., Hiroshima University, *Department of Material Science, JAERI

1. Introduction

For fusion reactor applications, there is an interest in copper and its alloys. Hydrogen and helium atoms are generated by nuclear transmutation in the fusion environment. These gas atoms play an important role on the evolution of the damage microstructure. It is well known that helium is active in cavity nucleation. Some studies have been carried out on hydrogen effects. However, it is not extensively characterized. In the present work, quantitative experiments were carried out to study the role of gas atoms (helium and hydrogen) on the evolution of the damage microstructure in irradiated materials. It is possible to control the concentration of gas atoms in irradiated metals by ion irradiation at high energy. We examined void formation in high energy ion irradiated pure copper by a single beam (5 MeV Cu) and a dual-beam (5 MeV Cu ion and 260 keV H ion, and 5MeV Ni ion and 600 keV He ion) irradiation. The ion energy was selected so that the projected range of the gas ions in copper might coincide with depth of peak damage (1.2 μm) calculated by the TRIM 95 code. Specimens for TEM cross sectional observation were prepared by a FIB (Focused Ion Beam) device. The relation between gas atoms and damage structure was derived from experimental results.

2. Experimental Procedure

The specimens used in this study were pure copper (Dowa Ministry Ltd.) with a nominal purity of 99.9999%. Annealed disks of 3mm in diameter and 0.05 mm thick were prepared [1]. The high energy ion irradiation was carried out with TIARA accelerator at the Taka saki- establishment of JAERI. The ions stop within 1 - 2 μm from the surface and damage was formed within this depth. The damage microstructure was observed as a function of the depth by utilizing an SMI9200 (Seiko Instrument Inc.) FIB microscope. The FIB generates 30 keV Ga ions and bombards the specimen surface with a glancing angle. Atoms on the surface are removed by sputtering. To preserve the surface position of ion-irradiated metals, we deposited Cu on the irradiated surface by electroplating to prevent erosion of the specimen surface [2,3]. In previous work, it was found that interstitial atoms form clusters throughout FIB-thinned specimens. It is very difficult to distinguish damage defects which are formed by high energy ion irradiation from FIB damage. To solve this problem, we developed a cryotransfer- FIB thinning technique, in which the specimen is cooled down to 100K on the FIB thinning holder (the Cryo-FIB technique) and transferred to a transmission electron microscope without warming up. This technique makes it possible to observe voids, even very small ones, in high energy ion irradiated metals [4]. In ion-irradiated metals at high temperature, voids, interstitial clusters and dislocations are formed. Even with the FIB technique mentioned above, it is difficult to observe the dislocation structure which is developed by clustering of interstitial atoms in irradiated specimen. To overcome this difficulty, we developed a TEM specimen preparation method which is a combination of Cryo-FIB thinning and electro-polishing. In annealed pure copper, many dot defects are observed with FIB thinning at room temperature. However in the case of thinning at 100K, defects were smaller than those with thinning at room temperature. Furthermore to remove regions damaged by the Ga ions, the specimens

were electro-polished in a solution of 33% HNO_3 and 67% ethanol cooled to -40°C at an applied potential of 6V for 6 sec. After electro-polishing, no dot defects were observed. It was found that the damage microstructure of ion-irradiated metals such as copper can be observed without FIB damage.

3. Results and Discussion

Fig. 1(a) shows the microstructure of pure copper irradiated at 300°C by 3MeV Cu ion. Many stacking fault tetrahedron (SFT) s were observed in the irradiated region. Figs. 1(b) and 1(c) show the microstructure observed by dislocation and void contrast in Cu and He dual beam irradiated copper at 300°C, respectively. Many voids were observed and the density of voids was 3.5 x 10^{22} m^{-3} at the peak of implanted He atoms. Number density and size of voids depended on the depth. The number density of voids gradually increased and the size of voids decreased with increasing dose and He concentration. In Cu and He irradiated copper at 400°C the number density of voids increased significantly at the depth corresponding to the range of helium atoms. Figs. 1(d) and 1(e) show the microstructure observed by dislocation and weak beam images in Cu and H dual beam irradiated copper at 300°C, respectively. Many SFTs were observed in the irradiated region, similar to the single ion irradiation results. In Cu and H irradiated copper at 300 and 400°C, no voids were observed. It is concluded that the total number of vacancies for Cu and H ion irradiation was smaller than that for

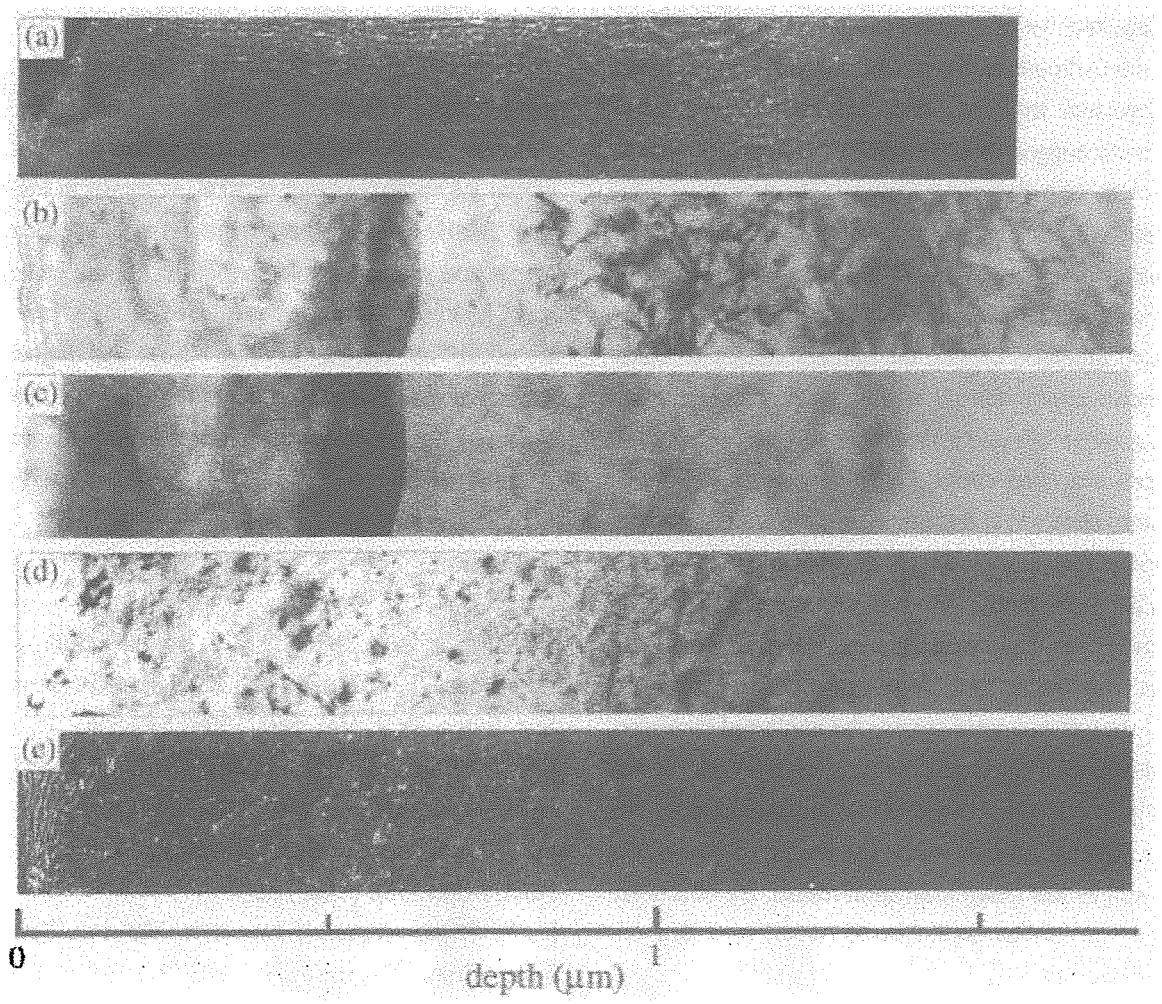


Fig. 1 The microstructure of ion irradiated pure copper at 300°C (a) 3MeV Cu ion (b) 5MeV Cu + 600keV He (dislocation contrast) (c) 5MeV Cu + 600keV He (void contrast) (d) 5MeV Cu + 260keV He (dislocation contrast) (d) 5MeV Cu + 260keV He (weak beam image).

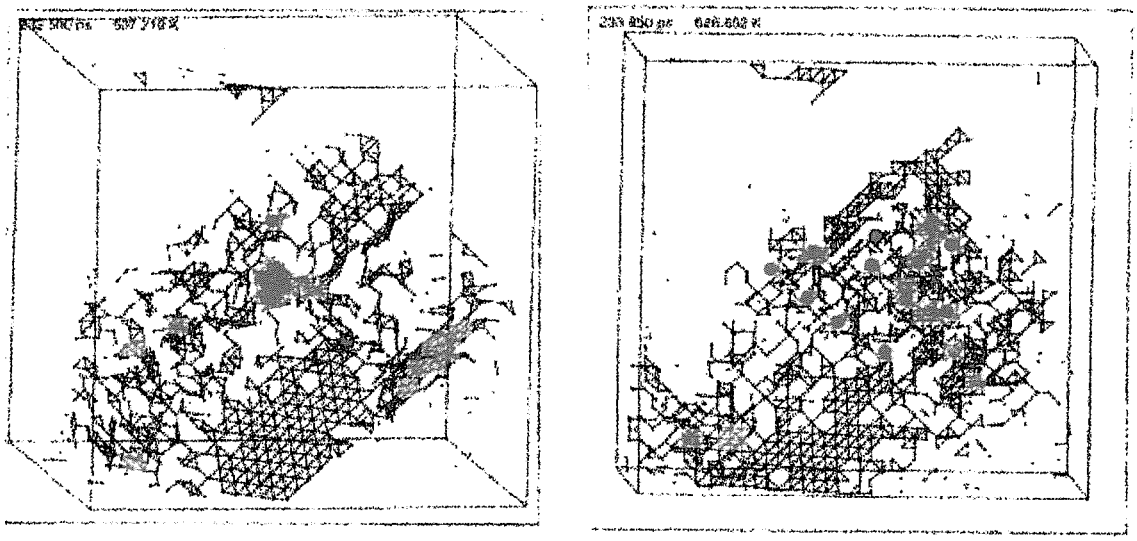


Fig. 2 Small circle shows vacancies and solid circle means He or H atom. (a) Helium atoms form a cluster in the vacancy cluster. (b) Hydrogen atoms scattered in the crystal.

Cu and He ion irradiation. It is considered that a large number of invisible vacancy clusters combined with hydrogen atoms or molecules are formed in the specimen irradiated with Cu and H ion. These results suggest that the mobility of vacancy clusters which trap hydrogen atoms is suppressed. In the pure copper irradiated at 500°C by a single beam (Ni ion), voids were observed, but the number density of voids was very low [6]. In the dual beam (Ni and He ion) irradiated copper, the number density of voids increased significantly at the depth corresponding to the range of helium ions. In dual beam (Ni and H ion) irradiated copper, only very large size voids were observed and the number density of voids was lower than that for the He dual beam irradiation [5]. The depth profile of voids was uniform in the Cu and H ion dual beam irradiation. Because diffusion of hydrogen is much higher than helium, effects of hydrogen can occur outside the implanted hydrogen distribution calculated by the TRIM95 code. In the triple beam (Ni, He and H ion) irradiated copper, the number density of voids was similar to that of Cu and He dual beam irradiation results. He effects on void nucleation appear to be much larger than H effects in Cu.

To investigate vacancies and gas atoms interaction, we carried out molecular dynamics computer simulations. The crystal was comprised of 32,000 atoms. After thermal equilibrium, 800 vacancies and 10 gas atoms were induced in the crystal. Figs. 2(a) and (b) show the results of the computer simulation. Helium atoms form a cluster within the vacancy cluster at 500K as shown in Fig. 2(a). The He cluster stabilized the spherical vacancy cluster and promoted void formation. On the other hand, hydrogen atoms were scattered in the crystal at 600K as shown in Fig. 2(b). At higher temperatures, He atoms scattered in the crystal like hydrogen. In that case, gas atoms did not promote void formation.

References

[1] I. Mukouda, Y. Shimomura, T. Iiyama Y. Katano, D. Yamaki, T. Nakazawa and K. Noda, Mat. Res. Soc. Symp. Proc. Vol. 540 (1999) 549-554.

[2] S. J. Zinkle and R.L. Sindelar, Nucl. Instr. and Meth. in Phys. Res. B16 (1986) 154.

[3] S. J. Zinkle, G. L. Kulcinski and R. W. Knoll, J. Nucl. Mater. 138 (1986) 46.

[4] Y. Shimomura and I. Mukouda, Mat. Res. Soc. Symp. Proc. Vol. 540 (1999) 527-532.

4.5 Synergistic Effects of Hydrogen and Helium on Microstructural Evolution in Vanadium Alloys by Triple Ion Beam Irradiation

N. Sekimura[1], S. Yonamine[1], T. Okita[1], A. Kurui[1], Y. Arai[1], T. Iwai[2], S. Ohnuki[3], A. Naito[4], S. Hamada[4] and Y. Miwa[4]
Department of Quantum Engineering and Systems Science, Univ. of Tokyo [1]
Research Center for Nuclear Science and Technology, Univ. of Tokyo [2]
Department of Materials Science and Engineering, Hokkaido University [3]
Materials Research Division, JAERI/Tokai [4]

1. Introduction

Vanadium alloys are potential blanket structural materials of a future DEMO reactor because of their excellent mechanical properties at elevated temperature and low induced radioactivity after neutron irradiation. Irradiation of 14 MeV neutrons produces He and H atoms at a high generation rate as well as displacement damage during irradiation. Microstructural evolution and resultant mechanical property changes in vanadium alloys are known to be strongly influenced by transmutation helium and hydrogen simultaneously produced during 14 MeV neutron irradiation. Therefore, the effect of high helium generation rate on microstructural evolution and mechanical property changes in vanadium has been investigated using DHCE (Dynamic Helium Charging Experiments) in fission reactors [1,2] and boron doping techniques [3].

In this study, multiple ion irradiation experiments are carried out to understand the effects of helium and hydrogen on the mechanisms of microstructural evolution in pure vanadium and vanadium alloys by varying the combination of heavy ion, helium and hydrogen irradiations systematically.

2. Experimental

We used the Triple Beam Irradiation Facility in the TIARA (Takasaki Ion Accelerators for Advanced Radiation Application), where three accelerators are simultaneously operated to irradiate small size specimens with heavy ions, helium ions and hydrogen ions.

V-5Cr and V-5Cr-5Ti alloys are prepared from 99.8 % pure vanadium by arc-melting and rolled to sheets of 0.2 mm in thickness. Table 1 shows impurity levels in the pure vanadium. These are cut into disks of 3mm in diameter, and annealed at 1273 K for 1 hour in high vacuum of 10^{-6} Pa wrapped within pure Zr foils, followed by rapid cooling.

These specimens are irradiated with 12 MeV Ni^{3+} ions to 30 dpa at 1700 nm from the surface with simultaneous implantation of helium and hydrogen by 1 MeV He^{+} and/or 350 keV H^{+} ions. Dual beam irradiation with 12MeV Ni^{3+} and 1MeV He^{+}, or 12MeV Ni^{3+} and 350KeV H^{+}, and single beam irradiation with 12MeV Ni^{3+} are also performed. Irradiation temperature is dynamicaly controlled at 873 K during irradiation. Typical damage rate is $4x10^{-4}$ dpa/sec. Two different injection rates, 10 and 20 appm/dpa, are used for both

helium and hydrogen irradiation.

About 1600 nm surface layer of the irradiated samples are sectioned away in a solution of 20% sulfuric acid and 80% methanol, and back-thinned to a perforation to observe the microstructural evolution in the peak damage region by TEM (transmission electron microscope) operated at 200 kV.

3. Results and Discussion

Very few cavities are detected in ternary V-5Cr-5Ti alloy irradiated with single ions to 30 dpa at 873 K. Simultaneous irradiation with hydrogen does not enhance cavity formation in V-5Cr-5Ti. In the recent ion irradiation experiments, V-5Cr-5Ti alloy also shows excellent swelling resistance at other irradiation temperatures even in the dual beam irradiation with heavy ions and hydrogen ions.

Co-implantation of helium at 873 K, however, produces cavities in V-5Cr-5Ti. Figure 1 compares observed cavity volume fraction in pure vanadium, V-5Cr and V-5Cr-5Ti irradiated with 12 MeV Ni^{3+} ions to 30 dpa at 873 K at 10 appm He/dpa with and without simultaneous irradiation of hydrogen. It should be noted that co-implanted hydrogen with helium also enhances swelling in vanadium alloys as well as pure vanadium.

Figure 2 shows cavity density and average cavity diameter in V-5Cr and V-5Cr-5Ti irradiated with 12 MeV Ni^{3+} ions to 30 dpa at 873 K at 10 appm He/dpa ratio as a function of H/dpa ratio. V-5Cr-5Ti is very resistant to cavity formation compared with V-5Cr. This is considered to come from titanium effects as trapping sites for interstitial impurity atoms such as oxygen and nitrogen. In the cases of triple beam irradiation with simultaneous implantation of hydrogen and helium, cavity number density increases with hydrogen implantation rate, whereas cavity density in V-5Cr binary alloy is not strongly influenced by hydrogen. At the H appm/dpa ratio of 20, cavity density in V-5Cr-5Ti is larger than that in V-5Cr, and cavities also grow larger in V-5Cr-5Ti.

Titanium atoms appear to play an important role in cavity nucleation in V-5Cr-5Ti alloy. Hydrogen may stabilize trapped helium clusters at Ti atoms. Titanium atoms were found to promote evolution of dislocation microstructure and to segregate around grain boundaries in V-5Cr-5Ti alloys irradiated at 873 and 973 K [4]. It is also found that co-implantation of helium at 873 K increases dislocation densities in both V-5Cr-5Ti and V-5Cr alloys [5].

4. Conclusion

Series of ion irradiation experiments in pure V and V alloys are performed using triple ion beam irradiations using the TIARA facility.

V-5Cr-5Ti is very resistant to cavity formation in the absence of helium. However, fine cavities are nucleated when helium is injected. Cavity nucleation and growth are further amplified when hydrogen is injected together.

References

[1] D. L. Smith, H. Matsui, L. R. Greenwood and B. A. Loomis, J. Nucl. Mater. 155-157 (1988)1359.

[2] H. Matsui, K. Fukumoto, D. L. Smith, Hee M. Chung, W. van Witzenburg, S. N. Votinov, J. Nucl. Mater. 233-237 (1996) 92.

[3] N. Sekimura, T. Iwai and F. A. Garner, J. Nucl. Mater., 233-237 (1996) 400.

[4] T. Iwai, N. Sekimura and F. A. Garner, J.

Nucl. Mater., 239 (1996) 157.
[5] N. Sekimura, S. Yonamine, T. Iwai, Y. Arai, A. Naito, Y. Miwa and S. Hamada, accepted in J. Nucl. Mater. (2000)

Table 1 Impurity levels of vanadium alloys used in this study (wt.ppm).

H	14	C	36	Al	200
O	120	Cr	300	Si	100
N	6	Fe	400	Cu	200

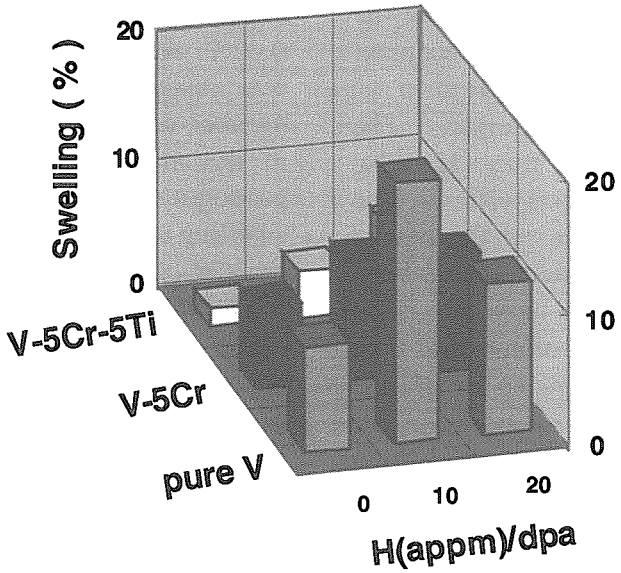


Figure 1 Cavity volume fraction in vanadium alloys irradiated with 12 MeV Ni^{3+} ions to 30 dpa at 873 K at He(appm)/dpa ratio of 10 with and without simultaneous irradiation of H.

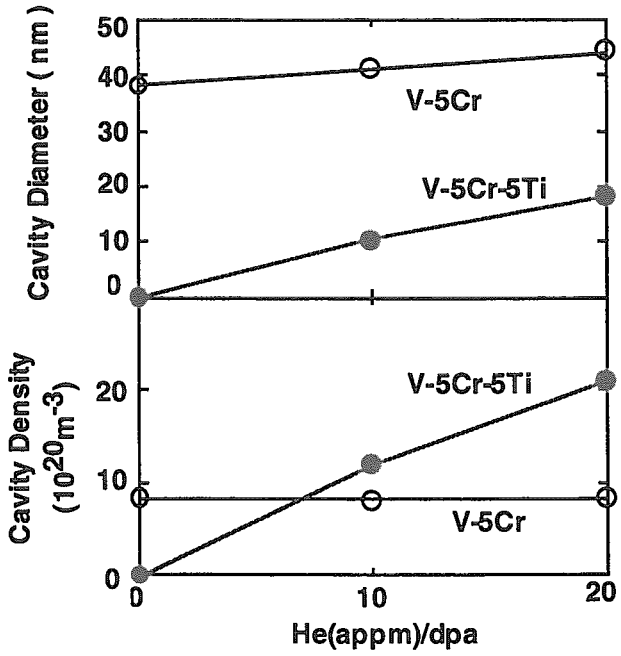


Figure 2 Cavity density and average diameter in V-5Cr and V-5Cr-5Ti irradiated with 12 MeV Ni^{3+} ions to 30 dpa at 873 K with simultaneous irradiation of He at He(appm)/dpa ratio of 10.

4.6 Effects of heat treatment and gas atom production on hardness and microstructure of F82H steel irradiated by dual/triple ion beams

Eiichi Wakai, Tomotsugu Sawai, Hiroyasu Tanigawa, Akira Naito, Tomitsugu Taguchi and Shiro Jitsukawa
Department of Materials Science, Tokai Research Establsihment, JAERI

1. Introduction

Low-activation ferritic/martensitic steels are candidate materials for the first wall and blanket structure of fusion reactors. The high-energy neutrons produced in the D-T fusion reaction induce displacement damage and generate gas atoms from (n, p) and (n,α) reactions in the materials. The presence of these gases may lead to degradation of mechanical properties. The effect of neutron irradiation on the tensile deformation of F82H steel has been reported. Shiba et al. [1,2] have described the tensile data obtained under the U.S. DOE/JAERI program, following irradiation in HFIR at 200 to 600°C for doses in the range 3-34 dpa, and the helium production effect on mechanical properties was investigated using isotope ^{10}B doping. A summary and discussion of the tensile data for 9-12Cr ferritic-martensitic steels irradiated under a variety of conditions has been presented by Rowcliffe et al. [3]. Recently, the swelling of F82H and the other 7-9Cr low-activation ferritic steels irradiated at 430°C to 67 dpa in FFTF was reported by Morimura et al. [4]; the swelling of F82H was 0.1%, and that of the other steels was 0.1- 0.7%. Maziasz and Klueh[5] had investigated the swelling versus helium production rate in 9Cr-1MoVNb(-0, -2Ni) and 12Cr-1MoVW(-0, -2Ni) steels irradiated at 400°C to 47 dpa, using the efficiency of helium production rate for HFIR and FFTF, and they indicated that the swelling of 0.1 to 0.4% depended on helium production. Recently, we have reported the effects of helium production and heat treatment on swelling behavior of F82H steels using ^{10}B, ^{58}Ni and ^{60}Ni doping. The irradiation was performed in the HFIR at 300 and 400°C to 51 dpa [6]. The swelling of tempered F82H-std and F82H doped with ^{10}B irradiated at 400°C was from 0.45 to 1.1 %, while the swelling of the non-tempered F82H doped with ^{58}Ni or ^{60}Ni was less than 0.02%. At 300°C the swelling in all steels was insignificant. In the F82H+Ni, high number densities of carbides were formed in the matrix at these temperatures. The production of helium atoms enhanced the swelling of the F82H steel. However, the non-tempered treatment for the F82H+Ni remarkably suppressed the swelling. The cause of low swelling in the F82H+Ni may be due to the formation of the high density of carbides acting as sinks or the decrease in mobility of vacancies that interacted with carbon atoms in matrix.

Purpose of the present study is to investigate the effect of heat treatment and gas atom production on hardening and microstructures of F82H steel irradiated by dual or triple beam conditions.

2. Experimental procedure

The chemical compositions of the F82H-std steel (IEA-heat, rolling No. KG820-2, sampling position 42W-16, grain size number 3.5) used in this study are given in Table 1. The heat treatment for F82H-std specimen was firstly normalized at 1040°C for 40 minutes in a vacuum followed by air-cooling. After that the specimens were tempered at 750°C for 1 hour in a vacuum followed by air-cooling. In order to investigate the effect of heat treatment and gas atoms on hardening and microstructures, four types of specimens were prepared. They are F82H-std, F82H-

Table 1
Chemical compositions of the F82H steel (IEA heat) used in this study

Alloys	Cr (wt%)	C	N	P	S	Al	Si	V	Ti	Mn	Ta	W
F82H-std	7.84	0.09	0.007	0.003	0.001	0.001	0.07	0.19	0.004	0.1	0.04	1.98

normalizing (this specimen was normalized at 1000°C for 30 min after the heat treatment of standard specimen), F82H-10min tempered (this was tempered at 740°C for 10min using the F82H-normalizing specimen), and F82H-20%CW. Standard 3 mm-diameter disks cut from 0.25 mm-thickness sheet stock were irradiated in the TIARA facility. It was performed under a simultaneous dual ion irradiation with 10.5 MeV Fe^{3+} ions and1.05 MeV He^{+} ions or a simultaneous triple ion irradiation with those and 380 keV H^{+} ions. He (appm)/dpa and H (appm)/dpa ratios are 15 and 15 (or 150) for dual and triple beam irradiation. The peak positions of damage, helium and hydrogen ions were all about 1.75 μm, which was calculated by using SRIM97 code. During the irradiation, the temperature of the surface in all specimens was continuously measured with Nikon's thermal vision system. After the irradiation, the hardness of the specimens was measured by using an ultra micro-indentation, UMIS-2000. The hardness measurement of the specimens was performed up to 25mN load at room temperature.

3. Results and discussion

Fig. 1 shows the dose dependence of hardness measured at room temperature in the F82H-std irradiated at 450°C to 50 dpa under dual beams of Fe^{3+} and He^{+} ions. Each data point is an average from 20 indentations. The hardness of F82H-std

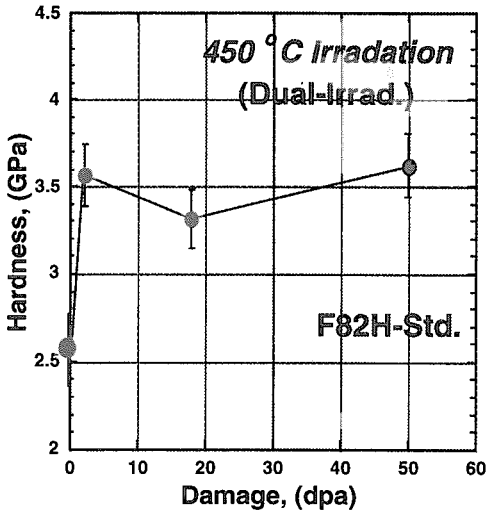


Fig.1. Dose dependence of hardness measured at room temperature in the F82H-std irradiated at 450°C to 50 dpa under dual beams of Fe^{3+} and He^{+} ions.(He(appm)/dpa=15)

before irradiation was about 2.5 GPa at room temperature. Radiation-hardening was observed in the specimens irradiated at 450°C, and the hardness increased rapidly during the first-damage increment, but it somewhat decreased at 18 dpa, and it again slightly increased at 50dpa. Fig. 2 shows the hardness of F82H-std, F82H-normalizing, F82H-10min tempered, and F82H-20%CW steels irradiated at 250 and 450°C to 2.3 dpa under dual beams of Fe^{3+} and He^{+} ions. Radiation-hardening was observed in the specimens irradiated at 250 and 450°C. The increases in hardness of

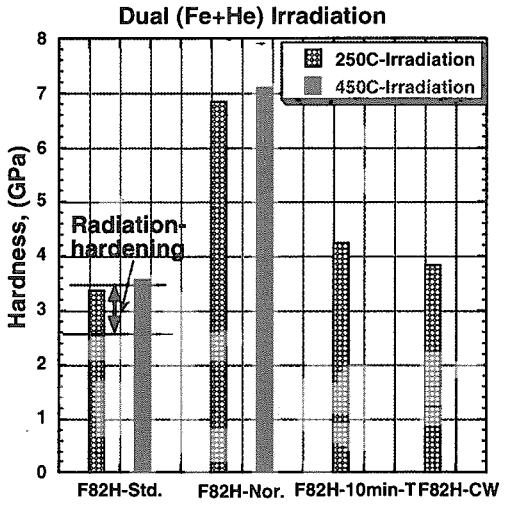


Fig. 2. Hardness of F82H-std, F82H-normalizing, F82H-10min tempered, and F82H-20%CW steels irradiated at 250 and 450°C to 2.3 dpa.

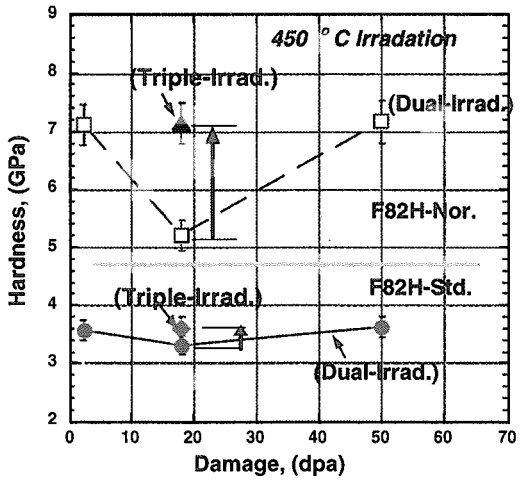


Fig. 3. Effect of triple beam on hardness of F82H steels irradiated at 450°C to 18 dpa. He(appm)/dpa=15, H(appm)/dpa=150.

F82H-std and F82H-normalizing specimens irradiated at 450°C were unexpectedly very similar to those irradiated at 250°C. The effect of triple beam in the F82H-std and F82H-normalizing irradiated at 450°C to 18 dpa was shown in Fig. 3. In both specimens the increase of hardness in triple beam condition was larger than that in dual beam condition. Large amounts of hydrogen atoms could affect on the formation and growth of cavity, and therefore we need to examine the relation between hardness and the density and size of cavity in further work.

Conclusions

Effects of heat treatment and gas atom production on hardening and microstructures of F82H irradiated by dual or triple beam condition were investigated. Radiation-hardening was observed in F82H-std and F82H-normalizing steels irradiated at 250°C and 450°C to 2.3 dpa under dual beam condition. The increases of hardness in the specimens irradiated at 450°C were unexpectedly very similar to those irradiated at 250°C. In the irradiation at 450°C, the increased hardness somewhat decreased at 18 dpa, and it again increased at 50 dpa. The triple beam in the F82H-std and F82H-normalizing irradiated at 450°C to 18 dpa enhanced the hardening.

References

(1) K. Shiba, I. Ioka, J. P. Robertson, M. Suzuki, and A. Hishinuma, Euromat-**96**(1996), p.265.

(2) K. Shiba, A. Hishinuma, to be published.

(3) F. Rowcliffe, J. P. Robertson, R. L. Klueh, K. Shiba, D. J. Alexander, M. L. Grossbeck, and S. Jitsukawa, J. Nucl. Mater., **258-263**(1998), pp. 1275-1279.

(4) T. Morimura, A. Kimura, and H. Matsui, J. Nucl. Mater., **239**(1996)118-125.

(5) P. J. Maziasz and R. L. Klueh, American Society for Testing and Materials-1046, Philadelphia, 1990, p. 35.

(6) E. Wakai, N. Hashimoto, J. P. Robertson, R.L. Klueh, K. Shiba, and S. Jistukawa, in: Proceedings of ICFRM-9, Cororado Springs, USA, 1999, J. Nucl. Mater., to be pubshied.

4.7 Evaluation of He Embrittlement in Reduced Activation Ferritic/Martensitic Steels

T. Hirose[1),3)], H. Tanigawa[1)], E. Wakai[1)], Y. Miwa[2)], S. Jitsukawa[1)], H. Sakasegawa[3)], Y. Katoh[3)], A. Kohyama[3)] and M. Narui[4)]

[1)] Department of Material Science, [2)] Department of Nuclear Energy System, JAERI

[3)] Institute of Advanced Energy, Kyoto University

[4)] Oarai branch, Institute for Material Research, Tohoku University

1. Introduction

Reduced activation ferritic steel, RAFs, is the leading candidate material for the first wall and blanket structures of the future D-T fusion reactors[1)]. Among the engineering issues of concern, fatigue properties are realized to be an important issue to be studied including neutron irradiation and transmutation He effect.

The objective of this work is to evaluate fatigue properties under fusion reactor condition. As the part of this work, He implantations to RAFs were carried out utilizing AVF Cyclotron accelerator in TIARA facility. And a new fatigue test machine for irradiated mini-sized specimen has been developed. The effect of specimen size on the fatigue properties was studied utilizing reduced activation ferritic steels; F82H and JLF-1. The correlation of the fatigue life characteristics and fracture mechanisms was investigated for full- and mini-sized specimens.

2. Experimental procedure

2.1 Development of Fatigue Test Machine for Irradiated Specimen

To develop mechanical testing machines for irradiated specimens, easy and remote-handling process is indispensable. Especially for fatigue tests, gripping of specimens and attaching of extensometers by remote handling is considered to be difficult. In this work, remote handling issues were regarded as the most important. For measuring strain, a laser extensometer was applied, which enables deformation monitoring during the test without any specimen contact[2)]. Figure 1 shows newly developed fatigue test machine for hot-cell usage. As shown in this figure, the laser extensometer consists of a transmitter and a receiver joint to an actuator.

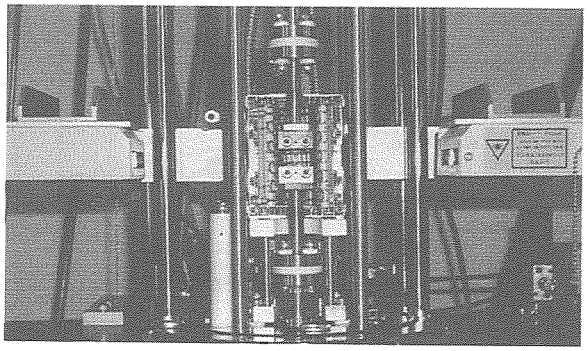


Fig. 1 Fatigue test machine for hot-cell usage

The specimen's waist with the unloaded condition was defined as the reference diameter. Strain was measured by measuring the deviation from the reference value at the waist portion. A measurement accuracy of 0.1μm was obtained by averaging the measured values. The measured strain value was also used for controlling the actuator during the test.

The upper limit of distance between the transmitter and receiver was about ~500mm, which is enough to install vacuum chamber in between. Strain measurement was carried out at outside of the chamber.

A unique clamping device was developed in order to grip SF-1 type specimen strictly during the test. The specimen needs to be parallel to load direction to avoid buckling. The clamping device consists of two counter plates. One plate has a groove along the load direction and a small pin. The other plate has a serrated surface. This device enabled remote handling operation.

2.2 Specimen

The materials used were F82H IEA heat (Fe-8Cr-2W-0.2V-0.04Ta), JLF-1 2nd large heat (Fe-9Cr-2W-0.2V-0.08Ta) and its TIG, tungsten inert gas, weldment[3, 4)]. To clarify the effect of specimen size on fatigue properties, two types of hourglass specimens have been fabricated. It is well known that the hourglass type specimen has good resistance to buckling. Furthermore the hourglass specimen is desirable for ion implantation, because fracture initiation site is limited to around the specimen's waist portion.

The ratio of root radius to diameter of waist portion, R/d of the both specimens was 8,

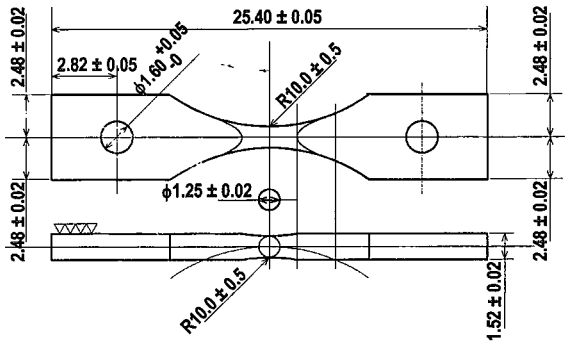


Fig. 2 SF-1 type fatigue specimen

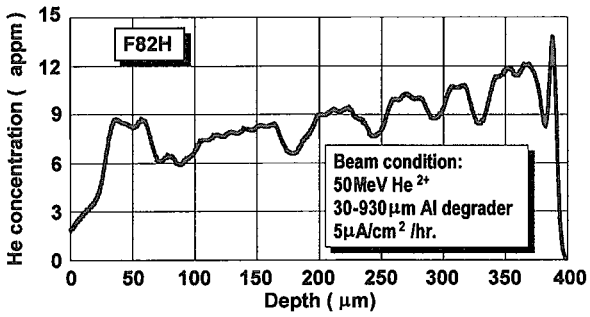


Fig. 3 Distribution of He concentrations

which satisfies the recommendations of ASTM E-606[5]. The diameter of waist for full- and mini-sized specimen was 6mm and 1.25mm, respectively. The mini-sized specimens called SF-1 (Fig. 2) are proposed to use in accelerator driven D-Li stripping reaction neutron sources, such as IFMIF[6]. The hourglass potion of SF-1 specimens was finished electrolytically.

2.3 Fatigue Test Condition

For full-sized specimens, an electrohydraulic servo-controlled testing machine with a 10kN load-cell was used. For SF-1 specimen, an electromotive testing machine with a 2kN load-cell was used. Diametral strain controlled fatigue tests were carried out with a triangular stress waveform and a total diametral strain range, $\Delta\varepsilon_d$ of 0.2% ~ 3.0%. The diametral strain rate was 0.04%/s, the stress condition was push-pull. $\Delta\varepsilon_d$ was converted to total axial strain range, $\Delta\varepsilon_a$, by the following formula described in ASTM E-606[5]

$$\Delta\varepsilon_a = (\sigma / E)(1-\nu_e) - 2\Delta\varepsilon_d \quad (1)$$

where:

σ : Applied stress, E : Elastic modulus

ν_e : Elastic Poisson's ratio

The number of cycles to failure, N_f, was defined as a point where a tensile peak stress decreased by 25% from an extrapolation curve of the tensile peak stress against number of cycle[7]. All tests were performed at an ambient temperature in air.

2.4 Helium implantation

The He implantation was carried out with AVF cyclotron accelerator at the TIARA facility. SF-1 specimens were implanted with energy-degraded 50 MeV He^{2+} ions. Fig. 3 shows the depth distribution of He concentration calculated by the TRIM95 code. As shown in this figure, the range was about ~400μm. He implantation was carried out on opposite two sides.

3. Results and Discussion

Laser extensometer and chucking device were successfully applied. Buckling did not occur even at large strain range of $\Delta\varepsilon_a$=6%. All specimens broke in the vicinity of the specimen's waist portion. The shape of hysteresis loop revealed that stress range and plastic strain range in each cycles did not depend on specimen size.

The N_f values with the SF-1 specimens were compared with those of full-sized specimens. The relationship between N_f and the converted total axial strain range, $\Delta\varepsilon_a$, is presented in Fig. 4. As shown in this figure, fatigue lifetime of JLF-1 TIG weldment was slightly shorter than that of its base metal, and strong size effect on fatigue lifetime was not observed[8, 9].

In the case of F82H, solid line represents results of full-sized cylindrical specimen of F82H[10]. Fatigue life of SF-1 hourglass specimen was slightly shorter than full-sized cylindrical specimen. However, in general, fatigue lifetime of hourglass specimen was shorter than that of cylindrical specimen. It is significant in high cycle region[7]. It was considered the specimen geometry affected fatigue lifetime.

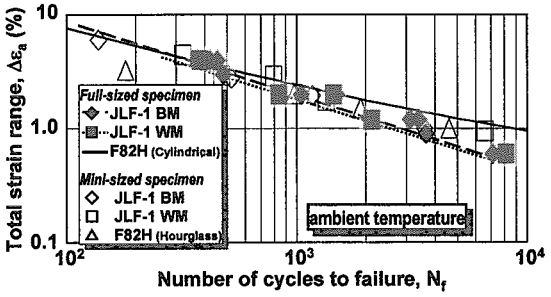


Fig. 4 Fatigue life curves

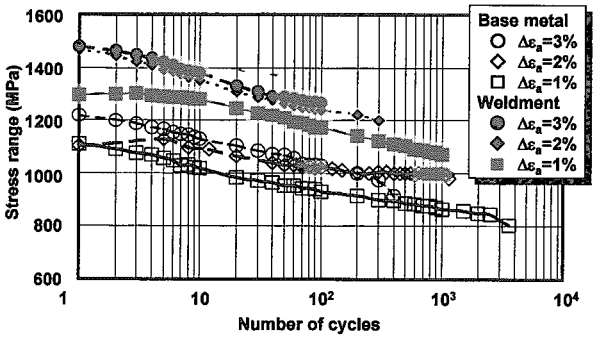


Fig. 5 Stress range of JLF-1 and its weldment

Cyclic stress response curves of JLF-1 and its TIG weldment are presented in Fig. 5. As shown in this figure, cyclic softening was observed in all tests. The tensile stress increased, however, at initial stage in several tests performed at higher strain range. On the other hand plastic strain range did not change during tests, except for the end of tests. It implies that the difference in both stress range and inclination of stress range did not depend on specimen size. The difference in stress range and inclination between specimen sizes was less than 5%. According to these results, fatigue properties are not sensitive to the specimen sizes studied in this work.

4. Summary

A miniature fatigue specimen test machine for a hot-laboratory has been successfully developed and the specimen size effect was studied. Diametral strain controlled fatigue tests on F82H and JLF-1 were carried out. Number of cycles to failure, plastic strain range and applied stress were not affected by the specimen size in this work. Cyclic softening was observed in all tests. Neutron irradiation and He implantation to F82H and JLF-1steel is ongoing. Post-irradiation fatigue test will be carried out in the near future.

References

1) A. Kohyama, A. Hishinuma, D.S. Gelles, R.L. Klueh, W. Dietz and K. Ehrlich, Journal of nuclear Materials 233-237 (1996) 138-147.
2) C. Brillaud, T. Meylogan and P. Salathe, ASTM STP 1270 (1996) 1144-1153.
3) A. Kohyama, Y. Kohno, M. Kuroda, A. Kimura and F. Wan, Journal of Nuclear Materials, 258-263 (1998) 1319-1323.
4) A. Nishimura, N. Inoue and T. Muroga, Journal of Nuclear Materials, 258-263 (1998) 1242-1247.
5) ASTM E-606, Annual book of ASTM, ASTM, 1996.
6) Y. Miwa, S. Jitsukawa and A. Hishinuma, Journal of Nuclear Materials, 258-263 (1998) 457-461.
7) A. Nishimura, T. Nagasaka, N. Inoue, T. Muroga and C. Namba, presented in ICFRM-9, to be published.
8) G. R. Rao, and B. A. Chin, ASTM STP 1125 (1992) 1095-1102.
9) G. R. Rao, and B. A. Chin, ASTM STP 1204 (1993) 267-274.
10) T. Ishii, K. Fukaya, Y. Nishiyama, M. Suzuki, and M. Eto, Journal of Nuclear Materials, 258-263 (1998) 1183-1186.

4.8 Cavity Formation in Reduced Activation Ferritic/Martensitic Steels Irradiated with Dual Ions

A. Naito, S. Jitsukawa, E. Wakai, H. Tanigawa, I. Ioka*, A. Hishinuma** and A. Kohyama***

Department of Material Science, JAERI, *Department of Nuclear Energy System, JAERI, **Department of Fusion Engineering Research, JAERI, *** Kyoto University

1. Introduction

Reduced activation ferritic/martensitic (RAF/M) steels have been considered as potential structural materials for the first wall of blanket (FWB) structures. D-T fusion neutrons will produce considerable amount of helium and hydrogen atoms in FWB structural materials by transmutation reactions during service. This may result in the acceleration of void swelling of the materials. The objective of this study is to clarify the effect of helium on cavity formation and swelling in RAF/M steels by the ion-irradiation experiments with high accuracy.

2. Experimental

The materials used are three kind of steels F82H (Fe-8Cr-2W-0.2V-0.04Ta), JLF-1 (Fe-9Cr-2W-0.2V-0.08Ta) and HT9 (Fe-12Cr-1Mo). Samples with 3mm in diameter and 0.2mm in thickness were irradiated with single ion beam of 11.3 MeV Fe^{3+} and dual ion beams of 11.3 MeV Fe^{3+} plus 1.2 MeV He^{+} at temperatures ranging from 400 to 500 C in the triple ion-beam irradiation facility of TIARA. Fig. 1 shows the theoretical depth profiles of displacement damage produced by iron ions and concentration of implanted helium calculated with TRIM-97 code. The displacement damage level and the implanted helium level were 60 dpa and 1200 appm at a peak depth of 1.9 μm,

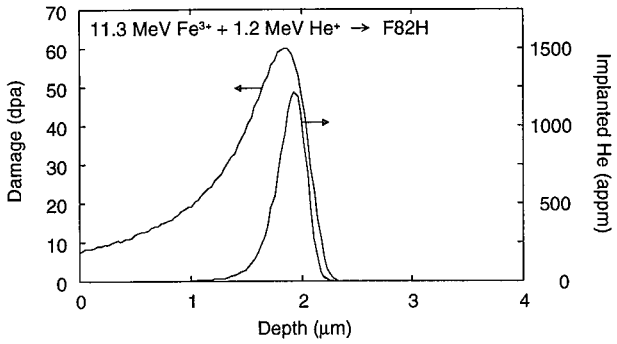


Fig. 1 Theoretical depth profiles of displacement damage produced by iron ions and concentration of implanted helium.

respectively.

After the irradiation, specimens for transmission electron microscopy (TEM) observation of a cross sectional view perpendicular to the incident surface were prepared from the irradiated samples. Nickel was electroplated on the both sides of an irradiated sample to a thickness greater than 3mm. The electroplated sample was sliced into 0.2mm thick sheet using a low speed diamond saw, and cut into 3 mm diameter disk. Then it was electropolished to perforation. A focused ion beam (FIB) processing system, FB-2000A attached with a micro sampling system was also employed to prepare TEM foils from the irradiated samples. The cross sectional microstructures were observed with a JEOL-2000FX operated at 200 kV.

3. Results

No cavity was observed in the specimens irradiated without He ions. On the other hand, cavities were observed in laths at the damage peak in the specimens irradiated with dual ion beams. The swelling behavior and its temperature dependence are different in three kind of steels as shown in Fig. 2. F82H showed the highest swelling resistance, and the largest swelling, 0.2 %, was observed at 500 C. The maximum cavity diameter in this condition reaches 20 nm. The largest swelling, 0.8 %, was observed in JLF-1 irradiated at 450 C, which contained large cavities up to 50 nm in diameter.

The swelling level at 450 C is lowered as the initial dislocation density is higher as shown in Fig. 3. The swelling may be suppressed due to higher initial dislocation density based on lower tempering temperature.

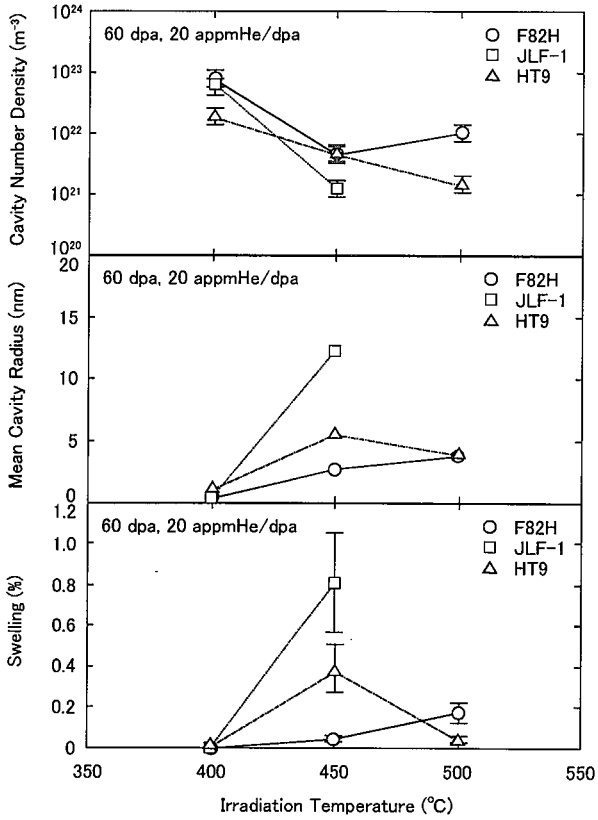


Fig. 2 Irradiation temperature dependence of cavity number density, mean cavity radius and swelling.

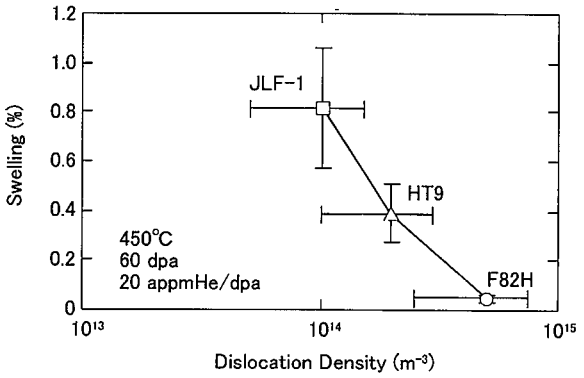


Fig. 3 Relationship between swelling level and initial dislocation density.

4.9 Basic study on the mechanisms of helium embrittlement and reduction of high temperature strength on reduced activation ferritic steel

H. Tanigawa [1], H. Abe [2], S. Jitsukawa [1], T. Iwai [3], H. Serizawa [4] and Yutai Katoh [5]
[1] Department of Material Science, [2] Department of Materials Development, JAERI
[3] Research Center for Nuclear Science and Technology, The University of Tokyo
[4] Joining and Welding Research Institute, Osaka University
[5] Institute of Advanced Energy, Kyoto University

1. Introduction

Reduced activation ferritic- martensitic steel, F82H (Fe-8Cr-2W-V-Ta), is one of the candidates for the first wall and blanket structural material for a D-T fusion reactor. It has been reported that transmutation-produced helium atoms from (n, α) reactions may play a significant role in the irradiation embrittlement and reduction of high temperature strength of the alloy during service. In order to avoid these critical reductions of the material strength, it is essential to understand the mechanisms of helium embrittlement and high temperature strength reduction.

There was a new conceptual approach to understand the mechanism of intergranular fracture, based on generalized Lindemann melting criterion for solid-state amorphization [1]. Generalized Lindemann melting criterion defines that the melting of metastable crystal occurres when the sum of dynamic and static mean square atom displacements (msd) reaches a critical value identical to that for melting of the perfect crystal. With this criterion, the crystal-to-glass (C-G) transformation, i.e. solid state amorphization, is simply melting of a critically disordered crystal at sufficiently low temperatures where the liquid exists in the glassy state. The point is that the melting criterion is independent of the physical origin of the static atomic displacement. So, the static atomic displacements induced by the segregation of impurities to the grain boundary or stress concentration, could induced melting. This suggests the possibility that all forms of intergranular fracture and the brittle behavior may have a common physical origin, namely local disorder-induced melting. Authors had shown that the crack tip region of intergranular fractured Al-Cu became amorphous during crack propagation on in situ TEM straining

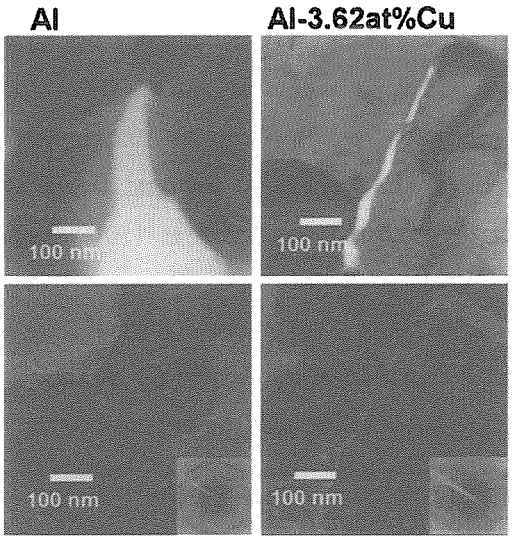


Fig.1 Bright field (upper row) and dark field (lower row) TEM images of cracked Al and Al-Cu thin foil. C-G transformed region (white contrasts in dark field image) on crack tip and grain boundary only observed in Al-Cu.

experiments (fig.1)[2], and confirmed the approach.

To demonstrate this approach is applicable to Fe based alloy, Fe-P alloy was selected for first trial, as the alloy was known to break at boundary with P addition[3], and to transform to amorphous phase with 11 to 13at% P addition at room temperature[4]. In this study, first P ion implantation had been done to confirm the critical P concentrations that evoke C-G transformation, and then in situ TEM straining experiments had been performed.

2. Experimental procedure

Material used in this study was high purity Fe-0.3at%P binary alloy. The impurity content (C, S , O, N, B) of the high purity iron

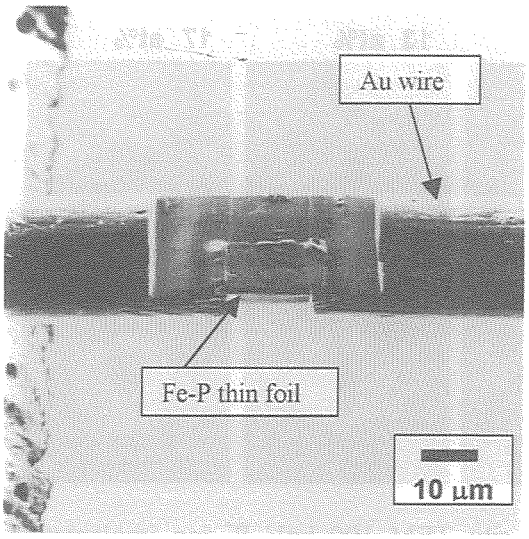


Fig.2 SIM images of TEM tensile specimen. Fe-P thin foil was loaded on Au wire.

was less than a few appm. Fe-P foil with fine grain was prepared with laser abrasion method. For the in situ TEM straining experiments, the foil was loaded on Au wire, which was welded on TEM tensile specimen (fig.2), using micro-sampling system in focused ion beam (FIB) processor (HITACHI FB-2000A). Then the foil was thinned to 100 nm thick with FIB processor and provided for the experiments. P implantation experiment was carried out at TIARA facility, JAERI Takasaki, using 400kV ion implanter and 400kV TEM (JEOL 4000FX). 100keV P^- ions were used for experiment as to implant the P ion into the middle of 100 nm thick Fe-P thin foil. Typical implantation rate was 0.1 at%P / min. In situ TEM straining experiment had been done using JEOL single tilt straining specimen holder.

3. Results and discussion

Figure 3 shows the results of P ion implantation experiment. It was clear from the figure that the C-G transformation occurred at grain boundary when 8 at% P was implanted, and started to occurr inside grains when 13at% P was implanted. Pre-experimental EDX analysis suggested that the P concentration at grain boundary is about 3 at%. So the C-G transformation occurred when 11 to 13 at% P was implanted in this study, and this result agreed with reported experimental results [4].

In situ TEM straining experiment had been done on as prepared Fe-P specimen, and on 6 at%P implanted Fe-P specimen. In both cases, no amorphous region, where it is suggested that the C-G transformation was occurred, had been observed before straining. As loading specimen, crack was induced in a very short time on both cases. Figures 4 and 5 show the TEM images of cracks induced on each specimens. On as-prepared Fe-P specimen (Fig. 4), the ductile crack was induced initially and stopped at a point, and from the crack tip, amorphous region was observed along the grain boundary. On 6 at% P implanted Fe-P specimen (Fig. 5), the ductile crack was also induced initially and stopped at a point, and amorphous region was observed at the triple point of grain boundaries near to the crack tip. Both results suggest that the stress concentration at the crack tip and segregated P at the grain boundary induced C-G transformation, and confirm the hypothesis that local disorder-induced melting may evoke intergranular fracture.

4. Summary

In situ TEM ion implantation and straining experiments on Fe-P binary alloy had been done to verify the hypothesis that local disorder-induced melting may evoke intergranular fracture, which is based on generalized Lindemann melting criterion.

(1) 100 keV P^- ion implantation has been done on Fe-0.3at%P and the critical percentage of P for C-G transformation was confirmed.
(2) Crack was induced to Fe-0.3at%P specimen and 6 at%P implanted Fe-0.3at%P specimen, and amorphous regions along grain boundary was observed ahead of crack tip.
(3) The hypothesis that local disorder-induced melting may evoke intergranular fracture.

References

1) P.R. Okamoto, N.Q. Lam and L.E. Rehn, Solid State Physics, (ed. H. Ehrenreich and F. Spaepen), 52 (1999) 1
2) H. Tanigawa, Ph.D. dissertation thesis, Kyoto University (1998)
3) K. Abiko, JAERI-memo 08-233 (1995) 140
4) G.Dietz, K. Richter, F. Stein and H.C. Schafer, Z. Phys. B Condensed Matter 81 (1990) 223

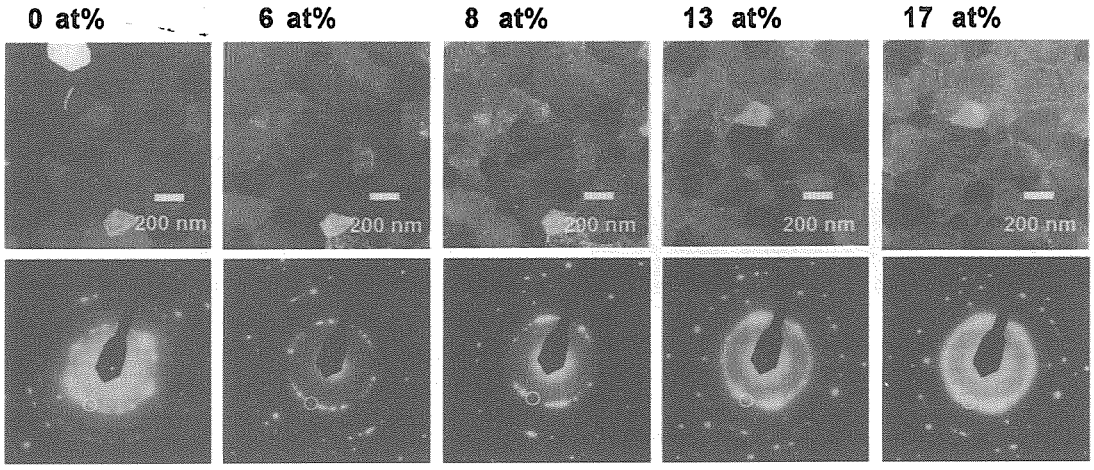


Fig.3 TEM dark field images obtained at in situ TEM 100 keV P^+ ion implantation experiments. All dark field images were obtained by selecting marked region of diffraction patterns by objective aperture



Fig.4 TEM dark field images of cracked Fe-0.3at%P. White contrast represents the amorphous regions induced by stress concentration ahead of crack tip and P segregation.

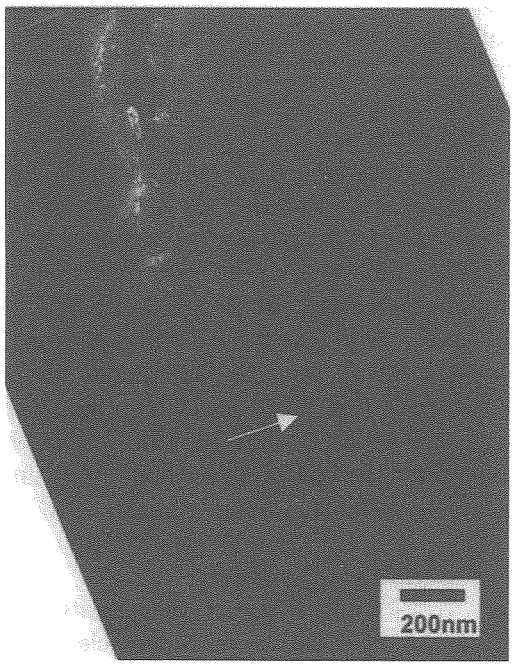


Fig.5 TEM dark field images of cracked 6at%P implanted Fe-0.3at%P. Indicated white contrast represents the amorphous regions on triple points of grain boundaries.

4.10 Research on Formation Process of Irradiation Defects for Light Water Reactor Pressure Vessel Steel

T. Tobita*, M. Suzuki*, Y. Idei*, A. Iwase**, K. Aizawa***, H. Amezawa****, N. Sekimura*****

*Department of Reactor Safety Research, **Materials Science, ***Advanced Basic Research Center, ****JMTR, JAERI, Tokai, *****The University of Tokyo.

1. INTRODUCTION

Fast neutron fluence with energy higher than 1 MeV is generally used as scaling parameters for irradiation induced embrittlement. However, the contribution of γ-ray, which has low knock-on energy, to irradiation embrittlement of RPV (Reactor Pressure Vessel) steel has not been taken into account in prediction formulas. In commercial nuclear reactor RPV steel, γ-ray contribution to irradiation damage is only several %. However, because defects are more likely to survive due to point defects production, γ-ray may have a potential to cause irradiation embrittlement in RPV steels.

When γ-ray is irradiated to the target material, high-energy electrons are produced through Compton effect, leading to the atomic displacements. We have no strong γ-source that makes enough radiation damage. Therefore, we simulated the γ-ray effects by high-energy electron irradiation.

In the previous report [1], we showed the dose dependence of hardening induced by electron irradiation in Fe-Cu model alloys. Then we compared the hardening with that by fast neutron irradiation by limited neutron data. In this report, we show additional results on electron and neutron irradiation hardening, with some microstructural characterization data.

2. EXPERIMENTS

The materials used were two kinds of Fe-Cu model alloys of different Cu contents. Chemical compositions of these materials are shown in Table 1. We used these materials for electron irradiation, thermal aging and material testing reactor irradiation. We evaluated irradiation embrittlement by Vickers hardness tests. Table 2 shows our test matrix.

Electron irradiation was performed at the TIARA Single-ended accelerator and the Accelerator No. 2 at Takasaki Establishment of Japan Atomic Energy Research Institute (JAERI). Electron energies used were 2 and 2.5MeV. Fig. 1A and 1B show the specimen set up for electron irradiation at each accelerator.

We measured the hardening value of the specimen before and after irradiation by using a Vickers hardness (Hv) tester. Test load was 500gf. We observed Cu precipitation of some hardened specimens using SANS (Small Angle Neutron Scattering).

The irradiation damage, dpa, was calculated using the Monte Carlo simulation code, EGS4 (Electron -Gamma Shower4[2]). Displacement energy for an Fe atom used in this calculation is 40 eV,

which is in accordance with ASTM recommendation[3].

Table 1 Chemical compositions of the materials (Wt%)

Material	Fe	Cu	C	Si	O	N
High Cu Alloy Fe-0.6%Cu	Bal.	0.61	0.002	0.002	0.015	0.0006
Low Cu Alloy Fe-0.02%Cu	Bal.	0.022	0.003	0.003	0.015	0.0006

Heat treated at 850°C - 2H & quenched.

Table 2 Test Matrix

	Electron Irradiation* 2.5MeV 10^{-5}~ 10^{-3} dpa 8×10^{-10} ~ 7×10^{-9} dpa/s	Neutron Irradiation 4×10^{-5}~2×10^{-2} dpa 7×10^{-11}、2×10^{-9} dpa/s	Thermal Aging
Hi Cu Alloy Fe-0.6wt%Cu	@ 215~310 °C	@ 240** & 250 °C***	@250~500°C
Low Cu Alloy Fe-0.02wt%Cu	@ 250 °C	@ 240** & 250 °C***	----------

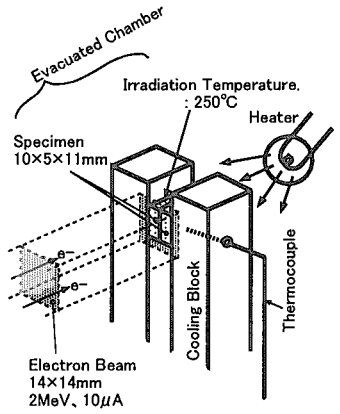


Fig. 1A Specimen setup for electron irradiation in TIARA

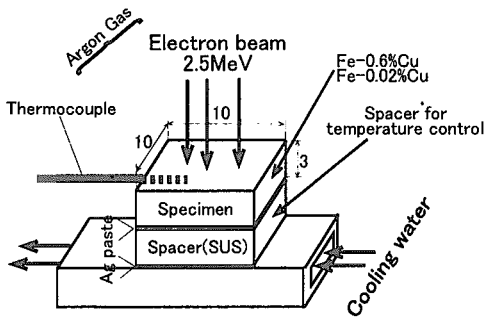


Fig. 1B Specimen set up for electron irradiation in ACCELERATOR No.2

3. RESULTS AND DISCUSSION

Fig.2A shows the relation between mean radius of the precipitates and electron fluence. Fig.2B shows number density of the precipitates as a function of electron fluence. With the increase of electron fluence, the size of the object becomes larger and the density becomes lower. This data suggests coarsing of Cu precipitation with electron irradiation. Then, Cu precipitation seems to be saturated at a higher fluence region. For Fe-0.02%Cu material, we could not observe the Cu precipitation.

Fig.3 shows the relation between hardening value and electron fluence at 250℃ irradiation. Each hardening data point represents the mean of 10 measurements. With the increase of electron fluence, hardening value becomes higher on each material. Fe-0.6%Cu material hardens rapidly from the low fluence region and seems to be saturated afterwards. We could not observe the hardening by thermal aging tests[1]. The followings are suggested. In the 0.02% Cu alloy, irradiation hardening is caused by matrix damage only. While in the 0.6%Cu alloy, irradiation hardening is the sum of matrix damage and Cu precipitation hardening.

Fig.4 shows the hardening as a function of calculated dpa for all specimens. Data for the same alloys irradiated at material testing reactors (JMTR and Yayoi reactor) are also plotted for comparison. The value calculated from SANS data with a Russel-Brown model[4] and Orowan model[5] are also shown in this figure. For Fe-0.02%Cu alloy, electron-irradiated data and neutron irradiated data show the same tendency. For Fe-0.6%Cu alloy, at lower dpa region and higher dpa region, the both data show the same tendency. Thus, irradiation

hardening can be scaled by dpa in these regions. However, in the Cu-precipitating stage (rapidly hardness increasing region), difference between electron irradiation and neutron irradiation is not clear because of the lack of overlapped data. Additional data by neutron irradiation is necessary. The Russel-Brown model shows good agreement with experiment value at lower dpa region. But, at higher dpa region, Orowan model seems to show better agreement. The calculation methods and the accuracy of precipitation measurement by SANS have to be examined more in detail.

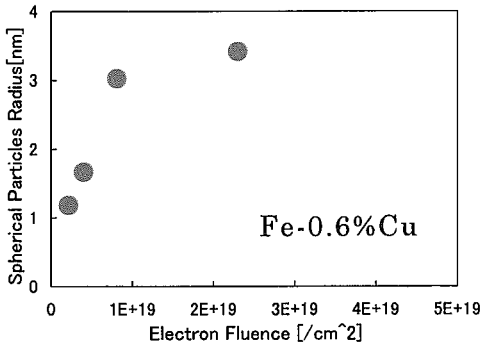


Fig.2A Spherical particle radius

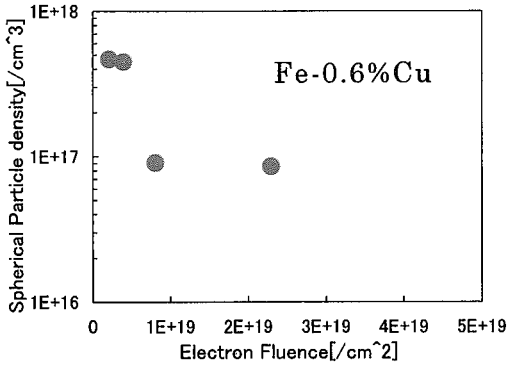


Fig.2B Number density of particle

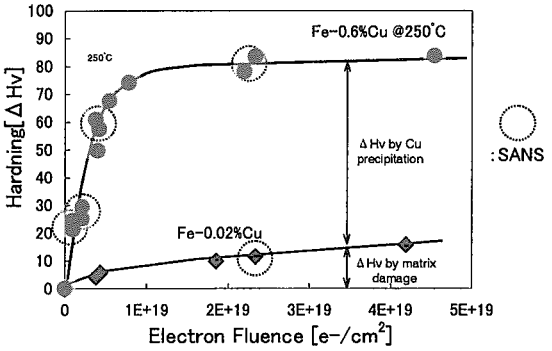


Fig.3 Vickers hardness of specimen surfaces irradiated by electron at 250°C

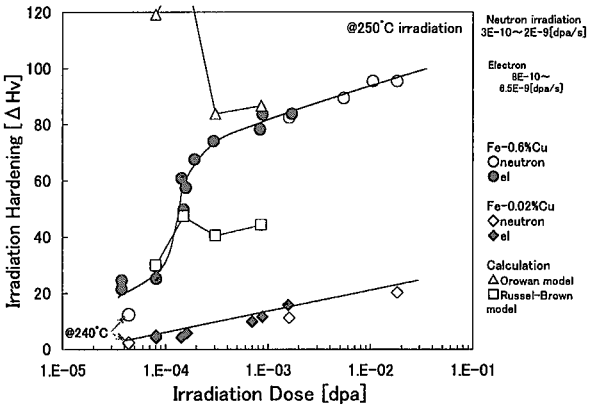


Fig. 4 Comparison of hardening by electron and fast neutron irradiation.

REFERENCES

[1] T. Tobita et.al. TIARA Annual Report 1998 ,p.123.

[2] W.R.Nelson, H.Hirayama, and D.W.O.Rogers, "The EGS4 Code System," SLAC-265, (1985).

[3] 1993 Annual book of ASTM Standers, Vol. 12. 02, (1993) p.171.

[4] Russel, K.C. and Brown, L.M. Acta Metallurgica, vol20, 1972, 20, pp969-974

[5] Philip M. Rice, et.al. Mat. Res. Soc. Symp. Proc. Vol.373, 1995, Materials Research Society.

4.11 Mechanical Characterization of Ion Implanted Layer by Microindentation Test Using Different Apex Angle Indenters

I.Ioka, M.Futakawa, T.Wakui* and A.Naito**
Department of Nuclear Energy System, JAERI, *Department of Mechanical Engineering, Niigata Univ., ** Department of Material Science, JAERI

1. Introduction

A triple ion beam facility at JAERI can be used to simulate a spallation neutron environment[1] by producing displacement damage in the material by simultaneously implanting H^+ and He^+ ions. However, the ion implanted area is limited to the very shallow surface layer of the specimen so that the irradiation damage is distributed around the thin layer. In previous report[2], we proposed a technique for deriving constants of the Swift's power low constitutive equation[3] ($\sigma=A(\varepsilon_0+\varepsilon)^n$, A: strength coefficient, ε_0: equivalent strain by cold rolling, n: strain hardening exponent) of the damaged parts by a microindentation test combined with an inverse analysis using a finite element method (FEM). It was assumed that the values of A and n were almost equal to those of the base material in the technique. The value of ε_0 was decided so that the analytical result by FEM may agree with the result of microindentation test.

In this study, the values of A, n and ε_0 were simultaneously obtained from the result of microindentation test using three kinds of trigonal pyramid indenters. The constitutive equation of nickel superalloy with high yield stress was deduced by the new technique in order to confirm the validity of the technique. Moreover, the constitutive equation of the ion implanted layer was estimated using the new technique.

2. Experimental

2.1 Derivation of the constitutive equation

By the microindentation test with the different apex angle, the gradient (S_{exp}) during loading was obtained from Load/Depth-Depth curve (P/h-h curve) of nickel superalloy shown in Fig.1.

The constitutive equation assumed the following Swift's power low curve.

$$\sigma=E\varepsilon, \qquad \sigma\leq\sigma_y \quad (1)$$

$$\sigma=A(\varepsilon_0+\varepsilon)^n,\ \varepsilon_0=(\sigma_y/A)^{1/n}-(\sigma_y/E), \qquad \sigma>\sigma_y \quad (2)$$

where E is Young's modulus and σ_y is yield stress. The Young's modulus is calculated from unloading part in the Load-Depth curve (P-h curve) of the microindentation test.

Relationships between the remainder of constitutive equation (A, n, σ_y) and the gradient (S) of the P/h-h curve on each indenter are obtained by the FEM analysis. A, n and σ_y are decided from the comparison of the result of the microindentation test with the analytical results[4].

2.2 Microindentation test

A testing machine, DUH-200 (Shimadzu Co.), was used for the microindentation test. A load was applied with a loading speed of 2.6mN/s, held 1 second and then removed. During loading and unloading, the load was continuously monitored along with the displacement with a resolution of 2mN and 0.01μm, respectively. Three kinds of indenter were selected so that the apex angle may become A_p/h^2=12.2, 24.5, 49.0. A_p and h are the projected area and the depth from the surface, respectively. The indenter with A_p/h^2=24.5 is correspondent to the Birkovich indenter. In the microindentation test, the maximum load was set to be 98mN, and the test frequency was 10 times for each.

2.3 Tensile test

The tensile test was carried out in order to confirm the constitutive equation obtained. Nickel superalloy used in the micro-indentation test was also used for the tensile test. The specimen is round bar type of 6mm in diameter and 32mm in length of gauge section. The tensile test was conducted at room temperature in air with strain rate of $4x10^{-4}$ 1/s.

2.4 Ion implantation

The material for ion implantation is SUS316L. Specimens are disks of 3mm in diameter with 0.2mm thickness. The electrochemically polished disk specimens were irradiated in triple (12MeV Ni^{3+}, 750keV He^{+} and 290keV H^{+}) ion beam modes at a temperature of 200°C. The SRIM97 code formerly known as TRIM[5] was used to compute the ion fluence and the displacement dose as a function of depth beneath the specimen surface. The displacement damage in the disk specimen is mainly attributed to Ni^{3+} ion implantation. The peak dose is about 22dpa around 2μm. The peak values of concentration of Ni, He and H atoms are about 6000appm, 2000appm and 20000appm, respectively. The peak positions of implanted He^{+} and H^{+} ions are controlled so that the effect of implanted Ni^{3+} ions can be neglected. The He/dpa and H/dpa ratios of the disk specimens are about 250 and 2400 at the depth of approximately 1.3μm.

3. Results and discussion

3.1 Verification of the constitutive equation

The P-h curves by the FEM analysis using the constitutive equation obtained and by tensile test are shown in Fig.2. Each constant of the constitutive equation is also shown in Fig.2. The analytical result showed good agreement with the experimental one. They agreed with each other also with respect to deformation at failure as shown in Fig.3.

3.2 Application to ion implanted layer

The P/h-h curves of the ion implanted specimen obtained from the microindentation test with different apex angle indenters are shown in Fig.4. The inflection point appears in each curve as shown in Fig.4, and it is possible to divide each curve into two regions. The curve in region Ⅰ reflects the change in properties of the ion implanted layer. In region Ⅱ, the properties of the base metal become more prominent rather than those of the ion implanted layer. Therefore, the constitutive equation of ion implanted layer was deduced by the gradient ($S_{exp.}$) in region Ⅰ.

The microindentation test with a spherical indenter was carried out for examining the validity of the constitutive equation deduced. The radius of the hemisphere apex of the spherical indenter is 5μm. The P-h curves obtained from the microindentation test with the spherical indenter and the analytical result are shown in Fig.5. The experimental result almost agreed with the analytical one using the constitutive equation deduced. From this fact, it was confirmed that this technique could apply to the derivation of the constitutive equation of the ion implanted layer.

4. Conclusion

For the ion implantation layer, the constitutive equation was deduced by the new technique that combined the microindentation test using different apex angle indenters with the FEM analysis. The validity of the constitutive equation deduced was confirmed by the comparison of the analytical result with the result from the microindention test

using the spherical indenter.

References

1) M.S.Wechsler, et al., Proc. of Sympo. on Materials for Spallation Neutron Sources, Florida, 23(1997).
2) I.Ioka et al., JAERI-Review 99-025, (1999) 140.
3) P.B.Mellor, J. Mech. Phys. Solids, 5(1956)5.
4) T.Wakui et al., Ibaraki-kouennkai, (1999)7-8.
5) J.F.Ziegler et al., "The Stopping and Range of Ion in Solids", vol.1, Pergamon Press, New York(1985).

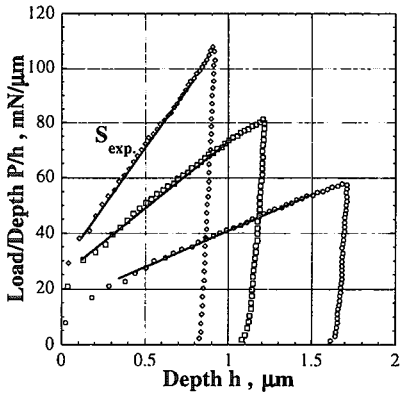


Fig.1 P/h-h curves of nickel superalloy

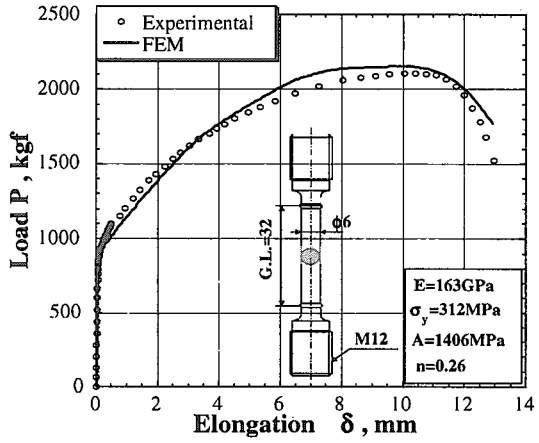


Fig.2 Load-Elongation curve of nickel

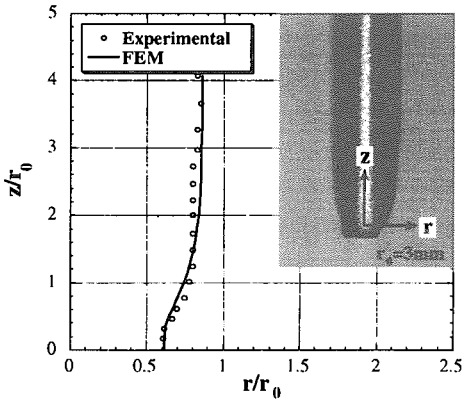


Fig.3 Deformation at failure from the analytical and experimental results

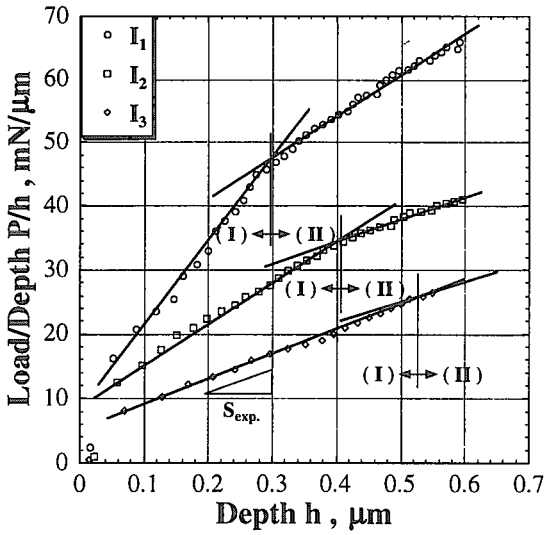


Fig.4 Load/Depth-Depth curves of ion implanted specimen using trigonal pyramid indenters

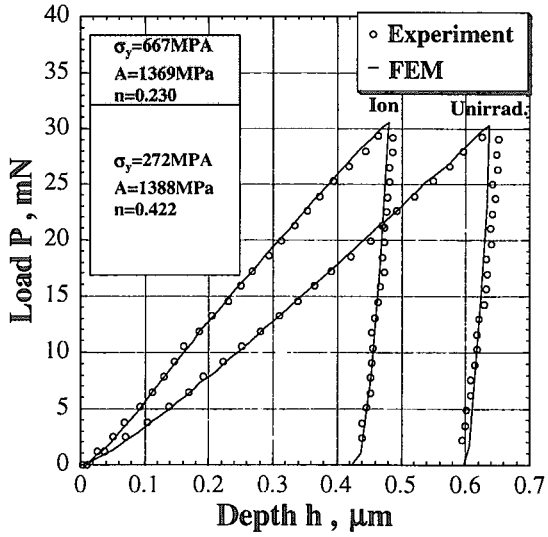


Fig.5 Experimental and analyzed Load-Depth curves using a spherical indenter.

4.12 Effect of Oxygen on Characteristics of Austenitic Stainless Steels as Cladding Tube in Light Water Reactor

S. Hamada, I. Ioka, C. Kato, K. Kiuchi

Department of Nuclear Energy System, JAERI

1. Introduction

The study and development of advanced fuel cladding tube materials for light water reactors with ultra high burn-up such as 100GWd/ton started in our laboratory. The characteristic changes of the cladding material irradiated in a reactor have been very influenced by irradiation -induced surface reactions from coolant and fuel sides as well as displacement damage by neutrons, hydrogen and helium atoms produced by nuclear transmutation reactions. Active chemical species such as H_2, O_2 H^+, O^{2-} are produced by radiolysis of water adjacent to the surface of a cladding tube in a light water reactor. Especially, it is reported that hydrogen of them can easily permeate into the material through the surface PDP (Plasma Driven Permeation)[1] at lower temperatures and affects the characteristics of the material. It is predicted that oxygen shows the similar behavior as hydrogen. These atoms will permeate into the cladding material through the surface and accumulate to grain boundaries. As a result, they will lead to ductility loss of a cladding tube without corrosion. Further, promoted diffusion of these atoms under the exposure of neutron and gamma ray would give more ductility loss and decrease of corrosion resistance at grain boundaries might occur. So far, the mechanism of such phenomenon has been hardly shown. Especially, even the phenomenon has not been observed for oxygen.

In order to clear the mechanism of this phenomenon from the viewpoint of microstructural change, which these atoms will induce, the ion irradiation experiments were carried out.

2. Experimental and results

Two types of stainless steels were choosenfor irradiation. The chemical composition of each material is 25Ni-17Cr-2-Mo-0.25Ti-Fe and 35Ni-17Cr-2Mo-0.3Ti-Fe, respectively. The triple beam irradiation apparatus was used for irradiation. In order to obtain the wider depth profile of incident ions, ions with various energies were employed for post experiments. In this study, oxygen ions with 1.0, 1.8 and 3.0MeV were irradiated to specimens at about 300℃. The depth profiles of oxygen atoms and displacement damage were calculated with TRIM code[2]. Fig. 1 shows the depth profiles of oxygen atoms and displacement damage. In the present study, the oxygen atoms content and displacement damage levels were 1500 to 2500 appm and 10dpa, respectively.

Hardness test, transmission electron microscopy observation of microstructural evolution and corrosion test for oxygen irradiated are planned and partially are in progress.

References

1) M. Takizawa et al. Plasma Fusion, 75 (1994) 432.

2) J. F. Ziegler et al. "The Stopping and Range of Ion in Solids" Vol.1, PREGAMON PRESS (1985).

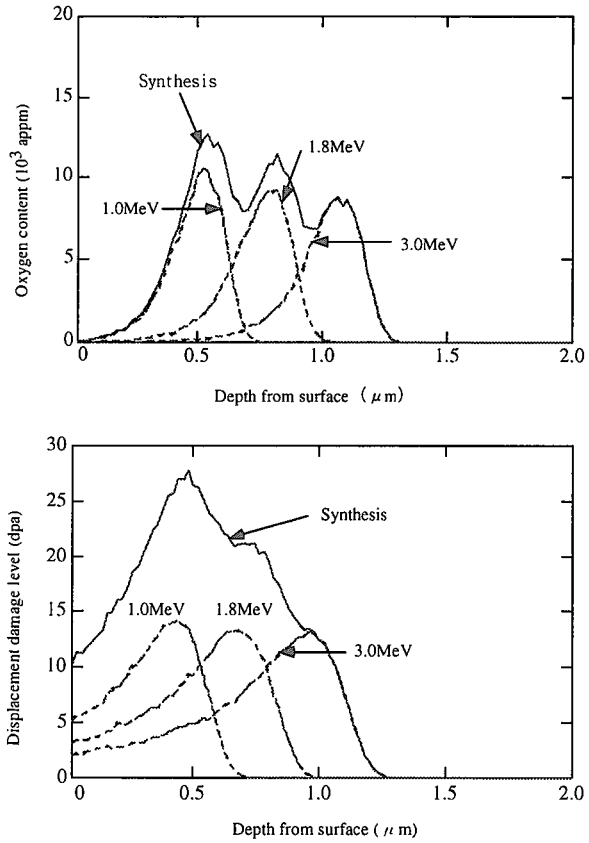


Fig. 1 Depth profiles of oxygen content (upper) and displacement damage level (lower) in stainless steel irradiated by oxygen ions with each energy of 1.0, 1.8 and 3.0MeV (1pμA/cm^2). Each broken line and solid line show depth profile for single energy and synthesis of depth profiles by three energies, respectively.

4.13 Investigation of the resonant vibration modes of self interstitial atoms in metals by low temperature specific heat measurement

M.Watanabe
Department of Materials Science, JAERI

1.Introduction

Some theories[1] predict the resonant vibration modes due to self interstitial atoms in metals, which have large amplitudes and low frequencies. These kinds of modes for a single defect presents an important problem for physics of lattice defect. The resonant vibration modes have important influence on properties of phonons. To verify the existence of these modes, we measured the specific heat of electron-irradiated fcc metal(Cu) and bcc metals(Mo, W) at low temperatures.

2.Experimental

The specimens used in this work were Cu, Mo and W single crystals with dimensions of $12\times12\times0.5\ mm^3$, $12^{\Phi}\times0.5\ mm^3$ and $8.8^{\Phi}\times0.5\ mm^3$. The irradiations with 2-MeV electrons to the dose of $7.73\times10^{17}/cm^2$, $6.49\times10^{17}/cm^2$ and $9.54\times10^{17}/cm^2$ at 19K, 23K and 25K, respectively, were performed by using the a low temperature irradiation facility interfaced to TIARA 3MV single-ended accelerator. Before and after irradiation, we measured the specific heat of the specimen under the adiabatic condition between 2K-60K.

3.Results and discussion

Fig. 1 shows the specific heat change in Cu<100> after irradiation to the dose of $7.73\times10^{17}/cm^2$ at 19K and subsequent 60K annealing[2]. Two peaks of specific heat changes were found. This temperature range is lower than the first stage of the recovery, and these peaks of specific heat changes can not be detected by electric resistance measurements, etc..

Figs. 2 and 3 show the specific heat change in Mo<100> after irradiation to the dose of $6.49\times10^{17}/cm^2$ at 23K and 300K annealing, respectively[3].

Figs. 4, 5 and 6 show the specific heat change in W<100> after irradiation to the dose of $6.49\times10^{17}/cm^2$ at 25K and 150K, 300 K annealing, respectively.

The specific heat change in Mo<100> and W<100> after irradiation well corresponded to recovery stage by the electric resistance measurement.

The specific heat which changed by the irradiation is recovered with increasing anneal temperature.

For Mo<100> and W<100>, the peaks of the specific heat change were observed, which originated from the resonance mode vibration similarly to that for Cu<100>.

Reference

1) A.Scholz and Chr.Lehmann, Phys.Rev.B6(1972)813.
2) M.Watanabe,A.Iwase,N.Ishikawa and Y.Chimi, TIARA Annual Report 1996, p92 (1997).
3) M.Watanabe,N.Ishikawa and Y.Chimi, TIARA Annual Report 1998, p119 (1999).

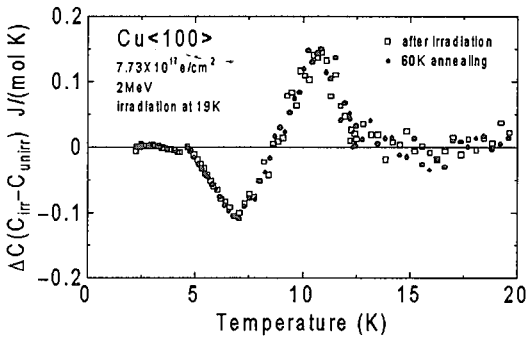


Fig.1. Specific heat change in Cu<100> after irradiation to the dose of 7.73 × 10^{17}e/cm ^{2} at 19K and 60K annealing.

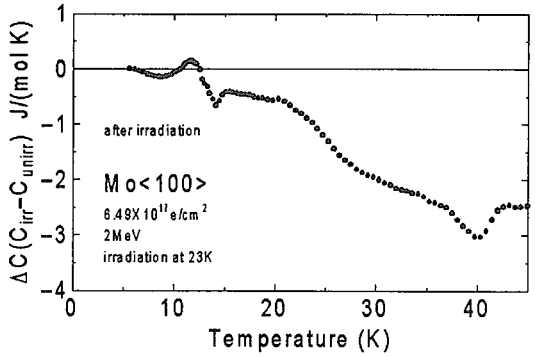


Fig.2. Specific heat change in Mo<100> after irradiation to the dose of 6.49 × 10^{17}e/cm ^{2} at 23K.

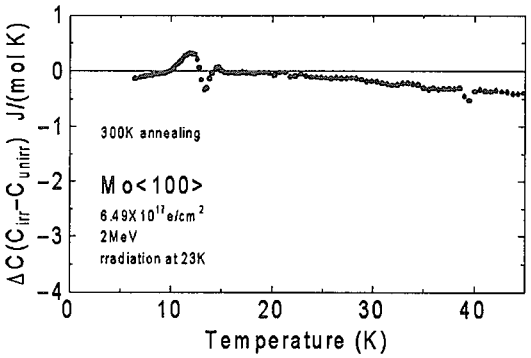


Fig.3. Specific heat change after 300 K annealing in Mo<100> irradiation to the dose of 6.49 × 10^{17}e/cm ^{2} at 23K.

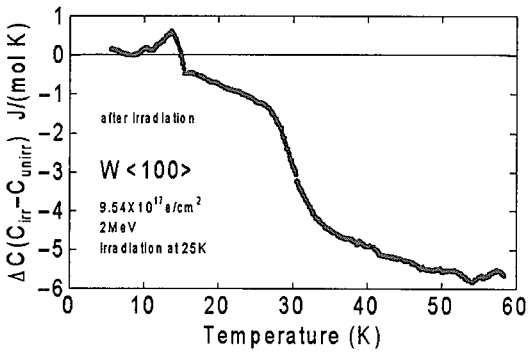


Fig.4. Specific heat change in W<100> after irradiation to the dose of 9.54 × 10^{17}e/cm ^{2} at 25K.

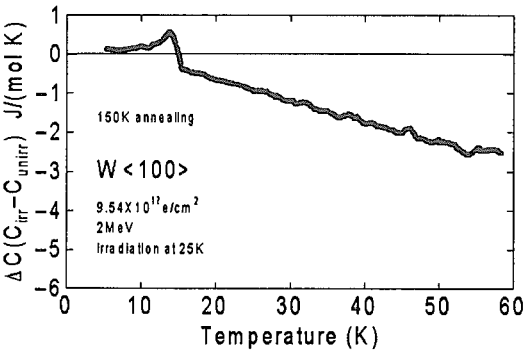


Fig. 5. Specific heat change after 150 K annealing in W<100> irradiation to the dose of 9.54 × 10^{17}e/cm ^{2} at 25K.

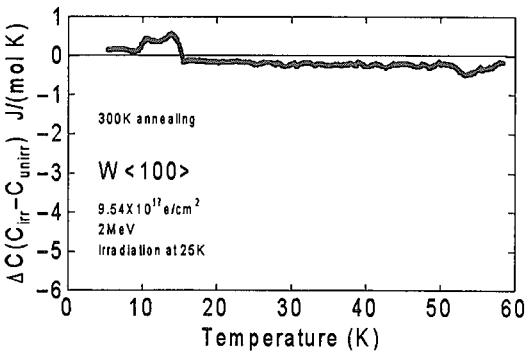


Fig. 6. Specific heat change after 300 K annealing in W<100> irradiation to the dose of 9.54 × 10^{17}e/cm ^{2} at 25K.

4.14 Effects of Electron Irradiation on Pd- H System

K. Yamakawa, Y. Chimi*, K. Adachi, A. Iwase*
Faculty of Engineering, Ehime University, *Department of Materials Science, JAERI,

1. Introduction

It is well known that hydrogen atoms in Pd exhibit the order- disorder transition around 50 K , which cause various anomalies in electrical resistivity[1,2], specific heat[3] and so on. We studied the effects of energetic electron irradiation on the order- disorder transition of hydrogen atoms in Pd- H at low temperatures.

2. Experimental Procedure

Polycrystalline Pd foil about 1.5 μm thick was loaded with hydrogen up to the atomic ratio of H/Pd = 0.5 by the electrolysis of 0.1 N H_2SO_4. In order to achieve the ordered state of hydrogen atoms at 10K, the $PdH_{0.5}$ specimen was gradually cooled down to 10 K. Then it was irradiated with 0.5 MeV electrons from the 3 MeV single- ended accelerator at TIARA. During the irradiation, the electrical resistivity was measured as a function of electron fluence. The temperature of the specimen was held at 10 K during irradiation and resistivity measurement.

3. Experimental Results

Figure 1 shows the dependence of electrical resistivity change on the electron fluence. The resistivity decreases linearly with increasing the electron fluence. In Pd- H system, it has been proved that the disordering of hydrogen atoms leads to the resistivity decrease. Therefore, the figure indicates that the disordering of hydrogen atoms is induced by electron irradiation. We have obtained the similar result in the high energy ion irradiated Pd- H system[4].

References

[1] T. Skoskiewics, B. Baranowski, Phys. Stat. Sol. 30(1968) K33.

[2] C. Herrero, F. D. Manchester, Phys. Lett. 86A(1981) 29.

[3] D. M. Nace, J. G. Aston, J. Am. Chem. Soc. 79(1957) 3623.

[4] Y. Chimi, K. Adachi, A. Iwase, N. Ishikawa, Y. Yamakawa, J. Alloys and Compounds, to be published.

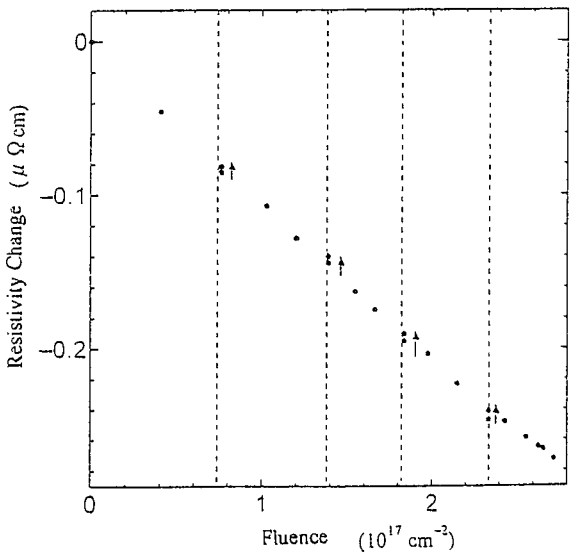


Fig. 1 Change in electrical resistivity of Pd- $H_{0.5}$ specimen as a function of electron fluence.

4.15 Negative Magnetoresistance of Pyrolytic Carbon and Effects of Low-Temperature Electron Irradiation †

N. Ishikawa, A. Iwase, T. Iwata, Y. Chimi, T. Nihira*
Department of Materials Science, JAERI, *Faculty of Engineering, Ibaraki University

Pyrolytic carbon that exhibited negative magnetoresistance was irradiated with 2MeV electrons at temperatures below 35K, and the changes in electronic transport properties such as zero-magnetic field resistivity, Hall coefficient, and magnetoresistance were measured as a function of electron fluence. With increasing electron fluence, the zero-field resistivity decreased, while the Hall coefficient and the absolute values of negative magnetoresistance increased. The experimental data were analyzed assuming that the densities of electrons and holes varied with the magnetic field.

Figure 1 shows that the carrier densities increase with the square of the magnetic field; the result is in good agreement with the Bright theory[1], in which the two-dimensional Landau levels are assumed to be broadened due to the defect scattering. Figure 2 shows the dependence of hole densities on the density of irradiation-produced vacancies for various magnetic fields. Figure 3 shows the linear dependence of p_0 and n_0 on $N_{v\text{-}irrad}$, where p_0 and n_0 are the zero-field densities of holes and electrons, respectively, and $N_{v\text{-}irrad}$ the density of irradiation-produced vacancies. The two straight lines in the figure intersect at a negative $N_{v\text{-}irrad}$ value, where p_0 and n_0 have a same value of N_0. The case $p_0=n_0$ means that there exist no acceptor defects (vacancies) in the specimen, and then the absolute value of the x axis at the intersecting point gives the density of intrinsic vacancies, $N_{v\text{-}intrinsic}$. This result indicates that both intrinsic defects and irradiation-produced defects act as electron acceptors. The addition of acceptors increases the ratio of hole density to electron density, p/n, resulting in the enhancement of the negative magnetoresistance.

The present results clarify that the negative magnetoresistance in pyrolytic carbon is caused by the existence of acceptor defects and the two-dimensional Landau levels, which are broadened by the defects. In addition, they suggest that the intrinsic acceptor defects in pyrolytic carbon are presumably vacancies.

Reference

1) A. A. Bright, Phys. Rev. B20(1979) 5142.

† Condensed from the article in Phys. Rev. B60(1999) 10811.

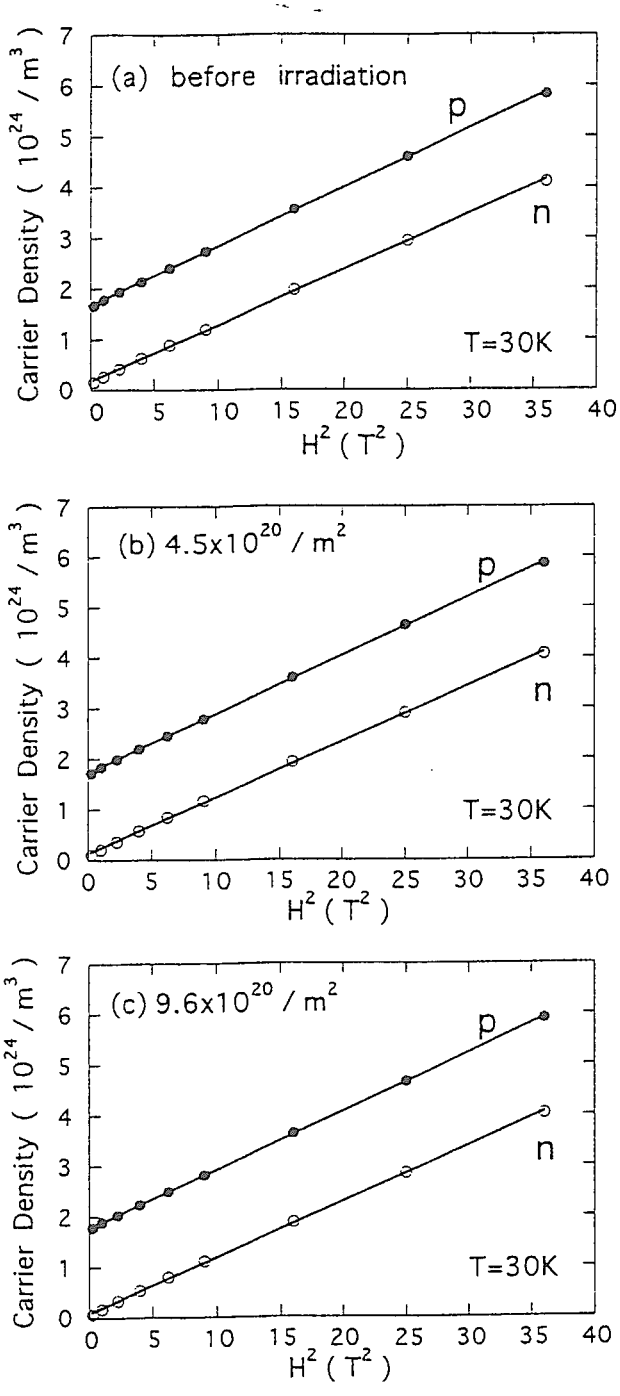


Fig. 1 Densities of holes and electrons at 30 K as a function of H^2 at various electron fluences; (a) before irradiation, (b) for 4.5x10^{20}/m^2, and (c) for 9.6x10^{20}/m^2.

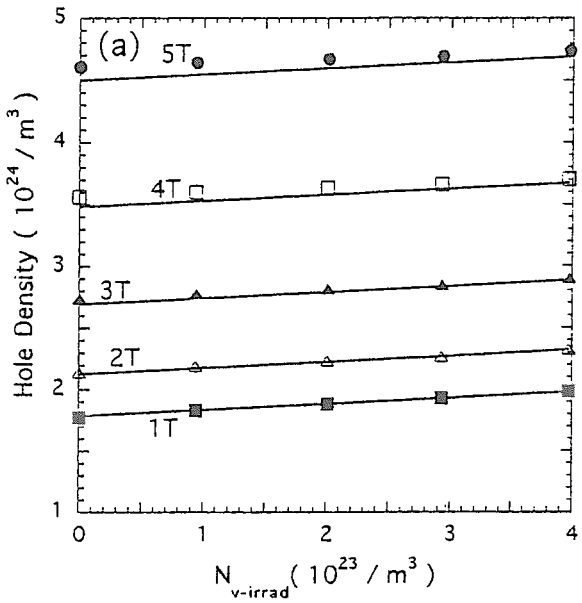


Fig. 2 $N_{v\text{-}irrad}$ dependence of hole density at 30 K for various magnetic fields.

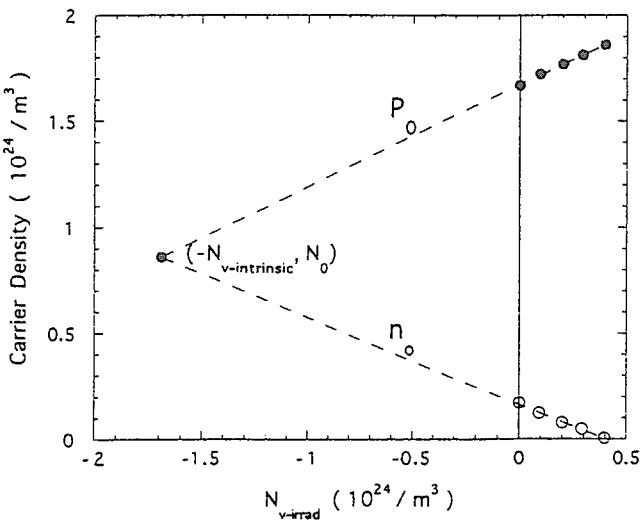


Fig. 3 $N_{v\text{-}irrad}$ dependence of p_0 and n_0. The straight lines for p_0 and n_0 are extrapolated to their intersecting point.

4.16 Measurement of Defect Recovery Spectrum in Al by means of Constant Heating Method

Y. Chimi, A. Iwase, N. Ishikawa
Department of Materials Science, JAERI

1. Introduction

For the study of the irradiation effects of materials, it is very important to know properties of irradiation-produced defects. In metals, especially, defect structure and/or activation energy for migration of defects are commonly obtained from the thermal stability of defects by means of the isochronal and/or the isothermal annealing methods[1]. However, these methods need enormous time and labor for the measurement, which leads to small amount of data and low temperature resolution.

In our recent studies[2-4], we have used the constant heating method, by which the change in a property due to irradiation has been extracted from the difference in temperature dependence of the property between before and after irradiation. In the present work, we measured the defect recovery spectrum in aluminum irradiated with electrons by means of the constant heating method, and verified the usefulness of the method.

2. Experimental Procedure

An aluminum thin film of 200nm thick was deposited on an α-Al_2O_3 single crystal substrate by vacuum evaporation and then annealed at 500°C for ~30min in pressure below 7×10^{-7} Torr. The specimen was irradiated with 2.0MeV electrons below ~16K from a 3MV single-ended accelerator in TIARA, JAERI-Takasaki. The increase in electrical resistivity of the specimen due to irradiation was 5.26~5.42nΩcm, which corresponded to defect concentration of ~13ppm. After the irradiation, the electrical resistivity of the specimen was measured by means of the constant heating method, i.e. raising the temperature of the specimen at a constant heating rate. The difference in resistivity between before and after irradiation indicates the amount of residual irradiation-produced defects surviving thermal disturbance at the temperature. The experiments were performed with four kinds of the heating rates (0.7, 2, 4 and 8K/min).

3. Results and Discussion

Figure 1 shows the defect recovery behavior, i.e. the increase in electrical resistivity of the specimen, $\Delta\rho$, normalized by the initial increase, $\Delta\rho_0$, as a function of temperature for each heating rate. The resistivity decreases with increasing the specimen temperature because of the recombination of the irradiation-produced defects. The defect recovery spectra, i.e. the temperature derivatives of the curves in Fig. 1 are shown in Fig. 2. Two kinds of peaks, which corresponds to the recovery sub-stages I_B and I_{D+E}[1], are observed around 20~25K and 35~40K, respectively. As can be seen in Fig. 2, the peak temperature for each sub-stage shifts to the higher temperature as the heating rate becomes higher. In principle, the activation energy for migration of defects can be derived from the peak temperature shift[5,6]. In the present experiment, however, the activation energy could not been obtained precisely because of a slight shift of the peak temperature. For obtaining the activation energy precisely, it is necessary that the defect recovery behavior is measured at a slower heating rate (<0.7K/min).

References

1) W. Schilling, G. Burger, K. Isebeck, H. Wenzl, in: A. Seeger, D. Schumacher, W. Schilling, J. Diehl (Eds.), Vacancies and Interstitials in Metals, North-Holland, Amsterdam, 1969, p. 255.
2) A. Iwase, T. Iwata, Nucl. Instrum. Meth. **B90** (1994) 322, and references therein.
3) Y. Chimi, A. Iwase, N. Ishikawa, J. Nucl. Mater. **271&272** (1999) 236.
4) Y. Chimi, A. Iwase, N. Ishikawa, N. Kuroda, T. Kambara, Nucl. Instrum. Meth. **B164-165** (2000) 408.
5) A.C. Damask, G.J. Dienes, in: Point Defects in Metals, Gordon and Breach, New York, 1963.
6) T. Iwata, J. Nucl. Mater. **133&134** (1985) 361.

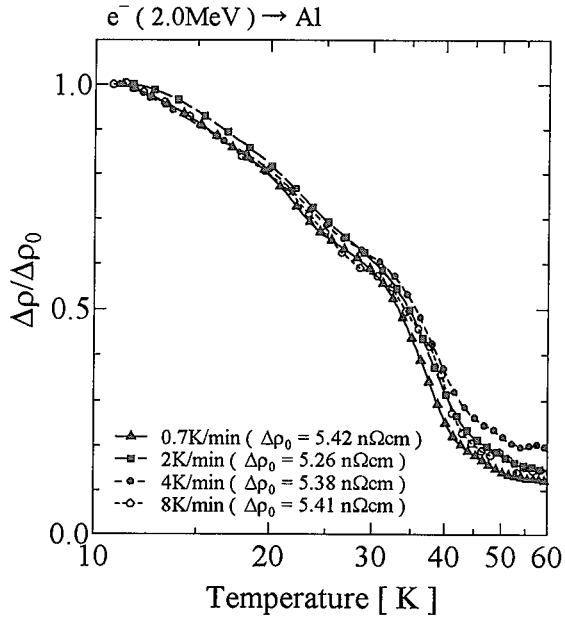


Fig. 1. Defect recovery behavior with four heating rates (0.7-8K/min).

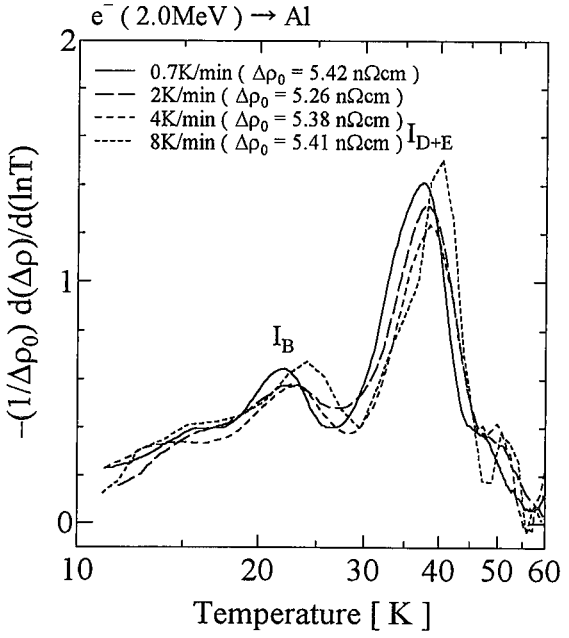


Fig. 2. Defect recovery spectra, which are temperature derivatives of the curves in Fig. 1, with four heating rates (0.7-8K/min).

4.17 Stability of dislocation loops in α-Al_2O_3 and $MgO{\bullet}nAl_2O_3$ crystals under displacive and ionizing radiation

Kazuhiro Yasuda[1], Chiken Kinoshita[1], Hiroaki Abe[2]

[1]Department of Applied Quantum Physics and Nuclear Engineering, Kyushu University, Hakozaki, Fukuoka 812-8581, Japan, [2]Department of Materials Development, JAERI, Watanuki, Takasaki 370-1292, Japan

1. Introduction

Stoichiometric magnesium aluminate spinel, $MgO{\bullet}Al_2O_3$, has been found to be sensitive to variations of displacive and nondisplacive irradiation spectra: the formation of dislocation loops is suppressed in $MgO{\bullet}Al_2O_3$ if high intensity of nondisplacive radiation is exposed with displacive radiation[1-3]. The mechanism of retardation of dislocation loop formation has not been clarified yet, but has been speculated to be due to ionization induced diffusion (IID) and radiation induced diffusion (RID)[1-3].

The retardation of loop formation has been also found in nonstoichiometric spinel, $MgO{\bullet}2.4Al_2O_3$, under concurrent irradiation with 300 keV O^+ ions and 200 keV electrons at 870 K[4]. However, the retardation effect was not appeared stronger than that observed in $MgO{\bullet}Al_2O_3$. In crystals of α-Al_2O_3, no significant retardation effect of loop formation is observed[4].

In the present paper, we shall discuss the reason for the different response in the formation process of dislocation loops among $MgO{\bullet}Al_2O_3$, $MgO{\bullet}2.4Al_2O_3$ and α-Al_2O_3 crystals. Special attention is paid on the stability of tiny dislocation loops under electron irradiation with energies from 100-200 keV, at which electron energy displacement damage is hardly expected in those crystals.

2. Experimental

Man-made single crystals of 'stoichiometric' $MgO{\bullet}Al_2O_3$ spinel with a (111) surface (Union Carbide), and 'nonstoichiometric' $MgO{\bullet}2.4Al_2O_3$ spinel with a (110) surface (Nakazumi Crystal) were used in the present study. Alpha alumina crystals, α-Al_2O_3 (Union Carbide), with a $(11\bar{2}0)$ surface were also used. These crystals were prepared to electron transparencies by ion-thinning with 6 keV Ar^+ ions. The ion-thinned specimens were subjected to in-situ observations under irradiation with a focused electron beam with energies from 100 to 200 keV. The stability of tiny dislocation loops, which were induced by ion-thinning process, was investigated under irradiation at 300 K with electron-flux ranging from of 0.5×10^{23} to 4.0×10^{23} e/m^2s. Temperature dependence of the stability of dislocation loops was also examined in α-Al_2O_3 under irradiation with 200 keV electrons at temperatures from 300 to 970 K.

3. Results and Discussion

Fig.1 shows the variation of the density of dislocation loops in $MgO{\bullet}2.4Al_2O_3$ and α-Al_2O_3, which were induced by 6 keV Ar^+ irradiation at 300 K, as a function of electron fluence under irradiation with 100, 150 and 200 keV electrons. Fig.1 also includes results obtained by Sato et al. on $MgO{\bullet}Al_2O_3$[5]. Dislocation loops in $MgO{\bullet}2.4Al_2O_3$ and α-Al_2O_3 are seen in fig.1 to be eliminated by electron irradiation at 300 K, as has been observed in $MgO{\bullet}Al_2O_3$[5]. It should also be noted here that the stability of dislocation loops is dependent of specimens: dislocation loops in $MgO{\bullet}Al_2O_3$ are less stable under electron irradiation than those in $MgO{\bullet}2.4Al_2O_3$ and α-Al_2O_3.

In order to quantify the elimination process of loops, a simple model is applied to the data in fig.1. Here an assumption is made that dislocation loops are eliminated through interactions with electrons in proportional to the density of loops (C_L), based on the results that the density of loops are likely decreased exponentially with electron fluence to

reach a saturation value at higher fluences. The differential equation of elimination process of dislocation loops is, therefore, given by

$$\frac{dC_L}{dt} = -\lambda\varphi C_L, \quad (1)$$

where φ is the electron flux, λ a constant and t irradiation time. The solution of eq. (1) is described as

$$C_L = C_L^0 \exp(-\lambda\varphi t), \quad (2)$$

where C_L^0 is the density of loops at t=0. Fig.2 summarizes the calculated values of λ for $MgO{\bullet}Al_2O_3$, $MgO{\bullet}2.4Al_2O_3$ and α-Al_2O_3 at 300 K as a function of electron energy. It is seen in fig.2 that the value of λ for $MgO{\bullet}2Al_2O_3$ ($52.9\times10^{-27}m^2$) at 200 keV electron irradiation is much higher than those for $MgO{\bullet}2.4Al_2O_3$ ($4.5\times10^{-27}m^2$) and Al_2O_3 ($13.0\times10^{-27}m^2$). Accordingly, from this results and the production rate of dislocation loops in $MgO{\bullet}Al_2O_3$, $MgO{\bullet}2.4Al_2O_3$ and α-Al_2O_3[6], the retardation of loop formation is understood to be most significant in $MgO{\bullet}Al_2O_3$, which possesses the lowest production rate and the lowest stability of dislocation loops. In contrast in α-Al_2O_3, no significant retardation effects are seen due to its high production rate and stability of loops under the irradiation condition. The retardation of loop nucleation in the crystals of MgO-Al_2O_3 system can be, therefore, explained as a competitive process of the production of dislocation loops under ion irradiation and the elimination of loops under electron irradiation.

The values of λ in fig.2 increase with decreasing electron-energy for all specimens investigated in the present study. This clearly indicates that the elimination of dislocation loops is not controlled by displacement process. Followings are considered as possible physical mechanisms for the elimination process of dislocation loops: (1) dislocation loops absorb structural and/or radiation-induced vacancies through the ionization induced diffusion (IID), (2) same mechanism as for (1) but through the radiation induced diffusion (RID) by receiving subthreshold nuclear energy, and (3) ionizing radiation makes dislocation loops unstable to dissociate into freely migrating interstitials. To test the above speculations, the temperature-dependence of the elimination process of dislocation loops was examined in α-Al_2O_3 under irradiation with 200 keV electrons, and the values obtained for λ are shown in fig.3. It can be seen in fig.3 that λ decreases with increasing irradiation temperature and reaches saturation value ($\sim4\times10^{-27}$ m^2) at temperatures higher than 650 K. The stability of loops is, therefore, understood to decrease with decreasing temperature under 200 keV electron irradiation.

If we suppose that the activation energy for vacancy diffusion is low enough to migrate to dislocation loops through the diffusion processes of IID and/or RID, the stability of the loops should decrease with increasing temperature because of their thermally activated process. The temperature-dependence of λ in fig.3 is, however, completely contrary to the above arguments, suggesting that the mechanisms (1) and (2) are not. The mechanism (3), on the other hand, involves the generation of free interstitials through the dissociation of loops, which recombine with vacancies (either structural or radiation induced vacancies) and/or to reach other dislocation loops. A portion of interstitials is, therefore, expected in this mechanism to contribute to the growth of dislocation loops. This idea leads to the increase in the stability of loop at higher temperatures where interstitials have enough mobility, and does not contradict the temperature-dependence shown in fig.3. Ionizing radiation of electrons is expected to contribute the increase in mobility of interstitials[1]. It is, therefore, concluded that the mechanism (3) is the most probable to explain the experimental results obtained in this study. Furthermore, a flow of interstitials to contribute to the increased growth rate of loops[7] can be explained only through the mechanisms (3) but not through the mechanism (1) and (2).

4. Conclusions

Tiny dislocation loops have been found to be unstable under low energy electron-irradiation in crystals of $MgO{\bullet}Al_2O_3$, $MgO{\bullet}2.4Al_2O_3$ and α-Al_2O_3. The stability of loops is higher in the order of $MgO{\bullet}2.4Al_2O_3$, α-Al_2O_3 and $MgO{\bullet}Al_2O_3$. This explains qualitatively the different response of the

retardation of loop formation, as a competitive process between loop formation under ion-irradiation and loop elimination under electron-irradiation. The most probable physical mechanism for the elimination process of dislocation loops is the dissociation of loops into free interstitials through the ionizing radiation.

References

[1] S.J. Zinkle, J. Nucl. Mater. 219 (1995) 113.

[2] K. Yasuda, R. Morisaki, C. Kinoshita, H. Abe and H. Naramoto, Proc. of 7th Int. Symp. on Advanced Nuclear Energy Research (Takasaki, Japan) (1997) 384.

[3] K. Yasuda, C. Kinoshita, R. Morisaki and H. Abe, Philos. Mag. A78 (1998) 583.

[4] K. Yasuda, C. Kinoshita, M. Ohmura and H. Abe, Nucl. Instr.and Meth. B166-167 (2000) 107.

[5] Y. Sato, C. Kinoshita and K. Nakai, JJAP series 2 Lattice Defects in Ceramics (1989) 105.

[6] The formation rate of dislocation loops is much higher in α-Al_2O_3 than that in $MgO{\bullet}Al_2O_3$ and $MgO{\bullet}2.4Al_2O_3$ under 300 keV O^+ ion irradiation at 870 K. The data for the accumulation process of loops can be seen in ref. [4].

[7] It has been found that larger dislocation loops are formed at the periphery of the focused electron beam under concurrent irradiation with ions and electrons. This suggests migration of interstitials from the center to the outside of the electron beam. The detail discussion can be seen in ref. [3] and [4].

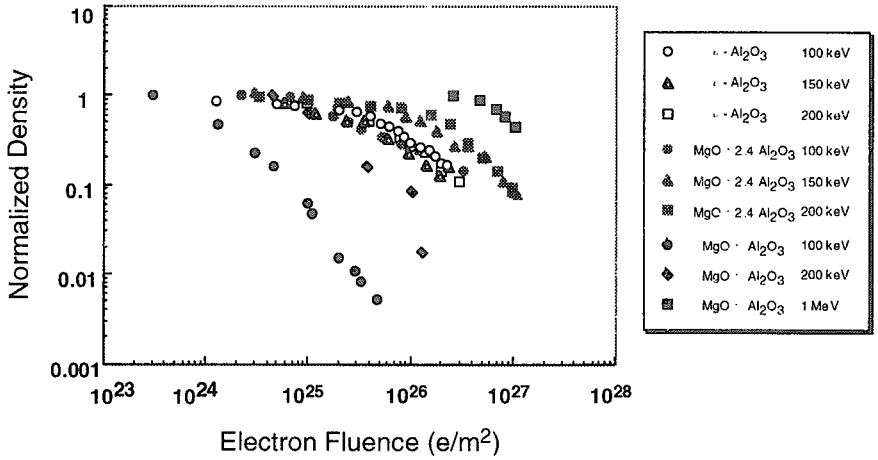


Fig. 1 Normalized density of dislocation loops in $MgO{\bullet}Al_2O_3$, $MgO{\bullet}2.4Al_2O_3$ and α-Al_2O_3 under irradiation with 100 to 1000 keV electrons at 300 K.

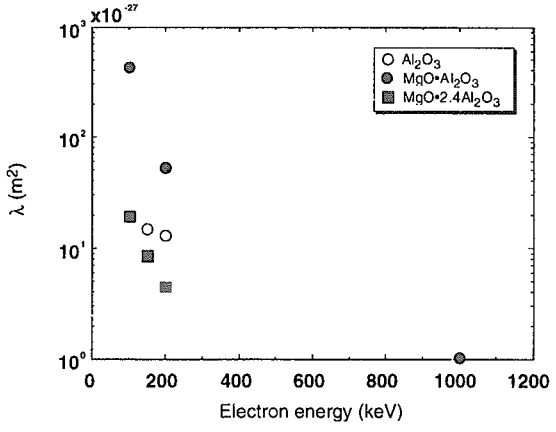


Fig.2 Variation of λ with electron energy at 300 K in $MgO{\bullet}Al_2O_3$, $MgO{\bullet}2.4Al_2O_3$ and α-Al_2O_3.

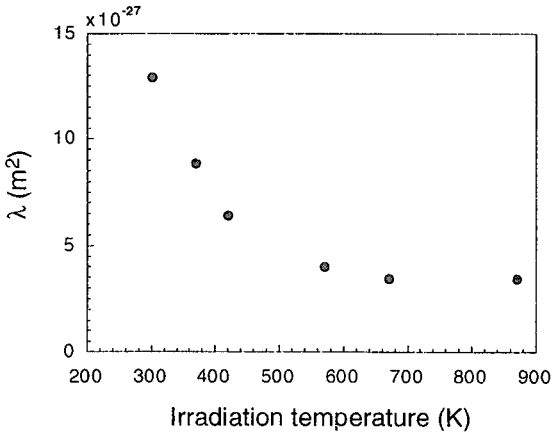


Fig. 3 Variation of λ with irradiation temperature in α-Al_2O_3 under irradiation with 200 keV electrons.

4.18 Carrier Control of β-$FeSi_2$ by 1.2 MeV-Au^{++} Ion Implantation

Y. Maeda, K. Umezawa, T. Ito, S. Yamamoto*, I. Nashiyama*
Department of Materials Sciences, Osaka Prefecture University
*Department of Materials Development, JAERI

1. Introduction

Semiconducting orthorhombic β-$FeSi_2$ consists of non-toxic and abundant elements, and is one of candidates which are adopted to ecologically friendly semiconductors (*i.e.* Kankyo semi-conductors) [1]. It has so large absorption nature that its application to high sensitive infrared photodetector or high efficiency solar cells is expected [2,3]. However, there is an important problem about carrier control of β-$FeSi_2$. In many cases of the ion-beam synthesis [4], *p-type* β-$FeSi_2$ was obtained and its carrier concentration was over 10^{19} cm^{-3}. It has been thought that this large carrier concentration comes from an iron vacancy in the lattice and the conduction type may be determined by compensation between some defects, but the detail mechanism of carrier generation has not yet made clear.

In this study, we investigated relationship between carrier generation and vacancies induced by high energy heavy ion implantation to find a dominant physical process for the carrier control.

2. Experiments

Two samples (Nos. 1 and 2) was prepared by an ion implantation of $^{56}Fe^{+}$ into ~500 μm thick FZ n-Si(001) with 2-8 Ωcm. The multiple ion implantation [4] was carried out at the energies of 100, 80 and 50 or 30 keV in this sequence. Its total dose was 1.5-2.0x10^{17} cm^{-2}. To form polycrystalline β-$FeSi_2$, before Au^{++} ion implantation the sample No.1 was annealed at 800 ℃ for 6 h in an Ar gas ambient in a rapid thermal anneal (RTA) furnace. Then both the samples No. 1 (annealed) and No. 2 (as-implanted) were implanted by 1.2 MeV-Au^{++} ions (dose: 8x10^{15} cm^{-2}), then annealed at 800 ℃ for 2h in an Ar gas ambient in a RTA furnace. The depth-profiles of Au and Fe were measured by Rutherford backscattering spectroscopy (RBS). The electrical resistivity and Hall measurements of the samples were carried out by a Van der Pauw four probes method at room temperature.

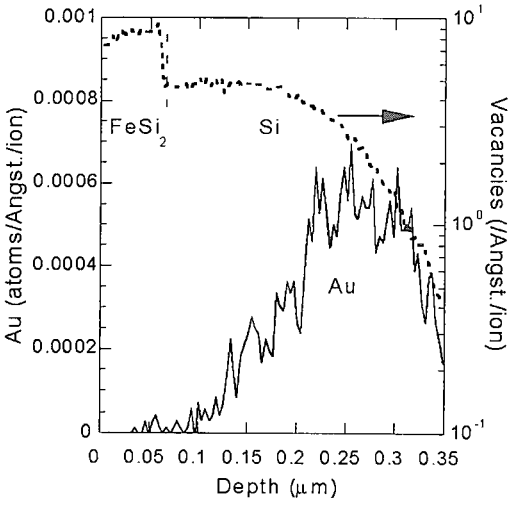


Fig.1 TRIM simulation of 1.2 Mev Au^{++} ion implantation into β-$FeSi_2$/Si layers.

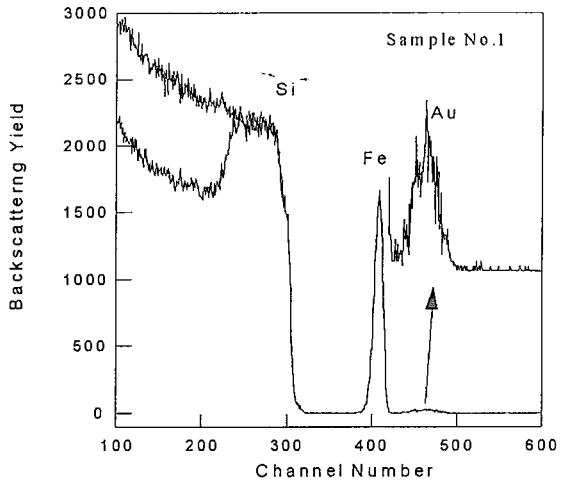
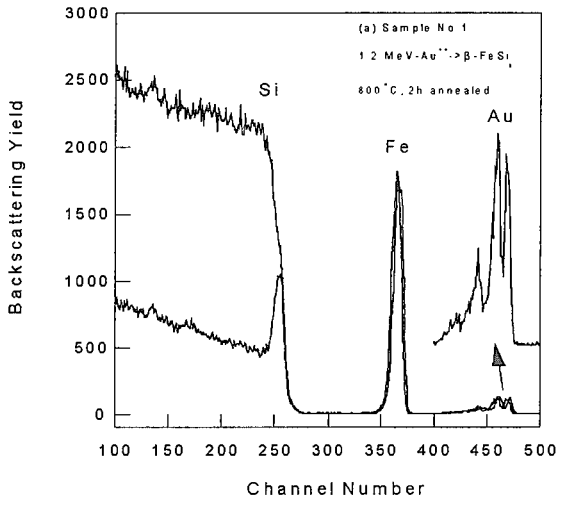


Fig.2 RBS spectra of the sample No.1 after Au^{++} ion implantation.



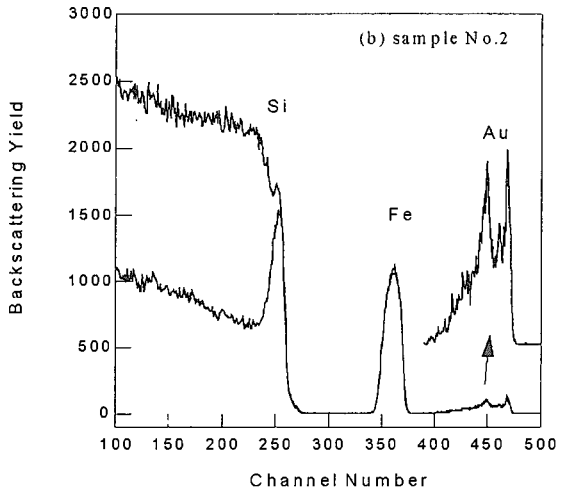


Fig.3 RBS spectra of the sample (a) No.1 and (b) No.2 after annealing at 800 °C for 2h.

3. Results and Discussion

Figure 1 shows a result of 1.2 MeV Au^{++} ion implantation obtained from a simulation of TRIM code about distributions of Au and total vacancies by ions and recoils. It shows that we can induce the uniform distribution of vacancies into the β-$FeSi_2$ layer (thickness:0.06 μm) and that Au atoms are mostly implanted not into β-$FeSi_2$ but into Si.

Figure 2 shows 2MeV $^4He^+$ RBS random and aligned spectra of the samples No.1 after Au^{++} ion implantation (before annealing). Before annealing, Au^{++} ion implanted β-$FeSi_2$ showed a completely random states. The χ_{min} of Si showed 73% which is much larger than that of 39 % in the initial Fe^+ ion implantation. The distribution of Au atoms showed mostly a simple Gaussian profile. Also in the sample No. 2, we observed the same features.

Figure 3 shows RBS spectra of the samples (a) No.1 and (b) No. 2 after annealing. In both samples, the redistribution of Au atoms showed the Ostwald ripening phenomenon (separation of profiles) from the simple Gaussian distribution at as-implanted states. In the No. 1 sample, it showed no change in the initial Fe distribution and concentration. The χ_{min} of Si decreased from 31.2% for the initial state to 21.3 % for Au^{++} ion implanted and annealed state. This shows that re-crystallization of implanted Si may be enhanced by vacancy introduction due to Au^{++} ion implantation.

On the other hand, in the sample No. 2, it showed broadening of the Fe distribution due to the Fe atom diffusion into Si, so that the Fe

concentration decreased significantly. The χ_{min} of Si was 31.2%, which was as same as the initial value (31%). In this case, it was observed that both Fe and Au diffusion was enhanced by induced vacancies. These different behaviors observed in the samples Nos. 1 and 2 may come from differences in their initial states. The initial state of the sample No.1 was β-$FeSi_2$ fully formed on Si, and that of the sample No.2 was Fe as-implanted Si without crystalline formation of β-$FeSi_2$. The Au^{++} ion implantation probably achieved enough amorphization of β-$FeSi_2$ (*amorphous* β-$FeSi_2$) as shown in Fig.1 in the sample No. 1, and increase in vacancies embedded in Fe implanted region and Si bulk in the sample No. 2. Therefore, crystallization of amorphous β-$FeSi_2$ is considered to be a dominant process without necessary of long distance atomic diffusion in the sample No. 1 during annealing. In the sample No. 2, nucleation and growth of β-$FeSi_2$ which need atomic diffusion enhanced by excess vacancies due to Au^{++} ion implantation (vacancy enhanced diffusion) is a dominant process, which is not different from the situation of usual Fe implanted samples. This enhanced diffusion of Fe can be seen in Fig.2(b). We measured electrical properties of these samples to determined their carrier concentration (N/cm^{-3}), conduction type and Hall mobility (cm^2/Vs). The as-implanted samples after Au^{++} ion implantation showed very high resistivity even at room temperature (294 K) because of their very random features, so we could not determined the accurate electrical properties using a conventional Hall measurement instrument.

The ion-beam synthesized β-$FeSi_2$ (the initial sample) showed *p-type* conduction with the hole mobility of 410 cm^2/Vs and the concentration of $1.02x10^{19}$ cm^{-3} at room temperature. The sample No. 1 showed change of the conduction from *p-type* to *n-type*. The Hall mobility of electrons was 202 cm^2/Vs, and the concentration was $5.1x10^{18}$ cm^{-3}. The sample No. 2 showed still p-type conduction, however, its Hall mobility of holes decreased and was 180 cm^2/Vs. The concentration increased and was $5.12x10^{19}$ cm^{-3}. The behavior observed in the sample No. 2 can be understood by taking the decrease of Fe concentration due to its enhanced diffusion into account. Deficiency of Fe makes vacancies in the lattice, so that vacancy-related holes increased. The decrease of the mobility may come from generation of some deep level traps or discontinuous morphology (precipitates). The reverse of conduction type observed in the sample No. 1 is cause by compensation of holes due to Fe vacancies and electrons probably due to Si vacancies highly induced by Au^{++} ion implantation into β-$FeSi_2$ lattice or due to donor levels made by implanted Au in β-$FeSi_2$.

We need further study about compensation mechanism of carriers of β-$FeSi_2$ by Au^{++} ion implantation in connection with roles of vacancies for carrier generation.

References

1) K. Miyake et al., Rev. Laser Eng. **28** (2000) 3.
2) H. Lange, Phys. Stat. Sol. (b)**201**(1997)3.
3) Y. Maeda et al., Rev. Laser Eng. **28** (2000) 93.
4) Y. Maeda et al., MRS Proc. **486** (1998) 329.

4.19 Formation process and stability of radiation-induced non-equilibrium phase in silicon

S. Ohnuki, S. Watanabe, T. Suda, M. Takeda, F. Arimoto,
S. Suzuki, H. Abe*
Department of Material Science, Hokkaido University, *Department of Material Development, JAERI

1. Introduction

It had been known silicon is easily transformed to amorphous phase during ion irradiation. In particularly polycrystalline silicon, the preferential amorphization (PA) on grain boundary (GB) takes place with 1.5 MeV Xe^+ irradiation at temperature range from 423 to 493 K[1]. This phenomenon could be considered as a thermodynamical process, because PA on GB depended on grain energy[2]. However, the mechanism of PA still remains not very well understood.

To obtain detail information on PA phenomenon, the in-situ observation under ion beam irradiation had been carried out[3]. In this study, we focused on effects of ion mass and the accelerating energy on PA. Especially, the critical fluence for amorphization, the crystallization temperature and the onset temperature of PA were investigated.

2. Experiment

Specimen was polycrystalline silicon about 200nm in thickness deposited on the oxide silicon by LPCVD method. Poly-Si was annealed at 1223K for 4 hours in Ar atmosphere. To obtain TEM observation specimen, the oxide silicon was resolved by HF solution after the annealing.

In-situ TEM observation was performed at IX irradiation port by using C^+, N^+ and Ar^+ of 100 – 300 keV, where the ion flux was 3.0 – 4.0 x 10^{17} /m^2s. The irradiation temperature ranged from 104 to 673 K.

The critical fluence was determined from the changing of selected area electron diffraction (SAED) pattern was used. SAED pattern of polycrystalline presented clearly diffraction spots, whereas SAED pattern of amorphous phase revealed halo ring. In this study, Ion irradiation was done until completely changing to amorphous phase.

For measuring the crystallization temperature, the preferential amorphous phase was firstly induced by irradiation at PA temperature. After the preferential amorphous phase introduction, ion irradiation was performed above higher than PA temperature. The crystallization temperature was decided by measuring c-a interface displacement rate, because c-a interface dose not move at the crystallization temperature. The onset temperature of PA was decided by in-situ TEM observation.

3. Results and Discussion

The critical fluence for the amorphization: Figure 1 shows the temperature dependence of the critical fluence at different irradiation conditions. The critical fluence was exponentially increased with increasing temperature. With increasing ion mass and decreasing the accelerating energy, the critical fluence became low fluence side, whereas the cutoff temperature became high temperature side.

The crystallization temperature: Figure 2 shows the relationship of the irradiation

temperature and the c-a interface displacement rate. The crystallization temperature was the cross point between the data line and the transverse axis. Table 1 shows the crystallization temperature at difference irradiation condition. With increasing ion mass and decreasing the accelerating energy, the crystallization temperature became high temperature.

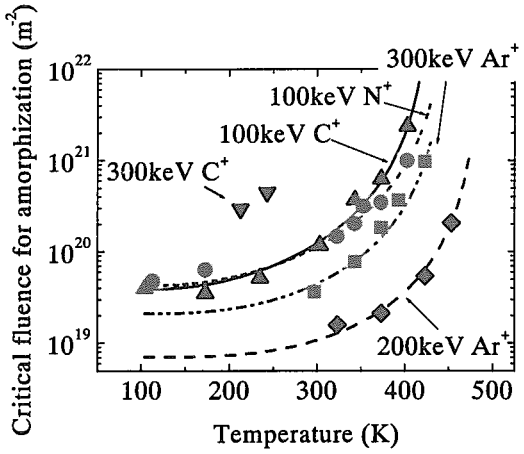


Figure 1 Temperature dependence the critical fluence for amorphization

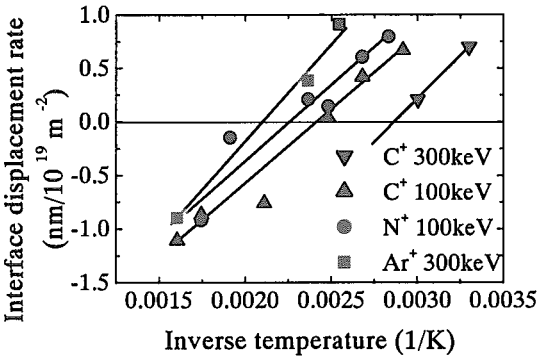


Figure 2 Relationship of the irradiation temperature and the c-a interface displacement rate. In vertical axis, positive and negative values mean amorphization and crystallization, respectively.

The onset temperature of PA: Figure 3 shows the structure of polycrystalline silicon above/below the temperature of PA during 300 keV C^+, 100 keV C^+ and 300 keV Ar^+ irradiation. The onset temperature became low temperature with increasing ion mass and the accelerating energy. Table 2 shows the onset temperature of PA at difference irradiation condition. The onset temperature also became the same results in difference irradiation condition.

Table 1 The crystallization temperature.

Ion/energy	Crystallization temperature, K
C^+ 300keV	350
C^+ 100keV	416
N^+ 100keV	444
Ar^+ 300keV	475
Ar^+ 200keV	–

Table 2 The minimum temperature for the onset of preferential amorphization on GB.

Ion/energy	Temperature, K
C^+ 300keV	243 – 300
C^+ 100keV	300 – 333
N^+ 100keV	300 – 333
Ar^+ 300keV	343– 373
Ar^+ 200keV	373 – 403

It is expected that these results will be corresponding to the magnitude of damage given from the irradiated ion. Accordingly, to estimate the energy used for damage formation, TRIM code calculation was performed. In the calculation, the displacement energy and lattice bonding energy were 16 eV and 2 eV, respectively. As a result, the energy used for damage formation within specimen thickness (200nm) increased as follows; 300 keV C^+ < 100 keV C^+ < 100 keV N^+ < 300 keV Ar^+ < 200

keV Ar^+. Assuming that the amount of introduced damage is in proportion to deposited energy from irradiated ion, it could be considered that the temperature for recovering damages become higher and the fluence for amorphization become lower.

4. Conclusion

With increasing ion mass and decreasing the accelerating energy, the critical fluence was decreased, and the temperature for crystallization PA was increased. These results have the equivalent tendency in the energy for the damege formation calculated by TRIM code within specimen thickness (200nm). It is confirmed that these phenomena are controlled by the balance between the energy deposition and recovery of defects, which are depended on ion-energy and temperature.

Reference

1) H. A. Atwater, et al., Appl. Phys. Lett., 56, 1990, 30-32
2) H. A. Atwater et al., Nucl. Instr. Meth. and Phis. Rev., B59/60, 1991, 386-390
3) M. Takeda et al., Mat. Res. Soc. Symp. Vol. 540, (1999) 37-41

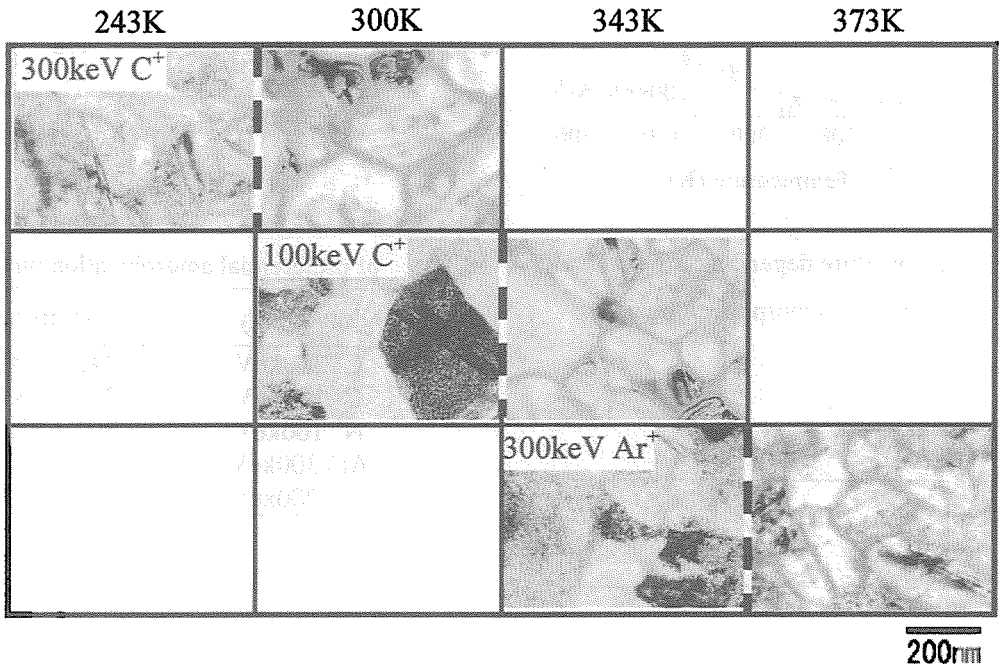


Figure 3 The structure of polycrystalline silicon above/below the temperature of preferential amorphization during 300 keV C^+, 100 keV C^+ and 300 keV Ar^+ irradiation. Above the temperature indicated at dash line, preferential amorphization occurs.

4.20 Ion Irradiation Effect on Carbon-related Thin Films

H. Naramoto, J. Vacik, S. Yamamoto*, K. Narumi, Y. Xu#
Advanced Science Research Center, JAERI
*Dept. of Materials Develop., JAERI/Takasaki

1. Introduction

The limited nature of mass-transport in the ion beam processing of materials guides us naturally into the interests in super-saturated systems[1] such as mixed one between immiscible substances (C_{60} and Ni). In such systems there might appear unexpected new phases based on the self-organization through the energy dissipation process[2]. Ion irradiation can convert C_{60} molecules at the specified position into different carbon allotropes in a controlled manner. Thus, the self-organization process can be complemented by ion irradiation so as to design the intended microstructure.

In this report are illustrated the irradiation effects of energetic heavy ions on the thermal diffusion behavior in a C_{60} sandwiched sample (Ni-poly./C_{60}(111)/ Ni(100) /MgO(100)).

2. Experimental

The epitaxially layered structure was prepared by changing the deposition temperatures with two different evaporation techniques. In Ni-poly./ C_{60}(111)/Ni(100)/MgO(100) sample, the first Ni(100) layer was deposited at 773K with electron bombardment heating, followed by the C_{60}(111) layer deposition at 393K with electrical heating. The top Ni layer was deposited at 393K not to deteriorate the C_{60} layer. The completely mixed layer between Ni and C_{60} was formed on MgO directly by simultaneous deposition of the relevant two substances.

The structural analysis before and after 7MeV $^{12}C^{2+}$ irradiation was performed with 2MeV $^{4}He^{+}$ RBS and X-ray diffraction. The topological changes were examined with a scanning electron microscope operated at 1keV not to destroy C_{60} molecules.

3. Results

<Pristine samples>: The C_{60} layer on Ni(100) shows the <111> oriented nature, and is kept to be crystalline up to 723K under Ar+3%H_2 reducing environment. In the temperature region between 723K and 923K the crystalline C_{60} layer was decomposed into C_{60} molecules and the transfer of C_{60} molecules through the top polycrystalline Ni layer was detected. After annealing at 923K, the original C_{60} layer changed into amorphous carbon phase. The annealing at 1073K relaxed the strains in Ni(100) layer, and the further annealing at 1173K resulted in Ni-based new phase with the co-existence of pure Ni phase.

<Irradiated sample>: The sandwiched sample was irradiated with 7MeV $^{12}C^{2+}$ ions at RT up to 1×10^{16} /cm^2, and was analyzed with X-ray diffraction and Rutherford backscattering techniques.

Fig. 1 compares the X-ray diffraction patterns from Ni-poly./C_{60}(111)/Ni(100)/ MgO(100) layered sample before and

after 7MeV $^{12}C^{2+}$ irradiation. One can see the considerable deterioration of crystalline C_{60} and Ni layers after the irradiation. The change of crystalline C_{60} layer can be inferred easily but not for the Ni layer. In another series of irradiation experiments, it was observed that the crystal quality was improved in the same kind of irradiation into Ni(100)/MgO(100) without C_{60} layer. Thus, the present result can be explained by taking into the forward injection of decomposed C_{60} molecules or carbon atoms into the epitaxial Ni layer.

Fig. 2 illustrates 2MeV $^{4}He^{+}$ Rutherford-backscattering (RBS) spectra from the same kind of layered sample. The sample was irradiated under the same condition as in Fig. 1, and annealed at 773K under flowing Ar+3%H2 mixture gas. In RBS spectrum from pristine and as-irradiated areas it is difficult to find out any difference in the carbon-contributed spectral region, probably because of the limited mass-resolution in RBS analysis. But after annealing at 773K, the big difference can be seen even in RBS spectra. In the spectrum from annealed pristine sample, the loss of carbon atoms can be identified clearly as the shift of bottom Ni layer into higher energy region around 400 Channels. But in the case of irradiated/annealed sample, any change can not be detected. The immobilization of carbon atoms(RBS analysis gives us the information with the atomic unit) after the ion irradiation can be attributed to the amorphous carbon phase and/or carbon-compound formation through the C_{60} molecules decomposition into carbon atoms by the intense electronic excitation when 7MeV $^{12}C^{2+}$ ion irradiation. The loss of carbon atoms in the pristine sample is also interesting because the loss of carbon atoms coincides with the appearance of C_{60} molecules on the top surface of Ni-poly./C_{60}(111)/Ni(100)/MgO(100) as assured with Raman measurement. At this stage of research it is difficult to remove a possibility that elastically flexible C_{60} molecules can diffuse along the grain boundary with big distortion but it seems more reasonable to consider the direct evaporation of C_{60} molecules through meso-pores formed in Ni-polycrystalline layer after annealing at 773K.

In the remaining part, the ion irradiation effect on C_{60}/Si is described without figure illustration. The analysis of bonding nature was made using a Raman spectroscopy. The C_{60} layer on Si substrate is rather homogeneous, and the details of vibrational features were recognized. After the irradiation with 360keV $^{40}Ar^{4+}$ ions up to 1×10^{14} Ar/cm^2, the film was changed into graphite-like structure with D and G-peaks in Raman spectrum. Further irradiation up to 1×10^{15} Ar/cm^2 converted the graphitic layer into amorphous carbon films.

References

1) H. Naramoto, S. Yamamoto and K. Narumi, Nucl. Instr. and Meth. B161-163 (2000) 534-538.
2) J. Vacik, S. Yamamoto, H. Naramoto, and K. Narumi, K. Miyashita, The 18th Fullerene General Sym.(Okazaki, Jan. 13-14, 2000).

On leave from Japan Science and Technology Corporation as a Domestic Research Fellow

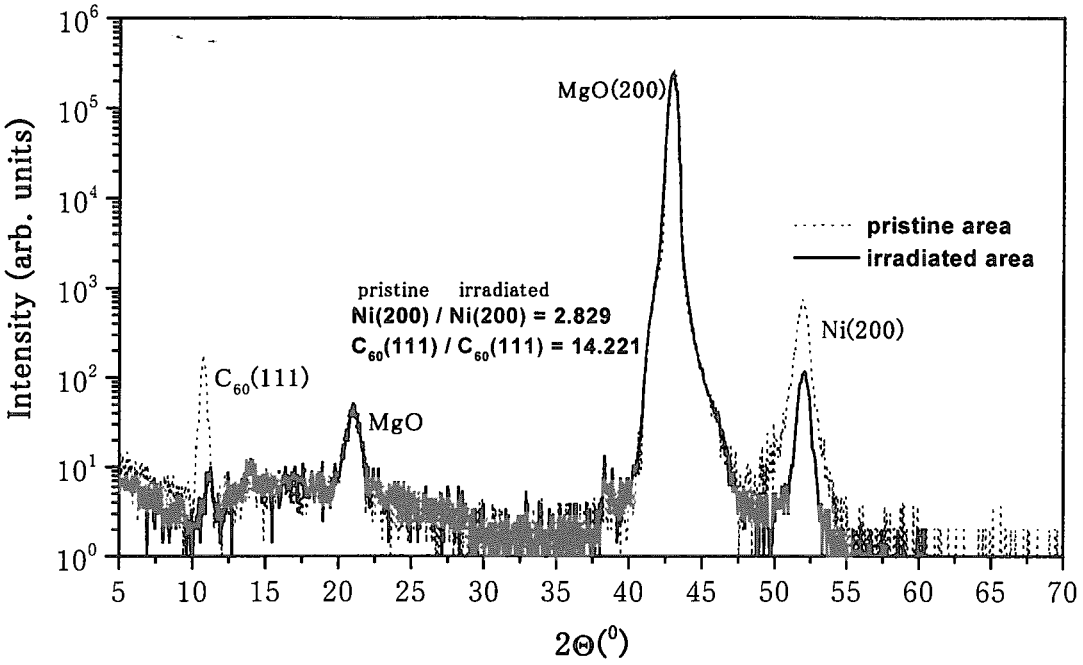


Fig. 1: X-ray diffraction pattern from Ni-poly/C_{60}(111)/ Ni(100)/ MgO(100) sample. The curve with a solid line corresponds to the irradiated area (7MeV $^{12}C^{2+}$, 1×10^{16} C/cm^2). The diffraction intensity for Ni and C_{60} is compared in pristine and irradiated samples at the center.

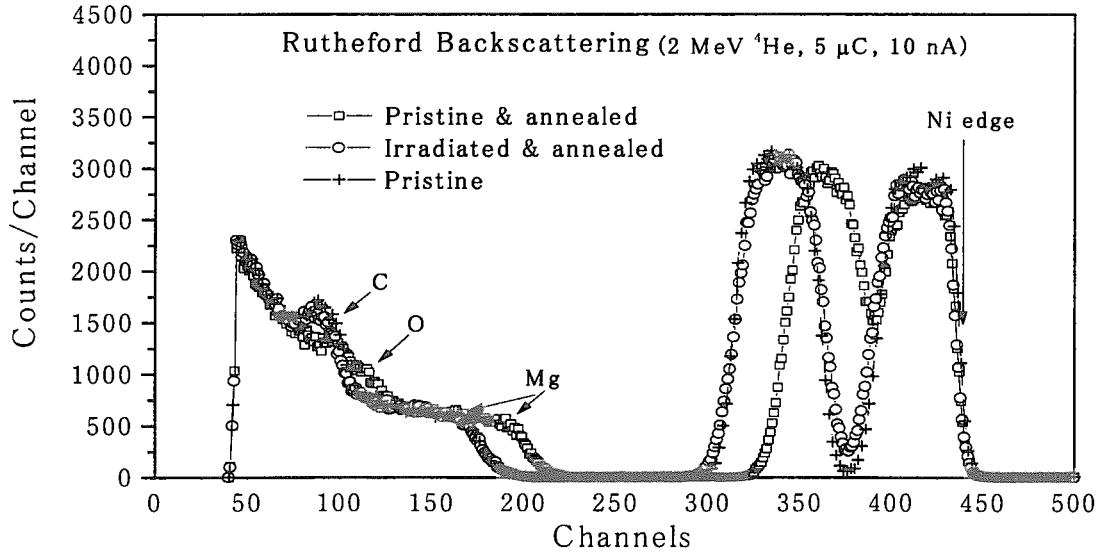


Fig. 2: 2MeV $^4He^+$ RBS spectra from the same sample in Fig. 2. The data with "+", "□" and "○" are from "pristine region before annealing", "pristine region after annealing" and "irradiated region after annealing", respectively.

4.21 Non-Equilibrium Growth of Ni+C_{60} on MgO(100)

J. Vacik[1,3], H. Naramoto[1], S. Yamamoto[2], K. Narumi[1]
[1]Advanced Science Research Center JAERI; [2]Department of Materials Development JAERI; [3]Nuclear Physics Institute, 250 68 Rez, Czech Republic

1. Introduction

Self-organization is a phenomenon often observed in nature. It appertains to various mono- and multi-component materials and sets in a broad range of spatio-temporal scales [see e.g. 1, 2]. It has been acknowledged that a simple universal insight, which would allow us to deduce the underlying physics of pattern-forming processes, does not exist. Nevertheless, many self-organized systems have similar structural features and evolution mechanisms and by understanding one, the other can be better comprehended.

Here we report on a new example of the self-organization observed in a thin film of the Ni+C_{60} co-mixture. The mesoscopic system of stripes, which was formed in the Ni+C_{60} system, draws attention to the unusual properties of the C_{60} - transitional metal intermixing.

2. Experimental

The Ni+C_{60} film was prepared by simultaneous Ni and C_{60} evaporation, using electron beam bombardment of the 99.99% pure Ni casters and resistive filament heating of the 99.9% pure C_{60} powder. The deposition rates of Ni and C_{60} were about 5 nm/min, the total thickness of the deposit (measured by the quartz microbalance placed in the vicinity of the sample) was about 300 nm. The co-deposition was performed under standard high vacuum conditions with the background pressure of about $5x10^{-7}$ Torr. The temperature of the substrate was kept at 500^0C during the deposition process; the cooling (uncontrolled) of the sample to RT set in immediately after deposition.

The final Ni+C_{60} film was analyzed by several techniques, e.g. by the laser scanning and Raman microscopes, X-ray diffraction and micro-Auger spectroscopy.

3. Results and discussion

In Fig. 1, a part of the periodic self-assembly of the Ni+C_{60} deposit is shown. It represents an array of tens of distinct stripe

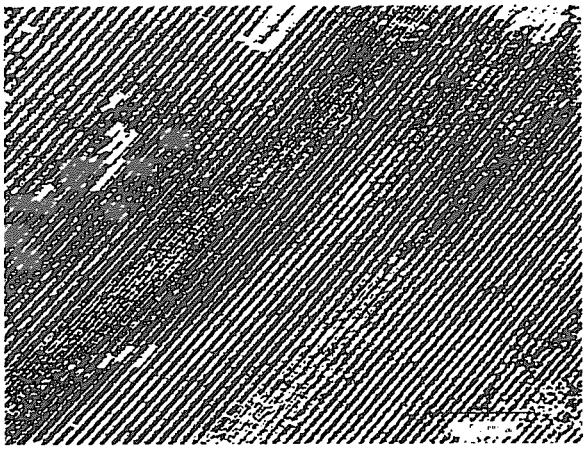


Fig. 1 Mesoscopic system of self-organized stripes evolved in the Ni+C_{60} co-mixture.

domains, several hundred of μm long, with a thickness and width of about 1 μm and spacing 1.5 μm. The analysis of the stripe system showed that each individual domain

consists of a dense pack of linearly arrayed 100-300 nm large Ni droplets, which are encapsulated in a thin layer of polymerized C_{60} molecules. The stripe domains are anchored in a thin common platform comprising a buffer Ni layer, epitaxialy grown on the MgO substrate, and an upper amorphous C (a-C) film. In Fig. 2, a structure of the stripe system, as it resulted from the thorough analysis, is demonstrated.

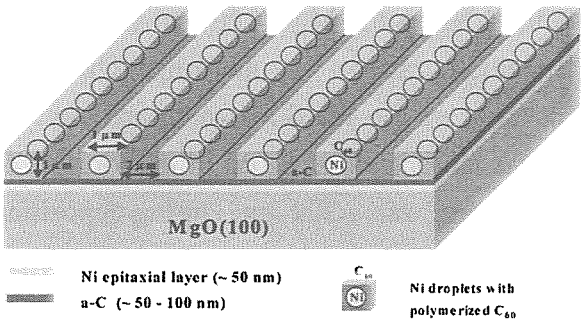


Fig. 2 Structure of the stripe system.

The observed phenomenon of the Ni+C_{60} self-organization provokes questions about the pattern formation mechanism. It has been found that in the Ni+C_{60} mixtures deposited at elevated temperatures, the C_{60} molecules tend to disintegrate and their fragments partly transform towards a-C structures. Due to the immiscibility of the C and Ni substances the growing amount of the a-C incites a thermodynamic instability (stress) in the system, which might result in a partitioning of the film. The immiscibility might be then viewed as a driving force of the Ni+C_{60} self-structuring. The mechanism of the stripes formation might be following: in the first period of the co-deposition Ni atoms nucleate on the MgO substrate and form a thin epitaxial layer. This process proceeds in the presence of fullerenes, however affects their integrity, i.e. the C_{60} molecules disintegrate and transform to a-C. The C_{60} disintegration continues till the a-C film is fully continual and forms a filter, which restrains further growth of epitaxial Ni buffer layer. In the following deposition stage an amorphous mixture of Ni and C_{60} is grown on the Ni/a-C platform, C_{60} partly disintegrates and Ni particles coalesce in to larger clusters. The third phase of the pattern formation might resemble the spinodal decomposition: in a certain place of the Ni+C_{60}/a-C co-mixture with a large thermodynamic instability the first domain is formed. It consists of the Ni and a-C components segregated due to their immiscibility. The birth of the two-sector Ni/a-C domain immediately generates a surplus of instability in the contiguous region (due to the sudden a-C concentration increase), which leads to the stress relaxation and creation of the second stripe domain. The next steps then follow the same algorithm. This progressive stress drift-and-release scenario is supposed to be a basic mechanism, which could lead to the observed periodic system of the stripe domains.

References

[1] P. Ball, *The Self-Made Tapestry,* Oxford University Press, New York, 1999

[2] P. Coveney and R. Highfield, *Frontiers of Complexity, Faber and Faber*, London, 1995

4.22 Epitaxial re-crystallization of the Ni/MgO(100) interface

J. Vacik[1,3], S. Yamamoto[2], H. Naramoto[1], K. Narumi[1]
[1]Advanced Science Research Center JAERI; [2]Department of Materials Development JAERI; [3]Nuclear Physics Institute, 250 68 Rez, Czech Republic

1. Introduction

Metal/ceramic [1] and particularly metal/oxide [2] thin film systems exhibit specific properties (e.g. magnetic, catalytic and tribological), which have received growing attention in various fields of industry (e.g. in microelectronics, surface engineering and advanced heterogenous catalysis). Despite the technological importance, however, the basic mechanisms, which govern the formation and eventually post-deposition re-structuring of the metal/oxide interfaces have not been fully understood. The fact that large changes in macroscopic properties are induced by relatively subtle alterations in microstructure stimulates the need to analyze the growth and structural evolution of the thin film systems with a broad scope of approaches.

The thin film growth techniques produce films with many defects, which can affect the physical properties of the materials. Since qualities of the systems take advantage from their clear crystallographic relations, much effort is devoted to preparation of the epitaxially grown defect-free systems. One of the suitable techniques used to improve crystalline quality of the thin films is thermal annealing. In this study, we applied thermal treatment to induce re-crystallization of the thin Ni films deposited on the MgO(100) substrates and to find the optimal conditions for preparation of the high quality single crystalline Ni films.

2. Experimental

A set of the Ni/MgO(100) systems were prepared by the vapor deposition of the 99.99% Ni on the MgO(100) substrate at the deposition rate ~ 5 nm/min. The total thickness of the Ni films (measured by the quartz microbalance placed in the vicinity of the sample) was ~ 300 nm. During deposition the substrates were kept at the temperature 500^0C. The background pressure in the vacuum chamber before and after deposition was ~ $5x10^{-7}$ Torr. The final Ni/MgO(100) systems were annealed in the Ar (+3% H_2) flow atmosphere between 500 and 1000^0C and systematically (after each 100^0C/1hr step) analyzed by Rutherford backscattering (RBS), X-ray diffraction (XRD) and atomic force microscopy (AFM).

3. Results and Discussion

As followed from the 2Θ-Θ scan and texture analysis, the Ni films were growing on the MgO(100) substrate epitaxially in a cube-on-cube texturing with the crystallographic relations MgO(100)||Ni(100) and MgO[100]||Ni[100]. Large lattice misfit (~ 16%) however induced in the Ni deposits considerable strain (which rapidly decayed away from the interface) and various

structural defects (e.g. interface dislocations). To reduce the inhomogeneities in the Ni films the systems were thermally annealed. The effect of the treatment is documented in Fig. 1, where series of the RBS spectra

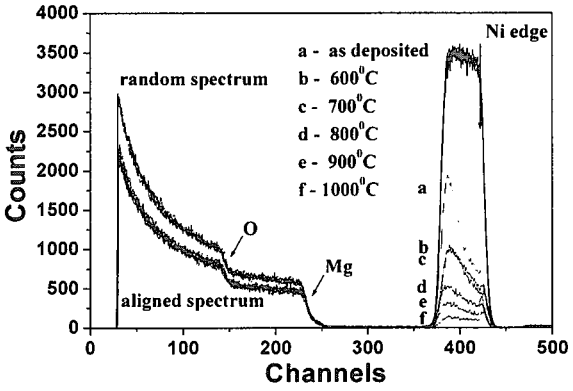


Fig. 1

(random and aligned) of the annealed Ni(100)/MgO(100) bi-crystal is shown. During thermal treatment the strain and defect density gradually decreased and at the temperature 1000^{0}C strain-free Ni films (though still containing imperfections) were obtained.

The evolution of the crystalline quality of the Ni films was studied in details by XRD. In Fig. 2, the development of rocking curves

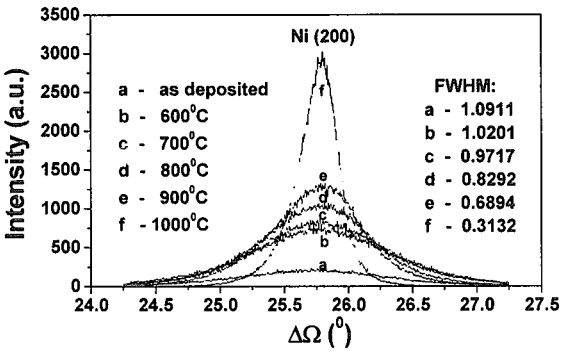


Fig. 2

(fixed at the Ni(200) reflections) is shown. As-deposited Ni films of rather low crystalline quality (FWHM < 1 ^{0}) have evolved towards the films with substantially improved epitaxy (FWHM ~ 0.3 ^{0}). Interestingly, the epitaxial re-structuring proceeded with the evident acceleration leap at the annealing temperature 1000^{0}C.

The re-crystallization of Ni deposits was studied also by AFM. In Fig. 3, AFM images of the Ni films before (a) and after annealing at 1000^{0}C (b) are shown. One can see the dramatic change in the surface morphology, about 200 nm large Ni crystallites coalesced towards the several μm large grains. The roughness (rms) before and after anealing decreased from 3.5 nm to 1.5 nm.

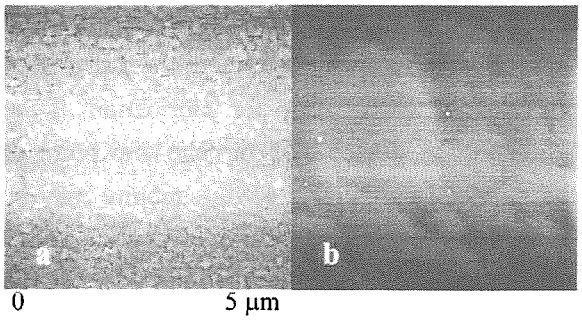


Fig. 3.

In conclusion, it was found that a high quality single crystalline Ni film can be prepared by vapor deposition on MgO(100) and subsequent thermal annealing at 1000^{0}C.

References

[1] F. Reniers, M. P. Delplancke, A. Asskali, V. Rooryck, and O. Van Sinay, Appl. Surf. Sci. 92, 35 (1996)

[2] H. Bialas and K. Heneka, Vacuum 45, 79 (1994)

4.23 Characterization of Steps on Annealed Sapphire Surfaces

Kazumasa Narumi and Hiroshi Naramoto
Advanced Science Research Center, JAERI

1. INTRODUCTION

Since the success of diamond synthesis by chemical vapor deposition (CVD)[1], many groups have done extensive investigation into diamond thin films. However, sufficiently uniform heteroepitaxial films have not been obtained yet, which are important for future application in diamond device technology. Although many candidate substrates for the heteroepitaxy of diamond have been selected from the various viewpoints[2], any systematic consideration has not been paid to control the substrate surface except for pretreatment to promote nucleation.

Sapphire has been used as a substrate for thin-film deposition because of its high purity, high chemical stability and high crystal quality and is now widely used for fabrication of the blue-emitting device[3]. From the viewpoint of the diamond epitaxial growth, sapphire may be promising: Recently, Yoshimoto *et al.* succeeded in epitaxial diamond growth on the (0001) surface of sapphire in an oxidizing environment[4]. From their results, one can reasonably deduce that one of the important keys to the epitaxial growth is to prepare an atomically smooth sapphire surface by controlled annealing in air[5]. They also showed a possibility to design the surface features of the sapphire substrate in an atomic scale, such as the terrace width and the step height, by controlling the misorientation from the crystallographic axis and the annealing condition[5]. In the present study, we investigate the changes of surface steps on sapphire substrates after systematic thermal annealing with an atomic force microscope (AFM).

2. EXPERIMENTAL

Sapphire single-crystal sheets with (0001) and (11$\bar{2}$0) plane were used as the specimen: The sheets were cut into pieces typically 5 × 5 × 0.3

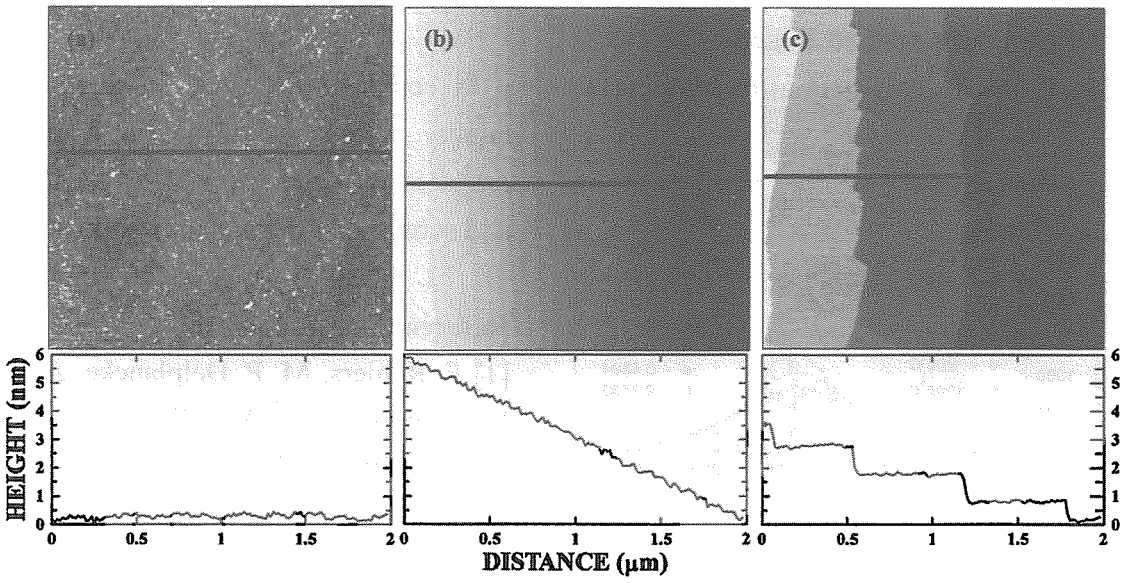


Figure 1. AFM images of the (11$\bar{2}$0) surfaces of sapphire (a) as-received, annealed (b) at 1100 °C for 1 hour and (c) at 1400 °C for 10 hours in air. The scanned area is 2 × 2 μm^2. Profile is taken along the line in the image.

mm^3. The specimens were cleaned with acetone and ethanol in an ultrasonic vibrator for 15 min, respectively and then rinsed in deionized water. Thermal annealing was performed in air or in a reducing environment, where Ar with 3 % H_2 was flowed at the rate of 200 cm^3/min in an electric furnace. After the annealing, the surface morphology was characterized with AFM (JEOL JSPM-4200). Although some specimens were observed several weeks after the annealing, there was no significant change in the surface morphology except some dust.

3. RESULTS AND DISCUSSION

When a macroscopic surface is slightly deviated from a low-index plane such as (0001) or $(11\bar{2}0)$, such a surface consists of the low-index plane and surface steps. Figure 1(a) shows the image of an as-received $(11\bar{2}0)$ surface, where step structure is slightly found though the surface was damaged. It is considered that such step structure was mechanically introduced during cutting and polishing process and determined geometrically by the misorientation. Figure 1(b) shows surface structure of a $(11\bar{2}0)$ surface of sapphire annealed for 1 hour at 1100 °C in air. The surface reflects the structure of the as-received one and consists of narrow terraces and steps whose height corresponds to the minimum unit of stacking sequence along the $[11\bar{2}0]$ axis (0.24 nm). On the other hand, surface structure of sapphire annealed for 10 hours at 1400 °C in air, shown in Fig. 1(c), is different from that annealed at 1100 °C: We observed steps, which are more than three times as high as those in Fig 1(b), followed by the expansion of terraces. Such step structure was not observed for specimens annealed at less than 1400 °C.

Depending on the temperature and the misorientation, the step density can be optimized in order to minimize the surface energy and during thermal annealing, the step density changes to lead to the reduction of the surface energy by sublimating surface atoms. In the present results, the surface that does not reflect the step structure of as-received specimens was observed for specimens annealed for 10 hours at 1400 °C. Thus we assumed that for annealing at 1400 °C, the step structure that is different from those the misorientation geometrically introduces

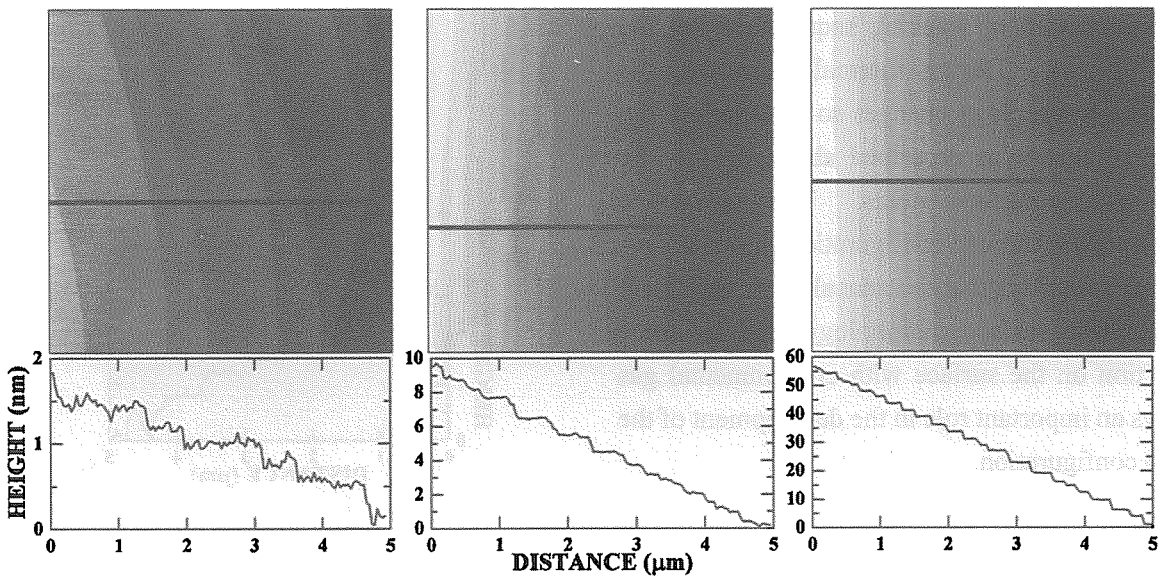


Figure 2. AFM images of the (0001) surfaces of sapphire annealed at 1400 °C for 10 hours in air. Misorientation is (a) 0.02°, (b) 0.09° and (c) 0.7°, respectively. Scanned area is 5 × 5 μm^2. Profile is taken along the line in the image.

appears.

In order to confirm the assumption, we observed dependence of the step structure on the misorientation for the (0001) surface of sapphire annealed for 10 hours at 1400 °C in air. It is shown in Fig. 2. As it is apparent in the figure, the step height becomes higher with the increasing misorientation followed by terrace-narrowing: For the surface with the misorientation of 0.02 °, the step height corresponds to the minimum unit of stacking sequence along the [0001] axis (0.22 nm). The step is more than a few times and ten times as high as the minimum unit of stacking sequence for the misorientation of 0.09 ° and 0.7 °, respectively. These results support our assumption and obviously show that it is possible to control the step structure by misorientation.

On the other hand, for annealing in a reducing environment, the situation is quite different: An AFM image of the (0001) surface of sapphire annealed for 1 hour at 1400 °C in the reducing environment is shown in Fig. 3. The surface is composed of meandering steps like inlets, holes, islands and atomically flat terraces. All the steps, holes and islands are as high as the minimum unit of stacking sequence along the [0001] axis. During thermal annealing, the surface morphology changes so as to reduce the surface energy as described above, mainly by sublimating surface atoms. The remarkable difference in the step configuration shown in Figs. 2 and 3 suggests that the annealing environment affects the surface morphology, that is, some reaction on the surface with environmental gas plays an important role in the development of the step configuration.

4. SUMMARY

Surface step structure of sapphire (0001) and (11$\bar{2}$0), which were annealed in air or in a reducing environment at 1000 to 1400 °C for 1 to 10 hours, was observed with AFM. The step structure on the annealed surfaces depends on the misorientation. An annealing environment also affects the surface morphology, especially the step configuration. It should be noticed that the present results show the probability to control the step structure on the sapphire surface.

References

1. J. C. Angus, H. A. Will and W. S. Stanko, J. Appl. Phys. **39** (1968) 2915.
2. T. Suzuki and A. Argoitia, Phys. Stat. Sol. (a), **154** (1996) 239.
3. For example, S. Nakamura, M. Senoh and T. Mukai, Appl. Phys. Lett. **62** (1993) 2390.
4. M. Yoshimoto, K. Yoshida, H. Maruta, Y. Hishitani, H. Koinuma, S. Nishio, M. Kakihana and T. Tachibana, Nature **399** (1999) 340.
5. M. Yoshimoto, T. Maeda, T. Ohnishi, H. Koinuma, O. Ishiyama, M. Shinohara, M. Kubo, R. Miura and A. Miyamoto, Appl. Phys. Lett. **67** (1995) 2615.

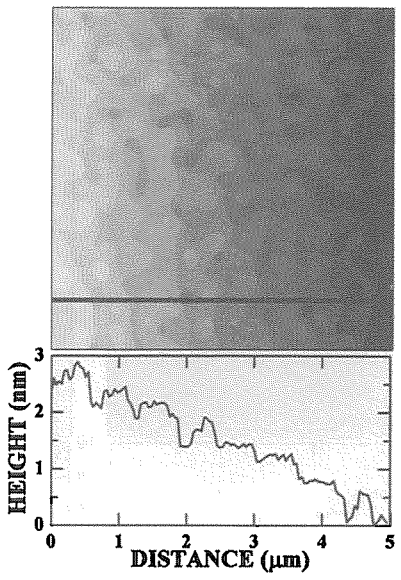


Figure 3. AFM image of the (0001) surface of sapphire annealed at 1400 °C for 1 hour in the reducing environment. Scanned area is 5 × 5 μm^2. Profile is taken along the line in the image.

4.24 Development of Micro-Processing Technique of Ceramics using Rare-Gas Ion Beam Irradiation

S. Ohtsuka[1], A. Hasegawa[2], M. Satou[2], K. Abe[2], T. Taguchi[3]

[1] Graduate School of Engineering, Tohoku University, [2] Department of Quantum Science and Energy Engineering, Tohoku University, [3] Department of Materials Development, JAERI

1. Introduction

Rare-gas ion-beam irradiation to a solid target causes microscopic surface morphology changes such as swelling, blistering and exfoliation due to accumulation of displacement damage and gas bubble formation. These surface morphology changes have been studied as radiation induced surface damages of materials [1,2]. We have shown that He-ion beam irradiation combined with a mask can be used to create as the mask pattern bumps on brittle and hard materials such as silicon carbide (SiC), diamond and sapphire, and also reported about the dependence of surface morphology changes on irradiation fluence and ion energy [3,4]. This surface shape modification technique may be useful as a fabrication process, which can be applied to hard or brittle materials.

To apply this phenomenon to a micro fabrication process, accuracy and fabrication efficiency will be important parameters. For example, damage production rate depends on ion mass and energy. The purpose of this work is to study the effect of ion mass on the surface morphology changes in order to obtain adequate irradiation condition from the view point of developing a micro-processing technique using rare-gas ion beam irradiation.

2. Experimental Method

A polycrystalline CVD processed β -SiC plate with a thickness of 0.5 mm was used as fabricated materials in this work. It was supplied by Mitsui Engineering and Shipbuilding Co., LTD [6]. A 25 μ m square-pattern grid mask made of copper was fixed to the surface to define the shape of the pattern on the irradiated surface. Rare-gas-ion irradiations in vacuum were carried out using a 400 kV ion implanter at the JAERI TIARA facility. The implanted ions were He^+, Ne^+, Ar^+ and Kr^+ -ion and the projectile energies were 30 keV, 110 keV, 200 keV and 380 keV, respectively. Figure 1 shows the calculated depth profile of the implanted ion concentration and the displacement damage in SiC using TRIM code[7] after $1x10^{21}$ ions/m^2 irradiation. The projected ranges of the He^+-ions and other ions are 0.20 μ m and 0.15 μ m, respectively. The projected range of the He^+-ions is larger than the other ions because of the limitation of lower accelerated energy of the ion implanter. The ratios of implanted gas atoms to displacement damage in the damage peak region are varied with ion type as follows: 25000 appm He/dpa, 2500 appm Ne/dpa, 1400 appm Ar/dpa and 830 appm Kr/dpa. This is due to the damage production efficiency resulted from the difference of ion mass. The irradiation fluence varied from $2.2x10^{18}$ to $2.0x10^{21}$ ions/m^2. Flux ranged from $9.9x10^{14}$ to $2.0x10^{18}$ ions/m^2/s. Irradiation temperature was measured using an infrared thermometer and the temperature was about 300 K.

Surface observation and quantitative measurement of surface morphology were conducted using an optical microscope and a scanning probe microscope (SPM) located at the Tohoku University Venture Business Laboratory (VBL).

3. Results

Figure 2 shows a typical optical microscope image of the surface of a specimen which was irradiated with 380 keV Kr^+-ion to a fluence of $1.0x10^{20}$ ions/m^2. A square-mask pattern was transferred on the specimen surface as an array of irradiation induced bumps. The bump array was formed uniformly in the whole irradiated area. This result shows that a relatively large area (about 1-10 cm^2) pattern can be processed using a spread ion beam.

Figure 3 shows a typical high-resolution SPM image of the Kr^+ ion irradiated specimen after an exposure of $1.1x10^{21}$ ions/m^2. As is shown in figure 3, a bump array with a height of ~30nm was obtained for a fluence, which ranged between 10^{19} to 10^{21} ions/m^2. The roughness of

the top surface of the bumps is the same as that of the unirradiated area. With increasing fluence, the top surface of the bump become irregular above 10^{21} ions/m^2. It may be attributed to blister formation in the implanted range.

The correlation between bump height and fluence is shown in figure 4. The height increases with fluence up to a fluence of $1x10^{21}$ ions/m^2. At this fluence, the bump height was ~ 40nm when using heavy ions. This shows that the bump height can be precisely controlled by the irradiated fluence. It can also be seen that heavy ions are more effective at creating bumps than lighter ions.

Linear swelling of the irradiated area (ΔL) was defined as follows.

$$\Delta L = h / R_p \times 100\ (\%)$$

where h is the bump height, R_p is the projected range of implanted ion. The dependence of linear swelling on fluence is shown in figure 5. For lower fluences, linear swelling increases remarkably up to 15 ~ 20%. Since it has been reported that 15% swelling occurs in crystalline SiC due to irradiation-induce-amorphization by a accumulation of displacement damage[2], the mechanism of bump-formation at lower fluence is thought to be amorphization-induced-swelling. This means about 30 nm of height is fluence independent bump height caused only by displacement damage. Actually, in the middle fluence region (above 10^{20} ions/m^2), swelling increases slightly with fluence. It is thought that the volume from the surface to the projected range has already become fully amorphized, and the mechanism of additional height increase may be swelling due to gas-bubble formation at in the region of the projected range depth. Above 10^{21} ion/m^2, bump height increase quickly. Blistering was observed in this region. Gas bubble coalescence and large lens shape gas bubble formation at the projected range became the dominant morphological change.

From the viewpoint of micro-processing of SiC, it will be expected that heavy ion irradiation such as Kr can create 30 nm high bumps on the surface without blistering within certain accuracy.

4. Summary

The effect of ion mass on surface morphology change was studied to apply rare-gas ion beam irradiation to micro-processing of ceramics. The results on SiC are summarized as follows:

(1) An array of bumps was transcribed on a SiC surface using a copper mask and ion irradiation.

(2) Bump-formation appears to be caused by swelling due to amorphization by accumulation of displacement damage and gas-bubble formation.

(3) The bump height increases with fluence up to about 10^{21} ions/m^2 and then blistering occurs. A bump height in the range of 20 to 40 nm was obtained by He, Ne, Ar and Kr irradiation.

(4) Heavy ion irradiation may permit microscopic scale surface morphology changes to SiC surfaces in a few minutes without an increase in surface roughness.

5. References

[1]S. K. Das and M. Kaminsky, Proc. Symp. Radiation Symp. Radiation Effects on Solid Surfaces, 25th August, Chicago, Advances in Chemistry series, 1975, pp.112

[2] J. M. Williams, C. M. McHargue and B. R. Appleton, Nucl. Instr. and Meth., Vol.209/210, 1983, 317

[3] S. Ohtsuka, A. Hasegawa, M. Satou and K. Abe, International Conference on Ion Implantation Technology Proceedings, Ion Implantation Technology -98, IEEE, 779-782, 1999

[4] S. Ohtsuka, A. Hasegawa, M. Satou and K. Abe, Proceeding of International Symposium on Enviroment-Conscious Innovative Materials Processing with Advanced Energy Sources, 424-427, 1999

[5]W. Wesch, Nucl. Instr. and Meth., Vol. B116, 1996,305

[6]Y. Chinose et al., Amorphous and Crystalline Silicon Carbide and Related Materials, Eds. M. M. Rahman et al., Springer Proceedings in Physics, Vol.43, Springer-Verlag, 1989,198

[7] J. F. Ziegler et al., The Stopping and Range of Ion in Solids, Pergamon Press, 1985

[8] I. A. H ϕ nstvet et al., Philos. Mag., Vol.A41, 1980, 201

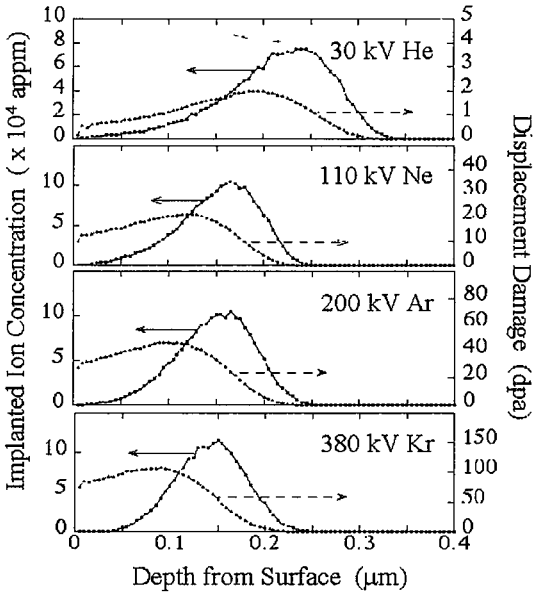


Figure 1 Depth profile of implanted ion concentration and displacement damage in SiC calculated with TRIM code [7]

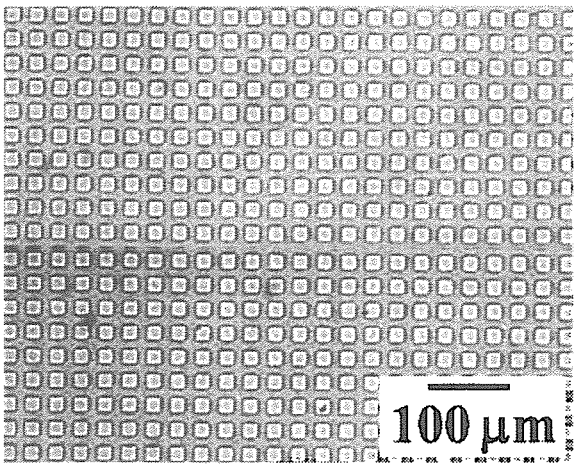


Figure 2 Optical microscopy of the 380keV Kr^+-ion irradiated SiC to the fluence of 1.0 x 10^{20} ions/m^2

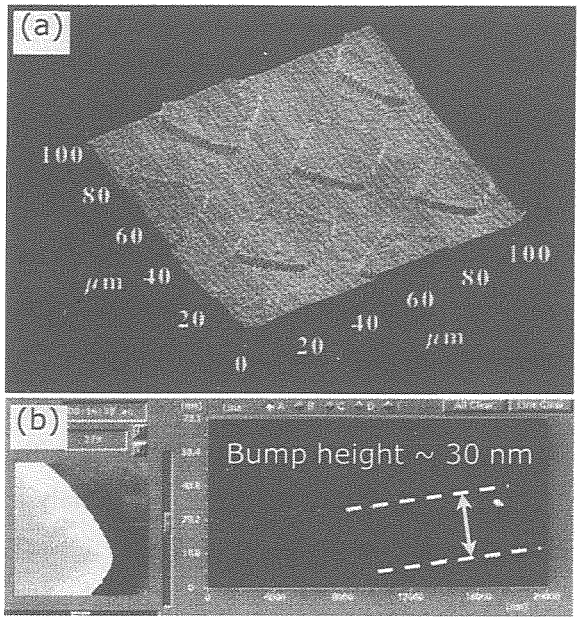


Figure 3 SPM observation results of 380keV Kr^+-ion irradiated SiC to the fluence of 1.0 x 10^{21} ions/m^2, (a) 3-dimensional image, (b) cross-sectional profile

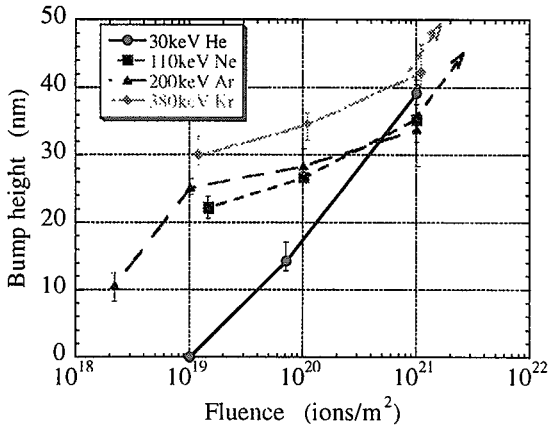


Figure 4 Dependence of bump height on fluence

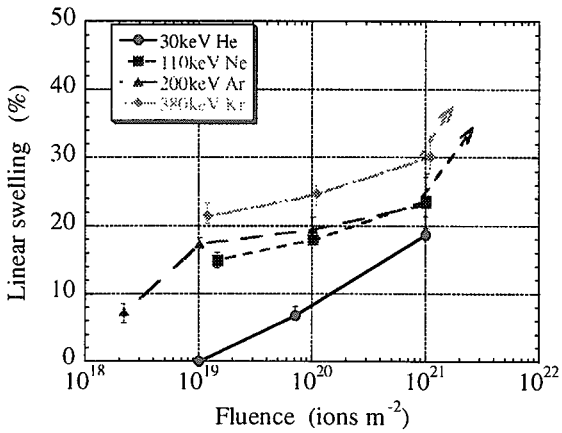


Figure 5 Dependence of linear swelling on fluence

4.25 Electrical and optical properties of Cr ion implanted TiO_2

T.Sumita, T.Yamaki, S.Yamamoto, H.Abe, A.Miyashita, I.Nashiyama
Department of Materials Development, JAERI

1.Introduction

Photocatalysis of titanium dioxide(TiO_2) has received great attention recently with the improvement of our concern about the environmental problem. However, its optical bandgap(3.0-3.2eV) is a disadvantage with regard to its application as a photocatalyst under the solar light.

The aim of this study is to create highly activated TiO_2 photocatalytic systems by using ion implantation technique. We expect the formation of 1)the graded structure assisting hole transport towards the surface[1,2] and/or 2)the layer allowing visible light at a certain depth of TiO_2. Here, we report electrical and optical properties of Cr ion implanted TiO_2.

2.Experimental

The samples were used <001> oriented TiO_2 rutile single crystal, which was cut 10mm × 10mm × 0.5mmt in size. Cr ion implantation was carried out at room temperature, with 150keV from the 400kV Ion Implantor of TIARA facility in JAERI-Takasaki and the doses between 5.5×10^{14} and $2.6 \times 10^{16}/cm^2$. All the implanted samples were annealed at 800℃ for 5h in air. The photoconductivity spectra were measured at room temperature, using as an excitation source a Xe lamp. The spectra have been corrected for the emission spectrum of the lamp. The optical transmission and reflection were measured with a ZEISS UV-VIS-NIR instrument. The RBS/channeling analysis with 2MeV He^+ ion beam from single-ended accelerator of TIARA were performed to get the information of damage recovery in implanted TiO_2 crystals.

3.Results and discussion

Figure 1 shows the photoconductivity spectra of Cr implanted TiO_2 for various doses after the annealing process and TiO_2 rutile crystal before implantation. The photoconductivity threshold energies of the implanted TiO_2 are decreased with increasing Cr doses from that of the original TiO_2. The threshold energies dependent on Cr doses were shifted to the visible light region.

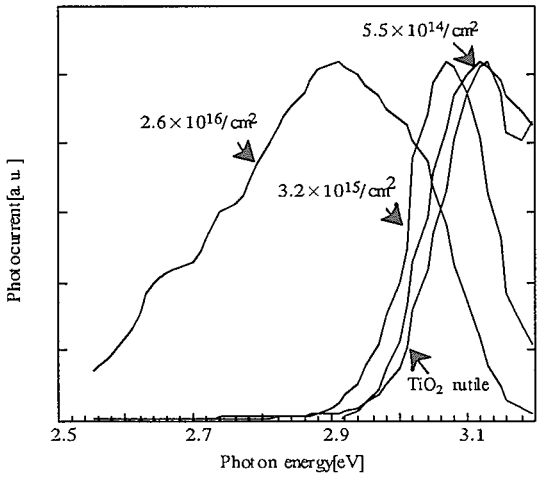


Fig.1 Photoconductivity spectra of Cr implanted TiO_2 for various doses.

Since TiO_2 is a semiconductor with a large bandgap, the optical bandgap E_g can be determined from absorption coefficient α. The α near the absorption edge was derived from the transmittance(T) and reflectivity(R) measured on the implanted TiO_2 with 2.6×10^{16}ions/cm^2 for Cr and TiO_2 rutile crystal. The α, which depends on the wavelength λ of incident light, can be obtained by using the following relationship, $T=(1-R)^2e^{-\alpha d}$, where d is thickness of the sample. When scattering effects are neglected, the α above the threshold of fundamental absorption follows the $(E-E_g)^2$ energy dependence characteristic of indirect allowed transitions, as shown by the $\alpha^{1/2}$ versus photon energy (E) plot in Figure 2. The α of Cr implanted layer was calculated from the depth of Cr distribution in TiO_2 crystal obtained by TRIM simulation. The optical bandgap of TiO_2 rutile crystal is estimated 2.92eV, which is good agreement with other reports[3]. In contrast to the TiO_2 crystal, the band gap of Cr implanted layer is decreased down to 2.07eV.

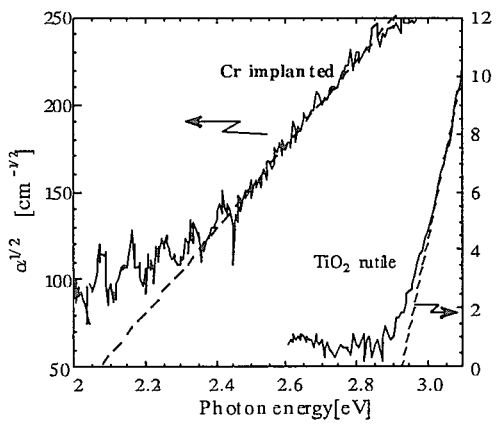


Fig.2 Optical absorption spectra of Cr implanted and normal TiO_2.

Figure 3 shows the RBS/channeling spectra, random(a) and aligned(b), for the Cr implanted TiO_2 after the annealing process. The aligned spectrum(b) shows the damage was recovered.

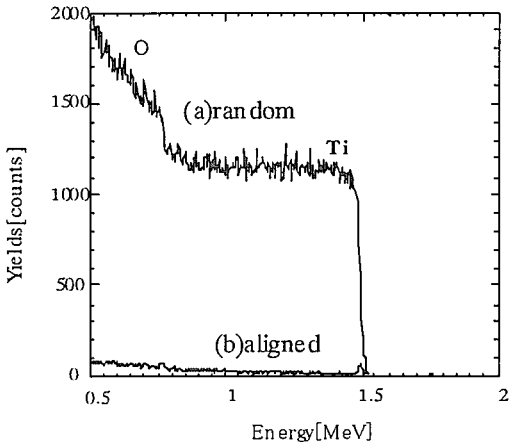


Fig.3 The RBS spectra of Cr implanted TiO_2

We carried out Nb[4] implantation and investigated the optical properties of the implanted samples. At the present, Cr ion is found to be one of the most effective for reducing the bandgap of TiO_2.

References

1) R.I.Bickley et al., J. Solid State Chem. 92, 178, 1991

2) T.Sumita et al., Nuclear. Instrum. Meth. Phys. Res. B, 148, 758, 1999

3) N.Martin et al., Thin Solid Films, 300, 113, 1997

4) Y.Aoki et al. Nuclear., Instrum. Meth. Phys. Res. B, 136, 400, 1998

4.26 Lattice defects created in quartz of uranium ores

S. Toyoda, K. Komuro*, and H. Isobe**
Department of Applied Physics, Faculty of Science, Okayama University of Science, *Intitute of Geoscience, University of Tsukuba, **Graduate School of Natural Science, Kumamoto University

Introduction

Migration of uranium and its daughter elements in forming uranium ore is an important issue to predict how these nuclei might move in natural environment after closing the site for radioactive waste disposal as well as to investigate uranium resource. This study investigates how radiation effects given to quartz by radiation from those nuclei are useful. The processes in nature to produce ESR (electron spin resonance) signals and cathode luminescence (CL) rims in quartz were investigated by implanting He^+ ions, by irradiating electron beam and gamma rays.

Experimental

He^+ ion of 4MeV and electrons of 500keV were irradiated to sliced synthetic quartz samples by the tandem accelerator at Takasaki Laboratory of Japan atomic Energy Research Institute. Each sample was divided into two for CL and ESR measurements. The former sample was put into regin before polishing. The other part was crushed into powder for ESR measurements.

CL measurements were done with a Luminoscope ELM-3R using an electron voltage of 13.5±1.0 kV, 0.85±0.10 μA under vacuum of 40-45 Torr. Photoes were taken with films of ASA1600.

ESR measurements were performed at room temperature with JEOL, RE-1X at Okayama Industry Technology Center. We used microwave power of 0.01mW, magnetic field scan of 5mT, magnetic field modulation amplitude of 0.1mT with 100kHz frequency. The intensity of the E_1' center in quartz was measured from a signal on an X-Y chart recorder. The samples were then heated at 170°C and at 300°C before following ESR measurements.

Results and Discussion

Cathodoluminescence

Orange CL rims were observed for samples irradiated by He^+ ions to more than 2×10^{-4} C/cm^2. The width of the rims was 12μm, being consistent with the range of the ions within quartz. This observation confirms that the CL rims observed in quartz of natural uranium ores have been created by α particles emitted by uranium and its daughter elements.

The lowest He^+ ion dose for which the CL rims were observed corresponds

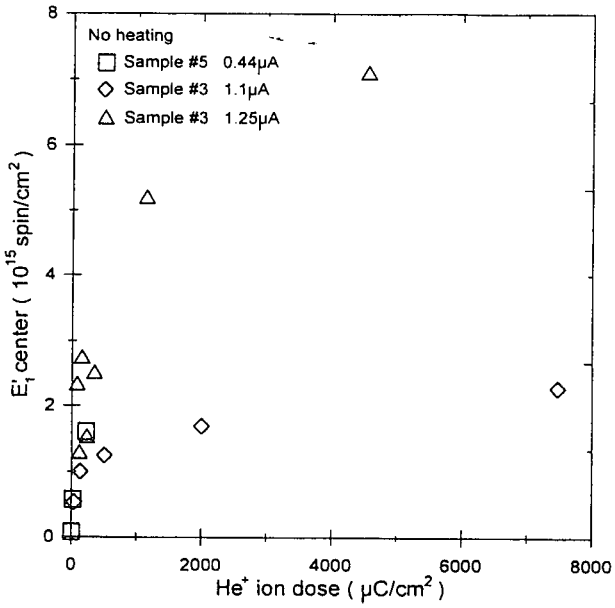


Fig. 1a The E_1' center signal intensities created by the 4MeV He^+ ion implantation.

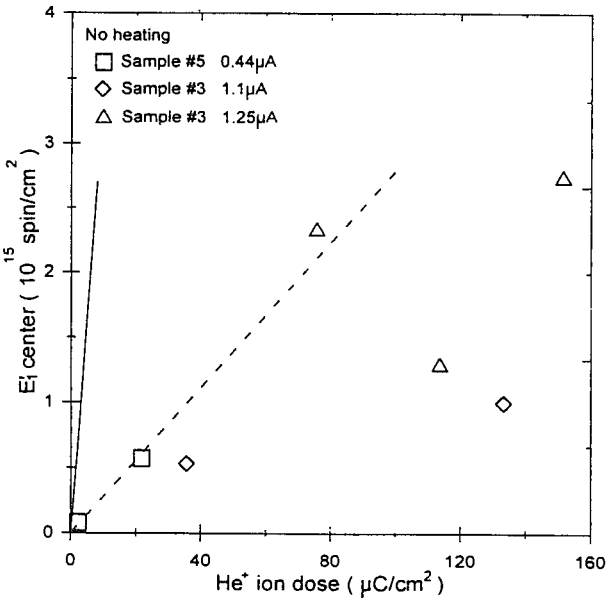


Fig. 1b Results of He^+ ion implantation where the lower dose part is enlarged.

to the specific ionization within quartz (number of ion pairs created per unit length) of 2.1×10^6.

ESR measurements

The intensities of the E_1' center in quartz were obtained as a function of doses of He^+ ions as shown in Fig. 1a and 1b. The intensities showed saturation for each sample. The difference would be due to sample dependence rather than the experimental error in measurements. Fig. 1b is enlargement of the lower dose region of Fig. 1a. The formation rate of the center was obtained as a G value (number of spins created per 100eV of absorbed radiation energy) by fitting a line to the part without saturation to be 1.1×10^{-4} This value is one order of magnitude lower than the value obtained by theoretical calculation named TRIM which was 1.3×10^{-3}. The difference would probably be because not all oxygen vacancies are paramagnetic but some of them may be diamagnetic.

The intensities of the E_1' center were also obtained as a function of electron dose as shown in Fig. 2. The G value was also obtained from the line fit to the points shown in this figure to be 4.3×10^{-5}

Assuming that the formation rate of the center by γ rays is the same as that of by electrons, the numbers of the centers created in a quartz grain of 1mm in diameter were calculated in case that the grain is placed in uranium of 1% for a year. By chance, these values coincide to be 3.2×10^9 spin/g, i.e. both processes create about same amount of defects in quartz.

However, the results of the annealing experiments indicate that only

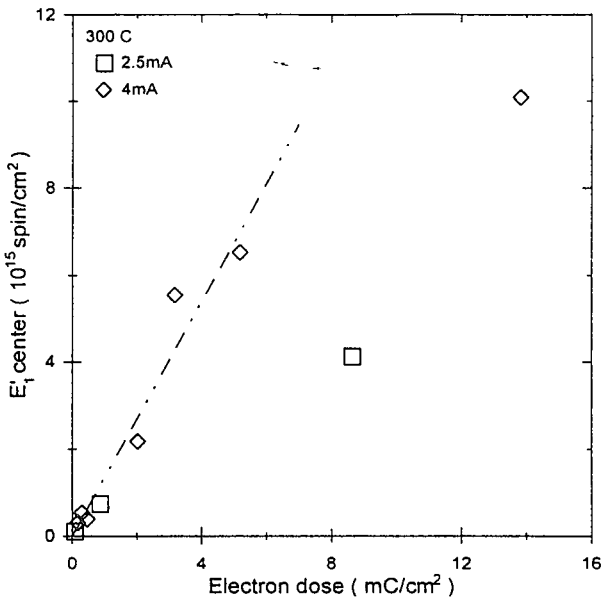


Fig. 2 The E_1' center signal intensities created by 500keV electron irradiation.

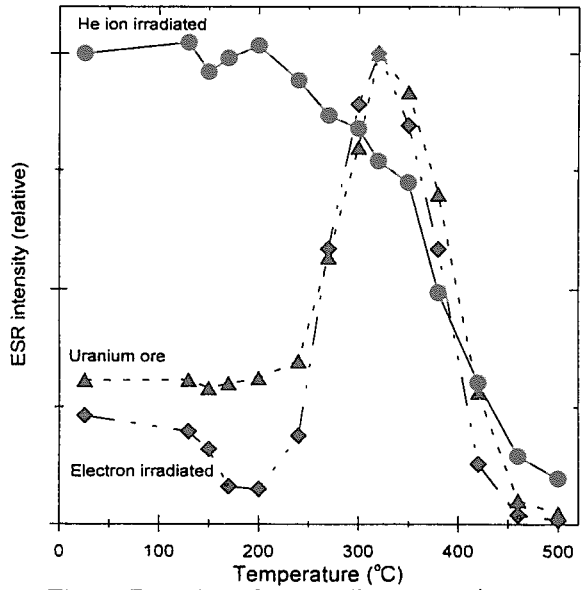


Fig. 3 Results of annealing experiments. The heating duration was 15 minutes at each temperature step.

β and γ rays create oxygen vacancies in quartz of uranium ore. The signal intensity of the E_1' center is known to increase with heating because electronic holes are transferred to diamagnetic oxygen vacancies to form paramagnetic E_1' centers. This feature was confirmed for quartz samples irradiated by electrons as shown in Fig. 3 while the intensity of the E_1' center created by He^+ ions was found to decrease monotonically. The sample taken from a uranium ore showed the same feature as the sample irradiated by electrons, indicating that the signal in quartz of uranium ore has been created by β and γ rays rather than α particles.

Conclusion

The present study showed that the CL rims are useful to estimate cumulative radiation dose given by α particles while ESR signals are associated with those given by β and γ rays. Futher studies would be needed to enable us to discuss uranium migration quantitatively with these two methods.

Acknowlegments

This work was supported by REIMEI Research fund provided by Japan Atomic Energy Research Institute.

5. Material Analysis

5.1 Hydrogen Distribution Features in Epitaxial Cu(111)/Nb(110) Multilayer Characterized with Ion Beam Analysis ····· 177
S. Yamamoto and H. Naramoto

5.2 Structure-sensitive Electron Spectroscopy: Continuum and Auger Electron Yields Induced by Fast Ions ····· 179
H. Kudo, K. Shibuya, N. Nakamura, K. Narumi, H. Naramoto and S. Yamamoto

5.3 Chemical Effect on X-Ray Spectra Induced by Multiple Inner-shell Ionization (III) ····· 181
N. Takeshima, K. Takahiro, K. Kawatsura, S. Yamamoto, I. Nashiyama, K. Narumi and H. Naramoto

5.4 Quantitative Analysis of Hydrogen in Solid Surface using Fast Neutrons Produced by Nuclear Reaction ····· 184
K. Saitoh, S. Nakao, T. Mizota, H. Niwa, Y. Saitoh, Y. Nakajima, S. Tajima and H. Naramoto

5.5 In-situ Observation of Formation of Graphitic Onions under Ion Implantation ····· 187
H. Abe

5.6 In-situ Observation of Growth Processes of Transition Metal Compound Thin Films by Ion-Implantaion ····· 190
Y. Kasukabe, H. Tani, Y. Yamada and H. Abe

5.7 Depth-selective Damage Analysis of C_n^+ (n=1-4) Cluster Irradiated Polycarbonate by a Variable-energy Positron Beam ····· 193
K. Hirata, Y. Saitoh, K. Narumi, Y. Kobayashi, A. Kawasuso, S. Okada and K. Arakawa

5.8 Positron Annihilation Study of Defects Produced in Pd by Ion Implantation and their Effects on Hydrogen Storage ····· 196
H. Abe, A. Uedono, S. Okada and H. Itoh

5.9 Magic Number Vacancy Clusters in Si by High Precision Positron Lifetime Measurements with Internal Positron Source of ^{22}Na ····· 199
M. Hasegawa, Y. Nagai, Z. Tang, K. Nakazuru, M. Maekawa, A. Kawasuso and S. Okada

This is a blank page.

5.1 Hydrogen Distribution Features in Epitaxial Cu(111)/Nb(110) Multilayer Characterized with Ion Beam Analysis

S. Yamamoto and H. Naramoto*
Dept. of Materials Development, JAERI
*Advanced Science Research Center, JAERI

1. Introduction

Recently, the hydrogen behavior in thin films and multilayers has been found to be interesting for structural changing of the host lattice and its electric proprieties. Also several differences in the hydrogen behavior between the thin films and the bulk, which are connected with interface conditions, have been observed. Several ion beam techniques are suitable to obtain the detail hydrogen profile in thin films and multilayers with good depth resolution. Particularly, ^{15}N-NRA technique has excellent depth resolution using very narrow resonant nuclear reaction at 6.385 MeV. In the present work, we have studied epitaxial Cu(111)/Nb(110) multilayer, deposited on the α-$Al_2O_3(1\bar{1}20)$ substrate by electron beam evaporation techniques in UHV. The structural analysis of the multilayer films was performed using RBS/channeling and XRD techniques. The hydrogen profiling of hydrogen charged multilayer samples was made by ^{15}N-NRA technique.

2. Experiment

Epitaxial Nb/Cu multilayers were deposited on the α-$Al_2O_3(1\bar{1}20)$ substrates using the electron beam evaporation technique. Both Nb and Cu films were deposited at the rate of about 0.2 nm/s. The α-Al_2O_3 substrate kept at 750°C for Nb and at 200°C for Cu. For the hydrogen charging procedure, the samples were transferred to a hydrogenation vessel connected with evaporation chamber and heated at 150°C for 30~60 min in H_2 atmosphere (99.9999% purity) passing through a liquid nitrogen cold trap.

For the ion beam analyses, 3 MV tandem and 3 MV single stage accelerators at JAERI/Takasaki were employed. The RBS/channeling analysis was carried out using $^4He^+$ ions with the energies of 2.0 to 2.7 MeV to examine the crystalline quality of the epitaxial films and the crystallographic relationship of each layer. The hydrogen profiling in the Nb/Cu multilayers was performed by employing ^{1}H (^{15}N, $\alpha\gamma$) ^{12}C the resonant nuclear reaction (^{15}N-NRA) at 6.385 MeV. The depth resolution of our experimental setup was about 8 nm in the near surface region. The yield from the characteristic γ-rays of the resonant nuclear reactions was measured as a function of the ^{15}N ion energy with a 3″ NaI(Tl) detector placed just behind the samples.

3. Results and discussion

Fig. 1 illustrates the random and aligned spectra from the Nb(49nm)/Cu(42 nm)/Nb(48nm) multilayer deposited on the α-Al_2O_3 $(1\bar{1}20)$ substrate. The minimum yield of the top Nb layer on the bCu layer is 0.091, which points out the high-quality growth of the layer even at the second period in Cu/Nb

bi-layer stacking. In epitaxial the Nb/Cu multilayer sample with a low hydrogen concentration, different hydrogen incorporation behavior was found. Fig. 2 shows a typical hydrogen concentration profile of an epitaxial Nb(110)/Cu(111) multilayered sample composed of three Cu(30 nm)/Nb(30 nm) periods deposited on the α-Al_2O_3 $(1\bar{1}20)$ substrate. In this figure, the hydrogen concentration was profiled from the top layer towards the substrate by increasing incident energy of the ^{15}N ions. The result shows that the hydrogen diffused up to the interface between the first Nb layer and α-Al_2O_3 substrate through Cu and Nb sequence during hydrogen charging process. Also there is no hydrogen incorporation in Cu layer and α-Al_2O_3 substrate. In this figure, the data were measured in 40 keV steps with increasing and decreasing incident energy to examine possible loss of hydrogen during the beam irradiation. It is well seem that the hydrogen concentration in the Nb layers between the Cu layers is remarkably low as compared with that in the first Nb layer on the α-Al_2O_3 substrate. It is thought that the reduction of the hydrogen concentration in Nb layers between Cu layers is related to interface condition. Similar measurements in a polycrystalline Nb/Cu multilayer with the same staking sequence showed that the hydrogen concentration in Nb layers are almost on the same level in low and high charged samples. The different behavior of the hydrogen incorporation was observed only in the epitaxial mulitayer samples with the low charged hydrogen.

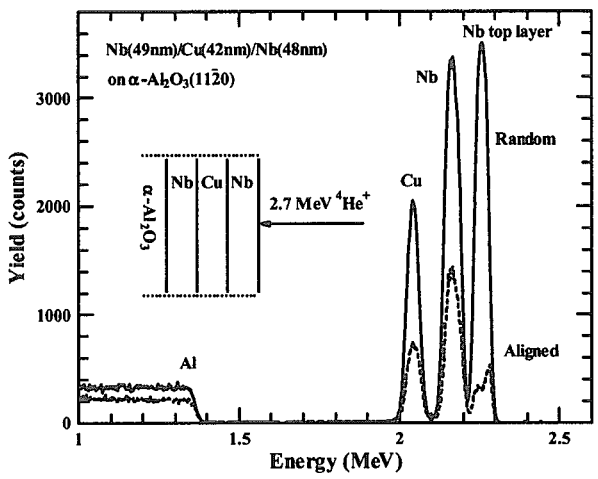


Fig. 1 RBS/channeling spectra of the 2.7 MeV $^4He^+$ ions from a Cu(111)/Nb(110) epitaxial multilayer composed of Nb 49 nm /Cu 42 nm / Nb 48 nm on α-Al_2O_3 $(1\bar{1}20)$ substrate. Aligned spectrum was measured around the major axis close to the <110> in top Nb layer.

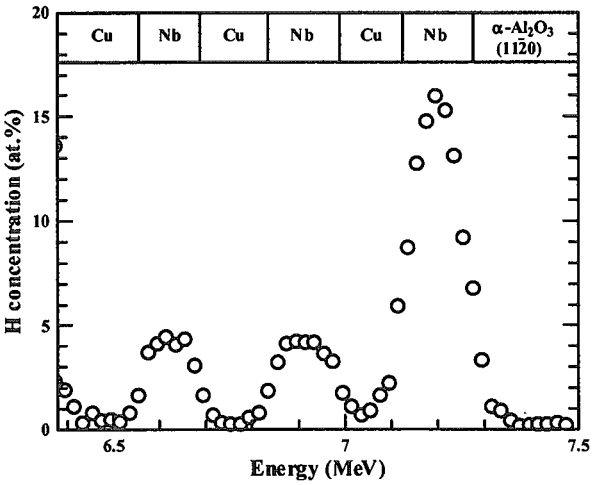


Fig. 2 The result of ^{15}N-NRA analysis of hydrogen-charged epitaxial Cu(111)/Nb(110) multilayer composed of three Cu(111)/Nb(110) sequence deposited on the α-Al_2O_3 $(1\bar{1}20)$ substrate. Thicknesses of the Cu and Nb layers are 30 nm each.

5.2 Structure-sensitive electron spectroscopy: continuum and Auger electron yields induced by fast ions

H. Kudo, K. Shibuya, N. Nakamura, K. Narumi*, H. Naramoto*, S. Yamamoto#
Institute of Applied Physics, Univ. of Tsukuba, *Advanced Science Research Center, JAERI, # Department of Material Development, JAERI

1. Introduction

The periodicity of crystal lattice affects ion-induced electron emission through the high-energy shadowing effect in the production process of the electrons[1]. However, there is another factor to be considered, i.e., the diffraction of escaping electrons which certainly affects the spatial distribution of the emitted electrons from a crystal target. While the diffraction effect is well known in photoelectron spectroscopy[2], equivalence for ion-induced electrons has not been investigated yet. We have confirmed existence of diffracted ion-induced Auger electrons, and compared its influence to that of the shadowing effect on the electron emission.

2. Forward scattering effect

In the Auger or photoelectronic processes concerning inner-shells of atoms, the monoenergetic electrons are emitted from the lattice sites of the crystal target irradiated with charged particles or photons. When the kinetic energy of the electrons is higher than several-hundred electron volts, the emission intensity is enhanced typically along the internuclear axes with short interatomic distances. This phenomenon is known as the forward scattering effect in Auger electron or photoelectron diffraction. Briefly, this is due to the *lens* effect of the attractive interaction potential between the electron and the neighboring atom(s), which focuses the otherwise spherically-emitted electron waves towards the internuclear directions.

It is important to note that the forward scattering effect is unexpected for the continuum electron yield, as reported previously, which is considerably contributed from the electrons escaped from a deep region of the crystal. For these electrons the focusing orbits are smeared out after suffering elastic as well as inelastic multiple scatterings in the outgoing paths. This is contrast to the case of the monoenergetic electron yield escaped at most through several surface layers. Physical aspects of the forward scattering effect have been well understood and are summarized in a review by Egelhoff[2] with emphasis on its applied use for local structure analysis of surfaces and interfaces.

3. Experiments

In the experiments, the Si KLL Auger electrons emitted from hydrogen-terminated surfaces of Si(100) and Si(111) have been measured[3]. The energy spectrum of Si K-shell Auger electrons has a dominant line at 1.62 keV. This is primarily due to $KL_{23}L_{23}$ transitions. The ion-induced electrons emitted from Si surfaces were energy-analyzed at a fixed angle of 160° with respect to the beam direction, using a 45° parallel-plate spectrometer of the double-deflection type with an angular acceptance of $\sim 6\times10^{-3}$ sr. The relative energy resolution of the spectrometer was

1.3%. The target crystals were bombarded by 4 MeV/u He^{2+} at room temperature under ultrahigh vacuum conditions (~5×10^{-7} Pa). The emission-angle dependence of the Auger electrons was measured by θ and φ tilts of the crystal with respect to the two orthogonal axes, using a three axis goniometer.

4. Results and discussion

Figure 1(a) shows the Si<100> forward scattering peak of the Auger electrons, observed for a H-terminated Si(100) surface. A typical shadowing pattern for Si(100) is also shown in Fig. 1(b). Note that the two figures are placed for the same crystallographic orientation. The two patterns are essentially similar, taking into account the reversed intensity due to the different sign of electric charge. However, the fringe of the Auger intensity peak at <100> is rotated by 45° compared to the shadowing pattern. This can be attributed to the short mean free path of the focused electron trajectory in the lattice[3]. The present results demonstrate applicability of the angle-resolved electron spectroscopy of ion-induced Auger electrons to surface structure analysis, especially in conjunction with the ion channeling technique.

References

1) Kudo et al., Nucl. Instr. and Meth. B115 (1996) 125.
2) W. F. Egelhoff Jr., in Ultrathin Magnetic Structures I, Chapter 5.2, Springer, Berlin 1994.
3) H. Kudo et al., Nucl. Instr. and Meth. B159 (1999) 241.

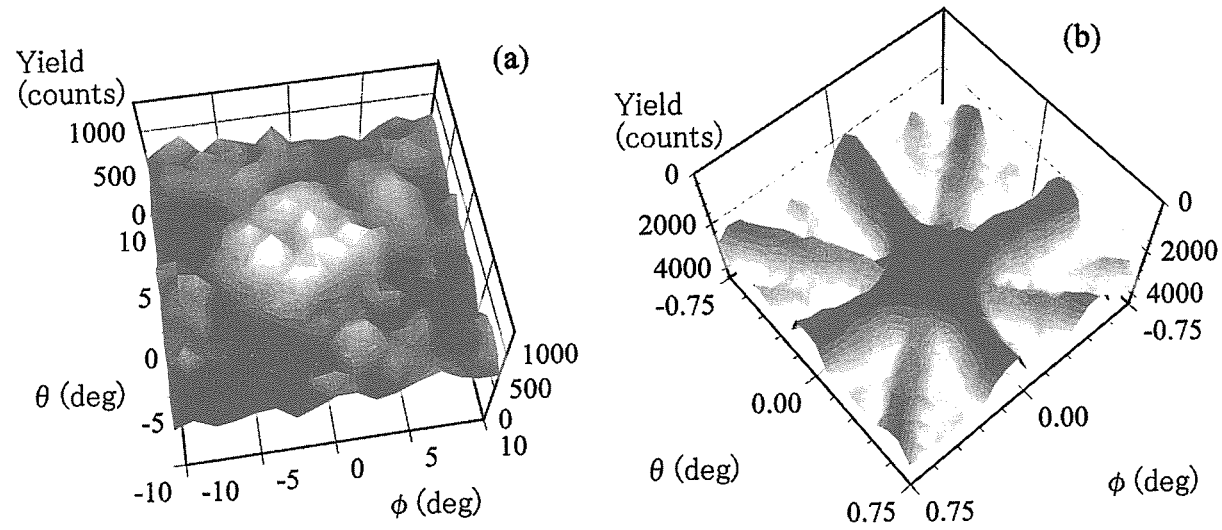


Fig. 1 (a) Angle-resolved pattern of Si KLL Auger electrons for Si(100), showing the forward scattering peak, and (b) High-energy shadowing pattern measured for continuum electron yields induced by 2 MeV H^+.

5.3 Chemical Effect on X-Ray Spectra Induced by Multiple Inner-Shell Ionization (III)

N. Takeshima, K. Takahiro, K. Kawatsura, S. Yamamoto*,
I. Nashiyama**, K. Narumi*** and H. Naramoto***

Faculty of Engineering and Design, Kyoto Institute of Technology,
*Department of Materials Development, JAERI, **HIREC,
***Advanced Science Research Center, JAERI

1. Introduction

X-ray emission spectroscopy has a wide application from atomic physics, radiation physics and chemistry, materials science and so on[1]. It is also well known that one of most useful methods for studying the interaction of fast heavy ions with atoms in a solid-state environment is X-ray emission spectroscopy. Many studies of projectile K or L X-ray emission spectra from fast heavy ions passing through inside thin or thick solid targets have been performed using different combinations of target and projectile atomic numbers[2,3].

In the present paper, we describe the measurements and the analysis of the spectra of Cu L X-rays emitted from Cu thick target bombarded by H, He, C, F and Si ions and, in the case of F ion impact, the spectra of F K X-rays emitted by F projectile traveling in a thick Cu target.

2. Experiments

The experiments were performed at the TIARA accelerator facility of JAERI in Takasaki using BL MD1of the 3 MV tandem accelerator for H, C, F and Si ion impacts, and BL SC1 of the 3 MV single-end accelerator for He ion impact. High energy H, He, C, F and Si ion beams have been bombarded on a thick Cu solid target. The typical beam current on the Cu target was about 0.5~2.0 μA. The Cu L X-ray emission spectra for H, He, C and Si ion impacts and the F K X-ray and Cu L X-ray emission spectra for F ion impact have been measured by using a high resolution X-ray crystal spectrometer with a step scan method[4-7]. The analyzing crystal used was a flat RbAP(100) single crystal. The X-ray detector was a gas flow type proportional counter with an entrance window of a thin polyester film of 1.0 μm thickness, which was operated with P-10 gas by applying +1600 V high voltage power.

3. Results and Discussion

The details on the high resolution Cu L X-ray emission spectra induced by H, He, C and Si ion impacts were already described in the previous papers[4-7]. In this paper, we focus on the X-ray spectra from fast F projectile ions and the thick Cu target.

Figure 1 shows the high resolution X-ray

emission spectra from a thick Cu target produced by 1.4 MeV F^{+}, 3.8 MeV F^{3+}, 7.6 MeV F^{3+} and 14 MeV F^{4+} ion impacts. The spectrum intensity was normalized at peak intensity of the Cu $L\alpha_{1,2}$ X-ray line, respectively. The relative intensity, $L\beta_1/L\alpha_{1,2}$ of the Cu target for F ion impact is larger at low energy than the one at high energy. This suggests that the X-ray production was induced by the quasi-molecular orbital formation during the collisions. The relative intensity, $L\beta_{3,4}/L\alpha_{1,2}$ impact is larger as increasing projectile energy. The peak energies of Lι and Lη region are shifted to the high energy side as increasing projectile energy. These indicate that the X rays are produced by direct Coulomb interaction. Beside the Cu L X-ray spectra, we observed intense X-ray spectra in the energy region of 650 ~ 800 eV in Fig. 1. They were identified as the K X-ray spectra from projectile F ions.

Figure 2 shows high resolution F K X-ray and Cu Lι and Lη X-ray spectra from 1.4 and 14 MeV F ion bombarded on a Cu target, which is the low energy part of Fig. 1. For 1.4 MeV F^{+} ion impact, F K satellite and hypersatellite lines[8] are clearly observed, which are distributed in Gaussian type. Here, F K satellite and hypersatellite lines mean that one or two F K-shell electrons are ionized and simultaneously F L-shell electrons are ionized. In this case, it is at the same collision conditions that a Cu atom with the same velocity of 1.4 MeV F ions collides with a F^{+} target. Therefore, in this velocity region, when one or two F K-shell electrons are ionized, the impact parameter is enough small to ionize the F L-shell electron with a probability of unity. So, the distribution of L-shell electron vacancy is Gaussian type. On the other hand, for 14 MeV F^{4+} ion impact (see upper part of Fig. 2), F K X-ray spectrum shows a special feature in shape. Projectile ions have a very high energy and a high charge state initially. When they entered inside the solid Cu target, projectile ions are excited and ionized to higher energy states and highly ionized state. The X-ray spectra during multiple collisions inside the target are originated mainly from 6+ and 7+ states of projectile F ions. These transitions are confirmed by the reference data of Kelly[9].

References

1) A. Meisel *et al*, "X-Ray Spectra and Chemical Binding" (Springer-Verlag, Berlin, 1989).
2) V. Horvat *et al.*, Phys. Rev. A 51, 363 (1995).
3) V. Horvat *et al.*, Phys. Rev. A 56, 1904 (1997).
4) H. Kageyama *et al.*, I. J. PIXE **5**, 203 (1995).
5) H. Kageyama *et al.*, Nucl. Instr. and Meth. Phys. Res. **B107**, 47 (1996).
6) K. Kawatsura *et al.*, I. J. PIXE **7**, 109 (1997).
7) K. Kawatsura *et al.*, Radiat. Phys. Chem. **49**, 617 (1997).
8) C.F Moore *et al.*, Phys. Lett. A **54**, 407 (1975).
9) R.L. Kelly, J. Phys. Chem. Ref. Data **16**, Suppl. 1 (1987).

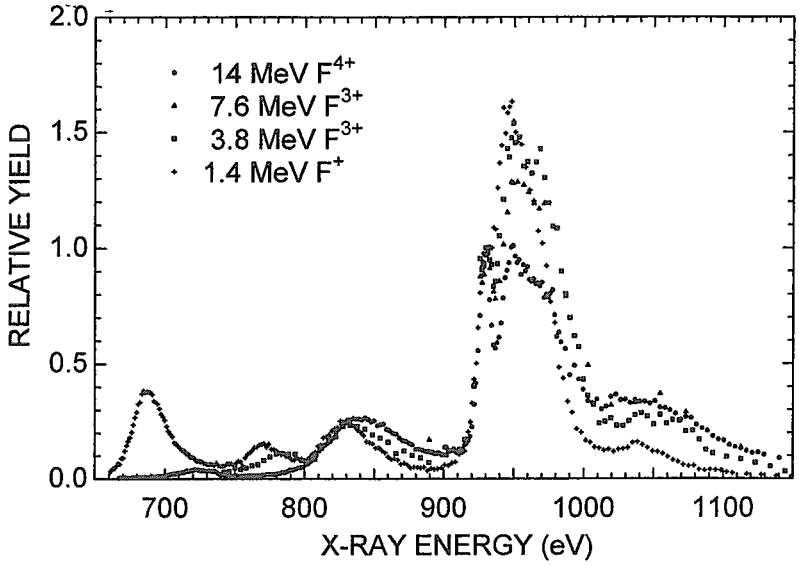


Fig. 1. F K X-ray and Cu L X-ray spectra from Cu target produced by 1.4 ~ 14 MeV F ion impacts.

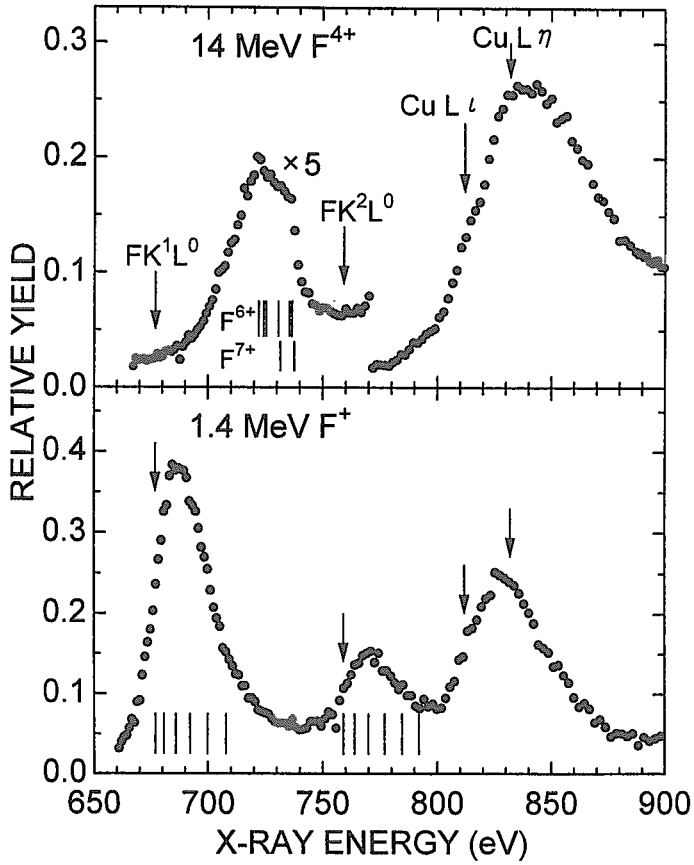


Fig. 2. Low energy part of F K X-ray and Cu L X-ray spectra from Cu target produced by 1.4 and 14 MeV F ion impacts

5.4 Quantitative Analysis of Hydrogen in Solid Surface Using Fast Neutrons Produced by Nuclear reaction

K.Saitoh, S.Nakao, T.Mizota, H.Niwa, Y.Saitoh*, Y.Nakajima*, S.Tajima* and H.Naramoto**

National Industrial Research Institute of Nagoya, Advanced Radiation Technology Center, JAERI*, Advanced Science Research Center, JAERI**

1. Introduction

Neutron elastic recoil detection analysis (NERD) would be a good nondestructive analytical method for light element, such as hydrogen iosotopes[1,2]. We have tried to establish NERD method using 0.5–5 MeV neutrons obtained by TIARA facility during last three years [2,3].

In this report, we report the results of NERD measurement and the analytical calculations for the cases of lower energy neutrons than 1 MeV.

2. Experimental

The experimental setup is almost similar to the last report[3]. Fast neutrons were obtained by the nuclear reaction $^{7}Li(p,n)^{7}Be$ (Q=-1.65 MeV) using a 2.4 MeV proton beam with an intensity of about 10μA. Li target films of 4μm were prepared by vacuum deposition of Li onto copper substrates. To prevent oxidation of the target film, an Au layer of about 40nm thickness was deposited on the surface.

NERD measurements were performed with a counter telescope consisting of a neutron entrance window, a sample holder, a ΔE-detector and an E-detector. Neutrons emitted from the neutron source to the forward direction were irradiated normally on the sample back surface through the entrance window. Recoil hydrogen atoms were detected by the ΔE-E type counter telescope system. For the ΔE-detector, a compact gridded ionization chamber[4] was used. The telescope was filled with Ar gas with 5% CO_2 to a pressure of 3 kPa. For the E-detector, a conventional Si surface barrier detector was used. Output signals from the two detectors are analyzed by a two-dimensional pulse height analyzing system (Laboratory Equipment LN9000) with a coincidence unit.

3. Results and discussion

In an ideal case of NERD measurement, i.e. both the energy spread of neutrons and the solid angle of detection system are infinitely zero, the energy spectrum of recoil particle can be presented by a simple formula. The relation between the depth z of atoms and the energy E(z) of recoil atoms at the surface is

$$E(z) = E_r - \int_0^z [dE/dx]_{E(x')} dx' \quad , \qquad (1)$$

where E_r is the primary recoil energy, $[dE/dx]_E$ the stopping power, and E(x') the energy of recoil atom as a function of path length x'. The energy spectrum f(E) of recoil particles at the surface is presented as

$$f(E) = \frac{\Phi_n t_m N_p(z) S_m \sigma_r \Omega_D}{[dE/dx]_{E(x)}} \quad , \qquad (2)$$

where Φ_n is the neutron flux rate, t_m the measurement time, $N_p(z)$ the concentration of atoms as a function of depth z, S_m the effective sample area, σ_r the differential cross section of the recoil atoms in the lab. system, and Ω_D the detector solid angle.

However, in actual cases, we must use a thick Li target to increase the neutron yield and use a finite solid angle of detection system to

increase the detection yield. Therefore, the main part of the analysis is to obtain the relation between a depth profile of the atoms and the measured spectrum, considering the finite experimental conditions. We have developed an analytical calculation program for the NERD analysis. In this program, the energy spread of neutrons due to the finite thickness of the target film, the angular dependence of neutrons energy, the energy dependence of particles on the recoil angle, and the energy loss in the ΔE detector were taken into account. The energy loss straggling of recoil particles in the sample and in the ΔE detector was also taken into account in the program. The geometry of the present NERD system and the experimental conditions are shown in Fig.1.

In Fig.2, measured NERD spectra from a thick polyethylene (PE) sheet and from a polyethylene terefthalate (PET) film of 2μm thickness are shown together. Also the theoretical spectra calculated from the eq.(2) and those corrected using the actual experimental conditions are shown in the same graph. It is found that, in the present experimental conditions, the measured NERD spectra are shifted to the lower energy, mainly due to the energy loss in the ΔE-detector. In addition, the depth resolution of measured spectra deteriorates significantly (more than 1μm for the PET case). The maximum analyzing depth is about 10 μm for the PET case.

The corrected energy spectra are in reasonable agreement with the measured ones. The differences between the measured and the calculated spectra may be due to the inaccuracy of the estimations of the detector resolution, the gas pressure and the film thickness.

4. Summary

Using low energy neutrons from the nuclear reaction $^{7}Li(p,n)^{7}Be$, energy spectra of recoil hydrogen atoms from a thick polyethylene and a PET film are successfully measured by the ΔE-E counter telescope. The measured spectra are in reasonable agreement with the theoretical predictions considering the experimental conditions. This shows that the NERD measurement with such low energy neutrons can be used for the depth profiling of hydrogen concentration in solid surface layer. The maximum depth of the analysis for the PET case is estimated to be about 10 μm and the depth resolution is 1-2 μm in these experimental conditions. The depth resolution can be improved by using a thinner Li target film and a small solid angle of the detection system.

References

1) B.G.Skorodonov, I.O.Yatsevich and Y. O.A.Zhukovsk, Nucl. Instr. Meth. B85 (1994) 301.
2) K.Saitoh, S.Nakao, H.Matsuda, H.Niwa, Y. Saitoh, Y.Nakajima, S.Tajima and H. Naramoto, JAERI TIARA Ann. Rep. 1997 p190-192.
3) K.Saitoh, S.Nakao, T.Mizota, H.Niwa, Y. Saitoh, Y.Nakajima, S.Tajima and H. Naramoto, JAERI TIARA Ann. Rep. 1998 p196-199.
4) T.Mizota, S.Nakao, H.Niwa and K. Saitoh, to be published in Jpn. J. Appl. Phys. (in print)

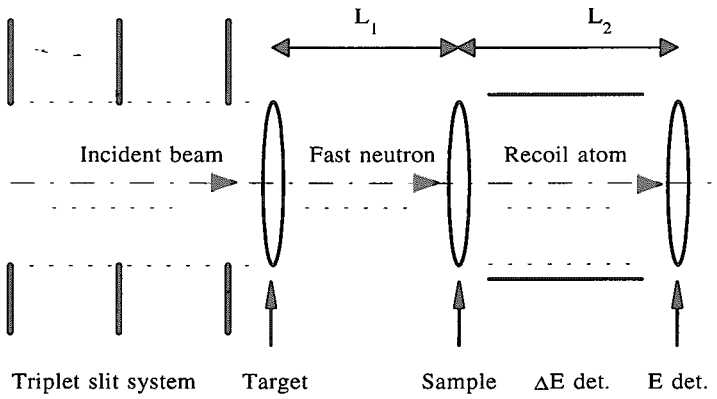


Fig.1 A schematic view of experimental condition of the present NERD measurements. The diameter of the target, sample and E-detector are 8 mm. Both distances between the target and the sample (L_1) and that between the sample and the E-detector (L_2) are 50mm.

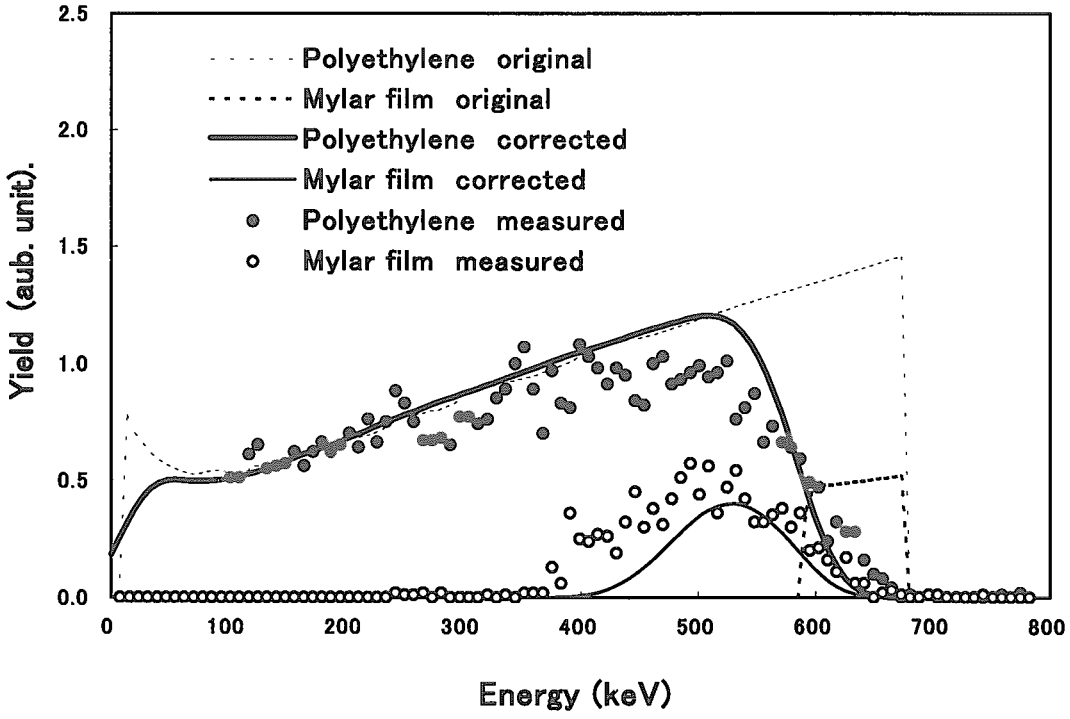


Fig.2 Measured and calculated spectra of recoil hydrogen atoms from a thick PE sheet and a 2 μm Mylar films. The calculated spectra were obtained from eq. (1) and considering the actual experimental conditions.

5.5 In-situ Observation of Formation of Graphitic Onions under Ion Implantation

Hiroaki Abe
Department of Materials Development, JAERI

1. Introduction

The spherical or ellipsoidal concentric graphitic clusters (carbon onions) have raised scientific and technological interests since they are expected as solid lubricants and others. The carbon onions have been formed, typically in transmission electron microscopes, due to high intensity of electron irradiation in soot [1]. The physical and chemical properties are still unknown because of extremely low production yield. Ion implantation could be the promising method for the mass production. In this work, we have performed in-situ [2] and ex-situ [3] observation of microstructural evolution of onions under ion implantation, together with high-resolution electron microscopic observation, for the purpose of clarifying their nucleation and growth mechanism.

2. Experiments

Mechanically polished polycrystalline copper substrates to an optical grade were used as implantation samples. Some of the samples were annealed at 773 K for 9 hrs prior to implantation. The substrates were implanted with 100 keV carbon ions at temperatures from 573 K to 973 K to the fluence from 5 x 10^{16} to 2 x 10^{18} ions/cm^2 at the Takasaki Ion Accelerators for Advanced Radiation Application (TIARA) in Japan Atomic Energy Research Institute (JAERI). Characterization of the microstructure was done by transmission electron microscopy (TEM) and by high-resolution electron microscopy (HREM) in JEM-4000FX. In-situ observation of microstructural evolution in copper at 783 K under 100 keV C^+ implantation was performed in well-annealed TEM samples (1273 K for 10 hrs). The microstructural evolution was videotaped and image processed in computers.

3. Results and Discussion

Spherical and ellipsoidal clusters were observed together with amorphous carbon layers at the temperature investigated as shown in Figure 1. The clusters were the assembly of concentric spherical or ellipsoidal graphitic layers with interlayer distance of 0.34 nm, determined by TEM, HREM, diffraction and energy loss spectroscopy. The carbon clusters consist of carbon onions and nanocapsules, former of which have their interiors completely filled up with graphitic shells, and the latter of which have cavities. Most all of the nanocapsules have hollow cores, while rarely observed were with copper particles. The morphology was evaluated from the Fresnel fringes around the cavities and particular contrast arising from

crystalline structure or from the thickness contrast. Fraction of carbon onions to the total number of the carbon clusters was about 10 ~ 20 % in defective polycrystalline substrates. The fraction seemed higher in the substrate with the better crystallinity. The averaged size of carbon clusters was about 10 nm in Cu implanted at 576 K to the fluence of 5 x 10^{17} C/cm^2. Above 677 K at the same fluence, the size distribution had peaks at 12 nm and at 24 or over, where onions and nanocapsules were major in the smaller and larger peaks, respectively. Especially at temperature above 973 K, huge onions whose diameter was even more than 100 nm were formed. The formation rate was, on the other hand, high at lower temperature and vice versa. It was about 2 x 10^{-7} clusters/ion in the substrate implanted at 576 K. The rate decreased one tenth and fortieth at 677 K and 973 K, respectively. Total amount of the carbon clusters was the order of 0.1 mg/cm^2 corresponding to 10^9 and 10^7 clusters/cm^2 at 573 K and 973 K, respectively.

The in-situ observation of microstructural evolution in copper under ion implantation was performed at 783 K. Throughout the irradiation, strain contrast features corresponding to incoming ions were observed. Energetic ions produce bunches of displacements, so-called displacement cascades, from which secondary defects such as dislocation loops are formed and raise the strain contrast [4]. Since the recombination of point defects is so enhanced at the temperature, the features disappeared in seconds as previously observed in Cu and Ni [5].

At the fluence of 1.1 x 10^{17} C/cm^2, we observed the whitish or blackish circular contrast features, whose size was about 5 nm in diameter. Both phase and strain contrast was observed, indicating that they were the second phase located inside of specimen. They were carbon onions, being stable and increase in size and number with implantation fluence. Onions grow about 14 nm in diameter by the further implantation of 1 x 10^{17} C/cm^2 (about 1hour). The growth rate of onions was roughly 9 nm/hr in the first one hour since they nucleated. Figure 2 (a) shows the phase contrast features corresponding to onions after implantation to the fluence of 4.6 x 10^{17} C/cm^2 at 783 K. Onions randomly distributed inside specimen, while they agglomerated at surface indicated by arrows. Cross-section of the TEM sample edge is usually wedge shape, where the evaporation rate is so high that change in surface morphology was observed in the real time scale. Ion irradiation seems to enhance evaporation, in addition to the high vapor pressure of copper comparing to other noble elements. We observed the evaporation made the embedded onions accumulate at the sample edge. Together with the phase contrast, they enhanced strain contrast in the surrounding media as shown in Figure 2 (b). The strain contrast was observed with a no-contrast line perpendicular to g vector, indicating that the onions nucleate inside enhancing isotropic strain in the media. Even in the onions agglomerated at sample edge, whose cross section is usually wedge-shape, we observed the copper thin

layers both over and under the onions. Evaporation rate must be much higher at 973 K, at which the atomic force microscopic observation found the agglomeration of onions at surface in copper implanted with 120 keV carbon ions [6], we presume the same mechanism worked in the experiments.

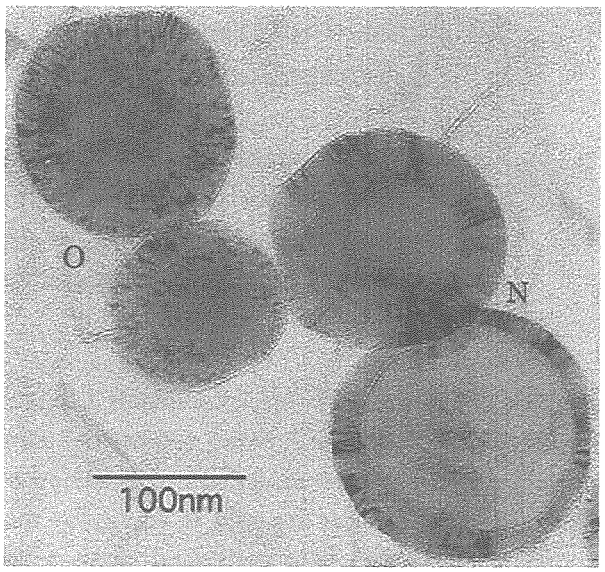


Figure 1. Carbon onions (O) and nanocapsules (N) formed by 160 keV C^+ fluence of 5 x 10^{17} C/cm^2 in copper at 973 K.

References

[1] D. Ugarte, Nature 359 (1992) 707.
[2] H. Abe, submitted to Diamond and Related Materials
[3] H. Abe, S. Yamamoto, A. Miyashita and K.E. Sickafus, submitted to J. Appl. Phys.
[4] K. Fukumoto, C. Kinoshita, H. Abe, K. Shinohara and M. Kutsuwada, J. Nucl. Mater. 179-181 (1991) 935-938.
[5] H. Sakaida, N. Sekimura and S. Ishino, J. Nucl. Mater. 179-181 (1991) 928.
[6] T. Cabioc'h, J.P. Riviere and J. Delafond, J. Mater. Sci. 30 (1995) 4787.

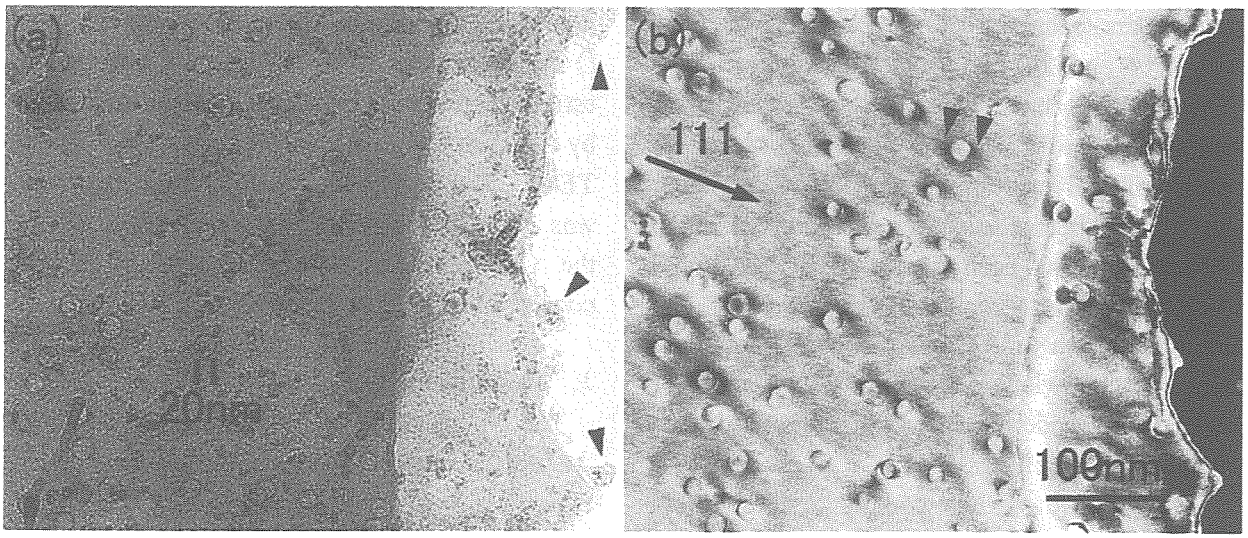


Figure 2. Bright-field (a) and center-dark-field (b) image in copper implanted with 100 keV C^+ ion fluence of 4.6 x 10^{17} C/cm^2 at 783 K showing strain and phase contrast, respectively. Arrows in (a) shows agglomeration of onions at surface, besides random distribution of onions inside sample. Isotropic strain contrast appears around onions as indicated with arrows in (b).

5.6 In-situ Observation of Growth Processes of Transition Metal Compound Thin Films by Ion-Implantation

Y. Kasukabe, H. Tani*, Y. Yamada*, H. Abe**
International Student Center/Department of Electronic Engineering, Tohoku University, *Department of Quantum Science and Energy Engineering, Tohoku University, **Department of Materials Development, JAERI.

1. Introduction

It is well known in transition metals that the valence d orbitals are more contracted than valence s and p orbitals and form a narrower band. The d orbitals are split in energy by the bonding interaction with the ligand atoms such as oxygen (O) and nitrogen (N) ones. The bonding interaction gives rise to transformations of the sublattice of transition metal compounds, and metallic as well as covalent and ionic properties, which make the compounds interesting for both technical applications such as hard coatings and diffusion barriers in microcircuits, and fundamental research[1]. The oxides of titanium (Ti), one of typical transition metals, are technologically important as catalyst supports and in photocatalytic applications[2]. These studies have revealed that properties of epitaxially-grown Ti oxide films are superior to those of polycrystalline ones. Then, much interest has been focused on the epitaxial films. Recently, it has been reported that NaCl-type TiN films were epitaxially grown by the N-implantation into evaporated Ti films[3]. However, knowledge of the growth processes of epitaxial Ti oxide films by O-implantation, is far from being complete.

The purpose of this work is first, to throw light on changes of the crystallographic structure of Ti films by O-implantation, using in-situ transmission electron microscopy (TEM), and then to discuss the epitaxial growth mechanism of Ti oxide films

2. Experimental

Detailed descriptions of the preparation of evaporated-Ti films were presented in the earlier paper[3]. The 100-nm-thick Ti films were deposited by an electron-beam heating method in an ultrahigh vacuum onto thermally cleaned NaCl substrates held at room temperature (RT). The ultimate pressure in the working chamber was less than 4×10^{-9} Torr. Oxygen ions (O^+) with 36 keV were implanted into the evaporated-Ti films at an angle of 30° to the surface normal. The implantation of O^+ was performed in the 400 kV analytical and high resolution TEM combined with ion accelerators at JAERI-Takasaki[4]. According to the results of Monte Carlo simulation using the TRIM code, the projected range of O^+ with 36 keV was 58 nm, and thus most of the implanted ions are thought to be retained inside the Ti films. The O concentrations in Ti films were able to be estimated from the implantation dose measured by a Faraday cage at the level of samples in the TEM. The maximum dose in this experiment was 3.29×10^{17} ions/cm^2, which corresponded to the O/Ti ratio of 0.58: the average atomic concentration of O in Ti films.

3. Results and discussions

The typical result of the TEM observation of the unimplanted Ti film is shown in Fig. 1. Figure 1(a) is an electron diffraction (ED) pattern taken from the 100-nm-thick Ti film. An analysis of Fig. 1 (a) indicates that hcp-Ti (lattice constants: a=0.296 nm, c=0.471 nm) and CaF_2-type TiH_x ($x \fallingdotseq 1.5$; lattice constant: a=0.441 nm) mainly exist in this film. The reflections indicated by the three-index system with an asterisk, * are obtained from TiH_x, whereas those indicated by four-index system are obtained from hcp-Ti. The bright field

(BF) image of Fig. 1(b) shows the band-like contrast indicated by an arrow, elongated in the <110> direction of TiH_x and NaCl. Figures 1(c) and 1(d) are, dark field (DF) images taken from reflections labeled 002* and $1\,\bar{1}\cdot 1$, respectively. The orientation relationships between the hcp-Ti and the NaCl substrate are $(03\cdot 5)$Ti//(001)NaCl and $[2\,\bar{1}\cdot 0]$Ti// $[\bar{1}\,10]$ NaCl: $(03\cdot 5)$-oriented hcp-Ti. On the other hand, the orientation relationship between the TiH_x and NaCl is $(110)TiH_x$//(001)NaCl and $[001]TiH_x$// [110]NaCl: (110)-oriented TiH_x. Figure 1 shows that (110)-oriented TiH_x grows mainly in the band-like contrast region, whereas epitaxial hcp-Ti grows only outside the band-like contrast regions as seen in Fig. 1(d).

Oxygen ions with 36 keV were implanted into the evaporated-Ti film which showed such ED pattern as Fig. 1(a). Figures 2(a) and 2(b) show, respectively, a typical ED pattern and BF image taken from the O-implanted Ti film with O/Ti=0.58. The DF image, Fig. 2(c) was taken from the 002 reflection in Fig. 2(a), whereas Fig. 2(d) was taken from the 200 reflection, where the reflections indicated by the three-index system are obtained from NaCl-type TiO_z. An analysis of Fig. 2 indicates that hcp-Ti (lattice constants: a=0.298 nm, c=0.491 nm) and TiO_z (lattice constant: a=0.421 nm) coexist in this film. The orientation relationships between hcp-Ti and NaCl are the same as those in unimplanted Ti films. Crystallites of TiO_z are grown in the two orientations; (110)-oriented TiO_z: $(110)TiO_z$ //(001)NaCl and $[001]TiO_z$ //[110]NaCl, and (001)-oriented TiO_z: (001) TiO_z //(001)NaCl and [100] TiO_z //[100]NaCl. It is noteworthy that reflections of TiH_x cannot be seen. Furthermore, it is revealed from Fig. 2 that (110)-oriented TiO_z crystallites are preferentially grown in the band-like contrast region indicated by an arrow, elongated in the <110> direction of NaCl and TiO_z. These suggest that the O-implantation induces the release of H from evaporated-Ti films containing TiH_x and the occupation of implanted-O atoms in octahedral sites of the H-escaped fcc Ti sublattice. This process results in the formation of the (110)-oriented TiO_z from (110)-oriented TiH_x without changing the orientation of the fcc-Ti sublattice.

On the other hand, (001)-oriented TiO_z

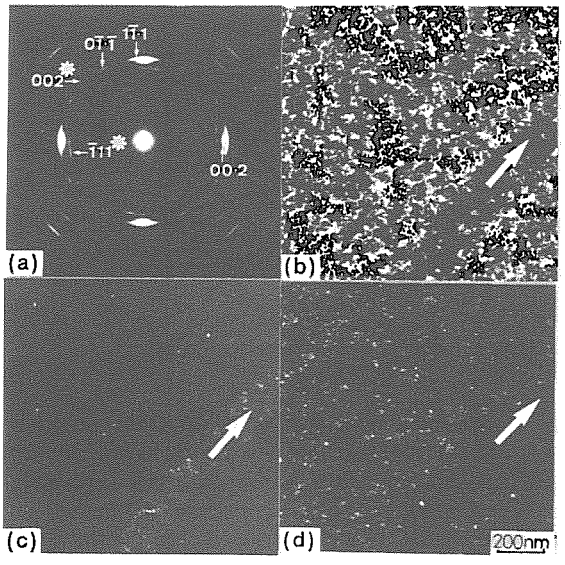


Fig. 1. ED pattern (a), and BF (b) and DF (c), (d) images taken from a 100-nm-thick Ti film. (c) and (d) were taken with the 002* reflection of TiH_x and the $1\,1\cdot 1$ reflection of hcp-Ti, respectively.

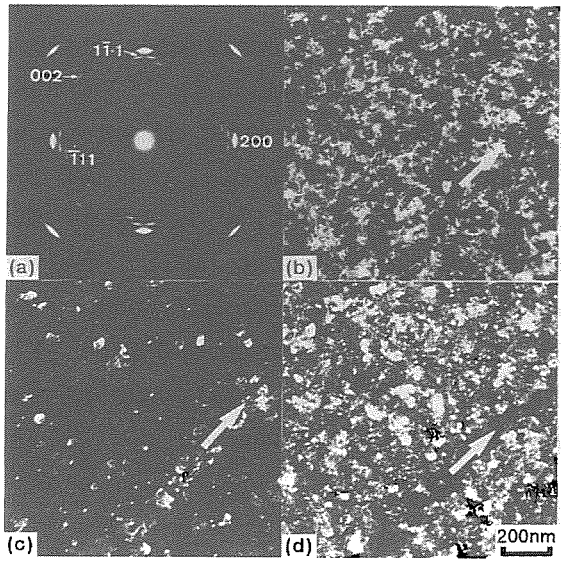


Fig. 2. ED pattern (a), and BF (b) and DF (c), (d) images taken from an O-implanted Ti film (O/Ti=0.58). (c) and (d) were taken with 002 and 200 reflections in (a), respectively.

crystallites grow preferentially outside the band-like contrast regions. It can be considered that the O-implantation into the (03 • 5)-oriented hcp-Ti leads to the epitaxial formation of the (001)-oriented TiO_z, as discussed below. Figure 3 shows the orientation relationship between (a) (03 • 5)-oriented hcp-Ti and (b) (001)-oriented fcc-Ti structures. Solid circles represent Ti atoms. Note that one of octahedral sites, which lies midway between F and K atoms in Fig. 3(a) corresponds to a midway site between F and K atoms in Fig. 3(b), which is an octahedral site in fcc-Ti. Thus, the occupation of octahedral sites in octahedra such as the GEFJKL in Fig. 3(a) by O leads to the occupation of octahedral sites of the transformed fcc-Ti by O. On the other hand, an octahedral sites in the BEKQAL octahedron in Fig. 3(a), which lies at the middle point between A and K atoms, is not an octahedral site in fcc-Ti, since in fcc-Ti (Fig. 3(b)) EKQA atoms form a rectangle, not a square. The PC*EKN*B* octahedron in Fig. 3(a) corresponds to the PCEKNB octahedron in Fig. 3(b). These mean that an O atom in the octahedral site of the BEKQAL octahedron in Fig. 3(a) diffuses to another octahedral site in newly formed octahedron such as the PCEKNB octahedron in Fig. 3(b), to form TiO_z. Therefore, it seems reasonable to conclude that the epitaxial growth of the (001)-oriented TiO_z can be caused by the transformation of hcp-Ti to fcc-Ti during the O-implantation, accompanied with the inheritance of the EFJK square and/or GEFJKL octahedron in Fig. 3(a), as well as the occupation of O in octahedral sites of the (001)-oriented fcc-Ti.

References

1) K. Sano, M. Oose and T. Kawakubo, Jpn. J. Appl. Phys. **34**, 3266,1995.

2) T. Suzuki and R. Souda, Surface Science **445**, 506, 2000.

3) Y. Kasukabe, N. Saito, M. Suzuki, Y. Yamada, Y. Fujino, S. Nagata, M. Kishimoto, and S. Yamaguchi, J. Vac. Sci. & Technol. **A16**, 482,1998.

4) H. Abe, H. Naramoto, K. Hojou, and S. Furuno, The TEM-Accelerators Facility at JAERI-Takasaki and its Application to Materials Science, JAERI-Research **96-047** (1996).

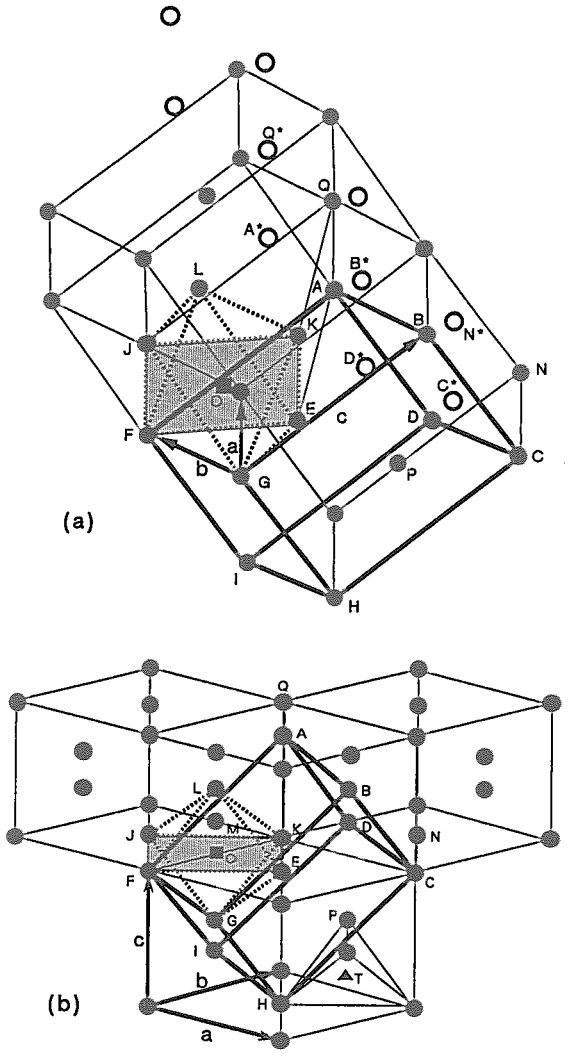


Fig. 3. Schematic representation of (a) (03•5)-oriented hcp-Ti and (b) (001)-oriented fcc-Ti structures. A unit cell of hcp- structure formed of A to I atoms in (a) can be transformed into a body-centred prismatic cell formed of A to I atoms in fcc-Ti in (b) by a shear. In (a), the open circles represent positions of Ti atoms shifted by the shear in order to obtain an fcc structure. The shifted C atom, for example, is represented by the open circle labeled C*. In (a) and (b), one of octahedral sites is marked by a solid square.

5.7 Depth-selective damage analysis of C_n^+(n=1-4) cluster irradiated polycarbonate by a variable-energy positron beam

K. Hirata, Y. Saitoh*, K. Narumi*, Y. Kobayashi, A. Kawasuso*, S. Okada* and K. Arakawa*

National Institute of Materials and Chemical Research, Tsukuba, Ibaraki 305-8565, Japan
*Advanced Radiation Technology Center, JAERI, Takasaki, Gumma 370-1292, Japan

1. Introduction

Implanted ions passing through a matter are slowed down by electronic and nuclear interaction with target atoms. On this slowing down process of implanted ions, irradiation damage is inevitably produced. Recent studies of cluster ion implantation revealed that the interactions of implanted cluster ions are different from those of single ions [1]. We applied a variable-energy positron beam to study damage produced by cluster ion irradiation for the first time and found that the *S* parameter at the near-surface region decreased with the increasing number of the atoms per one cluster [2]. In this paper, we estimate the thickness of the damaged layer, where a cluster effect at the near-surface region was observed.

2. Experimental

The C_n^+(n=1-4) ion irradiation to amorphous polycarbonate (PC) films with a thickness of 100 μ m and a density of 1.2 g/cm^3, which were kindly supplied by Mitubishi Chemical Co. Ltd., was carried out at JAERI/Takasaki [3]. Singly negative cluster ions were produced in a conventional Cs sputter ion source and injected into a 3MV tandem accelerator after mass separation. A small fraction of the negative cluster ions was stripped to singly positive ions and then accelerated at the second stage of the tandem accelerator, although most of the clusters were dissolved into the separated atoms by collision with a stripper N_2 gas in the terminal. The accelerated ions were analyzed by a separating magnet to obtain singly positive cluster ions. The implantation energy and dose of cluster ions were 0.5 MeV /atom (= 0.5 × n MeV/ion) and 1 × 10^{13} atoms/cm^2, respectively.

The variable-energy positron beam system at the National Institute of Materials and Chemical Research, details of which were described elsewhere [4,5], was used to measure positron annihilation Doppler broadening as a function of positron energy (*E*) between 80 eV and 30 keV. The spectra recorded with a high resolution Ge detector were characterized by the *S* parameter, which is the ratio of γ-ray counts in the central part of the 511 keV annihilation peak to the total counts contained in the whole peak.

3. Results and discussion

S-*E* curves for 0.5 MeV/atom-C_n^+ irradiated PC with a dose of 10^{13} atoms/cm^2 are shown in Fig. 1. The *S* parameters are normalized to the value for the unirradiated bulk sample. We can see in this figure that the *S* parameter at the near-surface region decreased with the increasing number of the atoms in one cluster.

When a cluster ion enters a material, the chemical bonds between cluster constituents are

immediately dissociated. The average distance between the tracks of the fragments increases with depth from the surface because of straggling and Coulomb repulsion between individual fragments. With further increasing of the depth from the surface, the average distance between the fragments originating from the same cluster becomes large enough to be considered as completely separated. Therefore, the irradiation damage at the near surface region is considerably influenced by cluster irradiation and the irradiation effect of individual ions becomes stronger with increasing of the depth from the surface.

Let us estimate the thickness of the cluster-irradiated region from the data in Fig. 1. The positron implantation profile $P(z,E)$ is often approximated by

$$P(z,E) = -\frac{d}{dz}\left[\exp(-\frac{z^2}{z0^2})\right] \quad \text{- (1)}$$

where $z_0 = (0.045/\rho)E^{1.6}$, ρ is the material density in g/cm^3 and E is the incident positron energy in keV [6]. The profile becomes increasingly broader with increasing incident positron energy because of enhancement of z_0 with positron energy. The depth dependence of S parameters of Fig. 1 is, thus, distorted. We assumed that the unfolded depth profiles for cluster-ion-irradiated samples could be divided into three regions: the cluster-ion-irradiated region, the single-ion-irradiated region and the bulk. The width and S of each region were fitted by means of a simple least-square analysis, so that the depth profiles folded with eq.(1) can reproduce the experimental data. In the analysis, the S parameter for the bulk region was fixed at 1 and that for the single-ion-irradiated region was equated to the value, which was obtained by fitting the data for single-ion-irradiated sample under the assumption that all damaged region is irradiated by single ions. The fitted values of thickness for the cluster region and the damaged region in total are listed in Table 1 and the depth dependence of the fitted S parameters is shown in Fig. 2. The average depths of implanted ions calculated by the TRIM code [7] are also included in the figure. The thickness of the cluster region, where the enhancement of irradiation damage is observed, is several nm for the studied energy of the implanted cluster ions.

References

[1] K. Narumi, K. Nakajima, K. Kimura, M. Mannami, Y. Saitoh, S. Yamamoto, Y. Aoki and H. Naramoto: Nucl. Instr. and Meth. in Phys. Res. B **135**, 77 (1998).

[2] K. Hirata, Y. Saitoh, Y. Kobayashi, A. Kawasuso, S. Okada and M. Saidoh: JAERI-Review **99-025**, 193 (1999).

[3] Y. Saitoh, K. Mizuhashi and S. Tajima: JAERI-Review **97-015**, 240 (1997).

[4] Y. Kobayashi, I. Kojima, S. Hishita, T. Suzuki, E. Asari and M. Kitajima: Phys. Rev. B**52**, 823 (1995).

[5] K. Hirata, Y. Kobayashi, S. Hishita, X. Zhao, Y. Itoh, T. Ohdaira, R. Suzuki and Y. Ujihira: Nucl. Instr. And Meth. in Phys. Res. B **121**, 267 (1997).

[6] Proceedings of Eighth Int. Conf. on Positron Annihilation, Gent, Belgium, 1988, eds. L. Dorikens- Vanpraet, M. Dorikens, D. Segers (World Scientific, Singapore, New, Jersey, Hong Kong, 1989) pp. 39-51.

[7] J. P. Biersack, L. G. Haggmark, Nucl. Instr. and Meth. **174**, 257 (1980).

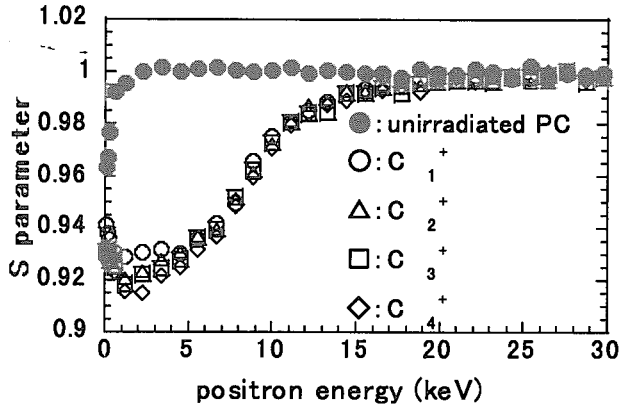


Fig. 1 *S-E* curves for unimplanted and 0.5 MeV/atom C_n^+-irradiated PC. Ion-implantation was performed under the condition of the same atomic dose (= 10^{13} atoms/cm^2).

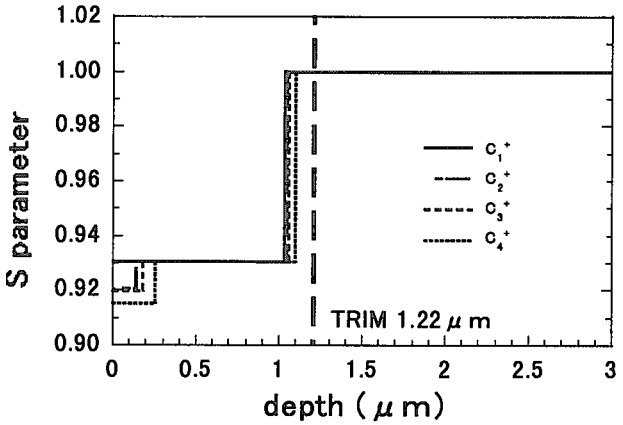


Fig. 2 Unfolded depth profiles of *S* parameter for PC irradiated with 0.5 MeV/atom C_n^+ with a dose of 1×10^{13} atoms/cm^2. We assumed that the unfolded depth profile can be approximated to a step function. The width and depth of the step were fitted by means of a simple least-square analysis.

Table 1 Fitted values of thickness for the cluster region and the damaged region in total. Diffusion of positron and positronium was not taken into account because their diffusion coefficients in PC are small. *S* parameters at positron energies below 1 keV were not included in the analysis.

Ion	energy (MeV/atom)	cluster region (μm)	total damaged region (μm)
C_1	0.5	---	1.01±0.02
C_2	0.5	0.14±0.04	1.05±0.02
C_3	0.5	0.18±0.03	1.06±0.02
C_4	0.5	0.25±0.03	1.10±0.02

5.8 Positron Annihilation Study of Defects Produced in Pd by Ion Implantation and Their Effects on Hydrogen Storage

H. ABE[1], A. UEDONO[2], S. OKADA[3] and H. ITOH[1]

[1] Department of Material Development, JAERI

[2] Institute of Applied Physics, University of Tsukuba

[3] Advanced Science Research Center, JAERI

1. INTRODUCTION

For practical use of palladium (Pd) as a hydrogen storage, it is important to improve the hydrogen solubility in the material. The hydrogen storage concentration and the rate of hydrogen absorption has been reported to depend strongly on the surface state of metals[1, 2]. Ion implantation is known to be a quite useful method for the surface modification of materials[2, 3]. Based on it, the hydrogen solubility in Pd is expected to have some effect on surface modification by ion implantation.

In order to examine the effects of ion implantation on the hydrogen absorption in Pd[4], we have implanted protons into Pd. Defects introduced by proton implantation was investigated by using positron annihilation measurements[5]. Hydrogen storage concentration and rate of hydrogen absorption in ion implanted Pd were also measured. Based on the obtained results, we discuss the correlation between ion implantation and hydrogen absorption in Pd.

2. EXPERIMENTAL

The samples used in this experiment were Pd sheets (99.99% purity) with a size of 10 x 10 x 0.1 mm^3. Before implantation, all Pd samples were annealed at 1073 K in a flowing pure N_2 gas (99.9998% purity). Ion implantation was performed with 100 keV-protons at dosed up to 1 x 10^{16} /cm^2.

Positron annihilation measurements made at University of Tsukuba[6]. Doppler-broadening profiles of annihilation γ-rays for the unimplanted and implanted samples were obtained at room temperature by using slow positron beams with energies up to 30 keV. A spectrum of annihilation γ-rays (total counts of 5 x 10^5) was measured with a Ge detector for each positron energy (E). The observed spectrum was characterized by the S-parameter, which is defined as the ratio of the yields in an energy range of 511±0.75 keV to the total yields. The S-E relation was analyzed by using a computer code VEPFIT[7] which can solve an equation of one-dimensional diffusion of positrons.

Hydrogen absorption measurements were also carried out for the unimplanted and implanted samples. After the introduction of each sample into a reaction tube, inner gas was exhausted to a vacuum level of 1 x 10^{-5}. Next, a pure H_2 gas (99.99999% purity) was introduced into the reaction tube, which is a component of a Sieverts' type apparatus, to a pressure of 1.52 x 10^3 Torr. To obtain the reaction rate of hydrogen in the samples, a change in the hydrogen pressure in the reaction tube was monitored. The total amount of hydrogen absorbed to the samples were derived from the difference between the saturated hydrogen pressure and the initial one.

3. RESULTS AND DISCUSSION

The S-E relation for the sample implanted with 1 x 10^{16} H^+/cm^2 is shown in Fig. 1. The data for the unimplanted sample is also represented in the figure for comparison. In the unimplanted sample, the S-parameter increases with decreasing positron energy, which is attributable to out-diffusion of positrons and their annihilation at the surface. The diffusion length of positrons (L) is

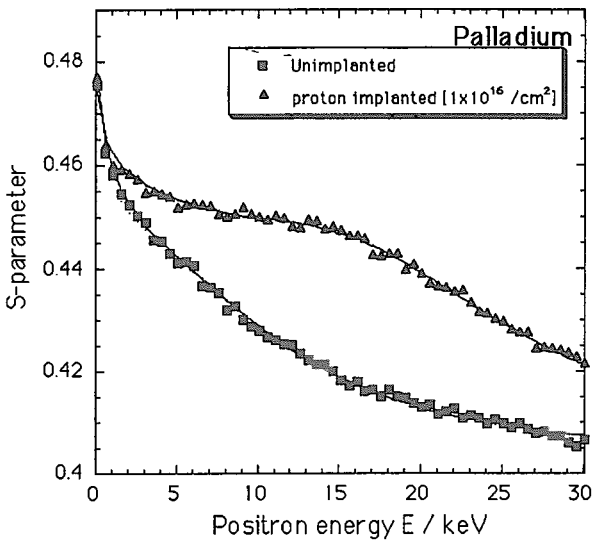


Fig.1. *S*-parameter as a function of incident positron energy (*E*) for the unimplanted and implanted Pd samples. The dose of protons was 1 x 10^{16} /cm^2. Fitting results are also represented by solid lines.

estimated to be 162±1 nm, which is close to the *L* values reported for pure Cu and Ni[8, 9]. This result suggests strongly high quality of the Pd samples used. For the implanted sample, large *S* values compared with those for the unimplanted Pd are obtained, as shown in Fig. 1. The increase of *S* indicates the formation of vacancy-type defects, probably vacancy clusters, due to proton implantation.

From a fitting to the *S-E* curve obtained for the implanted sample, the *S*-parameter and the depth of a defective region are obtained to be 0.4509±0.0001 and 400±10 nm, respectively. The latter value is in good agreement with the calculated range of defect production using TRIM[10]. The positron diffusion length is also estimated to be 37±2 nm. Such a small value of the diffusion length of positrons also indicates the generation of vacancy clusters in Pd.

To examine the influence of defects induced by implantation on hydrogen storage in Pd, we have measured the concentration of hydrogen absorbed in the unimplanted and implanted samples.

The results are shown in Fig. 2, where the ordinate indicates the ratio of absorbed hydrogen atoms to Pd atoms per unit volume (*H/Pd*). The maximum hydrogen concentration (*H/Pd* = 0.7) in the implanted sample is almost the same as that in the unimplanted one. This result can be explained by the fact that the volume of the implanted region is much smaller than the total volume. The absorption reaction rate (*r*) of hydrogen can be determined from a temporal change in the *H/Pd* value in a linear region[11]. In the unimplanted sample, the rate r_0 is estimated to be 2.41 x 10^{-3} /sec. On the other hand, the r_{imp} in the implanted sample is 1.61 x 10^{-3} /sec. These results show that the

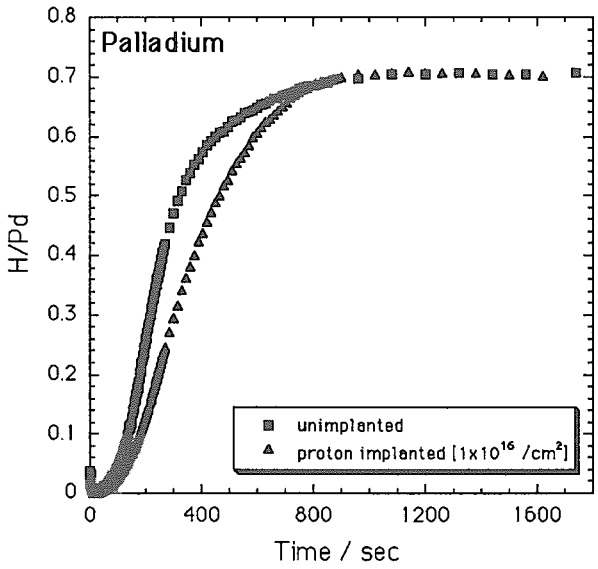


Fig.2. Change in the ratio of absorbed hydrogen atoms to Pd atoms per unit volume (*H/Pd*) for the unimplanted and implanted samples.

hydrogen absorption in ion implanted Pd occurs slowly compared with that in unimplanted Pd. This fact could be accounted for by the blocking effect of defects on the introduction of hydrogen into Pd. Similar hydrogen blocking and/or trapping effects of defects has been reported for several materials like Ni and Si[12-14]. Further investigations are

needed to clarify the mechanisms behind the observations.

ACKNOWLEDGEMENTS

The authors would like to appreciate Prof. H. Uchida and Dr. A. Komatsu in Tokai University and Dr. Z. Yoshida and his group members in Advanced Science Research Center of JAERI for their cooperation in the hydrogen absorption experiments as well as valuable discussion.

References

1) Y. Ohtani et al., J. Less-Common Metals 172-174 (1991), p.841.
2) H. Uchida, Int. J. Hydrogen Energy 24 (1999), p. 861.
3) H. Uchida et al., J. Alloys Comp. 293-295 (1999), p. 30.
4) T. Kuji et al., J. Alloys Comp. 293-295 (1999), p. 19.
5) P. Asoka-Kumar et al,. Appl. Phys. Lett. 57 (1990), p.1634.
6) A. Uedono et al., J. Appl. Phys. 87 (2000), p. 4119.
7) A. van Veen et al.,: AIP Conf. Proc. 218 (1990), p.171.
8) A. Uedono et al., Phy. Lett. A 129 (1988), p.249.
9) A. Uedono et al., J. Nuclear Materials 184 (1991), p.191.
10) J. F. Ziegler, *Handbook of Ion Implantation Technology* (Elsevier, Amsterdam 1992), p. 1.
11) P. Krueger, J. Phys. Chem. Solids, 54 (1993), p.1549.
12) J. E. Angelo et al., Modell. Simul. Mater. Sci. Eng. 3 (1995), p. 289.
13) H. Osono et al., J. Alloys Comp. 231 (1995), p. 41.
14) S. Kar et al., Appl. Phys. Lett. 60 (1992), p. 3001.

5.9 Magic Number Vacancy Clusters in Si by High Precision Positron Lifetime Measurements with Internal Positron Source of ^{22}Na

M. Hasegawa, Y. Nagai, Z. Tang, K. Nakazuru, M. Maekawa*, A. Kawasuso* and S. Okada*

Institute for Materials Research, Tohoku University;
*Department of Materials Development, JAERI, Takasaki

1. Introduction

Vacancy-type defects (vacancy and n-vacancy aggregation V_n) have crucial effects on various properties of the host materials and thus have been intensively studied. However, the natures of the V_n clusters, for example, those in Si generated during crystal growth and device fabrication by dry etching or ion implantation, are still unclear to a large extent. Based on a simple consideration of the number of dangling bonds induced by the vacancy clusters, Chadi and Chang[1] predicted that V_6 ring and V_{10} cage closed by four V_6 rings in Si are particularly stable (namely, they are magic vacancy clusters V_n with the magic numbers n=6 and 10), which is supported by a successive first-principles calculation. Recently we have evidenced for magic number vacancy clusters V_6, six-membered-ring vacancy clusters, in the basal planes of the crystal structure of graphite by combining positron annihilation experiments and first-principles calculations[2]. However, the magic V_n clusters in Si are not yet well evident experimentally due to the difficulties in identification of the vacancy clusters.

Positron annihilation techniques have been extensively used for studies of vacancy-type defects in Si. Especially positron lifetime is a sensitive tool to detect vacancy clusters in Si. Here to study magic number vacancy clusters V_6 and V_{10}, we employ a high precision positron lifetime measurements. Furthermore, to reduce ambiguity from the positron source component (Mylar or Kapton film component), we use an internal (in-situ) positron source of ^{22}Na induced by a nuclear reaction of high energy protons [$^{28}Si(p, ^{7}Be)^{22}Na$].

2. Experimental

In this study we prepared undoped Czchralski-grown (CZ) Si single crystal wafer samples (20x20x0.5mm). The content of oxygen in CZ-Si is a few tens of appm. These samples were stacked in an aluminum holder and cooled by He gas during irradiation. The stacked samples were irradiated with 70 MeV-protons from TIARA cyclotron to a fluence of $4x10^{17}$ cm^{-2}. The irradiation temperature was less than 100℃. The same samples were also irradiated at JMTR and JRR-3 with fast neutrons to doses to $3.4x10^{19}$ and $1.5x10^{20}n/cm^2$, respectively, below 100℃.

Positron lifetime measurements carried out on the stacked 4 samples at room temperature using a fast-fast spectrometer with a time resolution of 160 ps and an internal positron source of 22-Na (about 0.2MBq). The positron lifetime spectra were analyzed into continuous lifetime distributions by the computer program CONTIN[3], which is based on the theory of Laplace inversion. In this analysis, more than $1x10^7$ total counts were accumulated.

3. Results and Discussion

After irradiation positron lifetime spectra were well decomposed into two exponential components with time constants τ_i and relative intensities I_i (I=1,2 and $I_1 + I_2 = 1$).

Figure 1 shows isochronal annealing behavior of longer lifetime τ_2 and its intensity I_2 due to positron trapped at irradiation-induced vacancy clusters obtained from the usual two component analysis, PATFIT[4], of lifetime spectra of the neutron-irradiated samples. Positron lifetimes of vacancy clusters from first-principles calculations are presented on the right-hand vertical axis. In the as-irradiated state, the longer lifetime τ_2 of about 300 ps with I_2 more than 90% shows positrons are mostly trapped at divacancies. Around 200℃ the divacancies can migrate and thus form higher aggregations of vacancies. The sample of the lower dose irradiation of $3.4\text{x}10^{19}\text{n/cm}^2$ show a small increase in τ_2 by annealing below 400℃. The sample of the higher dose irradiation of $1.5\text{x}10^{20}\text{n/cm}^2$ show nearly the same annealing behavior of τ_2 below 300℃ with that of the lower dose irradiation. However, at 350 – 450℃ τ_2 of the higher dose irradiation is longer than that of the lower dose irradiation. These longer lifetimes for the higher dose suggest the larger vacancy clusters between 350 and 450℃. This stage corresponds to the vacancy aggregation process from V_2 to V_6.

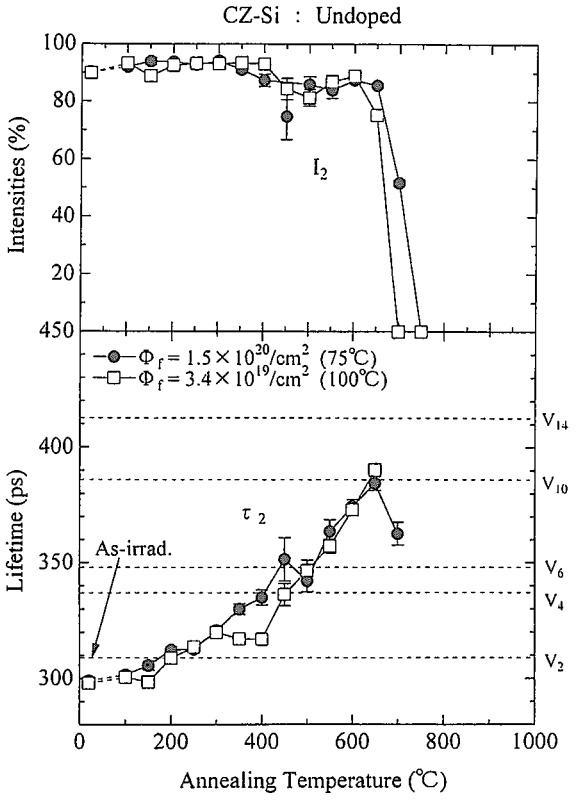


Figure 1. Post-irradiation annealing behavior of the longer positron lifetime components and its relative intensity I_2 in neutron-irradiated samples: On the right vertical axis, positron lifetimes at vacancy clusters obtained from a first-principles calculation are presented.

At about 500℃ τ_2 is about 350 ps which is corresponding to V6. Then τ_2 increases rapidly to about 385ps (V_{10}) with annealing temperature up to 650℃ in almost the same way both for the lower and higher dose irradiation. This strongly suggests that in this annealing temperature range vacancy aggregations of V_6 and V_{10} are preferentially formed and further that their fraction of the number densities nv10/nv6 is almost constant during this annealing temperature range. This coexisting of V6 and V10 will give nearly the same annealing behavior of τ_2 for the lower and the higher dose irradiation, which indicates that V_6 and V_{10} are the stable vacancy clusters.

To confirm the formation of the stable vacancy clusters, we employed CONTIN analysis of positron lifetime spectra with the total counts more than $1\text{x}10^7$. Figure 2 shows the positron annihilation rate distribution for the samples after proton irradiation and neutron irradiation against the annihilation rate λ : the positron lifetime is given by $\tau = 1/\lambda$. The peaks at 250 – 300 ps are due to the lifetime distribution from positrons trapped at vacancy-oxygen complexes and vacancy clusters in the as-irradiated states. To see the coexistence of V_6 and V_{10} , the internal positron source method has an advantage of being free from the source component from the ^{22}NaCl and the Mylar covering film; the source component of about 350ps (about 8%) gives nearly the same positron lifetimes of the magic number vacancy clusters and thus may causes

some ambiguity in the analysis of positron lifetimes for the vacancy clusters. To obtain stable results in the analysis of the longer lifetimes for the vacancy clusters, we have found that it is very necessary to accumulate the total counts more than $3x10^7$, as shown in Fig.2.

The internal source method is found to be promising in the analysis. However, the induced activity of 22-Na was too weak to give high total counts in usual run time of less than a few days. In future experiments it is very necessary to induce the activity of 1MBq. Now detailed experimental and theoretical studies are in progress.

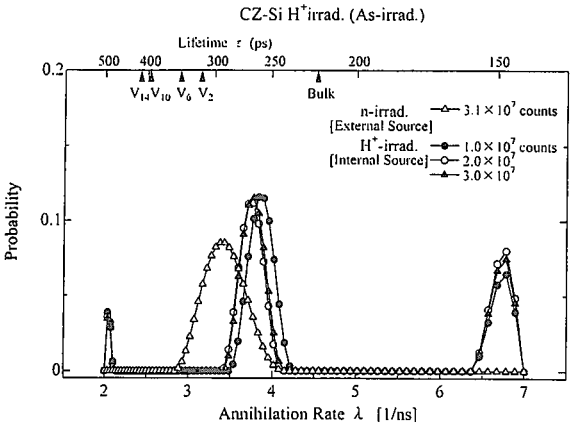


Figure 2. Positron annihilation rate distribution in the proton-irradiated sample containing the internal positron source. The distributions for the neutron irradiated sample with various total counts are also shown.

References

1) D.J. Chadi and K.J. Chang: Phys. Rev. **B38** (1988) 1523.

2) Z. Tang, M. Hasegawa, T. shimamura, Y. Nagai, T. Chiba, Y. Kawazoe, M. Takenaka, E. Kuramoto and T. Iwata: Phys. Rev. Lett. **82** (1999) 2532.

3) Y.C. Jean and G.H. Dai: Nucl. Instr. Meth. **B79** (1993) 356.

4) P. Kirkegaad, N.J. Pederson and M. Eldrup, PATFIT-88, Riso-M-2740 (Riso, 1989).

This is a blank page.

6. Nuclear Science and Radioisotope Production

6.1 Production of the Positron Emitters of Metallic Elements for Plant Physiology: ^{52}Fe ·····205
S. Watanabe, N.S. Ishioka, A. Osa, M. Koizumi and T. Sekine

6.2 Development of a Radioactive Endovascular Stent by Implantation of ^{133}Xe Ions (2) ·····207
S. Watanabe, A. Osa, N.S. Ishioka, M. Koizumi, T. Sekine,
A. Hasegawa and M. Yoshii

6.3 Effectiveness of ^{133}Xenon Implanted Radioactive Stent to Prevent Restenosis after Balloon Injury ·····208
A. Hasegawa, A. Miyajima, E. Okamoto, A. Nakano, M. Kurabayashi, S. Watanabe,
N.S. Ishioka, T. Sekine, A. Osa and M. Koizumi

6.4 Production of Polarized Beam of Unstable Nuclei via Ion Surface Interaction at Grazing Incidence and Tilted Foils ·····209
S. Ohya, T. Ohtsubo, J. Goto, Y. Izubuchi, H. Sato, T. Izumikawa, S. Muto,
A. Osa, M. Koizumi and T. Sekine

6.5 Internal Conversion Electron Measurements of Neutron-deficient Isotopes in Rare-earth Region with a Si (Li) Detector ·····211
M. Shibata, H. Yamamoto, K. Kawade, A. Taniguchi, A. Osa,
M. Koizumi and T. Sekine

6.6 Ion-source Development for the TIARA On-line Isotope Separator ·····213
M. Koizumi, A. Osa, T. Sekine, H. Katsuragawa, Jin-Wei-Guo, T. Wakui, Y. Ishida,
J. Sun-chan, H. Ishiyama and H. Miyatake

6.7 Systematic Behavior on Mössbauer Isomer Shifts of ^{133}Cs Implanted into Transition Metals ·····216
H. Muramatsu, K. Yoshikawa, H. Shimomura, T. Miura, S. Watanabe,
M. Koizumi, A. Osa and T. Sekine

This is a blank page.

6.1 Production of the positron emitters of metallic elements for plant physiology: ^{52}Fe

S. Watanabe, N. S. Ishioka, A. Osa*, M. Koizumi*and T. Sekine
Department of Radiation Research for Environment and Resources, JAERI,
Department of Materials Science, JAERI

1. Introduction

Since studies on physiological functions of plants were started in TIARA with the development of the positron emitting tracer imaging system (PETIS), positron emitters to be used for this purpose have been produced with the TIARA AVF cyclotron. We presented production methods of the positron emitter-labeled compounds [^{11}C]CO_2, [^{11}C]methionine, [^{13}N]NO_3^-/NO_2^-, [^{13}N]NH_4^+, [^{18}F]F^-, [^{18}F]FDG, [^{48}V]aqueous, [^{52}Mn] aqueous and [^{62}Zn] aqueous.[1, 2] The present paper describes a production method of the positron emitter ^{52}Fe.

Iron-52 decays with a half-life of 8.275 h 57% by positron emission and 43% by electron capture to ^{52m}Mn, and successively the daughter ^{52m}Mn decays with a half-life of 21.1 m 96.7% by positron emission and 1.6% by electron capture to stable ^{52}Cr and 1.75% by isomeric transition to ^{52}Mn. Manganese-52 decays with a half-life of 5.591 d 28% by positron emission and 72% by electron capture to stable ^{52}Cr.

Assuming that the ^{52}Fe in a plant is at radioactive equilibrium with the daughter ^{52m}Mn, and the ^{52m}Mn does not migrate far from the parent ^{52}Fe before the ^{52m}Mn decays, we can count the positron emissions from the ^{52m}Mn as those from the ^{52}Fe.

The amount of ^{52}Mn generated by the isomeric transition of ^{52m}Mn should be considered for the measurement with PETIS, because ^{52}Mn is also a positron emitter and long-lived. We will discuss the effect of the growth of ^{52}Mn in measurement.

2. Experimental

Iron-52 was produced in the ^{nat}Cr (α, xn) ^{52}Fe reaction by bombarding a 1500 μm thick chromium foil (natural isotopic composition, 99.99% purity, Goodfellow Metals Ltd.) with a 100-MeV alpha beam from the TIARA AVF cyclotron. About 3.5 MBq of ^{52}Fe was produced using a beam current of 3 μA for 2 hours. The radiochemical separation of the ^{52}Fe from the target was carried out by the method described by Fesser *et al.*[3] with two minor modifications as follows:

1) After the chromium target was dissolved in 12 M HCl, the hydrogen peroxide, which was added to ensure complete oxidation of the ^{52}Fe, was decomposed by boiling the solution in order to avoid the formation of bubbles in the anion exchange column;

2) For the elution of $^{52}Fe^{3+}$, 0.01 M HCl was adopted instead of 0.05 M HCl, because a solution with a low ionic strength must be supplied to plants.

The first 2 ml effluent of 0.01 M HCl with a relatively high radioactivity was supplied for experiments on plants. The radiochemical purity in the tracer solution was checked by γ-ray spectrometry using a HPGe detector.

3. Results and Discussion

In the γ-ray spectra of the final solution, no radiochemical impurity was found, as

shown in Fig. 1, except for the daughter ^{52m}Mn and the granddaughter ^{52}Mn.

The β^+-ray ratio $\beta^+(^{52}Mn)$ / $[\beta^+(^{52}Fe) + \beta^+ (^{52m}Mn)]$ was calculated as a function of time on the basis of their β^+ branchings and half-lives mentioned-above (Fig. 2). Eight hours after the end of bombardment, when a typical measurement in plant study ends, the ratio is 1.5 x 10^{-4}. Therefore, we can conclude that the effect of the ^{52}Mn growth is negligible in this plant study.

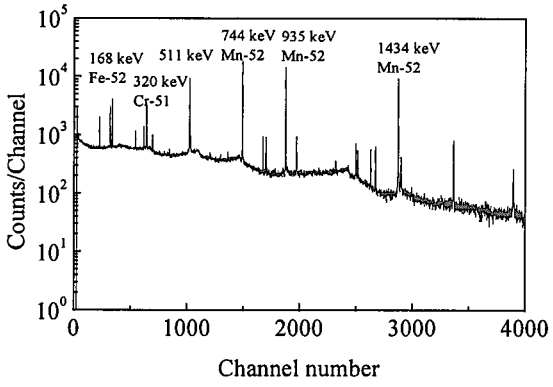


Fig. 1 a) A γ-ray spectrum of the irradiated target before chemical separation.

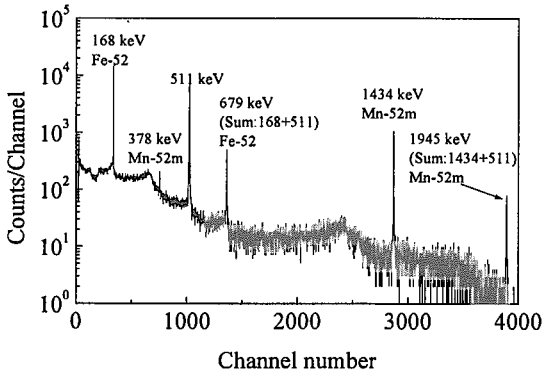


Fig. 1 b) A γ-ray spectrum of the final solution.

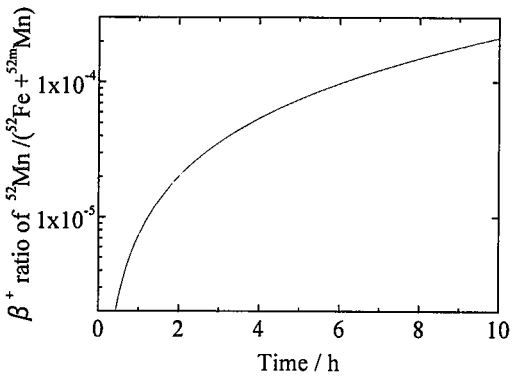


Fig. 2 The β^+-ray ratio $\beta^+(^{52}Mn)$ / $[\beta^+(^{52}Fe) + \beta^+ (^{52m}Mn)]$ with time from the end of bombardment.

References

1) N. S. Ishioka, H. Matsuoka, S. Watanabe, A. Osa, M. Koizumi, T. Kume, S. Matsuhashi, T. Fujimura, H. Uchida, A. Tsuji and T. Sekine, J. Radioanal. Nucl. Chem., 239 (1999) 417.

2) S. Watanabe, N. S. Ishioka, A. Osa, M. Koizumi and T. Sekine, JAERI-Review 99-025, 201-202 (1999).

3) A. Fessler, Z. B. Alfassi and S. M. Qaim, Radiochimica Acta, **65** (1994) 207.

6.2 Development of a Radioactive Endovascular Stent by Implantation of ^{133}Xe Ions (2)

S. Watanabe[1], A. Osa[2], N. S. Ishioka[1], M. Koizumi[2], T. Sekine[1], A. Hasegawa[3], M. Yoshii[3]
[1]Department of Radiation Research for Environment and Resources, [2]Department of Materials Science, [3]School of Medicine, Gunma University

Introduction

Stent angioplasty is carried out for the therapy of coronary stenosis derived from arteriosclerosis. However, restenosis, which is the re-narrowing of the blood vessel after stent angioplasty, occurs in about 20% of patients. In our animal experiment, we have shown that ^{133}Xe radioactive stents has a potential to suppress restenosis.[1)]

In order to apply the ^{133}Xe radioactive stents to therapy, sealed sources of the radioactive stents are desired for clinical use. Therefore, leak tests of the radioactive stents are carried out.

Leak test by JIS-z 4821 method

According to the regulations listed in the JIS (Japanese Industrial Standard) –z-4821, the second glade tests for temperature, external pressure, impact and puncture, were carried out for the radioactive stents containing up to about 600 kBq of ^{133}Xe. After each test, the leak of the ^{133}Xe from the radioactive stent was evaluated by a gaseous emanation test as follows. A radioactive stent was placed in a gas-tight vial. After 3 hours, the gaseous contents in the vial were transferred to another vacuum vial using a needle. The ^{133}Xe radioactivity in the vacuum vial was determined by γ-ray spectrometry using a HPGe detector.

The ^{133}Xe radioactivity leaked by each of the radioactive stent was less than 200 Bq per 12 hours, which is the upper limit for leak of gaseous radioactivity in the test.

Immersion test

In order to estimate the amount of ^{133}Xe leaked by the radioactive stents when the stent is implanted into a coronary artery, immersion tests of the radioactive stents were carried out. A radioactive stent immersed in water in a gas-tight vial was allowed to stand at 40°C over night. Both the water and the gaseous contents in the vial were transferred to another vacuum vial in the same manner described above.

The ^{133}Xe amount leaked by a radioactive stent was more than 200 Bq per 12 hours. This result can be explained as follows. The oxide film formed on the surface of the stainless steel, of which the stents are made, may be damaged upon production of a stent and by the implantation of ^{133}Xe ions. From the damaged points, the corrosion of the stainless steel may begin, when the stent is immersed, leaking the ^{133}Xe atoms.

To decrease a ^{133}Xe leak, we are planning to renovate the damaged oxide film of the stainless steel after implantation of ^{133}Xe.

References

1) S. Watanabe, A. Osa, T. Sekine, N. S. Ishioka, M. Koizumi, T. Kojima, A. Hasegawa, M. Yoshii, E. Okamoto, K. Aoyagi, A. Miyajima, R. Nagai, Appl. Radiat. Isot., **51** (1999) 197.

6.3 Effectiveness of ^{133}Xenon Implanted Radioactive Stent to Prevent Restenosis after Balloon Injury

A. Hasegawa, A. Miyajima , E. Okamoto, A. Nakano, M Kurabayasi,
*S. Watanabe, *N.S. Ishioka, *T. Sekine, *A. Osa, *M. Koizumi
Gunma University. School of Medicine, Second department of internalmedicine,
*Department of Radiation Research for Environment and Resources, JAERI

1. Introduction

Restenosis following successful percutaneous coronary revascularization continues to represent a major problem limiting the clinical efficacy ofthis procedure. The underlying mechanisms of restenosis are comprised of acombination of effects from vessel recoil, negative vascular remodeling,thrombus formation and neointimal hyperplasia. Endovascular irradiation (EI) inhibits balloon-induced neointima formation in animals. Continuous low-dose-rate radiation delivered by P-32 radioactive stents, decaying witha half-life of 14.3 days and emitting a β ray with a maximum energy of 1.711 MeV, failed to reduce neoimtimal formation after 4 and 12 weeks. The purpose of this study was to determine the effects of β -emitting radioactive stents by direct ion implantation of Xenon-133, decaying with a half-life of 5.25 days and emitting a β ray with a maximum energy of 0.346 MeV, on reduction in neointimal formation in rabbits.

2. Methods and Results

A total of 15 Xe-133 radioactive beta-emitting stents with an activity level of 0.13 to 2.65 μ Ci (n=12, 1.6$\pm$0.8 μ Ci ; group 1), and 33.5, 36.8, and 41.5 μ Ci (group 2) were implanted in the abdominal aorta of rabbits. Histomorphometry was performed at 4 weeks in group 1. The percent area stenosis, the ratio of the neointimal area divided by the medial area (area within external elastic lamina minus area within internal elastic lamina), for the racioactive stents (39 $\pm$ 18%) was significantly smaller than that for the nonradioactive stents (58$\pm$20% $p<0.05$). An intravascular ultrasound (IVUS) is a new cardiological diagnostic technique which provides detailed cross-sectional images of the vessel wall. We evaluated the stent lumen cross-sectional area (CSA) in group 2. The percent area stenosis was lower within the irradiated stent than within the non-irradiated stent (30.6 $\pm$ 1.8% vs 45.7$\pm$3.4% , $p<0.01$).

3. Conclusion

Neointima formation in rabbits aorta is markedly suppressed by a beta-particle-emitting stent incorporating the radioisotope Xenon-133 with a short half-life.

Reference

1) S, Watanabe et al., Appl. Radiat. Isot. 51(2), 197-202,1999

6.4 Production of polarized beam of unstable nuclei via ion surface interaction at grazing incidence and tilted foils

S. Ohya, T. Ohtsubo. J. Goto*, Y. Izubuchi*, H. Sato*, T. Izumikawa**, S. Muto***, A. Osa****, M. Koizumi**** and T. Sekine****
Department of Physics, Niigata University, *Graduate School of Science and Technology, Niigata University, **Radioisotope Center, Niigata University, ***KEK, ****Department of Material Science, JAERI

1. Introduction

The polarized nuclear beam is a powerful tool for studying not only nuclear physics but also condensed matter physics and fundamental physics. We can easily see the nuclear magnetic resonance (NMR) by detecting β rays. Therefore, many techniques to produce the nuclear polarization have been investigated. The asymmetrical atomic collision process is useful to obtain the nuclear polarization[1]. The ion beam surface interaction at grazing incidence (IBSIGI) yields a large orientation in the distribution of the orbital angular momenta of the reflected atoms and ions. The large degree of polarization after the surface interaction results in a considerable transfer of asymmetry into the atomic and nuclear spin system via the hyperfine interactions. Since 1975, Andrä and his co-workers[2] have investigated and developed the IBSIGI technique with stable nuclear beams. Freier[3] observed the large nuclear polarization of $P(^{14}N) \sim 22\%$. Recently Vanderpoorten et al.[4] applied this method to the unstable nuclear beam. They observed the large polarization of $P(^{13}N) = 11\%$ for ^{13}N by detecting the β-ray asymmetry.

We have studied the production of the polarized beam using Cs isotope beam, but the observed polarization was very small[5]. The small polarization may be due to the low velocity of Cs beam. Freier[3] studied the beam velocity dependence of the atomic and nuclear polarization of ^{14}N. Therefore, in the present work we used a ^{21}Na beam that is about 6 times faster than Cs beams. We also measured the polarization using tilted foil method.

2. Experimental details

A 50 keV ^{21}Na ($T_{1/2}$ = 22.47 s) beam from the on-line isotope separator (ISOL) at the Japan Atomic Energy Research Institute (JAERI) was used in this study. The Na activities were produced using $^{12}C(^{12}C, xnyp)$ reactions with a 75 MeV ^{12}C beam. They were ionized in a surface-ionization ion source of the mass separator and ^{21}Na ions were separated from other isotopes. The ^{21}Na beam was collimated by a narrow slit and bent onto the target of Si single crystal by an electric field of 360 V/cm. The scattered ions passed through a free space and implanted in a NaF single crystal stopper. The static magnetic field B_0 of 0.086 T parallel to the polarization axis was applied at the NaF stopper in order to maintain the nuclear polarization during the implantation. The cancellation-magnetic field were applied between the target and stopper, because the strong leakage field of B_0 decouples the atomic and nuclear spins. Typical magnetic field in the flight path was

less than 10 gauss. To detect the β-ray asymmetry , two sets of the plastic scintillator of 40 x 40 x 2 mm were placed at 0° and 180° with respect to the polarization axis. For the NMR, an rf oscillating field was applied perpendicular to B_0. The magnetic moment of ^{21}Na is known as $\mu(^{21}\mathrm{Na}) = +2.38630(10)\ \mu_N$ [4]. With the value of the magnetic moment and B_0 an expected value of the resonance frequency is calculated, and we applied the rf frequency of 1005 ± 50 kHz. The nuclear polarization was observed by the β-ray asymmetry change with the rf filed. For the tilted foil method we used thin (4 $\mu g/cm^2$) carbon foils which were tilted about 45 degree.

3. Results and Discussion

The experimental have done several runs. Figure 1 shows a typical result. Open circles are the experimental data and closed ones are the weighted mean. The observed polarization was 0.05(16)%. This value is comparable with the one of ^{124}Cs: $P(^{124}\mathrm{Cs}) = 0.22(13)\%$. We measured also the polarization with the tilted foil method. The result of polarization was 0.33(22)%. The origin of the small polarization is now unknown. We should check the beam quality and the system carefully.

References

1) H.J. Andrä, Hyp. Interact. 5, 403, 1978.
2) H. Winter and R. Zimmy, Hyp. Interact. 22, 237, 1985.
3) R. Freier and H. Winter, Hyp. Interact. 73, 323, 1992.
4) P. Raghavan, Atomic Data and Nuclear Data Table 42, 190, 1989.
5) T. Ohtsubo et al., Hyp. Interact. 120/121, 695, 1999.

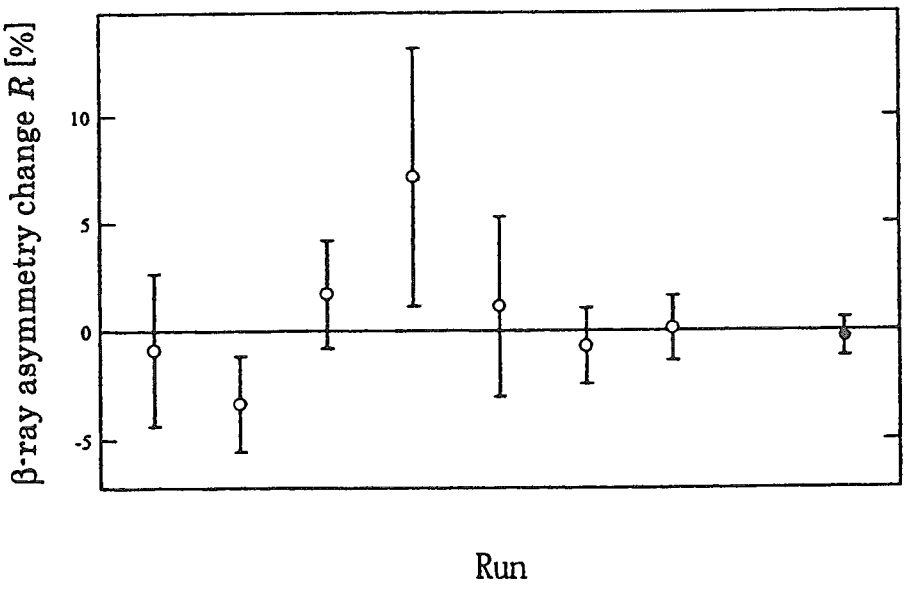


Fig. 1 Summary of experimental results of ^{21}Na.
The vertical axis shows the β-ray asymmetry change with the nuclear magnetic resonance by IBSIGI. Open circles show the experimental data. The closed circle shows the weighted mean of total data.

6.5 Internal Conversion Electron Measurements of Neutron-Deficient Isotopes in Rare-Earth Region with a Si(Li) Detector

M. Shibata, H. Yamamoto, K. Kawade, A. Taniguchi*, A. Osa**, M. Koizumi**, T. Sekine***

Department of Energy Engineering and Science, Nagoya University, *Research Reactor Institute, Kyoto University, **Department of Materials Science, JAERI, ***Department of Radiation Research for Environment and Resources, JAERI

1. Introduction

Spins and parities of excited states are important information for nuclear structure far from stability line. Multipolarity determination by means of internal conversion electron (ICE) measurements is an effective way to deduce parities experimentally. By using an on-line mass separator installed at the AVF cyclotron in JAERI, Takasaki, (TIARA-ISOL), Q_β and γ-γ angular correlation measurements have been carried out in the region of A=130 neutron-deficient rare-earth isotopes. In this year, a cooled Si(Li) detector was installed at the ISOL to measure ICEs in the decay of some La and Ba isotopes. The level structure in ^{126}Ba was intensively studied by in-beam spectroscopy[1,2]. It is also important to study with respect to ^{126}La decay including ICE measurements.

2. Experiment

For production of La and Ba isotopes, an Ar beam ($^{36}Ar^{8+}$, 195MeV) from the AVF cyclotron was irradiated on Mo targets (^{92}Mo : 97.4% enriched, ^{94}Mo : 93.9% enriched). The ^{126}La reaction products were ionized by a surface ionization technique in La monoxide (LaO^+) and mass-separated by the TAIRA-ISOL. The radioactive beams

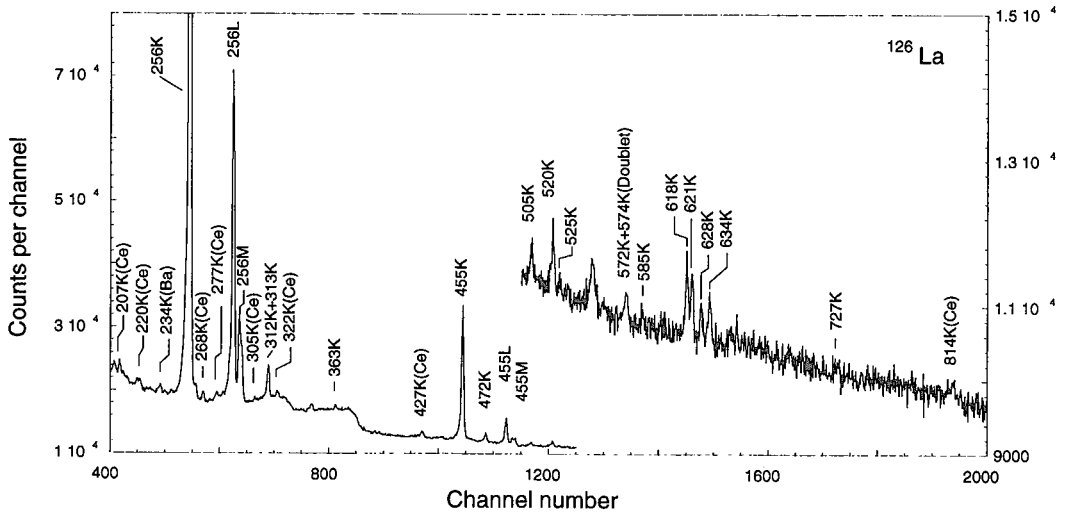


Fig.1 A singles spectrum of internal conversion electrons obtained with a Si(Li) detector in the decay of mass-separated beam of A=142. Electrons in the decay of both ^{126}La and ^{126}Ce were observed.

were implanted in a computer-controlled aluminized Mylar tape and transported to the counting position periodically. For measurements of ^{126}La decay, the tape was moved every 100 s, that is about 2 times the half-life of ^{126}La. (<50 s for low-spin and 54 s for high-spin[3]). At the counting position, a Si(Li) detector (300 mm^2×5 mm^t, provided from Eurisys co) for ICEs and a 38% HPGe detector for γ-rays were set in 180° geometry. Singles measurements were carried out with the detectors simultaneously. The decay of ^{126}La was measured for 16 hours totally.

3. Results and Discussion

A singles ICE spectrum in the decay of ^{126}La obtained with the Si(Li) detector is shown in Fig.1. This spectrum was obtained from the decay of ^{126}La for the first time. The ^{126}Ce, which is the parent nucleus of ^{126}La, was observed in the spectrum since it was also ionized in the condition of Cerium monoxide and it has almost the same half-life (50 s) of ^{126}La. The deduced k internal conversion coefficients (α_k) are shown in Fig.2 together with the theoretical values[4]. These values were deduced from the peak intensity ratios of electrons to γ-rays. The 256 keV γ-ray in ^{126}Ba was used for normalization since it was known as a pure E2 ($2^+ \rightarrow 0^+$) transition. Almost all the transitions were assigned to E2 or M1/E2 transitions.

According to the deduced multipolarities, parities of excited states in ^{126}Ba were determined. Upper limit values for two transitions, the 606.4 and 1031.4 keV γ-rays were set and these transitions were determined to be E1 transitions. Thus, the 1742 keV level in ^{126}Ba was determined to have odd-parity for the first time. Moreover, six levels were newly assigned to even-parities. The 1939 and 2056 keV levels were assigned to odd-parity states. The assignments of even-parity for the other levels were consistent with those of the previous

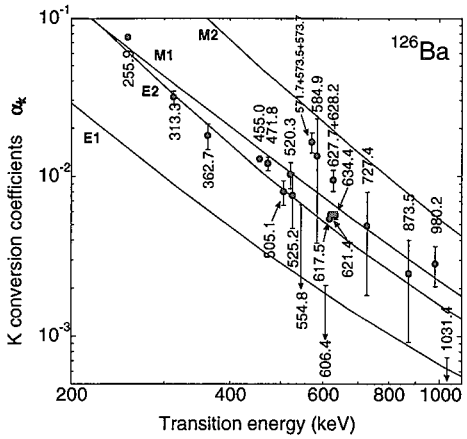


Fig.2 Experimental k conversion coefficients α_k and multipolarities of the transitions in ^{126}Ba. The solid lines indicate the theoretical conversion coefficients.

reports by in-beam spectroscopy.[1,2,5]

4. Conclusion

A Si(Li) detector for measurements of ICEs was installed at TIARA-ISOL. The k conversion coefficients for 22 transitions in ^{126}Ba were deduced from the decay of ^{126}La. We are constructing the decay scheme of ^{126}La including multipolarities, parities, the γ-γ coincidence relationships[3,5] and Q_β[6]. The Si(Li) detector enabled us to proceed much precise decay study.

References

1) K.Schiffer et al., Z. Phys. A-Atomic Nuclei, 327, 251, 1987.
2) D.Ward et al., Nucl. Phys.,A529,315, 1991.
3) Y.Kojima, Ph.D. thesis, Nagoya University.
4) F.Rösel et al., At. Data and Nucl. Data Tables, 21, 91, 1987.
5) M.Asai et al., Phys.Rev.,C56, 3045, 1997.
6) Y.Kojima et al., Appl. Radiat. Isot., 49, 829, 1998.

6.6 Ion-Source Development for the TIARA On-Line Isotope Separator

[1]Mitsuo KOIZUMI, [1]Akihiko OSA, [1]Toshiaki SEKINE, [2]Hidetsugu KATSURAGAWA, [2]Jin-Wei-Guo, [2]Takashi WAKUI, [3]Yoshihisa ISHIDA, [3]Jeong Sun-chan, [3]Hironobu ISHIYAMA, [3]Hiroari MIYATAKE
[1] Department of Materials Science, JAERI, [2]Toho University, [3]KEK

1. Introduction

The TIARA Isotope Separator On-Line (ISOL) mass-separates unstable nuclei produced in nuclear reactions between heavy ions accelerated by the AVF cyclotron and a target mounted in the ion source of the ISOL. The mass-separated ion beams have been applied to the decay study of neutron deficient unstable nuclei,[1] and to development of a polarization technique of radioactive ions for measurement of nuclear moments and/or electromagnetic fields in solids.[2] In order to proceed these studies, we are developing ion sources for the TIARA-ISOL. This report describes status of the laser ion source, [3] and available yields of ^{8}Li and ^{9}Li with a surface-ionization ion source.

2. Development of a Laser Ion Source

In spectroscopic study of nuclei far from stability with an ISOL, a mass-separated ion beam usually consists of some isobars. Signals from the nuclide of interest are often obscured by the background due to the decay of its isobars. In order to reduce the isobars other than the nuclide of interest, we are developing an element selective laser ion source.[3] Selecting an element with the ion source and separating a mass fraction with the mass-separator, the ISOL will provide an ion beam containing the nuclide of interest in high purity.

Our previous cavity of laser ion source had a large volume[3] and it seems that there existed a cold spot in the cavity, where reaction products were probably trapped. To avoid that, we have applied the cavity used as a surface-ionization ion source because it has been successfully used for extracting unstable nuclei with the TIARA-ISOL. Laser beams can be introduced into a 1.5-mm-diameter ion

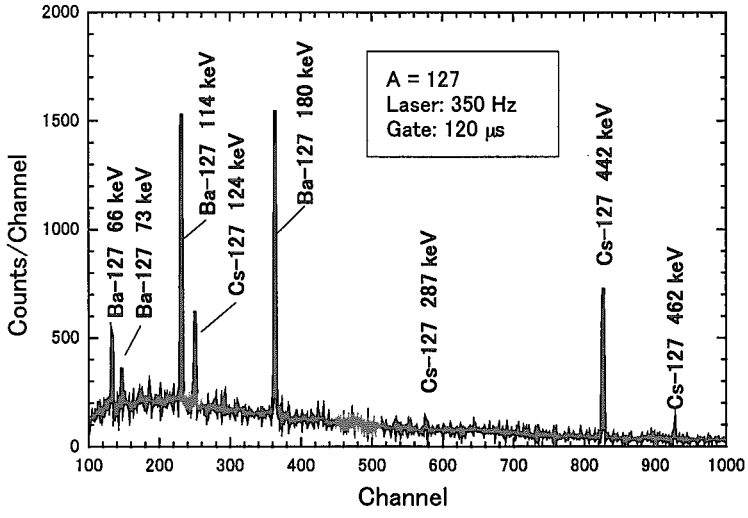


Fig. 1. A γ-ray spectrum at mass 127 measured at the tape transport system of the TIARA-ISOL.

extraction hole of the cavity.[4]

Because the cavity of an ion source used with an ISOL is heated up to about 2000 °C to evaporate product atoms, a certain number of atoms with low ionization potentials are also ionized through surface ionization, and then become a background. To suppress the surface ionization, we used a Nb foil with a low work function as the wall material of the cavity in the following experiment.

A fast deflector system has also been installed in the ISOL downstream after the analyzing magnet. This system can deflect an ion beam and prevent it to be transferred to the detector system; and when bunched photo-ions come, the system let them pass. It reduces surface ionized ion beams to come to the detector, and thus the signal to noise ratio will be improved.[4]

An on-line experiment of the laser ion source has been carried out with ^{127}Ba ($T_{1/2}$ = 12.7 min.) produced through ^{nat}Mo (^{36}Ar, 4p, yn) reactions. After mass-separation, γ-ray spectra at A=127 were measured with a tape transport system. The transitions from the $6s^2$ $^1S_0$ state to the 6s6p $^1P_1^\circ$ state (553.5 nm) and from the 6s6p $^1P_1^\circ$ state to the $5d_{5/2}$ 8d J=1 auto-ionization state[5] (389.6 nm) were used. The repetition rate of the lasers was 350 Hz. Figure 1 shows a γ-ray spectrum taken with a Ge detector. The gammas relevant to the decay of ^{127}Ba and ^{127}Cs were observed. The intensity of ^{127}Ba increased about 20% when laser beams were sent to the laser ion source, while no change was observed with that of ^{127}Cs. The efficiency of the laser ion source in photo-ionizing ^{127}Ba atoms was deduced to be about 0.04%, considering the production cross-section calculated with ALICE code, and the transport efficiency of the ISOL to be 50%.

3. Separation of Unstable Li Isotopes with a Surface-Ionization Ion Source

We have chosen the ^{12}C+^{nat}C reaction for production of unstable Na isotopes. A thick graphite sheet was mounted at the catcher position of the surface-ionization ion source, working as a target and a catcher foil. The carbon target was irradiated with 75-MeV $^{12}C^{3+}$ ions and reaction products of ^{20,21,24m,24g,25}Na were mass-separated as reported earlier.[4] The present paper reports another experiment with 220-MeV $^{12}C^{5+}$ ions to extend the mass range of reaction products.

The 220-MeV $^{12}C^{5+}$ beam was directed through an ion-source window made of 1.5-μm thick tantalum onto a target/catcher of 100-μm thick graphite. The reaction products diffused to the surface of the target/catcher were ionized in the surface-ionization ion source. The mass-separated product ions were transferred to a tape transport system, collected on an aluminized Mylar tape, and transported to a detection port. γ-singles measurements were performed with Ge detectors at the collection and the detection ports.

The mass range of Na isotopes produced was not extended by comparison with that of the reaction with the 75-MeV $^{12}C^{3+}$ beam. However, it should be mentioned that unstable Li isotopes, which are useful probes for materials science, were mass-separated. We concluded that unstable Li isotopes ^{8}Li ($T_{1/2}$=838 ms) and ^{9}Li ($T_{1/2}$=178 ms) were separated, from their data of mass, β-ray maximum energies (see Fig. 2) and half-lives estimated from growth curves of total β-ray counts. The experimental data are summarized in Table 1. The above-mentioned Na isotopes were considered to be produced in the fusion-evaporation reaction, while in the bombardment with the 220-MeV $^{12}C^{5+}$ beam (18.3 MeV/u), ^{8}Li and ^{9}Li were produced by the particle-transfer reaction or the fragmentation reaction.

Table 1 Experimental data on production and separation of ^{8}Li and ^{9}Li.

Primary beam:	$^{12}C^{5+}$ 220 MeV/~100 particle-nA
Target:	Graphite 90mg
Nuclear data:	^{8}Li $T_{1/2}$=838ms, Q_{β}=16 MeV ($E_{\beta max}$=13MeV)
	^{9}Li $T_{1/2}$=178.3ms, Q_{β}=13.6 MeV ($E_{\beta max}$=13.6MeV, $E_{\beta max}$=11.2MeV)
Source strength:	^{8}Li 1.1×10^{4} ion/s
	^{9}Li 300 ion/s

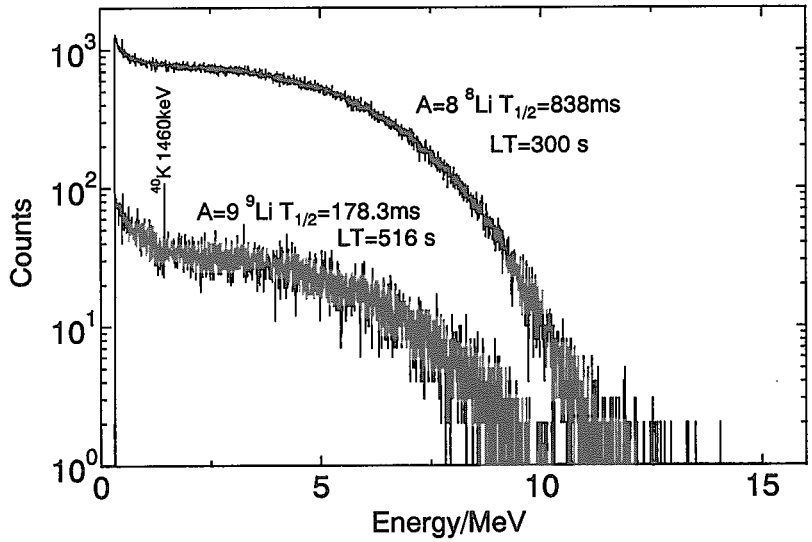


Fig. 2. β-ray spectra of ^{8}Li and ^{9}Li measured with a Ge detector.

References

[1] T. Sekine, S. Ichikawa, A. Osa, M. Koizumi, H. Iimura, K. Tsukada,I. Nishinaka, Y. Hatsukawa, Y. Nagame, M. Asai,Y. Kojima, T. Hirose, M. Shibata, H. Yamamoto, and K. Kawade, J. Radioanalytical and Nucl. Chem. 239 (1999) 127.

[2] T. Otsubo, S. Ohya, K. Hori, H. Kimura, S. Yachida, J. Goto, Y. Izubuchi, S. Muto, A. Osa, M. Koizumi, T. Sekine, Hyp. Interact., 120/121 (1999) 695.

[3] M. Koizumi, A. Osa, T. Sekine, and M. Kubota, Nucl. Instr. and Meth. B126 (1997) 100.

[4] A. Osa, M. Koizumi, T. Sekine, H.Katsuragawa, W.G. Jin, T. Wakui, TIARA Annual Report 1998.

[5] B. Willke and M. Mock, Phys. Rev. A43 (1991) 6433.

6.7 Systematic Behavior on Mössbauer Isomer Shifts of ^{133}Cs Implanted into Transition Metals

H. Muramatsu[1], K. Yoshikawa[1], H. Shimomura[1], T. Miura[2],
S. Watanabe[3], M. Koizumi[4], A. Osa[4], and T. Sekine[3,4]
[1]*Faculty of Education, Shinshu University,*
[2]*High Energy Accelerator Research Organization,*
[3]*Department of Radiation Reserch for Environment and Resources, JAERI*
[4]*Department of Materials Science, JAERI*

1. Introduction

The theory of isomer shift in metals, in general, is less developed than that in chemical compounds; the theoretical understanding to predict which parameters determine the isomer shifts in metals has not been established yet. For the ^{133}Cs, which is one of two isotopes of alkali metals for which the Mössbauer effect has so far been observed, and is an invaluable probe for the elucidation of the nature of chemical bondings in highly ionic compounds, some measurable differences between the isomer shifts of different chemical compounds have so far been found [1-3], although its chemistry makes us expect that the Mössbauer spectra of ^{133}Cs lack variety; that is, the cesium atom generally forms highly ionic compounds by losing a valence electron, which leaves behind a spherically symmetric and relatively inert core. The clear trend observed experimentally in the isomer shift of cesium halides is the increase with decreasing electronegativity of the halogen [3].

On the other hand, in the case of an impurity in metallic hosts or in alloys of cesium the widespread values of the isomer shift have been observed. Recent works [1] as well as early works [2] for the isomer shift of ^{133}Cs in some metallic lattices show that some of the observed values are unusually large; these values are much larger than those observed in any cesium compounds. The large isomer-shift values cannot be explained by the previous isomer-shift calibration constants of ^{133}Cs in terms of 6*s*-electron density. When these large isomer shifts are interpreted in terms of 6*s*-electron densities at the nucleus, an extremely high local pressure at the impurity sites should be considered, as pointed out by Pattyn et al. [4].

In this work, Mössbauer emission spectra of ^{133}Xe-implanted metal sources prepared by means of an electromagnetic isotope separator (EMIS) have been measured for the 81 keV transition of ^{133}Cs in order to understand the behavior of the isomer shift of ^{133}Cs atoms in transition metals and to find the parameter which determine the isomer shift in these matrices.

2. Experiment and data analysis

The source samples in this work were prepared by the implantation of ^{133}Xe ($T_{1/2}$=5.25 d), which decays to the Mössbauer level of ^{133}Cs. A radioactive ^{133}Xe gas was purchased from Amersham International (U.K.) with a small amount of fission xenon. Ion-implantation of ^{133}Xe was carried out at a terminal voltage of 20 or 40 kV at room temperature by means of an EMIS of JAERI-TIARA. The integrated dose of ^{133}Xe atoms was estimated to be 10^{13} atoms/cm^2 based on the radioactiv-

ity of the implanted samples. Host materials, into which ^{133}Xe was implanted, were polycrystalline foils of Al, Ti, V, Cr, Mn, Co, Ni, Cu, Mo, Rh, W and Pt with a purity of 99.0-99.99% and a thickness of 3-25 μm (purchased from Goodfellow Metals). These metallic foils were polished mechanically and washed with acetone before implantation.

Mössbauer spectra were measured using a single-line absorber of CsCl with 360 mg/cm^2 Cs thickness while keeping both the source and absorber at 4.2K. The 81 keV γ-rays of ^{133}Cs from an implanted source were detected with a thin NaI(Tl) scintillation detector. A constant acceleration drive with a triangular velocity shape was used at ±6 mm/s.

Most of the spectra obtained in the present work show complex ones; the radioactive atoms are introduced by implantation into more than one site. Then, the spectra were analyzed by decomposition into several components. In the least-squares fits of such spectra with single lines only, one single line is found in a large positive isomer-shift region with respect to a CsCl absorber. From the systematic isomer-shift studies on ^{133}Cs, however, it is unlikely to find isomer shifts larger than +0.1 mm/s with respect to a CsCl absorber [3,5]. Moreover, Campbell *et al.* [6] have shown that the quadrupole splitting e^2qQ_{ex} (Q_{ex}=-0.22 barn) of the 81 keV ($5/2^+$) state in ^{133}Cs is not negligible; it can be measured by Mössbauer spectroscopy for sufficiently large field gradients. Thus, a line at positive velocity in a spectrum belongs to a quadrupoletriplet which has a reasonable isomer shift. Referring to the systematic isomer-shift studies on ^{133}Cs by Pattyn and his coworkers [1] and considering the quadrupole splitting of the 81 keV ($5/2^+$) state, we analyzed the spectra obtained under the assumption that three single lines and two quadrupole triplets exist in a spectrum in accordance with the site assignment made by Reintsema *et al.* [7]. In this spectral analysis, the site having the largest isomer shift corresponds to a substitutional site and the rest of sites with smaller isomer shifts than this are assigned to be vacancy-associated ones. We then adopted the isomer-shift value of the substitutional site as the isomer shift in the metal of interest.

3. Results and discussion

For the systematic understanding of the isomer shift of ^{133}Cs atoms introduced as an impurity in various metallic hosts, many attempts have been made to find a correlation between the isomer shifts corresponding to the substitutional site and some physical and chemical properties of host materials: the atomic volume; the metallic bond radius; the Debye temperature; the Debye force-constant; the bulk modulus; the *d*-character in chemical bonds; and the electronegativity difference between host and impurity atoms. Among these macroscopic properties, we found close correlations of ^{133}Cs isomer shift with the Debye force constant, the bulk modulus (see FIG.1), and the electron density at the boundary of the Wigner-Seitz cell in the host-impurity system, n_{ws} [8]. These correlations thus obtained mean that an increase in the force constant between host atoms corresponds to an increase in the *s*-electron density localized at the Cs nucleus, that the rigidity of the host lattice strongly correlates to the isomer-shift value, and that a substantial part of the isomer shift must be related to the host conduction electrons, respectively.

A correlation between the isomer shift and the bulk modulus of the host metal, which is not observed in the case

of ^{57}Fe in metals, is unique for this Mössbauer atom having a relatively large atomic size. From the definition of the matrix compressibility K, i.e. $K=1/B$, where B is the bulk modulus, the larger B the smaller the lattice space available for the large Cs impurity atoms. Therefore, the volume contraction of the electronic orbitals of Cs impurity in the metallic host results in an increase in s-electron density. In the case of cesium in metals, this *compression effect* seems to be dominant for the determination of the isomer shifts due to its large atomic size, and it is conceived that other effects contributing to the isomer shift are concealed under it. Then, it is expected that the correlation obtained here for Cs impurity in metals may be generally used for the evaluation of the contribution of the compression effect to the isomer shift in other metal-impurity systems; if the subtraction of the compression effect from the isomer shift data of another Mössbauer nucleus in the metallic host can be realized with some manner or other, a certain parameter mainly determining the isomer shifts will be revealed. An application of this idea will soon appear elsewhere.

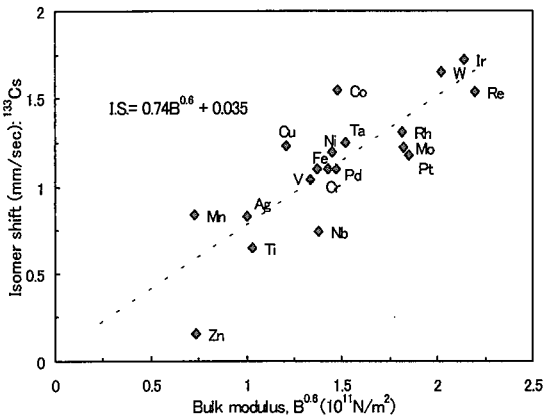


FIG.1. Isomer shift of the ^{133}Cs-impurity atom at the substitutional site in metal (relative to CsCl) against the bulk modulus of the metal.

References

[1] I. Dézsi, H. Pattyn, E. Verbiest and M. Van Rossum, Phys. Rev. B**39** (1989) 6321.

[2] H. de Waard and S. A. Drentje, Proc. Roy. Soc. A**311** (1969) 139.

[3] A. J. F. Boyle and G. L. Perlow, Phys. Rev. **149** (1966) 165.

[4]H.Patyn, M.M.Abd-Elmeguid, S.Bukshpan and J.Verheyden, Phys. Rev. B**51**, 10357 (1995).

[5] L. E. Campbell, in *Mössbauer Isomer Shifts*, edited by G. K. Shenoy and F. E.Wagner (North-Holland, Amsterdam, 1978), p.777.

[6] L. E. Campbell, G. L. Montet and G. J. Perlow, Phys. Rev. B**15** (1977)3318.

[7] S. R. Reintsema, E. Verbiest, J. Odeurs and H. Pattyn, J. Phys. F**9** (1979) 1511.

[8] H. Muramatsu, H. Ishii, E. Tanaka, M. Misawa, H. Ito, T. Miura, S. Muto, M. Koizumi, A. Osa, T. Sekine and M.Yanaga, J. Radioanal. Nucl. Chem., **239** (1999) 251.

7. Microbeam Application

7.1 Study on Uptake of Europium by the Mixture of Apatite and Smectite using RBS and Micro-PIXE ····· 221
T. Ohnuki, N. Kozai, M. Samadfam, S. Yamamoto, K. Narumi, H. Naramoto, T. Kamiya, T. Sakai and T. Murakami

7.2 Application of In-air Micro-PIXE Camera to the Metabolic Study of Cultured Single Cells ····· 224
A. Sugimoto, K. Ishii, S. Matsuyama, T. Satoh, H. Yamazaki, A. Tanaka, T. Amartivan, H. Endoh, Y. Oishi, H. Yuki, S. Sugihara, C. Akama, M. Satoh, T. Kamiya, T. Sakai, S. Oikawa, K. Arakawa and M. Saidoh

7.3 Application of Micro-PIXE to the Analysis of Single Raindrop and Single Aerosol Particle ··· 227
M. Kasahara, C.-J. Ma, S. Akashi, T. Kamiya, T. Sakai, S. Oikawa and T. Satoh

7.4 Target Preparation of Tissue Slices for In-air Micro-PIXE ····· 230
A. Tanaka, K. Kubota, K. Ishii, H. Fukuda, T. Akaizawa, T. Satoh, S. Matsuyama, H. Yamazaki, H. Yuki, T. Amartivan, H. Endoh, Y. Oishi, S. Sugihara, T. Kamiya, T. Sakai, M. Oikawa, K. Arakawa and M. Saidoh

7.5 Development of Atmospheric Micro-PIXE System for High-efficiency Elemental Analyses ··· 233
T. Kamiya, T. Sakai, M. Oikawa, K. Ishii, S. Matsuyama, T. Satoh and A. Sugimoto

7.6 Analysis of Uranium in Minerals by SEM, TEM, Micro-PIXE, XPS and XAFS ····· 236
T. Ohnuki, N. Kozai, M. Samadfam, R. Yasuda, T. Kamiya, T. Sakai and T. Murakami

7.7 Energy Stabilization Test for TIARA 3MV Single-ended Accelerator ····· 239
T. Sakai, T. Satoh, M. Oikawa, T. Kamiya and S. Uno

7.8 Development of the Measurement Method of Fluoride Distribution in Teeth ····· 242
M. Nomachi, K. Yasuda, H. Yamamoto, Y. Iwami, S. Ebisu, T. Kamiya, T. Sakai and M. Oikawa

7.9 Development of a High-energy Microbeam Single-ion-hit Technique for Bio-medical Applications ····· 245
T. Kamiya, T. Sakai, M. Oikawa, W. Yokota, Y. Kobayashi, M. Taguchi and M. Cholewa

7.10 Radiation Damage in Si PIN Diodes Induced by Heavy Ion Microbeam Single Hits ····· 248
T. Kamiya, T. Sakai, M. Oikawa and T. Hirao

This is a blank page.

7.1 Study on Uptake of Europium by the Mixture of Apatite and Smectite Using RBS and micro-PIXE

T. Ohnuki*, N. Kozai*, M. Samadfam*, S. Yamamoto**, K. Narumi***, H. Naramoto***, T. Kamiya****, T. Sakai**** and T. Murakami*****
Department of Environmental Science, JAERI*, Department of Materials Development, JAERI**, Advanced Science Research Center, JAERI***, Department of Material Development, JAERI****, Mineralogical Institute, The University of Tokyo******

1. Introduction

Migration of radionuclides through subsurface of earth should be studied to estimate the circulation of elements in terrestrial environment. Radionuclides are sorbed on minerals in soil and rock during the migration. Thus, sorption studies have been carried out by many research scientists. A major important question relating to sorption studies on soil and rock (mixture of components) is whether the sorption behavior on soil and rock can be estimated from the sorption behavior on the individual components of soil and rock.

It has been reported that a weighted average of the distribution ratio of each component can be used to determine the sorption of cesium and strontium by a mixture of minerals [1]. The present study was conducted to estimate the sorption behavior of europium, an analogue for trivalent TRU elements such as Am(III) and Cm(III), on soil by investigating the sorption to soil components.

Many components including clay minerals, metal oxides/hydroxides and phosphate minerals have performance for the sorption of europium. Europium is adsorbed strongly on phophate minerals [2]. It is reported that Eu aquo ions are sorbed rapidly at the highly polar apatite surface and the sorption equilibrium on apatite is attained in less than ten minutes [3]. It is well known that clay minerals are important sorbents that uptake cationic form of elements [4]. These results indicate that phosphate minerals and clay minerals play on important role in the sorption of europium. Although there are many components of the soil and rock, it is reasonable to study the europium sorption on soil and rock by using phosphate minerals and clay minerals. Smectite has been chosen as a representative clay mineral component, because it has a large distribution coefficient for cationic form of elements [5]

Sequential extraction technique for trace elements was usually used to examine adsorption behavior of elements by a mixture of minerals. This technique has been successfully applied to the separation of trace elements adsorbed on components in a mixture [6]. Since this technique is an indirect method, the evidence of the association of europium with each component in the mixture is desired. Since europium is hydrated, and form europium hydroxides that have low solubility, the concentration of europium in the sorption experiment was too low to be detected by electron probe microanalysis.

In the present study the association of europium with phosphate mineral and smectite by the sorption experiment of europium on the thin films. The depth profiles and the horizontal distributions of europium were obtained by Rutherford backscattering spectroscopy (RBS), and by micro-PIXE analysis, respectively.

2. Experimental

Sample

The single crystals of fluoroapatite from Cerro de Marcado, Durango, Mexico, were used. Powder samples of fluoroapatite were prepared by grinding to less than approximately 0.2 mm in diameter. The smectite was produced by the Kunimine Kogyo Co. Ltd., Japan, and originated from Tsukinuno, Japan. X-ray diffraction patterns of the fluoroapatite and the smectite showed that they did not contain measurable impurities.

Sorption experiments

All solutions were prepared with ultrapure DDI water and reagent-grade chemicals. Europium solutions were prepared by diluting the $Eu(NO_3)_3$ stock solution to contain europium concentrations of between $2.0x10^{-5}$ and $1.0x10^{-3}$ M. The pH of europium solutions were adjusted to 4.5 by adding small amounts of a 1 M NaOH or 1 M HCl solution.

Thin film of the mixture of smectite and fluoroapatite was formed on glassy carbon plate. The thin film was immersed in the europium solution for 2 days at 25 ℃. After the film separated from the solution, depth profiles of Eu, Al, Si, Ca, P and O in the film were obtained by 2.0 MeV He Rutherford Backscattering Spectroscope in the TIARA facility of JAERI. The surface distribution of Eu, P, Si, Al was determined by micro-PIXE system in the TIARA facility. The depth profiles of the same elements in the fresh mixture and smectite (not contacted with the Eu solution) were also measured as reference cases.

3. Results and discussion

RBS analysis of depth profile of europium:

Figure 1 shows RBS spectra for the thin and thick films of the mixture contacted with the europium solution. The RBS spectra of the fresh mixture and the fresh smectite are also shown in Fig. 1 as reference cases.

The RBS spectrum of the mixture shows that counts of the plateau for Ca (one of the element in fluoroapatite) in the thick film are constant. The peak for Ca in the RBS spectrum appeared at the same energy in both the thin and thick films of mixtures. These results indicate that fluoroapatite was present constantly in the mixture in the perpendicular direction from the surface of the mixture.

The peak for europium was observed in the RBS spectrum of the mixture after the sorption experiment. The peak width of the thick film for europium was larger than that of the thin film (Fig. 1). This indicates that europium deeply penetrated into the film of the mixture. Since the plateau for Eu was observed in the RBS spectrum of the thick film, europium is distributed uniformly into the mixture films from the surface.

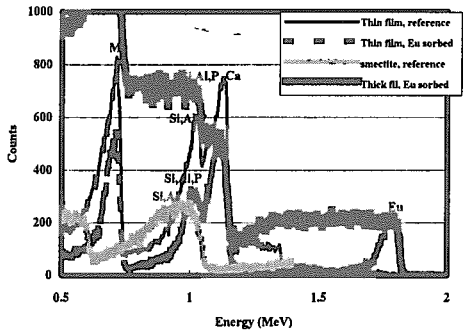


Fig. 1 RBS spectra of the mixture films.

Micro-PIXE analysis of horizontal distribution of europium

Figure 2 shows the distribution of europium and phosphate obtained by micro-PIXE in the thin film of the mixture contacted with europium solution. The brighter and darker areas in the right figure indicate the existence of fluoroapatite and smectite in the mixture, respectively.

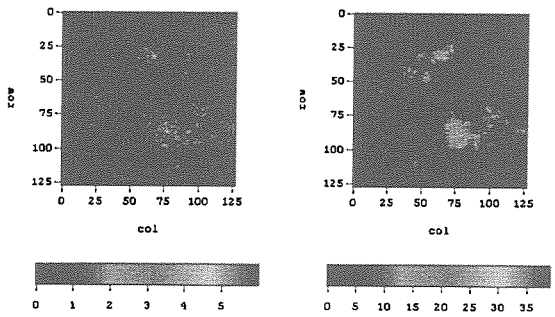


Fig. 2 Eu (left) and P (right) distributions obtained by micro-PIXE in the film of the mixture. Scan area: 100 x 100 μm.

This indicates that most of europium sorbed on the mixture was associated with fluoroapatite.

Almost all of europium was sorbed by smectite, when a 1 mM Eu of 30 ml was contacted with 0.1 g smectite for 1 day indicating that smectite has high performance on the uptake of europium from groundwater. Most of the sorbed europium was desorbed from smectite with 1 M KCl solution indicating europium was reversibly sorbed on smectite. Most of the sorbed europium on fluoroapatite was remained after contacting with 1 M KCl solution indicating that europium was irreversibly sorbed on fluoroapatite.

These suggest the uptake mechanism as follows. Europium sorbed by both floroapatite and smectite at the initial stage of uptake by the mixture. The europium sorbed on smectite can be desorbed, then is irreversibly sorbed on fluoroapatite. This sorption process derives the accumulation of europium on fluoroapatite in the mixtures.

Since fluoroapatite works as sink of the sorbed Eu by the mixure, the mixture of fluoroapatite and smectite is an effective material to remove rare earth elements from contaminated groundwater.

References

[1] Palmer D.A., et al., J. Inorg. Nucl. Chem., 43, 3317(1981).

[2] Ohnuki T., et al., J. Nucl. Sci. Tech., 34, 58-62(1997).

[3] McKelvey V. E., U. S. Geol. Suv. Prof. Paper 300, 1956, No. 300, 477-481. (1956),

[4] Robertson D.E., et al., US Nuclear Regulatory Commission NUREG/CR -3554 (1983).

[5] Ohnuki T., et al., Radiochimica Acta, 68, 203-207(1995).

7.2 Application of In-air Micro-PIXE Camera to the Metabolic Study of Cultured Single Cells

A.Sugimoto, K.Ishii, S.Matsuyama, T.Satoh, H.Yamazaki, A.Tanaka, T.Amartivan, H.Endoh, Y.Oishi, H.Yuki, S.Sugihara, C.Akama, and M.Satoh*
T.Kamiya**T.Sakai**S.Oikawa**K.Arakawa**M.Saidoh**
Department of Quantum Science and Energy Engineering, Tohoku Univ.
Department of Mechatronics and Precision Engineering, Tohoku Univ.*
Advanced Radiation Technology Center, JAERI**

1. Introduction

A micro-PIXE system was developed at the division of Takasaki Ion Accelerator for Advanced Radiation (TIARA) in Japan Atomic Energy Research Institute (JAERI). It consists of a micro-beam system[1] combined with a 3MV single-ended electrostatic accelerator, a beam position control, and X-ray detectors. We call a micro-PIXE camera since it provides us a picture of the elemental distribution in cells[2]. The microbeams are controlled in order to always scan on a region of interesting. When an X-ray is detected, the X-ray energy and the beam position are simultaneously measured for each event and these values are stored as a list mode. The sample can be analyzed in air and observed with a microscope during irradiation. The diagram of the principle is shown in Fig. 1.

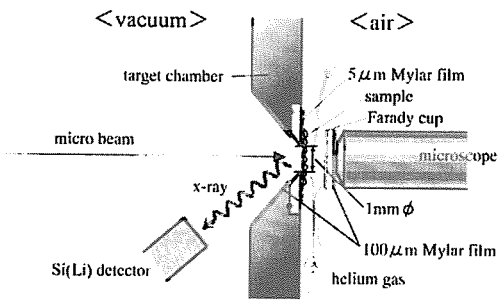


Fig. 1. Cross sectional view of the In-air Micro-PIXE.

We are planning to apply micro-PIXE camera to diagnosis in the cellular level (e.g. examination of effect of anti cancer drugs). For this purpose, we examined our system by analyzing bromodeoxyuridine (BrdU) taken in the DNA synthesis of cultured bovine aortic endothelial cells (BAECs)[3]. These cells form colonies of one layer in a culture dish and its single cells can be easily taken out. It is known that the metabolic period of the cells is about 24 hours and the cells take BrdU into their nucleus in the S phase.

2. Experimental

The size of BAEC is about 30μm and the cell has the shape of a polygon. BAECs were grown in the Dulbecco's modified Eagle medium supplemented with 10% inactivated fetal bovine serum and 1% penicillin-streptomycin.

Tris(hydroxymethyl)aminomethane-HNO_3 solution (pH=7.4) was prepared as a rinsing buffered solution which should be free from metallic ion for PIXE analysis[4]. Suspension containing the cells was dropped on a culture dish made of 5μm thick Mylar film and cultured in an automatic CO_2 incubator for a few days. Mylar film had been immersed in 5M sulfuric acid solution for 2 hours and washed with distilled water for 3 times. Because 5μm thick Mylar

film is too thin for treatment, we fixed it with a ring of glass and a viton ring (Fig. 2).

When the cells grew to 60% confluent, we changed the culture medium for fresh one in which BrdU (1:1000 to the medium) was supplemented. After incubation, we rinsed the culture medium several times with the buffered solution. The medium however still remained like as jelly covering the cells. We examined whether this rinsing lost the electrolytic element how much from the sample. Potassium and chlorine were observed in the PIXE spectra of the sample rinsed 3 times, but disappeared in that of 7 times. We chose the sample rinsed 3 times, though it still contained a small amount of medium. The rinsed sample was cooled in the liquid nitrogen, while it was soaked in the isopentane solution, and immediately, we free-dried for more than 24 hours .

The size of micro-beam spot of 2.6 MeV protons on the cell sample was about 1μm in diameter. X-rays were measured with a solid angle of 0.231 through a 60μm polypropylene film for stopping back scattered protons. The sample was cooled with helium gas during the irradiation.

3. Results and discussion

Figure 3 shows the X-ray spectrum and elemental map(128ch×128ch) of the cells in the region of 60μm ×60μm which were obtained by an image analysis software (Transform). It took 12 hours to obtain these images under beam currents of 30-40 pA. Major elements contained in the cells, P,S, and K were detected and a trace amount of Br could be clearly recognized. The peak of Ca is mainly contamination in the Mylar backing film. In Fig.3, the distribution of S will show the size of the cell. The elements of P, S, and K are concentrated in the central regions of the cells, which will be their nucleus. The mapping of Br presents that BrdU were used in the DNA synthesis of the nucleus.

The samples sometimes were happen to be melted during irradiation because of the remained medium. In fact, the sample washed 7 times scarcely melted. It was very effective to cool the samples by helium gas. The quantitative equation for micro-PIXE can be presented by,

$$m_A = \frac{1.602 \times 10^{-19} \times 128 \times 128 \times 4\pi}{6.023 \times 10^{23}} \times \frac{M_A}{\sigma^X \times eff \times ab} \times \frac{S}{Q \times d\Omega} \times Y_A$$

where m_A is the quantity of an element A in the cell, M_A is the mass number of A, σ^X is the production cross section of the characteristic X-rays of A, *eff* and *ab* is the detection efficiency and the absorption correction factor for the characteristic X-rays respectively, Q is the integrated beam currents, $d\Omega$ is the solid angle, S is an area in the picture of mapping and Y_A is counts of the characteristic X-rays of A in S. The quantitative analyses for the elements of P and Br were performed for the cells in Fig.3 and its results are presented in Table 1. This indicates the possibility of quantitative diagnosis by micro-PIXE camera in the clinical application. At present, we develop the system which utilizes micro PIXE camera through the internet in the remote location.

Table 1. Quantitative analysis of P and Br in BAECs

Cell Number	P [$\times 10^{-11}$g]	Br [$\times 10^{-13}$g]
1	1.91	9.51
2	1.40	3.92
3	1.25	4.84
4	0.768	2.77
5	0.995	1.61

References

1) T. Kamiya, T. Suda, and R. Tanaka, Nucl. Instr. And Meth. in Phys. Res. B104,43(1995).

2) S. Matsuyama, K. Ishii, A. Sugimoto, T. Satoh, K. Gotoh, H. Yamazaki, S.Iwasaki, K. Murozono, J.

Inoue, T. Hamano, S. Yokota, T. Sakai, T. Kamiya, and R. Tanaka, Internatinal Journal of PIXE, 8, 203(1998).

3) A. Sugimoto, K. Ishii, S. Matsuyama, T. Satoh, K. Gotoh, H. Yamazaki, C. Akama, M. Sato, T. Sakai, T. Kamiya, R. Tanaka, and M. Oikawa, International Journal of PIXE, 9, 151(1999).

4) S.A.E Johansson and J.L. Cambell, PIXE . A Novel Technique for Elemental Analysis, John Wiley & Sons (1988).

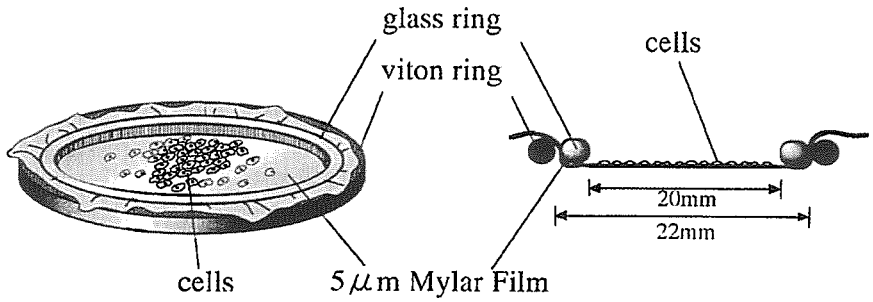


Fig. 2. Cell sample on the 5μm Mylar film fixed with a glass ring and a viton ring.

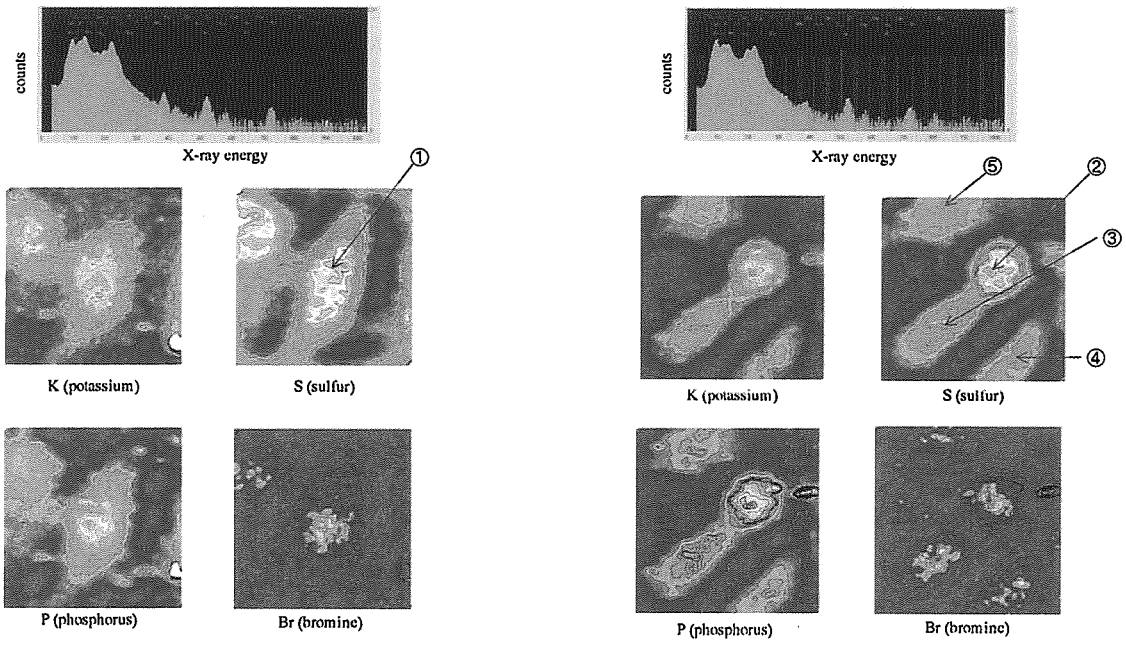


Fig3.X-ray spectra (log scale) and elemental maps of K,S,P and Br in the BAECs.

7.3 Application of Micro - PIXE to the Analysis of Single Raindrop and Single Aerosol Particle

M. Kasahara, C.- J. Ma, S. Akashi, T. Kamiya*, T. Sakai*,
S. Oikawa* and T. Satoh*
Graduate School of Energy Science, Kyoto University
*Advanced Radiation Technology Center, JAERI

1. Introduction

Until recently, not much has been known about the chemical constitution of individual cloud and raindrops. Fortunately, however, recent technologies such as capillary zone electrophoresis[1] and micro-PIXE[2] have provided new methods by which chemical analysis of single raindrops can be carried out. The analysis of single raindrops is expected to give new and interesting information about anthropogenic air pollution and drop formation processes in the atmosphere.

Also, a large number of studies on the Asian dust storm particles have been reported[3-6]. However, only a few studies on the Asian dust storm particles as the single particles, which can provide detailed information about the nature and compositions of the single particles were reported. Investigation of the properties of single aerosol particles is an essential prerequisite for understanding chemical reactions in the atmosphere.

In this study to determine the characteristics of single raindrops and Asian dust storm particles we tried to analyze their elemental components by Particle Induced X-ray Emission (PIXE) analysis. Furthermore, to acquire more detailed information such as inner – structure and mixing state in single raindrops and single Asian dust storm particles we measured their elemental concentration by micro-PIXE analysis.

2. Experiments

200 μl of collodion solution (3%) was mounted onto the 47 mm diameter non-hole Nuclepore filter just before raindrop sampling. Fallen drizzle and small sized raindrops were allowed to settle on the surface of collodion film without bounce off. Sampling of single raindrops using this collodion film method was newly performed at a height of 20 m above ground level of the Kyoto University building during rain events from September to November 1999. For sampling of ambient aerosols, Low Pressure Andersen Impactor sampler (LPAI) were operated at Kyoto University in Asian dust storm events during middle and end of April, 1999. For chemical analysis of raindrops collected on collodion film, PIXE analysis was applied.

To acquire more detailed information on the single raindrops and single Asian dust storm particles, micro-PIXE analysis was performed using the facilities of the Takasaki Ion Accelerators for Advanced Radiation Application. Detailed analytical procedures and experimental set-ups used for PIXE and micro-PIXE were described elsewhere.[7,8]

3. Results and Discussion

Application of collodion film method to the sampling of single rain droplets (diameter$\leqq$2.1 mm) was very successful. But, unfortunately, this collodion film method did not allow to sampling of raindrops larger than 2.1 mm diameter because of breakup of large raindrops when they collide with collodion film surface. Separated clean raindrop replicas formed on the collodion film are shown in Photo 1. The circle that appear in the center of each replica, probably represent the nucleation center from which cloud condensation nucleation was initiated. The size dependence of the elemental concentration of dissolved and suspended components in raindrops was obtained by PIXE analysis as illustrated in Fig. 1. It shows a strong decrease of every elemental concentration with increasing droplet diameter. Turner (1955) and Flossmann

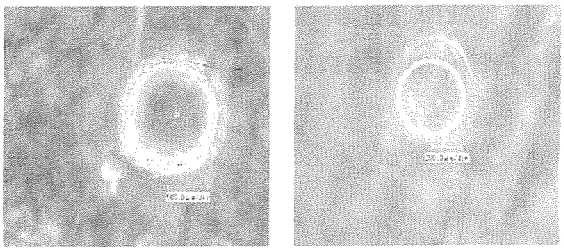


Photo 1 Raindrop replicas formed on the collodion film.

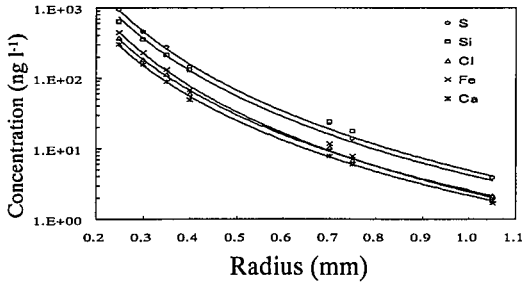


Fig. 1 Variation of elemental concentration as a function of raindrop size.

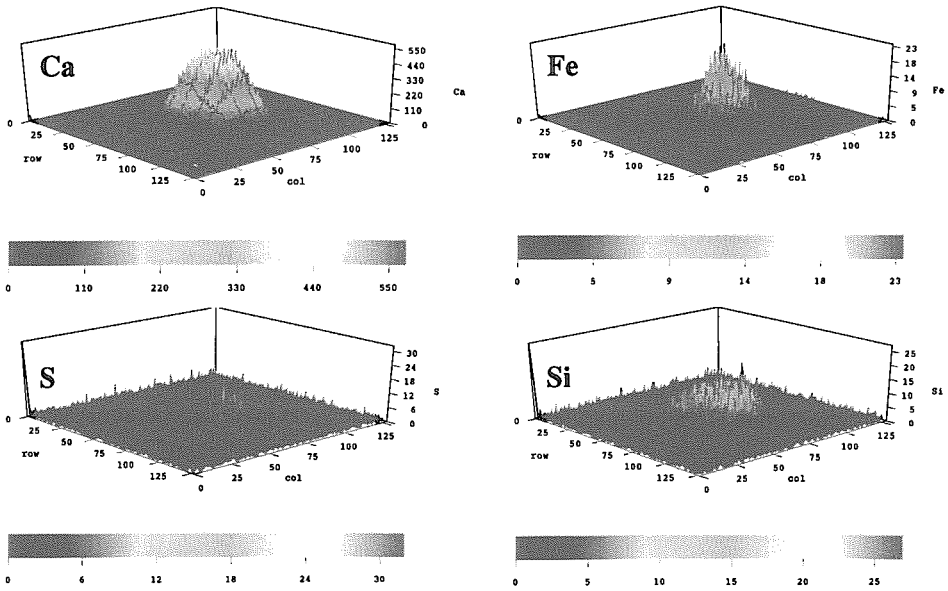


Fig. 2 Elemental maps obtained by micro-PIXE at the nucleation center of raindrop.

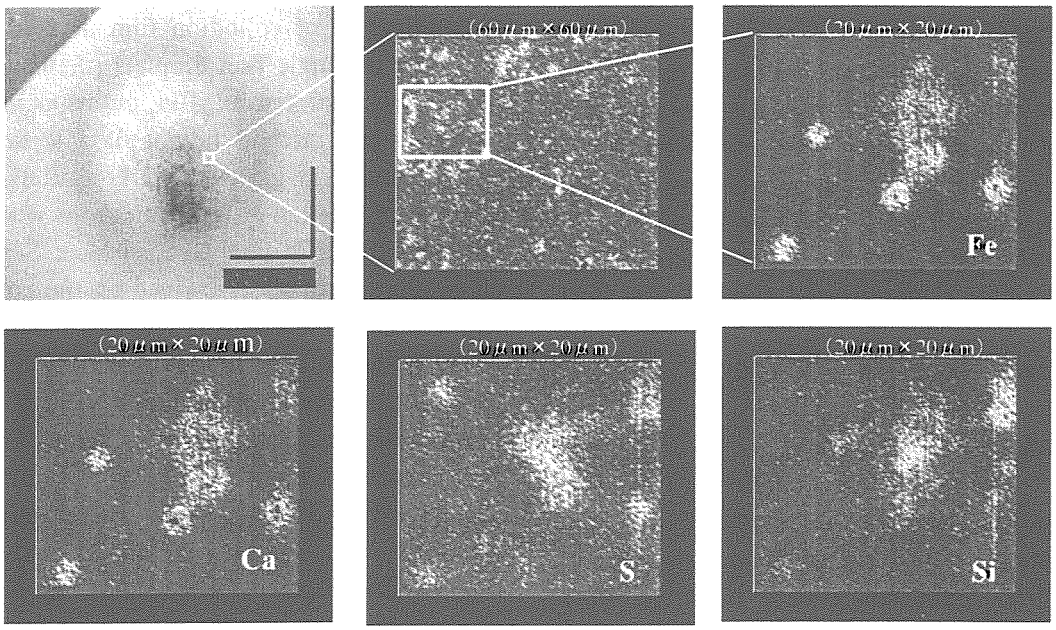


Fig. 3 Micro-PIXE elemental maps taken on separate single particles (50% e.c.d:1.17 μm).

(1994) reported that raindrops within the cloud or near the cloud base have nearly identical concentrations regardless of drop size[9,10]. On the other hand, it was found that dependence of concentration on drop diameter gave a continuous decrease in the concentration with increasing drop radius near and at the ground. It may, therefore, be concluded that dependence of elemental concentration on drop sizes measured near and at the ground is only due to below cloud influences. During rainfall from cloud base to ground, drops experience an increase in solute concentration due to evaporation and below cloud scavenging of particle and gases. In the size range of 200 to 2000 μm radius, the scavenging efficiency of particles and gases by drops decreases with increasing drop size. In addition, evaporations of falling rain mainly dominates the smallest drops.

In order to investigate more detailed information such as mixing state of elements on the single raindrop, micro - PIXE analytical measurement was also applied. The circles appeared in the center of every raindrop replica can be considered to be nucleation centers from which cloud condensation nucleation was initiated, as mentioned earlier. Fig. 2 shows the elemental maps obtained by micro-PIXE at the nucleation center of raindrop.

Some independent particles on the 5th stage (50% e.c.d:1.17 μm) of LPAI were analyzed by micro-PIXE. Separate single particle appearing in the full spectral area maps taken with 60 μm× 60 μm scanning size were subjected to individual spectrum measurements for elemental analysis. Fig. 3 shows the micro-PIXE elemental maps taken on separate single particles collected on Asian dust storm events. Image of top left in Fig. 3 shows one of the spots collected on the 5th stage of LPAI taken by digital microscope. Soil components such Ca, Fe and Si were found to be the most abundant component in and/or on each single particle. S was found in all the single particles. Every single particle existed as the mixing state of soil components and S. Even though, the composition of single particles was determined through the micro-PIXE analysis in this study, attempts at obtaining relative or absolute element concentration of single particles was not possible at the present micro-PIXE technical level.

4. Conclusion

Collodion film method newly applied in this study for the sampling of single raindrops was very successful. The size dependence of the elemental concentration of material dissolved and suspended in rain droplets obtained by PIXE analysis shows a strong decrease of every elemental concentration with increasing droplet diameter. It can be suggested that smaller raindrops should have higher elemental concentration because they have lower velocities and consequently longer lifetimes than larger ones. Soil originated components such as Si, Ca and Fe were found to be the most abundant component in and/or on nucleation center of raindrop by micro-PIXE analysis. S was found to be widely distributed. Our data supports that every single particle collected in Asian dust storm events existed as the mixing state of soil components and S.

References

1) Bachmann, K. et al. J. Atmos. Sci., 24, S421,1993
2) Ma C.-J. et al. The 3rd International Sym. on Bio-PIXE, 4O05, 16, 1999
3) Duce R. A. et al. Science, 209, 1522, 1980
4) Braaten D. A. et al. Atmos. Envir., 20, 1105, 1986
5) Zhang D. et al. J. Aero. Sci., 29, S217, 1998
6) Ma C.-J. et al. The 1st Asia Aerosol Conf. 330, 1999
7) Kasahara M. et al. Nuc. Inst. and Methods in Phys. Res., B118, 400, 1996
8) Ishii Y. et al. Nuc. Inst. and Methods in Phys. Res., B113, 75, 1996
9) Turner J. S. Wuart. JIR. Meteo. Soci., 81, 418, 1955
10) Flossman A. Atmos. Res., 32, 233, 1994

7.4 Target Preparation of Tissue Slices for In-air Micro-PIXE

A. Tanaka, K. Kubota*, K. Ishii, H. Fukuda*, T. Akaizawa*, T. Satoh,
S. Matsuyama, H. Yamazaki, H. Yuki, T. Amartivan, H. Endoh,
Y. Oishi, S. Sugihara, T. Kamiya**, T. Sakai**, M. Oikawa**,
K. Arakawa**, M. Saidoh**
Department of Quantum Science and Energy Engineering, Tohoku Univ.
Institute of Development, Aging and Cancer Tohoku Univ.*
Advanced Radiation Technology Center, JAERI**

1. Introduction

Micro-PIXE system is developed at the Takasaki ion accelerator for advanced radiation application (TIARA) in Japan Atomic Energy Research Institute (JAERI). Our micro-PIXE system is called micro-PIXE camera since it can take a picture of the elemental distribution in a cell. As reported previously[1], we established the target preparation of cultured cells for the in-air micro-PIXE camera and succeeded in getting elemental maps of a single endothelial cell (BAECs). The uptake quantity of the drug in the cell could be quantitatively evaluated by this method. This result suggests that the in-air micro-PIXE camera is suitable method for the clinical application. Not only analysis of the cultured cells but tissue sections are requested in the clinical application. The purpose of this work is to develop a sample preparation method for imaging elemental distribution of the tissue section by micro-PIXE camera. Bromodeoxyuridine (BrdU) and cisplatin were administered into rat tumor model. It is well known that, BrdU is taken into the nuclei of cells in the S-phase of the cell cycle. So the distribution of Br can be used the determination of the position of nucleus in the cell. And cisplatin (CDDP) is one of the compound of platinum coordination complexes used in cancer chemotherapy. The cytotoxic properties of cisplatin are the consequence of interactions with DNA. Therefore the effect of anti cancer drug can be examined by researching the distribution of Pt in the cell.

2. Micro-PIXE camera

Micro-PIXE camera consists of a micro-beam system combined with a 3MV single-ended electrostatic accelerator, a beam position control, and X-ray detectors. The micro-beams are scanned to analyze the elemental maps in the appointed region of the samples. When a X-ray is detected, the X-ray energy and the beam position are simultaneously measured for each event and these values are stored as a list mode. The sample can be analyzed in air and observed with a microscope during irradiation. The diagram of the principle is shown in Fig. 1.

3. Experimental

The tumor cells of LY80 were subcutaneously injected into the back of young male Donryu rats (weight 190-200g). A week after injection of the tumor cells, either CDDP (1.5ml/rat) or BrdU+FdU (fluorodeoxyuridine) (3ml/rat) were administrated into the rat. The rats were sacrificed by over dose of anesthesia with chloroform one

day after administration. Immediately after sacrifice, the tumor tissue and liver was taken and cut into an appropriate size. The section of tumor and liver were embedded in a medium (O.C.T. compound, Miles inc. USA) and frozen with liquid N_2. The frozen sections were cut into 10 μ m thick slices with a microtome under –25℃. The slices were placed on the surface of 4 μ m thick Mylar film. After air drying, we fixed it on the sample holder. The samples were inspected with a phase contrast microscopy, before and after irradiation. Other slices were stained by hematoxylin eosin (HE) and were inspected with an optical microscope at a magnification of 400x. The images with a microscope were compared with elemental distribution images obtained with the micro-PIXE camera.

Micro-beam spot size of 2.6 MeV protons was about 1 μ m on the cell sample. X-rays were measured with a solid angle of 0.231sr through a 60 μ m polypropylene film for stopping back scattered protons. The sample was cooled with helium gas during irradiation.

4. Results and Discussion

Figures 2 and 3 show the X-ray spectra and elemental mappings (30 μ m × 30 μ m) of the tumor tissue which administered by BrdU and CDDP, respectively. It took 3 hours and 6 hours to obtain the data of BudU and CDDP under beam currents of 30-40pA, respectively. In the case of cultured bovine aortic endothelial cells (BAECs)[2], the distribution of S showed the shape of the Cell, and the elements P, S, and K were concentrated in the nucleus of the cell. In addition, the bromine accumulated at the nucleus, when the BrdU has been administered. However, in Fig. 2 and Fig. 3, the shape of the cell and the position of the nucleus of the cell can not be recognized clearly, though it seems that the bromine is locally distributed. In Fig. 3, the peak of the L_α line of Pt does overlap with that of the K_β line of Zn. In consideration of K_α/K_β for Zn, the contribution of Pt- Lα is negligible small. And the liver sample sometimes melted during irradiation though it was cooled with the helium gas.

In our present work, we could not obtain the clear images of tissue sections. To improve this situation, we will develop several techniques in the target preparation. The freeze-dry might be useful in the case of tissue sections, while, in the present preparation, the sample is dried in the atmosphere. The thickness of slice is 10 μ m at present, this might be thinner than the size of the cell (~20 μ m) and we should examine the target samples with several thickness (>10 μ m). It might be effective to rinse cell slices in the target preparation, since the injured cells can be washed out from the surface of the slice.

References

1) S. Matsuyama, K. Ishii, A. Sugimoto, T. Satoh, K. Gotoh, H. Yamazaki, S. Iwasaki, K. Murozono, J. Inoue, T. Hamano, S. Yokota, T. Sakai, T. Kamiya, and R. Tanaka, International Journal of PIXE, 8, 203(1998).

2) A. Sugimoto, K. Ishii, S. Matsuyama, T. Satoh, K. Gotoh, H. Yamazaki, C. Akama, M. Sato, T. Sakai, T. Kamiya, R. Tanaka, and M. Oikawa, International Journal of PIXE, 9, 151(1999).

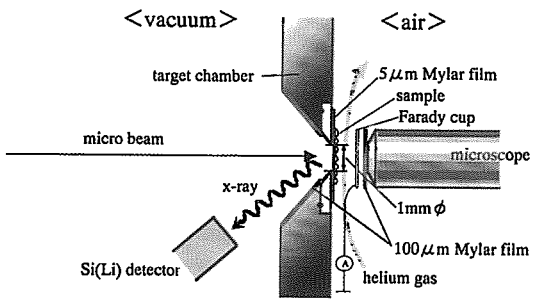


Fig. 1. Cross sectional view of the in-air Micro-PIXE.

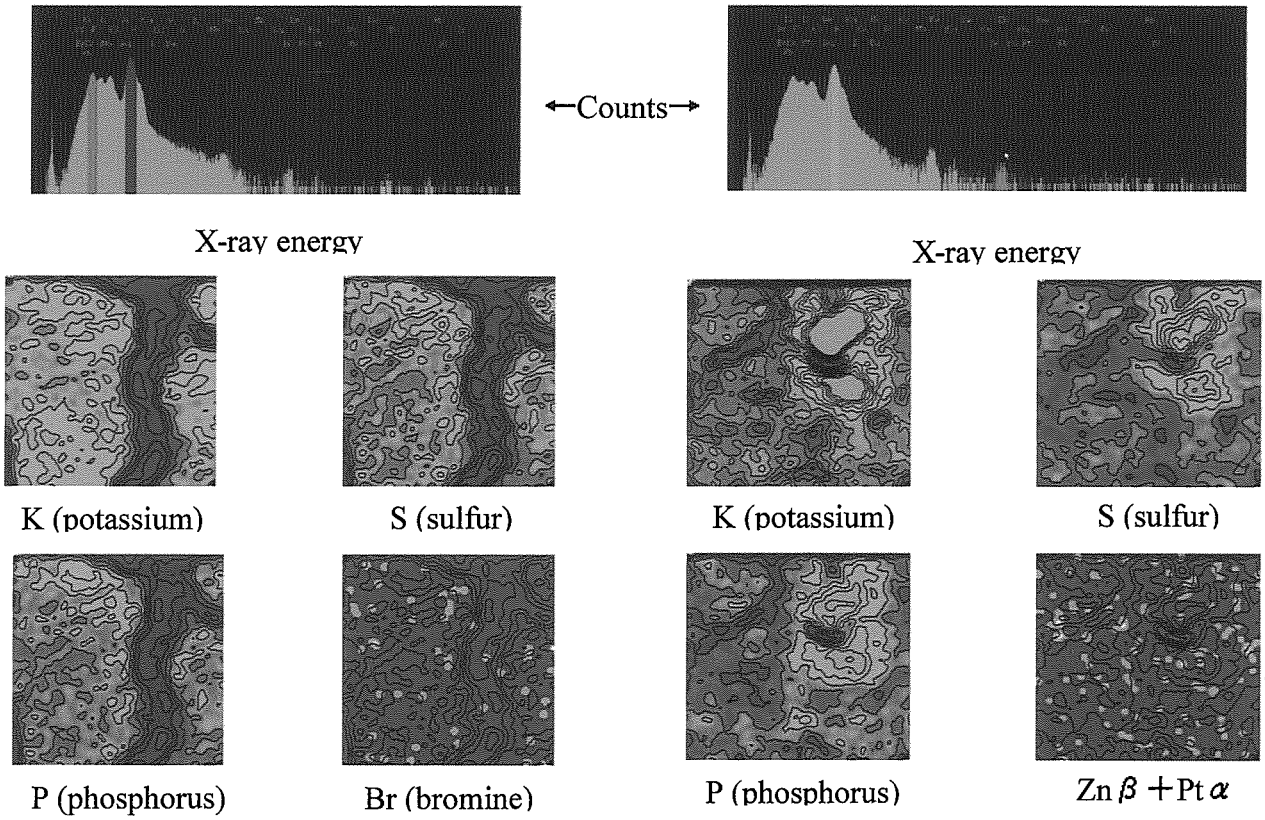


Fig2. X-ray spectrum an elemental mappings of the tumor cell (BrdU)

Fig3. X-ray spectrum an elemental mappings of the tumor cell (CDDP)

7.5 Development of Atmospheric Micro-PIXE System for High-efficiency Elemental Analyses,

T.Kamiya, T.Sakai, M.Oikawa, K.Ishii*, S.Matsuyama*, T.Satoh* and A.Sugimoto*,
Advanced Radiation Technology Centre, JAERI,
*The School of Engineering, Tohoku University.

1. Introduction

A technique of micro-PIXE is a powerful tool for local area elemental mapping of various kinds of samples. The light ion microbeam system in TIARA[1, 2] was designed mainly for this technique as well as other ion microbeam analyses, such as micro-RBS or micro-NRA. Furthermore, from the beginning of development, atmospheric analyses were aimed mainly for biological samples, while in almost all other systems analyzing samples are set in the vacuum chamber.

A target port of the light ion microbeam system is illustrated schematically in Fig. 1. The microbeams focus down to less than 1 μm at the exit window, a 5-μm thick polymer (Mylar or polyethylene terephthalate, PET) film stuck to a window holding disk, which has a 1 mm diameter center hole. Samples are attached on the window from the atmospheric side, or are prepared on the film and stuck to the disk. Mylar film, which also acts as a beam extraction window, needs to be tested on its tolerance to high-intensity microbeam irradiation.

Scanning transmission ion microscopy (STIM) technique was introduced to the light ion microbeam system, so as to make direct beam positioning to samples for subsequent micro-PIXE analyses in the atmosphere. STIM is a low current (less than fA level) and high efficient sample imaging technique, which does not induce radiation damage even to biological cells for beam positioning before micro-PIXE analysis. A Si PIN photodiode (cover glass removed) was set just behind the sample in the atmosphere to measure the energy of protons passing through the sample and the window. STIM images were obtained in several minutes, and corresponded with elemental maps obtained by subsequent micro-PIXE analyses.

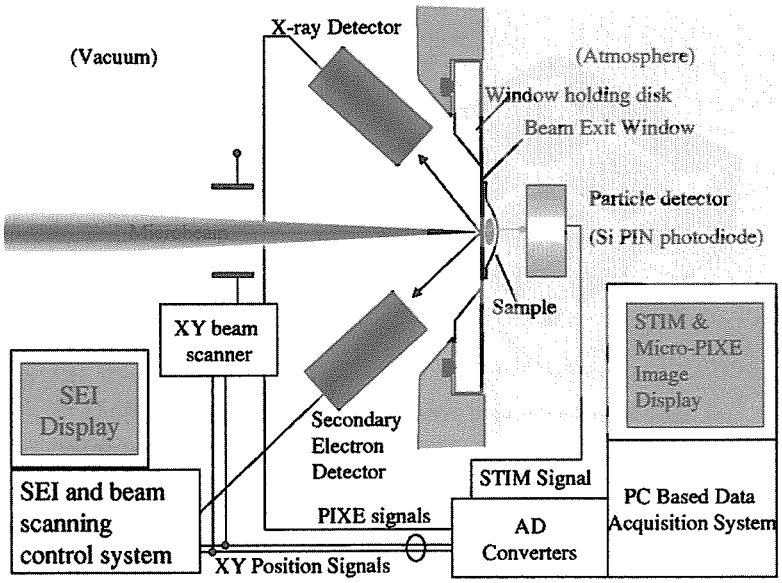


Fig. 1 Schematic view of the target port and block diagram of SEI (secondary electron imaging), STIM and micro-PIXE system.

This paper describes details of the experimental system, and shows preliminary results of STIM imaging and micro-PIXE analyses. It also mentions a future plan to introduce a large solid angle X-ray detection system for high-efficiency and short time analyses of large number of biological cells or other samples.

2. Irradiation Test of Beam Exit Windows

By setting a sample in the atmosphere, the varieties

Table 1 Change of thickness in irradiated area

	Atmosphere	Irradiation time	Beam current	Ion	Change of thickness
Mylar 5μm	Air	10 min	20 pA	2.5MeV H^+	1.62μm
Mylar 5μm	Air	30 min	20 pA	2.5MeV H^+	2.02μm
Mylar 5μm	Air	60 min	20 pA	2.5MeV H^+	2.34μm
Mylar 5μm	He	10 min	20 pA	2.5MeV H^+	1.90μm
Mylar 5μm	He	30 min	20 pA	2.5MeV H^+	2.30μm
Mylar 5μm	He	60 min	20 pA	2.5MeV H^+	2.25μm
Mylar 4μm	He	10 min	100 pA	2.5MeV H^+	1.17μm
Mylar 4μm	He	500 min	2 pA	2.5MeV H^+	1.39μm
Mylar 4μm	Air	20 min	50 pA	2.5MeV H^+	1.00μm
Mylar 4μm	Air	500 min	50 pA	2.5MeV H^+	1.56μm
Mylar 4μm	Air	5 min	100 pA	2.5MeV He^+	—
Mylar 4μm	He	5 min	100 pA	2.5MeV He^+	1.00μm
Mylar 4μm	Air	125 min	4 pA	2.5MeV He^+	2.20μm
Mylar 4μm	He	125 min	4 pA	2.5MeV He^+	1.09μm

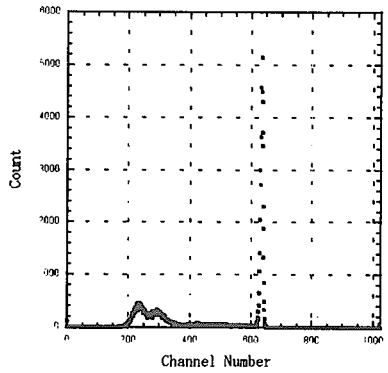
of analyzable samples can increase more easily than by that in the vacuum. But a window must be thin enough not to enlarge the beam spot on a target by multiple scattering in the window material. It must also be strong enough to stand atmospheric pressure. And most important thing is that it can stand high intensity microbeam irradiation in a small local area.

In the experiments, 5 and 4-μm thick Mylar films attached on to window holding disks were irradiated by 2.5 MeV H and He ion microbeams in 10 x 10 μm^2 areas. The conditions of irradiation were changed in the dose, the dose rate and the atmospheric gas (air and dry helium). Changes of the thickness by irradiation were observed for those irradiated area using a laser three-dimensional profile microscope (model VK-8500, Keyence, Japan) from the atmospheric side.

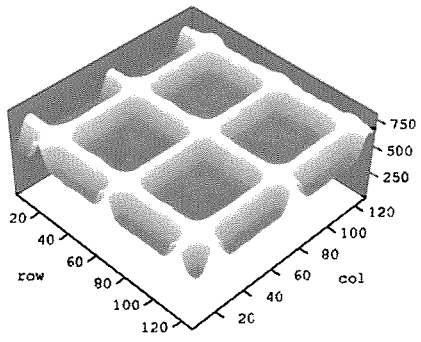
Results are summarized in Table 1. Less reduction of the thickness seems to be observed in the irradiation condition of lower dose or dose rate and in the He gas atmosphere. Further investigation is required to characterize this kind of radiation effect by longer and more intense irradiation to a smaller local area in real condition. Change of the chemical bond in irradiated film will be analyzed by a Fourier transform infrared spectrometer.

3. STIM Imaging

For the first test of STIM system, a copper grid (1,000 lines per inch) was used as a target with the beam current of less than fA order. An energy spectrum and a STIM image obtained with 2 MeV H microbeam are shown in Fig. 2. The highest energy peak in the spectrum is related to blank areas of the grid, and lower two peaks to bar area. The beam spot size can be reduced, but it is difficult to estimate it from the STIM image, because the bar of the grid has large variation of thickness at the edge.



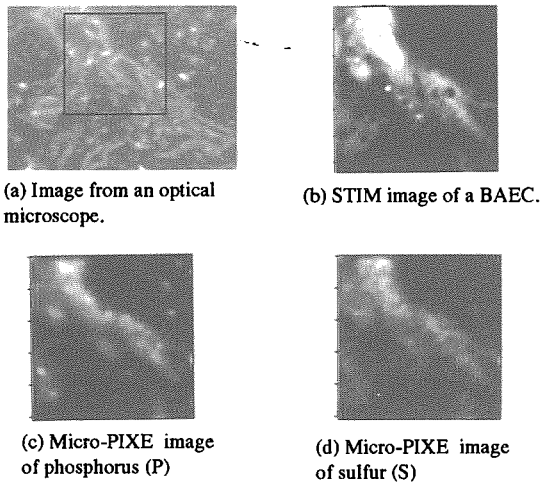
(a) Energy spectrum of 2 MeV proton passed through the copper grid



(b) Three dimensional view of STIM image of a copper grid (1,000 lines per inch). The width of bars is 6 μm and of blank 19 μm.

Fig. 2 STIM for a copper grid (1,000 lines per inch).

For the next test of STIM, bovine aortic endothelial cells (BAECs) were used as a sample. BAEC was selected as a test sample because it proliferates in a plane direction in culture



(a) Image from an optical microscope.

(b) STIM image of a BAEC.

(c) Micro-PIXE image of phosphorus (P)

(d) Micro-PIXE image of sulfur (S)

Fig. 3 Preliminary experiment of observing freeze-dried BAECs sample using (a) a optical microscope, (b) STIM and (c, d) micro-PIXE. An analyzed site of the sample is indicated by the square (60 x 60 μm^2) in the optical microscopic image, (a).

medium, so that it was just adequate to observe with an optical microscope and also to analyze with the STIM and the micro-PIXE system. BAECs were cultured in a petri dish, washed with buffer solution, and freeze-dried [3]. BAECs were observed by optical microscopy (Fig. 3a), and then analyzed by STIM with 60 x 60 μm^2 area, as shown in Fig. 3 (b). Micro-PIXE images of major elements were obtained, as shown in FIG. 3 (c), (d). Those images correspond to the STIM image. No trace elements were detected in this analysis.

4. Design of a large solid angle X-ray detector

A large solid angle X-ray detector was designed. By detecting X-rays efficiently with this, not only much better statistics or less time-consuming but also less radiation damage on samples can be expected in microbeam analyses for investigating trace elements in bio-medical samples. The detector is annular shaped and divided into many small cells to obtain the highest efficiency and to stand high count rate.

References

1)T.Kamiya, T.Sakai, T.Hamano, T.Suda and T.Hirao, Nucl. Instr. And Meth. B130 (1997) 285.

2)T.Kamiya, T.Suda and R.Tanaka, Nucl. Instr. And Meth. B118 (1996) 423.

3)A.Sugimoto, K.Ishii, S.Matsuyama, T.Satoh, K.Gotoh, H.Yamazaki; C.Akama, M.Sato, T.Sakai, T.Kamiya, M.Oikawa, M.Saidoh and R.Tanaka, Int. J. PIXE, 9 (1999) 151.

7.6 Analysis of Uranium in Minerals by SEM, TEM, micro-PIXE, XPS and XAFS

T. Ohnuki*, N. Kozai*, M. Samadfam*, R. Yasuda**, T. Kamiya***,
T. Sakai*** and T. Murakami****

Department of Environmental Science, JAERI*, Department of Hot Laboratories, JAERI**, Advanced Radiation Technology Center, JAERI***, Mineralogical Institute, The University of Tokyo****

1. Introduction

The two important oxidation states for uranium (U) in environment are IV and VI. The U(IV) is essentially insoluble in mildly acidic to alkaline groundwaters, whereas U(IV) solubility is commonly controlled by uraninite or coffinite. On the other hand, the U(VI) is potentially much more mobile, due in part to the higher solubilities of most U(VI) minerals[1]. The mobility of dissolved U in natural water is affected by processes such as adsorption or desorption of U ions and precipitation or dissolution of U-bearing minerals. Thus, oxidation states and chemical forms of U sorbed on minerals and/or U bearing minerals should be clarified to understand the behavior of U in environment.

The electron technology is introduced to mineralogical science in the 60's and early 70's. Mineralogical analysis using electron probe microanalysis (EPMA), scanning electron microscopy (SEM) and transmission electron microscopy (TEM) have been developed by employing this technique. Today SEM and EPMA are traditional methods to determine U concentrations and chemical forms of U-minerals from nm to μm scale in rock samples.

Application of high-energy ion beams also goes back to the early 70's. Particle induced X-ray emission (PIXE) is one of the possible methods detecting the elements in the level of ppm [2]. If we use the probe beams of μm order or less in diameter, U distribution in a rock sample can be determined with such the spatial resolution. A light ion microbeam system with the spatial resolution of less than 1 μm was constructed on a beam line of 3 MV single-ended accelerator in TIARA facility of Takasaki Establishment. Micro-PIXE (μ-PIXE) analyzing system was developed on TIARA facility for various elemental analyses with a sub-micron level spatial resolution [3]. Thus, mapping of U of ppm level is available by μ-PIXE.

X-ray absorption fine structure (XAFS) developed in 80's is a powerful method for structure and electronic state analyses, which can be used for not only crystalline but also non-crystalline materials under various environments. Fluorescent XAFS has higher sensitivity, thus is used for the materials containing low element concentration. XAFS and X-ray photoelectron spectroscopy (XPS) were used to analyze oxidation states and chemical forms of U in the U mineral samples [4].

Using above probes, we have analyzed the mineralogy, distribution and speciation of U-containing rock samples collected at the Koongarra U deposit, Australia [5], and have compared in terms of space resolution, detection limit in concentration, and empirical formula determination.

2. Experimental

Rock samples collected at the Koongarra U deposit, Australia were treated in two different ways; as thin sections and powder. Petrological thin sections of about 30 μm thick were made. The thin sections were initially checked by optical microscopy (OM), then were provided for the analyses by SEM and EPMA. Cores of 3 mm in diameter were drilled in interesting region of some of the thin sections. The ultramicrotomy and ion-thinning methods were critical for the examinations by TEM, and analytical electron microscopy (AEM).

Cores of 6 mm in diameter were drilled in interesting region of some of the thin sections. Proton beam with the energy of 2.5 MeV from the single-ended accelerator was used for μ-PIXE analysis. Beam spot was approximately 1 μm in diameter. X-ray detection system was similar to that used in EPMA analysis.

A thin film of a powder sample of U minerals was prepared for XAFS and XPS measurements. Co-precipitates of uranium and iron(III) and cupper(II) oxides/hydroxides were also provided for the XPS measurement.

L_{III} edge X-ray absorption spectra of U were measured in transmission mode and fluorescent mode at the BL-27 station of Photon Factory (PF) at the High Energy Accelerator Research Organization (KEK). Synchrotron radiation

from a storage ring operated at 2.5 GeV or 3.0 GeV was monochromatized with a Si(111) double crystal monochromator. XPS measurement was carried out at the same station in PF with 2104 eV monochromatized radiation.

3. Results and discussion

SEM and TEM analysis

Backscattering electron image (BEI) of apatite which is an accessory mineral in the host rock at Koongarra deposit shows that apatite in the sample of DDH 65-97 is surrounded with uranium-containing minerals (brightest area in Fig. 1)[6]. EPMA analysis of the U mineral shows that chemical component of the U mineral is expressed by $Mg(UO_2)_2(PO_4)_2 \cdot 10H_2O$. The mineral expressed by the formula is saleeite. Closer examination reveals that apatite grains are partly replaced by saleeite[7]. The cavities in the apatite grains were observed indicating that some of apatite was dissolved, and the dissolved constituents were transported downstream. Dissolution of apatite and formation of saleeite are expressed by:

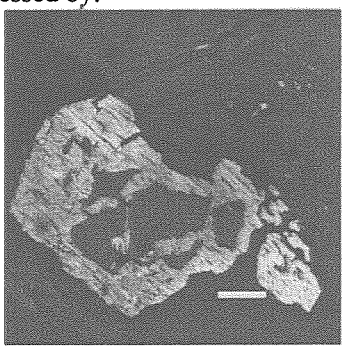


Figure 1 Backscattering image micrograph of apatite (A) surrounded with U grain (SL). Scale bar indicates 10 μm.

$$Ca_5(PO_4)_3F + H^+ + 2UO_2^{2+} + Mg^{2+} + 10\,H_2O = Mg(UO_2)_2(PO_4)_2 \cdot 10H_2O + HF + 5Ca^{2+} + PO_4^{3-}.$$

Intrestingly, though apatite contains calcium (Ca), the replacement of apatite by autunite ($Ca(UO_2)_2(PO_4)_2$) was not observed. The size of saleeite aggregates was 20 – 100 μm.

The OM micrograph of the polished thin section from DDH 60-65 shows that U is associated with iron (Fe) mineral, which occurs midstream from the uranium deposit. EPMA analysis shows that Fe mineral contains uranium of about several wt%. However, U mineral was not determined by EPMA. Constituents of the Fe mineral veins in sample DDH4-99, where we found U associated with phosphorous (P) by SEM-EDX, were examined by TEM. One of the U-bearing minerals was removed from the thin section and examined by TEM and AEM. The predominant crystalline phases in the Fe mineral veins are goethite and hematite, since most of the diffraction spots and rings can be attributed to these two minerals. Ferrihydrite, which is difficult to be identified using TEM or AEM , may coexist with goethite and hematite in the samples. A TEM micrograph indicates that small domains of goethite and hematite (mostly in the range 2 – 50 nm) are randomly oriented (Fig. 2)[7].

AEM indicates that U coexists with P, Mg and Cu. Phosphorous, Mg and Cu are probably derived from dissolution of apatite, chlorite and chalcopyrite of the host rock, respectively. The lattice fringes with spacing 1 nm was observed in TEM photograph. AEM spectrum did not give any formula of the U minerals, because size of U-bearing minerals is quite smaller than the detection area of AEM. However, the lattice fringe indicates that the mineral is saleeite of approximately 20 nm in size.

μ-PIXE analysis

Figure 2 shows the distribution of uranium and phosphate obtained by μ-PIXE in the thin section of the rock samples of DDH 65-97 (same position shown in Fig. 1). The brightest area in the right figure indicates the primary apatite. The outer rim around the primary apatite is darker than that in the primary apatite. Uranium is not present in the primary apatite, but in the rim (left figure). The primary apatite observed in the thin section from DDH 65-100, which is located slightly deeper position than DDH 65-97, does not contain any uranium. These indicate that some phosphate dissolved from the primary apatite and some uranium migrated from the primary ore react at the rim of the primary apatite to be mineralized to form saleeite. Spatial resolution by μ-PIXE was around 1 μm in the figure.

XAFS and XPS analysis

The energy of U L_{III} absorption edge of uranyl minerals is higher than that of uraninite. The structure of near edge spectra of U is also dependent on the oxidation state of U(IV and VI). Minimum U content of the sample for the near edge spectra was approximately 0.1 wt% by a fluorescent XAFS. The peak for U in the uraninite sample of ca. 0.1 mm in diameter installed in the indium foil was not detected by a transmission mode, but by a fluorescent XAFS.

XPS and XAFS analyses for U minerals show that absorption peak positions differ

between UO_2 and $UO_3 \cdot nH_2O$. And chemical shift of U(VI) peak of $U4f_{5/2}$ and $U4f_{7/2}$ from $UO_3 \cdot nH_2O$ to metatorbernite was higher than that from uraninite to $UO_3 \cdot nH_2O$. These indicate that XPS and XAFS are effective to determine not only oxidation state of U but empirical formula of U minerals.

Comparison among the probes

The comparison among the probes in terms of space resolution, sample preparation, detection limit and empirical formula determination are shown in Table 1. The spatial resolutions of the probes are in the order of TEM > SEM, μ-PIXE > XAFS, XPS. The lower detection limits of the probes are in the order of μ-PIXE < TEM, SEM < XAFS, XPS. Samples for XAFS and XPS are more easily prepared than those for μ-PIXE, SEM and TEM. Oxidation state of U was not determined by SEM and TEM, but by XAFS and XPS.

These results indicate that combination of the above probes can give us sufficient data on U speciation in not only in natural rock samples, but in solid samples obtained in the laboratory.

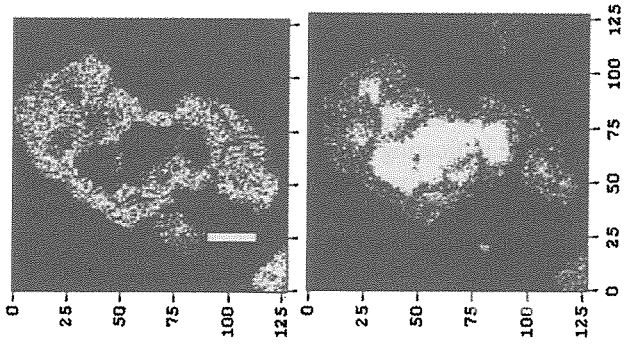


Fig. 2 U (left) and P (right) distributions obtained by μ-PIXE in and around apatite. Brighter spot shows higher concentration of elements. Scale bar: 10μm.

Table 1 Comparison between SEM, TEM, μ-PIXE, XAFS and XPS

Method	Resolution	Detection limit	Chemical formula	Oxidation state
SEM	μm	0.1wt%	Yes	No
TEM	nm	1 wt%	Yes	No
μ-PIXE	μm	1 ppm	Yes	No
XAFS	mm	1 wt%	Yes	Yes
XPS	mm	1 wt%	Yes	Yes

References

[1]Osmond J.K. and Ivanovich M., In M. Ivanovich and R. S. Harman eds. uranium series disequilibrium: Application to earth, marine, and environmental science (2nd Ed.) p259-289, Oxford University Press, Oxford(1992).

[2]Sueno S., Eur. J. Mineral., p1273-1297(1995).

[3]T.Kamiya, T.Suda and R.Tanaka, Nuclear Inst. Method B 118 447-450(1996).

[4]Duff M. C., et al., Geochim. Cosmochim. Acta, vol. 61, p73-81(1997).

[5]Murakami T., et al., ARAP final report Vol. 9, OECD/NEA, Paris(1992).

[6]Isobe H., Murakami T., Ewing R., J. Nucl Mat., 190. p174-187(1992).

[7]Murakami T., Ohnuki T., Isobe H., Sato T., American Mineralogist, 82, 888-899(1997).

7.7 Energy Stabilization Test for TIARA 3MV Single-ended Accelerator

T. Sakai, T. Satoh, M. Oikawa, T. Kamiya and S. Uno
Advanced Radiation Technology Center, JAERI

1. Introduction

Instability of a terminal voltage for electrostatic accelerators is one of the major problems in accelerator operations. This fluctuation expands an ion beam energy spread that decrease the transmission of the energy analyzing magnet and increase the fluctuation of beam current on targets. Especially, unstable beam current cause fatal errors in quantitative analysis such as micro-PIXE experiment which requires very narrow energy spread ($\Delta E/E \sim 10^{-5}$) of the ion beam[1].

The terminal voltage of TIARA 3 MV single-ended accelerator is sensed by the amount of down-charge current through high precision resistors which are located parallel to the high voltage multipliers. However these resistor are subject to the breakdown in the high voltage column. Once the resistor were degraded, the precise voltage on the terminal could not be sensed. This serious problem is still unsettled.

New energy analyzing slits and a difference amplifier circuit were designed and constructed to stabilize the energy of ions produced by the single-ended accelerator. In

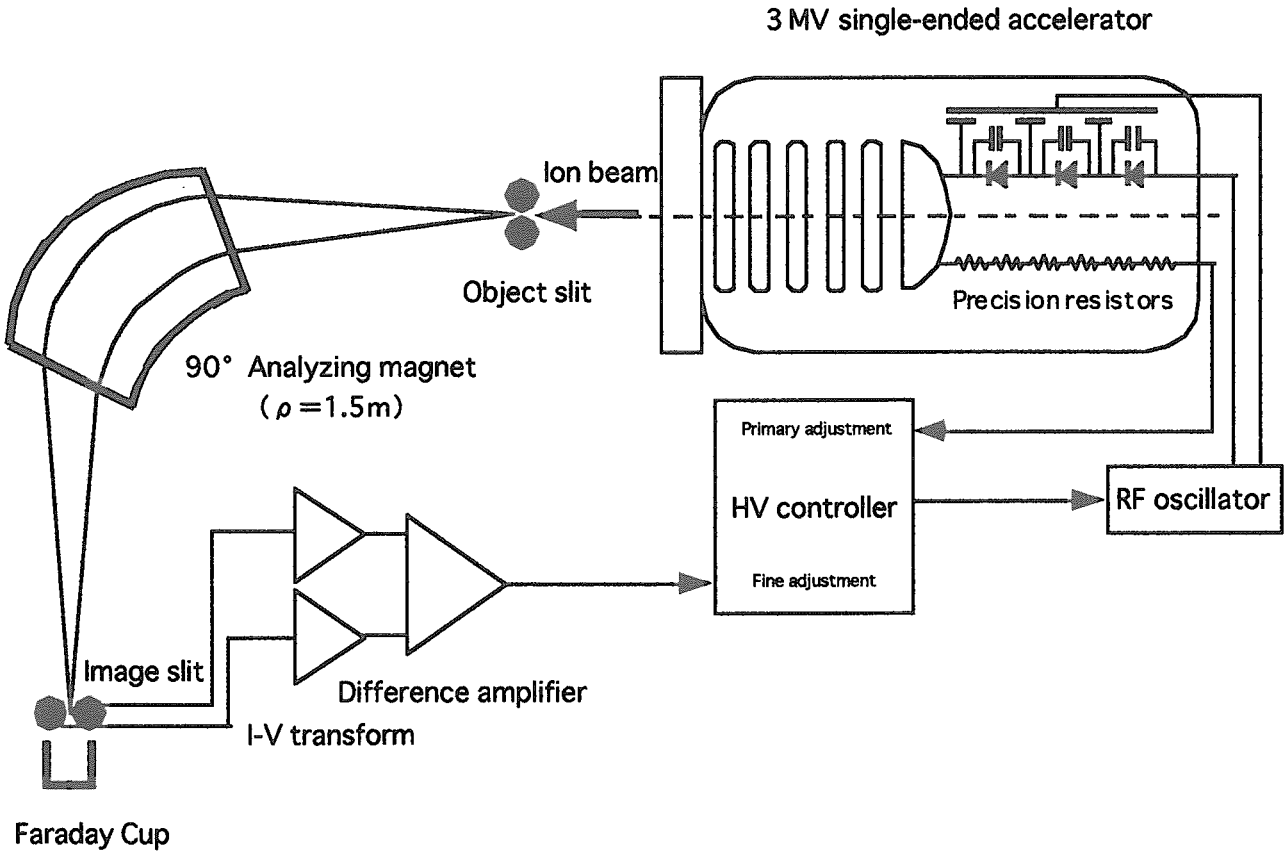


Fig.1 Schematic diagram of the energy analyzing and stabilizing systems

the present work, the new energy stabilizing system was combined to the accelerator and tested its performance.

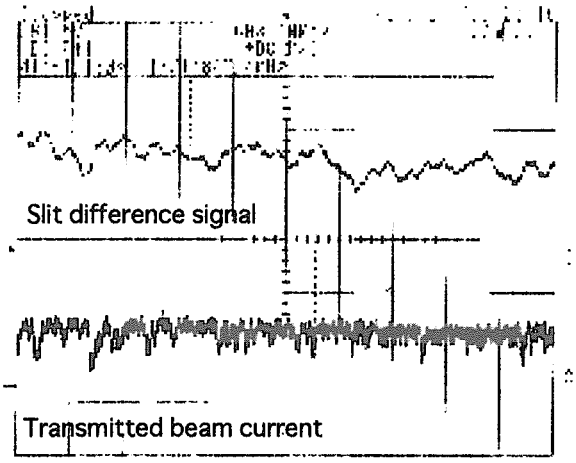
2. Instruments

The 3 MV single-ended accelerator is equipped with a balanced type Schenkel DC power supply as the high voltage generator[2]. The terminal voltage is only stabilized by the up-charge controller. The control signal is formed by comparing a high voltage monitoring signal and a setting signal. The controller has two source supplies, one is a primary supply and another is a fine adjuster. The tuning range of the latter is a thousandth of the former. In this work, a feedback signal, which was formed by a slit current balance, was fed to the fine tuning power supply.

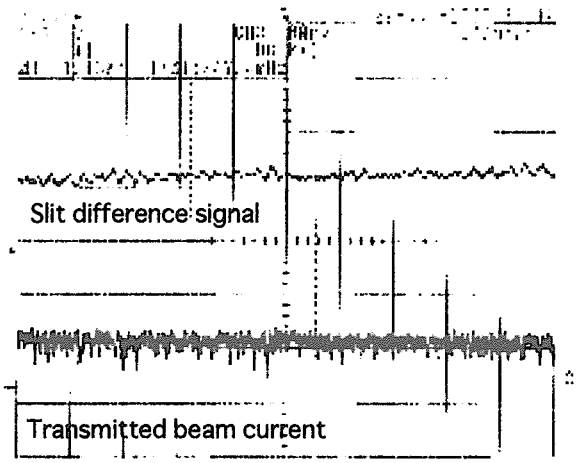
The image slit is assembled with a pair of cylindrical copper electrodes whose gap is 0.2 mm. Both low-energy and high-energy slit currents are amplified and fed into a difference amplifier. Conventional operational amplifiers (CA3140) were used in the circuit. The magnetic field of the 90° analyzing magnet was controlled by a NMR (Nuclear Magnetic Resonance) probe and a feedback system those resolution was better than 10^{-5}. Fig. 1 shows a diagram of the energy analyzing and stabilizing systems.

3. Results

The initial test was performed with 2 MV terminal voltage, extracting proton beam current of 1.5 μA at just after the object slit. Oscillographic traces of both the slit difference signal and the beam current of a Faraday cup at located just downstream from the image slit were measured as shown in Fig. 2. The results showed that the new system was effective to stabilize the voltage fluctuation in the frequency range of a few



(a) Slit amplifier system off



(b) Slit amplifier system on

Fig.2 The oscillographic traces of the slit difference signal and the beam current measured at a Faraday cup downstream from the image slit.

Hz. However higher frequency fluctuation still remained. The frequency range is limited by the response of the controller and the up-charge loading speed to the terminal.

More then one voltage stabilizer is used to minimize the fluctuation for the wide frequency range, although multiple-loop feedback instability[3] must be taken into

account. In future we are planning to adopt a terminal stabilizer[4)-5)], that is equipped with a voltage modulator between the ion source and the terminal, for further improvements.

Acknowledgement

We are grateful to S. Tajima and JAERI electrostatic accelerator group for their continuous assistance.

References

1) T. Kamiya, T. Suda and R. Tanaka, Nucl. Instr. and Meth. B118 (1996) 447.
2) Y. Saitoh et.al., Nucl. Instr. and Meth. B89 (1994) 23.
3) J. Takács, Energy Stabilization of Electrostatic Accelerators, (John Wiley & Sons, Chichester, 1997)
4) G. W. Roth and W. G. Weitkamp, Nucl. Instr. and Meth. 115 (1974) 501.
5) J. E. Cairns, M. W. Greene and J. A. Kuehner, Nucl. Instr. and Meth. 114 (1974) 489.

7.8 Development of the Measurement Method of Fluoride Distribution in Teeth.

M. Nomachi, K. Yasuda*, H. Yamamoto**, Y. Iwami**, S. Ebisu**, T. Kamiya***, T. Sakai***, and M. Oikawa***
Graduate school of Science, Osaka University
Wakasa-wan Energy Research Center*,
Graduate school of Dentistry, Osaka University**,
Advanced Radiation Technology Center, JAERI***

1.Introduction

In the field of dental research, fluoride ion, which exhibits cariostatic properties on hydroxyapatite[1-2], has been clinically applied in forms such as fluoride varnish, fluoride toothpaste, mouth rinse and dental materials. In spite of voluminous amount studies of fluoride uptake, the effect of fluoride on the caries has not been clear yet. Small atomic number of the fluoride in the periodic table prevents non-destructive quantitative chemical analysis.

In the present study, we report the fluoride uptake into the cavity wall by proton induced gamma-ray emission (PIGE) using a micro-beam apparatus. Beam spot size of the TIARA micro-beam apparatus is much smaller than that of the previous PIGE measurements[3-4]. We have developed the method to measure the beam current for thick targets such as teeth. It will be a powerful tool to measure microstructure of fluoride distribution.

2. Experimental setup

The 1.7 MeV proton beam accelerated by the TIARA single-ended accelerator was extracted to an external ion micro-beam apparatus[5]. The beam spot size was about 1 μ m with a beam current of about 100pA. The area of 500 μ m by 500 μ m was scanned at maximum[6].

We have used a nuclear reaction $^{19}F(p, \alpha\gamma)^{16}O$ for measuring fluoride density. The gamma rays of this reaction were detected with a 5" NaI(Tl) detector. Observed energy spectrum of the gamma rays is shown in Figure 1. The energy of the gamma ray of the reaction is much higher than the energy of background gamma rays generated by natural radioactivity, because the reaction has large Q-value. The measurement using the nuclear reaction has, therefore, very higher signal to noise ratio than the other methods.

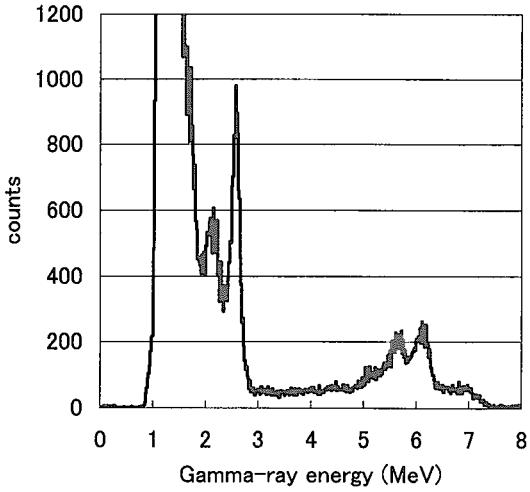


Fig.1. Gamma-ray energy spectrum measured by bombarding a fluoro-apatite target with 1.7 MeV proton-beam. Gamma rays are detected with a 5" NaI detector. Background gamma rays from natural radioactive sources are seen at ^{40}K:1.461MeV, ^{208}Tl:2.614MeV. Gamma rays from proton-fluoride nuclear reactions having energy of 6.143MeV, 7.112MeV and their one-photon escape peaks, are seen in higher energy region in the figure.

Density of calcium was measured by the X-ray. Proton induced X-rays were detected with a Si(Li) detector at the same time.

The specimens were thicker than the range of 1.7 MeV protons. Gamma-ray yield depends on the number of fluorine nuclei in the proton range. It is proportional to fluorine mass density in the case of similar chemical components. Gamma-rays yield from reference materials $Ca_{10}(PO_4)_6(OH)_{2-2x}F_{2x}$ (x=0, 0.1,0.5,1.0), which have similar chemical compounds to those of a

tooth, were measured. X-rays yield is also measured for the reference targets.

The measurement of the beam current is indispensable for quantitative measurements. In the case of thick targets like teeth, however, direct measurement is not possible. We monitored the beam current by measuring X-ray intensity from a 10 μm copper foil next to the measured region. The copper foil was bombarded for three seconds in every 30 seconds.

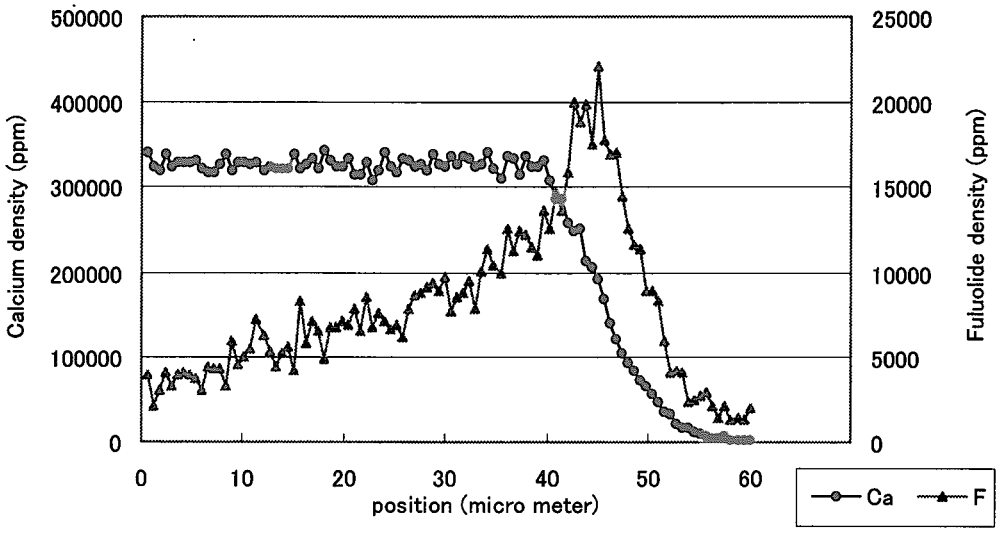


Fig.2. Distributions of calcium and fluoride in a human tooth for the etched specimen. The density is shown in mass ppm. The position is shown in micrometer. The spectrums are obtained in two-hours measurement. The edge in the calcium distribution indicates the cavity wall, since the region filled with the light-cured resin has no calcium. High concentration is observed near the cavity wall.

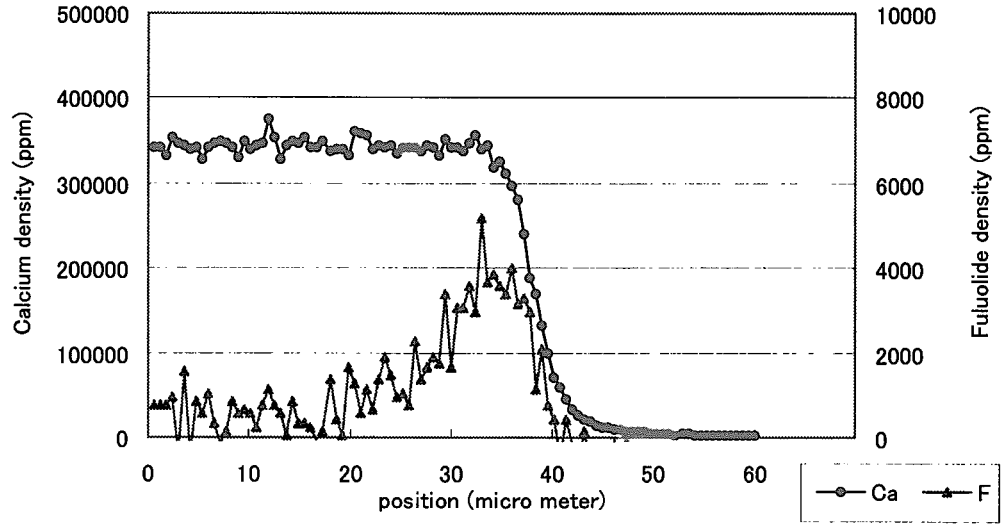


Fig.3. Distributions of calcium and fluoride in a human tooth are for the non-etched specimen. The density is shown in mass ppm. The position is shown in micrometer. The spectrums are obtained in two-hours measurement. The edge in the calcium distribution indicates the cavity wall, since the region filled with the light-cured resin has no calcium.

3. Measurements

Human premolar teeth were used as specimens. These teeth, which were extracted for orthodontic reasons within two months prior to the study, had no cracks, white spots nor enamel defects. Two specimens were prepared for the measurement. Class V cavities were positioned at 2.5mm up from the cementoenamel junction along the median line in the buccal face, the direction was toward the pulp and the shape was an elliptic pillar (1.5mm x 3.5mm x 1.5mm). The cavities were made with a water-cooled high-speed handpiece and diamondpoint. The cavity on one specimen was etched with acid, but that one the other specimen was not. The cavities were filled with the light-cured resin (Teethmate F-1, Kuraray Ltd, Osaka, Japan) as fluoride releasing material and cured for 80 sec. The teeth were coated with nail polish except for the filled cavity surface, immersed in a plastic capsule filled with 10ml of normal saline solution (saline) and kept at 37℃. After one-month immersion, the samples were removed from the saline, bisected longitudinally through the center of the cavity perpendicular to the axial wall with a precision saw (Isomet, Buehler Ltd., Lake Bluff, ILL USA). The fluoride concentration in the cavity wall adjacent to the filling material was measured on the surface of the bisected tooth.

4. Results

Figure 2 and 3 shows distribution of calcium and fluoride along the line perpendicular to the cavity wall in the specimens. The data were obtained in two-hour measurements with about 100pA-proton beam. Scan area was 84 μ m by 74 μ m. The distribution was obtained along 84 μ m with width of 10 μ m. The calcium and fluoride density is shown in mass ratio.

An edge of calcium distribution indicates the cavity wall. Comparing two specimens, the etched one has more fluoride concentration as high as 20000 ppm and the peak position is more inside as shown in the figure 2. The density at the peak is 4000 ppm in non-etched specimen as shown in the figure 3.

5. Summary

PIGE analysis provides very well signal to noise ratio for observing fluoride distribution. It is shown that quantitative measurements about 1000 ppm of fluoride or less, using the micron beam line at TIARA are feasible.

The small beam spot makes possible to resolve fine structures in fluoride distribution. Observed fluoride concentration in the narrow area shown in the present study can be seen only with sub-micron beam lines.

References

1) De Bruyn et al., *Jour. Biol. Buccalle,* **14**, 133 (1986)

2)W.E.Brown et al., *Caries Res.,* **11** *(Suppl.),* 118 (1977)

3) G.E.Coote, *Nucl. Instr. And Meth,* **B66** 191 (1992)

4) H.E. Zschau et al., *Nucl. Instr. And Meth.* **B66**, 292 (1992)

5) T. Sakai et al., *Biological Trace Element Research,* p77-82 Vols. **71-72**, (1999)

6) T. Sakai et al, *Nucl. Instr. And Meth.* **B136**, 1 (1998)

7.9 Development of a High-Energy Microbeam Single Ion Hit Technique for Bio-Medical Applications

T.Kamiya, T.Sakai, M.Oikawa, W.Yokota, Y.Kobayashi*, M.Taguchi* and M.Cholewa**
Advanced Radiation Technology Centre, JAERI
*Department of Radiation Research for Environment and Resources, JAERI
**The School of Physics, The University of Melbourne, Australia

1. Introduction

A single ion hit technique is useful to introduce large radiation effect to specific local area of various biological cells with single-ions. This kind of techniques has been developed at several facilities to hit individual cells in the atmosphere for bio-medical applications[1-3]. A similar technique has also been introduced to the high-energy microbeam system, which was installed on a vertical beam line of AVF-cyclotron in TIARA. Uniqueness of this system that it has been designed to irradiate living organisms with high-energy (more than 10 MeV/u) heavy ion beams, while others are with lower energy (several MeV/u) light ions. The beams have been collimated to about 10 μm in diameter; more than 95 % of the collimated ions were within the mono-energetic peak and delivered to the aimed local with 85-90 % of targeting accuracy.

A fundamental technology of single ion hit, which was applied to this system, was established at the heavy ion microbeam system connected to a 3 MV tandem accelerator[4,5]. An automated beam positioning technique, on the other hand, is required for single ion hit to individual cells in a crowd of those, which may be spread on a holder randomly. In order to get information of positions of adequate cells to be hit in a shorter period, automatic cell recognition system that consists of an optical microscope, sample stages and a computer system will be introduced.

This report outlines the single ion hit technique combined with the automated cell recognition and beam positioning system. It also presents future plans of technical development for its bio-medical application in JAERI Takasaki.

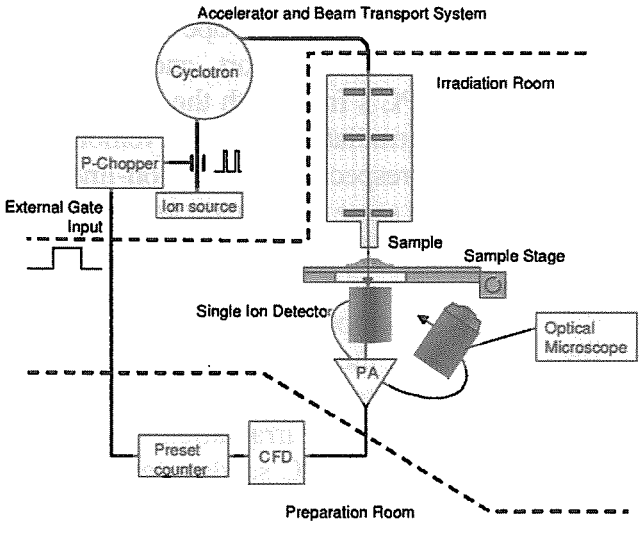


Fig. 1. Block diagram of the single ion hit system

2. Single ion hit System

A schematic diagram of the single ion hit system introduced to the AVF cyclotron machine and its vertical microbeam line [6], on course HZ, is shown in Fig. 1. The system consists of a single ion detector using a plastic scintillation counter and a fast beam switch using a P-chopper in the injection system of the cyclotron machine [7]. The scintillation counter, which occupies a port of the objective lens revolver in the optical microscope to observe samples on the stages, detects single ions passing

through a thin target. The P-chopper was designed to chop the DC beams into pulses spaced at intervals of from 1 μs to 1 ms. The single ion hits on the target can be realized by setting the P-chopper enable only in periods that a counter module is counting single ion detection signals up to any preset number.

260 MeV Ne and 460 MeV Ar ions were irradiated to CR-39 films for preliminary experiments. Fig. 2 shows an SEM image of a CR-39 irradiated by 460 MeV Ar ions and etched by NaOH solution. A pitch of the matrix is 50 μm controlled by movement of the sample stages. The number of ions to be irradiated onto each position was from 1 to 16. Some irregular and missing hits can be seen, due to noise and scattering at the exit-edge of the micro-capillary, respectively. Scattering effect was enhanced in the case of 260 MeV Ne ion irradiation, because it is lighter than an Ar ion.

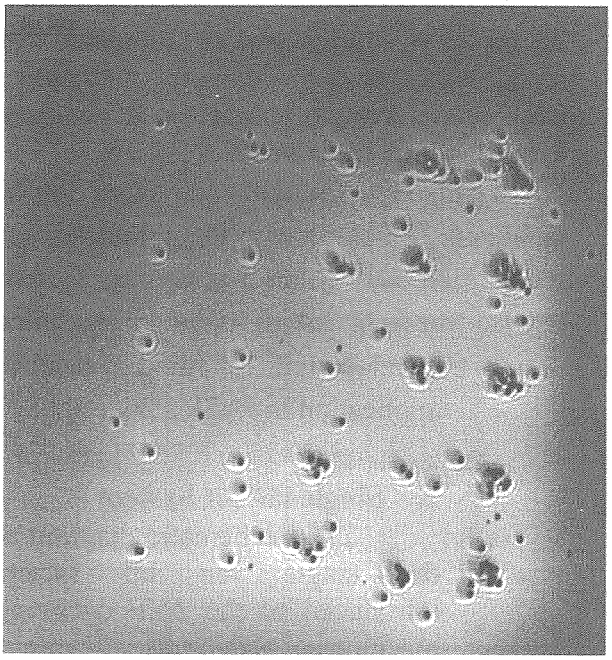


Fig.2. SEM image of CR-39 irradiated by 460 MeV Ar ions with 5 x 5 matrix positions and etched by NaOH solution. A pitch of the matrix is 50 μm controlled by movement of the sample stages. The number of ions to be irradiated onto each position was 1, 2, 4, 8 and 16 from the left side column to the right, respectively. Some irregular and missing hits can be seen.

3. Automated Cell Recognition and Beam Positioning System

So far, a spatial resolution of ion hits is 10 μm. It is small enough to irradiate biological cell with the size of 10 μm or more individually. In order to obtain statistically accurate results in a study of single ion irradiation effect, enough number of cells should be irradiated and investigated. An automated cell recognition and beam positioning system [8] was introduced to meet this requirement. A block diagram of the system is shown in Fig. 3. The system consists of an off-line and an on-line system.

The former is located at the heavy ion preparation room. The system consists of a high precision three-axis sample stage, an optical microscope, and a CCD camera to observe individual objects such as biological cells, a joystick to manipulate samples, and an off-line PC. The system controls the stage and takes images of samples containing scattered objects to recognize them individually using image processing with a positional reproducibility of less than 5 μm.

The later basically has the similar configuration to the former, but the sample stage and the microscope are located at the beam irradiation port and controlled by on-line PC's from both the preparation room and the irradiation room for remote and local control, respectively. The on-line stage can have the same coordinate as the off-line, if a fine fiducial mark is set at an adequate position in the sample plane. On-line PC uses common databases of recognized objects in the off-line system to revisit and irradiate the same object with the same accuracy. In irradiation processes, the on-line remote PC sends a 'enable' signal to a NIM counter module after each beam positioning process is completed and waits for a 'interval' signal flipping to zero, that is indicating irradiation completed.

4. Summary

A single ion hit system and an automated cell recognition beam positioning system was installed to the vertical microbeam line of the AVF cyclotron in TIARA. Irradiation tests for a CR-39 has been made with the single ion hit system. Tests of automated cell recognition and beam positioning will be made with damy sample and real cells. We also have a future plan to construct a focusing microbeam system on another beam line of the same cyclotron, so as to obtain higher positioning accuracy to hit local areas of cells, such as nuclei, mitochondria, chloroplasts, cell shells, and so on.

References

1)M.Folkard, B.Vojnovic, G.Schettino, M.Forsberg, G.Bowey, K.M.Prise, B.D.Michael, A.G.Michette and S.J.Pfauntsch, Nucl. Instr. And Meth. B130 (1997) 270.

2) C.R.Geard, D. J. Brenner, G. Randers-Pehrson, and S. A. Marino, *Nucl. Instr. and Meth.* B54, 411-416 (1991)

3) L.A.Braby, *Scanning Microscopy*, 6, 167-175 (1992)

4)T.Kamiya, T.Sakai, T.Hamano, T.Suda and T.Hirao, Nucl. Instr. And Meth. B130 (1997) 285.

5)T.Kamiya, T.Suda and R.Tanaka, Nucl. Instr. And Meth. B118 (1996) 423.

6)Y.Kobayashi, M.Taguchi, T.Shimizu, S.Okumura and H.Watanabe, J. Radiat. Res. 36(4) (1996) 290.

7)W.Yokota, M.Fuhuda, S.Okumura, K.Arakawa, Y.Nakamura, T.Nara, T.Agematsu and I.Ishibori, Rev. Sci. Instrum. 68(4), (1997) 1714.

8) M.S.Krochmal, G.Laken, I.D.Larsen, L.Fiddes, G.Parkhill, K.Dowse, Autoscan Systems Pty. Ltd., Australia

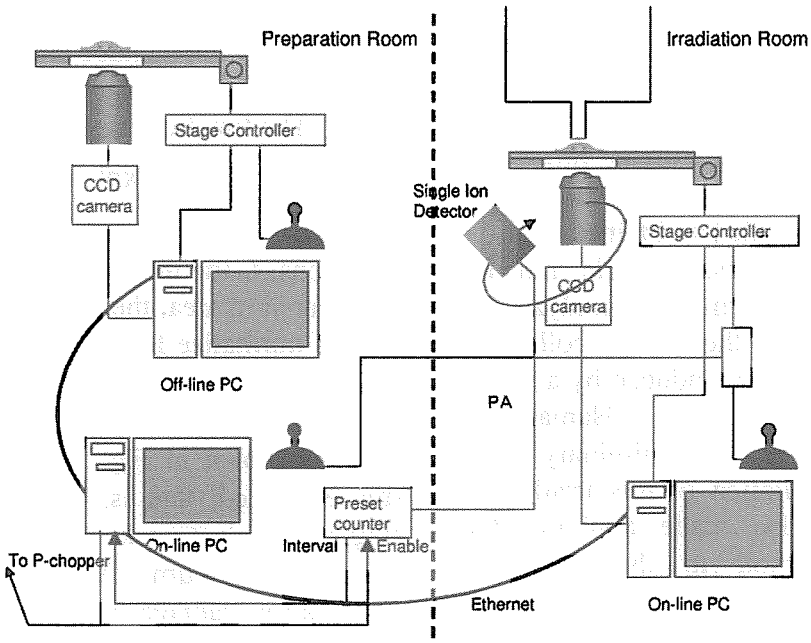


Fig. 3. Block diagram of the automated cell recognition and beam positioning system.

7.10 Radiation Damage in Si PIN Diodes Induced by Heavy Ion Microbeam Single Hits

T.Kamiya, T.Sakai, M.Oikawa and T.Hirao*
Advanced Radiation Technology Centre, JAERI
*Department of Materials Development, JAERI

1. Introduction

The single ion hit system [1-3] combined with the heavy ion microbeam system was originally designed to observe individual single even phenomena in semiconductor devices induced by single ion injections [4]. Observable subjects in such experiments are radiation effects by high-energy single ions. Properties of the charge generation and collection have been evaluated on various kinds of semiconductor devices.

However, a phenomenon induced by a heavy ion with a high LET consists not only of the charge generation and collection but also of radiation damage in crystal structure of the devices. Single event effects have been studied using the test devices as the targets of heavy ion microbeam to measure transient current pulse shapes with a digital sampling method. However, it was appear that 10^3 or more ion injections to obtain one clear transient pulse curve in this method also introduce damages in a local area of the device [4]. In order to investigate properties in the phenomenon individually, the further analyses should be made on obtained data.

In the present study, single ion hit experiments was performed to analyze the lateral extent of both the charge collection and the radiation damage induced by a single ion in a Si PIN diode (Hamamatsu Photonics, S1223-01) as a preliminary study [5]. Computer simulation of this irradiation experiment was also made applying the Monte Carlo method to the positional distribution of single ion hit of microbeam.

This paper will outline the experiments and the simulation and discuss on the result results from them.

2. Measurements and Analyses

As shown in a schematic draw in the previous report[6], the timing signal from a preamplifier connected to the diode, which was reversely biased with 20 V, is used for hit detection in the single ion hit system. Continual streams of about 10,000 15 MeV Ni, 9.72 MeV Si and 6.78 MeV O ions were injected into the sample with varying the areas from 1 x 1 to 50 x 50 μm^2 and setting the same range in the Si of 4.8 μm. The pulse height of single event transient current (E-out) from the diodes were measured and stored in a data collection system.

Results of measurement show that the reduction speed of the pulse height depends on the mass of incident ions and on the area of ion injection. But it doesn't seem to show their simple linear correlation.

In order to investigate the pulse height reduction property due to the difference of overlapping between the cross sectional area of each radiation damage and charge, Weibble function was introduced for least square fitting. The function used here is as follows,

$$I = I_0 \exp\left(-n^m / b^2\alpha\right)$$

where I is pulse height, n the number of ion injections, I_0 the initial value of I, b the width of a scanning area, therefore b^2 the irradiation area to normalize the radiation density, m the shape parameter and α the scale parameter.

Parameters, m and α, change depending on b as shown in Fig. 1. The parameter α is enhanced, that is, radiation effect by a single ion injection is reduced, in the region of b less than 2 μm. When the lateral extent of radiation damage, that is almost the same as the irradiation area, is confined in smaller area than that of charge collection one, some charge may keep to be collected in never-damaged area around the damaged one. The shape parameter m increases up to about 0.9 according to b, when b is less than 16-30

μm, and then saturates. This indicates that the type of damage effect gradually changes from initial failure type to accidental failure one.

3. Simulation

Radiation damage and charge collection in events in a 1000 ion irradiation on a fixed position were simulated in a two-dimensional field consisting of many small unit pixels with applying a simple model using a Monte Carlo method. Simulation was made on the following assumptions; (1) ions hit the sample randomly with the Gaussian distribution, (2) both radiation damage and charge generation take place uniformly in each pixel within their own extents, and (3) the amount of charge collection is evaluated as the total balance of the charge generated and consumed by accumulated damage in all pixels. A schematic draw is shown in Fig. 2.

Calculated data were also analyzed with the Weibull distribution function to estimate reproducibility for measured data. Relative correlation among parameters, the beam size, the lateral extent of an individual charge collection and radiation damage, and between amount of charge generated and consumed by a single ion injection were optimized, so that simulated result well reproduces measured data for the 15 MeV Ni irradiation to 1 x 1 μm^2 area. Fig. 3 and table 1 describe an optimized result of simulation and analysis compared with that of measurement.

The extent of charge collection seems to be more than ten times as large as that of radiation damage in radius and about twice as the beam size. About a sixth of generated charge seems to be consumed per ion injection within a damage extent.

4. Summary

Accumulation of damage effect by a stream of energetic heavy ion irradiation to various local areas was investigated by data analysis using Weibull distribution function and simulated by a two-dimensional simple model using Monte Carlo method. Since a spot size of utilized microbeams were around 1 μm, in analysis of measured data, enhancement of scale factors for smaller area in width of less than 2 μm is not contradictory to the simulation, that the area of charge collection is twice as large as the beam size in diameter. Simulation for various areas of irradiation will be made for further investigation.

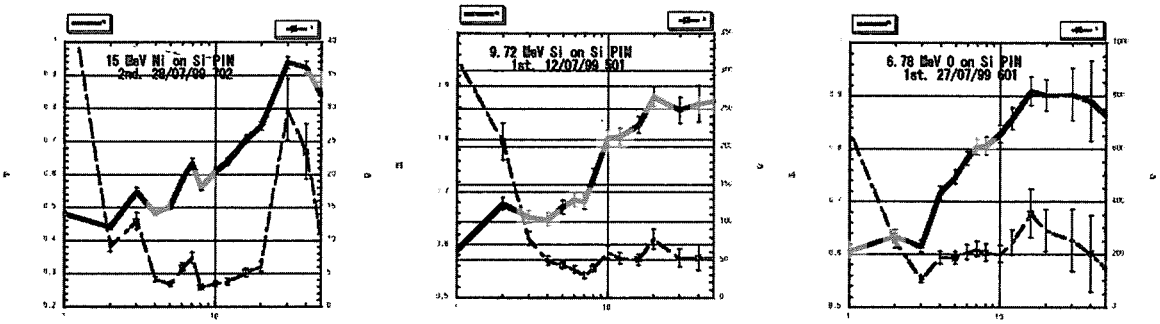
References

1)T.Kamiya, T.Sakai, T.Hamano, T.Suda and T.Hirao, Nucl. Instr. And Meth. B130 (1997) 285.
2)T.Kamiya, T.Suda and R.Tanaka, Nucl. Instr. And Meth. B118 (1996) 423.
3)T.Sakai, T.Hamano, T.Suda, T.Hirao and T.Kamiya, Nucl. Instr. And Meth. B130 (1997) 498.
4).Nashiyama, T.Hirao, T.Kamiya, H.Yutoh, T.Nishijima and H.Sekiguchi, IEEE Trans. On Nucl. Sci. 40, No.6 (1993) 1935.
5)T.Kamiya, T.Sakai, Y.Naitoh and T.Hirao, Nucl. Instr. And Meth. B158 (1999) 255.
6)T.Kamiya, T.Sakai, T.Hirao and Y.Naitoh, TIARA Ann. Rep. 1998, JAERI-Review, 99-025 (1999) 220.

Table 1. Parameters obtained by data analyses using the following Weibull distribution function for measured data in the case of 15 MeV Ni irradiation to 1 x 1 μm^2 area of the PIN diode and for simulated ones reproducing the measured. Note that b = 1, in this case.

$$I = I_0 \exp\left(-n^m/\alpha^b\right)$$

Parameters	Measured	Simulated
I_0	1942 ±23	1977 ±15
m	0.597 ±0.029	0.592 ±0.019
a	111 ±24	114 ±16



(a) (b) (c)

Fig. 1. Shape parameters *m* (rigid line) and scale parameter α (dashed) versus *b* for (a) 15 MeV Ni, (b) 9.72 MeV Si and (c) 6.78 MeV O, which have the same range in Si diode.

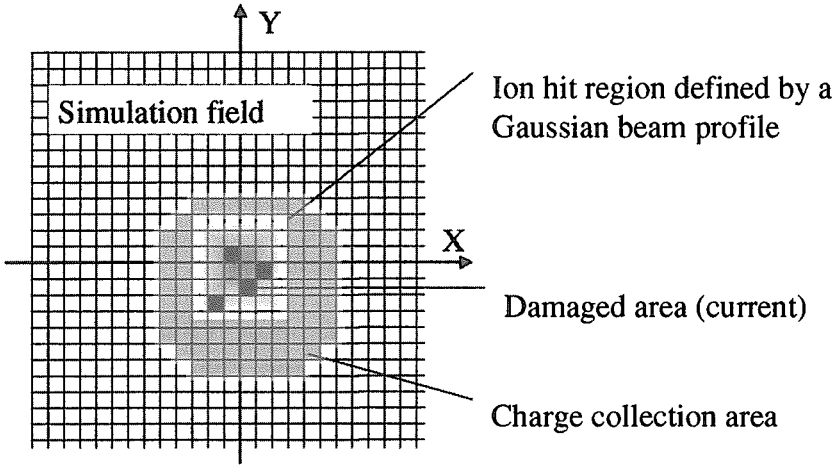
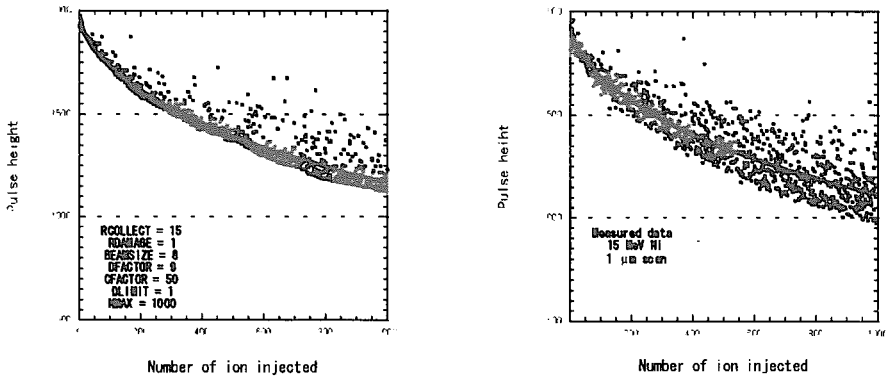


Fig. 2. Schematic draw of a simulation model for charge collection and damage generated by single ion injections. A simulation field consists of a matrix of pixels. A centroid of the ion hit region is set at the origin of the field. A current damaged area appears at the center of the charge collection area. Former damaged areas affect to the current charge collection.



(a) (b)

Fig. 3. (a) Optimized result of simulation and analysis with a Weiull disribution function in order to reproduce (b) measured data and analysis with the same function.

8. Radiation Shielding for Accelerator Facility

8.1 Measurements of Radioactivities of Residual Radionuclides
Generated by Heavy Ion Reactions below the Coulomb Barrier (II) ····· 253
Su. Tanaka, K. Nishimura, M. Hosono and M. Fukuda

8.2 Light Charged-particle Production in Proton-induced Reactions on
^{58}Ni, ^{90}Zr, ^{197}Au, and ^{209}Bi at 42 and 68 MeV ····· 256
Y. Watanabe, Y. Tanaka, Y. Matsuoka, K. Shin, M. Harada, S. Meigo, H. Nakashima,
H. Takada, T. Sasa, T. Fukahori, O. Iwamoto, S. Chiba and Su. Tanaka

8.3 Study of Cross Section Measurement Methods using the Self-TOF High Energy
Neutron Detector ····· 259
M. Sasaki, T. Nunomiya, T. Nakamura, N. Nakao, T. Shibata, Y. Nakane and Su. Tanaka

8.4 Measurement of Absorbed Dose Distributions in a Plastic Phantom Irradiated by
40- and 65- MeV Quasi-monoenergetic Neutrons ····· 262
Y. Nakane, Y. Sakamoto and Y. Harada

8.5 Charged-particle Production and Neutron Scattering Cross Sections for
55-75 MeV Neutrons ····· 265
M. Baba, M. Ibaraki, Y. Hirasawa, T. Miura, T. Hiroishi, T. Aoki, H. Nakashima,
S. Meigo and Su. Tanaka

This is a blank page.

8.1 Measurements of Radioactivities of Residual Radionuclides Generated by Heavy Ion Reactions below the Coulomb Barrier (II)

Su. Tanaka, K. Nishimura, M. Hosono, M. Fukuda
Advanced Radiation Technology Center, JAERI

1. Introduction

Recently accelerators are widely used for a variety of purposes. Radioactivity is induced in the accelerator components and target samples due to exposure to primary energetic ion beams and secondary neutrons. In the planning stage of experiments, estimation of the induced radioactivity is important for radiation protection to reduce the radioactivity and to minimize radiation exposure to personnel as well as the amount of radioactive wastes. An IRACM code system[1] was developed at JAERI to calculate the radioactivity and a gamma-ray dose rate. Estimation of the radioactivity is based on calculated activation cross sections for heavy ion induced reaction. To improve precision of radioactivity calculation, the calculated activation cross sections are required to be corrected by comparing with experimental data.

The motivation for studying radioactivities of residual radionuclides generated by heavy ion reactions at energies below the Coulomb barrier came from the importance of the radiation protection against light heavy ion (A < 20) reactions at low-energy accelerator facilities. But no theoretical method gives satisfactory explanation to the heavy ion reactions.[2] Hence we have measured radioactivity of residual radionuclides generated by $^{12}C+^{nat}C$, $^{11}B+^{nat}C$ and $^{7}Li+^{nat}C$ reactions using conventional gamma-spectrometry.[3] In a current year, we extended our earlier studies to measure the production of residual radionuclides from other heavy ion reactions $^{7}Li+Al$, $^{12}C+Al$, $^{16}O+Be$, $^{16}O+^{nat}C$, $^{19}F+Be$ and $^{19}F+^{nat}C$.

2. Experiment

The radioactivities of residual radionuclides were measured by the activation method using thick-targets of high purity material containing 99% Be, 99.8% ^{nat}C and 99.99% Al. The target was 25 mm high and 25 mm wide, and the thickness was determined overall to be larger than the projected range of each ion in the targets. The ^{7}Li, ^{11}B, ^{12}C, ^{16}O and ^{19}F ions accelerated by a 3MV Tandem accelerator at TIARA were delivered to a heavy ion irradiation system consisting of a target holder in a Faraday cup. The beam was uniformly scanned over an area of 10x10 mm^2 on the target. The number of ions was estimated from the integrated charge measured with the Farady cup. After the irradiation, gamma-rays emitted from the irradiated targets were measured by the HP-Ge (ORTEC Co. Ltd. GEM-30158: relative efficiency of 35.5%) with a energy resolution of 1.75 keV for 1333 keV gamma-ray. The gamma-ray spectra obtained after the decay of short life parent nuclides were used for the analysis of the residual radionuclide production.

The saturated activity Q at cooling time t was obtained by the following relation,

$$Q = \frac{C}{\varepsilon \cdot f_a f_s f_b \phi \cdot [1-\exp(-\lambda t_i)]\exp(-\lambda t)} \quad (1)$$

where

- C : peak area of the gamma-ray emitted from the radionuclides at cooling time t,
- ε : detector efficiency,
- f_a : correction factor of self-absorption,
- f_s : correction factor of sum-coincidence effect,
- f_b : branching ratio,
- ϕ : the number of incident ions,
- λ : decay constant,
- t_i: irradiation time.

The physical constants such as decay constant were taken from Ref. 4. The detector efficiency was measured by using calibrated radioactive standard gamma-ray sources. The error in the measured reaction rates resulted mainly from a statistical error of peak counts and a detector efficiency error. The statistical error of peak counts was less than 30 % in all cases. The detector efficiency error was estimated as 5 % from the calibration measurement with the standard sources. The other error concerning uncertainty of the number of incident ions, the decay constant, the gamma ray branching ratio, the irradiation time, the measuring time and the

cooling time was 5 % in all. Correction was not made for the decay of the parent nuclides in the calculation. The residual radionuclides investigated are shown in Table 1 with physical characteristics for the measurement.

3. Results and discussion

The residual radionuclides listed in Table 1 are identified from the photon energies and relation between the photon emission rate and the cooling time. The Coulomb barrier and a threshold energy of each reaction shown in Table 1 are calculated by THRES code[1]. In ^{7}Li+^{nat}C, ^{7}Li+Al and ^{11}B+^{nat}C reactions, it was found out that a 511 keV photon was originated in a positron annihilation radiation from ^{18}F. All the residual nuclide were produced from nuclide compounded of a projectile and target nuclide.

The measured saturated activity for the residual radionuclides is shown as a function of incident ion energy in Fig. 1. It is evident that the long-lives radionuclides are generated by the heavy ion reaction below the Coulomb barrier. The result indicates that estimation of the induced radioactivity even for the incident energy below the Coulomb barrier is required for the irradiation planning for the radiation protection.

In the present IRACM code system, an activation cross section library, ACSELA[1] was compiled for 57 elements and 136 nuclei for incident particles of n, p, d, He-4, C-12, N-14, O-16, Ne-20 and Ar-40. For precise estimation of the residual radioactivity, the ACSELA will be extended for the incident particles to all light heavy ions, and modified for all kind of heavy ion reactions at incident ion energies below and around the Coulomb barrier.

The authors are indebted to I. Kawashima, K. Matumoto and S. Kaneya for their helps in the irradiation and gamma-ray measurement.

References

1) Su. Tanaka et al., JAERI-Data/Code 97-019 (1997)
2) S.C. Wu et al., Nucl. Phys. A570, 387c (1994)
3) Su. Tanaka et al., JAERI-Review 99-025, p.231 (1999)
4) E. Brown et al., "Table of Radioactive Isotope", Jown Wiley & Sons, Inc.(1989)

Table 1 The Coulomb barrier and a threshold energy of each reactions for which the residual radionuclides are generated

Projectile	Target	E_γ (keV)	Residue	E_C (MeV)	E_{th} (MeV)	Reaction
^{7}Li	^{12}C	511	^{18}F	6.9	0	^{12}C(^{7}Li, n)^{18}F
	^{13}C	511	^{18}F	6.6	0	^{13}C(^{7}Li, 2n)^{18}F
^{7}Li	^{27}Al	511	^{18}F	10.2	----	^{27}Al(^{7}Li, x)^{18}F
^{11}B	^{12}C	511	^{18}F	13.0	2.7	^{12}C(^{11}B, α n)^{18}F
		1274	^{22}Na		0	^{12}C(^{11}B, n)^{22}Na
	^{13}C	511	^{18}F	12.3	11.7	^{13}C(^{11}B, α 2n)^{18}F
		1274	^{22}Na		0	^{13}C(^{11}B, 2n)^{22}Na
^{12}C	^{13}C	1368	^{24}Na	15.2	0	^{13}C(^{12}C, p)^{24}Na
^{12}C	^{27}Al	1368	^{24}Na	21.7	----	^{27}Al(^{12}C, x)^{24}Na
		146	^{34m}Cl		4.1	^{27}Al(^{12}C, α n)^{34m}Cl
^{16}O	^{9}Be	1368	^{24}Na	19.7	0	^{9}Be(^{16}O, p)^{24}Na
^{16}O	^{13}C	844	^{27}Mg	22.4	3.6	^{13}C(^{16}O, 2p)^{27}Mg
		1779	^{28}Al		0	^{13}C(^{16}O, p)^{28}Al
^{19}F	^{9}Be	1368	^{24}Na	24.1	0	^{9}Be(^{19}F, α)^{24}Na
		844	^{27}Mg		0	^{9}Be(^{19}F, p)^{27}Mg
^{19}F	^{12}C	1274	^{29}Al	28.7	0	^{12}C(^{19}F, 2p)^{29}Al
	^{13}C	1274	^{29}Al	27.0	0	^{13}C(^{19}F, p)^{29}Al

E_γ: Photon energy, E_C: Coulomb barrier, E_{th} :Threshold energy

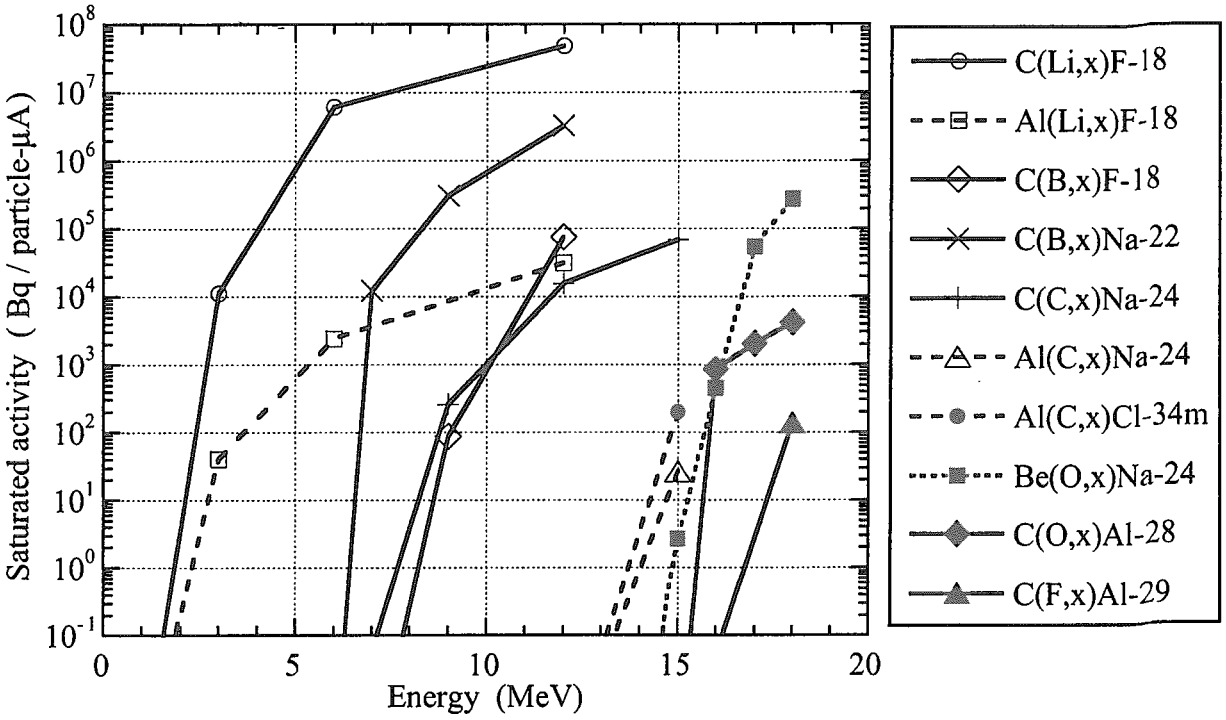


Fig.1 The measured saturated activity for the residual radionuclides as a function of incident ion energy

8.2 Light charged-particle production in proton-induced reactions on ^{58}Ni, ^{90}Zr, ^{197}Au, and ^{209}Bi at 42 and 68 MeV

Y. Watanabe[1], Y. Tanaka[1], Y. Matsuoka[1], K. Shin[2],
M. Harada[3], S. Meigo[3], H. Nakashima[3], H. Takada[3], T. Sasa[3], T. Fukahori[4],
O. Iwamoto[4], S. Chiba[5], and Su. Tanaka[6]

[1]Dept. of Advanced Energy Engineering Science, Kyushu Univ.,
[2]Dept. of Nuclear Engineering, Kyoto Univ.,
[3]Center for Neutron Science, JAERI, [4]Nuclear Data Center, JAERI,
[5]Advanced Science Research Center, JAERI,
[6]Advanced Radiation Technology Center, JAERI

1. Introduction

High-energy proton nuclear data are needed in various accelerator applications, such as accelerator-driven transmutation for nuclear waste, radiation damage estimation of semiconductor memory devices in space, and advanced proton therapy. In such applications, information on secondary particle production in nuclear reactions is indispensable for accurate calculations of high-energy proton transport in matter. In partcular, reliable double-differential cross sections (DDXs) of all emitted particles, i.e., the energy and angular distributions as a function of incident energy, play an important role in transport calculations with high accuracy. However, available systematic experimental data for protons are currently limited in a wide range of incident energy above 20 MeV.

Under these circumstances, we planned a systematic measurement of DDXs of light charged particles (protons, deuterons, tritons, ^{3}He and α-particles) emitted from proton-induced reactions in the incident energy range of protons accelerated using the TIARA facility. Following the measurement[1)] for ^{12}C and ^{27}Al done in 1998, we have meaured DDXs for ^{58}Ni, ^{90}Zr, ^{197}Au and ^{209}Bi at 42 and 68 MeV in the present work. In this report, the experimental results are compared with the latest evaluated data[2)]. Also, the dependence of target mass number on the DDXs and total yields of secondary particles is investigated.

2. Measurement

The experiments were carried out using 42 and 68 MeV proton beams delivered to the HB-1 beam line from the AVF cyclotron. The details of the experimental procedure have been reported elsewhere[1,3)].

The accelerated proton beam bombarded a thin target foil placed in the center of a scattering chamber 60 cm in diameter installed in the HB1 beam port. Energy distributions of light ions emitted from the target were measured using a ΔE-E counter telescope[4)] at 25, 30, 35, 45, 60, 75, 90, 120 and 150 degrees in the laboratory system. The counter telescope consisted of two thin silicon ΔE-detectors (30 μm and 500 μm in thickness, respectively), and a CsI(Tl) E-detector (18 mmϕ x 30 mm long) with photo-diode read-out. The targets used were self-supporting foils: ^{58}Ni (0.96 mg/cm^2 thick, 99.927% isotopic enrichment) and ^{90}Zr (0.62 mg/cm^2 thick, 97.62% isotopic enrichment), ^{197}Au (4.15 mg/cm^2 thick), and ^{nat}Bi (3.7 mg/cm^2 thick). It should be noted that ^{197}Au was used for 68 MeV and ^{nat}Bi for 42 MeV. The beam current was monitored by means of a current integrator connected to a beam dump placed 3 m downstream from the scattering chamber.

Pulse-height signals from each detector of the counter telescope were digitized and stored events by event using a PC-based data acquisition system with CAMAC. After particle identification by off-line processing of ΔE and E data, DDXs of all light charged-particles and angular distributions of elastic scattering were obtained.

3. Results

Figure 1 shows experimental DDXs of the ^{58}Ni(p,xp) reaction at 68 MeV. The structureless continuum spectra with forward-peaked angular distribution are observed in the intermediate outgoing energy region, where preequilibrium particle emission takes place mainly via multistep direct process.

In Fig.2, measured DDXs of emitted protons, deuterons, tritons, ^{3}He and α-particles are shown for a 68-MeV proton incident on ^{58}Ni, and are compared with LA150 evaluation[2]. Note that the LA150 evaluation has no data for ^{3}He. The evaluated DDXs are in good agreement with the measured DDXs of (p,xp), but not with the measured DDXs of the other light-ions (deuteron, triton, α-particle). In particular, the spectral shape for (p,xd) is largely different between the experimental and evaluated DDXs. The same is true for the result of (p,xd) reactions on ^{12}C and ^{27}Al[1]. Therefore, it would be necessary to examine the applicability of the pick-up model[5] used in preequilibrium deuteron emission calculations.

Angular distributions of secondary charged-particles were obtained by integration of DDXs over the outgoing energy region more than the threshold energy corresponding to each detectable lowest energy. The result for ^{58}Ni at 68 MeV (solid line) is shown with the LA150 evaluation (dashed lines) in Fig.3. It can be seen that the angular distributions of deuterons, triotons, and ^{3}He are steeper than those of protons and α-particles. This indicates that the particle emission via the direct process is more important for the former secondary particles. Agreement between the measurement and the LA150 evaluation is generally good.

Total yields of secondary charged-particles produced in 68 MeV(p,x) reactions are plotted as a function of target mass number in Fig.4. Proton production is the largest for ^{58}Ni. For ^{197}Au, the yields of ^{3}He and α-particles are obviously suppressed by a large Coulomb barrier, while the triton yield increases with increase in target mass number.

4. Concluding remarks

We have measured the DDXs of light charged-particles (p, d, t, ^{3}He and α) produced in proton-induced reactions on ^{58}Ni, ^{90}Zr, ^{197}Au and ^{209}Bi at 42 and 68 MeV. The obtained DDXs were compared with the latest LA150 evaluation. It was found that the latter reproduced the measured DDXs of protons satisfactorily, but the agreement was not so good for the other particles. In particular, the LA150 evaluation overestimated the high energy part of ^{58}Ni (p,xd) spectra as shown in the previous result for ^{12}C and ^{27}Al. In addition, hydrogen and helium production cross sections for 42 and 68 MeV were found to be the largest in the ^{58}Ni target region.

Finally, we expect that the data measured in this work will be useful in the evaluation of JENDL High Energy File which is now in progress.

Acknowledgments

The authors wish to thank the staff of AVF cyclotron facility for their cyclotron operation during the experiments. This work was undertaken as the Universities-JAERI Collaboration Research Project, and was also supported in part by a Grant-in-Aid for Scientific Research of the Ministry of Education, Science, and Culture (No. 09558059).

References

[1] M. Harada et al., J. Nucl. Scie. Technol. Suppl. 1, 687 (2000).

[2] M. B. Chadwick et al., Nucl. Sci. Eng., **131**, 293 (1999).

[3] Y. Tanaka, Master thesis, Kyushu University (2000), (in Japanese).

[4] M. Harada et al., Proc. of the 1996 Symp. on Nuclear Data, Nov. 21-22, Tokai, JAERI-Conf 97-005 (1997), p.240.

[5] C. Kalbach, Z. Phys. A **283**, 401 (1977).

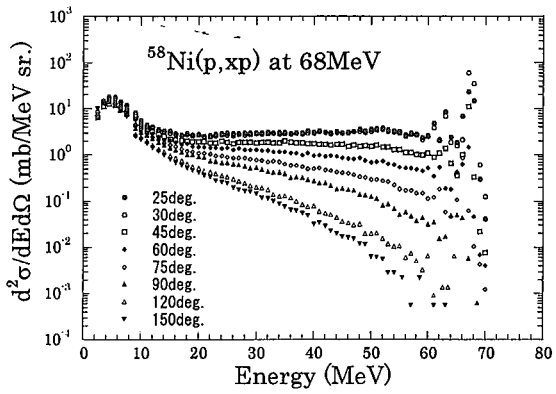


Fig. 1 Measured double differential cross sections of the ^{58}Ni (p,xp) reaction at 68 MeV.

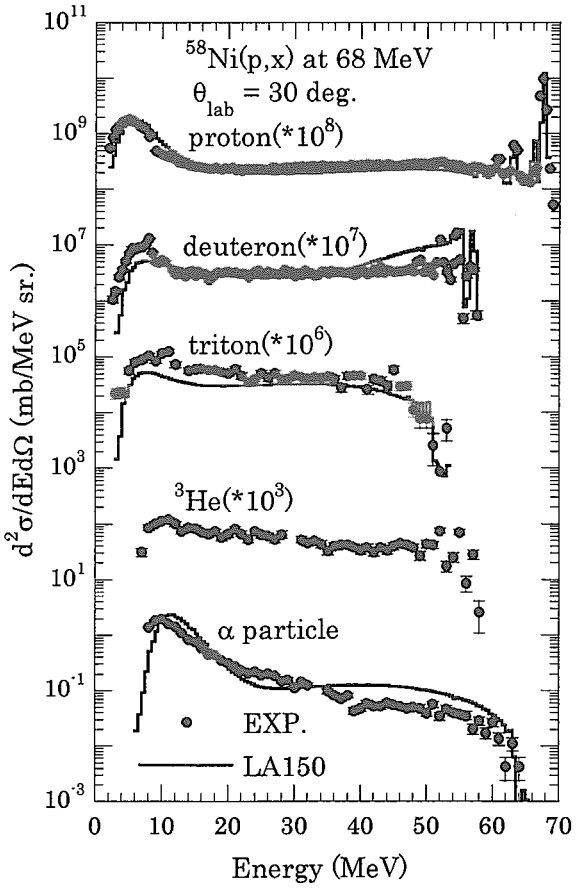


Fig. 2 Comparison of measured DDXs of protons, deuterons, tritons, ^{3}He, and α-particles produced by the p+^{58}Ni reaction at 68 MeV with LA150 evaluation[2].

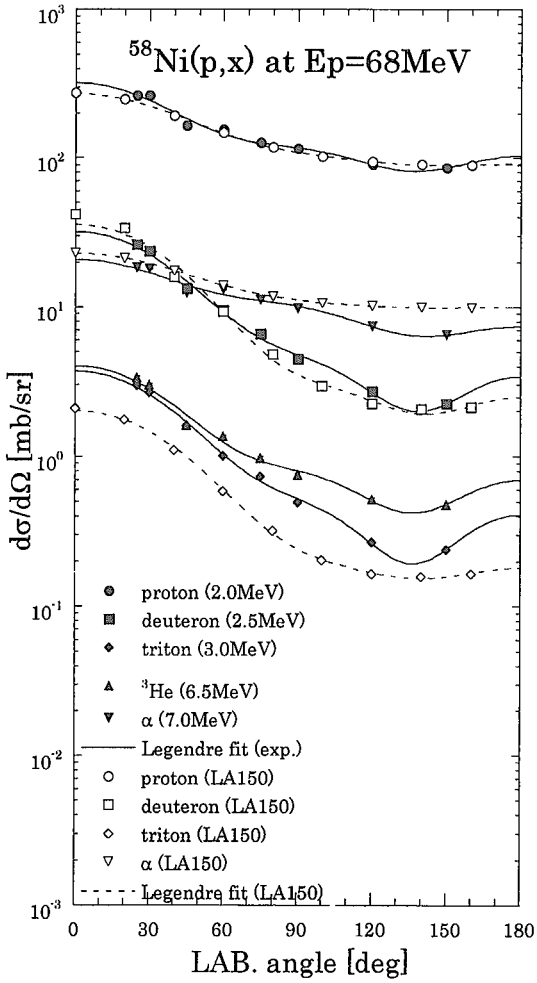


Fig. 3 Angular distributions of secondary charged-particles for the proton-induced reaction on ^{58}Ni at 68 MeV. The threshold energy (in MeV unit) is denoted in the parentheses for each particle.

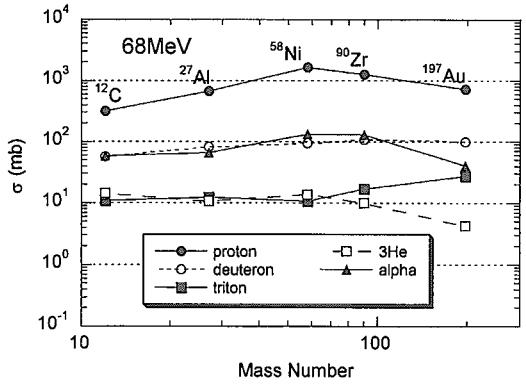


Fig.4 Dependence of experimental yields of secondary charged-particles on target mass number for an incident energy of 68 MeV.

8.3 Study of cross section measurement methods using the Self-TOF high energy neutron detector

Michiya SASAKI, Tomoya NUNOMIYA , Takashi NAKAMURA,
Noriaki NAKAO*, Tokushi SHIBATA*, Yoshihiro NAKANE**
Susumu TANAKA***
Department of Quantum Science and Energy Engineering, Tohoku University
*Radiation Science Center, KEK
**Center for Neutron Science, JAERI
***Advanced Radiation Technology Center, JAERI

1 Introduction

The Self-TOF detector which measures the neutron-induced proton time-of-flight (TOF) has been developed [1] [2] [3] for high energy neutron spectrometry by our group. This detector is composed of START and STOP detectors for measurement of proton energy by the TOF method. The START detector is a 80 mm diam. by 0.5 mm-thick and the STOP detector is a 130 mm diam. by 20 mm-thick NE102A plastic scintillator.

The performance of this detector was tested under the 40, 65, 132 and 207 MeV quasi-monoenergetic neutron fields at TIARA and RIKEN facilities. The detector was also applied for double differential cross section(DDX) measurements of charged particle production by neutrons.

2 Experiment

The schematic view of the experimental setup in the p-Li quasi-monoenergetic neutron field at TIARA is shown in Fig.1. The proton beams accelerated by a cyclotron are focused onto a natural Li target. Neutrons emerging from the Li target are transported down to the light ion room 3, and the detectors are located on the beam axis. The accelerated energies of protons, peak neutron energies and thicknesses of Li targets used in the experiments are indicated in Table 1.

Table 1: Proton energies, thicknesses of Li targets and peak neutron energies at each neutron field.

	E_p [MeV]	Li thickness [mm]	E_{npeak} [MeV]
TIARA	43	3.6	40
TIARA	68	5.2	65
RIKEN	135	10.0	132
RIKEN	210	10.0	207

The radiator is attached in front of the START detector. In neutron measurements, the recoiled proton energy from the radiator due to the H(n,p) elastic scattering reaction is measured between the START and the STOP detectors by the TOF method. The proton energy E_p is obtained from the proton flight time and the neutron energy E_n is then determined by $E_n = E_p/cos^2\theta$ where θ is the scattering angle. The contribution of incident protons, protons produced from carbon in the polyethylene radiator and from the START must be subtracted from the relevant events. By using three types of radiators, polyethylene, graphite and nothing, this contribution can be estimated[3].

In the charged particle measurements, Al and Cu radiators were also used and the charged particles generated from the radiators were measured by the same method. The contribution of incident protons, protons produced from other detectors can be subtracted by the similar analyses.

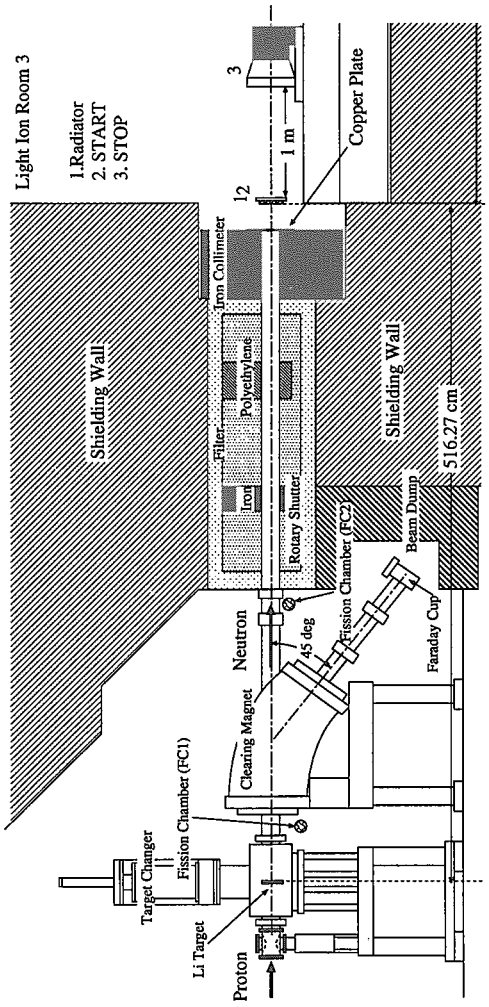


Figure 1: Experimental setup at TIARA.

3 Data analysis

The pulse height distributions of scintillation light outputs from the START and STOP detectors are stored with integrating - type ADC(LeCroy 2249W) which is gated by coincidence signals of the START and STOP detectors. The proton TOF is stored with TDC together with the neutron TOF spectra using the RF (Radio Frequency) signal from a cyclotron as a start signal. The events to be analyzed for estimation of neutron energy spectra are the proton events produced from a radiator. They can be selected by the two dimensional distribution of light outputs of the STOP detector and the recoiled proton TOF spectrum.

The proton energy spectra given for five radiators, polyethylene, graphite, copper, aluminum and nothing are determined from relativistic kinematics using the recoiled proton TOF spectra after correction of energy loss in the START scintillator. The proton events induced only by H(n,p) elastic scattering from polyethylene radiator, and that induced only by C(n,p), Cu(n,p) and Al(n,p) from each radiator can be obtained by the combination of the proton energy spectra as mentioned before.

4 Results and discussions

Table 2 shows the experimental data at TIARA and RIKEN together with the peak neutron fluences obtained by the PRT (Proton Recoil Telescope) and by Li activation methods[4]. The agreements of peak neutron fluences are satisfactry.

Figs. 2, 3 and 4 show the proton production DDXs of Cu, Al and C at 0 degree of 40 MeV neutrons, respectively. The high threshold energy (about 25 MeV) caused by the contamination of protons generated from the Li target.

5 Conclusions

The performance tests of the Self-TOF detector for measurements of neutrons were done at TIARA and RIKEN facilities. The contributions of carbon reaction in polyethylene radiator and background were able to be subtracted and succecefully measured charged particle DDXs at 0 degree by this simple measuring system.

Table 2: Comparison of the peak neutron fluences obtained by the Self-TOF detector and by the PRT and Li activation method.

E_n [MeV]	ϕ_1* [(MeV.sr)$^{-1}$]	ϕ_2**	ϕ_2/ϕ_1
40	4.075e+9	3.940e+9	0.967
65	4.425e+9	4.180e+9	0.945
132	1.018e+9	1.020e+9	1.002
208	1.057e+9	1.063e+9	1.006

*Obtained by PRT and Li activation.
**Obtained by the Self-TOF.

References

[1] M. Nakao et al., KEK Proc. of 11th Workshop on Radiat. Detec. and Their Uses, p102, (1997)

[2] N. Nakao et al., RIKEN Accel. Prog. Rep. 29 (1996)

[3] M. Sasaki et al., JAERI-Review 99-025, p237(1999)

[4] M. Takada et al., Nucl. Instrum. Methods, A 372, p253 (1996)

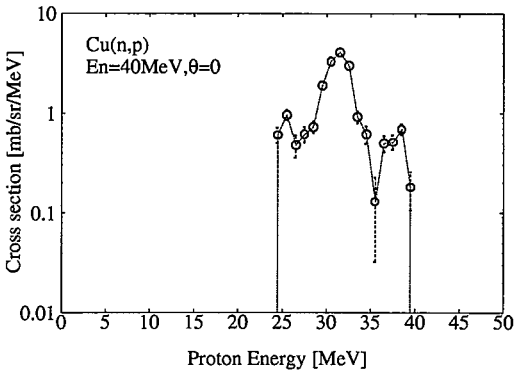


Figure 2: Cu(n,p) spectrum at 0 degree for 40 MeV neutron.

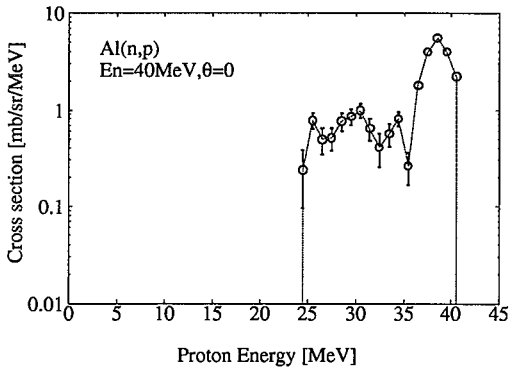


Figure 3: Al(n,p) spectrum at 0 degree for 40 MeV neutron.

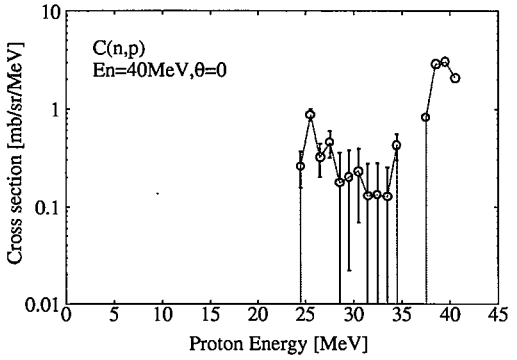


Figure 4: C(n,p) spectrum at 0 degree for 40 MeV neutron.

8.4 Measurement of Absorbed Dose Distributions in a Plastic Phantom Irradiated by 40- and 65-MeV Quasi-Monoenergetic Neutrons

Y. Nakane, Y. Sakamoto* and Y. Harada

Center for Neutron Science, JAERI, *Department of Health Physics, JAERI

1. Introduction

From the viewpoint of radiation protection including radiation shielding design at high energy accelerator facilities, it is important to establish an evaluation method of effective dose for high energy radiations above 20 MeV. The HERMES code system[1] has been extended to calculate the effective dose up to 10 GeV neutrons[2]. The accuracy of the code system for the dose evaluation, however, has not been validated experimentally for intermediate and high energy neutrons. For the validation of the code system for intermediate energy neutrons, absorbed dose distributions and microdosimetric spectra in a plastic phantom were measured with tissue equivalent detectors for 40- and 65-MeV quasi-monoenergetic neutrons at TIARA of JAERI. Measured dose distributions were compared with calculated ones

2. Experiments

Figure 1 shows a cross sectional view of the experimental arrangement. Quasi-monoenergetic source neutrons ("40 MeV" and "65 MeV") of about 40- and 65-MeV were produced in 3.6-mm and 5.2-mm thick ^{7}Li-targets (99.9% enriched) bombarded with 43- and 68-MeV protons, respectively. Source neutrons emitted in the forward direction were introduced to a 10.9-cm-diameter and 220-cm-long iron collimator embedded in a shielding wall and a 10.9-cm-diameter and 85-cm-long additional collimator on a movable stand, while proton beam penetrating through the target was bent down by a clearing magnet to a Faraday cup. A copper plate of 3-mm-thick was set at the exit of the additional collimator as a neutral proton beam stopper. The 30 x 30 x 30 cm^3 slab phantom made of polymethyl methacrylate (PMMA) was placed on the beam at the position of 558 cm from the Li target. Source neutron spectra above 10 MeV have been measured[3] by the TOF method with a 12.7-cm-diameter x 12.7-cm-long BC501A liquid scintillation detector as shown in Fig. 2. The intensity of neutrons at the irradiating position was monitored with the proton beam Faraday cup and two fission counters placed

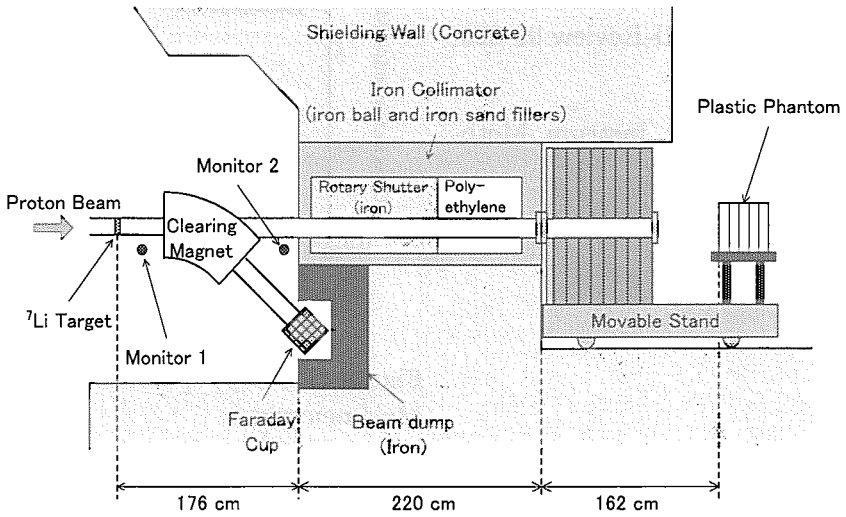


Fig. 1 Cross sectional view of the experimental arrangement

near the target and the collimator, of which efficiencies had been calibrated from the measurement[4] of absolute intensities by using a proton-recoil-counter-telescope (PRT). Error of neutron intensity monitoring was estimated to less than 7%. Absorbed dose distributions at the depth of 2, 5, 10, 15, 20 and 25 cm in the phantom were measured along the center line of the phantom by using a tissue equivalent proportional counter (TEPC) (Far West Technology Inc., Model LET-SW1/2) for the "40 MeV" and the "65 MeV" source neutrons. The counter consists of a 1.27-cm-diameter TE plastic sphere, a collecting wire of stainless steel and an 2.0 cm outer diameter aluminum shell outside the TE sphere used as a vacuum tight container. The counter was filled with a propane-based TE gas at the pressure of 9.03 kPa. To compare with the TEPC measurements, the distributions at the same positions were measured by using a tissue equivalent ionization chamber (TEIC) (Far West Technology Inc., Model IC-17) for the "65MeV" source neutrons. The detector has a spherical shape of TE plastic wall of 2.29 cm diameter. A methane-based TE gas flowed at 5 cm^3/min in the plastic wall.

In addition, energy spectra of source neutrons below 10 MeV were measured with a spherical multi-moderator spectrometer for the evaluation of dose contributions of neutrons below 10 MeV. The spectrometer was set on the beam at the position of 11.90m from the Li target. The spectrometer was also set at 50-cm off the beam axis to measure the spectrum of background neutrons. Using the spectra unfolded from the spectrometer measurements by using the SAND-II code[5], source neutron spectra at the Li target and the front surface of the phantom positions were evaluated with the MCNP-4B code[6] and a cross section data from the LA150 library[7] processed with NJOY94[8]. Evaluated spectra at the phantom position are shown in Fig. 3.

3. Calculations

Absorbed dose distributions in the phantom were calculated by using the code system given below. The absorbed dose caused by neutrons above 15 MeV was obtained from the deposition energy of charged particles from induced reactions calculated by the HETC-3STEP code, while that below 15 MeV was obtained from the Kerma factor given in ICRU 26[9] and neutron energy spectra calculated by the MORSE-CG/KFA code[1] with a multi-group cross section library processed from JENDL-3[10]. For comparison, the absorbed dose was also obtained for the whole energy region of neutrons from the Kerma factor and neutron energy

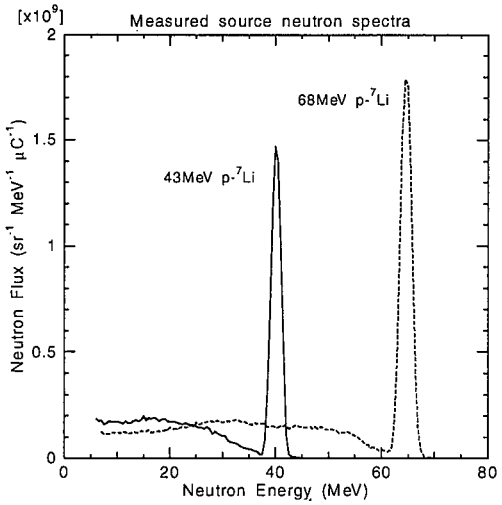


Fig. 2 Measured spectra of source neutrons by using the BC501A detector [3]

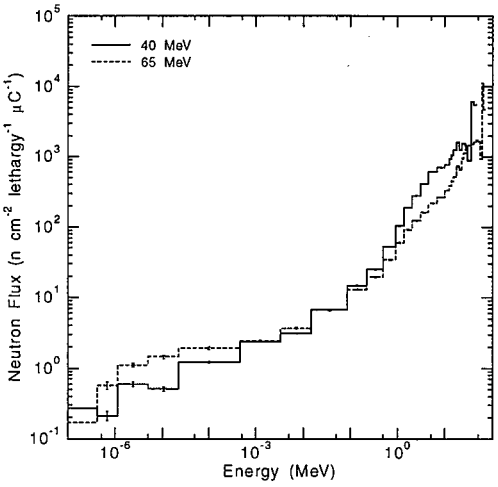


Fig. 3 Evaluated energy spectra of source neutrons at the front surface of the phantom

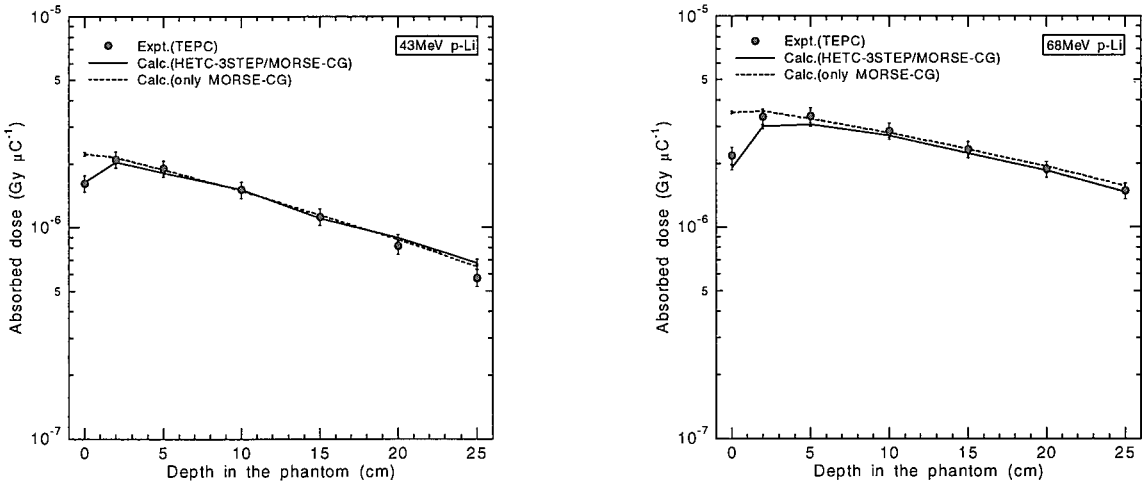
spectra calculated by the MORSE-CG code with the DLC-119/HILO86[11] multi-group cross section library up to 400 MeV.

4. Results and discussion

Figure 4 shows the results of measured and calculated absorbed dose distributions in the phantom. The calculated results of absorbed dose for the "40MeV" and the "65MeV" source neutrons by HETC-3STEP/MORSE-CG agree well with the experimental values within the error of 10% except for the value at the depth of 25 cm for the "40MeV" source neutron. With regard to absorbed dose distributions calculated for the whole energy region of neutrons by the MORSE-CG code, calculated results in the phantom are in good agreement with the experimental ones within 7% except for the value at the depth of 25cm, while those on the surface of the phantom are 38% and 60% higher than the measured ones for the "40MeV" and the "65MeV" source neutrons, respectively. These disagreements are ascribed to the Kerma approximation, in which the charged particles and recoil nuclide are assumed to lose the energy closely near the reaction point.

References

1) P. Cloth et al., KFA-IRE-EAN 12/88, 1988
2) N. Yoshizawa et al., J. Nucl. Sci. Technol., 35, 928, 1998
3) N. Nakao, H. Nakashima, T. Nakamura, Sh. Tanaka, Su. Tanaka, K. Shin, M. Baba, Y. Sakamoto and Y. Nakane, Ncul. Sci. Eng., 124, 228, 1996
4) M. Baba et al., Nucl. Instr. Meth., A 428, 454, 1999
5) W. N. McElroy et al., AFWL-TR-67-41, Vols. 1 through 4, Air Force Weapons Laboratory, 1967
6) "MCNP – A General Monte Carlo n-Particle Transport Code," Version 4B, LA-12625-M, Los Alamos National Laboratory, 1997
7) M. B. Chadwick et al., LA-UR-98-1825, Los Alamos National Laboratory, 1998
8) R. E. MacFarlane and D. W. Muir, LA-12740-M, Los Alamos National Laboratory, 1994
9) ICRU Report 26, "Neutron Dosimetry for Biology and Medicine", 1977
10) K. Shibata et al., JAERI 1319, 1990
11) R.G. Alsmiller Jr., J. M. Barnes and J. D. Drischler, ORNL/TM-9801, 1986



(a) "40MeV" source neutron (b) "65MeV" source neutron

Fig. 4 Measured and calculated absorbed dose distributions in the phantom

8.5 Charged-particle Production and Neutron Scattering Cross Sections for 55-75 MeV Neutrons

M.Baba, M.Ibaraki, Y.Hirasawa, T.Miura, T.Hiroishi, T.Aoki, H.Nakashima*, S.Meigo*, Su.Tanaka**
Graduate School of Quantum Science and Energy Engineering, Tohoku University
*Center for Neutron Science, JAERI, **Advanced Radiation Technology Center, JAERI

1. Introduction

Cross section data for medium-energy neutrons are required for shielding design and efficient utilization of intense accelerator facilities. We have conducted experiments on double-differential charged- particle emission (n,xz) cross sections and neutron elastic -scattering cross sections for 55 and 75 MeV neutrons at the ^{7}Li(p,n) mono-energetic neutron source of TIARA[1], employing specially developed spectrometers for secondary charged-particles and scattered neutrons[2-5]

During the last year, the experiment was extended to 65 MeV neutrons to study the energy dependence of cross sections and compare with the neutron scattering data by U.C. Davis group[6]. New (n,xz) data were obtained for iron and nickel, and elastic-scattering data for carbon, silicon, iron, zirconium and lead.

2. Experimental Apparatus

The experimental methods are described in ref.2-5. Source neutrons of 65 MeV were produced by the ^{7}Li(p,n) reaction with a ^{7}Li metal target, about 5.2 mm thick which corresponds to the energy loss of about 2 MeV. Neutrons were guided to the "Light Ion Room 3", and incident on the scattering chamber for (n,xz) measurement and then on the samples for scattering experiments. In this way, the (n,xz) and scattering experiments could be conducted concurrently for efficient use of the neutron beam.

3. Charged-particle Emission Cross Sections

The (n,xz) cross sections were measured using three wide-range spectrometers consisting of three-elements counter-telescope mounted to a vacuum chamber. Each telescope consists of a low-pressure gas proportional-counter (GPC), Si-SSD and a BaF_2 scintillater, and enables concurrent measurement from α particles of a few MeV upto $\sim$80 MeV protons. Samples were metallic plates of iron, 0.62-mm$\times$50-mm- diam, and nickel, 0.57-mm $\times$ 50-mm-diam. Data were gathered for pulse-heights of each counter, and TOF for SSD and BaF_2 using a CAMAC system as described in ref.3.

The data reduction method is described in refs.2 and 3. Raw data were corrected for the particle dependence of the BaF_2 light output and the particle energy loss in the samples.

Figures 1 shows double-differential (n,xz) data of iron and nickel for 65 MeV neutrons, in comparison with the LA-150 library[7] (solid-line). LA-150 generally reproduces the present data but tends to overemphasize the high energy parts, in particular for deuterons as seen also for 75 and 55 MeV neutrons. Figure 2 compares the present Fe(n,xp) data with the proton induced ^{56}Fe(p,xp) data at 61 MeV[8]. This figure shows significant contributions of the scattering process in high energy region at the forward emission angles.

4. Elastic Scattering Cross Sections

Scattered neutron spectra were measured by a TOF method using five NE213 liquid scintillation detectors, 12.5-cm-diam$\times$12.5-cm thick. The data were obtained at twenty-five laboratory angles between 2.6 and 53-deg. The flight paths were around 5 m for forward scattering angles and 2 m for backward angles. Scattering samples of elemental carbon

(5-cm-diam × 8-cm), silicon (5-cm-diam × 8-cm), iron (4-cm-diam × 6-cm), zirconium (3-cm-diam × 8cm), and lead (3-cm-diam × 6-cm) were placed around 10 m from the ^{7}Li target using a sample changer.

The absolute values of the cross section were determined relative to the incident neutron flux measured by the detectors for scattered neutrons. Experimental data were corrected for the effects of the inelastic-neutrons and finite-sample-size by the manner described in ref.4.

Fig. 3 shows the present results for 65 MeV neutrons together with the LA-150 library. LA-150 shows general agreement with our data for all nuclides, but underestimates at very forward angles, especially for lead up to ~ 15 %. This trend is the same as the 75 and 55 MeV cases as shown in angle-integrated elastic cross sections (Fig.4; angle-integrated values were obtained using the optical model calculation).

For the reason, LA-150 will overestimate the non-elastic (reaction) cross section which affects the neutron shielding calculations.

Figure 5 shows comparison of the present data with the U.C. Davis data. There are overestimate the non-elastic (reaction) cross section which affects the neutron shielding calculations.

Figure 5 shows comparison of the present data with the U.C. Davis data. There are significant difference between them. It was confirmed that the present data can be described consistently with the optical model potential which fit our 75 and 55 MeV data. It was also observed that the DLC119/HILO86 multi-group library[9] and the systematics used in the cascade/transport codes[10] show serious disagreement with the present results as noted for 75 and 55 MeV data[4,5].

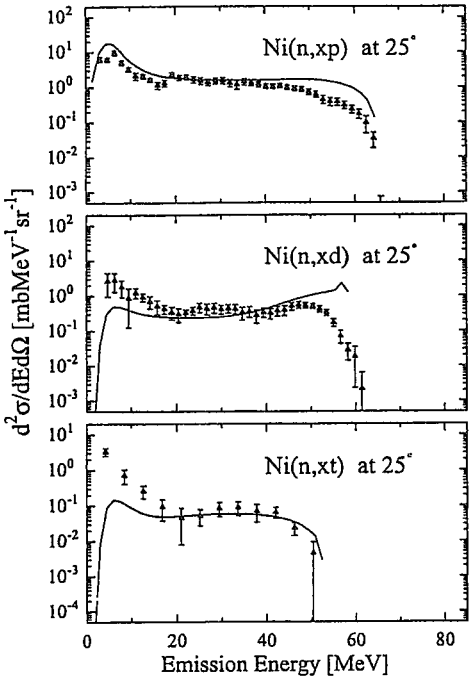


Fig.1: Results of (n,xz) cross section for 65 MeV neutrons, comapred with LA-150 library[7] (solid line).

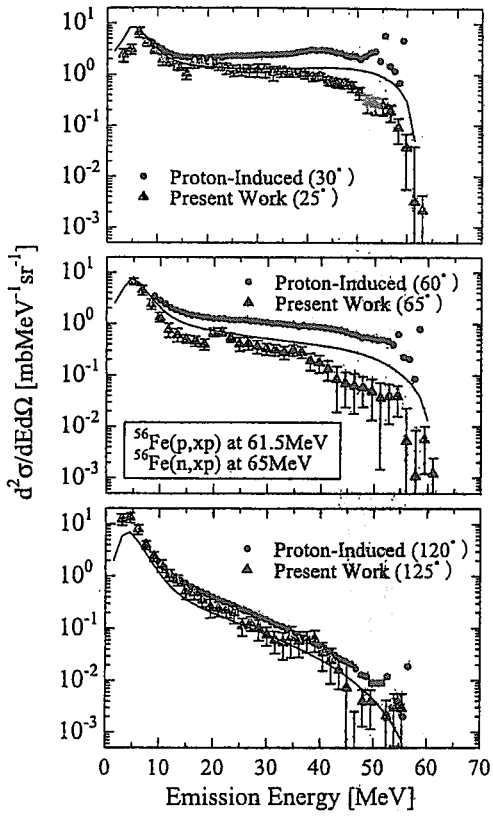


Fig.2: Comparison of the present Fe(n,xp) data for 65 MeV neutrons with the ^{56}Fe(p,xp) data at 61.5 MeV[8].

References.

1)M.Baba et al., Nucl. Instrum. Methods., A428, 454 (1999)
2)Y. Nauchi et al., J. Nucl. Sci. Technol., 36, 143 (1999)
3)Y. Hirasawa et al., JAERI-Conf. 2000-005 (2000) p.232
4)M.Ibaraki et al., Nucl. Instrum. Methods., A446/3, 536 (2000)
5)M.Ibaraki et al., J. Nucl. Sci. Technol., suppl.1 (May 2000), 683 (1999)
6)E.L.Hjort et al., Phys. Rev. C53 (1996) 237
7)M.B.Chadwick et al., Nucl. Sci. Eng., 131, 293 (1999)
8)F.E.Bertrand and R.W.Peele, ORNL-4456 (1969), Phys. Rev., C8, 1045 (1973)
9)R.G.Alsmiller and J.B.Barish, ORNL/TM-7818 (1981)
10)P.Cloth et al., Jul-2203 (Kern-forschungsanlage, Jeulich (1988)

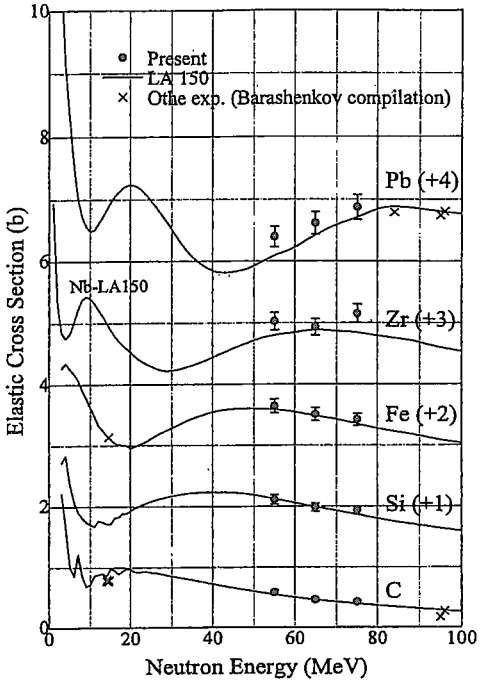


Fig.4: Angle-integrated elastic-scattering cross section for ten's of MeV neutrons.

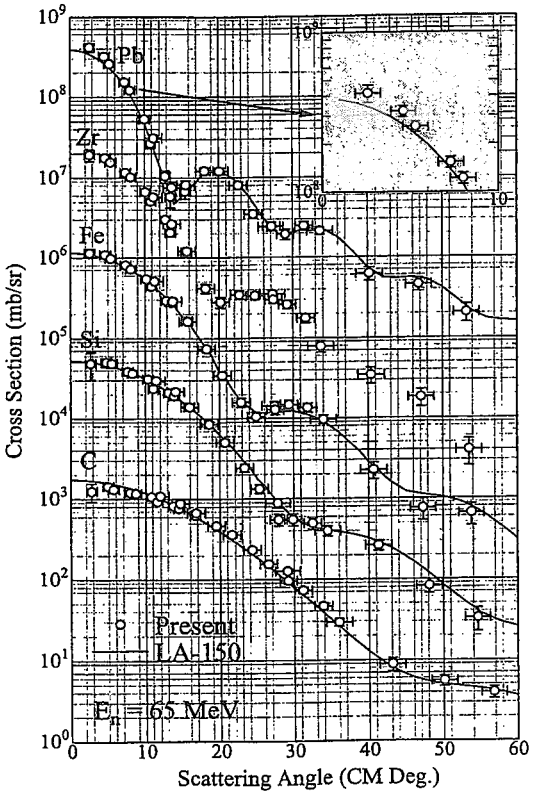


Fig.3: The present results of elastic-scattering cross section for 65 MeV neutrons, in comparison with the LA-150 library[7)]

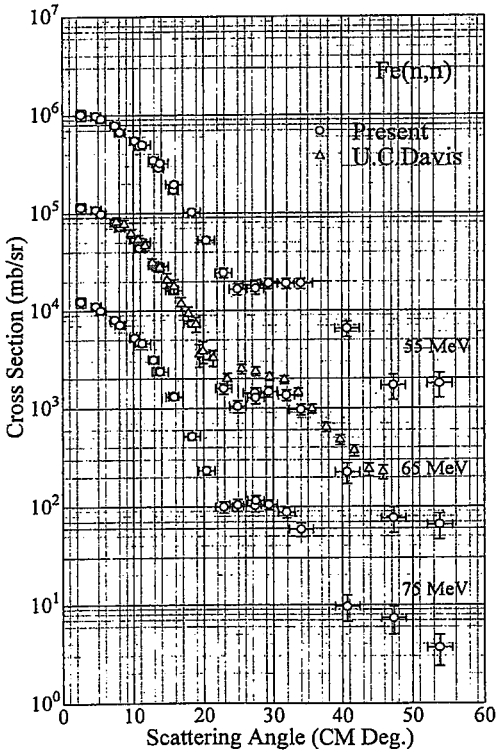


Fig.5: Comparison of differential neutron elastic-scattering scattering cross section.

This is a blank page.

9. Accelerator Technology

9.1 Beam Energy Measurement by the Time-of-flight Technique ····· 271
S. Okumura, K. Arakawa, M. Fukuda, I. Ishibori, H. Tamura, T. Agematsu, T. Nara, W. Yokota, S. Kurashima and T. Ishimoto

9.2 Acceleration Test of M/Q=2 and 4 Cocktail Beams and Study of Multiturn Extraction ····· 273
W. Yokota, M. Fukuda, S. Okumura, K. Arakawa, I. Ishibori, T. Nara, T. Agematsu, H. Tamura, S. Kurashima, Y. Nakamura and T. Ishimoto

9.3 Measurement of Beam Energy and Its Spread using Nuclear Reaction Resonances at the Single-ended Accelerator ····· 276
Y. Ishii, I. Takada, K. Mizuhashi, S. Saito, S. Uno, K. Ohkoshi, Y. Nakajima, A. Chiba, T. Kamiya, T. Sakai and S. Tajima

9.4 Prolongation of a Filament Lifetime using SF_6 Plasma Method ····· 279
K. Ohkoshi, Y. Saitoh, T. Kamiya, T. Sakai, T. Orimo, A. Ohmae, I. Takada and S. Tajima

9.5 Development of Transparent-type Beam Current Monitor ····· 280
Y. Nakajima, Y. Saitoh and S. Tajima

9.6 Cooling System for Beam Stabilization of JAERI AVF Cyclotron ····· 282
Y. Nakamura, S. Okumura, M. Sano, T. Nara, T. Ishimoto, S. Kurashima, W. Yokota, K. Arakawa, K. Saitoh, T. Fukuda, J. Kanakura, M. Fukuda, I. Ishibori, H. Tamura and T. Agematsu

9.7 Model Test of the Flat Top Cavity for the JAERI AVF Cyclotron ····· 285
Y. Kumata, Y. Fukumoto, K. Arakawa, Y. Nakamura and S. Kurashima

9.8 Present Status of JAERI AVF Cyclotron System ····· 288
Y. Nakamura, T. Nara, T. Agematsu, I. Ishibori, H. Tamura, S. Kurashima, W. Yokota, S. Okumura, K. Akaiwa, To. Yoshida, S. Ishiro, A. Matsumura, Y. Arakawa, Tu. Yoshida, S. Kanou and A. Ihara

9.9 Modification of the HY Beam Scanner for JAERI AVF Cyclotron ····· 291
T. Agematsu, S. Kurashima and Y. Nakamura

9.10 Improvement of the Switching Magnet Current Controller of Tandem Accelerator ····· 292
K. Mizuhashi, T. Miyoshi and S. Tajima

9.11 Renewal of the Computer Control System for JAERI AVF Cyclotron (II) ····· 294
T. Agematsu, K. Arakawa, Y. Nakamura and S. Ishiro

9.12 Renewal of Rotary Shutter for JAERI Cyclotron System ····· 296
I. Ishibori, Y. Nakamura, T. Torii and K. Suzuki

This is a blank page.

9.1 Beam Energy Measurement by the Time-of-flight Technique

S. Okumura, K. Arakawa, M. Fukuda, I. Ishibori, H. Tamura, T. Agematsu, T. Nara, W. Yokota, S. Kurashima, T. Ishimoto*
Advanced Radiation Technology Center, JAERI
*Department of Material Development, JAERI

1. Introduction

We have developed a movable time-of-flight (TOF) counter system[1-2] for precise measurement of the absolute energy and the energy width of a beam extracted from the cyclotron. Especially, the energy width is a very important parameter for production of a micro beam, which is constructing now. We are developing a flat-top acceleration system to provide a beam with small width of its energy enough for micro beam production.

A TOF method is easier way to determine the absolute energy for the variety of ion species with high precision better than the other energy measurement method such as the crossover technique and analyzing magnet. The precision of the energy measurement depends on uncertainty in measurement of the flight path length and the flight time. In order to achieve 10^{-3} precision of energy measurement, uncertainty less than 10^{-3} in both measurements of the flight path length and the flight time is needed. The flight path length can be obtained easily with uncertainty less than 10^{-3}, because a normal digital scale have enough precision. On the other hand, it is difficult to obtain enough precision in the flight time measurement, because the time accuracy of a normal time analyzing system is not so small, around 100ps, against the flight time, in this case a few ten nano seconds.

We have applied a time analyzer, pTA(ORTEC, model 9308), to measurement of the flight time, because its time resolution is superior to normal time analyzers.

2. Experimental setup

The system, shown in Fig.1, has two ion detectors: one is a transmission detector, a start detector, using a thin foil and an electron multiplier for production of a start signal when an ion pass through the detector, and the other, a stop detector, for production of a stop signal.

To achieve precise measurement of the beam energy, we adopted relative measurement of the length and the time difference, which eliminates inaccuracy of decision of the time and the length criteria. In this measurement, the length and the time difference have to be measured twice by moving the stop detector.

The detectors are installed in different vacuum chambers connected with bellows. The chamber for the stop detector can be moved at the maximum distance of 2 m. The relative change of the length can be measured with a magnetic scale with a precision less than 0.1 mm. The relative change of the time difference is obtained as a shift of the time spectrum peak measured with the pTA by using the relative timing signals from the start and stop detectors.

3. Measurements and Results

The proton beam accelerated with the cyclotron was transported to both of the start and stop detectors. Each signal from the detectors was fed into a constant fraction discriminator (ORTEC, model 935) to produce a suitable timing signal for the pTA. A personal computer was used to display spectral data, as shown in Fig.2.

We measured the beam energies of 20 and 70 MeV (nominal) proton beams. The accuracy of the energy measurements was almost achieved within 0.1 %, mainly for improvement of the time accuracy with the pTA. In these measurements, actual beam energies, 19.79 and 67.65 MeV, corresponding to nominal energies of 20 and 70 MeV, respectively.

The energy width of the 20 MeV proton beam was also estimated by using the width of the time spectra. In this case, the energy width ratio, dE/E, is about 0.3%.

Reference
1) S.Okumura et. al., JAERI Review 99-025, 249-250.
2) S.Okumura et. al., The 12th Sympo. on Accel. Sci. and Tech., Wako, Japan (1999) 471-472.

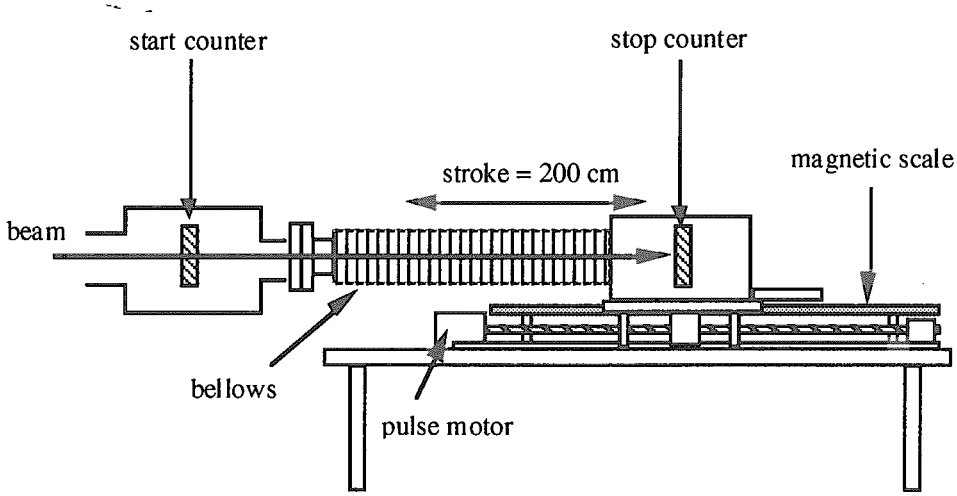


Fig. 1 Layout of the movable TOF counter system.

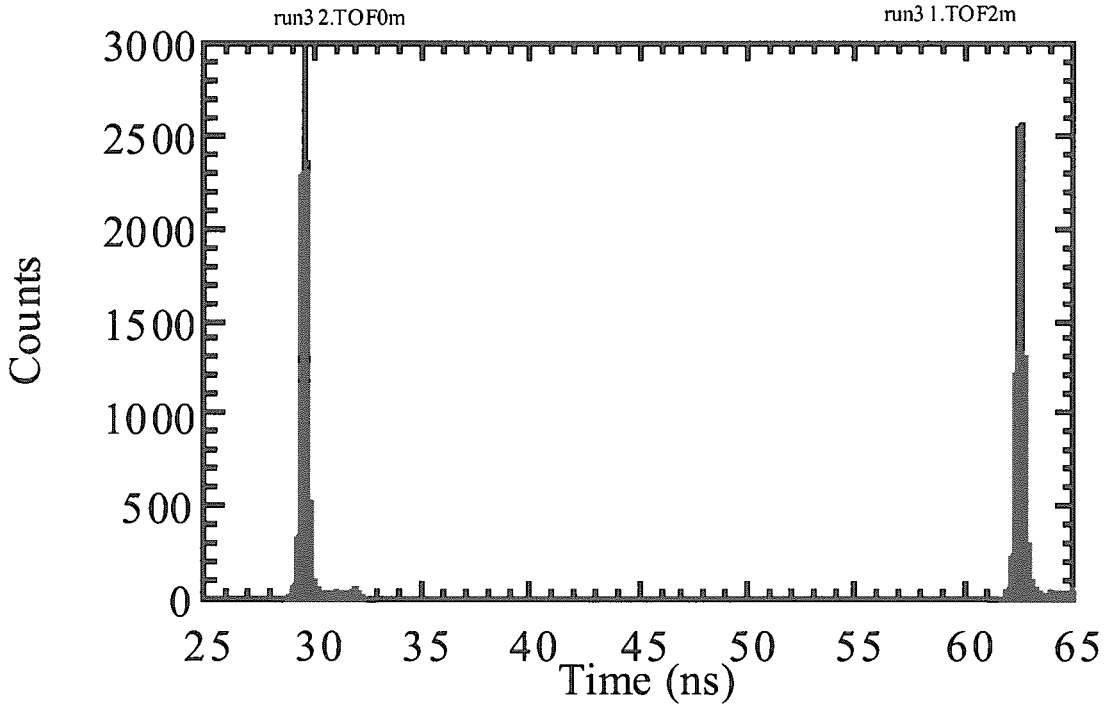


Fig. 2 Time spectra of 20 MeV proton beam. The left peak is measured at the initial point of the stop detector and the right one is measured at a 2m backward point.

9.2 Acceleration Test of M/Q=2 and 4 Cocktail Beams and Study of Multiturn Extraction

W. Yokota, M. Fukuda, S. Okumura, K. Arakawa, I. Ishibori, T. Nara, T. Agematsu, H. Tamura, S. Kurashima, Y. Nakamura, T. Ishimoto
Advanced Radiation Technology Center, JAERI

1. Introduction

The cocktail beam acceleration technique applied to a cyclotron permits us to quickly change ion species which have nearly equal mass-number to charge-number ratios (M/Q). It gives great advantage to research works which use wide range of LET, such as development of semiconductors for use in space environment. Now at TIARA, M/Q=5 cocktail ($^{15}N^{3+}$, $^{20}Ne^{4+}$, $^{40}Ar^{8+}$, $^{84}Kr^{17+}$) are available. In the case of M/Q=2 cocktail ($^{4}He^{2+}$, $^{12}C^{6+}$, $^{14}N^{7+}$, $^{16}O^{8+}$, $^{20}Ne^{10+}$, $^{36}Ar^{18+}$) and M/Q=4 cocktail ($^{4}He^{1+}$, $^{12}C^{3+}$, $^{16}O^{4+}$, $^{20}Ne^{5+}$, $^{36}Ar^{9+}$, $^{40}Ar^{10+}$, $^{84}Kr^{21+}$), there is a problem that there are more than one ion species in cyclotron beams. Ions of other than an objective species are impurities. We have developed various methods to reduce impurities for three years[1,2]. The final test acceleration of M/Q=2 and 4 cocktails was carried out to seek an efficient combination of the reduction methods for each impurity ion species. The obtained beam condition are summarized in section 2 with restrictions in purity, beam intensity and time to change ion species.

Control of multiturn extraction is indispensable to form single-pulse beams by using a combination of the P-chopper in the injection line and the S-chopper after the extraction of the JAERI cyclotron[3]. In order to establish a method to control the turn number of ion beams, time distribution of beam pulses was measured inside and outside the cyclotron. It has turned out that beam extraction has a greater impact on multiturn extraction than condition of internal beams. The details are described in section 3.

2. M/Q=2 and 4 Cocktail Beams

In order to reduce impurity ion species in beams accelerated with the cocktail beam acceleration technique, we developed the methods of (1) RF frequency shift[1], (2) application of low dee voltages[1], (3) injection of a single ion species into the cyclotron[2]. We use more than one methods to attain a low ratio of impurity ions or high purity, because each method gives insufficient reduction. The JAERI cyclotron can separate a couple of ion species whose M/Q difference satisfies $\Delta(M/Q)/(M/Q) \leq 6 \times 10^{-4}$. This ability is referred to as M/Q resolution. For example, $^{16}O^{4+}$ and $^{20}Ne^{5+}$ with much less $\Delta(M/Q)/(M/Q)$, 0.6×10^{-4}, intermix at a considerable ratio without application of the impurity reduction methods (see Table 1). Oxygen ions are always produced even when only neon gas is fed into an ECR ion source because oxygen atoms come from contaminations such as oil and water on the chamber wall. Therefore combined use of the reduction methods is necessary to lower oxygen ion content in neon beam down to 1×10^{-4}.

The final results of M/Q=2 and 4 cocktail beams are summarized in Table 1. Note that there are following restrictions when those cocktail beams are used for research experiments.

1. Beam intensities of M/Q=2 cocktails are small since all electrons are removed from

Table 1 Summary of M/Q=2 and 4 cocktail beam acceleration test. Numbers describe ratios of non-objective ions to an objective ion, and reduction methods and their results are shown in columns (a) to (f). In the case of M/Q=2, for which only values of Δ(M/Q)/(M/Q) are shown, differences from M/Q=4 are presence of ^{14}N and absence of ^{40}Ar and ^{84}Kr. Since M/Q differences of ^{14}N from ^{4}He and ^{12}C are moderately small, intermixture ratios among those ion species can be reduce to less than 1×10^{-4}.

M/Q	ion	Δ(M/Q)/(M/Q)	(a) standard cyclotron parameters	(b) intentional shift of RF frequency	(c) application of low dee voltages	(d) injection of a single ion species	(f) detune of dee voltages & magnetic field	note
4	$^{4}He^{1+}$	6.5×10^{-4}	○					
	$^{12}C^{3+}$	3.2×10^{-4}	O: 3×10^{-3}	○				C and O ions are always produced by ion source as backgroud
	$^{16}O^{4+}$	0.6×10^{-4}	C: 2×10^{-2} Ne: 3×10^{-2}	C: 3×10^{-3} Ne: 2×10^{-1}	C: 3×10^{-2}	○	C: 8×10^{-4} Ne: 2×10^{-4}	
	$^{20}Ne^{5+}$	5.2×10^{-4}	O: 4×10^{0} Ar: 1×10^{-1} C: 1×10^{-2}	×	O: 6×10^{-1} Ar: 6×10^{-2}	×	○	
	$^{36}Ar^{9+}$	0.3×10^{-4}	^{40}Ar: 3×10^{1}	×	×	×	×	approaches ○
	$^{40}Ar^{10+}$	1.2×10^{-4}	^{36}Ar: 1×10^{-2}	×	×	×	×	with purere isotope gas
	$^{84}Kr^{21+}$		Fe: 4×10^{0} Cr: 6×10^{0} * Ar: 1×10^{3} *	×	×	^{80}Kr: 1×10^{-1} Fe: 4×10^{-2} * Cr: 3×10^{-2} * Ar: 8×10^{-3}	×	approaches ○ by using $^{86}Kr^{22+}$

M/Q	ion	Δ(M/Q)/(M/Q)
2	$^{4}He^{2+}$	4.3×10^{-4}
	$^{14}N^{7+}$	2.2×10^{-4}
	$^{12}C^{6+}$	3.2×10^{-4}
	$^{16}O^{8+}$	0.6×10^{-4}
	$^{20}Ne^{10+}$	5.3×10^{-4}
	$^{36}Ar^{18+}$	

○ : ratio<1×10^{-4} × : insufficient effects on ratio reduction

* : coming from the plasma chamber wall of the ion source, and their M/Q differences from $^{84}Kr^{21+}$ are extremely small.

these ions. Especially $^{36}Ar^{18+}$, whose intensity is less than 1 epA, needs careful tune of the cyclotron.

2. Generally low impurity and high beam intensity are contradictory. For an impurity ratio less than 1×10^{-4}, beam intensity may be reduced by some orders of magnitude.
3. Purity is dependent on condition of the ion source and the cyclotron, and is poorly reproducible.
4. It takes a number of hours to reach to an impurity ratio less than 1×10^{-4}.
5. An impurity ratio of order of 1×10^{-3} can be attained usually within a few tens of minutes.
6. Production order of ion species must be determined so that Δ(M/Q)/(M/Q) between every species and the next (or the previous) one is larger than 3×10^{-4}, which is the minimum value for the reduction methods to be effective, since ions of previously used gas remain produced for some hours.

3. Multiturn Experiment

When radial expansion of an internal beam bunch at an extraction radius is larger than orbit separation, the beam bunch needs to turn a number of times to be completely extracted out of a cyclotron. This is called multiturn extraction and its turn number is the number of multiturn. We measured the radial expansion of a beam bunch at various radii and the number of multiturn, and studied their dependence on trim coil current, harmonic coil current, dee voltage and deflector voltage.

Beam of $^{4}He^{2+}$ from the ion source were chopped by the P-chopper to pulses of about 500 ns duration at several μs intervals and injected into the cyclotron. Each pulse was further divided into bunches at 60 ns intervals by dee voltage and accelerated up to 50 MeV. Internal beam bunches were observed with a digital storage oscilloscope by amplifying signals of beam current stopped on the radially-movable

probe of the cyclotron. Extracted beam pulses were measured with a plastic scintillator.

An example of time distribution of beam pulses is shown in Fig. 1. It turned out that a width of internal time distribution, which represents radial expansion of a beam bunch, was narrowed by changing harmonic coil currents as shown in Fig. 1-a and 1-b. On the other hand, Fig. 1-a' and 1-b' show that time distribution widths of the corresponding external beam pulses were inverted, which were extracted at different deflector voltages through multiturn extraction. This suggests that extraction is more decisive of the number of multiturn than internal beam bunch expansion in spite that the deflector voltage has no effect on internal beams. The measurement also revealed that trim coil currents and dee voltages affected time distribution of internal beams as well as harmonic coil currents. Furthermore all these parameters shift beam path into and inside the deflector. Therefore it is suggested that a part of pulses in the time distribution of internal beams were extracted from the cyclotron and radial expansion of internal beam bunch is not the only cause of multiturn extraction. As a result, we have to take a filtering effect of the deflector into account.

It should be noted that narrower time distribution widths of internal beam leads narrower ones of external beams. But it might be masked behind the large filtering effect.

Although usefulness of the filtering effect is unknown, its mechanism is worth investigating in detail at the next stage. Control of the internal time distribution width is necessary to reduce the multiturn number with less beam loss at the deflector.

References

1. W. Yokota et al., Proc. of the 12th Symposium on Accelerator Science and Technology, October 27-29, Wako, Saitama, 1999, pp. 127-129
2. I. Ishobori et al., Proc. of the 12th Symposium on Accelerator Science and Technology, October 27-29, Wako, Saitama, 1999, pp. 1453-455
3. W. Yokota et al., Rev. Sci. Instrum, 68 (1997) 1714

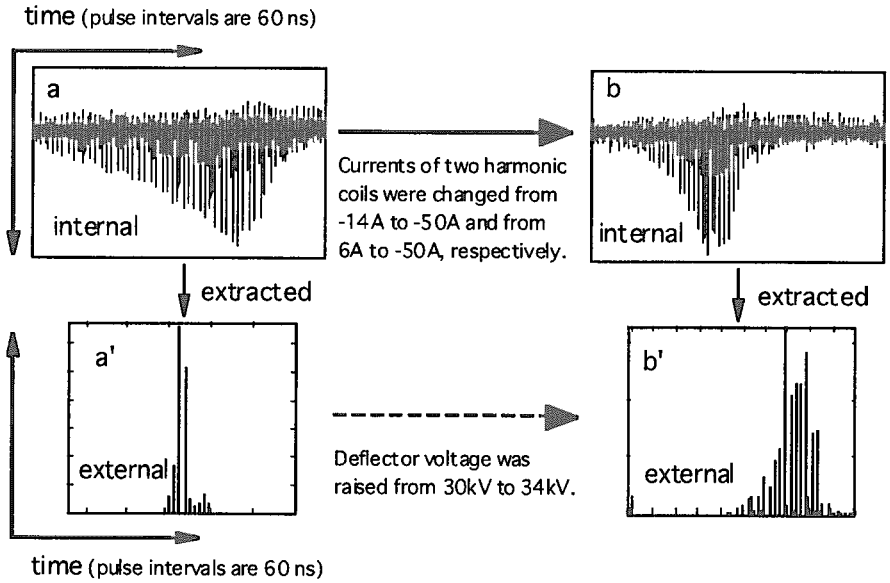


Fig.1 Change in internal and external beam pulse distribution. The internal distribution (a) is wider than (b) due to different harmonic coil currents. Whereas the external distribution (a') coming from (a) is much narrower than (b') from (b) because of different deflector voltage.

9.3 Measurement of Beam Energy and its Spread using Nuclear Reaction Resonances at the Single-ended Accelerator

Y.Ishii, I.Takada, K.Mizuhashi, S.Saito, S.Uno, K.Ohkoshi, Y.Nakajima, A.Chiba, T.Kamiya, T.Sakai and S.Tajima
Advanced Radiation Technology Cneter, JAERI

1. Introduction

Beam energy and its spread generated from the single-ended accelerator(voltage stability of $\pm 1\times10^{-5}$) has been measured using nuclear reaction resonances of $^{27}A\ell$ (p,γ)^{28}Si with the narrow resonance widths below 100eV. In the previous study, the beam energy was measured in the accuracy of 1×10^{-4} order employing the resonance energy of 992keV and 1317keV with their resonance widths of 100eV and 50eV, respectively. The accelerator was calibrated by comparing the beam energy measured by the reaction resonace to the beam energy based on the accelerator voltage[1]. The value of beam energy spread was only measured at the energy of 992keV. The value of beam energy spread was not, however, reproducible as following problem: (1)The statistical errors were increased in measurement data of γ-ray yield, because the SN ratio of its yield was small. (2)The calibration constant of the accelerator was often changed on the low voltage side at the same control voltage, because the voltage measurement and stability circuit was damaged by the discharges of the accelerator. In addition, the beam energy spread was changed widely[2] by the same cause. The main reason of the low SN ratio resulted in detecting various nuclear reactions by injecting the three kinds of beam in the target, e.g. H^+, H_2^+ and H_3^+, extracted from the accelerator without separation.

In this experiment, the SN ratio was improved by injecting only H^+ beam on the target. H^+ beam was separated from the three kinds of beam by the optimization of the operation parameters for the accelerator using secondary electrons retarding magnets equipped on the accelerator tube and the electrostatic focusing lens at the entrance of the tube. The discharge of the accelerator was reduced by exchanging the acceleration tube and enough conditioning of the accelerator. In addition, the energy spread at 1317keV was also measured by improving the measurement accuracy.

On the basis of these results, beam energy stability was evaluated at 992keV and 1317keV.

2. Eperimxental

The experimental chamber was connected with the 0° beam line to measure directly beam energy generated from the accelerator. A thin $A\ell$ target of 60nm in depth which was evaporated on Ta 0.3mm in thick was used for the experiment. As the voltage of the accelerator cannot be set in the resolution under 1kV, the injection beam energy was controlled by applying the voltage to the target insulated from the ground. The voltage of less than 5kV was applied by a high voltage power supply with a stability of 1×10^{-5} at 5kV. Although the γ-ray yields are generally normalized by measuring beam current injected in the target, the beam current cannot be measured because of applying voltage to the target. The beam current injected into the target was normalized by counting the protons that were scatted on the surface of its target using a SSD detector. The 2.5inch NaI detector was placed to the distance of about 20mm position from the target down stream of the beam to increase the detection efficiency of the γ-ray yield.

The reproducibility of the measurement data was improved by followings: (1)The aimed reaction was increased with injecting only H^+ by separating from three kinds of ion spices (H^+, H_2^+ and H_3^+). Thereby the SN ratio was improved to reduce the back ground noise. (2)The new accelerator tube was exchanged to reduce the electric discharge by changing the accelerator tube and enough conditioning it. The some divider electrodes which were equipped in the tube for dividing voltage were shorted because some insulation resistance values of the insulators among their electrodes were degraded by the electric discharge. Thereby the electric potential was not divided equally in the tube.

3. Results

Relation between γ-yield and beam energy on the basis of subtracting the target voltage from the acceleration voltage, called injection beam energy, was shown in Fig.1 at 992keV and 1317keV. The differences between the injection beam energy and the nuclear reaction energy were 0.5% and 0.6% at 992keV and 1317keV, respectively.

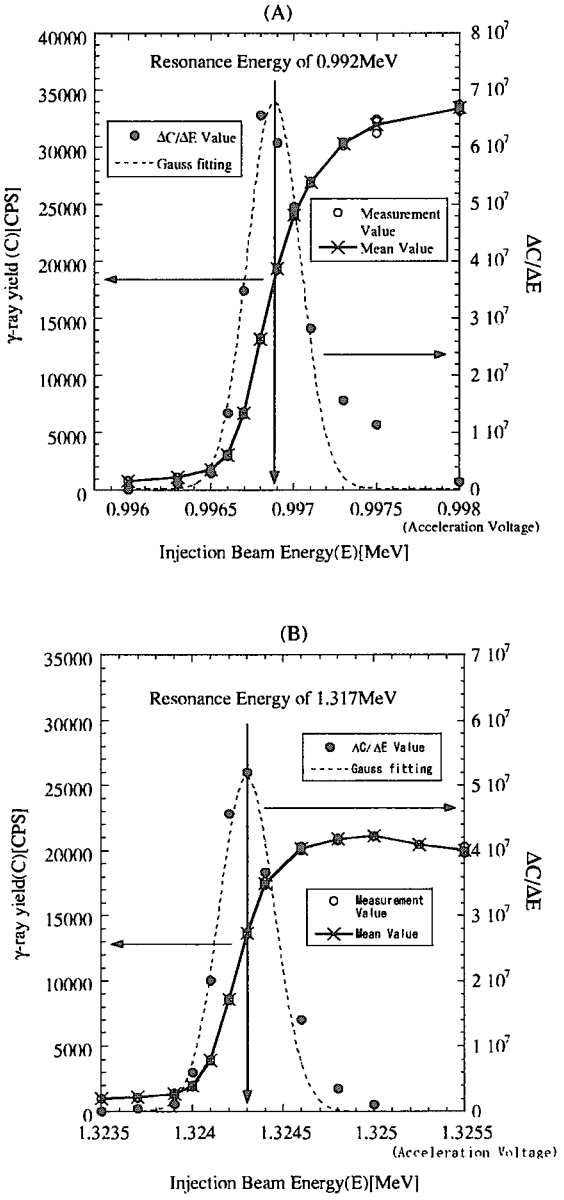


Fig.1 Measurement of beam energy and its spread at the resonance energy of 0.992MeV(A) and 1.317MeV(B). Injection Beam Energy represents beam energy based on subtracting the sample voltage from the acceleration voltage.

The beam energy widths were estimated at 320V and 310V with FWHM of the resonance peak. From these widths, the beam energy stability was evaluated at 3.2×10^{-4} and 2.4×10^{-4}. As compared with these results, the beam spreads were measured using the 90° analyzing magnet on the same accelerator condition by emplying the reactions. The results are shown in the Table-1. Each value is in 4.2×10^{-4} or less. The energy spread was reduced according as the beam energy was increased. The difference between the differential values(ΔE) of the resonance reaction and those of the 90° analyzing magnet was considered to originate from injecting beam in the analyzing magnet on the condition of deviating from the design orbit.

The beam energy stability was about 30 times larger than the voltage stability of $\pm1\times10^{-5}$. The voltage stability was measured without generating the beam. The energy stability was increased to generate about 10μA. In addition, the beam energy stability included the beam energy stability of the ion source, which is the RF ion source and placed in the high voltage terminal.

These measurements of the beam spreads were within the beam energy range of 1.3MeV. the measurement of the beam energy spread near 3MeV is required to study the linearity of its spread. On the other hand, the measurement of the beam energy spread generated from the ion source is important to evaluate the voltage stability on the condition of the beam generation. This measurement is demanded to improve the beam energy spread. The beam energy spread generated from the accelerator near 3MeV and the ion source will be measured in the next experiments. These experiments will enable us to generate the high stability beam.

Reference

1)Y.Ishii et al. TIARA annul report P.236(1995), JAERI-Review 95-019
2)Y.Ishii et al. TIARA annula report P.242(1996), JAER-Review 97-015
3)Y.Ishii et al. TIARA annul report p.268(1999), JAERI-Review 99-025

Table-1 Beam energy spread and stability

	Nuclear resonance reaction		90° analyzing magnet	
Energy(E)[MeV]	ΔE(FWHM)[V]	ΔE/E(stability)	ΔE(FWHM)[V]	ΔE/E(stability)
0.992	320	3.2×10^{-4}	420	4.2×10^{-4}
1.317	310	2.4×10^{-4}	370	2.8×10^{-4}

9.4 Prolongation of a Filament Lifetime using SF_6 Plasma Method

K.Ohkoshi, Y.Saitoh, T.Kamiya, T.Sakai,
T.Orimo*, A.Ohmae*, I.Takada and S.Tajima
Advanced Radiation Technology Center, JAERI
*Beam Operation Service, Co., Ltd.

1. Introduction

Variety of ions from proton to bismuth have been provided for various experiments by means of the 400kV ion implanter equipped with a Freeman ion source[1] in the TIARA facility[2]. Recently, irradiation of refractory materials, such as niobium (Nb), is attracted for material synthesis. In order to produce the ions of refractory materials by the Freeman ion source, the materials are put in the plasma chamber of the source and vaporized by the plasma. In case of the Freeman ion source, it requires much arc currents to produce the suitable ion beam current of the materials. It causes the filament lifetime to be shortened. In order to solve this problem, we applied the SF_6 plasma method[3].

This method is effective not only to produce the refractory material ions but also to prolong the lifetime of the filament[4].

2. Lifetime of Filament

Some materials were adhered to the surface of the tungsten (W) filament after an operation with the pure SF_6 plasma. We revealed that the materials were molybdenum (Mo) and W from the plasma chamber and the filament by the analyzing the materials with a micro particle-induced x-ray emission (micro-PIXE)[5] and an x-ray photoelectron spectroscopy (XPS).

The Mo and W are fluorinated in the SF_6 plasma. The fluoride metals adhered to the filament were decomposed into metals and fluorines by heat of the filament, and the metals are adhered on the surface of the filament.

The amount of stuck Mo and W to the filament was larger than that of the lost W from the filament in pure SF_6 plasma operation, therefore the diameter of the filament gradually increased and the resistance decreased. The reduction of the filament resistance makes plasma unstable. We tried to apply the increment of the filament diameter to prolong the filament lifetime. In order to prolong the lifetime of the filament, it is important that the amount of the lost W from the filament balances that of the stuck metals from the chamber wall and the filament itself. The balance can be adjusted with changing the arc current and the gas flow of the source. In the test operation to generate Nb^+, we obtained the balanced condition in the arc current of about 0.19A and the gas flow of the 0.4sccm. We could increase the beam current of Nb^+ from 5 to 10μA and prolong the filament lifetime from 6h to more than 86h. A filament could be hardly consumed with the SF_6 plasma method. The filaments after operation with the SF_6 plasma method and the Ar heating method, and virgin filament are shown in Fig.1.

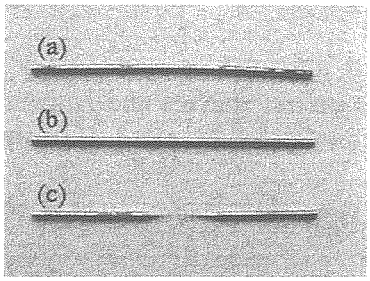


Fig.1 Filament after operation with (a)SF_6 plasma method, (c)Ar heating method, and (b)virgin filament.

However, the plasma chamber becomes dirty by long time operation with pure SF_6 plasma, and it makes plasma unstable. We tested beam generation using the mixture gases of SF_6 and Ar in the ratio of about 1-20 to avoid the problem. In this case, the ion beam current of refractory material with the mixture gas is a little lower than that with pure SF_6. However, there were the effects of prolonging the lifetime of filaments, of stabilizing plasma and also of minimizing corrosive dirt that make the maintenance term of the source short.

Using this technique, we are almost free from worry about a filament lifetime.

References

1) J.H.Freeman, Nucl. Instrum. Methods 109, 477 (1973)
2) Y.Saitoh, S.Tajima et al., Nucl. Instrum. Methods Phys. Res. B 89, 23 (1994)
3) K.Ohkoshi, Y.Saitoh et al.,TIARA Annual Report (Vol.7), p238 (1997)
4) K.Ohkoshi, Y.Saitoh et al., Rev. Sci. Instrum.71, 1174 (2000)
5) T.Sakai et al., Nucl. Instrum. Methods Phys. Res. 390, 136 (1998)

9.5 Development of Transparent-type Beam Current Monitor

Y.Nakajima, Y.Saitoh and S.Tajima
Advanced Radiation Technology Center, JAERI

1.Introduction

We are developing a transparent-type beam current monitor which is required measuring beam current for multiple coincide irradiation in TIARA facility. We measured characteristics of secondary electron emitted from wire probe, and we confirmed following facts.

(1) The amount of secondary electron is increased linearly with increase of the beam current.

(2) The amount of secondary electron depends on ion species and its energy, and it is explained by electric stopping-power logics.

In this time, we made a test device which does not depend on the beam energy and ion species, and we acquired fundamental data of it.

2.Experimental

Fig.1 shows structure of test device consisted of a wire mesh, five electrodes and an aperture. The wire mesh, 0.03mm in diameter and 0.85mm in interval, is movable and is inserted into the gap of the center electrode by the air actuator when measuring the beam current.

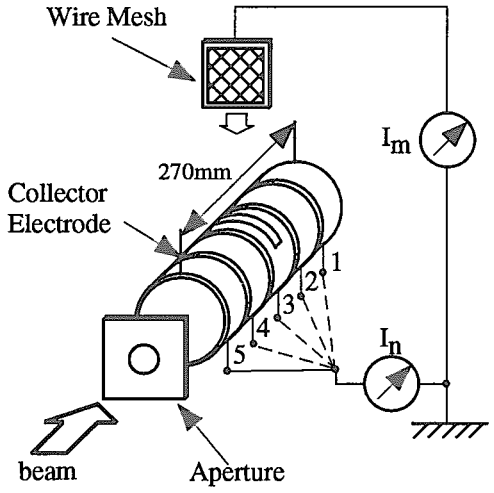


Fig.1 Structure of test device

The current of the mesh and each electrode can be measured individually. The mesh current, I_m, is represented as following equation (1).

$$I_m = I_f \cdot R_o \cdot q + I_s \quad (1)$$

where I_f is measured beam current by Faraday Cup equipped just after the device when wire mesh is not inserted, R_o is a ratio of lost beam at the mesh to I_f, q is charge state of ion beam and I_s is secondary electron current which is emitted from wire mesh inserted. R_o has already measured by Faraday Cup while inserting and pulling-out the mesh to the beam, and determined R_o=0.07. The secondary electron distributions from the wire mesh were measured by the five collector electrodes.

In the next step, we measured the change of mesh current while supplying negative voltage to No.1 and No.5 electrodes as shown in Fig.2.

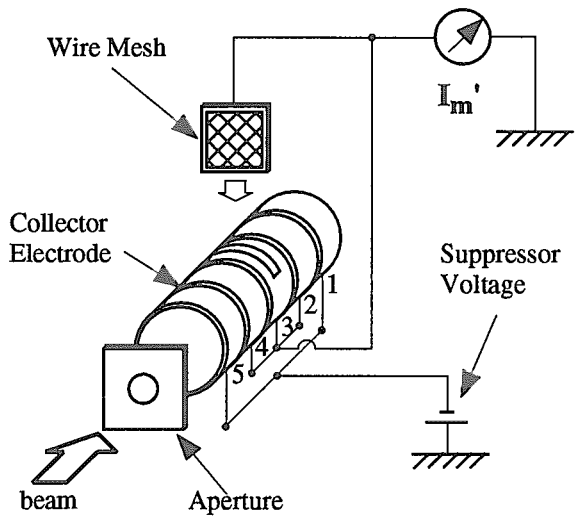


Fig.2 Measuring circuit of relationship between mesh current and suppressor voltage

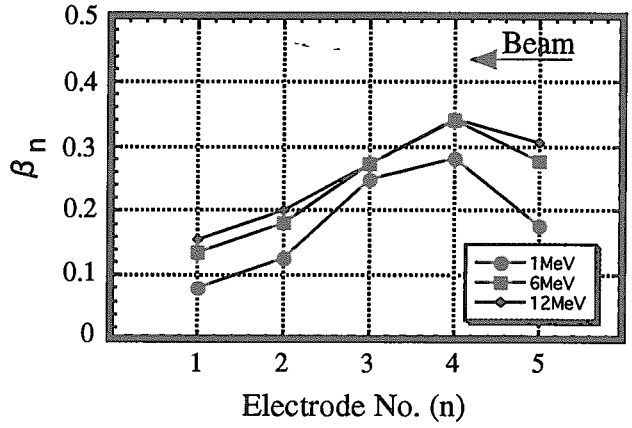


Fig.3 Distribution of secondary electron

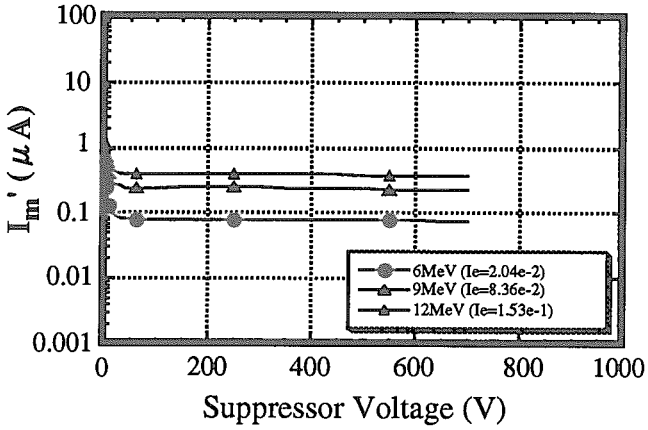


Fig.4 Relation between suppressor voltage and mesh current

3.Results

Fig.3 shows the secondary electron distributions induced nickel ion of energy from 1MeV to 12MeV. Ratio of secondary electron and beam current at the Faraday cup , β_n, are calculated as follows.

$$\beta_n = I_n / I_f \cdot q \quad (n=1,2,3,4,5) \qquad (2)$$

where I_n is measured secondary electron current for n-th electrode. Almost of secondary electrons emitted from the mesh distribute to backward, and they increase with the beam energy.

Fig.4 shows change of the mesh current induced by nickel ion, I_m', when increasing suppressor voltage supplied to No.1 and No.5 electrodes. The mesh current depends on suppressor voltage because then secondary electron were gone back to the mesh by electric field formed both electrodes.

In the Fig.4, I_e is the expected currents calculated by $I_e = q \cdot I_f \cdot Ro$. The ratios of I_m' and I_e are 4.0, 3.0 and 3.2 at beam energy of 6 MeV, 9MeV and 12MeV respectively . These suggest that a part of secondary electrons lost somewhere or R_o will not be constant for each beam condition. We are continuously going to try to find them.

References

1) S.Tajima, I.Takada, et al., JAERI-Tech 96-029(1996)
2) Y.Nakajima, Y.Saito, S.Tajima, TIARA Annual Report 1998(JAERI-Review 99-025),262-263

9.6 Cooling System for Beam Stabilization of JAERI AVF Cyclotron

Y. Nakamura, S. Okumura, M. Sano*, T. Nara, T. Ishimoto, S. Kurashima, W. Yokota, K. Arakawa, K. Saitoh*, T. Fukuda*, J. Kanakura*, M. Fukuda, I. Ishibori, H. Tamura and T. Agematsu

Advanced Radiation Technology Center, JAERI
*Quantum Equipment Division, Sumitomo Heavy Industries, Ltd.

1. Introduction

We have ascertained that the instability of ion beam extracted from the cyclotron comes from the magnetic field drift (MFD). Three possibilities, which are thought the cause of the MFD, have been proposed so far. One is geometrical change of the effective cyclotron acceleration gap, the other is temperature dependence on magnetization itself and another is the change of spin density in specific volume. We have measured many temperatures around the cyclotron yoke and surface on the spiral sector, magnetic field in the acceleration gap and displacement between upper and lower side yokes in order to investigate the beam instability of the JAERI AVF cyclotron [1), 2)]. As a result, we found out certainly that the principal cause of the MFD originated from slight change of the effective acceleration gap. Therefore, we decided to carry out some measures for beam stabilization of the cyclotron.

2. Drift of Magnetic Field

A lot of temperatures around the cyclotron were measured continuously by means of the precise platinum resistance thermometers and C-C thermocouples. An average reducing rate of the magnetic field in the cyclotron was estimated at about –0.14 mT/K when the cyclotron was operated at 2.04 T of magnetic field value using a NMR probe positioned on the hill part of the sector. On the other hand, this rate for the AGOR superconducting cyclotron has been estimated theoretically at the value of –0.16 mT/K at base field of 2.23 T [3)]. Strangely enough, both values are nearly same although two cyclotrons have considerably different structure.

As a temporary standard, if the change of beam transmission is allowed up to about ±10 %, the MFD needs to be suppressed within 0.057 mT as estimated from Fig. 1. Therefore, temperature change at many positions connected with the MFD has also to be restricted below 0.4 ℃.

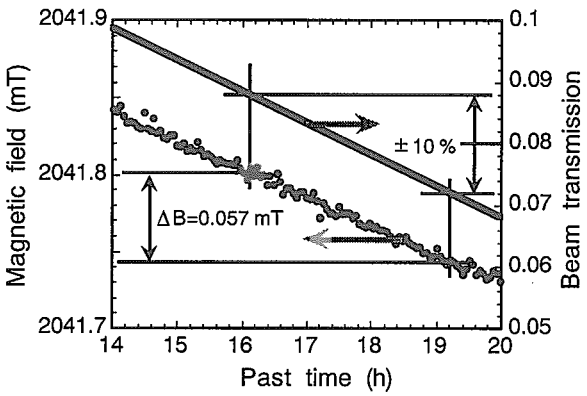


Fig. 1 Initial reduction of magnetic field and beam transmission under operation of $^{36}Ar^{8+}$ 195 MeV.

3. Heat Analysis

Some heat sources in the cyclotron exist as shown in Fig. 2. A great part of these quantities is supplied through thin PET sheet 0.75 mm thick directly from the main coil stacks. Other minor heat sources are supposed the trimming coils of twelve pairs, earth plate and dee electrodes by RF power

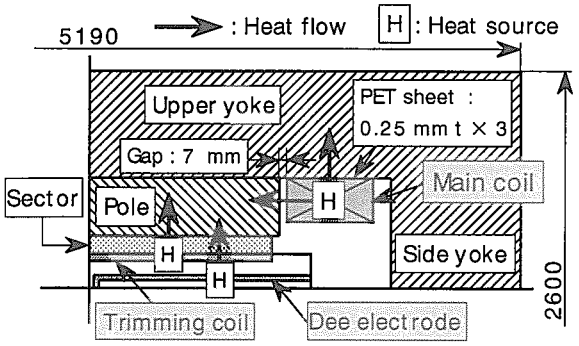


Fig. 2 Various heat sources in 1/4 sectional view of the cyclotron.

consumption. The thermal analysis code "NASTLAN" consisted of finite element method was used for three-dimensional heat analysis.

An example of heat analysis before the measures for beam stabilization is shown in Fig. 3. Using a 1/8 model of the cyclotron, the input data were chosen the values under operation condition of $^{36}Ar^{8+}$ 195 MeV. The temperatures in the whole cyclotron body are set 30 ℃ at the start of heat analysis. The highest temperature in the cyclotron attains to 50 ℃ after 50 hours past.

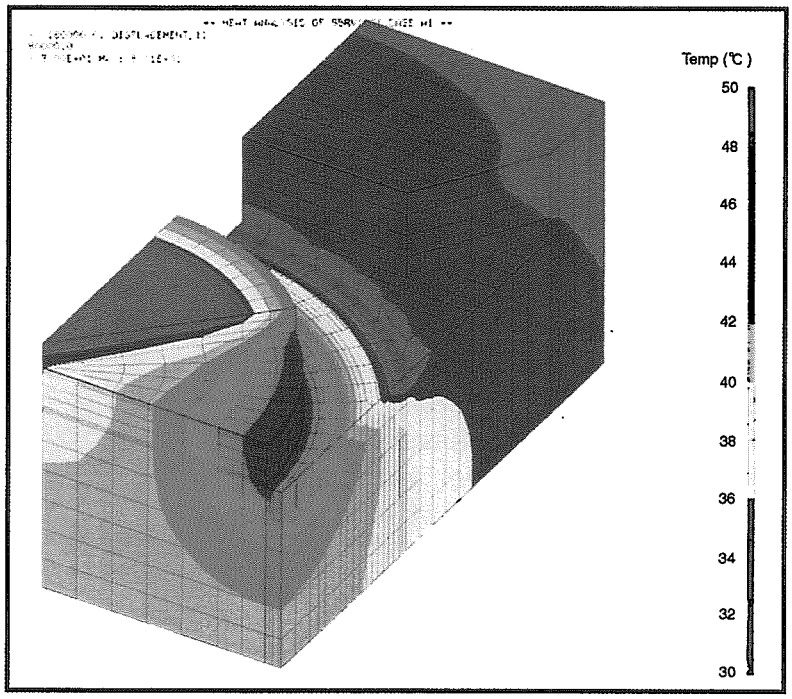


Fig. 3 An example of heat analysis before the measures for beam stabilization of the cyclotron.

If the following measures for beam stabilization of the cyclotron are accomplished completely, temperature increases everywhere in the cyclotron body are estimated below 0.4 ℃ under the same analytical condition.

4. Outline of Measures

In regard to the actual measures, a cooling jacket system was inserted between main coil and upper/lower yoke so that the

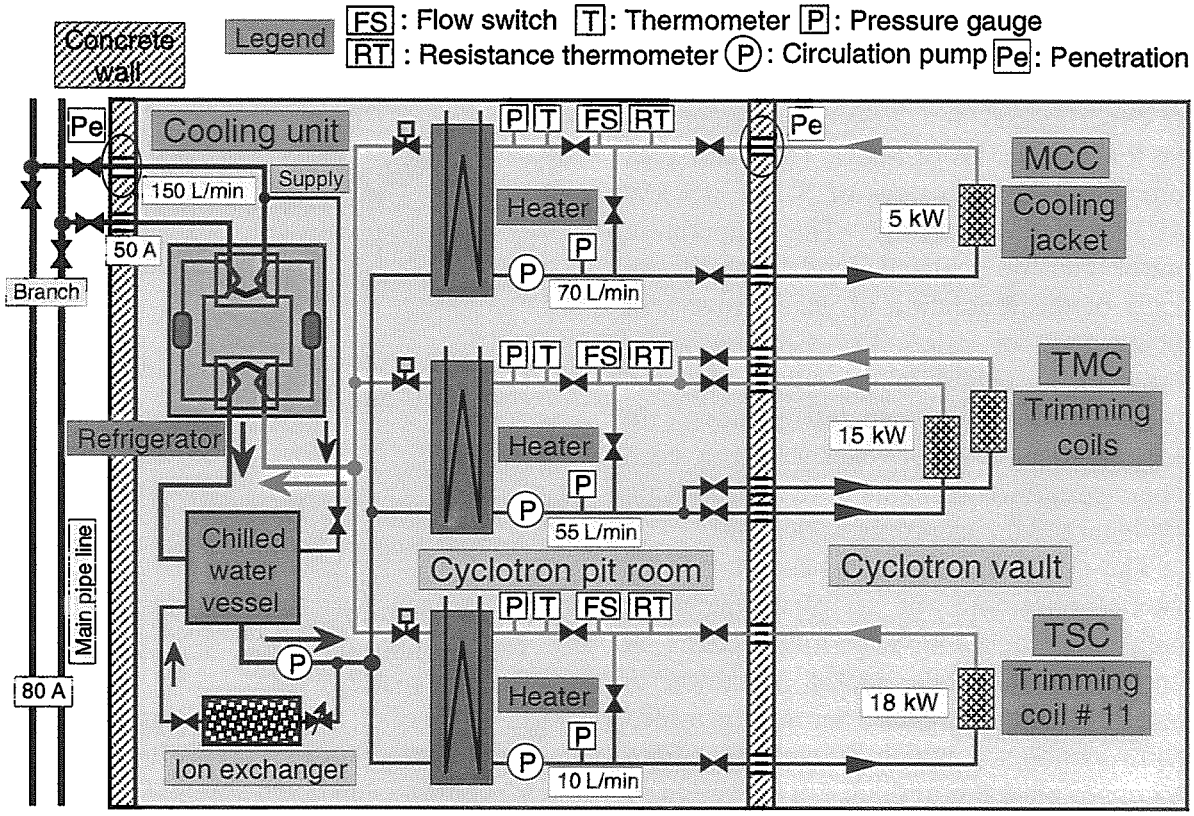


Fig. 4 An outline of cooling system for beam stabilization of JAERI AVF cyclotron.

heat conducted from the main coil can be shut out perfectly. However, we could not find out absolutely the efficient method to remove the heat transferred side surface of the pole through the narrow air gap of 7 mm because of difficulties from engineering aspect.

The trimming coils positioned directly on the spiral sectors can remove efficiently the heat dissipated into the vacuum chamber. For the sake of this purpose, an exclusive cooling system for trimming coils was installed so as to control independently by the separation from the existing cyclotron cooling system.

Furthermore, air ventilation in the cyclotron pit room was improved slightly by the installation of four blowing fans.

5. Construction of Cooling System

An outline of the whole cooling system is shown in Fig. 4. The cooling system roughly consists of three loops. One (MCC) is for the cooling jacket of the main coil, the other (TSC) is for trimming coil No. 11 which is the biggest power consumption among twelve trimming coils and another (TMC) is also for the residual eleven trimming coils except No. 11. Based on our experimental and analytical results, the heat load capacities of MCC, TMC and TSC were designed the values of 5 kW, 15 kW and 18 kW, respectively. The temperature control can be realized fundamentally by means of the regulation of water flow with the accuracy of ±0.5 ℃. Chilling water below 10 ℃ stored in the small adiabatic vessel is supplied by two refrigerators. In the operational mode of water warming, each heater assembled into the water circulation loop is turned on according to demand.

The MCC consists of two set of the jacket, furthermore one set of the jacket is roughly separated into large four pieces. A principal piece of the jacket is shown in Fig. 5. This jacket piece has a long folded hollow conductor which is embedded into the copper plate 8 mm thick. The weight of this piece is about 35 kg. For the insertion of cooling jacket, movement of the main coil stack was needed to bear the enough space between the main coil and yoke surfaces. In case of the upper main coil, the coil stack which has the weight of about 4.5 tons was supported by the vacuum chamber.

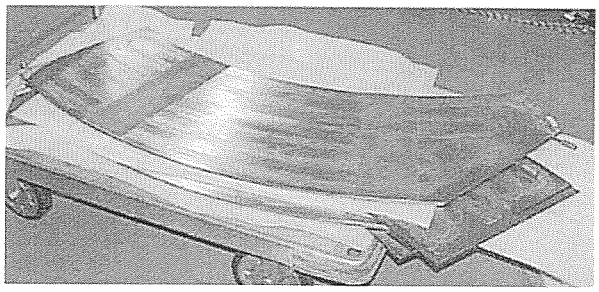


Fig. 5 Principal piece of the cooling jacket put on the cart.

A tentative result of temperature control for the cooling system is shown in Fig. 6. The deviation of control temperature by the averaging treatment of inlet and outlet water temperature is regulated completely within ± 0.1 ℃ for both systems of TMC and MCC.

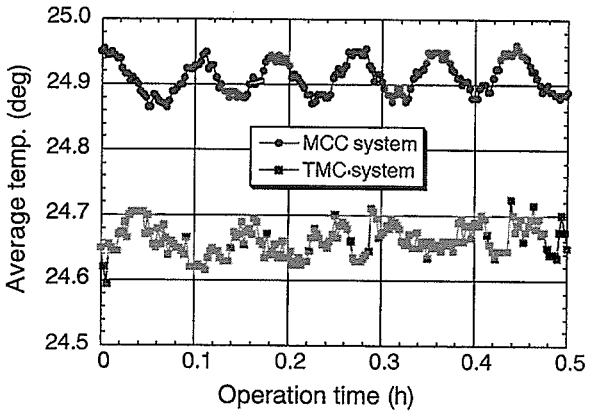


Fig. 6 An example of temperature control for MCC and TMC system.

References

1) M. Fukuda, S. Okumura, *et al.*, TIARA Annual Report 1998 (JAERI-Review, 99-025)
2) S. Okumura, K. Arakawa, *et al.*, Proc. of 12th Sympo. on Accel. Sci. and Technol., Wako, Japan (1999)
3) L. P. Roobol, S. Brandenburg and H. W. Schreuder, Proc. of 15th Int. Conf. on Cyclotrons and Their Applications, Caen, France (1998)

9.7 Model Test of the Flat Top Cavity for the JAERI AVF Cyclotron

Y. Kumata*, Y. Fukumoto*, K. Arakawa , Y. Nakamura, S.Kurashima

*Quantum Equipment Division, Sumitomo Heavy Industries Ltd,
Advanced Radiation Technology Center, JAERI

1. Introduction

The JAERI AVF cyclotron has been dedicated to various applications as biotechnology, material science, radiation chemistry, nuclear science and radioisotope production.

The ion micro beam is available to study the changes of cellular structure and function by single ion hit and to develop a cell surgery technique in the field of biotechnology. A specific site of living cell is exposed to ion beams focused to around 1 μm in diameter. The energy width is a very important parameter for production of a micro beam.

We are going to decrease the beam energy spread with using flat-top cavity for micro beam production. For this purpose, the 3rd or 5th order higher frequency voltage is superimposed to the fundamental accelerating voltage [1].

According to the report from NAC AVF cyclotron, the phase acceptance is to be increased by factor two [2].

2. Model Cavity

Figure 1 shows the cross section of the coaxial flat-top (FT) cavity. The inner and outer diameters are 40 mm and 200 mm, respectively. The length of cavity is adjusted by a moving short from 40 mm to 1000 mm. The FT cavity is coupled to the main acceleration cavity with using capacitive coupler whose size is 150 mm by 150 mm. And its gap is variable from 5 mm to 50 mm.

3. Experimental

We measured the resonant frequency and Q-value from 11 MHz to 20 MHz of

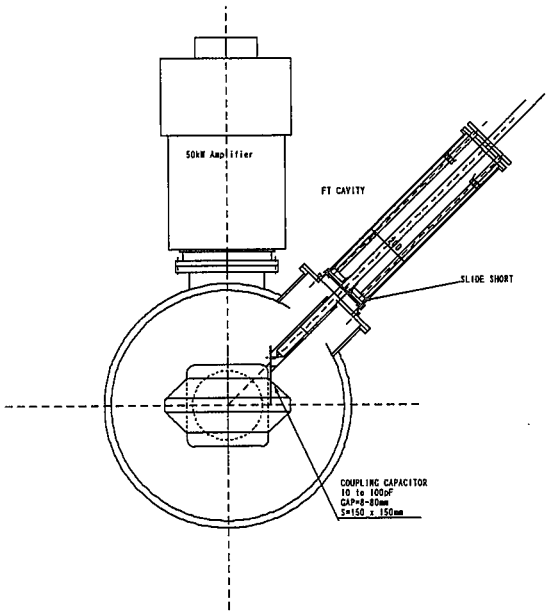


Fig. 1 Cross section of the FT cavity. The FT cavity is coupled to the main cavity perpendicularly. The sliding short is adjusted to get the suitable resonant frequency from 55 to 100 MHz.

fundamental frequency (f0). The frequency of the FT cavity is just 5 times of the fundamental frequency, i.e. it is from 55 to 100 MHz. The resonant frequency vs. cavity length is shown in Fig. 2. The FT resonant frequency is affected not only by the FT cavity length (L3) but also by the coupling capacitor (C3). For example, the cavity length is 350 mm and coupling capacitor gap is 6 mm to achieve 55 MHz, 50 mm and 25 mm at 100 MHz, respectively.

The measured Q-value is shown in Fig. 3. The FT cavity has relatively low Q-value at the lower frequency. It depends on the length of the FT cavity, because its wall loss is increased accordingly. The Q-value of the main cavity doesn't change even though the FT cavity was

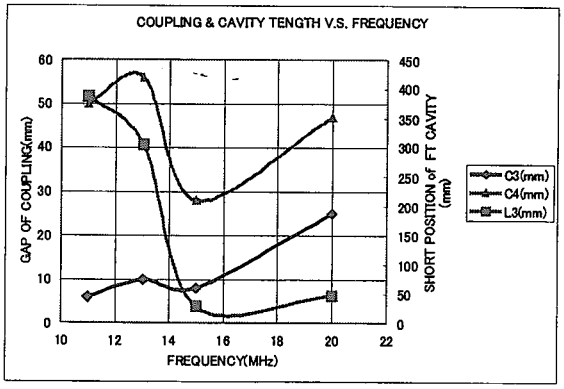


Fig. 2 FT cavity length (L3) and coupling capacitor gap (C3) vs. fundamental frequency. C4 is the gap of the capacitive power feeder on the FT cavity.

coupled. It means that the power loss of the fundamental frequency on the FT cavity is small.

A voltage superimposing test has been achieved using measurement system shown in Fig. 4. The fundamental frequency power is fed through the anode electrode of the main tetrode (4CW50000E). The 5th order

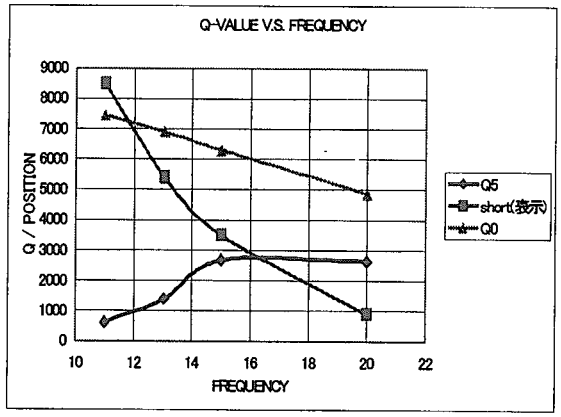


Fig. 3 Q-Value of FT cavity (Q5) and main cavity (Q0) vs. fundamental frequency.

frequency power is fed through the capacitive feeder located on the FT cavity. The input impedance of the FT cavity is adjusted to 50Ω changing the capacitor gap (C4). The induced voltage on the dee electrode is measured by a capacitive pick-up whose dividing ratio is about 1/1000. Two synthesizers are used to generate the fundamental frequency and the 5th order frequency. These signals are synchronized

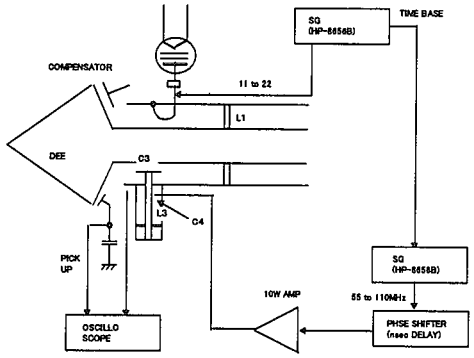


Fig. 4 Block diagram of the voltage mixing test.

using time base signal from one synthesizer to the other. The relative phase between the two signals are adjusted by a variable delay line. A typical wave form at 20 MHz operation is shown in Fig. 5. The flat-top width is about 6 ns and it is equivalent to the phase of 40 degree. Similar wave forms have been obtained at 15, 13 and 11 MHz.

The calculated phase acceptance is expanded

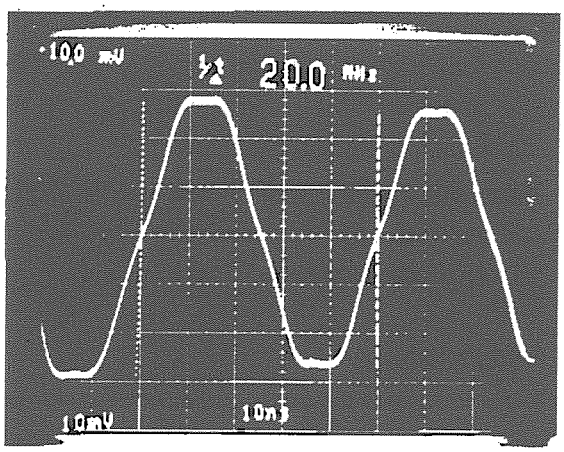


Fig. 5 Generated voltage wave form on the dee electrode. The 5th order FT voltage is superimposed to fundamental frequency voltage. The flat-top width is about 40 degree.

about 3 times up to 0.5 radian (30 degree) as shown in Fig. 6. The energy variation of the extracted beam is expected under 0.1%.

Power consumption in the FT cavity is calculated from the input power and the induced dee voltage. The input power is deduced from

the output level of the signal generator. The dee voltage is measured by the capacitive pick up. The expected power consumption is shown in Fig. 7.

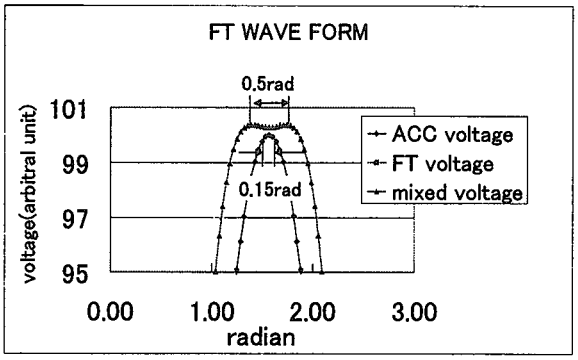


Fig. 6 Comparison of the simple sine curve and calculated mixed voltage. The phase width is about 0.15 and 0.5 radian, respectively.

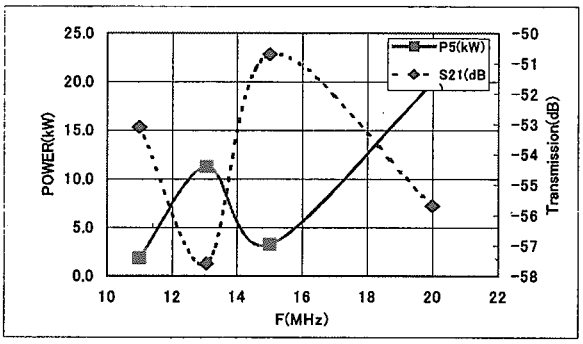


Fig. 7 Expected power consumption in the FT cavity. The solid line shows the power consumption and dotted line shows the transmission factor (S21) from the FT feeder to the voltage pick-up.

4. Discussion

The maximum frequency is limited to 100 MHz because the inductance around the capacitive coupler might be too large. It would be necessary to enlarge the inner diameter of the coaxial FT cavity. It will be also helpful for reducing the power consumption.

Theoretical calculation using one dimensional transmission line model is achieved to find the way to reduce the power consumption and to achieve the maximum frequency of 110 MHz. The calculation shows the smaller capacitance of the coupling C (C3) will cause larger power consumption.

Acknowledgement

The authors would like to thank to Dr. Shinozuka in Tohoku University and Dr. Goto, Mr. Kohara in RIKEN for lending us their equipment for the test.

References

1) S. Kohara, et al., *Model Test of a Resonator for Flat-Top Acceleration System in RIKEN AVF Cyclotron,* Proceedings of the 12th Symposium on Accelerator Science and Technology, Wako, Japan, p227 (1999)

2) J.L.Coradie, et al., *A Flat-top Acceleration System for The NAC Light Ion Injector Cyclotron.* , Proceedings of 14th International Conference , South Africa, p249, (1995)

9.8 Present Status of JAERI AVF Cyclotron System

Y. Nakamura, T. Nara, T. Agematsu, I. Ishibori, H. Tamura, S. Kurashima, W. Yokota, S. Okumura, K. Akaiwa*, To. Yoshida*, S. Ishiro*, A. Matsumura*, Y. Arakawa*, Tu. Yoshida*, S. Kanou* and A. Ihara*

Advanced Radiation Technology Center, JAERI
* Beam Operation Service, Co., Ltd.

1. Introduction

The JAERI AVF cyclotron system in TIARA has been operated smoothly without any serious troubles since the first extraction of $^4He^{2+}$ 50 MeV ion in March 1991 [1), 2)]. A cumulative operation time of the cyclotron amounted to 26200 hours at the end of March in 2000. Operation time is constantly about 3200 hours every year after 1993 as shown in Fig. 1.

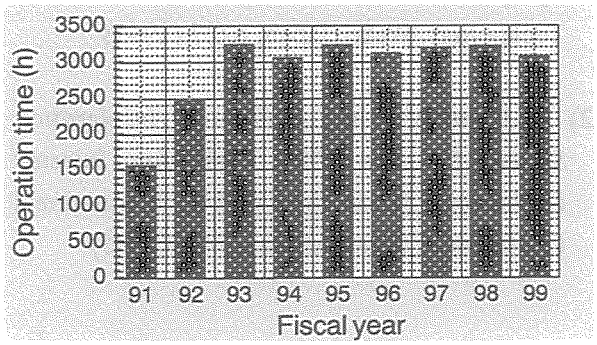


Fig. 1 Yearly operation time since 1991.

2 Present Status

2.1 Measures for beam stabilization

An energetic effort by our cyclotron group has been continued for the stabilization of the JAERI AVF cyclotron for several years. As the result, the measures for the cyclotron stabilization were carried out in March, 2000 [3), 4)]. Principal measures consist of two items [5)]. One is the insertion of the cooling jacket between the main coil stack and upper/lower yoke. The other is the alteration to an exclusive cooling line from the existing one for the trimming coils.

2.2 Renewal of magnetic channel, its probe and power supply

The material for the top head of magnetic channel (MC) probe was changed to graphite from tantalum to decrease the radioactivation as shown in Fig. 2. For this modification, the size of this head became large. Therefore, the body of the MC, is shown in Fig. 3, was also needed to reduce own size, although the magnetic ability had to be maintained the same as old one.

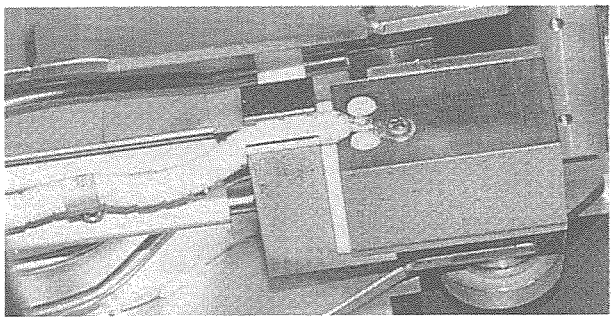


Fig. 2 New probe head made of graphite instead of tantalum.

The new power supply for the MC was reinforced the maximum output current up to 1430 A from 1300 A with the purpose of keeping the magnetic performance.

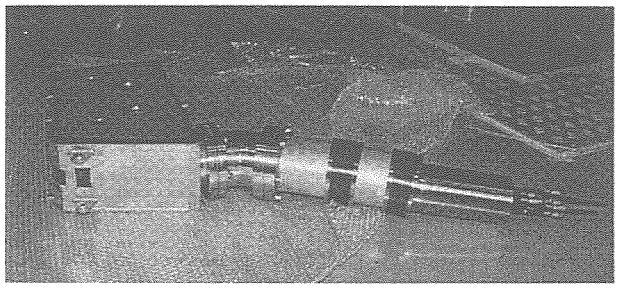


Fig. 3 Magnetic channel before installation.

2.3 Improvement of devices

A beam scanner (BSHY) driven by triangular wave is positioned along the HB beam course. The BSHY had a little poor uniformity because the distortions at the top and central part of the triangular wave were observed. The BSHB was modified its wave shape which is not included in any distortions. The fluence uniformity of the BSHB was largely improved from ± 28 % to ± 4% [6)].

A rotary shutter (RSHB) embedded into the shielding wall through the HB beam course was exchanged [7)]. The RSHB was operated the busiest among nine rotary shutters. The number of operations had been counted up 3500 at that time before the exchange since the installation in 1990.

Significant air leakage through the driving shaft of the RSHB had been observed whenever it was rotated.

The renewal rotary shutter was performed some improvements as the followings: 1) the change of vacuum seal from double O-rings ("cap-seal") to magnetic fluid seal, 2) the modification of driving mechanism from pneumatic rotary actuator to stepping motor, 3) the reconstruction of the polyethylene shielder with covering stainless steel plate to diminish the outgassing into the vacuum environment, etc.

2.4 Maintenance and repair

A vacuum tube (4CW-800B) of pre-amplifier in RF circuit was exchanged to new one because it was diagnosed to become worse in the inspection.

Several power supplies were taken care of their performances and conditions. A number of plastic (nylon) tubes for water-cooling in the some power supplies were exchanged to new ones. Many shunt resistors assembled into some power supplies were also replaced with new types made of "Zeranin" or "Manganin".

Serious deterioration of the vacuum in the cyclotron occurred for the insertion of the modified NMR probe. It was thought that the outgassing from the plastic (PVC) wire connected to the probe was increased by RF heating. The insulation material of the PVC wire was changed to polyimide which has an excellent property against heat and radiation.

A lot of optical fiber cables were also laid from cyclotron vault and several ion rooms to cyclotron control room for some measure-ments and data acquisition.

Many valves equipped with the water cooling system in the ion injection line were altered to reliable ones owing to the insufficient closing performance.

In the periodical maintenance working at last summer, principal routine items were carried out as belows:

(1) Confirmation of original positions about some probes, two phase slits, a deflector, the MC, a gradient corrector, etc.,
(2) Cleaning the deflector electrodes,
(3) Inspection of RF system and evaluation of RF characteristics,
(4) Scheduled replacement nylon tubes with rubber horses for cooling water in the beam transport system,
(5) Exchange of lubrication oil for about 50 rotary pumps,
(6) Exchange of back-up batteries for many programmable controllers (once for five years).

There were no serious problems in the periodical maintenance, especially.

3. Beam Acceleration Test

$^{56}Fe^{15+}$ 400 MeV ion was accelerated successfully first as a sort of metallic ions. This ion was produced steadily by means of MIVOC method using "HYPER-NANOGAN". And, this beam was utilized immediately for research purpose after the acceleration test.

An acceleration of $^{12}C^{6+}$ 320 MeV ion which is one of the cocktail beams of M/Q=2 series was also continued energetically until the midnight of Saturday from Friday evening in last May. This beam was also irradiated tentatively to some seeds of bio-samples.

Furthermore, $^{36}Ar^{18+}$ 970 MeV ion which is almost close to 1 GeV, has the highest energy so far using the JAERI AVF cyclotron, was tried to develop for the future use.

In regard to cocktail beams of M/Q=2 and M/Q=4, steady our effort has been done for the survey of practical conditions of the beam delivered to the users [8), 9)]. It is rather difficult to separate clearly the single species among several cocktail ions when the difference of the M/Q ratio between objective ion and neighbor one is the almost same as the proper resolution of the 930 cyclotron. However, we find out that the reduction of dee voltage is very effective to choose single species in addition to slight frequency shift of the master oscillator. We will be able to deliver these cocktail beams to the users in spite of a little limitations.

A number of ion species accelerated by JAERI AVF cyclotron so far are listed in Table 1. The symbols of "T_{ext}" and "T_{all}" described in Table 1 are defined by the ratio of the beam current detected on the main probe at r=900 mm to that with the Faraday cup just after the cyclotron, and the ratio between two beam currents injected into and extracted from the cyclotron, respectively.

At the present time, we can not deliver several species among these with enough intensity for the users because of the aggravation of the transmission efficiencies induced to repeated utilization for a long time, although we have sometimes tried to recover the efficiencies.

4. The Others

A preliminary measurement for flat-topping acceleration was done at CYRIC in Tohoku University [10]. The model cavity borrowed from RIKEN was transported there, then also assembled into the CYRIC 930 cyclotron. Several useful data were obtained for consideration of flat-topping acceleration on JAERI 930 cyclotron.

A future reconstructing plan for whole cyclotron cooling system was investigated comprehensively from the viewpoint of engineering aspect [11]. Based on this plan, additional budget will be proposed to realize the reconstruction.

References

1) K. Arakawa, Y. Nakamura, *et al.*, TIARA Annual Report 1998 (JAERI-Review 99-025)
2) H. Tamura, K. Arakawa, *et al.*, Proc. 12th Sympo. on Accel. Sci. and Technol., Wako, Japan (1999)
3) S. Okumura, K. Arakawa, *et al.*, Proc. 12th Sympo. on Accel. Sci. and Technol., Wako, Japan (1999)
4) M. Fukuda, S. Okumura, *et al.*, TIARA Annual Report 1998 (JAERI-Review 99-025)
5) Y. Nakamura, S. Okumura, *et al.*, in this annual report
6) T. Agematsu, S. Kurashima, *et al.*, in this annual report
7) I. Ishibori, Y. Nakamura, *et al.*, in this annual report
8) W. Yokota, M. Fukuda, *et al.*, Proc. 12th Sympo. on Accel. Sci. and Technol., Wako, Japan (1999)
9) W. Yokota, S. Okumura, *et al.*, in this annual report
10) Y. Kumata, Y. Fukumoto, *et al.*, in this annual report
11) N. Ohnuma, private communication

Table 1 The list of ion species accelerated by JAERI AVF cyclotron.

Ion species	Energy (MeV)	Beam (eμA)	Text (%)	Tall (%)
H^+	10	12	80	27
	20	5	77	23
	30	5	67	22
	45	30	79	14
	50	5	44	14
	55	5	63	14
	60	5	57	22
	65	7	62	12
	70	5	42	12
	80	3	47	13
	90	10	48	7.7
D^+	10	11	29	3.7
	20	5.6	80	16
	35	40	59	13
	50	20	49	7.2
$^4He^{2+}$	20	5.5	69	12
	30	10	42	10
	50	20	62	22
	100	10	32	10
	108	1.6	M/Q=2	
$^{12}C^{3+}$	75	2	M/Q=4	
$^{12}C^{5+}$	220	0.25	77	22
$^{12}C^{6+}$	320	0.0025	M/Q=2	
$^{14}N^{3+}$	67	4	43	10
$^{15}N^{3+}$	56	0.70	M/Q=5	5.0
$^{16}O^{4+}$	100	5	M/Q=4	22
$^{16}O^{5+}$	100	4	34	21
$^{16}O^{6+}$	160	1.9	58	21
$^{16}O^{7+}$	225	1	82	13
$^{16}O^{7+}$	335	0.1	41	6
$^{16}O^{8+}$	430	0.0045	M/Q=2	
$^{20}Ne^{4+}$	75	1.5	M/Q=5	6.6
$^{20}Ne^{5+}$	125	0.01	M/Q=4	
$^{20}Ne^{6+}$	120	1.6	53	18
$^{20}Ne^{7+}$	260	0.33	70	19
$^{20}Ne^{8+}$	350	1.5	63	23
$^{20}Ne^{10+}$	540	10^5 cps	M/Q=2	
$^{36}Ar^{8+}$	195	2.5	73	13
$^{36}Ar^{10+}$	195	0.1	43	1.2
$^{36}Ar^{18+}$	970	10^5 cps	M/Q=2	
$^{40}Ar^{8+}$	150	2.4	M/Q=5	6.2
	175	3	73	15
$^{40}Ar^{10+}$	250	0.2	M/Q=4	
$^{40}Ar^{11+}$	330	0.7	86	22
$^{40}Ar^{13+}$	460	0.03	63	24
$^{56}Fe^{15+}$	400	0.55	66	23
$^{84}Kr^{17+}$	320	0.08	M/Q=5	5.0
$^{84}Kr^{18+}$	400	0.04	60	2
$^{84}Kr^{20+}$	520	0.06	72	22
$^{84}Kr^{21+}$	525	0.0032	M/Q=4	
$^{129}Xe^{23+}$	450	0.2	72	11

M/Q = 2, 4 and 5 : Cocktail beams
Color : added ion species on previous table

9.9 Modification of the HY Beam Scanner for JAERI AVF Cyclotron

T. Agematsu, S. Kurashima, Y. Nakamura
Advanced Radiation Technology Center, JAERI

1. The Beam Scanners

JAERI AVF cyclotron has the ion beam scanners for large area irradiation. The beam scanners are installed on three beam courses (HY, LD and LX). The ion beam is two-dimensionally scanned by using a pair of laminated electromagnets fed with excitation current alternating in triangular wave.

The power supply of the LD course scanner was improved in FY 1993, because the poor uniformity on the scanned beam distribution caused by the distortion of the output current wave form of the power supply of was found [1]. However, the HY and the LX course scanners have been not improved so far.

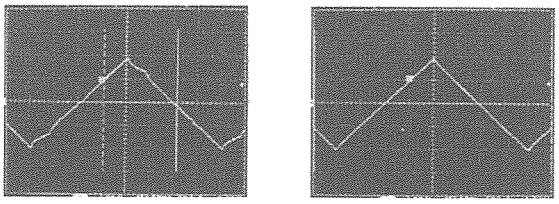
For recent progress of the experiments, the users of the HY course are looking forward to improving the uniformity like the modified LD scanner for a long time. Therefore the power supply of the HY scanner was improved in the end of FY 1999. The technical detail and the final result of this modification are the almost same as the LD scanner which has been already reported [2,3].

2. Results

To remove the distortions in triangular wave of the HY beam scanner, we improved the power supply for the direction of 50 Hz scanning. The circuit was replaced by a single end push pull (SEPP) circuit without polarity change. As the result, the distortions were removed completely as shown in Fig. 1. The uniformity of fluence distribution by beam scanning evaluated by the computer simulation [2,3]. As a result, it improved from ±28% to ±4% as shown in Fig. 2.

References

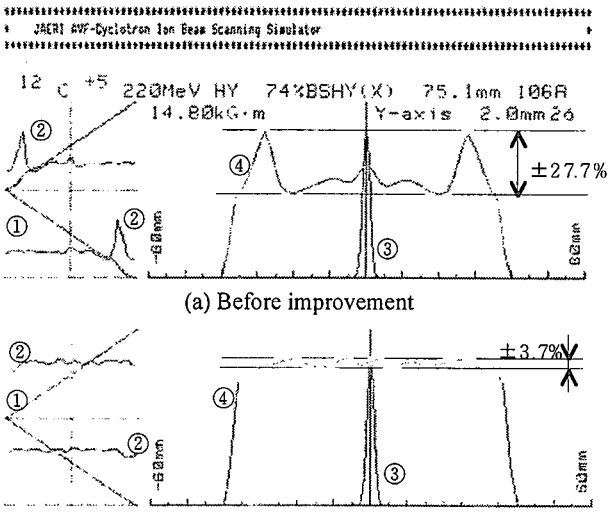
1) S. Okumura et al., JAERI TIARA Annual Report Vol. 3 (1993), p202.
2) T. Agematsu et al., JAERI-M 94-071
3) T. Agematsu et al., JAERI-Conf 95-003, Proc. ' 6th Japan-China Bilateral Symp. Radiat. Chem', (1994) p46



(a) Before (b) After

Fig. 1 An example of the scanning wave.

Photograph (a) is before and (b) is after improvement. The scanning frequency is 50 Hz in the vertical direction of the HY scanner.



(a) Before improvement

(b) After improvement

Fig. 2 An example of the simulated fluence distribution along the vertical direction of the HY scanner.

① Scanning wave. ② Differentiated wave by time to beam position. ③ Distribution of the non scanning beam. ④ Fluence distribution.

9.10 Improvement of the Switching Magnet Current Controller of Tandem Accelerator

K. Mizuhashi, * T. Miyoshi and S. Tajima
Advanced Radiation Technology Center, JAERI
* Kudo Electric Co. Ltd.

1. Introduction

The tandem accelerator has good stability of 3×10^{-4} at 3MV terminal voltage. The stability of the terminal voltage directly decided energy stability of the accelerated ion beam. An accelerated ion beam is deflected by the switching magnet and transferred to an experiment chamber. When an ion beam pass through the switching magnet, the X axis position of an ion beam is drifted by the fluctuation of ion energy and magnetic field. About the deflective width, the relation between beam energy and magnetic field is given by,

$$\frac{dB}{B}=\frac{1}{2}\cdot\frac{dE}{E},$$

where B is magnetic field and E beam energy. Therefore, the variation of ripple and drift by magnetic field stability of 1.5×10^{-4} is the same as a value with ion energy stability 3×10^{-4}. So we decided a specification of the switching magnet which has better stability than 1×10^{-4} for the excitation current. And current stability of this magnet is 5×10^{-5}. After warm up for three hours, the control signal of the magnet excitation current reaches within the range of 5×10^{-5} drift. So the operator must hourly adjust the ion beam position in the experimental chamber for first three hours.

2. Improvement

The main improved points are two parts. Old magnet current controller uses a shunt resistance to measure current in the magnet coil. New magnet current controller replaces the shunt resistance with a DCCT (Direct Current Current Transformer) that has temperature coefficient of 0.22(ppm/℃). The temperature coefficient of the shunt resistance was 20(ppm/℃) and the total temperature coefficient for the old magnet current controller was 191(ppm/℃). The other hand, some circuit resisters are used in the current controller are replaced with new circuit resisters which have better temperature coefficient. And to get the smaller total temperature coefficient , the number of circuit resisters in the magnet current controller are reduced. After improvement of the magnet current controller, the total temperature coefficient(K_t) is 15.1(ppm/℃) given by ,

$$Kt=\sqrt{(0.22)^2+(15)^2+(0.08)^2+(0.07)^2+(0.4)^2\cdot4+1^2}=15.1\ (\mathrm{ppm/℃}),$$

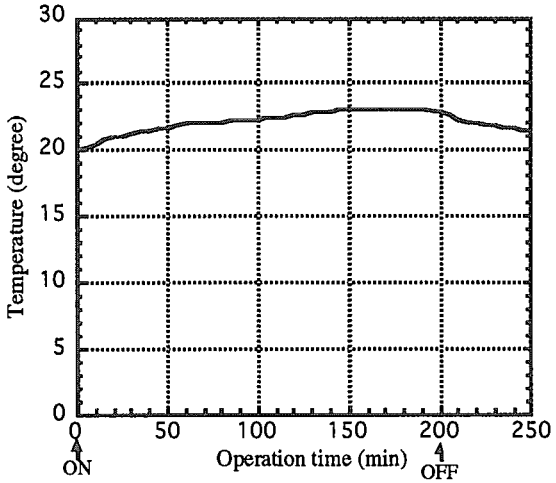


Fig. 1 Initial change of inside temperature for the magnet current controller under output current 420 (A).

where temperature coefficient of DCCT is 0.22(ppm/℃), standard voltage power supply 15 (ppm/℃), amplifier1 0.08(ppm/℃), amplifier2 0.07(ppm/℃), resisters 0.4 (ppm/℃) and burden resistance 1(ppm/℃).

3. Result

The magnet system is operated by full power (420 A) for three hours at before and after improved the magnet current control circuit. We observed the measurement signal of magnet current. The detective voltage signal of 420(A) is about 5040(mV) by the DCCT and 1262.4(mV) by the shunt resistance.

The results of an operation test are as follows:

After the elapse of three hours, temperature of the power controller inside increased from 20.1(℃) to 23 (℃), and the temperature almost saturates as shown in Fig.1. The error on the current controlled signal is induced by the temperature difference (△T) of 2.9(℃). Before the improvement, the error of controlled signal was about 554 (ppm) by the temperature difference of 2.9(℃) in calculation, but on the other hand the measured value was about 650 (ppm). The error on new magnet control system was about 44 (ppm) in calculation within the same environment. And the measured value was about 25 (ppm). Results of the stability test on the magnet current under output current 420(A) are shown in fig.2. After test condition of 420(A), the next stability test under the output current of 127(A) was started as shown in Fig.3. The temperature of magnet current controller inside is decreased and therefore the current changing ratio shows a negative value. From these data, the current changing ratio (7×10^{-5}) of the 127(A) operating is worse than it of 420(A) operating with 2.5×10^{-5}. Because the denominator of the 127 (A) operating is smaller than it of 420 (A) operating. This operation is rare case and the current is usually controlled from 0 (A) to 127 (A). So the temperature difference is smaller than above value.

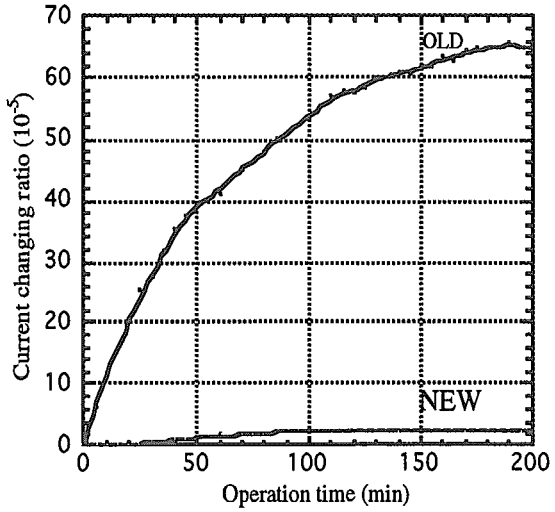


Fig.2 Stability of the magnet current under output current 420 (A).

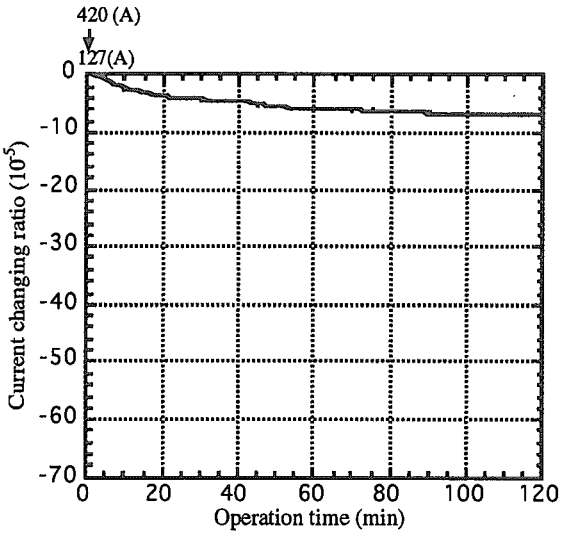


Fig.3 Stability of the magnet current under output current 127 (A).

By the improvement of the controller circuit, the controller has good current stability below 5×10^{-5} for beam in drift. The control signal almost does not depend on temperature. So large beam drift by temperature change was removed.

9.11 Renewal of the Computer Control System for JAERI AVF Cyclotron (II)

T. Agematsu, K. Arakawa, Y. Nakamura, S. Ishiro*
Advanced Radiation Technology Center, JAERI,
*Beam Operation Service, Co., Ltd.

1. Introduction

The former computer control system for the JAERI AVF cyclotron had been operated over ten years. In FY 1998, we renewed the control computers, man-machine interface and principal software of the control [1]. The old three mini-computers (VAX, DEC) were replaced to personal computers (PC) based on the Windows NT. The full replacement of the control system was completed in September 1999 [2]. The old system was operated until the end of March 2000 for the backup of the new system.

2. New Control System

All of the software for the control system was rewritten newly using InTouch, Delphi and C language. InTouch, which is principal language for the control program, is a process control tool for Graphic User Interface (GUI) .

The new control sequences were reconstructed in consideration of our many experiences for the cyclotron operation.

2.1 Upgraded Software

As shown in Fig.1, a graphic sequence of each device on the CRT was designed based on the actual arrangement of the devices, therefore operator can select easily the parameters for the devices. It makes the parameter adjustment of the devices easy with using the six rotary encoders.

The temporary store/recall function for the adjustment parameter was available only one parameter in the old computer control system. In the new system the function was realized to accept the many parameters during adjustment term, therefore operator are not necessary to remember the any parameters before and after adjustment in the cyclotron tuning.

2.2 Data Server

In order to keep the data certainly of the control system, we constructed the data server system based on the Windows NT Server. The control computers and the data server computer make a closed network.

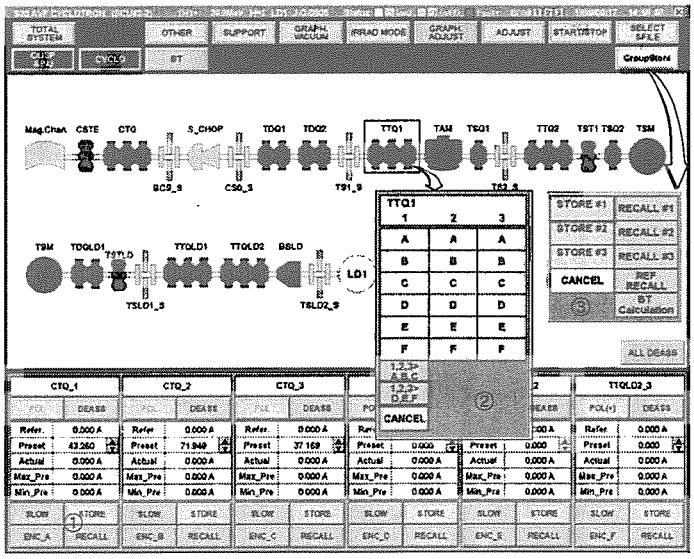


Fig.1 The graphical display for selecting and assigning the parameters for the beam transport group.

① The Store/Recall function switch of the parameter. ② The popup menu for assigning the parameters with the mouse. ③ The expanded Store/Recall function menu for all parameters of the adjustment term.

3. Conclusion

In FY 1999, the renewal of the computer control system for JAERI AVF cyclotron was completed. We will be able to operate smoothly the control system of the cyclotron over the future by this work.

References

1) T. Agematsu et al., JAERI-Review 99-025
' JAERI TIARA Annual Report 1998 ', p257.
2) T. Agematsu et al., "Construction of Personal Computer Control System for the JAERI AVF Cyclotron", Proc. of the 12th Sympo. On Accel. Sci. and Tech., Wako, Japan (1999), p450.

9.12 Renewal of Rotary Shutter for JAERI Cyclotron System

I.Ishibori, Y. Nakamura, T. Torii* and K. Suzuki*

Advanced Radiation Technology Center, JAERI,
* Fusion & Accelerator Development Center, Hitachi Ltd.

1. Introduction

In order to shield the radiation generated from the cyclotron and the beam transports, nine rotary shutters have been installed into the shielding walls between switching magnet room and several ion rooms. A rotary shutter (RS) consists of the iron columns for shielding against gamma rays and the laminated polyethylene discs against neutrons and a driving mechanism. Double vacuum sealing using "cap-seal" was adopted to evacuate differentially for driving shaft of the RS.

The number of operations for the RS along the HB course already amounted to about 3500 before the removal although it was designed as allowable operations up to 2000 times. As a result, a meaningful vacuum leakage had occurred by the deterioration of the cap-seal [1]. Therefore, we fabricated a new RS which was improved some performances, also replaced with this.

2. Consideration of Specification

Principal dimensions for shielding structure were not modified quite because the shielding ability of the renewed RS had to be maintained equivalently. However, some improvements possessed with excellent performance were carried out as followings.

(1) The vacuum seal for the driving shaft was changed to magnetic fluid seal from cap-seal as shown in Fig. 1. The maximum times of allowable operations times were designed up to 10000. A driving mechanism for rotation movement was also modified to electric stepping motor from pneumatic rotary actuator. And, this stepping motor was put at near position from the wall surface to be exchanged easily in case of trouble .

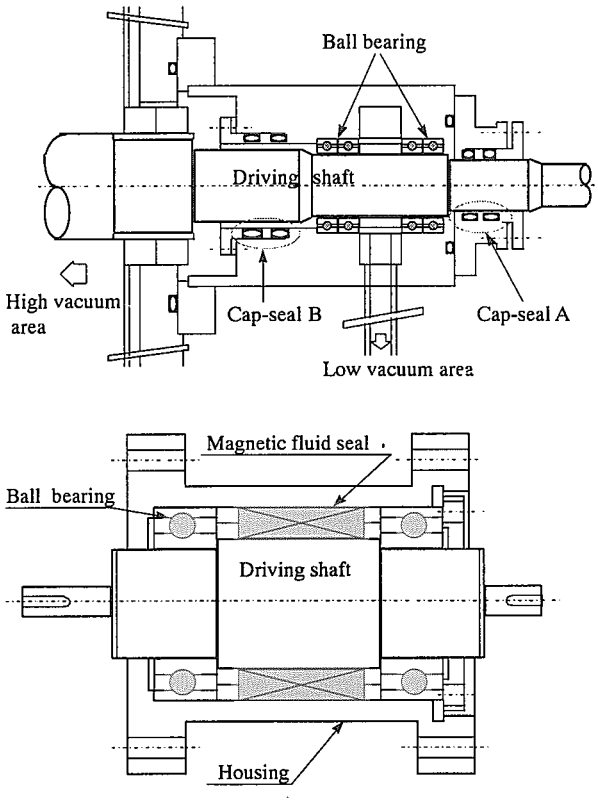


Fig.1 Modification of vacuum seal. Upper: before the renewal, Lower: after the renewal.

(2) The polyethylene discs for neutron shielding were covered with stainless steel plate in order to reduce the outgassing generated from the surface of these discs.

(3) A rotary pump was also replaced a new turbo-molecular pump (TMP) which can be evacuated directly the high vacuum region connected with the beam transport duct.

3. Fabrication of Supporting Devices for Working

Because the renewal of the RS has been scheduled every second year in the future, some supporting devices were prepared to make removal and installation working efficiently as below.

(1) The "support bed" is equipped with free ball bearings which can be moved vertically by pneumatic actuator. As the support bed is designed so as to handle up to 3 tons, this can easily deal with the body itself of the RS including the auxiliary shielding material (ASM).

(2) A "cyclone" system consisted two large vacuum cleaners and filtration vessels, is used to suck up only the iron sand which is one of the ASM's. The ASM around the RS body is made by mixing of iron sand and small iron balls that are utilized usually in "pachinko" games.

4. Factory Test

Prior to the installation, factory test was carried out to make sure the durability of the operations up to 10000 times. The test results in the factory were shown in Table 1. The durability in regard to the driving mechanism and vacuum seal was confirmed, since leakage rates at principal parts and the currents through the driving motor were not almost changed.

Of course, after the factory test, the driving motor and the magnetic fluid seal were exchanged to new ones.

5. Exchange and Installation

The body of the RS has to be imbedded in the shielding wall so that significant air gap is not existed around it. The installation condition for auxiliary shielding downstream the RS is shown in Fig. 2. The ASM is divided into plenty of small bags which are packed by thick plastic film doubly. And, the condition of the RS before the insertion into the shielding wall is also shown in Fig. 3. The body of the RS is buried into the ASM enclosed

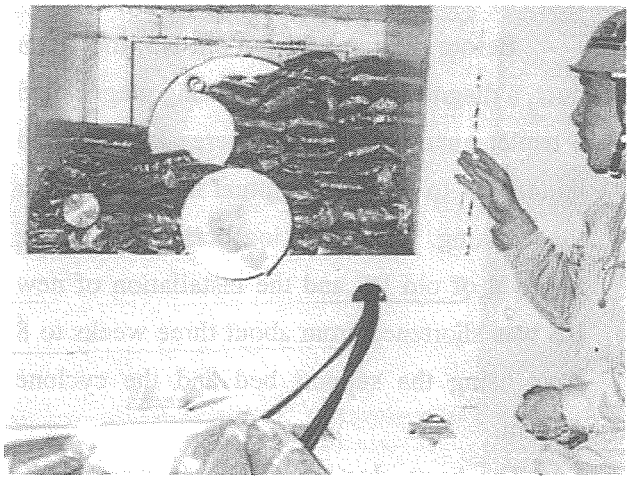


Fig.2 Auxiliary shielding downstream the RS.

by iron thick plates.

Owing to the recycling the ASM, the rate of the radioactivation of the ASM was needed to estimate surely. For this purpose, the activation along the shielding depth was measured by sampling of the part in the ASM before the renewal working of the RS. The result of measurement is shown in Fig. 4. Radioactivity at the position of the RS body was evaluated at below 10^{-5} Bq/g by the



Fig.3 New rotary shutter set on the support bed before the insertion.

extrapolation based on the data. Therefore, a particular radiation control was not need for the renewal working.

Before the removal the old RS, the beam duct, a diagnostic station, a steering magnet and a triplet quadruple magnet were also removed tentatively to avoid the mutual interference for the working. The working period during the removal of old RS and the installation of new RS was shortened from about three weeks to 8 days using the support bed and the cyclone system.

The beam duct and some electromagnets were returned again to their original positions with good precision within ±0.5 mm. All of the working for renewal of the RS was completed for about two weeks.

Finally, we confirmed that new RS and these devices were operated smoothly.

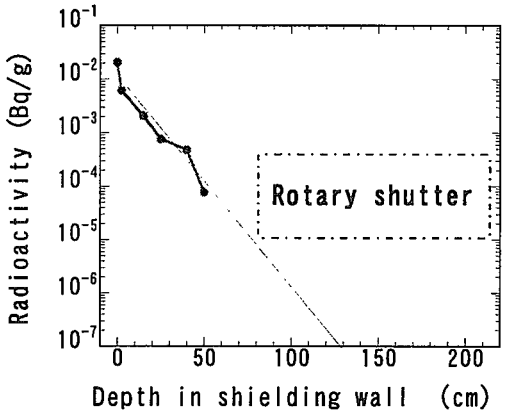


Fig.4 Measurement result of radioactivity for auxiliary shielding material.

6. Summary

The improvements for reliability and durability were realized since the expansion of the life time the for driving mechanism and the reduction of outgassing into the high vacuum were done certainly.

In the future, we have to be planning to renew residual eight RS's in consideration of operation condition of this RS.

Reference

(1)Y.Nakamura, TIARA Annual report p232-234 (1997)

Table 1 The results of factory test.

Number of operation	0	1000	3000	5000	8000	10000
Part of helium leak test	Leak rate $\times 10^{-11}$ (Pa•m^3/s)					
Fixed shutter	4.5	5.6	5.1	5.3	7.1	5.4
Gasket of TMP	4.5	5.6	5.1	5.3	7.1	5.4
O ring	4.5	5.6	5.1	5.3	7.1	5.4
Magnetic fluid seal	4.5	5.6	5.1	5.3	7.1	5.4
Driving motor	Load current (A)					
Close ⇨ open	1.06	1.06	1.06	1.06	1.08	1.07
Opening	0.20	0.20	0.20	0.19	0.19	0.19
Open ⇨ close	0.67	0.67	0.67	0.67	0.67	0.69
Closing	0.17	0.17	0.17	0.17	0.16	0.16

10. Status of TIARA 1999

10.1 Utilization of TIARA Facilities ····· 301
Utilization and Coordination Division
10.2 Operation of JAERI AVF Cyclotron System ····· 303
Y. Nakamura, T. Nara, T. Agematsu, I. Ishibori, H. Tamura, S. Kurashima,
W. Yokota, S. Okumura, K. Akaiwa, To. Yoshida, S. Ishiro, A. Matsumura,
Tu. Yoshida, Y. Arakawa, S. Kanou, A. Ihara and H. Suto
10.3 Operation of the Electrostatic Accelerators ····· 304
I. Takada, K. Mizuhashi, S. Uno, K. Ohkoshi, Y. Nakajima, Y. Saitoh,
Y. Ishii, T. Kamiya and T. Sakai
10.4 Radiation Control & Radioactive Waste Management in TIARA ····· 305
Safety Division & Utilities and Maintenance Division
Department of Administrative Services, JAERI

This is a blank page.

10.1 Utilization of TIARA Facilities

Utilization and Coordination Division,

Advanced Radiation Technology Center, JAERI

1. Introduction

TIARA is a center of the ion accelerator facilities composed of four ion accelerators, the AVF cyclotron, the 3MV tandem accelerator, the 3MV single-ended accelerator, and the 400kV ion implanter. These accelerators have been fully served for ion beam applications since January 1994.

2. Utilization System

TIARA is opened for public use: it receives applications of the experimental subjects in wide areas once a year from outside users as well as JAERI staffs. The subjects and these own utilizable beam times are approved after the official investigation by Subcommittee for TIARA under Advisory Council for JAERI's Research Facilities, which are both publicly organized since 1999. To attain an effective outcome of the research program, the utilization time of each accelerator is fairly allotted to the subjects three times in a year based on the approved beam time.

Charges for the utilization are remitted in the case that a contract of the joint research between JAERI and a university or a company or that of the projective joint research between JAERI and universities is made. The results of research have to be published at the TIARA Research Review Meeting and in the JAERI TIARA Annual Report. There is another system of visitor use with charges but without the publication duty.

3. Experimental subject approved

Number of subjects using cyclotron approved in FY1999 for the experiment was 52 while the total number using three electrostatic accelerators was 51 as shown in Table 1. Table 2 shows the number allotted to users under various contracts.

Table 1. Number of experimental subjects at various research fields.

Accelerators / Fields of research	Number of subjects	
	Cyclotron	Electrostatic accelerators
Materials for space	3	4
Materials for fusion	3	11
Biotechnology	23	2
Functional material	2	21
RI & nuclear sci.	5	0
Radiation chemistry	7	2
Basic technology	9	11
Total	52	51

Table 2. Number of experimental subjects at various relations with users.

Accelerators / Relations with visitors		Number of subjects	
		Cyclotron	Electrostatic accelerators
JAERI only	Takasaki Establishment	18	14
	Others	3	11
Cooperative research with university		9	13
Projective joint research between JAERI and universities		12	8
Joint research with private company or governmental institute		10	5
Total		52	51

4. Allotted time to users

The cyclotron has been continuously operated from Monday to Friday. The utilization time for the cyclotron is allotted by the hour. In case of the electrostatic accelerators, on the other hand, the utilization time is allotted by the day either from 9 a.m. to 6 p.m.: (A mode), or from 9 a.m. to 10 p.m.: (B mode).

As shown in Table 3, the cyclotron was used at the various research fields, while the electrostatic accelerators were mainly used in the field of functional material and material for fusion. The ratios of allotted time to JAERI staffs were 35% in the cyclotron utilization and 54% in the utilization of other electrostatic accelerators as shown in Table 4.

Table 3. Utilization of the accelerators in FY1999 at various research fields.

Accelerators / Fields of research	Utilization time at each period															
	Cyclotron (hours)				Tandem accelerator (days)				Single-ended accelerator (days)				Ion implanter (days)			
	99-1	99-2	99-3	total	99-1	99-2	99-3	total	99-1	99-2	99-3	total	99-1	99-2	99-3	total
Material for space	160	108	52	320	8	8	10	26	-	-	-	-	11	11	7	29
Material for fusion	0	0	30.5	30.5	18	10	14	42	14	11	13	38	12	9	10	31
Biotechnology	339	249.5	115.5	704	3	3	1	7	-	-	-	-	-	-	-	-
Functional material	17	16	6	39	14	19	12	45	17	22	18	57	20	21	20	61
RI & nuclear science	119	98	44	261	-	-	-	-	-	-	-	-	-	-	-	-
Radiation chemistry	98	76	37.5	211.5	4	4	3	11	-	-	-	-	-	-	-	-
Basic technology	319	200	114	633	10	11	8	29	25	21	16	62	2	1	1	4
total	1052	747.5	399.5	2199	57	55	48	160	56	54	47	157	45	42	38	125

Table 4. Utilization of the accelerators in FY1999 at various relations with users.

Relation with visitors / Accelerators		Utilization time at each period															
		Cyclotron (hours)				Tandem accelerator (days)				Single-ended accelerator(days)				Ion implanter (days)			
		99-1	99-2	99-3	total	99-1	99-2	99-3	total	99-1	99-2	99-3	total	99-1	99-2	99-3	total
JAERI Only	Takasaki Establishment	434	258	171	863	24	30	26	80	18	15	11	44	24	24	20	68
	others	0	0	30.5	30.5	7	1	6	14	7	11	17	35	4	2	4	10
Cooperative research with universities		161	118	63	342	9	7	1	17	4	8	2	14	8	8	7	23
Projective joint research between JAERI and universities		269	245	71	585	10	9	8	27	25	19	17	61	8	7	5	20
Joint research with company or governmental institute		188	126.5	64	378.5	7	8	7	22	2	1	0	3	1	1	2	4
Visitors use with charges		89	179	111.5	379.5	2	2	2	6	1	0	0	1	6	6	4	16
Total		1141	926.5	511	2578.5	59	57	50	166	57	54	47	166	51	48	42	141

10.2 Operation of JAERI AVF Cyclotron System

Y. Nakamura, T. Nara, T. Agematsu, I. Ishibori, H. Tamura, S. Kurashima, W. Yokota, S. Okumura, K. Akaiwa*, To. Yoshida*, S. Ishiro*, A. Matsumura*, Tu. Yoshida*, Y. Arakawa*, S. Kanou*, A. Ihara* and H. Suto*

Advanced Radiation Technology Center, JAERI
*Beam Operation Service, Co., Ltd.

The JAERI AVF cyclotron system was smoothly operated according to a beam time allotment. The total operation time through FY 1999 amounted to 3070 hours, although the cyclotron system had been stopped during one month of last March as mentioned below.

The operation time for every month is shown in Fig.1. The ratios of operation time used for experiments including visitor's use with charge, tuning, beam development and machine study were 80.6%, 16.6% and 2.8%, respectively. Twenty-eight kinds of ion species, as quite same as last year, were also delivered for various experiments.

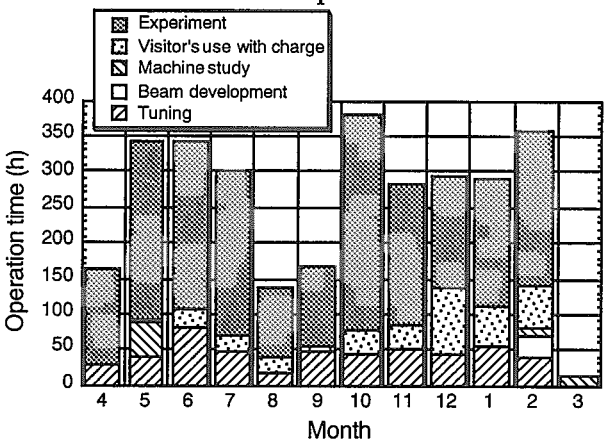


Fig. 1 Monthly operation time in FY 1999.

Regular yearly overhaul was done for four weeks in summer.

In last March, a countermeasure for the cyclotron stabilization was carried out. Principal two items were the insertion of the cooling jacket between the main coil and yoke, and the separation to an exclusive cooling line for the trimming coils.

The rotary shutter (RSHB) equipped with HB beam course was exchanged to the new one that was improved some functions such as vacuum seal structure, outgassing rate and driving mechanism owing to the deterioration of the performance by frequent operation.

The beam scanner (BSHY) positioned for the HB1 target port was also improved as to possess the complete linearity of triangular wave because of poor uniformity for the irradiation in wide area.

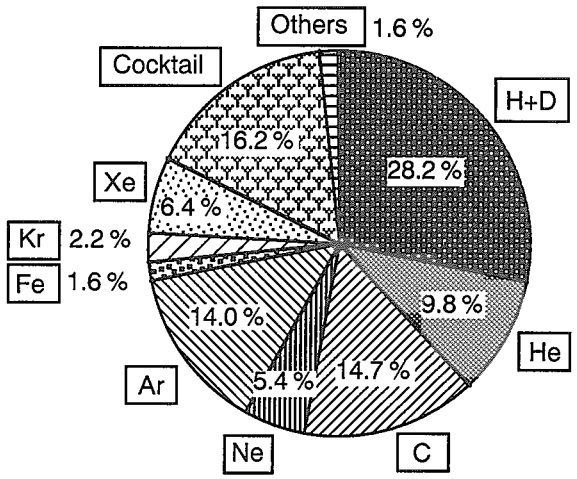


Fig.2 The percentages of accelerated ion species during FY 1999.

Figure 2 shows the percentages of accelerated ions. The summed rate of heavy ions and cocktail ones occupied about 70 % to total time, while the beam time for light ions was also 28 % of all as shown in Fig. 2.

Especially, $^{56}Fe^{15+}$ 400 MeV ion beam of 0.55 eμA was successfully accelerated first as a sort of metallic ions using the "HYPER-NANOGAN".

The frequencies of particles, energies and beam courses are shown in Fig. 3. The number of the alterations for beam course amounted to 232, which was the greatest so far. And the frequencies of particle and energy change also increase gradually year by year.

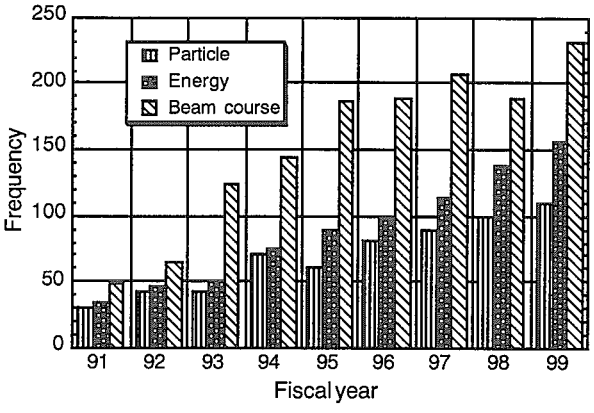


Fig. 3 Frequencies of particles, energies and beam courses since 1991.

10.3 Operation of the Electrostatic Accelerators

I. Takada, K.Mizuhashi, S. Uno, K. Ohkoshi, Y. Nakajima,
Y. Saitoh, Y. Ishii, T. Kamiya and T. Sakai

Advanced Radiation Technology Center, JAERI

1. Operation

The Electrostatic accelerators except the single-ended were operated smoothly for various experiments in FY 1999. The operation of the single-ended accelerator was suspended by trouble of accelerating tube and damage of Thermo Mechanical Leak(TML) for nineteen days. The total operation time for each accelerator in this fiscal year was 2,098 hours for the tandem accelerator, 2,593 hours for the single-ended accelerator and 1,867 hours for the 400kV ion implanter, respectively. Monthly and yearly operation time for each accelerator are shown in Fig.1 and Fig.2.

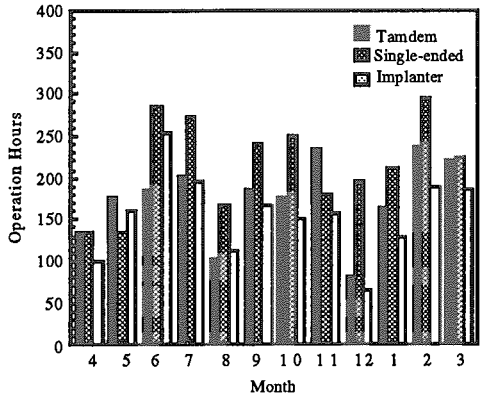


Fig. 1 Monthly operation time for each accelerator in FY 1999.

2. Maintenance

The maintenances for the accelerators were carried out in April, August and December. During these terms several improvement and renewals were performed as follows;

For the tandem accelerator; 1) The SF6 gas insulation performance which was deteriorated by use for a long time were exchanged with new one in January.

For the single-ended accelerator; 2) The magnet power supplies of BMS-3 and BMSA-1 were exchanged with high current stability ones.
3) The bearing used Motor Generator were replaced with new ones because they were operated over 10,000 hours and noisy. 4) The TML which was made pin-hole by SF6 decompositions was exchanged twice with new one.

For the 400kV ion implanter. 5) The exchange of damaged insulator by sparks scheduled in March was carried over in the next fiscal year. 6) The magnet power supplies of BMI-1, BMI-2 and BMI-3 were exchanged with high current stability ones.

3. Development

We made a practical test of compact ECR source about several ion equipping with the ion implanter and succeeded in the generation of Ar^{+6} beams of 1eμA with good stability. In order to establish the on-line beam monitor technique, we accumulated the data of secondary electron from the fixed meshes of wire induced by H,C,Ni and Au ions. We made a new type resister assembly to prevent damage by sparks and were tested with setting The accelerator.

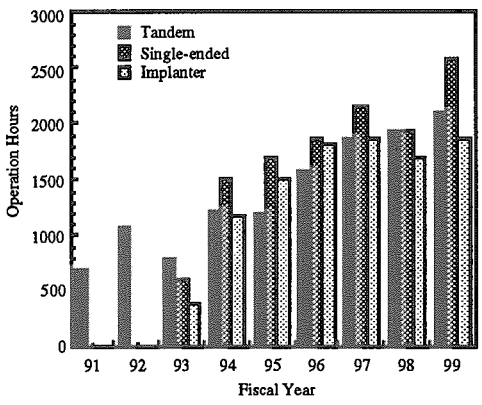


Fig.2 Yearly operation time for each accelerator since 1991

10.4 Radiation Control & Radioactive Waste Management in TIARA

Safety Division & Utilities and Maintenance Division
Department of Administrative Services, JAERI

1. Radiation Control

1.1 Individual monitoring

(1) Individual monitoring for the radiation workers

Table 1 shows a distribution on effective dose equivalent of the radiation workers in FY 1999. The effective dose equivalent values of almost workers were less than 0.2 mSv (minimum detectable dose equivalent).

Maximum dose equivalent was 1.6 mSv/y due to the overhauling of the cyclotron.

(2) Individual monitoring for the visitors and others

Table 2 shows number of persons who have been temporally entered the radiation controlled areas. The effective dose equivalent of all persons were less than 0.2 mSv.

Table1. Distributions on the effective dose equivalent in FY 1999.

Persons / Items \ Periods		Number of persons			
		1st quarter	2nd quarter	3rd quarter	4th quarter
Distribution range on effective dose equivalent HE:Effective dose equivalent[*1] (mSv)	HE < 0.2	510	564	554	596
	0.2 ≦HE ≦ 1.0	5	8	0	8
	1.0 <HE ≦ 5.0	0	0	0	0
	5.0 <HE ≦ 50.0	0	0	0	0
	50.0< HE	0	0	0	0
Persons for radiation control(A)		515	572	554	604
Exposure above 1 mSv	Persons(B)	0	0	0	0
	(B)/(A)×100(%)	0	0	0	0
Mass effective dose equivalent (Person・mSv)		1.6	3.8	0.0	4.0
Mean dose equivalent (mSv)		0.00	0.01	0.00	0.01
Maximum dose equivalent (mSv)		0.4	0.8	0.0	0.8

[*1] Not detected according to internal exposure.

Table 2. Number of temporary entrance persons to radiation controlled areas in FY 1999.

Persons / Periods / Temporary entrance persons	Number of persons				
	1st quarter	2nd quarter	3rd quarter	4th quarter	Total
Visitor and other	366	404	608	266	1644

1.2 Monitoring of radioactive gases

Table 3 shows the maximum radioactive concentrations and total activities for radioactive gases released from TIARA's stack, during each quarter of FY 1999.

The least amount of ^{41}Ar, ^{13}N and ^{11}C were detected for some time during operation of the cyclotron, but the pulverized substance (^{65}Zn, etc) were not detected.

Table 3. Monitoring results of released gaseous radioactivities in FY 1999.

Nuclide	Items / Periods	1st quarter	2nd quarter	3rd quarter	4th quarter	Total
^{41}Ar	Maxmum concentration (Bq/cm^3)	1.2×10^{-4}	7.9×10^{-4}	1.8×10^{-4}	$<5.4\times10^{-5}$	7.9×10^{-4}
	activity (Bq)	9.4×10^{8}	2.1×10^{9}	8.4×10^{8}	2.6×10^{7}	3.9×10^{9}
^{13}N	Maxmum concentration (Bq/cm^3)	6.7×10^{-4}	—	$<5.4\times10^{-5}$	$<5.4\times10^{-5}$	6.7×10^{-4}
	activity (Bq)	1.6×10^{9}	—	3.2×10^{6}	3.7×10^{6}	1.6×10^{9}
^{11}C	Maxmum concentration (Bq/cm^3)	—	$<5.4\times10^{-5}$	$<5.4\times10^{-5}$	—	$<5.4\times10^{-5}$
	activity (Bq)	—	3.3×10^{6}	6.9×10^{6}	—	1.0×10^{7}
^{65}Zn	Maxmum concentration (Bq/cm^3)	$<5.1\times10^{-10}$	$<6.0\times10^{-10}$	$<5.4\times10^{-10}$	$<5.1\times10^{-10}$	$<6.0\times10^{-10}$
	activity (Bq)	0	0	0	0	0

1.3 Monitoring for external radiation and surface contamination

External radiation monitoring was routinely carried out in/around the radiation controlled areas and surface contamination monitoring was also carried out. Neither unusual value of dose equivalent rate nor surface contamination were detected.

Figure 1 displays a typical example of distribution of the dose equivalent rate at the radiation controlled area in the cyclotron building.

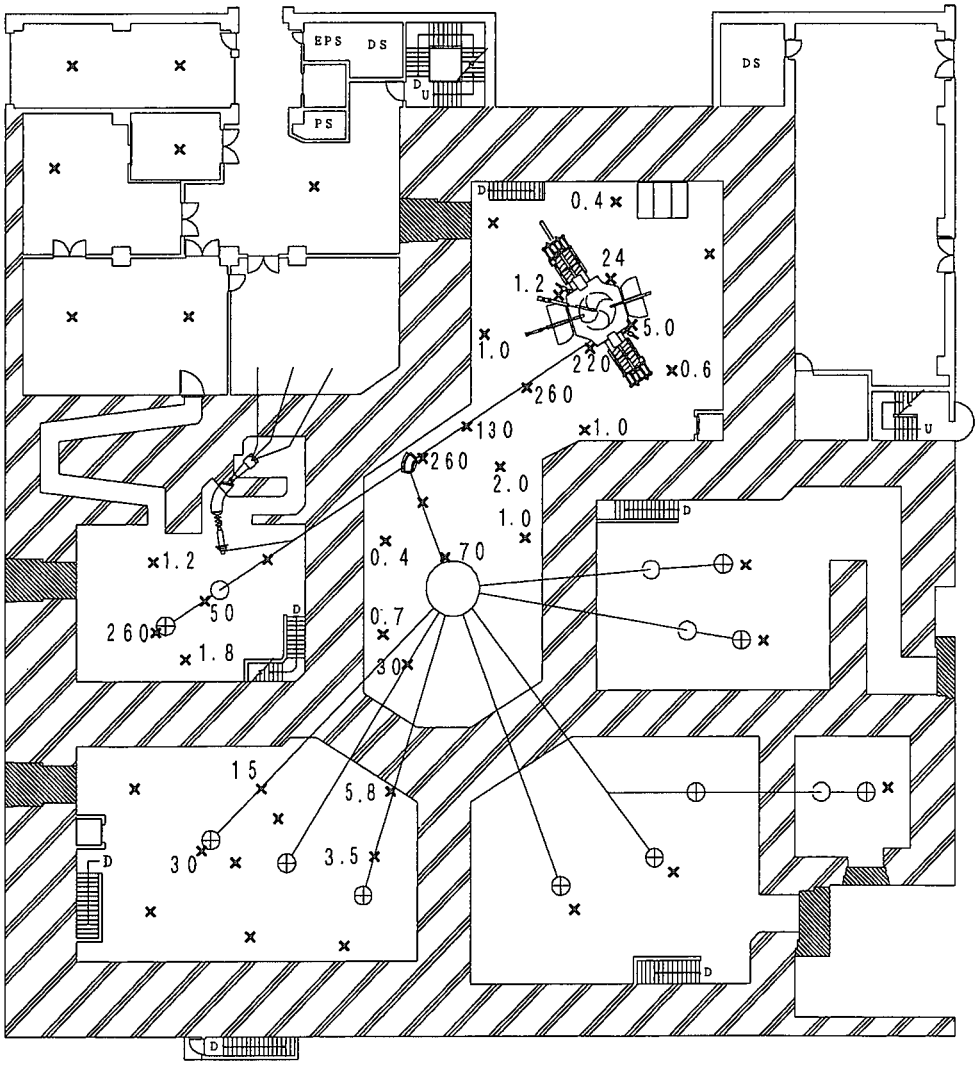


Fig.1 Dose rate distribution at the radiation controlled area in the cyclotron building.
Date measured : March 24, 2000
Measuring position : Indicated with × above 1m from floor
Unit : μSv/h(numeric less than 0.2 μSv/h are not indicated)

2. Radioactive Waste Management

2.1 Solid wastes

Table 4 shows the amounts of solid wastes at various properties and kinds generated in each quarter of FY 1999. Main wastes were combustible filters for exhaust air. Compressible wastes were generated mainly by the cyclotron maintenance.

2.2 Liquid waste was almost waste water ("inorganic" in Table 5) generated with chemical experiments and operation of air conditioning units installed in each room of the first class radiation controlled area. Larger quantities of the wastewater in summer season (2nd quarter) are mainly due to condensed water is treated by evaporation, and condensed water is reused in the controlled area. Only small amounts of residue are generated by the evaporation because the waste quality is very pure.

The evaporation residue and sludge are solidified by cement in a stainless steel drum. The residue and sludge of ca. 100 liter makes one cement solidify of 200-litter drum.

Table 4. Radioactive solid wastes generated in FY 1999.

Amounts / Items	Amounts of generation in each periods (m^3)					Number of package /drum
	1st quarter	2nd quarter	3rd quarter	4th quarter	Total	
Category A*	1.04	1.16	0.90	5.79	8.89	
1)Combustible	0.88	0.72	0.52	0.50	2.62	17**
2)Incombustible	0.16	0.44	0.38	5.29	6.27	0
Compressible	0.16	0.44	0.38	0.20	1.18	8**
Filters	0	0	0	5.09	5.09	47
Incompressible	0	0	0	0	0	0
Ion exchange resin	0	0	0	0	0	0
(Cement solidify)	0	0	0	0	0	0
Category B*	0	0	0	0	0	
1)Incombustible	0	0	0	0	0	0

* defined by dose at the outer surface of container : (A) < 2 mSv/h ≦ (B)

** 200-liter drum

Table 5. Radioactive liquid waste generated in FY 1999.

Amounts / Items	Amounts of generation in each periods (m^3)					Number of package /drum
	1st quarter	2nd quarter	3rd quarter	4th quarter	Total	
Category A*	12.81	27.22	7.53	4.62	52.18	
1)Inorganic	12.71	27.22	7.53	4.52	51.98	treatment
2)Organic	0	0	0	0	0	0
Organic	0	0	0	0	0	0
Oil	0	0	0	0	0	0
3)Sludge	0.1	0	0	0.10	0.20	1
Category B*	0	0	0	0	0	
1)Inorganic	0	0	0	0	0	0
2)Organic	0	0	0	0	0	
Organic	0	0	0	0	0	0
Oil	0	0	0	0	0	0
3)Sludge	0	0	0	0	0	0
Evaporation residue	0	0	0	0.20	0.20	2

* defined by concentrations in Bq/cm^3(β, γ) : (A) < 3.7×10 ≦ (B) < 3.7×10^4

Appendix

Appendix 1. List of Publication ····· 311
A 1.1 Publications in Journal ····· 311
A 1.2 Publications in Proceeding ····· 317
Appendix 2. Type of Research Collaboration ····· 323
Appendix 3. Organization and Personnel of TIARA ····· 325

This is a blank page.

Appendix 1. LIST OF PUBLICATION

A1.1. Publications in Journal

9J01
T. Ohshima, M. Yoshikawa, H. Itoh, Y. Aoki and I. Nashiyama,
γ -ray Irradiation Effects on 6H-SiC MOSFET,
Material Science Engineering, **B61-62**, 480 (1999)
I SCS 92003

9J02
A. Uedono, S. Tanigawa, T. Ohshima, H. Itoh, M. Yoshikawa, I. Nashiyama, T. Frank, G. Pensl, R. Suzuki, T. Ohdaira and T. Mikado,
Crystallization of an amorphous Layer in P^+-implanted 6H-SiC Studied by Monoenergetic Positron Beams
J. Appl. Phys., **87**, 4119 (2000).
I SCS 92003

9J03
A. Uedono, S. Tanigawa, T. Ohshima, H. Itoh, Y. Aoki, M. Yoshikawa and I. Nashiyama,
Oxygen-related Defects in O^+-implanted 6H-SiC Studied by a Monoenergetic Positron Beam
J. Appl. Phys., **86**, 5392 (1999)
I SCS 92003

9J04
T. Ohshima, K. Abe, H. Itoh, M. Yoshikawa, K. Kojioma, I. Nashiyama and S. Okada,
Electrical Activation of Phosphorus-donors Introduced in 6H-SiC by Hot-implantation
Appl. Phys., **A70** (in press)
I SCS 92003

9J05
T. Tanaka, T. Ohshima, H. Itoh, S. Okada, A. Wakahara, and A. Yoshida,
Effect of Mg Ion Implantation on Electrical Properties of $CuInSe_2$ Thin Films
J. Appl. Phys., **87**, 3283(2000)
I SCS 92004

9J06
K. Hamada, M. Inoue, A. Tanaka and H. Watanabe,
Potato Virus Y-resistant Mutation Induced by the Combination Treatment of Ion Beam Exposure and another Culture in *Nicotiana tabacum* L.
Plant Biotechnology, **16**, 285(1999)
C BIT 91008

9J07
Y. Hase, K. Shimono, M. Inoue, A. Tanaka and H. Watanabe,
Biological Effects of Ion Beams in *Nicotiana tabacum* L.
Radiation and Environmental Biophysics, **38**, 111(1999)
C BIT 91008

9J08
N. Sermkiattipong, M. Takigami, S. Pongpat, O. Sukusudej, S. Charoen and H. Ito,
Decomposition of Dark Brown Pigments in Molasses Wastewater by Mutant Strains of Aspergillus usamii and Coriolus versicolor
Biocontrol Science, **4(2)**, 109 (1999)
C BIT 91015

9J09
A. Amsal, M. Takigami and H. Ito,
Increased Digestibility of Raw Starches by Mutant Strains of Aspergillus awamori
Food Sci. Technol. Res., **5(2)**, 153 (1999)
C BIT 91015

9J10
Y. Kabayashi, M. Taguchi and H. Watanabe,
Use of a Collimated Heavy Ion Microbeam for Irradiating Cells Individually
Radiation research, **153**, 228(2000)
C BIT 91016

9J11
Z.-L. Tu, S. Yamasaki, K. Shirai, R. Kanekatsu, K. Kiguchi, Y. Kobayashi, M. Taguchi and H. Watanabe,
Effects of General and Local Irradiation of Heavy Ion Beams on the Development and Morphogenesis of the Silkworm, *Bombyx mori*
J. Seric. Sci. Jpn., **68**, 443 (1999)
C BIT 91017

9J12
Z.-L. Tu, K. Shirai, R. Kanekatsu, K. Kiguchi, Y. Kobayashi, M. Taguchi and H. Watanabe,
Effects of Local Heavy Ion Beam Irradiation on the Hemopoietic Organs of the Silkworm, *Bombyx mori*

J. Seric. Sci. Jpn., **68**, 491(1999)
C BIT 91017

9J13
H. Matsunami, Y. Arima, K. Watanabe, N. S. Ishioka, S. Watanabe, A. Osa, T. Sekine, H. Uchida, A. Tsuji, S. Matsuhashi, T. Itoh and T. Kume,
Positional Relationship between ^{13}N-nitrate Uptake-and Rhizobium Infectible Sites on a Single Root of Common Bean and soybean: An Application of Positron Emitting Tracer Imaging System (PETIS)
Soil Science and Plant Nutrition, **45(4)**, 955(1999)
C BIT 91022, 81024, 71017

9J14
H. Nakanishi, N. Bughio, S. Matsuhashi, N.S. Ishioka, H. Uchida, A. Tsuji, A. Osa, T. Sekine, T. Kume and S. Mori,
Visualizing Real Time 11C Methionine Translocation in Fe-sufficient and Fe-deficient Barely using a Positron Emitting Tracer Imaging System (PETIS)
J. Experimental Botany, **50**, 637(1999)
C BIT 91024

9J15
M. Taguchi, Y. Matsumoto, M. Moriyama, H. Namba, Y. Aoki and H. Hiratsuka,
Effect of Specific Energy of Heavy Ions for 1,2,4,5-Tetracyanobenzene Radical Anion Formation
Radiat. Phys. Chem., **58**, 123 (2000)
C RCO 91007

9J16
M. Taguchi, H. Namba, K. Furukawa and S. Ohno,
Energy Distribution around a 175 MeV Ar Ion in Argon at the Density of Water
Radiat. Phys. Chem., **55**, 511 (1999)
C RCO 91040

9J17
S. Ohno, K. Furukawa, M. Taguchi, H. Namba and H. Watanabe,
Predicted Radiolysis Yield in a Fricke Solution Irradiated with Various Heavy Ions
Radiat. Phys. Chem., **55**, 503 (1999)
C RCO 91040

9J18
S. Seki, Y. Kunimi, Y. Sakurai and S. Tagawa,
High-sensitive Negative Resist Materials Based on Polysilane Derivatives
J. Photopolym. Sci. Technol, **13**, 395 (2000)
C RCO 91043

9J19
S. Seki, Y. Kunimi, K. Nishida, K. Aramaki and S. Tagawa,
Optical Properties of Pyrrolyl-substituted Polysilanes
J. Organomet. Chem., (in press.)
C RCO 91043

9J20
S. Seki, Y. Sakurai, K. Maeda, Y. Kunimi and S. Tagawa,
Studies on the Negative Resist Material Based on Polysilanes for EB and X-ray Lithography
Jpn. J. Appl. Phys. (in press.)
C RCO 91043

9J21
S. Seki, Y. Yoshida and S. Tagawa,
Radical Anions of Polysilane Derivatives Studied by Pulse Radiolysis
Radiat. Phys. Chem. (in press.)
C RCO 91043

9J22
Y. Kunimi, S. Seki and S. Tagawa,
Investigation on Hole Drift Mobility in Poly(*n*-hexylphenylsilane)
Solid State Commun., **114**, 469 (2000)
S RCO 91043

9J23
M. Tashiro, P. K. Pujari, S. Seki, Y. Honda, S. Nishijima and S. Tagawa,
Studies on Thermally Induced Structural Changes in Silicon Based Polymers by Positron Annihilation
Radiat. Phys. Chem. (in press.)
S RCO 91043

9J24
S. Seki, Y. Yoshida, S. Tagawa, K. Asai, K. Ishigure, K. Furukawa, M. Fujiki and N. Matsumoto,
Effects of Structural Defects on Hole Drift Mobility in Aryl-substituted Polysilanes,
Phil. Mag. ,**B79**, 1631 (1999)
C RCO 91043

9J25
S. Seki, K. Maeda, Y. Kunimi, Y. Yoshida, S. Tagawa, H. Kudoh, M. Sugimoto, T. Sasuga, T. Seguchi, T. Iwai, H. Shibata, K. Asai and K. Ishigure,
Ion Beam Induced Crosslinking Reactions in Poly(di-*n*-hexylsilane)
J. Phys. Chem., **B103**, 3043 (1999)
C RCO 91043

9J26
S. Seki, Y. Yoshida, S. Tagawa and K. Asai,
Electronic Structure of Radical Anions and Cations of Polysilanes with Structural Defects
Macromolecules, **32**, 1080 (1999)
C RCO 91043

9J27
Y. Katano, T. Aruga, S. Yamamoto, T. Nakazawa, D. Yamaki and K. Noda,
Effects of Co-Implanted Oxygen or Aluminum Atmos on Hydrogen Migrations and Damage Structures in Multiple-Beam Irradiated Al_2O_3
J. Nucl. Mater. (In press.)
T, I, S IOM 92007

9J28
I. Mukouda and Y. Shimomura,
Damage Evolution in Neutron-irradiated Cu during Neutron Irradiation
J. Nucl. Mater., **271&272**, 230 (1999)
T, I, S IOM 92008

9J29
Y. Shimomura, I. Mukouda and K. Sugio,
Computer Simulation on the Void Formation in Neutron-irradiated Cu and Ni at High Temperature
J. Nucl. Mater., 271&272, 225 (1999)
T, I, S IOM 92008

9J30
Y. Shimomura, I. Mukouda, K. Sugio and P. Zhao,
Atomistic Processes of Damage Evolution in Neutron-irradiated Cu and Ni at High Temperature
Radiation Effects and Defect in Solids, **148**, 127 (1999)
T, I, S IOM 92008

9J31
N. Sekimura, Y. Shirao, H. Yamguchi, S. Yonamine and Y. Arai,
Defect Cluster Formation in Vanadium Irradiated with Heavy Ions
J. Nucl. Mater., **271&272**, 63(1999)
T, S, I IOM 92009

9J32
N. Sekimura, S. Yonamine, T. Iwai, Y. Arai, A. Naito, Y. Miwa and S. Hamada,
Synergistic Effects of Hydrogen and Helium on Microstructual Evolution in Vanadium Alloys by Triple Ion Beam Irradiation
J. Nucl. Mater. (to be published)
T, S, I IOM 92009

9J33
S. Nogami, A. Hasegawa, K. Abe, T. Taguchi and R. Yamada,
Effect of Dual-beam-Irradiation by Helium and Carbon Ions on Microstructure Development of SiC/SiC Composites
J. Nucl. Mater. (in press.)
T, S IOM 92010

9J34
I. Ioka, A. Naito, K. Shiba, J.P. Robertson, S. Jitsukawa and A. Hishinuma,
Effect of Annealing on the Tensile Properties of Irradiated Austenitic Stainless Steel
J. Nucl. Mater., **258**, 1664 (1998)
T, S IOM 92014

9J35
K. Yasuda, C. Kinoshita, M. Ohmura and H. Abe,
Production and Stability of Dislocation Loops in an MgO-Al_2O_3 System under Concurrent Irradiation with Ions and Electrons
Nucl. Instr. and Meth. in Phys. Res., **B166-167**, 107(2000)
I IOM 92020

9J36
T. Soeda, S. Matsumura, J. Hayata and C. Kinoshita,
Quantitative Electron Diffraction Study of Cation Configuration and Irradiation Induced Displacement in Magnesium Aluminate Spinel Crystals
J. Electron Microscopy, **48 (5)**, 531(1999)
I IOM 92020

9J37
Y. Maeda, K. Umezawa, S. Yamamoto and I. Nashiyama,

Effect of Au Ion Implantation on Electrical Properties of Ion Beam Synthesized β-$FeSi_2$
Nucl. Instr. and Meth. in Phys. Res., **B** (to be submitted)
T, S IOM 92021

9J38
F. Arimoto, M. Takeda, T. Suda, S. Watanabe, S. Ohnuki, H. Takahashi, H. Abe and H. Naramoto,
Formation and Stability of Metallic Silicides during Ion-Beam-Mixing in Systems of Mo/Si and Ti/Si,
Materials Transactions, JIM, **40(5)**, 408(1999)
T IOM 92022

9J39
Z.J. Zhang, K. Narumi, H. Naramoto, Z.P. Wu, S. Yamamoto and A. Miyashita,
The Effect of Sputtering Ions on the Structure and Properties of Diamond-like Carbon Films
J. Phys.:Condens. Matter, **11**, L273(1999)
I IOM 92025

9J40
K. Yamakawa,
Hydrogen Migration in Pd-H Alloy Around 50K Anomaly at Various Hydrogen Concentrations
J. Phys.: Condens.Matter, **11(44)**, 8681(1999)
S IOM 92027

9J41
K. Yamakawa and H. Maeta,
Migration of Hydrogen in Yttrium at Low Temperatures
J. Alloys and Comp., **93-95**, 341(1999)
S IOM 92027

9J42
K.Yamakawa and H. Maeta,
Migration of Hydrogen Isotopes in Pd and Pd-Fe Dilute Alloys at Low Temperatures
J. Japan Inst. Metals, **63 (7)**, 866 (1999)
S IOM 92027

9J43
K. Yamakawa,
Migration of Hydrogen in Rare-Earth Metals at the Disorder-Oder Transition
J. Phys.: Condense Matter, **11**, L261(1999)
S IOM 92027

9J44
A. Iwase, N. Ishikawa, T. Iwata, Y. Chimi and T. Nihira,
Negative Magnetoresistance of Pyrolytic Carbon and Effects of Low-Temperature Electron Irradiation
Phys. Rev., **B60**, 10811 (1999)
S IOM 92028

9J45
A. Uedono, S. Tanigawa, T. Ohshima, H. Itoh, Y. Aoki, M. Yoshikawa and I. Nashiyama,
Oxygen-related Defects in O^+-implanted 6H-SiC Studied by Monoenergetic Positron Beams
J. Appl. Phys., **86**, 5392(1999)
I IOM 92031

9J46
T. Ohshima, A. Uedono, H. Itoh, M. Yoshikawa, K. Kojima, I. Nashiyama, S. Okada and K. Abe,
Relationship between Donor Activation and Defect Annealing in 6H-SiC Hot-implanted with Phosphorus Ions
Materials Science Forum, **338-342**, 857(2000)
I IOM 92031

9J47
T. Ohnuki, N. Kozai, H. Isobe, T. Murakami, S. Yamamoto, K. Narumi and H. Naramoto,
Sorption Mechanism of Europium During Alteration of Albite
Radiochemica Acta., **86**, 161(1999)
T, C IOM 92036

9J48
H. Abe, S. Yamamoto, A. Miyashita and K.E. Sickafus,
Formation Mechanism of Carbon Onions and Nanocapsules under Ion Implantation in Cupper
J. Appl. Phys. (submitted)
I MAN 92019

9J49
H. Kudo, S. Seki, K. Sumitomo, K. Narumi, S. Yamamoto and H. Naramoto,
Ion-induced Electron Measurements using Crystal Targets Overlaid with Noncrystalline Layers
Nucl. Instr. and Meth. in Phys. Res., **B164**, 897 (2000)
S MAN 92023

9J50
H. Kudo, K. Shibuya, N. Nakamura, T. Azuma and S. Seki,
Forward Scattering Peaks of Ion-induced Auger Electrons
Nucl. Instr. Meth. in Phys. Res, **B159**, 241 (1999)
S MAN 92023

9J51
H. Kudo, N. Nakamura, K. Shibuya, K. Narumi, S. Yamamoto, H. Naramoto, K. Sumitomo and S. Seki,
Ion-induced Electron Emission from Si Crystal Targets Covered with Noncrystalline Si Layers
Nucl. Instr. and Meth. in Phys. Res. (to be published.)
I MAN 92023

9J52
K. Kawatsura, N. Shimatani, T. Igarashi, T. Inoue, N. Terazawa, S. Arai, Y. Aoki, S. Yamamoto, K. Narumi, H. Naramoto, Y. Horino, Y. Mokuno and K. Fujii,
Radiation-Induced Amorphization and Recrystallization of α-SiC Single Crystal
J. Nucl. Mater., **271/272**, 11 (1999)
T, S MAN 92024

9J53
T. Mitamura, K. Kawatsura, R. Takahashi, T. Adachi, T. Igarashi, S. Arai, N. Masuda, Y. Aoki, S. Yamamoto, K. Narumi, H. Naramoto, Y. Horino, Y. Mokuno and K. Fujii,
Radiation Effect of 200 keV and 1 MeV Ni Ion on MgO Single Crystal
J. Nucl. Mater. **271/272**, 15 (1999)
T, I, S MAN 92024

9J54
T. Mitamura, K. Kawatsura, T. Nakae, T. Igarashi, T. Inoue, S. Arai, Y. Aoki, S. Yamamoto, K. Narumi, H. Naramoto, Y. Horino, Y. Mokuno, K. Fujii, M. Terasawa, H. Uchida, K. Koterazawa, K. Takahiro, S. Nagata, and S. Yamaguchi,
Radiation Damage and Radiation-Induced Segregation in Single Crystal Stainless Steel by RBS and PIXE Channeling
J. Nucl. Mater., **271/272**, 21 (1999).
S MAN 92024

9J55
Z. Zhang, K. Narumi, H. Naramoto, S. Yamamoto and A. Miyashita,
x-ray and Fourier transformed Infrared Investigation of β-SiC Growth by ion Implantation
J. Phys. D: Appl. Phys., **32**, 2236(1999)
I MAN 92025

9J56
S. Yamamoto and H. Naramoto,
Hydrogen Distribution Characterization in Cu(111)/Nb(110) Multilayer Using Ion Beam Analysis
Nucl. Instr. And Meth. in Phys. Res., **B161-163**, 605(2000)
T, S MAN 92018

9J57
H. Naramoto, S. Yamamoto and K. Narumi,
RBS/Channeling Analysis of Implanted Immiscible Species
Nucl. Instr. and Meth. in Phys. Res., **B161-163**, 534(2000)
S, I MAN 92025

9J58
K. Takahiro, A. Kunimatsu, S. Nagata, S. Yamaguchi, S. Yamamoto, Y. Aoki and H. Naramoto,
Crystal Structure and Optical Absorption of Au Implanted MgO, $SrTiO_3$ and $LiNbO_3$ Crystals
Nucl. Instr. and Meth. in Phys. Res., **B152**, 314(1999)
S, I MAN 92025

9J59
T. Sakai, Y. Naitoh, T. Kamiya, S. Matsuyama, K. Gotoh, S. Yokota, H. Yamasaki and K. Ishii,
AN Extrnal Ion Microbeam for Studies of Biological Samples
Biological Trace Element Research, **71-72,** 77 (1999)
S ACT 92040

9J60
C.-J. Ma, M. Kasahara and S. Tohno,
Application of PIXE to the Analysis of Single Raindrops Sampled as a Function of their Size
Air & waste Management Association(to be submitted)
S MAN 92046

9J61
C.-J. Ma, M. Kasahara, R. Holler and T. Kamiya,
Characterization of Single Particles and Bulk Aerosol Samples in Japan During the Asian Dust-storm Period

Atmospheric Environment (to be submitted)
S MAN 92046

9J62
H. Muramatsu, H. Ishii, E. Tanaka, M. Misawa, H. Ito, T. Miura, S. Muto, M. Koizumi, A. Osa, T. Sekine and M.Yanaga,
Mössbauer Spectroscopy of ^{133}Cs Following the Decay of ^{133}Xe Atoms Implanted in Metals
J. Radioanal. Nucl. Chem., **239,** 251 (1999)
O NRI 91033

9J63
T. Ohtsubo, S. Ohya, K. Hori, K. Kimura, S. Yachida, J. Goto, Y. Izubuchi, S. Muto, T. Sekine, M. Koizumi and A. Osa,
Polarized Beam of Unstable Nuclei via Ion Beam Surface Interaction at Grazing Incidence
Hyp. Int., **120/121**, 695(1999)
C NRI 91035

9J64
Su. Tanaka, M. Fukuda, K. Nishimura, M. Hosono, H. Watanabe and N. Yamano,
The IRAC Code System to Calculate Activity and Transmutation in the TIARA Facility
J. Nucl. Sci. Technol., **Suppl. 1**, 840 (2000)
C RSH 91048

9J65
M. Harada, Y. Watanabe, A. Yamamoto, Y. Tanaka, Sun Weili, K. Shin, S. Meigo, O. Iwamoto, H. Nakashima, H. Takada, S. Chiba, T. Fukahori, T. Sasa and Su. Tanaka,
Measurements of Double Differential Cross Sections of Secondary Charged-Particles Produced by Proton-Induced Reaction at Several Tens of MeV
J. Nucl. Scie. Technol. **Suppl. 1**, p.687 (2000)
C RSH 91049

9J66
M. Ibaraki, M. Baba, T. Miura, Y. Nauchi, Y. Hirasawa, N. Hirakawa, H. Nakashima, S. Meigo, O. Iwamoto and Su. Tanaka,
Experimental Method for Neutron Elastic Scattering Cross section Measurement in 40-90 MeV Region at TIARA
Nucl. Instr. and Meth. in Phys. Res., **A446/3**, 536(2000)
C RSH 9152

9J67
W. Yokota, Y. Saitoh, T. Nara, Y. Ishii and K. Arakawa,
Magnetic Field Modification of 18 GHz Electron Cyclotron Resonance Ion Source at the Japan Atomic Energy Research Institute
Rev. Sci. Instrum., **71,** 906 (2000)
C ACT 91045

9J68
T. Kamiya, T. Sakai, Y. Naitoh, M. Oikawa, T. Hamano and T. Hirao,
Automated Single Ion Hit at JAERI Heavy Ion Microbeam to Observe Individual Radiation Damage
Nucl. Instr. and Meth. in Phys. Res., B158, 255(1999)
T ACT 92039

9J69
K. Ohokoshi, Y. Saitoh and S. Tajima,
New Ion Generation Method with SF6 Plasma
Chemistry and Chemical Industry, **52**, 1409(1999)
I ACT 92042

9J070
K. Ohokoshi, Y. Saitoh and S. Tajima,
Prolongation of Filament Lifetime by using SF6 Plasm
Review of Scientific Instruments, **71**, 1174(2000)
I ACT 92042

A1.2 Publications in Proceeding

9C01
N. Nemoto, H. Shindou, S. Kuboyama, S. Matsuda, H. Itoh, S. Okada and I. Nashiyama,
Relationship between Single-Event Upset Immunity and Fabrication Processes of Recent Memories
Abs. of the 5th European conference radiation and its Effects on Components and System (Fontervraud France, Sept. 1999), RADECS99, F-24
C SCS 91002

9C02
M. Saidoh, M. Fukuda, K. Arakawa, S. Tajima, H. Sunaga, K. Yotsumoto, T. Kamiya, R. Tanaka, T. Hirao, I. Nashiyama, H. Itoh, S. Okada, N. Nemoto, S. Kuboyama and S. Matsuda,
The Irradiation Facilities for The radiation Tolerance Testing of Semiconductor Devices for Space Use in Japan
Proc. of the IEEE Radiation Effects Data Workshop (Norfolk Virginia USA, July 1999), p.117
C SCS 91002

9C03
N. Nemoto, H. Shindou, A. Makihara, S. Kuboyama, S. Matsuda, K. Sugimoto, I. Nashiyama and H. Itoh,
Development of 1M Gate CMOS Gate Array
Abs. of European Space Components Conference (Noordwijk The Netherlands, Mar. 2000), p148
C SCS 91002

9C04
T. Ohshima, M. Yoshikawa, H. Itoh, K. Kojima, S. Okada and I. Nashiyama,
Influence of Post-Oxidation Annealing on Electrical Characteristics in 6H-SiC MOSFETs
Proc. of Int. Conf. on Silicon Carbide and Related Materials 1999 (Research Triangle Park, NC, USA, Oct. 10-15 1999), ICSCRM'99, p.1299
I SCS 92003

9C05
T. Ohshima, A. Uedono, H. Itoh, M. Yoshikawa, K. Kojima, S. Okada, I. Nashiyama, K. Abe and S. Tanigawa,
Relationship between Donor Activation and Defect Annealing in 6H-SiC Hot-Implanted with Phosphorous Ions
Proc. of Int. Conf. on Silicon Carbide and Related Materials 1999 (Research Triangle Park, NC, USA, Oct. 10-15 1999), ICSCRM'99, p857
I SCS 92003

9C06
T. Tanaka, T. Ohshima, H. Itoh, S. Okada, A. Wakahara, and A. Yoshida,
Mg Ion Implantation in $CuInSe_2$ Thin Films
Proc. of the 11th Int. Photovoltaic Science and Engineering Conf. (Sapporo, Sept. 20-22 1999), P-1-89
I SCS 92004

9C07
T. Tanaka, Min-Ho Kim, A. Wakahara, T. Ohshima, H. Itoh, S. Okada and A. Yoshida,
Characterization of Mg-implanted $CuInSe_2$ Thin Films
Proc. of the 18th Sympo. on Electric Materials (July 1999) p.13
I SCS 92004

9C08
Y. Hase, A. Tanaka, T. Baba and H. Watanabe,
Analysis of Petal and Sepal-specific Floral Mutant, *sepl* in Arabidopsis
Proc. of 2000 Annual Meeting of the Japanese Soc. of Plant Physiologists (Nagoya, Mar. 27-29 2000) (Plant Cell Physiology, **41** (suppl.), 215 (2000))
C BIT 92017

9C09
H. Yamaguchi, S. Nagatomi, A. Tanaka, N. Shikazono, T. Morishita and K.Degi,
Mutation Induction with Ion Beam Irradiation in Rose
Proc. of 2000 Autumn Meeting of Japanese Soc. for Horticultural Science (J. Japan. Soc. Hort. Sci., **69** (suppl.2), 2000 (in press.))
C BIT 91013

9C10
Y. Kobayashi, M. Taguchi and H. Watanabe,
Local Irradiation of Biological Systems using a Collimated Heavy Ion Microbeam
KODANSHA SCIENTIFIC " Risk Evaluation of Cosmic-Ray Exposure in Long-Term Manned Space Mission" (ed. by K. Fukitaka, H. Majima, K. Ando,

H. Yasuda, M. Suzuki), p. 51(1999)
C BIT 91016

9C11
Y. Kobayashi, M. Taguchi, T. Fujimura, T.V. Khoa, T. Kamiya, H. Watanabe and K. Yamamoto,
The Effect of Single Ion Irradiation on Mammalian Cells
Abs. of the 9th TIARA Research Review Meeting (Takasaki 22-23, June 2000), p. 19
C BIT 91016

9C12
Z.-L. Tu, K.Shirai, R.Kanekatsu, Y. Kobayashi, M. Taguchi and H. Watanabe,
Radiosurgery by Heavy Ion Beams for Biological Study of the Silkworm, *Bombyx mori*
Proc. of the 4th China Int. Silk Conf. (Yinchuan, May 2000), p. 13
C BIT 91017

9C13
H. Matsunami, Y. Arima, K. Watanabe, S. Matsuhashi, N. S. Ishioka, H. Uchida and T. Kume,
$^{13}NO_3^-$-N-uptake-site on the Common Bean Root Relating to Combined Nitrogen Stress on the Root-nodulation (in Japanese)
Proc. of the 35th Annual Meeting on Radioisotopes in the Physical Sciences and Industries (Tokyo, June 1998), p.6
C BIT 71017

9C14
H. Matsunami, Y. Arima, K. Watanabe, N. S. Ishioka, S. Watanabe, A. Osa, T. Sekine, H. Uchida, A. Tsuji, S. Matsuhashi, T. Itoh and T. Kume,
$^{13}NO_3^-$-N-uptake-site on a Single Root of Leguminous Crops Relating to Combined Nitrogen Stress on the Root-nodulation (in Japanese)
Abs. of the 8th TIARA Research Review Meeting (Takasaki, June 1999), P.136
C BIT 81024, 71017

9C15
H. Matsunami, Y. Arima, K. Watanabe, M. Iizuka, S. Matsuhashi, N. S. Ishioka, S. Watanabe, T. Itoh, C. Mizuniwa, T. Sekine, S. Hashimoto, A. Osa, H. Uchida and A. Tsuji,
$^{13}NO_3^-$-N and $^{13}NO_4^+$-N -uptake-site on a Single Root of Leguminous Crops Relating to Combined Nitrogen Stress on the Root-nodulation (in Japanese)
Abs. of the 9th TIARA Research Review Meeting (Takasaki, June 2000), p.124,
C BIT 91022, 81024, 71017

9C16
Y. Sasuga, K. Ichikawa, R. Toyohuku, Y. Oono, H. Uchimiya and H. Takenaga,
Identification of Brassinolide-insensitive Mutants in Arabidopsis by Ion Beam Irradiation
Proc. of '99 Sympo. on Japanese Soc. of Soil Science and Plant Nutrition (Ueda, June 10-11 1999)), p.14
C BIT 81022

9C17
Y. Sasuga, K. Ichikawa, R. Kuwano, Y. Oono, Y. Kobayashi, S. Tanaka and H. Takenaga,
Isolation and Analysis of Brassinolide-insensitive Mutant from *Arabidopsis Thaliana* Irradiated with Ion Beam
Proc. of '00 Sympo. on Japanese Soc. for Plant Cell and Molecular Biology, (Sizuoka , July 24-25 2000), p. 160
C BIT 91020

9C18
H. Hayashi, H. Mano, N. Suzui, S. Matsuhashi, C. Mizuniwa, T. Ito, S. Hashimoto, N. Ishioka, T. Watanabe, T. Sekine, A. Osa, H. Uchida, A. Tsuji and M. Chino,
Visualization of Short-term Translocation of (^{13}N-NO_3) in Rice Plants
Proc. of the 37th Annual Meeting on Radioisotopes in the Physical Sciences and Industries (Tokyo, June 2000), p.20
C BIT 91025

9C19
M. Taguchi, X. Yujie, M. Moriyama, Y. Kobayashi, H. Hiratsuka and S. Ohno,
Yields of Tyrosine Isomers in the Radiolysis of Aqueous Phenylalanine Solution by Energetic Heavy Ions
Proc. of Int. Sympo. on Prospects for Application of Radiation Toward the 21st Century (Tokyo, Mar. 13-17, 2000), p.127
C RCO 91007

9C20
S. Ohno, K. Furukawa, M. Taguchi, T. Kojima and H. Watanabe,
An Ion-track Structure Model Based on Experimental Measurements and its Application to Calculate the Radiolysis Yields
Proc. of Int. Sympo. on Prospects for Application of Radiation Toward the 21st Century (Tokyo, Mar. 13-17 2000), p.5
C RCO 91040

9C21
M. Asano, H. Koshikawa, Y. Maekawa, R. Spohr and M. Yoshida,
Size-exclusion Separation of Poly(ethylene glycol)s through Thermo-responsive Ion-track filters
Proc. of Int. Sympo. on Prospects for application of Radiation towards the 21st century (Tokyo, March 13-17, 2000), p.125
C 91038 RCO

9C22
H. Koizumi,
Formation and Reactions of Free Radicals in the Radiolysis of Organic Materials by Ion Beams
Proc. of the 8th Japan-China Bilateral Sympo. on Radiation Chemistry (Kyoto, Oct. 1999), p.314
C 91041 RCO

9C23
S. Seki, K. Maeda, Y. Kunimi, S. Tagawa, Y. Yoshida, H. Kudoh, M. Sugimoto, Y. Morita, T. Seguchi, T. Iwai, H. Shibata, K. Asai and K. Ishigure,
Ion Track Structure in Poly(di-*n*-hexylsilane)
Proc. of the 8th Japan-China Bilateral Sympo. on Radiation chemistry (Kyoto, Oct. 1999), p.287
C RCO 91043

9C24
S. Seki, K. Nishida, Y. Kunimi, Y. Yoshida and S. Tagawa,
Electronic Structure of σ-conjugated System of Polysilanes Studied by Electron Beam Pulse Radiolysis
Proc. of IEEE the 13th ICDL, 646(1999)
C RCO 91043

9C25
T. Kojima, H. Sunaga, H. Takizawa and H. Tachibana,
Application of Thin Film Dosimeters to 3-45 MeV/amu Ion Beams
Proc. of the 8th Japan-China Bilateral Sympo. on Radiation Chemistry, (Kyoto, Oct. 25-29 1999), p. 310
C RCO 91046

9C26
M. Watanabe, N. Ishikawa and Y. Chimi,
Investigation of the Resonant Vibration Modes of Self Interstitial Atoms in Metals
Abs. of the 9th TIARA Research Review Meeting (Takasaki, June 2000), p.86
S IOM 92005

9C27
T. Tobita, M. Suzuki, A. Iwase, K. Aizawa and Y. Idei ,
Basic Study of Irradiation Embrittlement Caused by γ -rays on Light Water Reactor Pressure Vessel
Proc. of the 36th Annual Meeting of the Atomic Energy Soc. of Japan, (Kinki Univ., Mar. 1998) p.454
S IOM 92006

9C28
T. Tobita, M. Suzuki, A. Iwase, K. Aizawa and Y. Idei
Study on γ -ray Induced Embrittlement of Light Water Reactor Pressure Vessel Steel
Proc. of the 15th Int. Conf. on Structural Mechanics in Reactor Technology (Seoul, Korea, August 15-20, 1999), vol. X –205
S IOM 92006

9C29
I. Ioka, M.Futakawa and T.Wakui,
Mechanical Characterization on Ion Irradiated Thin Surface Layer by Nanoindentation Technique with Inverse Analysis
Proc. of the 7th Int. Conf. on Nuclear Engineering (Tokyo, April 19-23 1999) ICONE-7095
T, I, S IOM 92014

9C30
S. Yamamoto, A. Miyashita, H. Naramoto and I. Nashiyama,
Growth and Characterization of Epitaxial Ti Films on α -Al_2O_3 Substrate

Proc. of the Japan Institute of Metals Fall Meeting 1999
S IOM 92018

9C31
K. Yasuda, T. Inoue, S. Sakamoto, C. Kinoshita and S. Matsumura, H. Abe and K.E. Sickafus,
Radiation Damage Effects in Cubic-stabilized Zirconia: Extended Defect Formation under Electron Irradiation
Annual Reports of the HVEME Laboratory, Kyushu University, **22**, 7(1999)
I IOM 92020

9C32
C. Kinoshita, S. Matsumura, K. Yasuda, T. Soeda, and M. Noujima,
Irradiated Microstructure of Magnesium Aluminate Spinel and their Controlling Factors
Mater. Res. Soc. Sympo. Proceedings, **540**, 287(1999)
I IOM 92020

9C33
K. Yasuda, T. Watanabe, S. Matsumura and C. Kinoshita,
Disordering kinetics in Ni_4Mo under irradiation with electrons and ions
Proc. of Solid-Solid Phase Transformations, Edited by Koiwa, et al., Japan Institute of Metals, p. 405 (1999)
I IOM 92020

9C34
M. Takeda, S. Ohnuki, S. Watanabe, H. Abe,
H. Naramoto, P.R. Okamoto and N.Q. Lam,
Effect of Stress and Impurities on Preferential Amorphization on Grain Boundaries in Polycrystalline

Proc. of Silicon Mater. Res. Soc. Sympo., **540**, 37 (1999)
I IOM 92022

9C35
K. Narumi, S. Yamamoto and H. Naramoto,
SPM Characterization of Substrate Surfaces Prepared for Carbon-Related-Film Deposition
The Mater. Res. Soc. Sympo. Proceedings Series, **587**
O IOM, MAN 92026

9C36
A. Arai, K. Hirata, T. Sekiguchi, A. Kawasuso,
B. Y. Kobayashi and S. Okada,
Effect of Radiation Damage on Luminescence of Erbium-implanted SiO_2/Si Studied by Slow Positron Beam
Proc. of the 6th Int. Workshop on Positron and Positronium Chemistry (Tsukuba, June 1999), p.54
I IOM 92031

9C37
T. Sumita, T. Yamaki, S. Yamamoto, H. Abe,
A. Miyashita and I. Nashiyama,
Electrical and Optical Properties of Ion Implanted TiO_2
Extended Abs. of the 47th Spring Meeting (Tokyo, Mar. 2000), the Japan Soc. of Applied Physics and Related Societies, No.2 p.583
I IOM 92050

9C38
T. Yamaki, T. Sumita, S. Yamamoto, A Miyashita and I. Nashiyama,
Preparation of Highly Oriented TiO_2 Thin Films by Pulsed Laser Deposition
Abs. of the 78th National Meeting of the Chemical Society of Japan (Funabashi Japan, March 2000), No 1, p.69
O IOM 92050

9C39
H. Abe,
Nucleation of Carbon Onions and Nanocapsules under Ion Implantation at High Temperature
Proc. of the 11th European Conference on Diamond-like Materials, Nanotubes, Nitrides and Silicon Carbides (Diamond 2000)
I MAN 92019

9C40
M. Kasahara, S. Tohno, S. Akashi and C.J. Ma,
Single Particle Analysis – Its Importance in Aerosol Research
Proc. of the First Asian Aerosol Conf. (Nagoya, July 1999), p.136
S MAN 92046

9C41
C.-J. Ma, M. Kasahara, S. Tohno, Y. Onishi and K.-C. Whoang,
Application of PIXE to the Analysis of Single

Raindrops Sampled as a Function of their Size
Proc. of the 3rd Int. Sympo. on Bio-PIXE (Kyoto, Nov. 1999), p.31
S MAN 92046

9C42
Sugimoto, K. Ishii, S. Matsuyama, T. Satoh,
T. Sakai, T. Kamiya, M. Oikawa, M. Saidoh and R. Tanaka,
Application of Micro-PIXE Camera to Elemental Analysis of a Single Cell
Proc. of the 3rd Int. Sympo. on Bio-PIXE (Uji, Japan, Nov. 16-19 1999)
(*Int. J. of PIEX*, **8**, 151(1999))
S ACT 92048

9C43
T. Kamiya, T. Sakai, M. Oikawa, T. Satoh, K. Ishii, A. Sugimoto and S. Matsuyama,
STIM Imaging for Mammalian Cell Samples before Micro-PIXE Analysis in Air Environment at JAERI Takasaki Light Ion Microbeam System
Proc. of the 3rd Int. Sympo. on Bio-PIXE (Uji, Japan, Nov. 16-19 1999)
(*Int. J. of PIEX*, **8**, 217(1999))
S ACT 92048

9C44
T. Ohnuki, N. Kozai, M. Samadfam, T. Kamiya,
T. Sakai and T. Murakami,
Speciation of Uranium in Materials by SEM, TEM, μ-PIXE, XPS and XAFS
Proc. of OECD/NEA workshop on Evaluation of Speciation Technology (Oct. 26-28, 1999 at JAERI Japan), OECD/NEA, Paris (in press)
T, C MAN 82049

9C45
Y. Nakane and Y. Sakamoto,
Dose Distributions in a Plastic Phantom Irradiated by 40- and 65-MeV Quasi-Monoenergetic Neutrons
Proc. of 10th International Congress of the Int. Radiation Protection Association (Hiroshima, May 2000), IRPA-109, p-3b-155
C RSH 91051

9C46
M. Ibaraki, M. Baba, T. Miura, Y. Nauchi,
Y. Hirasawa, N. Hirakawa, H. Nakashima,
S. Meigo, O. Iwamoto and S. Tanaka,
Measurement of Elastic Scattering Cross Sections for Carbon, Silicon, Iron, Zirconium and Lead for 75 MeV Neutrons
Proc. of the 9th Int. Conf. on Radiation Shielding (Tsukuba, Oct. 1999)
(*J. Nucl. Sci. Technol.*, supl.1, p.683(2000))
C RSH 91052

9C47
M. Baba, T. Sanami, Y. Nauchi, Y. Hirasawa,
H. Nakashima, S. Meigo, S. Tanaka and
N. Hirakawa,
Measurement of Differential Neutron-Induced Charged-Particle Emission Cross Sections for 5-75 MeV Neutrons
Proc. of the 10th Int. Conf. on Reactor Dosimetry (Osaka, Sept. 1999),
C RSH 91052

9C48
M. Baba,
Nuclear Data Measurement for 40-90 MeV Neutrons at TIARA
Proc. of 1999 Nuclear Data Sympo., JAERI
(JAERI-Conf 2000-005, p.32)
C RSH 91052

9C49
Y. Hirasawa, M. Baba, Y. Nauchi, M. Ibaraki,
T. Miura, T. Hiroishi, T. Aoki, H. Nakashima,
S. Meigo and S. Tanaka,
Measurements of Double-differential Charged-particle Production Cross Sections for 55, 65, 75 MeV Neutrons
Proc. of 1999 Nuclear Data Sympo., JAERI
(JAERI-Conf 2000-005 p.232)
C RSH 91052

9C50
M. Ibaraki, H. Nakashima, S. Meigo, M. Baba,
T. Miura, Y. Nauchi, Y. Hirasawa, T. Hiroishi,
T. Aoki and S. Tanaka,
Measurement of Elastic Scattering and Total Non-Elastic Cross Sections for 40-80 MeV Neutrons at TIARA
Proc. of 1999 Nuclear Data Sympo., JAERI
(JAERI-Conf 2000-005 p.243)
C RSH 91052

9C51
K. Ohkoshi, Y. Saitoh and S. Tajima,
Prolongation of a Filament Lifetime using SF_6

Plasma method
Proc. of the 8th Int. Conf. on Ion SOURCES (Sep. 1999)
(Rev. of Scientific Instruments, **71**(2), 1174)
I ACT 92042

9C52
S. Okumura, K. Arakawa, M. Fukuda, I. Ishiboi, H. Tamura, T. Agematsu, T. Nara and W. Yokota,
Beam Energy Measurement by the Time-of-flight Technique
Proc. of the 12th Sympo. on Accel. Sci. and tech. (Wako Japan, Oct. 1999), p.471
C ACT 91044

9C53
W. Yokota, M. Fukuda, S. Okumura, K. Arakawa, H. Tamura, I. Ishibori, T. Agematsu, T. Nara, and Y. Nakamura,
Cocktail Beam Acceleration Technique at JAERI AVF Cyclotron (I)
Proc. of the 12th Sympo. on Accel. Sci. and Tech. (Wako Japan, Oct. 1999), p.127
C ACT 91045

9C54
I. Ishibori, M. Fukuda, S. Okumura, K. Arakawa, H. Tamura, W. Yokota, T. Agematsu, T. Nara and Y. Nakamura,
Cocktail Beam Acceleration Technique at JAERI AVF Cyclotron (II)
Proc. of the 12th Sympo. on Accel. Sci. and Tech. (Wako Japan, Oct. 1999), p453,
C ACT 91045

9C55
W. Yokota, Y. Saitoh, T. Nara, Y. Ishii, K. Arakawa and K. Ohkoshi,
Status of ECR Ion Sources at JAERI
Proc. of the 14th Int. Workshop on ECR Ion Sources (Geneva, May 1999), p.172
O ACT 91045

9C56
T. Nara, W. Yokota, Y. Saitoh, Y. Ishii, and K. Arakawa,
Beam Generation Test for HYPERNANOGAN and Modification of 18GHz ECR Ion Source
Proc. of the 12th Sympo. on Accel. Sci. and Tech. (Wako Japan, Oct. 1999), p.209
O ACT 91045

9C57
H. Tamura, K. Arakawa, Y. Nakamura, W. Yokota, M. Fukuda, T. Nara, T. Agematsu, S. Okumura and I. Ishibori,
Status Report on the JAERI AVF Cyclotron
Proc. of the 12th Sympo. on Accel. Sci. and Tech. (Wako Japan, Oct. 1999), p.171
C STA off line

9C58
T. Agematsu, K. Arakawa, S. Ishiro and M. Tachibana,
Construction of Personal Computer Control System for JAERI AVF Cyclotron
Proc. of the 12th Sympo. on Accel. Sci. and Tech., (Wako Japan, Oct. 1999), p450
C STA off line

9C59
S. Tajima, I. Takada, K. Mizuhashi, S. Uno, K. Ohkoshi, Y. Nakajima, Y. Saitoh, Y.Ishii, T. Sakai and T. Kamiya,
Status of TIARA Accelerators at JAERI Takasaki
Proc. of 12th Workshop on Tanadem Accel. and Tech., (Kyoto, July 1999)
T, S, I ACT 92042

9C60
K. Mizuhashi, T. Kitano, S. Kanai, M. Ishii, and S. Tajima,
Transmission of the Takasaki Tandem Accelerator
Proc. of 12th Workshop on Tanadem Accel. and Tech., (Kyoto, July 1999)
T ACT 92042

9C61
Y. Nakajima, Y. Saitoh and S. Tajima,
Beam Curent Monitor with Secondary Electron from the Moving Wire Probe
Proc. of 12th Workshop on Tanadem Accel. and Tech., (Kyoto, July 1999)
T, I ACT 92042

Appendix 2. Type of Research Collaboration

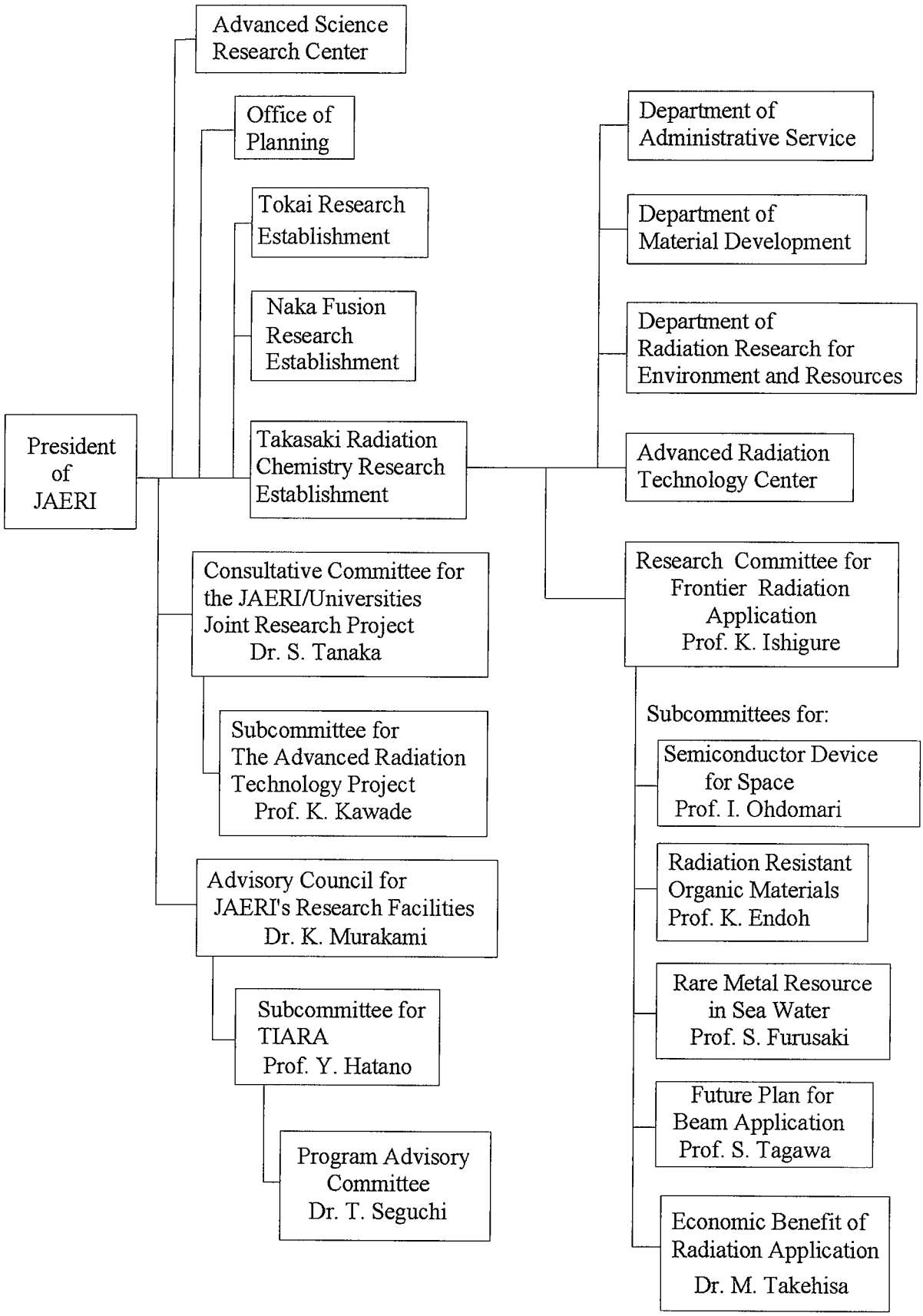
Section of this Report	Research Program Number	Type of Research Collaborations*	Section of this Report	Research Program Number	Type of Research Collaborations*
1.1	91001	JAERI	4.12	92015	Joint Res.
1.2	91002	Joint Res.	4.13	92005	JAERI
1.3	91003/92002	Joint Res.	4.14	92027	Coop.Res.Univ.
1.4	92001	JAERI	4.15	92028	JAERI
1.5	92003	JAERI	4.16	92029	JAERI
1.6	92004	Coop.Res.Univ.	4.17	92020	Coop.Res.Univ.
1.7	91030/92030	Coop.Res.Univ.	4.18	92021	Coop.Res.Univ.
			4.19	92022	Coop.Res.Univ.
2.1	91007	JAERI	4.20	92025	JAERI
2.2	91008	Coop.Res.Univ.	4.21	92025	JAERI
2.3	91009	Joint Res.	4.22	92025	JAERI
2.4	91010	Joint Res.	4.23	92026	JAERI
2.5	91011	Joint Res.	4.24	92033	Coop.Res.Univ.
2.6	91012	JAERI	4.25	92050	JAERI
2.7	92013	Joint Res.	4.26	92051	JAERI
2.8	91014	Joint Res.			
2.9	91015	JAERI	5.1	92018	JAERI
2.10	91016	JAERI	5.2	92023	Coop.Res.Univ.
2.11	91017	Coop.Res.Univ	5.3	92024	Coop.Res.Univ.
2.12	91018	Coop.Res.Univ	5.4	92043	Joint Res.
2.13	91019	Joint Res.	5.5	92019	JAERI
2.14	91020	Coop.Res.Univ	5.6	92034	Coop.Res.Univ.
2.15	91021	JAERI	5.7	92032	Joint Res.
2.16	91022	Proj.Res.Univ.	5.8	92031	JAERI
2.17	91023	Proj.Res.Univ.	5.9	91031	Coop.Res.Univ.
2.18	91024	Proj.Res.Univ.			
2.19	91025	Proj.Res.Univ.	6.1	91032	JAERI
2.20	91026	Proj.Res.Univ.	6.2	91032	JAERI
2.21	91027	Joint Res.	6.3	off line	Coop.Res.Univ.
2.23	92017	JAERI	6.4	91035	Proj.Res.Univ.
			6.5	91036	Proj.Res.Univ.
3.1	91037/92037	Joint Res.	6.6	91033/91034	JAERI & Proj.Res.Univ.
3.2	91038	JAERI	6.7	off line	Coop.Res.Univ.
3.3	91041	Coop.Res.Univ.			
3.4	91042	Coop.Res.Univ.	7.1	92036	JAERI
3.5	91043	Coop.Res.Univ.	7.2	92045	Proj.Res.Univ.
3.6	91040	JAERI	73	92046	Proj.Res.Univ.
3.7	91046	JAERI	7.4	92047	Proj.Res.Univ.
			7.5	92048	Proj.Res.Univ.
4.1	91005	JAERI	7.6	92049	JAERI
4.2	92010	Proj.Res.Univ.	7.7	92040	JAERI
4.3	92007	Proj.Res.Univ.	7.8	92041	Coop.Res.Univ.
4.4	92008	Proj.Res.Univ.	7.9	91047	JAERI
4.5	92009	Proj.Res.Univ.	7.10	92039	JAERI
4.6	92011	JAERI			
4.7	91006	JAERI	8.1	91048/82044	JAERI
4.8	92012	JAERI	8.2	91049	Proj.Res.Univ.
4.9	82013	JAERI	8.3	91050	Proj.Res.Univ.
4.10	92006	JAERI	8.4	91051	Proj.Res.Univ.
4.11	92014	JAERI	8.5	91052	Proj.Res.Univ.

Section of this Report	Research Program Number	Type of Research Collaborations*
9.1	91044	JAERI
9.2	91045	JAERI
9.3	92042	JAERI
9.4	92042	JAERI
9.5	92042	JAERI
9.6	off line	JAERI
9.7	off line	JAERI
9.8	off line	JAERI
9.9	off line	JAERI
9.10	off line	JAERI
9.11	off line	JAERI
9.12	off line	JAERI

*Joint Res.: Joint research with private company or governmental institution
Coop. Res. Univ.: Cooperative research with a university or universities #
Proj. Res.Univ.: The JAERI-Universities Joint Research Project #
#For administration of these programs, we appreciate the cooperation of:
Research Center for Nuclear Science and Technology, The University of Tokyo.

Appendix 3. Organization and Personnel of TIARA (FY 1999)

1) Organization for the Research and Development of Advanced Radiation Technology



2) Personnel for the Administration, Operation and Control of TIARA

Advanced Radiation Technology Center

Director	M. Saidoh

Administration Division

General Manager	T. Sekino
Staff Member	K. Morishita, M. Nakata

Utilization and Coordination Division

General Manager	Su. Tanaka
Staff Member	K. Nishimura, M. Hosono

Ion Accelerator Operation Division

General Manager	S. Tajima

Group of Cyclotron Operation

Staff Member	Y. Nakamura, T. Nara, T. Agematsu, I. Ishibori, H. Tamura, S. Kurashima

Group of Electrostatic Accelerators Operation

Staff Member	I. Takada, K. Mizuhashi, S. Uno, K. Ohkoshi, Y. Nakajima, A. Chiba

Ion Beam Engineering Division

Head	K. Arakawa
Staff Member	T. Kojima, W. Yokota, H. Tachibana, M. Fukuda, T. Kamiya, S. Okumura, Y. Saito, Y. Ishii, T. Sakai, S.Oikawa

Irradiation Service Division

General Manager	K. Yotsumoto
Staff Member	H. Sunaga , T. Kanazawa, H. Kaneko, T. Haneda, Y. Haruyama, H. Takizawa

Department of Administrative Services

Safety Division

Staff Member	T. Niino, H. Miyauchi

(Radiation Monitoring and Control in TIARA)

Utilities and Maintenance Division

Staff Member	J. Yoshii, S. Kaneko, Y. Takayama

(Radioactive Waste Management and Utility Control in TIARA)

国際単位系（SI）と換算表

表1　SI基本単位および補助単位

量	名称	記号
長さ	メートル	m
質量	キログラム	kg
時間	秒	s
電流	アンペア	A
熱力学温度	ケルビン	K
物質量	モル	mol
光度	カンデラ	cd
平面角	ラジアン	rad
立体角	ステラジアン	sr

表2　SIと併用される単位

名称	記号
分，時，日	min，h，d
度，分，秒	°，′，″
リットル	l，L
トン	t
電子ボルト	eV
原子質量単位	u

1 eV=1.60218×10^{-19}J

1 u=1.66054×10^{-27}kg

表3　固有の名称をもつSI組立単位

量	名称	記号	他のSI単位による表現
周波数	ヘルツ	Hz	s^{-1}
力	ニュートン	N	$m\cdot kg/s^2$
圧力，応力	パスカル	Pa	N/m^2
エネルギー，仕事，熱量	ジュール	J	N·m
工率，放射束	ワット	W	J/s
電気量，電荷	クーロン	C	A·s
電位，電圧，起電力	ボルト	V	W/A
静電容量	ファラド	F	C/V
電気抵抗	オーム	Ω	V/A
コンダクタンス	ジーメンス	S	A/V
磁束	ウェーバ	Wb	V·s
磁束密度	テスラ	T	Wb/m^2
インダクタンス	ヘンリー	H	Wb/A
セルシウス温度	セルシウス度	℃	
光束	ルーメン	lm	cd·sr
照度	ルクス	lx	lm/m^2
放射能	ベクレル	Bq	s^{-1}
吸収線量	グレイ	Gy	J/kg
線量等量	シーベルト	Sv	J/kg

表4　SIと共に暫定的に維持される単位

名称	記号
オングストローム	Å
バーン	b
バール	bar
ガル	Gal
キュリー	Ci
レントゲン	R
ラド	rad
レム	rem

1 Å=0.1nm=10^{-10}m

1 b=100fm^2=10^{-28}m^2

1 bar=0.1MPa=10^{5}Pa

1 Gal=1cm/s^2=10^{-2}m/s^2

1 Ci=3.7×10^{10}Bq

1 R=2.58×10^{-4}C/kg

1 rad=1cGy=10^{-2}Gy

1 rem=1cSv=10^{-2}Sv

表5　SI接頭語

倍数	接頭語	記号
10^{18}	エクサ	E
10^{15}	ペタ	P
10^{12}	テラ	T
10^{9}	ギガ	G
10^{6}	メガ	M
10^{3}	キロ	k
10^{2}	ヘクト	h
10^{1}	デカ	da
10^{-1}	デシ	d
10^{-2}	センチ	c
10^{-3}	ミリ	m
10^{-6}	マイクロ	μ
10^{-9}	ナノ	n
10^{-12}	ピコ	p
10^{-15}	フェムト	f
10^{-18}	アト	a

(注)

1．表1－5は「国際単位系」第5版，国際度量衡局1985年刊行による。ただし，1 eVおよび1 uの値はCODATAの1986年推奨値によった。

2．表4には海里，ノット，アール，ヘクタールも含まれているが日常の単位なのでここでは省略した。

3．barは，JISでは流体の圧力を表わす場合に限り表2のカテゴリーに分類されている。

4．EC閣僚理事会指令ではbar，barnおよび「血圧の単位」mmHgを表2のカテゴリーに入れている。

換算表

力	N(=10^{5}dyn)	kgf	lbf
	1	0.101972	0.224809
	9.80665	1	2.20462
	4.44822	0.453592	1

粘度　1 Pa·s(N·s/m^2)=10 P(ポアズ)(g/(cm·s))

動粘度　1m^2/s=10^{4}St(ストークス)(cm^2/s)

圧力	MPa(=10bar)	kgf/cm^2	atm	mmHg(Torr)	lbf/in^2(psi)
	1	10.1972	9.86923	7.50062×10^3	145.038
	0.0980665	1	0.967841	735.559	14.2233
	0.101325	1.03323	1	760	14.6959
	1.33322×10^{-4}	1.35951×10^{-3}	1.31579×10^{-3}	1	1.93368×10^{-2}
	6.89476×10^{-3}	7.03070×10^{-2}	6.80460×10^{-2}	51.7149	1

エネルギー・仕事・熱量	J(=10^7 erg)	kgf·m	kW·h	cal(計量法)	Btu	ft·lbf	eV
	1	0.101972	2.77778×10^{-7}	0.238889	9.47813×10^{-4}	0.737562	6.24150×10^{18}
	9.80665	1	2.72407×10^{-6}	2.34270	9.29487×10^{-3}	7.23301	6.12082×10^{19}
	3.6×10^6	3.67098×10^5	1	8.59999×10^5	3412.13	2.65522×10^6	2.24694×10^{25}
	4.18605	0.426858	1.16279×10^{-6}	1	3.96759×10^{-3}	3.08747	2.61272×10^{19}
	1055.06	107.586	2.93072×10^{-4}	252.042	1	778.172	6.58515×10^{21}
	1.35582	0.138255	3.76616×10^{-7}	0.323890	1.28506×10^{-3}	1	8.46233×10^{18}
	1.60218×10^{-19}	1.63377×10^{-20}	4.45050×10^{-26}	3.82743×10^{-20}	1.51857×10^{-22}	1.18171×10^{-19}	1

1 cal= 4.18605J（計量法）

= 4.184J（熱化学）

= 4.1855J（15℃）

= 4.1868J（国際蒸気表

仕事率　1 PS(仏馬力)

= 75 kgf·m/s

= 735.499W

放射能	Bq	Ci
	1	2.70270×10^{-11}
	3.7×10^{10}	1

吸収線量	Gy	rad
	1	100
	0.01	1

照射線量	C/kg	R
	1	3876
	2.58×10^{-4}	1

線量当量	Sv	rem
	1	100
	0.01	1

(86年12月26日現在)

